

MATER. TEHNOL.	LETNIK VOLUME	49	ŠTEV. NO.	6	STR. P.	845–1018	LJUBLJANA SLOVENIJA	NOV.–DEC. 2015
-------------------	------------------	----	--------------	---	------------	----------	------------------------	-------------------

VSEBINA – CONTENTS

PREGLEDNI ČLANEK – REVIEW ARTICLE

Problems and normative evaluation of bond-strength tests for coated reinforcement and concrete

Problemi in normativna ocena preizkusov trdnosti vezi med armaturo s prekritjem in betonom

P. Pokorný, M. Kouřil, J. Stouřil, P. Bouška, P. Simon, P. Juránek 847

IZVIRNI ZNANSTVENI ČLANKI – ORIGINAL SCIENTIFIC ARTICLES

Modeling of occurrence of surface defects of C45 steel with genetic programming

Modeliranje pojava površinskih napak pri jeklu C45 z genetskim programiranjem

M. Kovačič, R. Jager 857

Effects of various helically angled grinding wheels on the surface roughness and roundness in grinding cylindrical surfaces

Vpliv različnih kotov vijačnice pri brusilnih kolutih na hrapavost površine in okroglost pri brušenju valjastih površin

M. Gavas, M. Kina, U. Köklü 865

Characterization of cast-iron gradient castings

Karakterizacija litoželeznega gradientnega ulitka

D. Mitrović, P. Mrvar, M. Petrič 871

Comparative mechanical and corrosion studies on magnesium, zinc and iron alloys as biodegradable metals

Primerjalna študija mehanskih in korozijskih lastnosti biorazgradljivih zlitin magnezija, cinka in železa

D. Vojtěch, J. Kubásek, J. Čapek, I. Pospíšilová 877

Microstructural changes of fine-grained concrete exposed to a sulfate attack

Mikrostrukturne spremembe drobnozrnatega betona, izpostavljenega sulfatu

M. Vyšvařil, P. Bayer, M. Rovnaníková 883

Effect of thermomechanical treatment on the corrosion behaviour of Si- and Al-containing high-Mn austenitic steel with Nb and Ti micro-additions

Vpliv termomehanske obdelave na korozijsko vedenje manganskega avstenitnega jekla z vsebnostjo Si in Al, mikrolegiranega z Nb in Ti

A. Grajcar, A. Plachcińska, S. Topolska, M. Kciuk 889

Surface free energy of hydrophobic coatings of hybrid-fiber-reinforced high-performance concrete

Prosta energija površine hidrofobnih premazov na visokozmogljivem betonu, ojačanem s hibridnimi vlakni

D. Barnat-Hunek, P. Smarzewski 895

Developing continuous-casting-process control based on advanced mathematical modelling

Uporaba naprednega matematičnega modeliranja za razvoj kontrole postopka kontinuirnega ulivanja

J. Falkus, K. Miłkowska-Piszczek 903

Elastic behaviour of magnesia-chrome refractories at elevated temperatures

Elastično vedenje ognjevzdržnih gradiv magnezija-krom pri povišanih temperaturah

I. Jastrzębska, J. Szczerba, J. Szlęzak, E. Śniezek, Z. Pędzich 913

Study on the magnetization-reversal behavior of annealed Sm-Fe-Co-Si-Cu ribbons

Študij vedenja pri obratu magnetizacije žarjenih trakov Sm-Fe-Co-Si-Cu

M. Dośpiał, S. Garus, M. Nabialek 919

Evaluation of the chitosan-coating effectiveness on a dental titanium alloy in terms of microbial and fibroblastic attachment and the effect of aging

Ocena učinkovitosti nanosa hitozana na oprijemanje mikrobov in fibroblastov na dentalni titanovi zlitini ter na pojav staranja

U. T. Kalyoncuoglu, B. Yilmaz, S. Gungor, Z. Evis, P. Uyar, G. Akca, G. Kansu 925

Structure and properties of the carburised surface layer on 35CrSiMn5-5-4 steel after nanostructurization treatment

Struktura in lastnosti naogljčene površine jekla 35CrSiMn5-5-4 po nanostrukturni obdelavi

E. Skolek, K. Wasiak, W. A. Świątnicki 933

Optimization of the surface roughness by applying the Taguchi technique for the turning of stainless steel under cooling conditions

Uporaba Taguchi-jeve metode za optimiranje hrapavosti površine pri struženju nerjavnega jekla z ohlajanjem

M. Sarıkaya 941

Effect of cryogenic treatment applied to M42 HSS drills on the machinability of Ti-6Al-4V alloy Vpliv podhlajevanja svedrov M42 HSS na obdelovalnost zlitine Ti-6Al-4V T. Krivak, U. Šeker	949
Load-capacity prediction for the carbon- or glass-fibre-reinforced plastic part of a wrapped pin joint Napoved nosilnosti plastičnih delov zatičnega spoja, ojačanega z ogljikovimi ali steklastimi vlakni J. Krystek, R. Kottner	957
A meshless model of electromagnetic braking for the continuous casting of steel Brezmrežni model elektromagnetnega zaviranja pri kontinuiranem ulivanju jekla K. Mramor, R. Vertnik, B. Šarler	961
Non-singular method of fundamental solutions for three-dimensional isotropic elasticity problems with displacement boundary conditions Nesingularna metoda fundamentalnih rešitev za deformacijo tridimenzijskih elastičnih problemov z deformacijskimi robnimi pogoji Q. Liu, B. Šarler	969
Solid-state sintering of $(K_{0,5}Na_{0,5})NbO_3$ synthesized from an alkali-carbonate-based low-temperature calcined powder Sintranje v trdnem keramike $(K_{0,5}Na_{0,5})NbO_3$, sintetizirane iz nizkotemperaturno kalciniranega prahu, pripravljenega na osnovi alkalijskih karbonatov M. Feizpour, T. Ebadzadeh, D. Jenko	975
Stability of close-cell Al foams depending on the usage of different foaming agents Stabilnost aluminijevih pen z zaprto poroznostjo glede na uporabo različnih penilnih sredstev I. Paulin	983
STROKOVNI ČLANEK – PROFESSIONAL ARTICLE	
Evolution of the microstructure and magnetic properties of a cobalt-silicon-based alloy in the early stages of mechanical milling Razvoj mikrostrukture in magnetnih lastnosti zlitine Co-Si v začetnem stadiju mehanskega legiranja W. Rattanasakulthong, C. Sirisathitkul, P. F. Rogl	989
IN MEMORIAM	
Prof. dr. Milan Trbižan	993
LETNO KAZALO – INDEX	
Letnik 49 (2015), 1–6 – Volume 49 (2015), 1–6	995

PROBLEMS AND NORMATIVE EVALUATION OF BOND-STRENGTH TESTS FOR COATED REINFORCEMENT AND CONCRETE

PROBLEMI IN NORMATIVNA OCENA PREIZKUSOV TRDNOSTI VEZI MED ARMATURO S PREKRITJEM IN BETONOM

**Petr Pokorný¹, Milan Kouřil¹, Jan Stoužil¹, Petr Bouška², Pavel Simon³,
Pavel Juránek⁴**

¹Institute of Chemical Technology in Prague, Department of Metals and Corrosion Engineering, Technická 5, 166 28 Prague 6, Czech Republic

²Czech Technical University in Prague, Klokner Institute, Šolínova 7, 166 08 Prague 6, Czech Republic

³Ing. Vladimír Fišer, Mlýnská 68, 602 00 Brno, Czech Republic

⁴Technical and Test Institute for Constructions Prague – Brno Branch, Hněvkovského 77, 617 00 Brno, Czech Republic
Pokornyt@vscht.cz

Prejem rokopisa – received: 2014-09-13; sprejem za objavo – accepted for publication: 2015-01-05

doi:10.17222/mit.2014.227

This paper focuses on the problems of the bond-strength between concrete and reinforcement and defines the basic factors affecting the quality of the bond. Two types of coated concrete reinforcement (the zinc- and epoxy-coated) and methods of testing their bond-strength with concrete are described. The goal of this work is to generalize the results of the bond-strength tests so that they would consider only the influence of the corrosion of the zinc-coated reinforcement in fresh concrete or, in the case of the epoxy-coated reinforcement, its probable constriction during the testing. Based on described standards, it is recommended to use the pull-out test to obtain these generalized results: two Czech standards (Bond-strength test of the reinforcement cast in prisms, Beam-strength test of the reinforcement in cubes) and a RILEM recommendation.

Keywords: concrete, corrosion of concrete reinforcement, bond-strength, bond-strength tests, hot-dip galvanized reinforcement, epoxy-coated reinforcement, standards

Članek obravnava probleme trdnosti vezi med betonom in armaturo ter določa osnovne faktorje, ki vplivajo na kvaliteto vezi. Opisani sta dve vrsti prekritja armature (prekritje s cinkom in prekritje z epoksi smolo) in kako se preizkusi njihova trdnost vezi z betonom. Cilj tega dela je bil dobiti rezultate preizkusov trdnosti vezi, ki bi upoštevali samo vpliv korozije pri armaturi, pokriti s cinkom v svežem betonu ali, v primeru armature, pokrite z epoksi smolo, na njeno zoženje med preizkusom. Na podlagi opisanih standardov se priporoča preizkus izpuljenja, da se dobi posplošene rezultate: dva češka standarda (Preizkus trdnosti vezi betona ulitega v prizme, Preizkus trdnosti betonske kocke) in RILEM-priporočilo.

Ključne besede: beton, korozija armature v betonu, trdnost vezi, preizkusi trdnosti vezi, vroče cinkana armatura, armatura z nanosom epoksi smole, standardi

1 INTRODUCTION

The durability of reinforced-concrete structures is always limited by the corrosion of carbon-steel reinforcement. The volume of corrosion products is significantly larger (2–6-times) than the volume of the original non-corroded reinforcements, thus creating a stress leading to the formation of cracks in the initial stages of concrete solidification, eventually resulting in a disintegration of the concrete cover. The initiation of reinforcement corrosion corresponds to the carbonation of the concrete cover by CO₂ (the carbon steel becomes active due to a pH reduction of the alkaline pore solution) and/or, more frequently, a local attack by penetrating chlorides (deicing salt, seawater). A disintegration of the concrete cover propagates the attack to the other parts of the reinforcement. A reduction of the reinforcement diameter by the corrosion poses a significant threat to the static function of the construction. The whole corroded reinforcement often needs to be replaced at great expenses to repair the construction.^{1–3}

The prolongation of the longevity of concrete reinforcement basically falls into two categories. The first one involves a change in the concrete properties to increase the compactness of the concrete cover (the concretes with a low water-cement ratio, a better concrete densification, final application of various concrete plasticizers or other changes to the concrete composition). Special cements with a suitable ash substituting the cement provide another way to increase the compactness – these concretes can have higher mechanical properties, a lower inherited porosity and, therefore, lower penetration of water, oxygen and corrosion stimulators.⁴ A surface modification with a barrier effect slowing down the penetration of carbon dioxide and chlorides such as paint or an organosilane surface modification (the surface becomes hydrophobic) are also not negligible.

The second category focuses on the reinforcement. Its examples are corrosion inhibitors, a cathodic protection, the coating of the reinforcement or application of a

reinforcement from another material (stainless steel, composite reinforcement).^{5,6}

A significant advantage of stainless steel, compared to carbon steel, is its high resistance to a low-pH pore solution. Its resistance to chloride-containing environment depends on the composition of the steel – certain types are prone to a localized corrosion attack. Nevertheless, the critical chloride concentration causing the activation of steel can be up to 15× higher than that for carbon steel.^{7,8} Similarly to carbon steel, the resistance of stainless steel is limited by the state of its surface. The scales formed during hot-working or welding have a strong detrimental effect on its corrosion resistance. It was discovered that even an increase in the pH from 12.5 to 13.5 improves the corrosion resistance less than the removal of the surface.⁹

The surface finish of a steel reinforcement can enhance the corrosion resistance of the reinforcement in a concrete environment while the core of the reinforcement maintains all of its necessary mechanical properties (weldability, tensile and compressive strengths, fatigue strength, etc.). Currently, the feasibility of hot-dip galvanized coating and powder-plastic coating is being discussed. However, these kinds of reinforcement protection cannot be employed until the bond between the concrete and these new surface-modified reinforcements has been thoroughly studied.¹⁰

2 CONCRETE-REINFORCEMENT BOND-STRENGTH

A perfect and permanent bond between all steel-reinforcement components and concrete is the basic requirement for the static cooperation of both materials. The quality of the bond depends on their reciprocal cohesion, the bond durability corresponds to the similarity of their thermal-expansion coefficients and the corrosion resistance of the reinforcement material. Different thermal-expansion coefficients cause both materials to behave differently during temperature changes, thus negatively affecting their bond.¹¹

The concrete-reinforcement bond is generally a combination of all the factors affecting the movement of reinforcement during a transformation of a concrete structures reinforced by steel. It is thus important for the reinforcement components to change similarly to the concrete during loading and prevent their movement.^{11,12}

The total bond-strength (B_s) between concrete and its reinforcement is a combination of three factors from the bond-strength formula: adhesion factor f_{ad} which includes the effect of the small surface defects of the reinforcement, friction factor f_f which takes into account small surface unevenness of the reinforcement causing friction and, finally, mechanical bonding factor f_{mech} which includes the effect of the surface geometry (ribs, imprints, warping, etc.). The bond-strength formula is written as Equation (1):¹³

$$B_s = f_{ad} + f_f + f_{mech} \quad (1)$$

The factors mentioned above do not have even effects on the bond-strength. The mechanical bonding factor has the greatest effect on the bond-strength. The reason for this is the fact the above factors also necessarily include the effects of the mechanical properties of concrete – its local hardness (included in the friction factor) and compressive strength (included in the mechanical bonding factor). The adhesion factor is strongly affected by the concrete porosity – a high porosity decreases the effect of the physicochemical interactions at the interface which are always short-range. The bond is formed by hydrating concrete penetrating the reinforcement-surface defects, creating a mechanical bond. The mechanical bond becomes strengthened, to some extent, during the concrete's aging due to its constriction around the reinforcement.^{12,13}

The tensile forces of the reinforcement must be transferred to the concrete in the less-stressed areas and the reinforcement must be well bound. Bond length l_b is defined as the length of the reinforcement inside the concrete necessary for the reinforcement to crack (during pulling) instead of being torn out of the concrete. Tangential stress (τ_b) occurs on the surface of the reinforcement – the force (F) is distributed unevenly along the reinforcement; for the sake of simplicity, the average value is typically used in structures design. This value is given by Equation (2) (u is the rod diameter, l_b is the length of the rod set in concrete):

$$\tau_b = \frac{F}{ul_b} \quad (2)$$

Considering the bond-strength, we can define the limit bond length according to Equation (3) (f_{yk} is the characteristic yield strength of the reinforcement rod, Φ is the nominal diameter of the reinforcement rod, f_{bd} is the design value of the ultimate bond stress):

$$l_b = \frac{\Phi}{4} \frac{f_{yk}}{f_{bd}} \quad (3)$$

The key to correctly calculate the sufficient bond length is the reinforcement-concrete bond-strength. In mathematical models, the bond-strength is represented by the design value of the ultimate bond stress f_{bd} which can be calculated, for ribbed reinforcements, from Equation (4) (η_1 is the factor including the aging conditions and the position of the reinforcement rod during the casting of concrete, η_2 is the factor including the normative diameter of the reinforcement rod, f_{ctd} is the design tensile strength that should not exceed the value set for the C60/75 concrete strength class):¹²

$$f_{bd} = 2.25\eta_1\eta_2f_{ctd} \quad (4)$$

When assessing the effect of concrete on the strength of its bond with the reinforcement, it is generally important for the cement content in the concrete to be high, since the hydrating cement must adhere well to the rein-

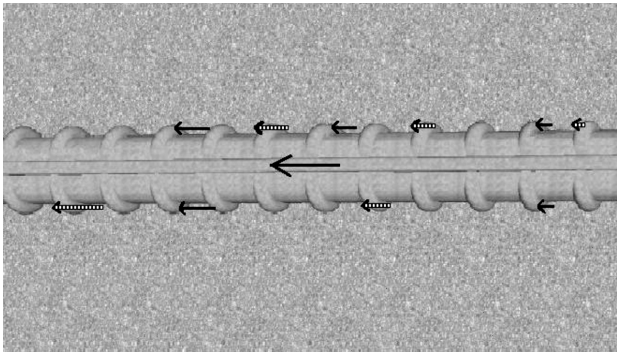


Figure 1: Idealized effect (compressive – dotted vectors and tensile – full length vectors) of ribbed rod reinforcement in the beginning stages of loading (black vector shows the strain direction)

Slika 1: Idealiziran vpliv (tlačni – črtkasti vektorji in natezni – polnočrtni vektorji) rebraste palice armature v začetnem stadiju obremenitve (črni vektor kaže smer deformacije)

forcement rods. Concrete must also be well compacted. Single rods must be covered by concrete on all sides and the minimum cover thickness must be maintained. As shown above in Equation (4), the position of the reinforcement in concrete also has an effect on its final strength. The horizontal rods closer to the bottom have a better bond-strength than those closer to the top surface. The reason for this is a gradual settlement of the concrete. This is more significant for the concretes with a higher mixing-water content.

The surface of a reinforcement plays a major role. It needs to be rough and clean, suitably degraded and rust-free. When a load is applied to the reinforcement, the ribbings stress the concrete in their vicinity, creating a transverse tensile stress, eventually causing the concrete to crack behind the ribbings, relative to the trajectory of the applied load (**Figures 1 and 2**). A higher loading causes the shear strength of concrete to be exceeded and the reinforcement rod to "cut out" of the concrete (**Figure 3**).^{12,14}

The bond-strength of concrete is mainly determined by the mechanical bonding factor; for the ribbed bar

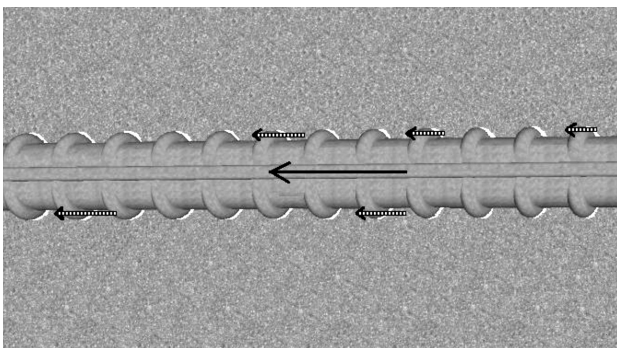


Figure 2: Idealized model of reinforcement movement (black vector), when the bond is broken (dotted vectors show the compressive forces on the concrete caused by the ribs)

Slika 2: Idealiziran model premikanja armature (črni vektor), ko se povezava prekine (črtkasti vektorji kažejo tlačne sile na beton, ki jih povzročijo rebra)

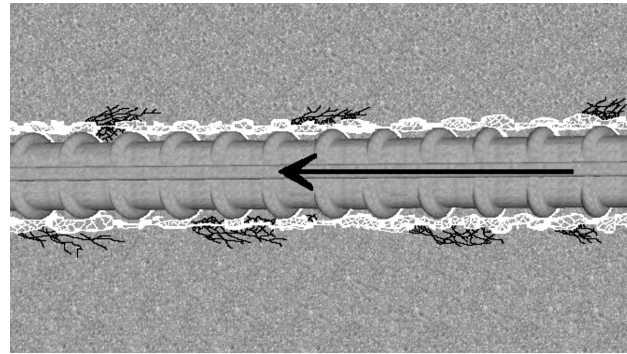


Figure 3: Idealized model depicting cutting-out of the ribbed reinforcement right before its pull-off of concrete. Longitudinal crack spreads through concrete closely above the ribs.

Slika 3: Idealiziran model prikazuje izpuljenje rebraste armature tik pred njenim izpuljenjem iz betona. Vzdolžne razpoke se širijo skozi beton, tik nad rebri.

reinforcement, the bond-strength depends on the relative rib area f_R that can be calculated from the rib geometry using Equation (5), while the area of a single rib F_R needs to be calculated using Equation (6) (d is the nominal reinforcement-bar diameter, c is the distance between the centers of two adjacent ribs, β is the angle of the rib inclination, n is the number of crosswise rows on the rod perimeter, m is the number of differently angled ribs in a column, q is the number of crosswise longitudinal ribs for cold-bent rods, P is the number of threads of the rib spiral, a_k' is the average height of longitudinal ribs, $a_{s,i}$ is the average height of the i parts of the ribs divided in p parts with a Δl length, **Figures 4 and 5**). The second addend applies only to cold-bent rods and is neglected if it exceeds 30 % of the total value of f_R .^{15,16}

$$f_R = \frac{1}{\pi d} \sum_{i=1}^n \frac{(1/m) \sum_{j=1}^m F_{R,i,j} \sin \beta_{i,j}}{c_i} + \frac{1}{P} \sum_{k=1}^q a'_k \quad (5)$$

$$F_R = \sum_{i=1}^p (a_{s,i} \Delta l) \quad (6)$$

The desired values of the relative rib surface and their shapes are given in the design standards. The minimum

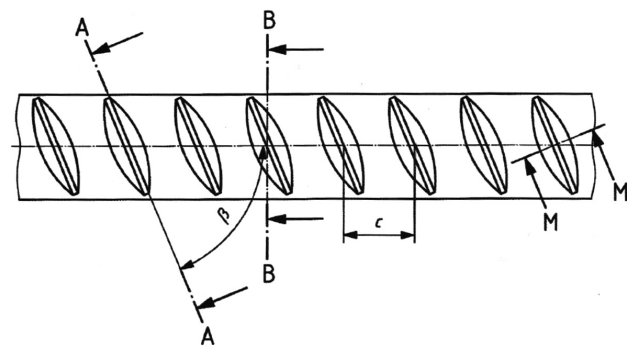


Figure 4: Detail of a rib configuration for a calculation of the relative rib surface f_R

Slika 4: Podrobnosti konfiguracije reber za izračun relativne površine reber f_R

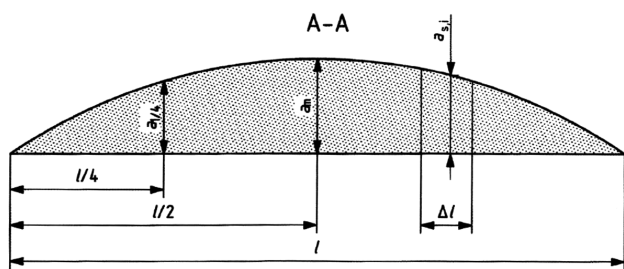


Figure 5: Cross-section of a rib for a calculation of the rib surface F_R
 Slika 5: Prerez rebra za izračun površine F_R rebra

relative surface $f_{R,min}$, related to the nominative bar diameter, is usually known. The nominal evaluation of the minimum relative rod surface is shown in Table 1.¹⁵

Table 1: Evaluation of minimum relative surface of ribs to ensure a good strength of the bond with bars, foils and also welded nets¹⁵

Tabela 1: Ocena minimalnih površin reber za zagotovitev dobre trdnosti vezave s palicami, folijami in tudi z varjenimi mrežami¹⁵

nominal diameter of reinforcement d_s/mm	minimum relative rib surface ($f_{R,min}$)
5–6	0.035
6.5–2	0.040
> 12	0.056

3 PROBLEMS OF CONCRETE-REINFORCEMENT BOND-STRENGTH TESTS

The available standards recommend two experimental set-ups to determine the reinforcement-concrete bond-strength. The first of them is based on pulling out a steel-bar reinforcement set from the concrete. The second set-up is basically a 4-point beaming test – a determination of the bond-strength for bent concrete girders, a girder test, a beam test, etc.

Both methods produce quite different results which make an objective assessment of the concrete-reinforcement bond-strength difficult. Nonetheless, comparing the data obtained with a repeated measurement using the same method is also somewhat complicated. For both methods, the non-objectivity of the measurements come from the standards themselves. In the case of the pull-out test of a reinforcement with a bonding component (indentation, rib, corrugation), the concrete is disintegrated during the test (Figure 3). The results are, therefore, strongly dependent on the strength of the concrete. Also, the results of "the beam test" cannot be used to make a general statement about the bond-strength – the forced bending momentum creates a compressive stress in the upper part of the beam and a tensile stress in the lower part. Any reasonably changed experimental set-up still cannot provide us with the data disregarding the mechanical properties of concrete.

These influences can be ignored using a modified pull-out test with a smooth-surface reinforcement. However, the reinforcement must be perfectly aligned with the central axis of the fixed concrete sample so that there

is no compressive stress. The data from these bond-strength tests for concrete and reinforcement cannot be used to make general assumptions about the real bond-strength since they are also influenced by many other factors. On the other hand, the results of a smooth reinforcement-concrete bond-strength test are of no practical use since the bond is primarily facilitated by the bonding components which are considered in the static calculations.^{15,17}

3.1 Bond-strength of a coated reinforcement

Coating provides the reinforcement with a surface barrier which increases the time until the surface activation of the steel. A supplementary reinforcement coating can thus be used to prolong the longevity of iron-concrete constructions. However, the strength of the bond between the coating and the concrete must be correctly evaluated. A reduced coated reinforcement-concrete bond-strength, even on a scale of percent units, can make its practical application much more difficult. The reason for this is the concern about the static reliability, especially in the applications with high requirements – constructions with very high load-bearing capacities, dynamically stressed constructions. A reduced bond-strength can be solved by increasing the bond length or adding bonding profiles. A less effective alternative to this is a surface modification of the reinforcement (increasing the surface area of the bonding elements, i.e., ribs, indentations, corrugations, etc.). Increasing the bond length increases the cost of the construction; the coating requires additional concrete-reinforcement bond-strength tests to be performed (using the reinforcement with a modified surface). Two surface modifications are discussed: the hot-dip galvanized coating and the epoxy coating.¹⁵

A comparison of the bond-strength results between the coated and non-coated reinforcements of the same surface geometry must be done according to the standardized tests. A correct interpretation of the data is also of great importance. The bond-strength must also be measured when the reinforcement surface geometry, the concrete's chemical composition and other factors altering the bonding interaction are changed.

3.1.1 Hot-dip galvanized reinforcement

The suitability of a hot-dip galvanized (zinc) coating for a concrete steel reinforcement is still arguable. This modification provably has a positive effect on the resistance to chlorides and also on the resistance to carbonated concrete.^{2,18} However, zinc actively corrodes in fresh concrete (alkaline, pH often exceeds 13.0) producing hydrogen. Hydrogen increases the porosity of the concrete and reduces the adhesion factor, thus also reducing the total bond-strength. After the zinc coating actively corrodes in fresh concrete, the remaining coating does not always exhibit sufficient quality.^{17,19} Other authors verified the initial reduction of the

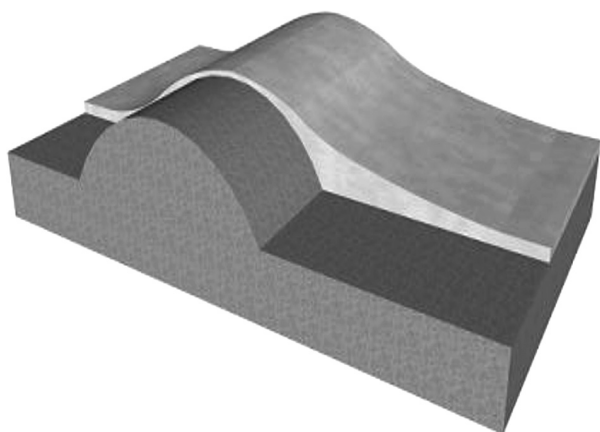


Figure 6: Model comparing the geometries of ribbed reinforcement with and without zinc coating

Slika 6: Model primerjave geometrije rebraste armature z nanosom cinka in brez njega

bond-strength; however, this is later compensated by zinc corrosion products ($\text{Zn}(\text{OH})_2$) resulting from the concrete carbonation and filling in the pores.^{20–22}

Another group of authors claim that a zinc-coated reinforcement easily becomes passivated in an environment with a pH value of 13.3 by forming non-soluble $\text{Ca}[\text{Zn}(\text{OH})_3]_2 \cdot 2\text{H}_2\text{O}$; sulphate anions also have a positive effect on passivation.^{23–29} Another phenomenon – apart from the negative effect of zinc on the corrosion resistance of a reinforcement – a detrimental effect of zinc during the concrete hardening also needs to be mentioned. It was proven that zincates slow down the hardening of concrete and, with regard to the water content in concrete, they can extremely deteriorate the mechanical properties of concrete.^{30–32} Poor results for a zinc-coated ribbed reinforcement are sometimes explained with the smoothening of the surface by the zinc coating itself. A lower bond-strength corresponds to a lower relative rib surface f_R , thus reducing the factor of mechanical bonding in the bond-strength equation B_s . According to these authors, hot-dip zinc coating can result in the formation of an uneven coating – thicker at one heel of a rib (depending on how the rod was removed from the zinc bath) and very thin at the top of the rib (**Figures 6 and 7**).¹³ Others observed a reduced bond-strength for the hot-dip galvanized reinforcement even after a 28-day curing of the concrete.^{33,34}

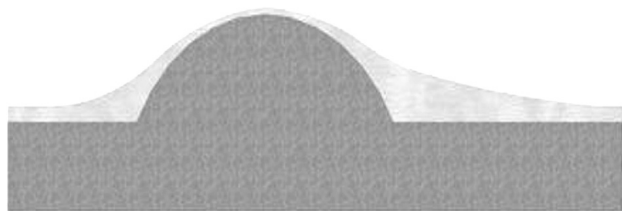


Figure 7: Cross-section model comparing the heights of the rib of non-coated and coated ribbed reinforcement from **Figure 6**

Slika 7: Model prereza, ki primerja višino rebra pri rebrasti armaturi z nanosom in brez njega s **slike 6**

3.1.2 Epoxy-coated reinforcement

The main problem of this type of coating is its mechanical resistance – it is very fragile and its manipulation is therefore problematic. Coating defects are formed during the bending, being set in the concrete, and often also during its fabrication. Another disadvantage is the necessity of welding prior to coating. A coated reinforcement can be linked only by sockets.⁸ The cracking of a coated reinforcement stored at a temperature below 10 °C was also observed.³⁵ Corrosion products of steel forming on the surface of a reinforcement can also damage the epoxy coating.³⁶ A perfect compact coating can prolong the longevity of concrete-steel constructions, but the problem lies in the strength of its bond with the concrete. Experts agree that an epoxy-coated reinforcement has a decreased strength of the bond with the concrete (sometimes even by 20–25 %). The recognized reasons for this include the concrete not adhering well to the reinforcement and creating only a small number of physico-chemical interactions, the smoothening of the ribs done in the way similar to the one used for the zinc-coated reinforcement, or an elastic deformation of the epoxy coating during the loading. Epoxy-coated reinforcements usually have higher bond lengths and other anchoring modifications.^{37–40}

4 DETAILED DESCRIPTION AND CHARACTERIZATION OF THE STANDARDS

The following text sums up the standards and recommendations for the arrangement, conditions and evaluation of bond-strength tests (ČSN standards, RILEM recommendations).

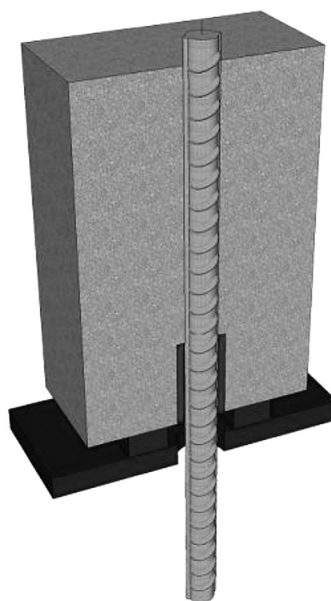


Figure 8: Schematics of the pull-out-test experimental set-up (concrete prism)

Slika 8: Shematski prikaz preizkusa izpuljenja (betonska prizma)

4.1 ČSN 73 1328 (determination of the concrete-reinforcement bond-strength)⁴¹

This standard is the basic regulation for evaluating the bond-strength of the concrete with the components described above. It deals with both dense and aggregate concrete – the aggregate can be both dense and porous. The standard does not evaluate the effect of the reinforcement surface on the bond-strength. In this standard, the bond-strength is defined as the shear strength of the concrete (in the shear strength τ_m [MPa], $\tau_m = P_m/(a \cdot o)$, a is the bond length, o is the diameter of the reinforcement) when the pull-out of the reinforcement from the concrete is 0.001 mm to 0.002 mm. The bond-strength is thus defined as the shear strength on the tensile-stressed bar perimeter – this value is defined during the projecting of iron-concrete constructions.

4.1.1 Determination of the steel-concrete bond-strength for a bar-shaped reinforcement

Prior to the test, three cubic samples with 20 cm or 15 cm edge diameters, from the same concrete (i.e., an identical production and treatment procedure), are manufactured for the concrete-cube strength test. For the bond-strength test, bars of precise dimensions are manufactured using a reinforcement bar. To ensure that this bar is right in the axis of the concrete sample, it is inserted in a tube placed in the bottom part. The fresh concrete must be prevented from entering the tube. The bond length is the length of the concrete sample reduced by the length of the anchoring tube. The result is the arithmetic average value from three measurements (three parallel samples of one reinforcement type) of the bond-strength measured after 28 days of curing. The results that differ by more than 20 % from the average are discarded (Figure 8).

4.1.2 Strength of the bond between the steel and concrete in beam-stressed girders

Similarly to the previous case, it is recommended to verify the concrete-cube strength prior to the test. Rectangular cross-section girders are used for this sample. Their dimensions are chosen to correspond to the bond lengths of the reinforcements (Figure 9). The test rein-

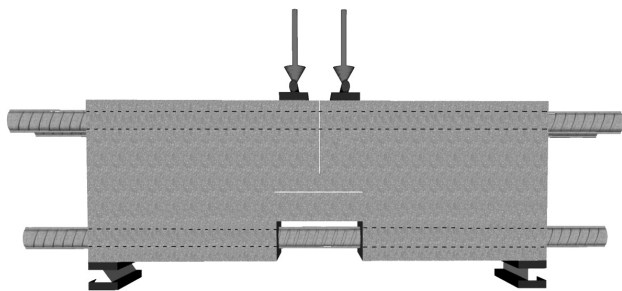


Figure 9: Schematics of reinforced girder prepared for a beam test with arrows showing the applied force

Slika 9: Shematski prikaz ojačanega nosilca, pripravljenega za upogibni preizkus, puščici kažeta uporabljeno silo

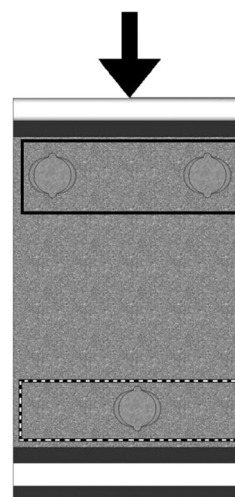


Figure 10: Cross-section of the beam-test girder sample: compressed part (full line) and tensile-stressed part (dotted line)

Slika 10: Prerez nosilca za upogibni preizkus: tlačni del (polna črta) in natežno obremenjen del (črtkasta črta)

forcement is set in the pulled part of the girder (i.e., the part where the bending stress is manifested as the tensile stress); the sample also contains two auxiliary reinforcement bars in the compressed part. The girder is also equipped with two closed clamps in the middle of the tensile-stressed part with an artificial interstice reaching about half of the girder's height. There is also a very narrow interstice in the tensile-stressed part. Both interstices are present to provide a suitable load-distribution path. The bottom reinforcement is also partially exposed so that its deformation can be easily measured.

The reinforcements in this set-up are set in tubes to ensure a precise settlement in the concrete and prevent their deformation during the loading. There are steel spikes in the heads of the girder with deviation meters for measuring the movement of the reinforcement towards the inner part of the girder (Figure 10). The test takes place after 28 d of curing the concrete in specified conditions. During the test, several parameters are measured: the bending of the girder, which is measured in the middle part with an accuracy of 0.001 mm, the deformation of the middle part of the bottom reinforcement (an accuracy of 0.0001 mm), the shift of the reinforcement towards the inner part of the girder (an accuracy of 0.001 mm) and the pulling strength during the first decrease of the bond-strength (a reinforcement shift of 0.002 mm). The test is repeated three times with the same reinforcement type and an arithmetic value is calculated. The strength values should not vary by more than 20 % from the average value.

4.2 ČSN 73 1333 (testing the bond-strength of prestressing reinforcement in concrete)⁴²

This standard can be used for testing the bond-strength of prestressing reinforcement with common compacted or compacted light concrete from an artificial porous aggregate. This test is used to assess the bond-

strength of the prestressing reinforcement in prestressed concrete. On the other hand, this standard cannot be used for assessing the effect of a construction loading on the strength of a bond of a prestressed reinforcement with the concrete (e.g., dynamically loaded constructions). It is important that this standard considers the mechanical bond between a prestressed reinforcement and the modified surface (imprints, ribs, corrugation, etc.) to be the deciding factor for anchoring the reinforcement in concrete.

Concrete hinders the movement of the reinforcement by pressing against its surface inhomogeneities. Bonding is defined as a reliable and safe transfer of the prestressing force from a prestressing reinforcement to concrete. The initial shift of the prestressing reinforcement is defined by the standard as a "slip".

Similarly to the previous one, this standard also recommends two experimental set-ups: the testing of girders and of cubes. The testing of girders allows us to assess the bond-strength between a prestressing reinforcement and new-type surface modifications. The testing of cubes is viable for a study of the effects of various factors (surface modification of the reinforcement, composition, processing and treatment of concrete) on the bond-strength.

Three samples are tested after 28 d of the curing. The composition, the processing and curing process are precisely defined.

4.2.1 Testing of the bond-strength of girders

This standard evaluates the change in a prestressing-force value before and after a slip of the reinforcement inside a concrete sample. The slip length defining the bond-strength is defined as 0.001 mm. The girder geometry is different from the girder in the ČSN 73 1328 standard. The cross-section of the girder is also rectangular; however, it only contains one or two tested prestressing reinforcement(s). The tail pieces of the reinforcement are anchored struts so that it cannot slip more than $\times 10^{-4}$ of its length between the anchoring points. The girder is usually equipped with detectors measuring the total longitudinal transformation (at least five on all the sides along the girder). The positions of dial deviation meters are similar to the ones defined in ČSN 73 1328.

The relative longitudinal girder transformation is the average value of all the values from the total longitudinal transformation of the opposite sides. The transformation magnitude versus time is plotted alongside the girder for every test stage. The changes in the prestressing force alongside the girder and the bond length are estimated from these plots. In this case, the bond length is considered to be the distance between the head of the reinforcement and the place where the transformation magnitude stops increasing. The reinforcement shift is the value from a dial deviation meter diminished by the

value of the elastic shortening between the meter and the head of the girder.

The total value of the bond length is the average value calculated from the values taken up to six hours after introducing the prestressing load on both sides of all three girders (six values). The total value of the prestressing-reinforcement shift is calculated similarly, but from the reinforcement components (6–12 values). Individual values must not differ by more than 20 % from the average value.

4.2.2 Testing of the bond-strength of cubes

During this test, a non-prestressed reinforcement is pulled out of a concrete cube. The set-up is similar to the one for the bond-strength test of the reinforcement and bars described in ČSN 73 1328. The bond-strength is calculated from the force necessary to pull the reinforcement out and from the shift of the other end of the reinforcement inside the concrete.

The cubes must be produced in such a way that the reinforcement rod is the cube's axis. The standard recommends the use of wooden trapezoidal laths to prevent the movement of the reinforcement. One lath is placed diagonally on the bottom of the mold, the other one is placed on top of it. The tailpieces of the reinforcement rod are placed in the holes of the laths.

The load of the prestressing reinforcement is measured by deviation with a 0.001 mm accuracy.

The force to pull the reinforcement out of the cube is increased in 8–12 steps with a short pause (30 s) between the steps. The force for each step is increased smoothly and slowly so that each step takes 20 s.

The deviation is first measured before the loading, then a couple of steps before its maximum value and also after this value is exceeded. During the test, several values are monitored: the force during the first shift of the reinforcement inside the concrete sample F_{or} , the maximum force F_{max} and F_{lim} which is the force acting when the reinforcement is being continuously pulled inside the sample without the need to increase this force. The stress of the bonding layer depends on F_{or} , F_{max} and F_{lim} and it is calculated with Equation (1), where l is the

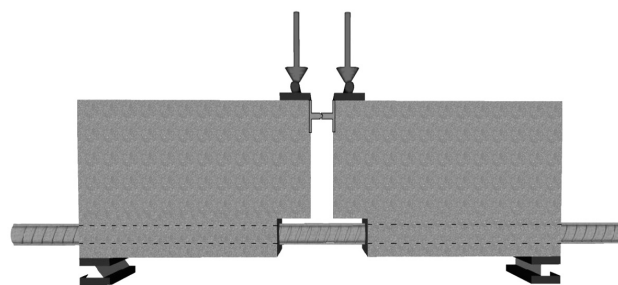


Figure 11: Schematics of a reinforced beam prepared for a beam test with arrows showing the applied forces and a connecting hinge according to RILEM RC5

Slika 11: Shematski prikaz ojačanega nosilca, pripravljenega za upogibni preizkus. Puščici kažeta uporabljeni sili in povezovalni tečaj, skladno z RILEM RC5

length of the reinforcement set in the concrete and a is the nominal perimeter length of the reinforcement:

$$\tau_x = \frac{F_x}{l_u} \quad (7)$$

The calculated stresses τ_{or} , τ_{max} , τ_{lim} for the bonding layer are the average values of all the values of at least three measurements (three cube samples). Individual values must not vary by more than 30 % from the average value.

4.3 RC5 (bond test for reinforcement steel 1: beam test)

RC5 is one of the basic RILEM recommendations dealing with another modification of the beam test. This procedure can be used to verify the bond-strength between common reinforcement and normal concrete, and also between prestressed constructions and concrete. An experimental set-up is depicted in **Figure 11**. Two separate concrete blocks are, at the bottom, connected by a reinforcement, whose bond-strength is to be measured. The reinforcement bar is again set into tubes to ensure its proper alignment and a precise bond length. The top parts of the blocks are connected by a separating hinge with a similar purpose as that of the interstices in the other set-ups. The hinge dimensions, the geometry of the supporting beams, the diameter of the reinforcement bars, the length and height of the concrete blocks and other parameters divide this test into two set-up groups – types A and B. The inward shift of the reinforcement inside the block is measured on both sides. The locations of dial deviation meters are identical to the ones defined in ČSN 73 1328.

Similarly to the other standards, this recommendation also requires the use of non-corroded, properly degreased test samples. The surface modifications must not affect the geometry of the tested reinforcement bar. The standard defines the concrete composition (aggregate and gravel) in terms of a viable granulometry; the water content is strictly defined. Again, the compressive strength of the cubes is verified.

The bond-strength is measured after a 28 d curing in precisely defined conditions. After setting the test beam on a mobile ball or triangle support, a force is applied to the top part of the girder, symmetrically to both blocks. The force is applied continuously so that the next-step magnitude of the force is reached in up to 30 s. After reaching the desired value, the applied force is held at that value for 120 s. The shift of the bar towards the inside of the block is measured (an accuracy of 0.001 mm); in addition, a measurement is taken for each step. The test continues until exceeding the bond-strength between the concrete and the reinforcement.⁴³

4.4 RC6 (bond test for reinforcement steel 2: pull-out test)

The RILEM recommendation also provides an alternative "pull-out test" described in the ČSN standards. A non-prestressed steel reinforcement with a minimum of 10 mm in diameter is recommended for a bond-strength measurement using this method. This test is recommended for the bond-strength testing of the reinforcements with different types of surface geometry. Considering the statistical evaluation, a minimum of 5 parallel samples is recommended. It is also recommended to set the reinforcement in a cubic concrete block. Again, the shift of the reinforcement towards the inside of the block is measured by a suitable deviation meter placed on the top part of the non-stressed reinforcement. The bond length of the reinforcement and the dimensions of the cube are chosen in such a way that they are proportional to the ratio between the bond length and the reinforcement-bar diameter. The reinforcement bar is, again, precisely inserted in a plastic tube which is suitably protected against the fresh-concrete contamination. The standard defines the preparation process and the composition of the concrete, its processing during the curing and the verification of its cubic compressive strength. The testing continues until a complete loss of the cohesion between the concrete and the reinforcement takes place. The result of this test is a loading curve $F = f(\Delta l)$. The loading force must be, similarly to the beam test (RC5), proportional to the diameter of the reinforcement bar and it must be continually increased (the rate of the increase must be steady).

The most important result of this experiment is the stress determined for the bonding layer, calculated from the loading force after the 28 d curing of the concrete.⁴⁴

5 CONCLUSION

A good bond-strength between any reinforcement type and concrete is one of the main prerequisites for a reliable static function of steel-concrete constructions. The bond-strength is affected by many factors: the adhesive forces between concrete and reinforcement, the friction forces caused by the surface inhomogeneities of the flat parts of the reinforcement, the surface geometry (ribs, imprints and corrugations), the composition and mechanical properties of the used concrete, its processing, curing time and also the position of the reinforcement in the concrete.

To make a valid generalization about the effect of the corrosion of hot-dip galvanized steel or the constriction of epoxy coating, it is necessary to use the methods that minimize the effect of the concrete's mechanical properties on the measured bond-strength. The only suitable method is the pull-out test (the bond-strength test of bars and cubes). A very important requirement of this test is that the reinforcement must be placed along the longitudinal axis of the concrete sample so that the pulled-out

reinforcement bar does not generate pressure forces. This can be achieved by using the tubes set in the concrete – the reinforcement rod is inserted in these tubes and a proper alignment is ensured, unlike when using anchoring agents which are not part of the mold.

Acknowledgement

This work was accomplished with the financial support from Specific University Research (MSMT No. 20/2014), the Grant Agency of the Czech Republic, reg. number 14-20856S and the Technological Agency of the Czech Republic, TA02030164.

6 REFERENCES

- M. Collepardi, *Moderní beton*, ČKAIT, Praha 2009
- P. Pokorný, The influence of galvanized steel on bond strength with concrete, 56 (2012) 4, 119–135, doi: 10.2478/v10227-011-0020-9
- P. Novák, Z. Dong, L. Joska, *Koroze ocelové výztuže v betonu*, *Koroze a ochrana materiálu*, 40 (1996), 2–7
- A. R. Boža, I. B. Topçu, M. Öztürk, Effect of fly-ash amount and cement type on the corrosion performance of the steel embedded in concrete, *Mater. Tehnol.*, 46 (2012) 5, 511–518
- L. Bertolini, B. Elsner, P. Pedferri, R. Polder, *Corrosion of Steel in Concrete (Prevention, Diagnosis, Repair)*, Wiley-VCH, Weinheim 2004
- H. Böhm, *Corrosion in reinforced concrete structures*, WP, Cornwall 2005
- S. M. Alvarez, A. Bautista, F. Valesco, Influence of process parameters on the corrosion resistance of corrugated austenitic and duplex stainless steels, *Mater. Tehnol.*, 47 (2013) 3, 317–321
- M. Kouřil, J. Stouřil, J. Bystrianský, R. Malá, P. Novák, *Korozivzdorné oceli pro výztuže betonu*, *Koroze a ochrana materiálu*, 46 (2002), 62–67
- M. Kouřil, P. Novák, M. Bojko, Threshold chloride concentration for stainless steels activation in concrete pore solution, *Cement and Concrete Research*, 40 (2010), 431–436, doi:10.1016/j.cemconres.2009.11.005
- P. Aitcin, *Vysokohodnotný beton*, ČKAIT, Praha 2005
- F. Škvára, *Technologie anorganických pojiv II.*, VŠCHT Praha, Praha 1995
- J. Procházka, P. Štěpánek, J. Krátký, A. Kohoutková, J. Vašková, *Navrhování betonových konstrukcí 1 – Prvky z prostého železového betonu*, ČBS, Praha 2007
- <http://www.tekna.no/ikbViewer/Content/225411/F40%20-%20Sistonen%20-%202005-09-02%20FINAL.pdf>, 2. 6. 2012
- P. Pytlík, *Technologie betonu*, VUT Brno, Brno 2000
- ČSN EN 1992 -1 -1: *Navrhování betonových konstrukcí - Část 1. 1.: Obecná pravidla a pravidla pro pozemní stavby* (leden 2006)
- ČSN EN ISO 15630-1: *Ocel pro výztuž a předpínání do betonu - Zkušební metody - Část 1: Tyče, válcovaný drát a drát pro výztuž do betonu* (květen 2011)
- M. Kouřil, Š. Krtička, P. Novák, *Soudržnost zinkované oceli s betonem*, *Koroze a ochrana materiálu*, 51 (2007), 80–83
- S. R. Yeomans, *Galvanized steel reinforcement in concrete*, Elsevier, Canberra 2004
- K. Wienerová, M. Kouřil, J. Stouřil, *Koroze a ochrana zinkované oceli v betonu*, *Koroze a ochrana materiálu*, 54 (2010), 148–154
- A. Bautista, J. A. Gonzales, Analysis of the protective efficiency of galvanizing against corrosion of reinforcements embedded in chloride contaminated concrete, *Cement and Concrete Research*, 26 (1996), 215–224, doi:10.1016/0008-8846(95)00215-4
- O. Kayali, S. R. Yeomans, Bond of ribbed galvanized reinforcing steel in concrete, *Cement & Concrete Composites*, 22 (2000), 459–467, doi:10.1016/S0958-9465(00)00049-4
- O. Kayali, S. R. Yeomans, Bond and slip of coated reinforcement in concrete, *Construction and Building Materials*, 9 (1995), 219–226, doi:10.1016/0950-0618(95)00024-A
- A. Macías, C. Andrade, Corrosion of galvanized steel in dilute Ca(OH)₂ solutions (pH 11.1–12.6), *British Corrosion Journal*, 22 (1987), 162–171, doi:10.1179/000705987798271505
- A. Macías, C. Andrade, Corrosion of galvanized steel reinforcements in alkaline solutions, Part 1: Electrochemical results, *British Corrosion Journal*, 22 (1987), 113–118, doi:10.1179/000705987798271631
- A. Macías, C. Andrade, Corrosion of galvanized steel reinforcements in alkaline solutions, Part 2: SEM study and identification of corrosion products, *British Corrosion Journal*, 22 (1987), 119–129, doi:10.1179/000705987798271749
- C. Andrade, J. D. Holst, U. Nürnberger, J. D. Whiteley, N. Woodman, *Protection System for Reinforcement (Chapter 2 – Hot dip galvanizing)*. CEB – Bulletin D'Information, No. 211, Lousanne 1992
- A. Macías, C. Andrade, Corrosion rate of galvanized steel immersed in saturated solutions of Ca(OH)₂ in the pH range 12–13.8, *British Corrosion Journal*, 18 (1983), 82–87, doi:10.1179/000705983798273912
- M. T. Blanco, A. Macías, C. Andrade, SEM study of the corrosion products of galvanized reinforcements immersed in solutions in the pH range 12.6–13.6, *British Corrosion Journal*, 19 (1984), 41–48, doi:10.1179/000705984798273524
- A. Macías, C. Andrade, Galvanized steel behaviour in Ca(OH)₂ saturated solutions containing SO₄²⁻ ions, *Cement and Concrete Research*, 17 (1987), 307–316, doi:10.1016/0008-8846(87)90113-X
- P. Rovnaníková, *Problémy spojené s použitím pozinkované výztuže do betonu*, *Koroze a ochrana materiálu*, 46 (2002), 104–107
- I. F. Olmo, E. Chacon, A. Irabien, Influence of lead, zinc, iron (III) and chromium (III) oxides on the setting time and strength development of Portland cement, *Cement and Concrete Research*, 31 (2001), 1213–1219
- C. Tashiro, H. Takahashi, M. Kanaya, I. Hirakida, R. Yoshida, Hardening property of cement mortar adding heavy metal compound and solubility of heavy metal from hardened mortar, *Cement and Concrete Research*, 7 (1977), 283–290, doi:10.1016/0008-8846(77)90090-4
- A. Maldonado, O. Quiroz-Zavala, L. Diaz-Ballote, Bond between galvanized steel and concrete prepared with limestone aggregates, *Anticorrosion Methods and Materials*, 57 (2010), 305–313, doi:10.1108/00035591011087163
- Ch. Tashiro, S. Tatibana, Bond strength between C3S paste and iron, cooper or zinc wire and microstructure of interface, *Cement and Concrete Research*, 13 (1983), 377–382, doi:10.1016/0008-8846(83)90037-6
- M. Bojko, *Dizertační práce*, VŠCHT Praha, Praha 2007
- A. R. Cusens, Z. Yu, Pullout tests of epoxy-coated reinforcement in concrete, *Cement and Concrete Composites*, 14 (1992), 269–276, doi:10.1016/0958-9465(92)90025-Q
- K. Kobayashi, K. Takewaka, Experimental studies on epoxy coated reinforcing steel for corrosion protection, *The International Journal of Cement Composites and Lightweight Concrete*, 6 (1984), 99–116, doi:10.1016/0262-5075(84)90039-3
- J. J. Assaad, C. A. Issa, Bond strength of epoxy coated bars in under-water concrete, *Construction and Building Materials*, 30 (2011), 667–674, doi:10.1016/j.conbuildmat.2011.12.047
- M. M. El-Hawary, Evaluation of bond strength of epoxy-coated bars in concrete exposed to marine environment, *Construction and Building Materials*, 13 (1999), 357–362, doi:10.1016/S0950-0618(99)00042-2

⁴⁰ R. Swamy, S. Koyama, Epoxy coated rebars the panacea for steel corrosion in concrete, *Construction and Building Materials*, 3 (1989), 86–91, doi:10.1016/S0950-0618(89)80006-6

⁴¹ ČSN 73 1328: Stanovení soudržnosti oceli s betonem, 1971

⁴² ČSN 73 1333: Zkoušení soudržnosti předpínací výztuže s betonem, 1990

⁴³ Technical Recommendations for the Testing and Use of Construction Materials (RILEM) RC5: Bond test for reinforcement steel – 1. Beam test, 1982

⁴⁴ Technical Recommendations for the Testing and Use of Construction Materials (RILEM) RC6: Bond test for reinforcement steel – 2. Pull-out test, 1983

MODELING OF OCCURRENCE OF SURFACE DEFECTS OF C45 STEEL WITH GENETIC PROGRAMMING

MODELIRANJE POJAVA POVRŠINSKIH NAPAK PRI JEKLU C45 Z GENETSKIM PROGRAMIRANJEM

Miha Kovačič¹, Robert Jager²

¹Štore Steel, d. o. o., Železarska cesta 3, 3220 Štore, Slovenia

²Laboratory for Multiphase Processes, University of Nova Gorica, Vipavska 13, 5000 Nova Gorica, Slovenia
miha.kovacic@store-steel.si

Prejem rokopisa – received: 2013-12-09; sprejem za objavo – accepted for publication: 2015-02-18

doi:10.17222/mit.2013.304

Carbon steel C45 with an increased content of carbon is used for tempering in the automotive industry for highly stressed parts (axles, shafts), machine parts, screws, drills for wood, axes, knives, hammers and similar. In the present work an attempt of analyzing the influences of different steelmaking parameters is presented. On the basis of the monitored data about the casting-temperature changes, the total oxygen, the number of added aluminum rods, the chemical analyses before and after steelmaking, the added lime, the aluminum-cored wire, the calcium-silicon-cored wire, the sulphur-cored wire, the rolling dimensions, the casting speed, the opening of the ladle nozzle with oxygen and surface defects (scrap fraction) on rolled bars, a mathematical model was obtained with the help of the genetic programming method. The results show that the most influential parameters for the surface-defect occurrence on the C45 steel are the opening of the ladle nozzle with oxygen and aluminum. On the basis of the results, the steelmaking technology was changed. Instead of the aluminium-killed steelmaking technology the aluminium-calcium-free (ACF) steelmaking technology was used. The batches from an aluminium-calcium-free steelmaking period statistically have a significantly lower level of surface defects (scrap fraction). The scrap fraction was reduced from the average of 68.45 % to 1.92 % – by more than 35 times.

Keywords: mechanical engineering, metallurgy, steel, C45 steel, making steel, casting steel, steel plant, billet surface defects, genetic programming

Jeklo C45 je ogljikovo jeklo za poboljšanje s povečano koncentracijo ogljika. Uporablja se za obremenjene dele v avtomobilski industriji (osi, gredi), za dele strojev, vijake, svedre za les, sekire, nože, kladiva in podobno. V članku je predstavljen poskus analize vplivov različnih parametrov pri postopku izdelave omenjenega jekla. Na podlagi zbranih podatkov o spremembi livne temperature, aktivnega kisika (kisik v talini), dodanih aluminijevih palic, analiz kemijskih elementov med izdelavo jekla in po njej, dodanega apna, dodanega aluminija, kalcij-silicija ter žvepla v obliki žice, dimenzij valjanca, hitrosti litja, podžiganja in podatkov o površinskih napakah (delež izmeta) valjanih palic smo izdelali matematični model z genetskim programiranjem. Rezultati modeliranja genetskega programiranja so pokazali, da sta podžiganje in aluminij tista parametra, ki najbolj vplivata na nastajanje napak v jeklu C45 in imata torej največji vpliv na izmet. Na podlagi rezultatov se je spremenila tehnologija izdelave jekla. Namesto tehnologije z dodatkom aluminija se je uporabila tehnologija aluminium-calcium-free (ACF). Šarže, izdelane v obdobju izdelave jekla s to tehnologijo, imajo statistično značilno manj površinskih napak (izmeta). Izmet se je v povprečju zmanjšal iz 68,45 % na 1,92 % – več kot 35-krat.

Ključne besede: strojništvo, metalurgija, jeklo, jeklo C45, izdelava jekla, ulivanje jekla, jeklarna, površinske napake na gredici, genetsko programiranje

1 INTRODUCTION

The basic concerns about the development of the continuous-casting technology are associated with finding the source generating surface defects and taking proper measures to prevent and remedy them where appropriate.¹⁻³

A literature review shows that there are three basic ways of modeling surface defects:

- experimental approach⁴,
- computational fluid dynamics¹⁻³ and
- artificial-intelligence approach which effectively combines the above-mentioned approaches.⁵⁻¹⁰

The authors^{5,6} propose an interaction between the numerical heat-transfer model and the artificial-intelligence heuristic-search method, linked to a knowledge base for the continuous casting. A two-dimensional

heat-transfer model was developed using the finite-difference method and applied to real continuous-casting conditions. The heuristic search method, aided by a knowledge base, explores the technological and metallurgical parameter settings in order to find optimized cooling conditions, resulting in a defect-free billet production with the minimum metallurgical period.

The paper by Tirian et al.⁷ describes a neural-network-based strategy for crack prediction aimed at improving the steel-casting process performance by decreasing the number of crack-generated failure cases. A neural system for estimating the crack-detection probability was designed, implemented, tested and integrated into an adaptive control system.

A simulated annealing-optimization algorithm was used for a multicriteria optimization procedure to determine appropriate process-parameter values for producing

quality products in a continuous-casting system.⁸ A total of 17 critical-quality conditions were identified; these had to be satisfied to prevent defect formations during the casting. An objective function, formulated as a loss function, was used so that all 17 critical conditions were satisfied simultaneously.

The article by Sanz-García et al.⁹ deals with three successful experiences gained from genetic algorithms and the finite-element method in order to solve engineering-optimization problems in connection with the surface-defect occurrence during continuous casting.

A set of metamodels was developed to satisfy the necessary process conditions connected to one or more continuous-casting parameters.¹⁰ The values of these parameters were determined so that all the process conditions were satisfied simultaneously, ensuring that the product had the desired quality.

This paper discusses the use of the genetic-programming method for predicting the occurrence of surface defects on rolled C45 steel, used for highly stressed parts in the automotive industry, with respect to the influences of several steelmaking parameters. Genetic programming is one of the more general and recently developed approaches of evolutionary algorithms. Similarly to some other machine-learning approaches such as artificial neural networks, genetic algorithms, particle-swarm optimization and gravitational search algorithm (see examples¹¹⁻¹⁴), genetic programming can be used for solving a wide spectrum of engineering and other problems.

The problem is described in Section 2. In the subsequent section the effect of the proposed concept and the results of the defect-occurrence prediction are presented. A practical implementation of the modeling is presented in Section 4 and, finally, the main contributions of the performed research and guidelines for further research are given in the last section.

2 EXPERIMENTAL BACKGROUND

Steelmaking begins with scrap melting in an electric-arc furnace. After the melting of the scrap and carburizing agents, the carbon carriers, in general, are coke, anthracite, graphite and slag additives, which regulate the basicity, viscosity, thermal and electric conductivities, desulphurization, dephosphorization, neutrality towards the furnace fireproof linings and capability to filter non-metallic inclusions.^{1,2}

The melting bath heated up to the tapping temperature according to further treatment procedures is discharged into the casting ladle after the electric-arc-furnace melting.

The standard steelmaking procedure (in a ladle furnace) for C45 consists of:

1. Melt-temperature measurement. Depending on the temperature the melt is additionally heated.

2. Visual checking of the slag's viscosity and amount. The slag should be properly dense. In the case of not having enough slag, lime and bauxite should be added. The argon flux should also be appropriate.
3. Chemical analysis.
4. On the basis of the chemical composition, corrective alloying is performed and argon stirring is also consequently increased.
5. If necessary, aluminum and sulfur wires are added.
6. Chemical analysis.
7. On the basis of the chemical composition, fine corrective alloying is performed (CaSi and aluminum wires). During the alloying moderate argon stirring is performed. The melt should also be properly covered with slag due to a possible melt reoxidation. In the end a sulfur wire is added.
8. Melt-temperature measurement.

After achieving the proper melt temperature in the melting bath the billets are continuously cast. The melting bath flows through the sliding-gate system and ladle shroud towards the tundish.

During the casting it may be necessary to use the oxygen lance to cut through the ladle slide gate and pour the liquid steel through it. In good steelmaking practice, we want to have a minimum number of such batches because the oxygen that is blown into the melt causes a re-oxidation of the melt and impurities may be formed.¹⁵

After filling up the tundish, the mould filling system with tundish stoppers and submerged pouring tubes is established. Billets with a square section of 180 mm are cast. After reaching a certain melting-bath level the potentiometer starts the flattening system which drags a billet out of the mould. In this way continuous casting is established. The billet goes through the cooling zone toward the gas cutters where it is cut and laid off onto the cooling bed.

The cooled-down billets are reheated, according to the prescribed temperature, in the continuous-heating furnace. After the heating the billets are hot rolled in a strand of rolls. Steel bars are cooled on the cooling bed. After the cooling they are cut with hot shears to different lengths.

In line with the customer specifications, after the rolling the cut bars are inspected on the automatic control line (**Figure 1**) equipped with three inspection units:

- anti-mixing control (FÖRSTER MAGNATEST, eddy current),
- surface-defect control (FÖRSTER CYRCOFLUX, magnetic-flux leakage) and
- internal-defect control (KRAUTKRAMER ROWA 90/160, ultrasound).

The minimum detectable surface-defect depth and length are 0.15 mm and 12.5 mm, respectively. Regarding the inspection speed and type of the ultrasonic head, the minimum detectable inner-defect sizes are 0.8 mm and 1.2 mm. Due to blind areas and the type of the



Figure 1: Automatic control line in Štore Steel Ltd.

Slika 1: Samodejna kontrolna linija v Štore Steel, d. o. o.

internal defects, the control unit detects 85 % of the material volume.

The data for the analysis was collected on the basis of 34 batches of the C45 steel consecutively inspected (automatic control line) in Štore Steel Ltd. (Table 1) from January to December 2010. The data was taken from the technological documentation of the cast batches and from the chemical archive. The goal was to get as wide a range of influential parameters as possible. These are:

- Active oxygen O_2 ($\times 10^{-6}$): It influences the aluminum addition and, consequently, the aluminum-oxide content. It is measured with a temperature probe before the tapping.
- Lime CaO (kg): It is added during the tapping and it helps create additional slag which is needed also during the ladle-furnace treatment.
- Calcium carbonate (kg): It is added during the tapping to reduce the slag density.
- Aluminum bricks (kg): They are added during the tapping in order to deoxidize the melt (the killed steel). Their amount depends on the active-oxygen content.

- The presence of the slag in the electric-arc furnace: The slag in the electric-arc furnace is the slag that was unintentionally poured into the ladle during the tapping. The electric-arc-furnace operator adjusts the tapping according to the melt quantity and tap-hole dimensions. The slag in the electric-arc furnace negatively influences the processing of the melt in the ladle furnace. Chemical and physical reactions evolve within a time shift or it can happen that they do not evolve at all.
- Aluminium wire (m): It is added to the ladle furnace according to the working instructions. It binds oxygen into aluminium oxides.
- CaSi wire (m): Calcium is added for melt modifying. It is proportional with the aluminium content. The modification is, in fact, the ability of calcium to bind unwanted inclusions and transport them into the slag.
- $t_{Al-CaSi}$ (min): This is the time between the additions of aluminium and CaSi wires.
- Sulphur wire (m): It is added to form MnS inclusions which increase the machinability.
- The contents of Al, Ca, S at the beginning of the melt's ladle-furnace treatment (%)
- The final contents of Al, Ca and S (%)
- ΔT (°C): This is the temperature difference between the actual and prescribed casting temperatures measured in the tundish.
- n_s : This is the number of the strands used during the casting. A continuous caster has three strands, but it can happen that the inner nozzle becomes clogged and the casting is, therefore, performed with fewer strands. Proportionally, the casting lasts longer and, consequently, the melt temperature drops influencing the casting speed.
- The casting speed (m/min): It depends on the steel chemical composition and the melt temperature.
- The casting-speed variation (m/min): Due to temperature drops the casting speed must be changed.
- n_{Ino} : This is the number of the ladle-nozzle openings with the oxygen lance.
- The rolled-bar diameter (mm)

Table 1: Experimental data

Tabela 1: Eksperimentalni podatki

Batch	Electric-arc-furnace parameters				Ladle-furnace parameters											Casting parameters				Scrap (%)		
	$O_2 \times 10^{-6}$	CaO (kg)	CaCO ₃ (kg)	Al bricks (kg)	slag	Al wire (m)	CaSi wire (m)	$t_{(Al-CaSi)}$ (min)	S wire (m)	Al ₁ (%)	Si ₁ (%)	Ca ₁ (%)	Al ₂ (%)	S ₂ (%)	Ca ₂ (%)	ΔT (°C)	strands	Δv /(m/min)	v /(m/min)		ladle-nozzle openings	diameter (mm)
1	367.8	670	40	65	0	130	80	10	110	0.013	0.02	0.005	0.028	0.027	0.025	40	3	0	1.73	0	37	27.42
1	367.8	670	40	65	0	130	80	10	110	0.013	0.02	0.005	0.028	0.027	0.025	40	3	0	1.73	0	44	33.29
2	357.3	600	60	82	0	90	90	10	105	0.01	0.045	0.003	0.029	0.029	0.035	55	3	0	1.65	0	28	18.91
2	357.3	600	60	82	0	90	90	10	105	0.01	0.045	0.003	0.029	0.029	0.035	55	3	0	1.65	0	33	30.92
3	444.7	600	30	60	0	140	70	29	120	0.007	0.015	0.002	0.03	0.031	0.027	42	3	0	1.65	0	37	33.67

4	338.5	600	30	63	0	65	80	14	140	0.025	0.034	0.002	0.025	0.034	0.026	39	3	0	1.73	2	28	24.58
4	338.5	600	30	63	0	65	80	14	140	0.025	0.034	0.002	0.025	0.034	0.026	39	3	0	1.73	2	30	49.22
4	338.5	600	30	63	0	65	80	14	140	0.025	0.034	0.002	0.025	0.034	0.026	39	3	0	1.73	2	44	45.74
5	620.7	600	30	60	0	165	87	52	130	0.021	0.026	0.002	0.027	0.03	0.022	44	3	0	1.73	1	28	12.88
5	620.7	600	30	60	0	165	87	52	130	0.021	0.026	0.002	0.027	0.03	0.022	44	3	0	1.73	1	37	17.78
6	210.1	600	30	60	1	125	90	21	135	0.019	0.021	0.004	0.023	0.024	0.03	45	3	0	1.73	1	30	15.69
7	506.5	720	40	70	0	70	96	17	120	0.006	0.02	0.002	0.035	0.02	0.037	39	3	0	1.73	0	33	32.88
8	203.3	600	50	50	0	70	80	30	60	0.021	0.045	0.001	0.034	0.029	0.028	46	3	0.05	1.68	0	44	26.58
9	352.9	650	40	70	0	70	90	45	120	0.022	0.043	0.001	0.03	0.026	0.033	45	3	0	1.73	0	33	35.11
9	352.9	650	40	70	0	70	90	45	120	0.022	0.043	0.001	0.03	0.026	0.033	45	3	0	1.73	0	37	32.16
10	216.7	600	30	55	0	20	85	10	80	0.035	0.038	0.001	0.029	0.026	0.03	50	3	0	1.68	1	37	18.13
11	767.2	600	40	70	0	80	90	45	90	0.022	0.026	0.001	0.034	0.028	0.029	26	2	0	1.83	1	28	29.2
11	767.2	600	40	70	0	80	90	45	90	0.022	0.026	0.001	0.034	0.028	0.029	26	2	0	1.83	1	33	31.88
11	767.2	600	40	70	0	80	90	45	90	0.022	0.026	0.001	0.034	0.028	0.029	26	2	0	1.83	1	37	23.81
12	222.2	600	40	55	0	90	90	80	135	0.019	0.037	0.001	0.028	0.026	0.027	50	3	0	1.68	0	30	58.5
12	222.2	600	40	55	0	90	90	80	135	0.019	0.037	0.001	0.028	0.026	0.027	50	3	0	1.68	0	33	68.33
12	222.2	600	40	55	0	90	90	80	135	0.019	0.037	0.001	0.028	0.026	0.027	50	3	0	1.68	0	44	26.85
13	313.2	640	40	62	0	0	90	/	70	0.037	0.033	0.004	0.032	0.033	0.027	45	3	0.05	1.73	2	37	46.87
14	544.8	600	40	75	0	105	100	40	140	0.015	0.034	0.001	0.029	0.025	0.033	40	3	0	1.73	0	44	37.67
14	544.8	600	40	75	0	105	100	40	140	0.015	0.034	0.001	0.029	0.025	0.033	40	3	0	1.73	0	37	61.15
15	513.6	600	60	45	0	50	75	10	130	0.021	0.03	0.003	0.03	0.024	0.031	53	3	0	1.63	0	44	33.39
15	513.6	600	60	45	0	50	75	10	130	0.021	0.03	0.003	0.03	0.024	0.031	53	3	0	1.63	0	28	53.25
16	560.1	760	70	60	0	75	85	11	173	0.029	0.014	0.001	0.033	0.029	0.034	48	3	0.05	1.68	0	30	37.74
16	560.1	760	70	60	0	75	85	11	173	0.029	0.014	0.001	0.033	0.029	0.034	48	3	0.05	1.68	0	37	50.29
16	560.1	760	70	60	0	75	85	11	173	0.029	0.014	0.001	0.033	0.029	0.034	48	3	0.05	1.68	0	30	5.216
17	163.6	600	70	55	0	70	85	14	120	0.023	0.037	0.001	0.033	0.03	0.027	47	3	0	1.73	0	44	23.76
17	163.6	600	70	55	0	70	85	14	120	0.023	0.037	0.001	0.033	0.03	0.027	47	3	0	1.73	0	37	63.09
18	320.6	600	30	62	0	225	85	60	200	0.007	0.019	0.002	0.028	0.023	0.035	40	3	0	1.73	4	28	4.732
19	162.6	600	30	66	0	0	80	/	70	0.04	0.041	0.002	0.032	0.038	0.036	42	2	0.12	1.85	2	33	4.762
20	317.8	600	30	62	0	90	80	24	130	0.031	0.022	0.004	0.039	0.032	0.038	50	3	0	1.68	1	28	11.27
20	317.8	600	30	62	0	90	80	24	130	0.031	0.022	0.004	0.039	0.032	0.038	50	3	0	1.68	1	30	56.41
21	313	600	40	62	0	100	90	55	135	0.017	0.026	0.002	0.028	0.023	0.031	46	3	0	1.73	3	37	11.08
21	313	600	40	62	0	100	90	55	135	0.017	0.026	0.002	0.028	0.023	0.031	46	3	0	1.73	3	30	14.81
21	313	600	40	62	0	100	90	55	135	0.017	0.026	0.002	0.028	0.023	0.031	46	3	0	1.73	3	37	27.12
22	371.3	600	20	65	0	115	95	18	120	0.017	0.018	0.001	0.031	0.035	0.034	40	3	0	1.73	1	30	38.47
22	371.3	600	20	65	0	115	95	18	120	0.017	0.018	0.001	0.031	0.035	0.034	40	3	0	1.73	1	37	37.12
23	327	600	20	65	0	25	95	15	105	0.032	0.02	0.003	0.028	0.027	0.041	40	3	0	1.73	0	53	68.78
23	327	600	20	65	0	25	95	15	105	0.032	0.02	0.003	0.028	0.027	0.041	40	3	0	1.73	0	37	46.86
24	170.6	600	25	45	0	145	80	38	0	0.017	0.02	0.001	0.029	0.033	0.026	42	3	0	1.73	1	53	18.11
25	630.6	600	30	70	0	125	80	20	133	0.012	0.036	0.005	0.032	0.028	0.026	48	3	0	1.73	1	44	24.85
25	630.6	600	30	70	0	125	80	20	133	0.012	0.036	0.005	0.032	0.028	0.026	48	3	0	1.73	1	37	25.43
26	248	600	40	65	0	110	85	40	75	0.015	0.031	0.002	0.029	0.034	0.025	43	3	0	1.73	0	44	25.38
27	355.7	600	30	70	0	80	85	13	70	0.02	0.026	0.001	0.033	0.03	0.019	51	3	0	1.68	0	33	50
27	355.7	600	30	70	0	80	85	13	70	0.02	0.026	0.001	0.033	0.03	0.019	51	3	0	1.68	0	37	64.21
28	155.8	600	70	60	0	120	85	33	120	0.01	0.03	0.001	0.029	0.035	0.024	42	3	0	1.73	1	33	18.56
28	155.8	600	70	60	0	120	85	33	120	0.01	0.03	0.001	0.029	0.035	0.024	42	3	0	1.73	1	37	35.6
29	205.6	600	40	55	0	110	85	6	107	0.011	0.04	0.002	0.033	0.023	0.03	45	3	0	1.73	0	44	22.81
30	267.1	600	40	60	0	50	75	10	95	0.025	0.033	0.001	0.03	0.027	0.031	46	3	0.05	1.68	0	37	23.84
30	267.1	600	40	60	0	50	75	10	95	0.025	0.033	0.001	0.03	0.027	0.031	46	3	0.05	1.68	0	37	7.297
31	348.4	600	40	60	0	120	75	40	105	0.015	0.023	0.002	0.029	0.024	0.028	41	3	0.05	1.68	1	44	9.655
32	652.6	650	40	80	1	90	80	10	145	0.019	0.024	0.002	0.032	0.023	0.031	51	3	0	1.68	1	30	8.411
32	652.6	650	40	80	1	90	80	10	145	0.019	0.024	0.002	0.032	0.023	0.031	51	3	0	1.68	1	44	35.27
33	184.8	600	30	55	0	150	80	40	115	0.01	0.022	0.002	0.031	0.029	0.032	45	3	0.05	1.68	1	30	16.29
33	184.8	600	30	55	0	150	80	40	115	0.01	0.022	0.002	0.031	0.029	0.032	45	3	0.05	1.68	1	33	23.68
34	455.4	600	30	58	0	120	90	63	110	0.024	0.02	0.002	0.026	0.021	0.027	44	3	0	1.73	1	37	35.61
34	455.4	600	30	58	0	120	90	63	110	0.024	0.02	0.002	0.026	0.021	0.027	44	3	0	1.73	1	44	29.76
34	455.4	600	30	58	0	120	90	63	110	0.024	0.02	0.002	0.026	0.021	0.027	44	3	0	1.73	1	37	35.03
34	455.4	600	30	58	0	120	90	63	110	0.024	0.02	0.002	0.026	0.021	0.027	44	3	0	1.73	1	44	38.83

3 MODELING OF OCCURRENCE OF SURFACE DEFECTS WITH GENETIC PROGRAMMING

Genetic programming is probably the most general evolutionary optimization method.¹⁵⁻¹⁹ The organisms that undergo an adaptation are in fact mathematical expressions (models) for a nozzle-opening prediction consisting of the available function genes (i.e., the basic arithmetical functions) and terminal genes (i.e., independent input parameters and random floating-point constants). In our case the models consist of the function genes of addition (+), subtraction (-), multiplication (×) and division (/) and terminal genes of active oxygen O₂ (O₂), lime (CaO), calcium carbonate (CaCO₃), aluminum bricks (Alb), the electric-arc-furnace slag presence (slag), the aluminium wire (Alw), the CaSi wire (CaSiw), the time between the additions of aluminium and CaSi wires (tAl-CaSi), the sulphur wire (Sw), the contents of Al (Al), Ca (Ca) and S (S) at the beginning of the melt's ladle-furnace treatment, the final contents of Al (Al), Ca (Ca) and S (S), the temperature difference between the actual and prescribed casting temperatures measured in the tundish (dT), the number of strands used during the casting (ns), the casting speed (vc), the casting-speed variation (vvc), the number of ladle-nozzle openings with the oxygen lance (nlno) and the rolled-bar diameter (d).

Random computer programs of various forms and lengths are generated by means of selected genes at the beginning of the simulated evolution. Afterwards, the varying of the computer programs during several iterations, known as generations, is performed by means of genetic operations. For the progress of the population only the reproduction and crossover are sufficient. After the completion of the variation in the computer programs a new generation is obtained that is evaluated and compared with the experimental data.

The process of changing and evaluating the organisms is repeated until the termination criterion of the process is fulfilled. This is the prescribed maximum number of generations.

For the process of simulated evolutions the following evolutionary parameters were selected: the population of organisms: 500, the greatest number of generations: 100, the reproduction probability of 0.4, the crossover probability of 0.6, the greatest permissible depth when creating a population: 6, the greatest permissible depth after the operation of a crossover of two organisms: 10, and the smallest permissible depth of organisms when generating new organisms: 2. Genetic operations of the reproduction and crossover were used. For the selection of organisms the tournament method with a tournament size of 7 was used. For the model fitness, the average square of deviation from the monitored data was selected. It is defined as:

$$\Delta = \frac{\sum_{i=1}^n \Delta_i^2}{n} \tag{1}$$

where n is the size of the monitored data and Δ_i is the square of deviation of a single sample data. The deviation of a single sample data, produced by an individual organism, is simply:

$$\Delta_i = E_i - G_i \tag{2}$$

where E_i and G_i are the actual and the predicted scrap fractions (which depend only on surface defects), respectively.

We developed 100 independent civilizations of mathematical models for the scrap-fraction prediction. Each civilization has the most successful organism – the mathematical model for the scrap-fraction prediction. The best most successful organism from all of the civilizations is presented here:

$$\begin{aligned} & -5.20857 + \frac{CaSiw(dT - \frac{nlno}{ns})}{Alw(CaSiw - d)} + \frac{CaSiw - ns}{CaSiw - dnlno} + \frac{Alw^2(dT - ns)}{CaSiw^2 d} + \\ & \frac{Alw \left(dT + \frac{Alw(-d+dT)}{CaSiw} - \frac{Alw^4}{CaSiw^3 ns \left(\frac{nlno}{-d+dT} + ns \right)} \right)}{CaSiw \left(d + \frac{dT - ns}{-d+dT} \right)} + \\ & \frac{Alw \left(ns + \frac{CaSiw - \frac{CaSiw}{CaSiw - d + \frac{nlno}{-d+dT}}}{CaSiw - \frac{Alw(CaSiw - d)}{1 + \frac{nlno}{CaSiw - d + \frac{nlno}{-d+dT}}}} \right)}{CaSiw} + \\ & \frac{\left(CaSiw - \frac{Alw(-CaK + CaSiw)}{CaSiw} \right) \left(CaSiw + \frac{CaSiw(CaSiw - ns)}{Alw(CaSiw - d)} + \frac{(CaSiw - ns)}{CaSiw - \frac{CaSiw}{-d}} - dnlno - \frac{(-CaSiw + dT)(CaSiw - ns)}{\left(1 + \frac{dT - ns}{-CaSiw - d + \frac{nlno}{-d+dT}} \right) (dT - ns)} \right)}{SI} + \\ & \frac{-1.73619 + nlno + \frac{dT - ns}{CaSiw - d}}{SI} + \\ & \frac{Al5 \left(-1.73619 + \frac{CaSiw(CaSiw - nlno) \left(-1.73619 + \frac{1}{nlno} + \frac{Alw^2}{CaSiw d ns} \right)}{Alw(dT - ns)} + \frac{CaSiw(CaSiw - d)nlno ns}{Alw^2} + \frac{-1.73619 + nlno + \frac{Alw^2(dT - ns)}{CaSiw^2 d}}{SI} \right)}{SI} + \\ & \frac{CaSiw(CaSiw - nlno) ns}{Alw \left(Alw + \frac{Alw}{(-d+dT) ns} \right) vvcvc} + Alb \end{aligned} \tag{3}$$

with the average relative deviation of 12.03 %.

The randomly driven process builds the fittest and most complex models from generation to generation and uses the ingredients that are most suitable for the experimental environment adaptation. For curiosity's sake, an analysis of the genes (parameters) excluded from the models is presented in **Figure 2**.

On the basis of the number of genes excluded from 100 obtained mathematical models we can assume the influence of the parameters on the scrap fraction. It is clear from the figure that out of 100 genetically obtained mathematical models only 12 models do not include the parameter of aluminium blocks and only 3 out of 100 models do not include the parameter of the number of ladle-nozzle openings. So, we can deduct that aluminium blocks and ladle-nozzle openings with an oxygen lance

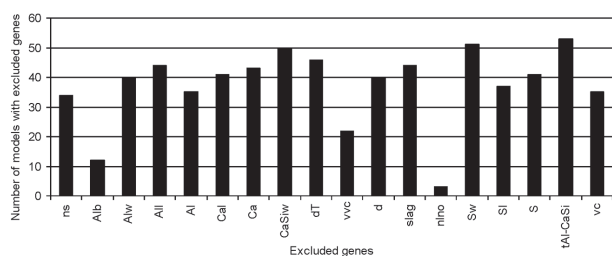


Figure 2: Frequency of the genes excluded from the best 100 mathematical models for scrap fraction

Slika 2: Frekvenca izločenih genov na podlagi najboljših 100 matematičnih modelov za delež izmeta

are probably the most important parameters influencing the occurrence of surface defects.

4 PRACTICAL IMPLEMENTATION OF THE MODELING RESULTS

At the beginning of 2011, the aluminium-calcium-free (ACF) steelmaking technology was used for the C45 steel instead of the aluminium-killed steelmaking technology. The data for the analysis was collected on the basis of 17 consecutively inspected batches of the C45 steel (automatic control line) in Štore Steel Ltd. (Table 2).

Table 2: Automatic-control-line results (scrap fractions) for 17 consecutively inspected batches (automatic control line) of C45 steel made with aluminium-calcium-free steelmaking technology

Tabela 2: Rezultati samodejne kontrolne linije (delež izmeta) za 17 zaporedno pregledanih šarž jekla C45, izdelanih po tehnologiji aluminium-calcium-free

Batch	Scrap %
1	0
2	1.036
2	2.102
3	2.042
3	2.809
4	0.642
5	0.877
6	2.889
7	0.902
8	1.731
9	1.512
10	3.218
11	1.570
12	2.345
13	0.520
14	0.700
15	4.757
16	1.086
17	5.695

The data was analyzed using Microsoft Excel. The α parameter was set at $\alpha = 0.05$.

The t-test for unequal variances was used to compare the differences between the two populations. The results of the comparison of the automatic control results ob-

tained during the aluminium-killed steelmaking period (Table 1) and aluminium-calcium-free steelmaking period (Table 2) are presented in Table 3.

Table 3: Comparison of automatic-control results obtained during aluminium-killed steelmaking period (Table 1) and aluminium-calcium-free steelmaking period (Table 2)

Tabela 3: Primerjava rezultatov samodejne kontrolne linije, pridobljenih v obdobju izdelave jekla na podlagi tehnologije z dodajanjem aluminija (tabela 1) in med obdobjem uporabe tehnologije aluminium-calcium-free (tabela 2)

	Al-killed steelmaking	ACF steelmaking
Mean	68.45302471	1.917526316
Variance	260.6865252	2.146430596
Observations	61	19
Hypothesized mean difference	0	
df	63	
t-stat	31.76825617	
$P(T \leq t)$ one-tail	8.65978E-41	
t critical one-tail	1.669402222	
$P(T \leq t)$ two-tail	1.73196E-40	
t critical two-tail	1.998340522	

t-test: two-sample assuming unequal variances

The comparison shows that there is a statistically significant difference between the batches made within the aluminium-killed steelmaking period and aluminium-calcium-free steelmaking period ($p < 0.05$). The batches from the aluminium-calcium-free steelmaking period statistically have a significantly smaller amount of surface defects (scrap percentage).

5 CONCLUSION

The purpose of this paper was to reduce surface defects (scrap fraction) on the C45 steel. The influences of the casting-temperature changes, the total oxygen, the number of added aluminum rods, the chemical analyses before and after steelmaking, added lime, aluminum-cored wire, calcium-silicon-cored wire, sulphur-cored wire, the rolling dimensions, the casting speed, the opening of the ladle nozzle with oxygen on the surface defects of rolled bars were analyzed. The data for the analysis was collected on the basis of 34 consecutively inspected (automatic control line) batches of the C45 steel in Štore Steel Ltd. The data was taken from the technological documentation of the cast batches and from the chemical archive. Afterwards a model for a scrap-fraction prediction was developed with the genetic-programming method allowing an evolution of better and better model variants during the simulation. There were 100 different models and only the best was used for the scrap-fraction prediction. The relative average deviation of the actual scrap fraction from the predicted scrap fraction was 12.03 %. Also, the frequencies of the genes excluded from the best 100 mathematical

models for the scrap fraction were analyzed. The results show that the most influential parameters for the surface defects occurring on the C45 steel are the opening of the ladle nozzle with the oxygen lance and aluminum (blocks). According to the results, the steelmaking technology was changed. At the end of 2009 and at the beginning of 2010 the aluminium-calcium-free (ACF) steelmaking technology was used with the C45 steel instead of the aluminium-killed steelmaking technology. The t-test for unequal variances was used to compare the differences between the automatic-control results obtained during the aluminium-killed steelmaking period and the aluminium-calcium-free steelmaking period. The batches from the aluminium-calcium-free steelmaking period statistically had a significantly smaller amount of surface defects (scrap percentage). The scrap fraction was reduced from the average of 68.45 % to 1.92 % – by more than 35 times. In future the implemented procedure can be applied to several steel grades.

6 REFERENCES

- ¹ W. R. Irving, *Continuous casting of steel*, Institute of Materials, London 1993
- ² C. Reilly, N. R. Green, M. R. Jolly, The present state of modeling entrainment defects in the shape casting process, *Applied Mathematical Modelling*, 37 (2013) 3, 611–628, doi:10.1016/j.apm.2012.04.032
- ³ J. Stetina, T. Mauder, L. F. Klimes, Increasing the surface temperature during the straightening of a continuously cast slab, *Mater. Tehnol.*, 47 (2013) 3, 311–316
- ⁴ Q. Lu, R. Yang, X. Wang, J. Zhang, W. Wang, Water modeling of mold powder entrapment in slab continuous casting mold, *Journal of University of Science and Technology Beijing, Mineral, Metallurgy, Material*, 14 (2007) 5, 399–404, doi:10.1016/S1005-8850(07)60079-6
- ⁵ N. Cheung, A. Garcia, The use of a heuristic search technique for the optimization of quality of steel billets produced by continuous casting, *Engineering Applications of Artificial Intelligence*, 14 (2001) 2, 229–238, doi:10.1016/S0952-1976(00)00075-0
- ⁶ N. Cheung, C. A. Santos, J. A. Spim, A. Garcia, Application of a heuristic search technique for the improvement of spray zones cooling conditions in continuously cast steel billets, *Applied Mathematical Modelling*, 30 (2006) 1, 104–115, doi:10.1016/j.apm.2005.03.008
- ⁷ G. O. Tirian, I. Filip, G. Proștean, Adaptive control system for continuous steel casting based on neural networks and fuzzy logic, *Neurocomputing*, 125 (2014), 236–245, doi:10.1016/j.neucom.2012.11.052
- ⁸ M. S. Kulkarni, A. Subash Babu, Managing quality in continuous casting process using product quality model and simulated annealing, *Journal of Materials Processing Technology*, 166 (2005) 2, 294–306, doi:10.1016/j.jmatprotec.2004.09.073
- ⁹ A. Sanz-García, A. V. Pernía-Espinoza, R. Fernández-Martínez, F. J. Martínez-de-Pisón-Ascacibar, Combining genetic algorithms and the finite element method to improve steel industrial processes, *Journal of Applied Logic*, 10 (2012) 4, 298–308, doi:10.1016/j.jal.2012.07.006
- ¹⁰ M. S. Kulkarni, A. S. Babu, Optimization of Continuous Casting Using Simulation, *Materials and Manufacturing Processes*, 20 (2005) 4, 595–606, doi:10.1081/AMP-200041874
- ¹¹ M. Hrelja, S. Klancnik, T. Irgolic, M. Paulic, Z. Jurkovic, J. Balic, M. Brezocnik, Particle swarm optimization approach for modelling a turning process, *Advances in Production Engineering & Management*, 9 (2014) 1, 21–30, doi:10.14743/apem2014.1.173
- ¹² M. Hrelja, S. Klancnik, J. Balic, M. Brezocnik, Modelling of a turning process using the gravitational search algorithm, *International Journal of Simulation Modelling*, 13 (2014) 1, 30–41, doi:10.2507/IJSIMM13(1)3.248
- ¹³ M. Chandrasekaran, D. Devarasiddappa, Artificial neural network modeling for surface roughness prediction in cylindrical grinding of Al-SiCp metal matrix composites and ANOVA analysis, *Advances in Production Engineering & Management*, 9 (2014) 2, 59–70, doi:10.14743/apem2014.2.176
- ¹⁴ X. W. Huang, X. Y. Zhao, X. L. Ma, An improved genetic algorithm for job-shop scheduling problem with process sequence flexibility, *International Journal of Simulation Modelling*, 13 (2014) 4, 510–522, doi:10.2507/IJSIMM13(4)CO20
- ¹⁵ M. Kovačič, B. Jurjovec, L. Krajnc, Ladle nozzle opening and genetic programming, *Mater. Tehnol.*, 48 (2014) 1, 23–26
- ¹⁶ M. Kovačič, B. Šarler, Application of the genetic programming for increasing the soft annealing productivity in steel industry, *Materials and Manufacturing Processes*, 24 (2009) 3, 369–374, doi:10.1080/10426910802679634
- ¹⁷ M. Kovačič, S. Senčič, Modeling of PM10 emission with genetic programming, *Mater. Tehnol.*, 46 (2012) 5, 453–457
- ¹⁸ M. Kovačič, P. Uratnik, M. Brezočnik, R. Turk, Prediction of the bending capability of rolled metal sheet by genetic programming, *Materials and Manufacturing Processes*, 22 (2007) 5, 634–640, doi:10.1080/10426910701323326
- ¹⁹ J. R. Koza, *Genetic programming III*, Morgan Kaufmann, San Francisco 1999

EFFECTS OF VARIOUS HELICALLY ANGLED GRINDING WHEELS ON THE SURFACE ROUGHNESS AND ROUNDNESS IN GRINDING CYLINDRICAL SURFACES

VPLIV RAZLIČNIH KOTOV VIJAČNICE PRI BRUSILNIH KOLUTIH NA HRAPAVOST POVRŠINE IN OKROGLOST PRI BRUŠENJU VALJASTIH POVRŠIN

Muammer Gavas¹, Muammer Kına², Uğur Köklü³

¹Department of Manufacturing Engineering, Dumlupınar University, Kütahya, Turkey

²Istanbul Arel University, Istanbul, Turkey

³Department of Mechanical Engineering, Karamanoglu Mehmetbey University, Karaman, Turkey
ugurkoklu@gmail.com

Prejem rokopisa – received: 2014-04-07; sprejem za objavo – accepted for publication: 2015-01-05

doi:10.17222/mit.2014.065

Grinding is generally used in the final step of machining metallic materials to achieve the necessary surface quality and dimensions. Grinding wheels with flat surfaces are commonly used in the process of grinding. However, due to the fact that there is a great deal of contact length (corresponding to the grinding-wheel width) between the grinding wheel and the workpiece, effective cooling during the grinding process may not be possible and, consequently, the heat in the deformation region is increased. Due to these reasons, some undesired results such as an unqualified surface and a roundness error take place. Various profiles of the grinding wheel were, therefore, proposed to improve the surface quality and decrease the roundness error by modifying the grinding wheel and developing various methods. In this study, AISI 1050, AISI 4140 and AISI 7131 steel materials were subjected to the cylindrical-grinding process using wheels helically grooved at 15 °, 30 ° and 45 ° and the obtained results such as the average surface roughness and roundness errors were compared with the results of the flat-surface grinding wheels. The experimental results show that the surface roughness and roundness error are reduced when using a helically grooved grinding wheel and, thus, the quality of the machined parts is improved.

Keywords: cylindrical grinding, helically grooved grinding wheel, roundness error, surface roughness

Brušenje se navadno uporablja kot končna stopnja obdelave kovinskih materialov za zagotovitev kvalitete površine in mer. Pri postopku brušenja se navadno uporabljajo brusni koloti z ravno površino. Vendar pa je zaradi velike kontakne dolžine (odvisno od širine brusilnega koluta) med brusilnim kolutom in obdelovancem oteženo učinkovito ohlajanje, zato se področje deformacije ogreva. Lahko se pojavijo neželeni rezultati, kot so neustrezna površina in napaka okroglosti. Za izboljšanje kvalitete površine in zmanjšanje napak okroglosti so predlagani modificirani brusilni koloti z različnimi profili in različne metode. V tej študiji so bila jekla AISI 1050, AISI 4140 in AISI 7131 okroglo brušena s koloti z vijačnim utorom 15 °, 30 ° in 45 °. Dobljeni rezultati, kot sta povprečna hrapavost površine in napaka okroglosti, so bili primerjani s tistimi, dobljenimi z brusilnimi koloti z ravno površino. Rezultati kažejo, da se površinska hrapavost in napaka okroglosti zmanjšujeta pri uporabi brusilnih kolotov z vijačnim utorom, torej se kvaliteta strojnih delov izboljša.

Ključne besede: okroglo brušenje, brusni kolot z vijačnim utorom, napaka okroglosti, hrapavost površine

1 INTRODUCTION

A better surface quality and higher efficiency are the prerequisites for today's machining industry in order for it to be more competitive since modern manufacturing processes require shorter production time and higher-precision components.¹ Compared with the other material-removal processes such as turning, milling and boring, the grinding process is more complex and more difficult to control.² Grinding is a finishing process, broadly used in the manufacturing of the components requiring fine tolerances, a good surface finish and a higher dimensional and geometrical accuracy.^{3,4} In spite of all the good results of this finishing process, there are some phenomena that affect the results. These are the chattering and vibration of the machine and workpiece, burning, unacceptable changes in the surface layer, and microcracks and burns that cause surface defects, in-

creasing the surface roughness and other defects. These defects are caused by clamping the workpiece, the course and magnitude of the grinding-wheel wear, and the stiffness of the whole machine-tool/workpiece fixture system.^{5,6}

The effects of a discontinuous workpiece material on the grinding performance were investigated by researchers.^{7,8} To control and improve the grinding performance we would have to manufacture engineered grinding wheels with a desirable topography to optimize the metal-cutting process. One example of such a design is a grooved wheel.⁹ Several studies confirmed that intermittent grinding not only decreases the grinding force, specific energy, surface burn, waviness and temperature but also optimizes the material-removal rate.¹⁰⁻¹² Fan and Miller¹² developed a force model for grinding with segmental wheels. Both experimental and analytical results

show that the average grinding force decreases and the peak force increases due to segmental wheels, as compared to conventional wheels. Larger spaces between the segments further reduce the average force and increase the surface roughness and peak force. Kim et al.¹³, Jin and Meng¹⁴ constructed discontinuous grinding wheels (DGWs) with multi-porous grooves. Their study illustrated that DGWs significantly improved the grinding performance and surface roughness.

Shaji and Radhakrishnan¹⁵ used slotted wheels with graphite integrated into the slots. Three such wheels were developed with a varying number of the slots for lubricant sandwiching. The results showed that the surface roughness and residual stress were lower in the case of the graphite-slotted wheels. The results of the experiments with helically grooved wheels grinding four different materials were reported by Gavas et al.⁵ Their study illustrated that the ground-surface roughness decreased for some materials in comparison to the conventional grinding. The roundness slightly increased for brass and AISI 1010, but did not change for the AISI 1040 and AISI 2080 steels. Zhang¹⁶ conducted helical scan grinding (HSG) on brittle materials such as ceramics and glass, and ductile materials such as steel. The experimental results showed that HSG not only improved the ground-surface finish, but also decreased the adhesion of the workpiece material to the cutting grits in the grinding of tough materials such as stainless steel SUS304, and the fracture area in the grinding of brittle materials such as ceramics.

Zhang and Uematsu¹⁷ analytically studied this topic to find the difference in the surface-generation mechanism between HSG and traverse grinding, and they proposed models for predicting the surface roughness in HSG. Both the experimental results and analysis show that the ground-surface roughness decreases with the helix angle and reaches the limiting surface-roughness value at the critical helix angle, which is dependent on the speed ratio. The HSG method is more effective in improving the ground-surface roughness for large and/or coarse wheels than for small and/or fine wheels. Recently, Nguyen and Zhang¹⁸ investigated the performance of a segmented-grinding-wheel system and succeeded to maintain the sharpness of the active cutting edges while minimizing the ploughing and rubbing deformations of ground workpieces.

Using the intermittent grinding wheels, the characteristics of the grinding force, temperature, surface roughness and geometric error were evaluated by Kwak and Ha.¹⁹ With the results of the experiments with conventional and intermittent wheels, it was proven that the intermittent wheel appeared to be superior in various aspects such as the grinding force, the temperature and the geometric error, showing little deterioration of the surface roughness. Tawakoli and Azarhoushang²⁰ investigated the feasibility of intermittent grinding with a segmented wheel, using two ceramic-matrix composite ma-

terials. The grinding forces, surface roughness, surface profile, elastic deformation and tool wear were compared when grinding the ceramic-matrix composites with segmented and normal diamond wheels. The finer surface roughness obtained with the conventional grinding, compared to the intermittent grinding with a T-tool wheel, was due to a higher number of active cutting edges and more rubbing in the process.

In this paper, the results of the grinding experiments with helically grooved wheels used on three materials are presented and compared with those obtained with the conventional method. The grinding experiments were conducted on the AISI 1050, AISI 4140 and AISI 7131 steel materials, with three helically grooved grinding wheels. The surface roughness and roundness were studied as the performance criteria and better results were achieved when using the wheels helically grooved at 15 ° and 30 ° than a flat-surface wheel.

2 EXPERIMENTAL PROCEDURE

2.1 Preparation of helically grooved grinding wheels

The grinding tests were performed on a horizontal spindle-type cylindrical-grinding machine with four aluminum-oxide grinding wheels. All the wheels used in the experiments had the same specifications. However, one of the grinding wheels had a flat surface. This type is called the flat-surface grinding wheel (FSGW). The other grinding wheels with different helix angles were manufactured for this study. These types are called helically grooved grinding wheels with angles of 15 ° (HGGW 15 °), 30 ° (HGGW 30 °), and 45 ° (HGGW 45 °).

Figure 1 shows schematic drawings of the dimensions of

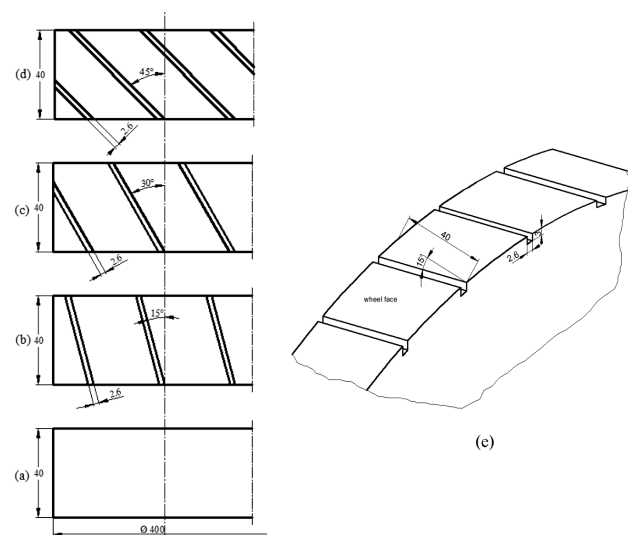


Figure 1: Dimensions of the grinding wheels: a) FSGW, b) HGGW 15 °, c) HGGW 30 ° and d) HGGW 45 ° (dimensions in millimeters), e) isometric perspective of HGGW 15 °

Slika 1: Dimenzije brusnih kolutov: a) FSGW, b) HGGW 15 °, c) HGGW 30 ° in d) HGGW 45 ° (dimenzije v milimetrih), e) izometrična perspektiva HGGW 15 °

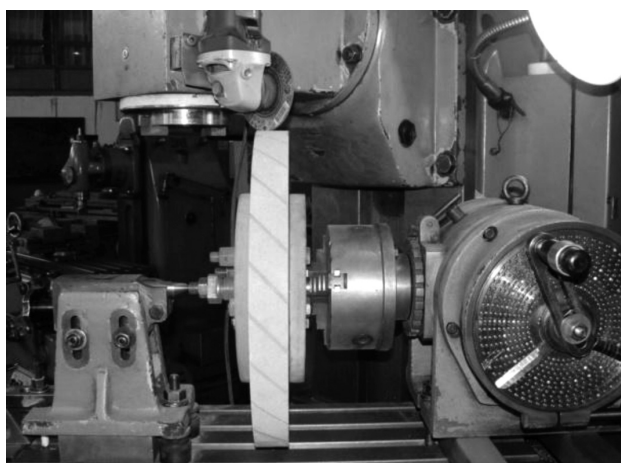


Figure 2: Forming of helical grooves on a grinding wheel with a cut-off disc

Slika 2: Izdelava vijačnega utora na brusnem kolutu z rezalno ploščico

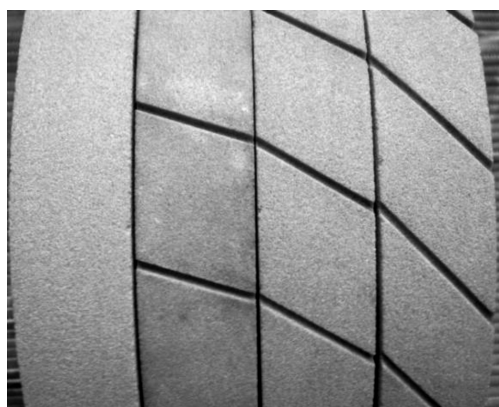


Figure 3: Photograph of FSGW and HGGWs

Slika 3: Posnetek FSGW in HGGW

the conventional grinding wheel and helically grooved grinding wheels (HGGWs).

The helical grooves at the angles of 15 °, 30 °, and 45 ° on the circumference of the grinding wheels were cut in with a universal milling machine using a cut-off disc in the angle grinder. The HGGWs were made by cutting radial grooves with a helical profile. These grinding wheels consisted of 24 equal grooves on the circumference of a grinding wheel. The width and depth of each groove was 2.6 mm and 3 mm, respectively. The forming of the helical grooves on a grinding wheel with a cut-off disc is shown in **Figure 2**. FSGW and HGGWs with different helix angles are shown in **Figure 3**.²¹

2.2 Materials, grinding parameters and the measurement procedure

The materials used in this study were AISI 1050, AISI 4140, and AISI 7131; the chemical compositions and hardness values of the materials are listed in **Table 1** and the dimensions of the workpieces are shown in **Figure 4**. Grinding-test bar specimens with a diameter 39 mm and length 170 mm were prepared by turning them directly from the as-received materials.

The grinding conditions and dimensions of the specimens were the same for both methods. In the grinding experiments, a horizontal spindle-type cylindrical-grinding machine with aluminum-oxide grinding wheels with dimensions of 400 mm × 40 mm × 127 mm and a constant wheel speed of 1570 r/min was used. Furthermore, these elements were common. 60-K-6-V indicates a wheel grain size of 60, hardness K, structure 6 and a vitrified bond. The selection was based on a wide industrial application of grinding wheels. Before each grinding experiment, the grinding wheel was dressed using a single-point diamond dresser to produce a sharp, clean wheel surface. During the grinding process, a water-soluble metalworking fluid diluted to 1 : 5 was supplied to the grinding zone, and the coolant flow rate from the outlet was 8 L/min. During all the experiments, the

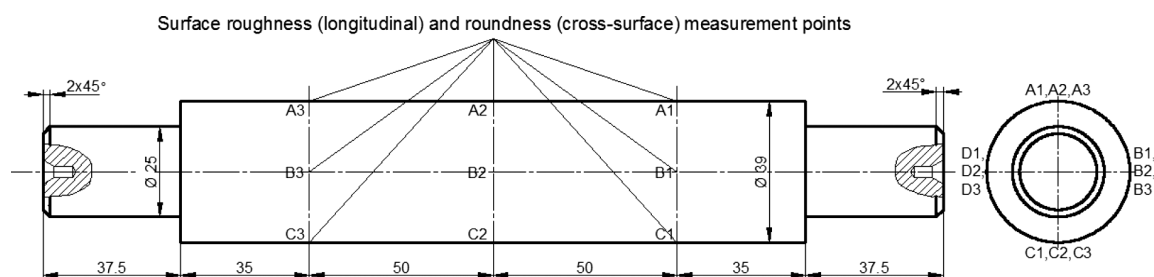


Figure 4: Dimensions and measurement points for the surface roughness and roundness of a grinding workpiece used in the experiments

Slika 4: Dimenzije in točke merjenja hrapavosti površine in okroglosti na obdelovancu, uporabljenem pri preizkusih

Table 1: Chemical compositions (w/%) and hardness of the materials used in the experiment

Tabela 1: Kemijske sestave (w/%) in trdote materialov, uporabljenih pri preizkusih

Materials	C	Si	Mn	P	S	Cr	Mo	Hardness (HRB)
AISI 1050	0.47–0.55	0.15–0.35	0.60–0.90	0.04	0.05	–	–	96
AISI 4140	0.35–0.44	0.15–0.40	0.60–0.90	0.035	0.035	0.80–1.10	–	99
AISI 7131	0.14–0.19	0.15–0.40	1.00–1.30	0.035	0.035	0.80–1.10	0.15–0.25	115

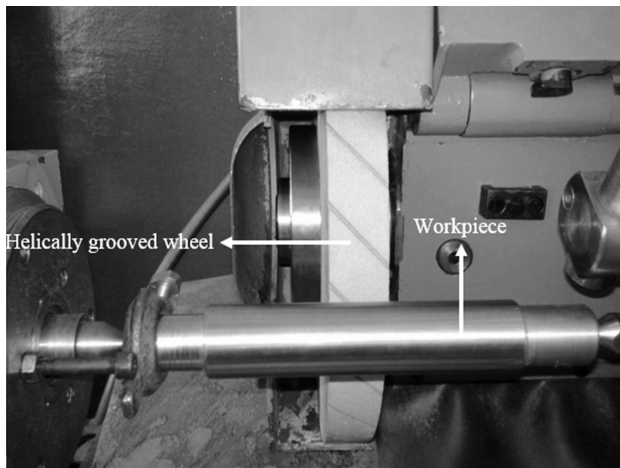


Figure 5: Experimental set-up
Slika 5: Eksperimentalni sestav

grinding length (170 mm), workpiece diameter (39 mm), depth of cut (10 μm) and feed rate (1.57 mm/r) were used. In addition, each work material was ground for 5 min before measuring the surface roughness and roundness error. The experimental set-up is shown in Figure 5.

The measurement points for the surface roughness and waviness of the work material are shown in Figure 4. Each test specimen was measured on 12 different points (A1, A2, A3), (B1, B2, B3), (C1, C2, C3), and (D1, D2, D3) for the surface roughness. For the roundness, each test specimen was measured on three points (1, 2, and 3). In this study, the surface roughness (R_a , the arithmetic average) of each machined workpiece was measured using a surface roughness tester (Mahr Perthen) with a 4 mm cut-off length. In addition, a recorder that transfers the obtained values onto a graphic was also used. The roundness was measured with a round test instrument (Mitutoyo RA-114) in the same locations.

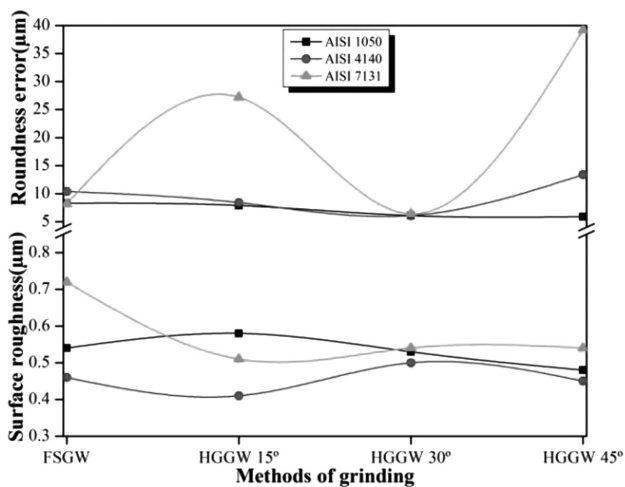


Figure 6: Ground surface roughness and roundness for FSGW and HGGWs

Slika 6: Brušena površinska hrapavost in okroglost pri FSGW in HGGW

3 RESULTS AND DISCUSSION

The experimental results for the surface roughness of three steels at the same grinding conditions using both FSGW and HGGWs are shown in Figure 6. Each surface-roughness value was obtained by averaging 12 measurements. One of these 12 measurements was used to represent the surface roughness of the ground part. It is obvious that both the material type and the grinding method have an effect on the surface roughness. The highest surface roughness was obtained for the AISI 7131 steel ground with FSGW. The effect of the material type on the surface roughness is often attributed to the difference in the hardness of different materials.⁵

Generally, the surface roughness obtained with HGGWs is better than that obtained with FSGW. It is apparent that HGGW 45° gives better surface finishes of the three steels than FSGW. As the grooves on the circumference of a grinding wheel decrease the grinding force, temperature¹⁵ and contact length between the workpiece and the grinding wheel, and enough cutting fluid is being delivered to the wheel-workpiece interface,¹³ it is, consequently, expected that HGGWs are better in terms of the ground-surface quality.^{21,22}

Figures 6 and 7 show a comparison of the roundness of the ground workpieces produced with FSGW and HGGWs under the same grinding conditions. It is obvious that both the material type and the grinding method have an effect on the roundness. Generally, the roundness obtained with HGGWs is better than that obtained with FSGW. When the roundness values obtained

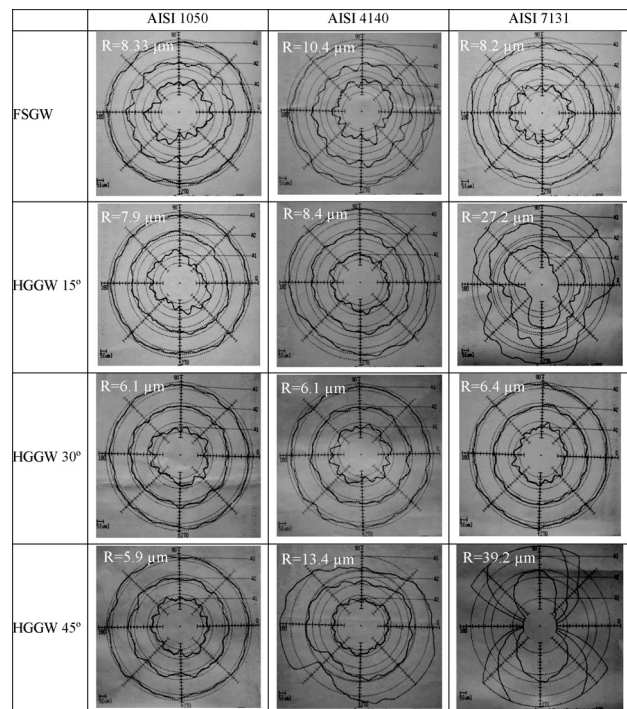


Figure 7: Profiles of the ground surfaces produced with FSGW and HGGWs

Slika 7: Profil brušenih površin pri FSGW in HGGW

with FSGW and HGGWs are compared, it is clearly seen that the roundness error increased for the AISI 7131 steel, while the AISI 1050 and AISI 4140 steels behave in an identical manner during the grinding in view of the roundness error. For comparison, the roundness values of the three steels ground in the FSGW and HGGW processes are shown in **Figure 7**. Among the HGGWs, HGGW 30 ° seemed to generate the lowest roundness. Consequently, the grinding with helically grooved wheels (HGGW 15 ° and HGGW 30 °) increases the roundness quality, while the AISI 7131 steel showed conflicting behavior, namely, the roundness increased for the this material.

The AISI 7131 steel and HGGW 45 ° showed unexpected behavior; namely, the surface roughness and roundness increased for this material. This is explained with the segmentation of the grinding wheel, reducing the number of static and kinematic cutting edges and, hence, the rubbing regime, which is one of the important mechanisms for improving the surface roughness. Additionally, the uncut-chip thickness increases with the decrease in the kinematic cutting edges. Tawakoli and Azarhoushang²⁰ suggested the following relation (Equation (1)) involving R_t (the distance between the highest peak and the deepest valley of the profile of the total evaluation length or, in other words, the total height of the profile) and the uncut-chip thickness h_{cu} :

$$R_t \propto \frac{h_{cu}^{4/3}}{a_e^{1/3}} \approx \left(\frac{v_{ft}}{v_c} \frac{1}{C_{kin} r \sqrt{d_s}} \right)^{2/3} \quad (1)$$

where h_{cu} is the uncut-chip thickness, a_e is the depth of cut, v_{ft} is the feed speed, v_c is the cutting speed, d_s is the wheel diameter, r is the grain-cutting-point shape factor, and C_{kin} is the kinematic cutting-edge density.

4 CONCLUSIONS

In this study, grinding operations of a flat-surface wheel and helically grooved wheels were performed on three different steels (AISI 1050, AISI 4140 and AISI 7131) under the same grinding conditions, except for the grinding-wheel profile. The surface roughness and roundness obtained from these processes were demonstrated. Both the material type and the grinding method have an effect on the surface roughness and roundness. The experimental results show that, generally, the surface roughness and roundness obtained with a helically grooved grinding wheel are better than in the case of conventional grinding. Additionally, among the helically grooved wheels, HGGW 30 ° seemed to generate a lower roundness than the other two HGGWs and FSGW. Consequently, grinding with helically grooved wheels (HGGW 15 ° and HGGW 30 °) increased the surface roughness and roundness, while the AISI 7131 steel showed conflicting behavior, namely, the roundness of this material was increased.

5 REFERENCES

- M. Ubartas, V. Ostaševičius, S. Samper, V. Jūrėnas, R. Daukševičius, Experimental investigation of vibrational drilling, *Mechanika*, 17 (2011) 4, 368–373, doi:10.5755/j01.mech.17.4.563
- X. Tian, J. P. Huissoon, Q. Xu, B. Peng, Dimensional error analysis and its intelligent pre-compensation in cnc grinding, *International Journal of Advanced Manufacturing Technology*, 36 (2008) 1–2, 28–33, doi:10.1007/s00170-006-0813-y
- M. Chandrasekaran, M. Muralidhar, C. M. Krishna, U. S. Dixit, Application of soft computing techniques in machining performance prediction and optimization: a literature review, *International Journal of Advanced Manufacturing Technology*, 46 (2010) 5–8, 445–464, doi:10.1007/s00170-009-2104-x
- P. L. Tso, S. Y. Yang, The compensation of geometrical errors on forming grinding, *Journal of Materials Processing Technology*, 73 (1998) 1–3, 82–88, doi:10.1016/S0924-0136(97)00216-1
- M. Gavas, İ. Karacan, E. Kaya, A novel method to improve surface quality in cylindrical grinding, *Experimental Techniques*, 35 (2011) 1, 26–32, doi:10.1111/j.1747-1567.2009.00575.x
- F. Holesovsky, M. Hrala, Integrity of ground cylindrical surface, *Journal of Materials Processing Technology*, 153–154 (1999), 714–721, doi:10.1016/j.jmatprotec.2004.04.180
- U. Köklü, Optimisation of machining parameters in interrupted cylindrical grinding using the Grey-based Taguchi method, *International Journal of Computer Integrated Manufacturing*, 26 (2013) 8, 696–702, doi:10.1080/0951192X.2012.749537
- M. Kurt, U. Köklü, Minimization of the shape error in the interrupted grinding process by using Taguchi method, *Mechanika*, 18 (2012) 6, 677–682, doi:10.5755/j01.mech.18.6.3163
- J. F. G. Oliveira, A. C. Bottene, T. V. França, A novel dressing technique for texturing of ground surfaces, *CIRP Annals – Manufacturing Technology*, 59 (2010), 361–364, doi:10.1016/j.cirp.2010.03.119
- K. Nakayama, J. Takagi, T. Abe, Grinding wheel with helical grooves – an attempt to improve the grinding performance, *CIRP Annals – Manufacturing Technology*, 25 (1977) 1, 133–138
- K. W. Lee, P. K. Wong, J. H. Zhang, Study on the grinding of advanced ceramics with slotted diamond wheels, *Journal of Materials Processing Technology*, 100 (2000) 1–3, 230–235, doi:10.1016/S0924-0136(00)00403-9
- X. Fan, M. H. Miller, Force analysis for grinding with segmental wheels, *Machining Science and Technology*, 10 (2006) 4, 435–455, doi:10.1080/10910340600996142
- J. D. Kim, Y. H. Kang, D. X. Jin, Y. S. Lee, Development of discontinuous grinding wheel with multi-porous grooves, *International Journal of Machine Tools and Manufacture*, 37 (1997) 11, 1611–1624, doi:10.1016/S0890-6955(97)00005-9
- D. X. Jin, Z. Meng, Research for discontinuous grinding wheel with multi porous grooves, *Key Engineering Materials*, 259–260 (2004), 117–121, doi:10.4028/www.scientific.net/KEM.259-260.117
- S. Shaji, V. Radhakrishnan, Application of solid lubricants in grinding: investigations on graphite sandwiched grinding wheels, *Machining Science and Technology*, 7 (2003) 1, 137–155, doi:10.1081/MST-120018959
- B. Zhang, Helical scan grinding of brittle and ductile materials, *Journal of Materials Processing Technology*, 91 (1999) 1–3, 196–205, doi:10.1016/S0924-0136(98)00420-8
- B. Zhang, T. Uematsu, Surface generation mechanism in helical scan grinding: an analytical study, *Journal of Materials Processing Technology*, 91 (1999) 1–3, 206–214, doi:10.1016/S0924-0136(98)00415-4
- T. Nguyen, L. C. Zhang, Performance of a new segmented grinding wheel system, *International Journal of Machine Tools & Manufacture*, 49 (2009) 3–4, 291–296, doi:10.1016/j.ijmactools.2008.10.015
- J. S. Kwak, M. K. Ha, Force modelling and machining characteristics of the intermittent grinding wheels, *KSME International Journal*, 15 (2001) 3, 351–356

- ²⁰ T. Tawakoli, B. Azarhoushang, Intermittent grinding of ceramic matrix composites (CMCs) utilizing a developed segmented wheel, *International Journal of Machine Tools & Manufacture*, 51 (2011) 2, 112–119, doi:10.1016/j.ijmachtools.2010.11.002
- ²¹ M. Kına, Effect of Various Helical Angled Grinding Wheel to Surface Roughness and Roundness in Grinding of Cylindrical Surfaces, MSc Thesis, Kutahya, 2011
- ²² U. Köklü, Grinding with helically grooved wheels, *Proceedings of the Institution of Mechanical Engineers, Part E: Journal of Process Mechanical Engineering*, 228 (2014) 1, 33–42, doi:10.1177/0954408912470775

CHARACTERIZATION OF CAST-IRON GRADIENT CASTINGS

KARAKTERIZACIJA LITOŽELEZNEGA GRADIENTNEGA ULITKA

Danijel Mitrović¹, Primož Mrvar², Mitja Petrič²

¹Livar d.d., Slovenska cesta 43, 1295 Ivančna Gorica, Slovenia

²Department of Materials and Metallurgy, Faculty of Natural Sciences and Engineering, University of Ljubljana, Aškerčeva 12, 1000 Ljubljana, Slovenia

Danijel.Mitrovic@livar.si, Primoz.Mrvar@omm.ntf.uni-lj.si, Mitja.Petric@omm.ntf.uni-lj.si

Prejem rokopisa – received: 2014-07-07; sprejem za objavo – accepted for publication: 2014-12-08

doi:10.17222/mit.2014.102

This work deals with the topic of composed castings, also called gradient castings. The characterization of the microstructures and the subsequently monitored mechanical properties of the composite castings are discussed. The production technology is a combination of the horizontal centrifugal casting of alloyed white cast iron followed by an intermediate layer of flake grey cast iron and gravity casting of the core, which occurs in the third sequence. The core was made of spheroidal grey cast iron. The research was focused on the intermediate layer and a metallographic analysis of the intermediate layer, which is crucial for the defects and the lifetime of rolls.

The TCW program was used for the thermodynamic calculations of equilibrium phases in order to prove that the phases present in the microstructures were determined with light and scanning electron microscopy (SEM). Dilatometry in the solid state was done for all three layers to study the behavior of composed rolls during the thermal loading. The densities of microstructural constituents were calculated with the TAPP 2.2 software to explain the distribution of the phases in the intermediate layer. Additionally, the linear hardness and the tensile strength at room and higher temperatures were measured.

Keywords: composite casting, centrifugal casting, gravity casting, intermediate layer, microstructure

V predstavljenem delu smo opredelili in karakterizirali mikrostrukturne sestavine ter spremljali mehanske lastnosti kompozitnega ulitka. Tehnologija izdelave je kombinacija horizontalnega in centrifugalnega litja legirane bele litine in kasneje sive litine (dve sekvenci) ter gravitacijskega litja jedra, ki se pojavi v tretji sekvenci. Jedro je izdelano iz sive litine s kroglastim grafitom. Raziskava je bila usmerjena na vmesno plast, ki je ulita iz sive litine z lamelnim grafitom in je ključnega pomena za pojav napak na valjih oziroma za trajnostno dobo valjev.

Uporabili smo naslednje preiskovalne metode: program TCW za termodinamični izračun faznih ravnotežnih faz v povezavi s svetlobno in elektronsko mikroskopijo, dilatometrijo v trdnem stanju za ugotavljanje razlik pri krčenju in širjenju vseh plasti, izračun gostot mikrostrukturnih komponent s programom TAPP 2.2 za določevanje razporeditve karbidov med strjevanjem, linearne meritve trdot ter natezne trdnosti pri sobni in povišanih temperaturah.

Ključne besede: kompozitni ulitek, centrifugalno litje, gravitacijsko litje, vmesna plast, mikrostruktura

1 INTRODUCTION

Centrifugal pouring technology is a casting process, where metal can be poured and solidified in a rotating permanent mold under the influence of the centrifugal force.¹ The direction of solidification in the centrifugal process differs from that in the sand casting. Due to a rapid transfer of heat to the permanent mold, crystallization starts on the outer surface of the casting and progresses towards the inside. The result is a fine-grained surface crust. Further solidification towards the interior takes place with the growth of dendrite crystals.² Dendrites can have an equiaxed or columnar shape, depending on the thermal gradient during the solidification.³

A cast roll can be produced as a gradient casting composed of a hard steel shell as the working layer and a tough core. The microstructure of the working layer of a roll after the solidification depends on the chemical composition of the alloy. The main microstructural constituent is austenite (γ) that solidified in the form of dendrites, followed by a eutectic, which consists of austenite and carbides.⁴ The type of the carbides is determined by the chemical composition. Usually the

alloys for rolls are alloyed with Cr, Ni, W, Mo and V.^{5,6} For a chromium-white-cast-iron working layer, it is desirable to have as little as possible of the retained austenite in the matrix and no pearlite phase in the microstructure.

In the as-cast state, the matrix contains a substantial proportion of the residual austenite (30–60 %) that has to decompose with a single or multistage heat treatment in order to achieve the required microstructure, containing small and evenly distributed $M_{23}C_6$ type carbides in the α -metallic matrix.⁷ Due to their high hardness and uniform distribution in the matrix, secondary carbides are of a great importance for the wear resistance. The target mechanical properties are obtained with the heat treatment, where a casting is heated to the austenitizing temperature and control cooled to room temperature. Such a treatment allows a good control over the segregation of the secondary carbides in a temperature range from 800 °C to 1050 °C.

Rolls can be produced by forging or by casting. Cast rolls are often produced as gradient castings made of more than one material. The outer layer of a casting, or

Table 1: Chemical analysis of a gradient casting (w%)**Tabela 1:** Kemijska analiza gradientnega ulitka (w%)

	C	Si	Mn	P	S	Cr	Ni	Mo	Mg	Cu	Sn	Al	V	Ti	W	Co	Fe
Working layer	2.799	0.703	0.965	0.030	0.037	16.681	1.433	1.154	0.003	0.081	0.000	0.0000	0.296	0.000	0.000	0.000	75.818
Intermediate layer	3.118	1.034	0.342	0.026	0.010	0.129	0.247	0.029	0.000	0.039	0.005	0.0013	0.012	0.006	0.009	0.018	94.965
Core	3.002	2.734	0.366	0.031	0.007	0.131	0.247	0.029	0.099	0.039	0.007	0.0229	0.013	0.007	0.009	0.017	93.198

the working layer, made with horizontal centrifugal casting, is followed by a centrifugally cast intermediate layer and the final layer is the gravity-cast core made of spheroidal cast iron. The working layer is often made of chromium white cast iron to achieve the hardness and wear resistance. The intermediate layer is a sort of grey cast iron, creating a good bond between the working layer and the core; and the core is made of nodular cast iron to obtain ductility during the casting.^{8,9} The bonding between the working layer and the core is important since poor bonding can cause bond-related spalls.¹⁰

The aim of the paper is to describe the formation and types of the carbides in the intermediate layer and the bonding between the working layer and the core. The bonding is crucial for the defects and lifetime of a roll. Also, the mechanical properties across the cross-section are determined and the mechanism of a possible crack formation is explained.

2 EXPERIMENTAL WORK

The analyses were carried out on the samples taken from the working layer, the intermediate layer and the core. Light microscopy, scanning electron microscopy (SEM) with an EDS analysis, tensile tests at various temperatures, hardness measurements and a dilatometric analysis were carried out. The densities of the solidified phases were calculated with the TAPP 2.2 program and

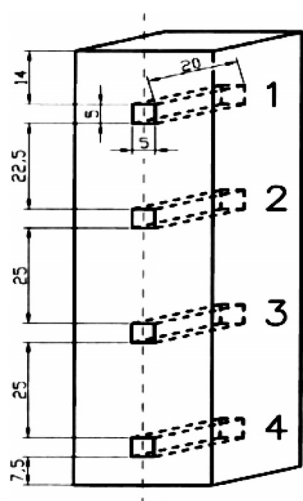


Figure 1: Presentation of the sampling for a dilatometric analysis (sample 1 – working layer, sample 2 – working layer, sample 3 – intermediate layer, sample 4 – core)

Slika 1: Predstavitev vzorčenja za dilatometriko analizo (vzorec 1 – delovna plast, vzorec 2 – delovna plast, vzorec 3 – vmesna plast, vzorec 4 – jedro)

the thermodynamic-phase equilibrium calculations were performed with the Thermo-Calc software.

The analyses were carried out on the samples taken from the working layer, the intermediate layer and the core, at a depth of approximately 80 mm into the roll. Metallographic samples were taken from all three layers and metallographically prepared by grinding, polishing and etching with 2 % Nital. The samples for the tensile tests were taken from the working layer in the longitudinal direction of a roll. The test pieces had round cross-sections with a diameter of 10 mm. The test pieces for dilatometric analyses were taken from all three layers of a roll as indicated in **Figure 1**. The test pieces had dimensions of 5 mm × 5 mm × 20 mm. The dilatometric analyses were carried out at a heating rate of 20 K/s, up to 1100 °C, at which the samples were held for 5 min and then cooled at the same rate to 400 °C.

The microstructure was analyzed with light microscopy using an Olympus BX61 microscope and with scanning electron microscopy using a JEOL JSM-5600 electron microscope equipped with EDS. The tensile tests at elevated temperatures were carried out according to the EN ISO 6892 standard, using an Instron 1255 machine at room temperature and at (300, 400, 500, 600, 700 and 800) °C. Rockwell-hardness measurements were performed using an Instron Tukon 2100 B machine and a dilatometric analysis performed by a BÄHR DIL 801 instrument, on the area from the surface of a roll up to 80 mm into the depth of the roll, every 2–5 mm. The densities of the solidified microstructural phases were calculated with the TAPP 2.2 program and the thermodynamic-phase equilibrium calculations were performed with the Thermo-Calc software.

Chemical compositions of all three layers are presented in **Table 1**.

3 RESULTS AND DISCUSSION

Figure 2 presents the boundary area of the working layer, the intermediate layer and the core. The microstructure of the working layer consists of austenite and carbides since the alloy is rich in chromium and molybdenum. The intermediate layer, which merges with the core, is highly rich in M_7C_3 carbides. During the first stage of the solidification of the intermediate layer, the formation of primary austenite crystals occurs in the liquid melt, which, due to the centrifugal force and the density higher than the rest of the melt, starts to move in the direction of the working layer. The melt of the intermediate layer re-melts and merges with a thin layer

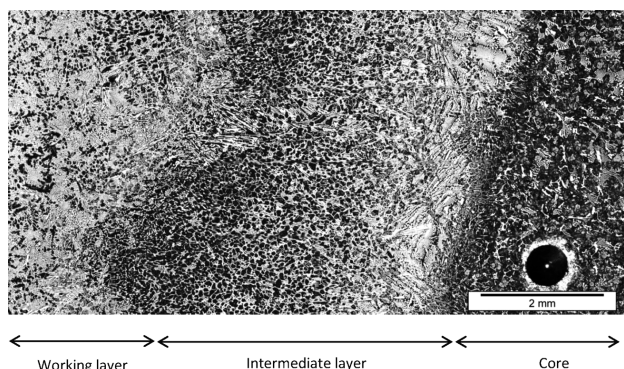


Figure 2: Macrostructure of the working layer, the intermediate layer and the core

Slika 2: Makroposnetek delovne plasti, vmesne plasti in jedra

of the working layer and some carbide-promoting elements, especially chromium, dissolve in the intermediate melt, causing the formation of carbide sand due to a lower density in comparison with γ , deposited at the interface of the intermediate layer and the core. A large amount of carbides can be clearly seen on **Figure 2**. A sufficient solidification interval and lower cooling rates cause an intermediate layer stratified in this way, which is an undesirable microstructure. The carbides that are not evenly dispersed in the metal matrix represent the brittle layer of the casting.

Figure 3 shows the isopleth phase diagram of the working-layer material. The solidification starts with the solidification of austenite, followed by a eutectic reaction with the solidification of the M_7C_3 type carbides between 1260 °C and 1230 °C. The precipitation of the $M_{23}C_6$ type carbides takes place at 820 °C.

Figure 4a shows a SEM microphotograph of the working layer, where the large particles are the carbides that solidified during the eutectic reactions. The EDS

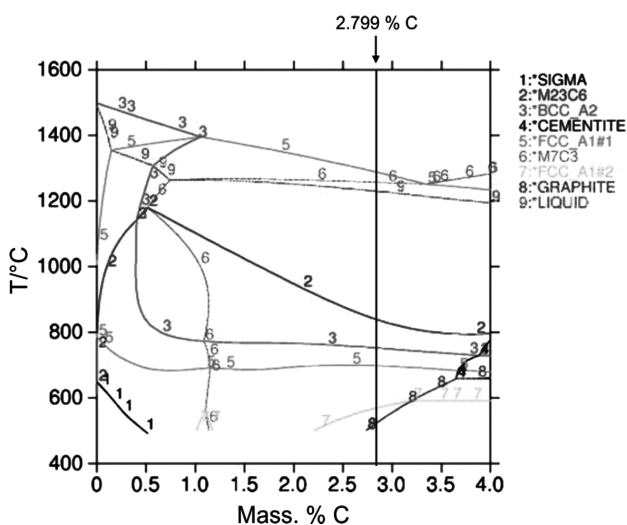


Figure 3: Isopleth phase diagram of the working layer with marked chemical composition

Slika 3: Izopletni fazni diagram delovne plasti z označeno kemijsko sestavo

analysis shows that this phase includes the M_7C_3 type carbides. Smaller particles in the matrix are the $M_{23}C_6$ type carbides that precipitated in the solid state from the solid solution of austenite. According to Vitry et al.⁶ the M_7C_3 and $M_{23}C_6$ type carbides should be chromium carbides, but from the EDS analyses it is clear that these carbides are mainly chromium and iron carbides with some small amounts of V and Mo. The types of carbides are the same as predicted by the thermodynamic calculations from **Figure 3**. It is clear that practically the whole austenite was transformed into martensite during the heat treatment. The intermediate layer also contains carbides, determined with the EDS analysis to be of the M_7C_3 type, as seen on **Figure 4b**. There is a small amount of smaller particles of secondary carbides $M_{23}C_6$ distributed

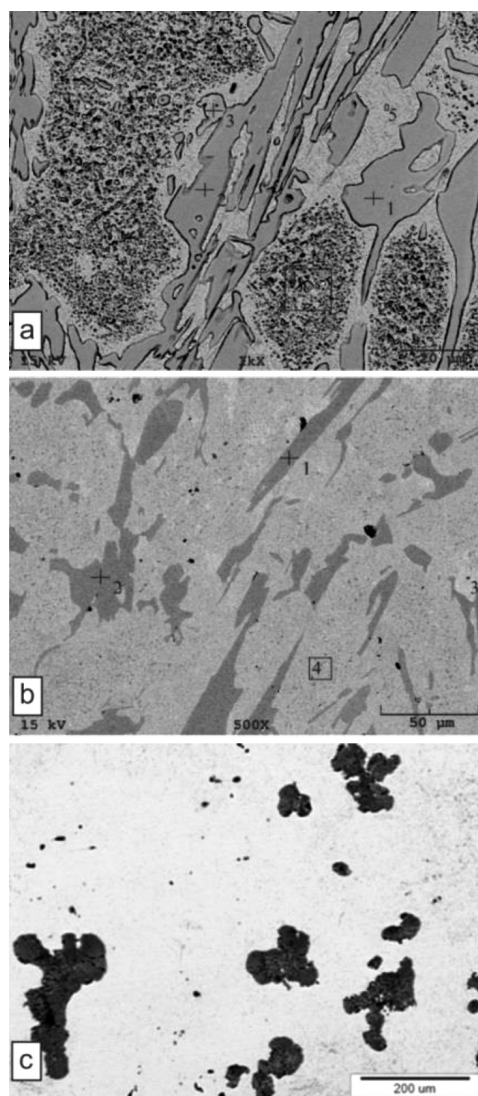


Figure 4: Microstructures of all three layers: a) SEM microphotograph of working layer, b) SEM microphotograph of intermediate layer and c) light microphotograph of core

Slika 4: Mikrostrukture vseh treh plasti: a) SEM-mikroskopija delovne plasti, b) SEM-mikroskopija vmesne plasti ter c) svetlobna mikroskopija jedra

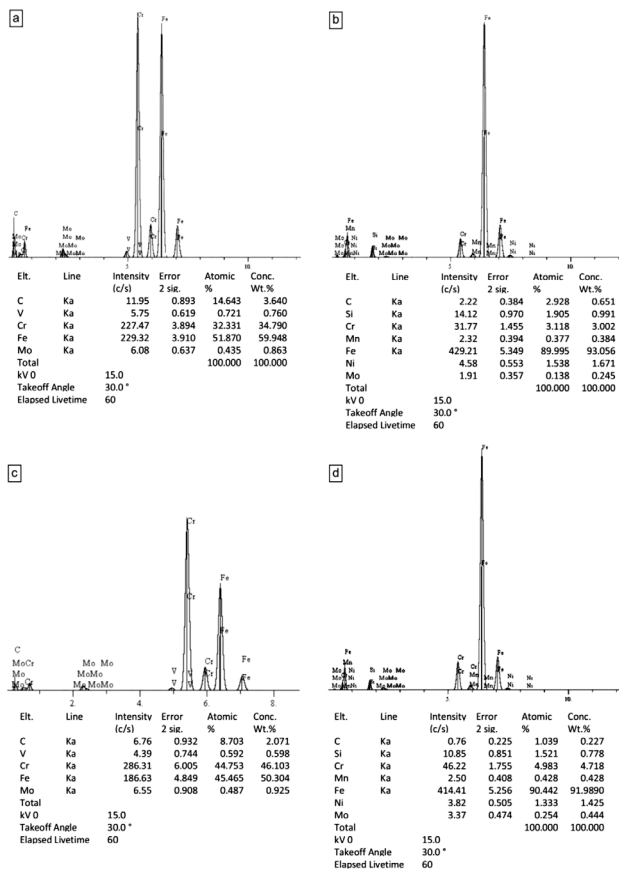


Figure 5: EDS spectra of phases: a) M₇C₃ carbide, spot 1 on Figure 4b, b) martensite, spot 3 on Figure 4b, c) carbides M₂₃C₆, spot 6 on Figure 4a and d) martensite with carbide M₂₃C₆, spot 4 on Figure 4b

Slika 5: EDS-spektri faz: a) M₇C₃ karbida, območje 1 na sliki 4b, b) martenzit, območje 3 na sliki 4b, c) karbid M₂₃C₆, območje 6 na sliki 4a ter d) martenzit s karbidi M₂₃C₆, območje 3 na sliki 4b

in the martensite matrix; this amount is much lower since the concentration of the carbide-promoting elements is much lower than in the working layer. Figure 4c shows a light microphotograph of the core in the polished state, where graphite can be seen in the iron matrix. Graphite is expected to be in the nodule-like form, but here this is not the case, probably due to an insufficient Mg-treatment and a burn-off of Mg during the long solidification time of the core.

Figure 5 presents EDS spectra of the analyzed microstructural constituents marked on Figures 4a and 4b.

With the help of the TAPP 2.2 program, the densities of the eutectic M₇C₃ carbides and austenite at the reference solidification temperature were calculated. The density of carbides M₇C₃ at the temperature of precipitation is 6.738 kg/dm³; austenite has a density of a 6.99 kg/dm³ at the temperature of precipitation. Given the relative differences in the density between the austenite, the carbides and the melt in the solidification stage of the intermediate layer, it seems that the stratification of both microstructural ingredients takes place. In the first stage,

austenite dendrites appear and they are pushed by the centrifugal forces and a higher density in the direction towards the working layer. When the temperature of the remaining melt falls within the scope of the eutectic solidification, leading to the development of a nucleation and growth of the carbides they are pushed in the direction of the interface between the intermediate layer and the core since the carbides have a lower density than the austenite. The difference in the density between the austenite and carbides is only 0.3 kg/dm³, but it is much more significant at a centrifugal force of 120 G leading to an inhomogeneous microstructure development.

Rockwell-hardness measurements were carried out in the area between the surface of the casting and the depth of 80 mm. Figure 6a presents the hardness of the working layer, which is around 61 HRC up to the depth of 60 mm where the intermediate layer starts. In this layer the hardness starts to descend and continues to descend in the core too where it drops to only 32 HRC.

The tensile tests (Figure 6b) of the working layer at different temperatures show that the tensile strength is lowered by about 10 % at 400 °C and, at higher temperatures, it declines even faster and reaches only 200 MPa at 700 °C. This means that the working layer has a tendency to form cracks during the cooling of the casting,

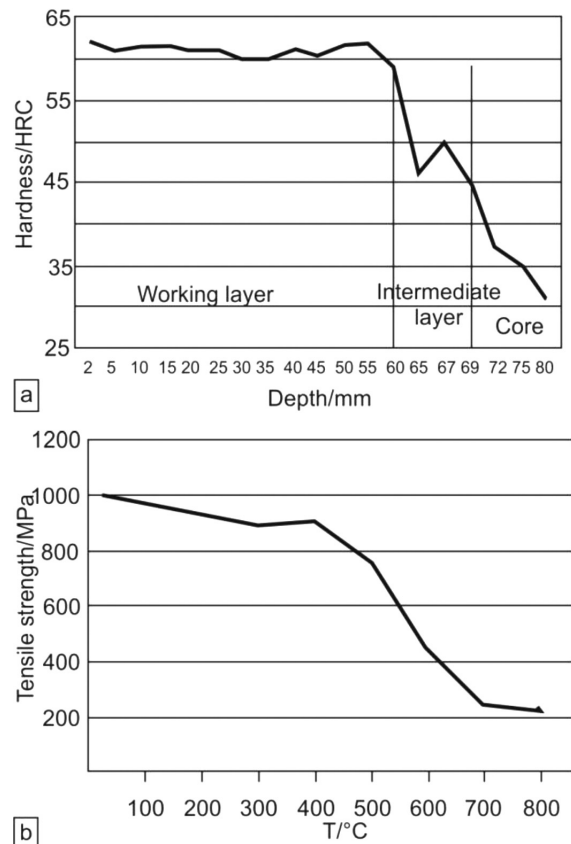


Figure 6: Mechanical properties: a) hardness and b) tensile strength at different temperatures

Slika 6: Mehanske lastnosti: a) trdota ter b) natezna trdnost pri različnih temperaturah

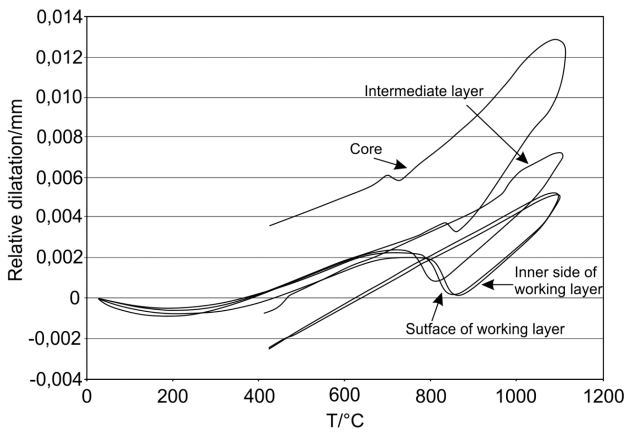


Figure 7: Dilatation curves of the samples at different layers
Slika 7: Dilatacijske krivulje vzorcev razliĉnih plasti

since the core has a much higher temperature, causing the tensile stresses in the working layer.

Figure 7 presents a dilatometric analysis of four samples, two from the working layer, one from the intermediate layer and one from the core. We can see that the working layer has the lowest dilatation in the temperature range from room temperature to up to 1100 °C. The intermediate layer has a slightly higher dilatation at the highest temperature, but the core has the highest dilatation. These differences in dilatation cause high internal stresses during the cooling of the gradient casting. It is clear that when the casting is being cooled from the surface side, the working layer is shrinking faster than the core, which causes the tensile stresses in the working layer and these might lead to a crack formation. A similar situation takes place during the heat treatment, where the whole casting is heated to the austenitizing temperature and the core expands more than the working layer, causing tensile stresses again. On **Figure 7** we can see that the quantitative difference in dilatation of the samples is 0.055 mm at 1000 °C which is not an insignificant value.

4 CONCLUSIONS

The solidification of three different layers was determined in the present work. It is clear that the intermediate layer re-melts the working layer and some carbide-promoting elements dissolve in the intermediate liquid layer, causing the formation of the M_7C_3 type carbides during the solidification. The working layer consists also of secondary carbides of the $M_{23}C_6$ type. This finding is confirmed by a thermodynamic calculation, which shows that the solidification of austenite is followed by the solidification of the M_7C_3 type carbide eutectic and a further precipitation of the $M_{23}C_6$ carbides.

The M_7C_3 type carbides have a lower density than austenite; as a result, at a slow solidification rate of the intermediate layer, the formed carbides are pushed by

high centrifugal forces into the inner part of the layer. In this way, an inhomogeneous microstructure is obtained, which is inappropriate for the lifetime of the roll.

The tensile strength of the working layer is not changed until the temperature reaches 500 °C, and then it is rapidly lowered, which can lead to a casting failure if such working temperatures occur also during the lifetime.

The hardness of the gradient-casting cross-section is on a decrease towards the intermediate layer, which is the result of a lower concentration of primary and secondary carbides.

A dilatometric analysis showed big differences in the linear thermal-expansion coefficients of different layers. The difference in dilatation between the working layer and the core is 0.055 mm at 1000 °C. Such differences in the contraction or expansion during the cooling and heating of the solidification process, heat treatment or during the working cycles of a roll can cause stresses that may exceed the ultimate tensile strength of the working layer, initiating a crack that may result in a roll failure.

5 REFERENCES

- Manual for centrifugal casting of rolls, Valji Štore, Valji Štore, d. o. o., Štore 1986
- J. P. Breyer, G. Walmag, Metallurgy of High Chromium-Molybdenum White Iron and Steel Rolls, Rolls for the Metalworking Industries, Iron and Steel Society, Warendale 2002, 29–40
- W. Wolczynski, E. Guzik, W. Wajda, D. Jedrzejczyk, B. Kania, M. Kostrzewa, CET in Solidifying Roll – Thermal Gradient Field Analysis, Archives of Metallurgy and Materials, 57 (2012) 1, 105–117, doi:10.2478/v10172-011-0159-9
- M. Yamamoto, I. Narita, H. Miyahara, Fractal Analysis of Solidification Microstructure of High Carbon High Alloy Cast Roll Manufactured by Centrifugal Casting, Tetsu To Hagane – Journal of the Iron and Steel Institute of Japan, 99 (2013) 2, 72–79, doi:10.2355/tetsutohagane.99.72
- M. Kang, Y. Suh, Y. J. Oh, Y. K. Lee, The effects of vanadium on the microstructure and wear resistance of centrifugally cast Ni-hard rolls, Journal of Alloys and Compounds, 609 (2014), 25–32, doi:10.1016/j.jallcom.2014.04.184
- V. Vitry, S. Nardone, J. P. Breyer, M. Sinnaeve, F. Delaunois, Microstructure of two centrifugal cast high speed steels for hot strip mills applications, Materials and Design, 34 (2012), 372–378, doi:10.1016/j.matdes.2011.07.041
- F. Golobranc, Preoblikovanje, Vol. 1, Fakulteta za strojništvo, Ljubljana 1991
- G. Rivera, P. R. Calvillo, R. Boeri, Y. Houbaert, J. Sikora, Examination of the solidification macrostructure of spheroidal and flake graphite cast irons using DAAS and EBSD, Materials Characterization, 59 (2008) 9, 1342–1348, doi:10.1016/j.matchar.2007.11.009
- Y. Bai, Y. Luan, N. Song, X. Kang, D. Li, Y. Li, Chemical Compositions, Microstructure and Mechanical Properties of Roll Core used Ductile Iron in Centrifugal Casting Composite Rolls, Journal of Materials Science and Technology, 28 (2012) 9, 853–858, doi:10.1016/S1005-0302(12)60142-X
- Roll Failures Manual, Hot Mill Cast Work Rolls, 1st ed., CAEF – The European Foundry Association - Roll Section, Duesseldorf 2002, p. 10

COMPARATIVE MECHANICAL AND CORROSION STUDIES ON MAGNESIUM, ZINC AND IRON ALLOYS AS BIODEGRADABLE METALS

PRIMERJALNA ŠTUDIJA MEHANSKIH IN KOROZIJSKIH LASTNOSTI BIORAZGRADLJIVIH ZLITIN MAGNEZIJA, CINKA IN ŽELEZA

Dalibor Vojtěch, Jiří Kubásek, Jaroslav Čapek, Iva Pospíšilová

Department of Metals and Corrosion Engineering, Institute of Chemical Technology, Technická 5, 166 28 Prague 6, Czech Republic
Dalibor.Vojtech@vscht.cz

Prejem rokopisa – received: 2014-07-30; sprejem za objavo – accepted for publication: 2014-12-11

doi:10.17222/mit.2014.129

In this paper, selected magnesium, zinc and iron biodegradable alloys were studied as prospective biomaterials for temporary medical implants like stents and fixation devices for fractured bones. Mechanical properties of the alloys were characterized with hardness and tensile tests. In-vitro corrosion behavior was studied using immersion tests in a simulated physiological solution (SPS, 9 g/L NaCl) to roughly estimate the in-vivo biodegradation rates of implants. It was found that the Mg and Zn alloys were limited by a tensile strength of 370 MPa, while the tensile strength of the Fe alloys achieved 530 MPa. The main advantage of the Mg alloys is that their Young's modulus of elasticity is similar to that of the human bone. However, the corrosion tests revealed that the Mg-based alloys showed the highest corrosion rates in the SPS, ranging between 0.6 mm and 4.0 mm per year, which is above the tolerable degradation rates of implants. The corrosion rates of the Zn alloys were between 0.3 mm and 0.6 mm per year and the slowest corrosion rates of approximately 0.2 mm per year were observed for the Fe alloys. The results indicate that all three kinds of alloys meet the mechanical requirements for the load-bearing implants. From the corrosion-behavior point of view, the Zn- and Fe-based "slowly corroding" alloys appear as promising alternatives to the Mg-based alloys.

Keywords: biodegradable metal, magnesium, zinc, iron, mechanical properties, corrosion

Članek obravnava študij izbranih magnezijevih, cinkovih in železovih potencialnih biorazgradljivih zlitin kot obetajočih biomaterialov začasne medicinske vsadke, kot so opornice in pripomočki za utrjevanje zlomljenih kosti. Mehanske lastnosti zlitin so bile določene z merjenjem trdote in z nateznimi preizkusi. Korozijski preizkusi in vitro so bili izvršeni s pomakanjem v simulirano fiziološko raztopino (SPS, 9 g/L NaCl) za grobo oceno in vivo hitrosti biorazgradnje implantatov. Ugotovljeno je, da so zlitine Mg in Zn omejene z natezno trdnostjo 370 MPa, medtem ko je natezna trdnost Fe-zlitin dosegla 530 MPa. Glavna prednost Mg-zlitin je v podobnem Young-ovem modulu elastičnosti, ki je podoben kot pri človeški kosti. Vendar pa so korozijski preizkusi pokazali pri zlitinah na osnovi Mg največje korozijske hitrosti v SPS, med 0,6 mm in 4,0 mm na leto, kar je nad dopustno hitrostjo degradacije implantata. Korozijske hitrosti Zn zlitin so bile med 0,3 mm in 0,6 mm na leto, najnižje hitrosti korozije, okrog 0,2 mm na leto, pa so bile opažene pri Fe-zlitinah. Rezultati so pokazali, da vse tri vrste zlitin ustrezajo mehanskim zahtevam za obremenjene implantate. S stališča korozijskega vedenja so zlitine na osnovi Zn in Fe "zlitine s počasno korozijo" in se kažejo kot obetajoče nadomestilo za zlitine na osnovi Mg.

Ključne besede: biorazgradljive kovine, magnezij, cink, železo, mehanske lastnosti, korozija

1 INTRODUCTION

Metallic biomaterials have been used in bone and joint replacements, fractured-bone fixation devices, stents, dental implants, etc., for a long time. The advantage of metals over polymers or ceramics is in higher strength and toughness. In addition, metals can be simply processed with the established technologies like casting, forming, powder metallurgy, machining. The most important metallic biomaterials in the current use are stainless steels (SUS 316L), titanium alloys (Ti, Ti-6Al-4V, Ti-6Al-7Nb), cobalt alloys (Co-Cr-Mo), superelastic Ni-Ti, noble-metal alloys (Au, Pd, dental amalgams – Hg-Ag-Cu-Sn).¹ All these kinds of materials show a high corrosion resistance to human-body fluids due to the noble nature and/or spontaneous passivation and are, therefore, considered as bio-inert materials.²

Besides the bio-inert materials, biodegradable materials have attracted a great attention. The term biodegradability means that a material progressively corrodes and degrades in the body environment.^{3,4} Products of this degradation are not toxic, allergic or carcinogenic and they are readily excreted by the human body.³ Biodegradable materials can be used for the implants whose functions in the human body are only temporary, like fixation devices (screws, plates) for fractured bones and stents.³⁻⁵ When using inert biomaterials in bone-fixation devices, a second surgery is often necessary to remove them after the healing process of the bone has completed. In contrast, a biodegradable material slowly degrades in the human body and is progressively replaced by the growing tissue. No second surgery is needed which significantly reduces the inconvenience to

the patient, morbidity and health cost. Among the biodegradable materials, polymeric materials (for example poly-lactic acid – PLA) are commonly used at present, but their disadvantages are a low mechanical strength and hardness.⁵ For this reason, research and development activities all over the world are also focused on metallic biodegradable alloys with a higher strength, hardness and toughness as compared to the polymers.

Biodegradable alloys should have a good biocompatibility with the human body tissues. This basic requirement limits a number of possible candidates to three metals, magnesium, zinc and iron.³

Magnesium is generally considered as a relatively non-toxic metal. It is essential for proper biological functions of the human body. Its recommended daily value is about 400 mg.⁶ Magnesium supports the growth of the bone tissue, heart functions, the neurologic system, etc.^{7–10} Overdoses of magnesium are unlikely to occur because the metal absorption is efficiently controlled by the metabolism and excess amounts are excreted by the kidneys.¹⁰ There are many studies covering the mechanical, corrosion, in-vitro and in-vivo biocompatibility of the Mg alloys.^{11,12} On the basis of these studies, magnesium alloys are generally believed to show a good combination of mechanical performance and biocompatibility depending on the actual alloying elements present. However, the main drawbacks of most of the investigated biodegradable Mg alloys are excessive in-vivo corrosion rates.^{4–10}

Iron is also an essential element for proper biological functions, mainly for the transfer of oxygen by blood.¹³ The recommended daily value of Fe is about 10 mg.⁶ Regarding the biocompatibility of iron-based alloys, there are a number of reported results,^{14–16} but they are often controversial. In order to explain the discrepancies between biocompatibility tests, more in-vitro and in-vivo experiments are needed.

Zinc supports the immune system, the proper functions of taste, smell, etc.^{11,17} Like Mg, Zn is also a component of many food supplements, therefore, it is considered as relatively non-toxic. Its recommended daily value is about 40 mg, but short-term overdoses of up to 100 mg do not cause significant health problems¹⁸. Zinc has been considered as a prospective biodegradable implant material only for a relatively short time;¹⁹ therefore, the in-vitro and in-vivo biocompatibility tests with zinc alloys are very limited. However, the tests reported recently indicate a good biocompatibility of Zn.²⁰

In the present work, magnesium, zinc, iron and their alloys are studied with respect to their mechanical and corrosion properties. Appropriate alloying of Mg, Zn and Fe can positively modify their mechanical, corrosion and physical properties, which are important for potential medical applications. In the available literature many alloying elements are proposed for these purposes,^{3–19} but in this study Mg-RE (RE = rare earth metals, Gd, Nd, Y), Zn-Mg and Fe-Mn based alloys were selected, be-

cause all these alloying systems are generally considered as relatively safe and acceptable for a potential medical use.³

2 EXPERIMENTS

Chemical compositions of the investigated Mg, Zn and Fe alloys are summarized in **Table 1**. Magnesium and iron alloys were prepared by melting pure metals in a vacuum-induction furnace under argon. Zinc alloys were prepared by melting pure metals in air. The alloys were cast into cast-iron metal molds (Mg, Zn) or sand molds (Fe) to prepare ingots of 20 mm in diameter and 150 mm in length. Parts of the as-cast ingots of Mg and Zn alloys were hot extruded at a temperature of 400 °C, an extrusion ratio of 10 : 1 and a rate of 5 mm/min to prepare rods of 6 mm in diameter. Ingots of iron alloys were hot forged at 850 °C into rods of 6 mm in diameter.

Table 1: Designations and chemical compositions of the studied alloys (w/%)

Tabela 1: Oznake in kemijska sestava preiskovanih zlitin (w/%)

Alloy designation	Element (w/%)						
	Mg	Zn	Fe	Gd	Nd	Y	Mn
Mg	> 99.8	-	0.02	-	-	-	-
Mg-3Gd	bal.	-	0.01	2.7	-	-	-
Mg-3Gd-1Y	bal.	-	0.01	2.6	-	0.8	-
Mg-3Nd-4Y	bal.	-	-	-	2.8	4.2	-
Zn	-	> 99.8	-	-	-	-	-
Zn-1Mg	0.9	bal.	-	-	-	-	-
Zn-2Mg	1.6	bal.	-	-	-	-	-
Fe	-	-	> 99.7	-	-	-	-
Fe-30Mn	-	-	bal.	-	-	-	30.5

The microstructures of the alloys were examined using light (LM) and scanning electron microscopy with energy dispersive spectrometry (SEM + EDS) and X-ray diffraction (XRD). Mechanical properties were characterized with the Vickers-hardness (HV 5) and tensile testing. The tensile tests were carried out on a LabTest 5.250SP1-VM universal loading machine at a deformation rate of 1 mm/min.

In the human body any implant is exposed to fluids containing complicated water solutions of inorganic salts (chlorides, phosphates, etc.), organic compounds (glucose, amino acids, etc.) and biological matter (proteins, cells, etc.). In this study, the biological environment was simulated with a simple NaCl solution, in which the concentration of chlorides is similar to that in the blood plasma. This simulated physiological solution (SPS) contained 9 g/L NaCl, 7×10^{-6} of dissolved oxygen and its initial pH was 6.2 due to dissolved CO₂. The corrosion behavior was characterized with in-vitro immersion tests in the SPS. The alloy samples were immersed in the SPS for 168 h at 37 °C. Afterwards, the corrosion products were chemically removed and the corrosion rates were then calculated, in mm/year, using the weight losses measured with a balance.

3 RESULTS AND DISCUSSION

3.1 Mechanical properties

The Vickers hardness (HV 5), the ultimate tensile strength (UTS) and the elongation (E) are summarized in **Figure 1**. As expected, pure Mg and Zn show the lowest hardness and strength levels that do not exceed 50 HV 5 and 130 MPa, respectively (**Figures 1a** and **1b**). In contrast, pure iron has higher hardness and tensile-strength values of approximately 100 HV 5 and 300 MPa in the as-forged state. **Figure 1** also demonstrates that both the

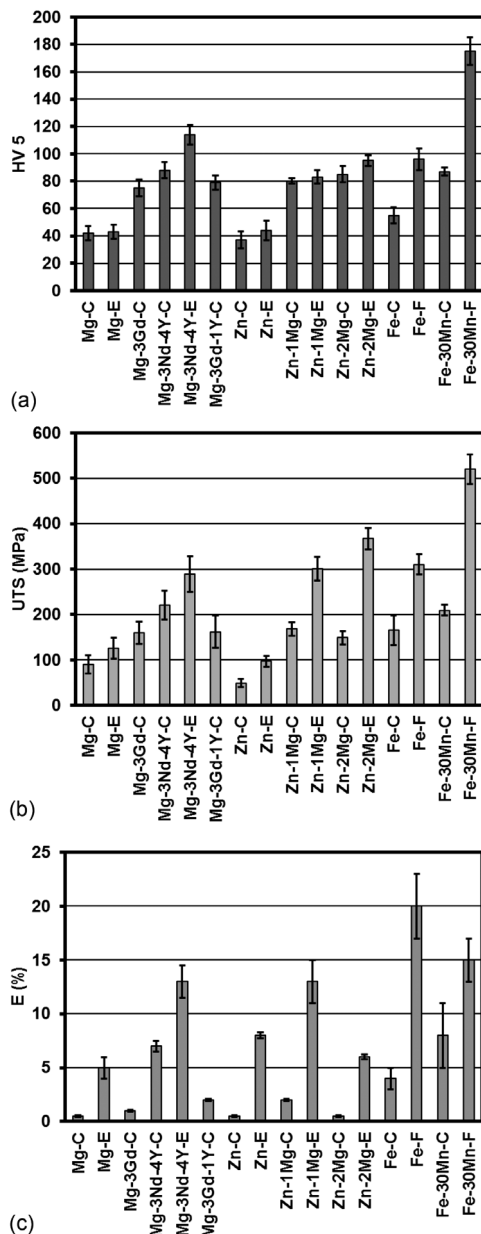


Figure 1: a) Vickers hardness (HV 5), b) ultimate tensile strength (UTS) and c) elongation (E) of the investigated alloys (C – as cast, E – as hot extruded, F – as hot forged)

Slika 1: a) Trdota po Vickersu (HV 5), b) natezna trdnost (UTS) in c) raztezek (E) preiskovanih zlitin (C – ulito stanje, E – vroče ekstrudirano, F – vroče kovano)

hardness and the strength of all three groups of alloys increase with the increasing concentrations of the alloying elements due to the solid-solution strengthening and hardening and due to the influence of the intermetallic phases present in the structures. Moreover, positive influences of hot-extrusion or hot-forging operations on the hardness, the strength and the elongation are observed. The reason for the influence is the fact that hot-forming steps cause an elimination of casting defects, dynamic recrystallization and structural refinement, as is illustrated for the Zn-2Mg alloy in **Figure 2**. The as-cast Zn-2Mg alloy (**Figure 2a**) is composed of primary Zn dendrites (light) and an interdendritic network of a Zn + Mg₂Zn₁₁ eutectic mixture (dark). A detailed view of the eutectic is seen in the insert in **Figure 2a**. Hot extrusion (**Figure 2b**) partially breaks down the continuous eutectic network and the structure becomes oriented parallel to the extrusion direction. The dynamic recrystallization occurring in the Zn grains (light) results in the formation of equi-axed and refined Zn grains. The average grain size in these regions is 15 μ m, which is more than a three-fold reduction in comparison with the primary dendrites in the as-cast alloy (50 μ m).

Figure 1 shows that among the Mg-based alloys, the highest hardness (114 HV 5) and strength (290 MPa) are measured for the hot-extruded Mg-3Nd-4Y alloy due to the presence of the recrystallized and fine-grained structure. This alloy also shows a good elongation of 13 % (**Figure 1c**). Magnesium additions to zinc lead to significant hardening and strengthening of the Zn-Mg alloys. The hot-extruded Zn-2Mg alloy shows the highest hardness (95 HV 5) and tensile strength (367 MPa). But the elongation of this alloy is only 6 %. On the other hand, the Zn-1Mg alloy exhibits a slightly lower tensile strength (301 MPa) but a considerably higher plasticity (elongation of 13 %). As it was expected, the hot-forged Fe-30Mn alloy exhibits the highest hardness (175 HV 5) and strength (530 MPa) among all the studied alloys. The reason is that manganese remains dissolved in γ -Fe, stabilizing the austenitic structure to the room temperature (as proved with XRD) and causing significant solid-solution hardening and strengthening. Moreover, this material also shows an acceptable elongation of 15 %.

It is important to compare the mechanical characteristics of novel biodegradable alloys shown in **Figure 1** with those of today's commercial biodegradable polymers, for example, the poly-lactic acid (PLA). It is known that the tensile strength of the PLA does not exceed 60 MPa.¹ Therefore, all three groups of metallic biodegradable materials show significantly higher strength levels than the PLA which is of a great importance for load-bearing implants like fixation screws, nails or plates. The advantage of the Mg alloys over the Zn and Fe alloys is a low density (≈ 3 g/cm³) similar to that of the bone (≈ 2 g/cm³) and also a low Young's modulus (≈ 50 GPa). A low modulus is desirable for a proper

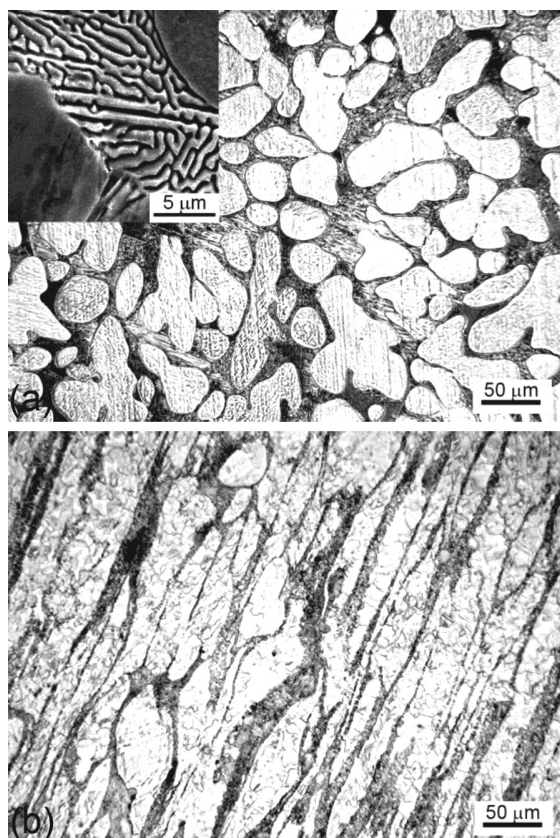


Figure 2: Microstructures of the Zn-2Mg alloy: a) as cast, b) as hot extruded (LM, SEM)

Slika 2: Mikrostruktura Zn-2Mg-zlitine: a) ulito stanje, b) vroče ekstrudirano (SM, SEM)

transfer of mechanical loading between the implant and the bone and for a proper healing process of the bone. The Zn alloys show a strength similar to the Mg alloys but higher density and modulus of elasticity. The Fe alloys are characterized by the highest strength, exhibiting also high density and modulus. As demonstrated in the following section, the advantages of Zn and Fe over Mg are in their lower corrosion rates.

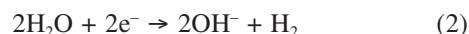
3.2 Corrosion behavior

Figure 3 summarizes the corrosion rates of the alloys in the SPS.

It is observed that, of all the materials, pure Mg corrodes at the highest rate (4 mm per year). The fast corrosion is caused by the presence of impurities, mainly Fe, in magnesium (**Table 1**). It is known that more noble metallic impurities like Fe, Ni, Cu and Co strongly accelerate the corrosion of Mg by forming cathodic sites and micro-galvanic cells with the Mg matrix.^{11,12} All the Mg-RE alloys studied show slower corrosion rates in the SPS than Mg. The Mg-3Gd alloy corrodes at the lowest rate (0.6 mm per year). The rare-earth metals reduce the corrosion rate by forming RE-Fe intermetallic phases, which decrease the galvanic effects between the Mg matrix and cathodic impurities. **Figure 3** also indicates

that the corrosion rates slightly increase with an increase in the total RE concentration. This may be due to higher volume fractions of the intermetallic phases and the resulting galvanic effects. In comparison with the Mg alloys, the Fe and Zn alloys exhibit significantly lower corrosion rates ranging between 0.2 mm and 0.6 mm per year. The differences between the three groups of alloys are related to different mechanisms of the corrosion process:

Magnesium is the least noble of the three metals studied as its standard potential is -2.4 V (vs. SHE).² It thus shows a high tendency to dissolve in water solutions. Magnesium corrosion includes anodic metal dissolution (Equation (1)) and cathodic water decomposition (Equation (2)) to form gaseous hydrogen and to alkalize the solution.^{11,12} The corrosion rate of a magnesium implant that is too fast is thus undesirable because both corrosion products have adverse effects on the biocompatibility by negatively influencing the tissue adherence and healing.²¹ In the alkaline solutions, surface corrosion products may form, but these products are broken down in the presence of Cl^- anions in the SPS:



It is important that the corrosion of the Mg alloys is not controlled by the access of oxidizing species (for example, dissolved oxygen) to the metal. For this reason, it may proceed relatively rapidly even in neutral-water solutions (**Figure 3**). The chloride ions present in the SPS generally accelerate the corrosion process.

Iron is the most noble of all the three metals investigated as its standard potential is -0.4 V (vs. SHE).² Therefore, its tendency to dissolve is the lowest. The corrosion process includes anodic dissolution and, in contrast to Mg, cathodic reduction of dissolved oxygen

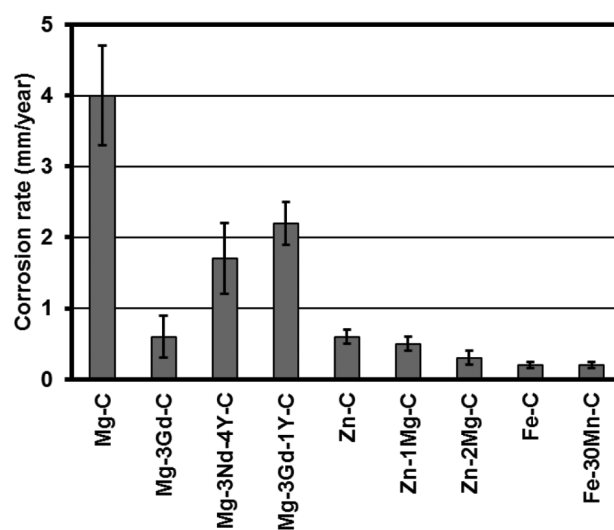


Figure 3: Corrosion rates of the alloys in the SPS measured with immersion tests

Slika 3: Korozijske hitrosti zlitin, potopljenih v SPS

(Equations (3) and (4)). The low corrosion rates of the Fe alloys in the SPS (**Figure 3**) can be attributed to the fact that the corrosion of Fe needs dissolved oxygen whose concentration in the SPS is low. In addition, the corrosion of Fe in neutral solutions is accompanied by the formation of more or less protective corrosion products on the surface. Another positive feature of iron is that its corrosion in neutral solutions does not produce gaseous hydrogen, which would negatively influence the tissue healing around the implant:



Zinc nobility is between those of Mg and Fe. The standard potential is -0.8 V (vs. SHE).² The corrosion of zinc shows some similarity with iron (Equations (5) and (6)) because it is controlled by dissolved oxygen in the neutral SPS. Therefore, the corrosion process is relatively slow (**Figure 3**). Zinc is also easily covered with protective the passive films of corrosion products in neutral and slightly alkaline solutions. Like in the case of iron, hydrogen gas is not generally formed during the corrosion of zinc in neutral solutions. All the above features are good prerequisites for low corrosion rates of zinc implants in human body fluids:



Regarding the corrosion process of a biodegradable implant in vivo, it is important to know which corrosion rate is acceptable for a particular application. Too fast an in-vivo degradation of an implant is undesirable because such an implant would degrade before the completion of the healing process. In the case of fixation devices of fractured bones, it is necessary that the implants mechanically fix the bones for a certain minimum period depending on the implant type, design, location, the surrounding tissue, etc. The requirement may be, for example, that a fixation screw must keep 95 % of its original load-bearing capability for at least six weeks after the implantation.²² In other words, the corrosion of the screw should not reduce its cross-section by more than 5 %, providing the maximum acceptable corrosion rate of 0.4 mm per year. **Figure 3** indicates that the Fe and Zn alloys meet this requirement and that some Mg-RE alloys approach the acceptable corrosion rate. It should be noted that real in-vivo environments contain, in addition to chlorides, like the ones contained by the SPS used in this study, also various organic and inorganic compounds which, in contrast to chlorides, retard the corrosion process by forming protective surface films. For this reason, an in-vivo corrosion would be probably slower than the corrosion in the simple SPS and some Mg-RE alloys would thus also fall into the acceptable range.²³

4 CONCLUSIONS

In this study, biodegradable Mg, Fe and Zn alloys were compared with regard to mechanical and corrosion properties. It can be concluded that all of these materials show significantly higher strengths than the commercial biodegradable material (PLA). They are thus promising materials for highly loaded implants. In the case of Mg, there are still concerns regarding high corrosion rates, hydrogen-gas release and local alkalization. The main positive feature of the Zn and Fe alloys is their slow corrosion due to the absence of the gaseous-hydrogen release. In addition, the Fe alloys show the highest strength among all the studied materials.

Acknowledgements

The authors wish to thank the Czech Science Foundation for the financial support of this research (project no. P108/12/G043).

5 REFERENCES

- J. R. Davis, Handbook of Materials for Medical Devices, ASM International, Materials Park 2003, doi:10.1361/hmmd2003p001
- D. E. J. Talbot, Corrosion Science and Technology, CRC Press, London 2007
- Y. F. Zheng, X. N. Gu, F. Witte, Biodegradable metals, Materials Science and Engineering R, 77 (2014), 1–34, doi:10.1016/j.mser.2014.01.001
- F. Witte, The history of biodegradable magnesium implants: A review, Acta Biomaterialia, 6 (2010), 1680–1692, doi:10.1016/j.actbio.2010.02.028
- B. R. Zeng, W. Dietzel, F. Witte, N. Hort, C. Blawert, Progress and Challenge for Magnesium Alloys as Biomaterials, Advanced Engineering Materials, 10 (2008), B3–B14, doi:10.1002/adem.200800035
- Y. Chen, Z. Xu, C. Smith, J. Sankar, Recent advances on the development of magnesium alloys for biodegradable implants, Acta Biomaterialia, 10 (2014), 4561–4573, doi:10.1016/j.mser.2014.01.001
- Y. Xin, T. Hu, P. K. Chu, In vitro studies of biomedical magnesium alloys in a simulated physiological environment: A review, Acta Biomaterialia, 7 (2011), 1452–1459, doi:10.1016/j.actbio.2010.12.004
- X. N. Gu, Y. F. Zheng, A review on magnesium alloys as biodegradable materials, Frontiers of Materials Science in China, 4 (2010), 111–115, doi:10.1007/s11706-010-0024-1
- H. Waizy, J. M. Seitz, J. Reifenrath, A. Weizbauer, F. W. Bach, A. M. Lindenberg, B. Denkena, H. Windhagen, Biodegradable magnesium implants for orthopedic applications, Journal of Materials Science, 48 (2013), 39–50, doi:10.1007/s10853-012-6572-2
- M. P. Staiger, A. M. Pietak, J. Huadmai, G. Dias, Magnesium and its alloys as orthopedic biomaterials: A review, Biomaterials, 27 (2006), 1728–1734, doi:10.1016/j.biomaterials.2005.10.003
- F. Witte, N. Hort, C. Vogt, S. Cohen, K. U. Kainer, R. Willumeit, F. Feyerabend, Degradable biomaterials based on magnesium corrosion, Current Opinion in Solid State and Materials Science, 12 (2008), 63–72, doi:10.1016/j.cossms.2009.04.001
- A. Atrens, M. Liu, N. I. Z. Abidin, Corrosion mechanism applicable to biodegradable magnesium implants, Materials Science and Engineering B, 176 (2011), 1609–1636, doi:10.1016/j.mseb.2010.12.017

- ¹³ A. H. Yusop, A. A. Bakir, N. A. Shaharom, M. R. A. Kadir, H. Hermawan, Porous biodegradable Metals for Hard Tissue Scaffolds: A Review, *International Journal of Biomaterials*, 2012 (**2012**), 1–10, doi:10.1155/2012/641430
- ¹⁴ B. Wegener, B. Sievers, S. Utschneider, P. Müller, V. Jansson, Microstructure, cytotoxicity and corrosion of powder-metallurgical iron alloys for biodegradable bone replacement materials, *Materials Science and Engineering B*, 176 (**2011**), 1789–1796, doi:10.1016/j.mseb.2011.04.017
- ¹⁵ M. Moravej, D. Mantovani, Biodegradable Metals for Cardiovascular Stent Application: Interests and New Opportunities, *International Journal of Molecular Science*, 12 (**2011**), 4250–4270, doi:10.3390/ijms12074250
- ¹⁶ H. Hermawan, D. Dubé, D. Mantovani, Developments in metallic biodegradable stents, *Acta Biomaterialia*, 6 (**2010**), 1693–1697, doi:10.1016/j.actbio.2009.10.006
- ¹⁷ S. Zhang, X. Zhang, Ch. Zhao, J. Li, Y. Song, Ch. Xie, H. Tao, Y. Zhang, Y. He, Y. Jiang, Y. Bian, Research on an Mg-Zn alloy as a degradable biomaterial, *Acta Biomaterialia*, 6 (**2010**), 626–640, doi:10.1016/j.actbio.2009.06.028
- ¹⁸ G. J. Fosmire, Zinc toxicity, *American Journal of Clinical Nutrition*, 51 (**1990**), 225–227
- ¹⁹ D. Vojtěch, J. Kubásek, J. Šerák, P. Novák, Mechanical and corrosion properties of newly developed biodegradable Zn-based alloys for bone fixation, *Acta Biomaterialia*, 7 (**2011**), 3515–3522, doi:10.1016/j.actbio.2011.05.008
- ²⁰ P. K. Bowen, J. Drelich, J. Goldman, Zinc Exhibits Ideal Physiological Corrosion Behavior for Bioabsorbable Stents, *Advanced Materials*, 25 (**2013**), 2577–2582, doi:10.1002/adma.201300226
- ²¹ J. Wang, J. Tang, P. Zhang, Y. Li, J. Wang, Y. Lai, L. Qin, Surface modification of magnesium alloys developed for bioabsorbable orthopedic implants: A general review, *Journal of Biomedical Materials Research Part B*, 100B (**2012**), 1691–1701, doi:10.1002/jbm.b.32707
- ²² Private discussions
- ²³ F. Witte, J. Fischer, J. Nellesen, H. A. Crostack, V. Kaese, A. Pisch, F. Beckmann, H. Windhagen, In vitro and in vivo corrosion measurements of magnesium alloys, *Biomaterials*, 27 (**2006**), 1013–1018, doi:10.1016/j.biomaterials.2005.07.037

MICROSTRUCTURAL CHANGES OF FINE-GRAINED CONCRETE EXPOSED TO A SULFATE ATTACK

MIKROSTRUKTURNE SPREMENBE DROBNOZRNATEGA BETONA, IZPOSTAVLJENEGA SULFATU

Martin Vyšvařil, Patrik Bayer, Markéta Rovnaníková

Brno University of Technology, Faculty of Civil Engineering, Institute of Chemistry, Žižkova 17, 602 00 Brno, Czech Republic
vysvaril.m@fce.vutbr.cz

Prejem rokopisa – received: 2014-07-30; sprejem za objavo – accepted for publication: 2015-01-05

doi:10.17222/mit.2014.138

Sulfate attack is one of the major threats to durability of concrete constructions and it becomes a major destructor of sewage-collection systems where concrete sewer pipes are exposed to sulfates. The most frequent biodeterioration in sewage pipes is caused by biogenic sulfuric-acid corrosion. During this attack, the pH of the surfaces of concrete sewer pipes is reduced and chemical reactions lead to the cracking and scaling of the concrete material, accelerated by the sewage flow. This paper is focused on the sulfate attack on fine-grained concrete where the effect of a 0.5 % sulfuric-acid solution on the microstructural changes of various types of concrete after a treatment for a period of 6 months was investigated with mercury intrusion porosimetry and scanning electron microscopy. It was found that the total porosity of most samples was decreased after the sulfate attack, indicated by the products of the sulfate corrosion filling in the pores of the concrete. The smallest changes in the microstructure were observed in the samples made from sulfate-resisting cements. The formation of the locations rich in sulfur, iron and aluminum during the sulfate attack of the concrete was determined by mapping the chemical-element distribution.

Keywords: sulfate attack, porosity, microstructure, ettringite, gypsum

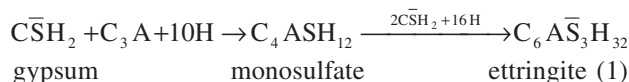
Izpostavitev sulfatom je ena od glavnih groženj za obstojnost betonskih struktur in postaja glavni uničevalec v sistemih zbiranja odpadka, kjer so betonske cevi izpostavljene sulfatom. Najpogostejša biorazgradnja betonskih cevi za zbiranje odpadka je povzročena z biogensko korozijo z žvepleno kislino. Med tem napadom se pH površine zmanjša in kemijske reakcije, pospešene s tokom odpadka, povzročijo pokanje in luščenje materiala iz betona. Članek obravnava vpliv izpostavitve sulfatov na drobnozrnat beton, kjer je bil preiskovan učinek raztopine žveplene kisline 0,5 % na mikrostrukturne spremembe različnih vrst betonov po izpostavitvi 6 mesecev. Uporabljena je bila porozimetrija z vdorom živega srebra in vrstična elektronska mikroskopija. Ugotovljeno je bilo, da je bila skupna poroznost vzorcev zmanjšana po učinkovanju sulfata, kar kaže, da se pore v proizvodih napolnijo s produkti sulfatne korozije. Najmanjše spremembe mikrostrukture so bile opažene pri vzorcih izdelanih betonov, odpornih proti sulfatom. V betonu, izpostavljenem sulfatom, je bil nastanek področij, bogatih z žveplom, železom in aluminijem določen z razporeditvijo kemijskih elementov.

Ključne besede: izpostavitev sulfatom, poroznost, mikrostruktura, etringit, sadra

1 INTRODUCTION

Durability of concrete has become a very relevant issue in construction projects over the last decades. Sulfate attack is one of the major threats to the durability of concrete constructions and it is a major destructor in sewage-collection systems where concrete sewer pipes are exposed to sulfates. The sulfates originate from the waste water as well as from the biogenic activity of bacteria – microbiologically induced concrete corrosion (MICC).¹ The most frequent biodeterioration in sewage pipes is caused by biogenic sulfuric-acid corrosion.^{1,2} During this attack, the pH of the surfaces of concrete sewer pipes is reduced and chemical reactions lead to the cracking and scaling of the concrete material accelerated by the sewage flow. The rate of the loss of a concrete material can be 3–6 mm per year, thereby the breaking-out of steel reinforcement can take place, resulting in the subsequent corrosion of the steel reinforcement.³ From this aspect, a sulfate attack in the sewage system is very dangerous, especially in the areas with waste water rich in sulfates or H₂S.

The formation of ettringite (AFt) from calcium sulfate (gypsum) and C₃A via monosulfate (AFm), according to Equation (1), is the main chemical reaction of the sulfate attack on concrete.⁴ Gypsum is the primary product of the chemical sulfate attack on concrete (formed by the reaction of sulfate anion with calcium hydroxide):



Ettringite has a relative low density (1.75 g cm⁻³) in comparison to, e.g., the C-S-H phase (2.0 g cm⁻³) and a considerably larger volume than the initial compounds, therefore its formation provides a potential stress in the hardened cement paste.⁵ The theoretical volume increase varies depending on the source of the available aluminum. The sources of reactive aluminum are AFm phases (monosulfate, monocarbonate) and calcium aluminate originating from the clinker phases (C₃A, C₄AF). The ettringite formation can be reduced by lowering the C₃A content in the cement. According to the European stan-

dards EN 196 and EN 197, sulfate-resistant cements are limited in the C_3A content to $< 3\%$ and the Al_2O_3 content to $< 5\%$.

Systematic studies and reviews were done to evaluate the deterioration processes of the secondary-ettringite formation due to an external sulfate attack on hydrated cement paste, mortar and concrete.^{4,6,7} The results showed that the amounts of C_3A (0–8 %) in the cement systems do not necessarily protect them from a sulfate deterioration. In contrast, the w/c ratio of the investigated samples had a major impact on the failure time of the samples during 40 years of exposure under real conditions. The permeability (porosity) of concrete samples has a major influence on the deterioration of the samples. It is generally agreed that the alumino-ferrite phase (C_4AF) seems to be less important with regard to the secondary-ettringite formation during a sulfate attack due to its lower reaction kinetics.^{8,9} The formation of secondary ettringite from C_4AF in the presence of gypsum (sulfate) and the formation of aluminum- (AH_3) and iron-hydroxide (FH_3) are given in Equation (2):



Besides ettringite, gypsum can also form during a sulfate attack, especially in highly concentrated sulfate solutions.^{10,11} The influence of a gypsum formation on the performance of cement pastes, mortars and concretes was studied in detail by many authors.^{6,12–14} It was suggested that the secondary-gypsum formation is related to the amount of alite (C_3S) in the cement system due to the possibility of a portlandite formation. The transformation of portlandite into gypsum can cause an expansion, usually later, during the sulfate exposure, and the softening of the near-surface regions due to the gypsum formation was also observed. The softening was attributed to the decalcification of the C-S-H phase.

At lower temperatures, thaumasite ($CaSiO_3 \cdot CaSO_4 \cdot CaCO_3 \cdot 15H_2O$; C_3SSCH_{15}) is formed in addition to ettringite as a result of the reaction between C-S-H and SO_4^{2-} , CO_2 or CO_3^{2-} , and water. The AFt phase is structurally similar to ettringite, with Al^{3+} substituted by Si^{4+} . Thaumasite is more stable at lower temperatures since silicon tends to adopt the octahedral co-ordination. However, thaumasite is formed also at temperatures around 20 °C and above.^{15,16} Once thaumasite is formed, it remains stable up to 30 °C.¹⁷ The formation of thaumasite always needs a source of carbonate which can be supplied from the limestone contained in the cement itself. The damage due to the thaumasite formation was investigated by various authors.^{18–21}

Thus, the interactions of sulfate ions with the cement matrix result in a disruption of the concrete and a significant loss of the mechanical strength and mass, and it leads to a reduction of the service life of concrete composites.

This paper is focused on the sulfate attack on fine-grained concrete, investigating the effect of 0.5 % sulfuric acid (simulating *MICC*) on the microstructural

changes of various types of concrete after a treatment for the period of six months. The changes in the microstructure were determined with mercury intrusion porosimetry and scanning electron microscope. The aim of this study was to compare the resistances of various types of concrete against the sulfate attack, in view of the microstructural changes that may result in a disintegration and the subsequent loss of the concrete material.

2 MATERIALS AND METHODS

Fine-grained concrete specimens (40 mm × 40 mm × 160 mm) were prepared with a water-to-binder ratio of 0.45 and three fractions of quartz sand according to Czech standard CSN 72 1200, with designations PG 1 (< 0.5 mm), PG 2 (0.5–1 mm) and PG 3 (1–2.5 mm), in the weight-to-binder ratio of 1 : 1 : 1 : 1. Seven concrete mixtures with different compositions of the binder were prepared: PC – Portland cement CEM I 42.5 R (100 %); SRP – sulfate-resisting Portland cement (100 %); SRS – sulfate-resisting slag cement CEM III/B 32.5 N-SV (100 %); MK – metakaolin (20 %), Portland cement (80 %); GL – ground limestone (20 %), Portland cement (80 %); GBFS – granulated blast-furnace slag (20 %), Portland cement (80 %) and FA – low-calcium fly ash (20 %), Portland cement (80 %). The mixtures with the supplementary cementing materials (metakaolin, limestone, slag and fly ash) corresponded to Portland blended cements according to European standard EN 197-1. The chemical compositions and physical properties of the initial materials are given in **Table 1**. The specimens were unmolded 24 h after the casting under laboratory conditions ($t = (22 \pm 2)$ °C, R. H. was (55 ± 5) %) and

Table 1: Chemical compositions and physical properties of initial materials in mass fractions, w/%

Tabela 1: Kemijska sestava in fizikalne lastnosti izhodnih materialov v masnih deležih, w/%

Materials	PC	SRP	SRS	MK	GL	GBFS	FA	
Chemical composition	CaO	61.48	60.92	47.53	0.20	54.73	34.81	3.60
	SiO ₂	21.26	21.88	32.84	58.70	0.81	39.78	53.70
	Al ₂ O ₃	5.08	3.65	6.01	38.50	0.32	8.17	24.62
	Fe ₂ O ₃	3.64	4.36	1.54	0.72	0.10	1.54	7.91
	SO ₃	2.42	2.39	2.30	0.02	0.05	0.46	0.96
	MgO	0.86	3.15	7.21	0.38	0.38	13.22	1.67
	Na ₂ O	0.12	0.41	0.32	0.04	–	–	0.85
	K ₂ O	0.91	0.86	0.65	0.85	–	–	2.62
	MnO	0.07	0.11	0.03	–	0.01	0.89	–
	TiO ₂	0.29	0.34	0.41	0.49	–	0.24	1.03
	Cr ₂ O ₃	–	–	–	–	–	0.14	–
	P ₂ O ₅	–	–	–	–	–	0.03	2.25
L.O.I.	4.17	1.97	0.82	1.67	43.99	1.48	2.82	
Physical properties	SSA (m ² kg ⁻¹)	360	685	504	13060	390	384	340
	SG (kg m ⁻³)	3120	2650	2950	1070	2700	2810	2300

Note: "–" ... not tested

placed into a water bath for another 27 d. Afterwards, the specimens were air-dried for 24 h and then the pore structures of the samples were studied to determine the total porosity and the pore-size distribution with high-pressure mercury intrusion porosimetry using a Micromeritics PoreSizer 9310 porosimeter, and the microstructures of samples were observed with a scanning electron microscope, MIRA3 (TESCAN), equipped with an EDX probe.

Subsequently, the test samples were covered with a protective coat to prevent drying and they were placed into a solution of 0.5 % H_2SO_4 for a period of six months. The concentration of the sulfuric acid was chosen in accordance with the literature.²² The solution level was maintained at a height of 5 mm and the solutions were weekly renewed. After six months, the samples were slit lengthwise and the changes in their microstructures were studied with high-pressure mercury intrusion porosimetry and scanning electron microscope. Attention was paid mainly to the lower parts of the samples, near the H_2SO_4 solution.



Figure 1: Lower part of SRP concrete sample after being in H_2SO_4 0.5 % for 6 months

Slika 1: Spodnji del SRP-betonskega vzorca po namakanju 6 mesecev v H_2SO_4 0,5 %

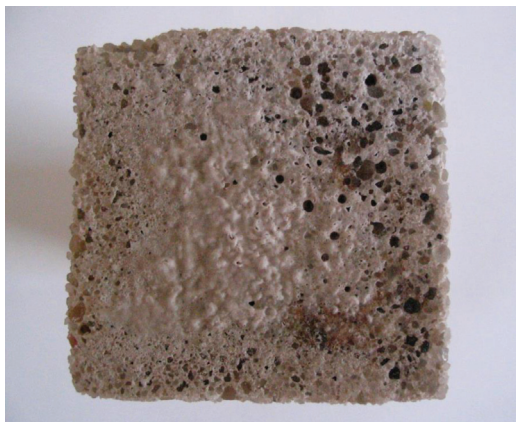


Figure 2: Immersed part of SRP concrete sample after being in H_2SO_4 0.5 % for 6 months

Slika 2: Potopljeni del SRP-betonskega vzorca po namakanju 6 mesecev v H_2SO_4 0,5 %

3 RESULTS AND DISCUSSION

3.1 Visual appearance

After being in 0.5 % H_2SO_4 for six months, a visible degradation of the submerged part occurred on all the investigated samples and the creation of a rust layer on the periphery of each sample, just above the level of the acid, took place. **Figure 1** illustrates the effect of the 0.5 % sulfuric acid on the SRP-concrete sample. A detailed view of the immersed part of the sample is shown in **Figure 2**. There are well recognizable exposed aggregates and white precipitates of gypsum ($CaSO_4 \cdot 2H_2O$) on the surface.

3.2 Changes in the porosity

It was found that all the concrete samples had almost identical pore distributions before the sulfate attack. The samples mainly contained pores with a diameter of 0.1 μm (**Figure 3**). The largest porosity was observed for the FA concrete and the lowest for the SRS concrete. The results of the determination of the cumulative pore volumes of the samples exposed to the sulfate attack for six months are also in **Figure 3**. The pore-size distribution remained approximately the same, but the samples had a slightly higher amount of the pores with a diameter below 0.1 μm . This means that larger pores were filled in to a certain degree by the products of the reactions of the

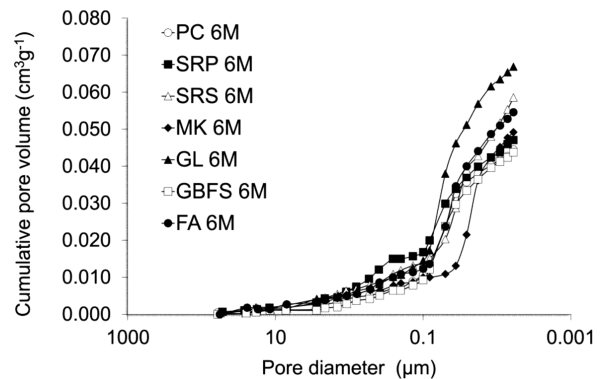
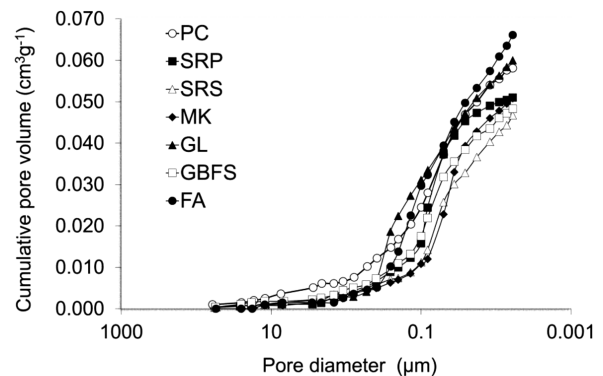


Figure 3: Pore-size distribution of the investigated concrete samples before and after a 6-month (6M) exposure to H_2SO_4 0.5 %

Slika 3: Razporeditev velikosti por v preiskovanih vzorcih betona pred 6-mesečno (6M) izpostavitvijo H_2SO_4 0,5 % in po njej

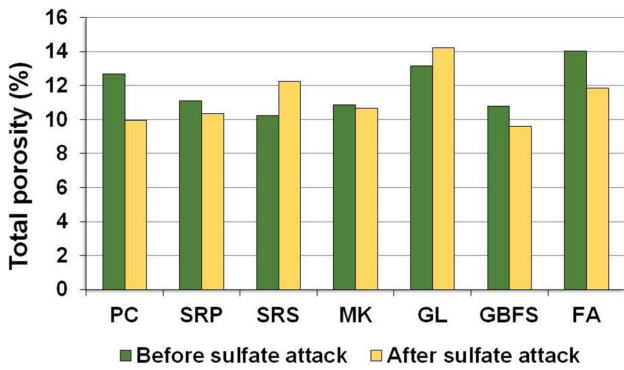


Figure 4: Total porosity of the concrete samples before and after a 6-month exposure to 0.5 % H₂SO₄

Slika 4: Skupna poroznost betonskih vzorcev pred 6-mesečno izpostavitvijo H₂SO₄ 0,5 % in po njej

sulfate attack. The total porosities of the investigated concrete samples are depicted in **Figure 4**. The reduction in the total porosity of most samples occurred after the sulfate attack, which indicates that the pores were filled in by the products of the sulfate corrosion of the concrete.

The most significant decrease was observed for the PC and FA concretes. Conversely, for the SRS and GL concretes, an increase in the total porosity was found. In the case of the SRS concrete, it is apparently due to the low porosity before the sulfate attack, prohibiting a smooth crystallization of the sulfate-corrosion products in the pores and a disruption of the microstructures of the samples. The increase in the total porosity of the GL concrete is in accordance with the conclusions of E. F.

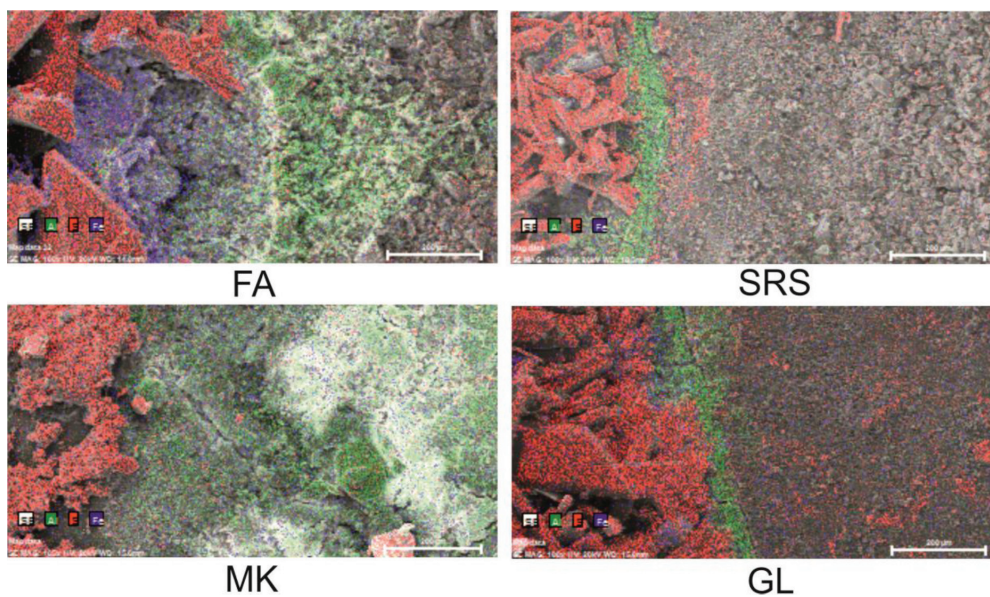


Figure 5: Distribution of sulfur (red), aluminum (green) and iron (blue) on the surfaces of lower parts of lengthwise slices of the selected types of concrete samples obtained with EDX SEM

Slika 5: EDX-SEM-razporeditev žvepla (rdeče), aluminija (zeleno) in železa (modro) na površini spodnjega dela vzdolžnega prereza izbranih vrst betona

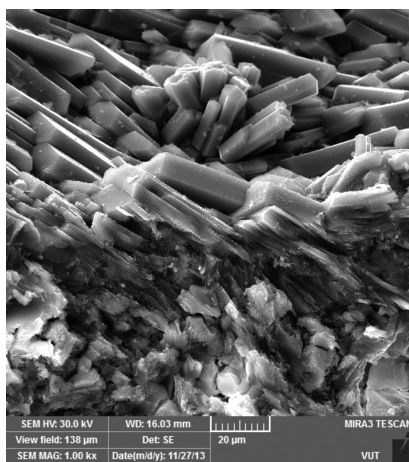


Figure 6: SEM image of gypsum identified in the structure of submerged part of PC-concrete sample after a 6-month sulfate attack

Slika 6: SEM-posnetek sadre, dobljene v potopljenem delu PC-betonskega vzorca po 6-mesečni izpostavitvi sulfatu

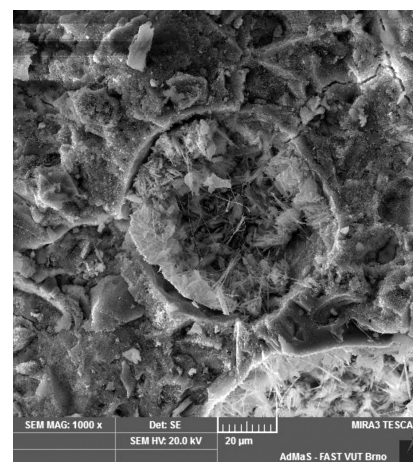


Figure 7: SEM image of microstructure of PC-concrete sample after a 6-month sulfate attack

Slika 7: SEM-posnetek mikrostrukture vzorca PC-betona po 6-mesečni izpostavitvi sulfatu

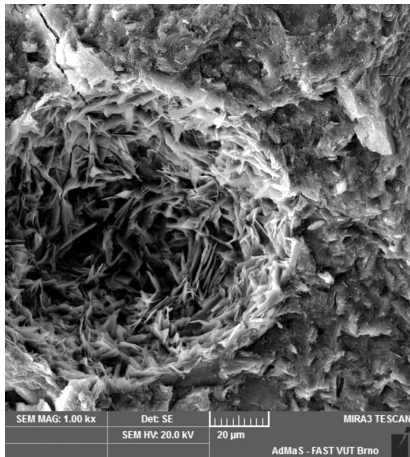


Figure 8: SEM image of microstructure of MK-concrete sample after a 6-month sulfate attack

Slika 8: SEM-posnetek mikrostrukture vzorca MK-betona po 6-mesečni izpostavitvi sulfatu

Irassar et al.¹² He found that a concrete containing a limestone filler is more susceptible to a sulfate attack and less durable than the corresponding plain mortar, as indicated by its larger expansion, greater surface deterioration, deeper transition zone of the attack, larger deposition of gypsum and higher degree of the CH depletion.

3.3 Changes in the microstructure

By mapping the chemical-element distribution on the surface of the lower part of the lengthwise slice of each samples, the presence of the locations rich in sulfur, iron and aluminum was determined. In the lowest parts of the samples, sulfur prevailed in the gypsum form. Using EDX REM, an aluminum-rich zone, identified as hydrated $\text{Al}(\text{OH})_3$, was located just above the gypsum. The presence of $\text{Al}(\text{OH})_3$ is presumably caused by the formation of ettringite from C_4AF in the presence of gypsum

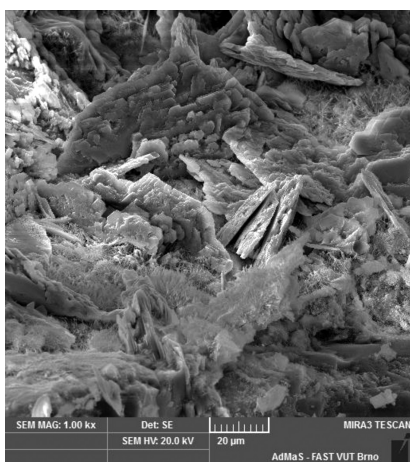


Figure 9: SEM image of microstructure of GL-concrete sample after a 6-month sulfate attack

Slika 9: SEM-posnetek mikrostrukture vzorca GL-betona po 6-mesečni izpostavitvi sulfatu

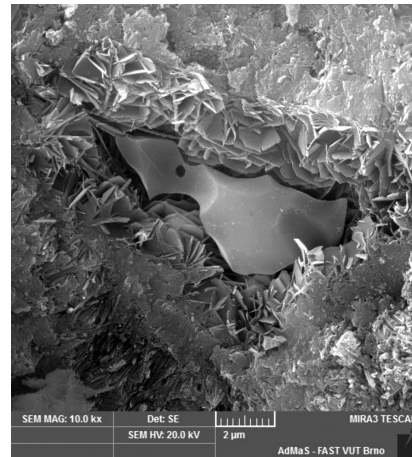


Figure 10: SEM image of microstructure of GBFS-concrete sample after a 6-month sulfate attack – detail of a partially reacted slag grain

Slika 10: SEM-posnetek mikrostrukture vzorca GBFS-betona po 6-mesečni izpostavitvi sulfatu – detajl delno zreagirane zrna žilindre

(Equation (2)). Thus, it can be concluded that even during a six-month sulfate attack, ettringite forms from C_4AF . In the case of the samples made from the materials with a high iron content (FA, PC, SRP), the zone rich in iron was present between the sulfur and aluminum locations. The iron compound was not sufficiently established; it is just known that it is a silicate without aluminum. The identification of this compound is still in process. Selected EDX REM images of the mapped chemical-element distributions are shown in **Figure 5**. The PC-, SRP- and FA-concrete samples had very similar distributions of chemical elements, and so did SRS and GBFS. The MK sample did not have a narrow zone rich in aluminum because of a high aluminum content in the used metakaolin.

In the submerged parts of all the investigated samples, typical prismatic gypsum crystals were identified with EDX SEM (**Figure 6**). The pores of the PC-concrete sample were largely filled with the crystalline

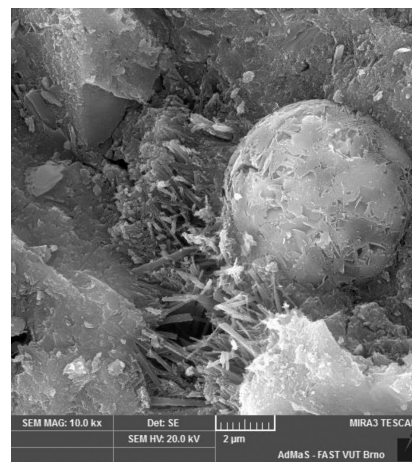


Figure 11: SEM image of microstructure of FA-concrete sample after a 6-month sulfate attack

Slika 11: SEM-posnetek mikrostrukture vzorca FA-betona po 6-mesečni izpostavitvi sulfatu

products of the sulfate attack, particularly with the typical needle crystals of ettringite (**Figure 7**), confirming the reduction in the total porosity. Of all the investigated concrete samples, the SRP- and SRS-concrete samples showed the smallest changes in the microstructures as just small amounts of ettringite were identified.

In the microstructures of the MK- and GL-concrete samples, a lot of portlandite in typical hexagonal crystals was identified on the surfaces of the pores (**Figures 8 and 9**), in contrast to the microstructures of these samples before the sulfate attack. An increased amount of portlandite in the pores was observed in all the studied samples, but for the MK and GL samples, this amount was enormous. This increased presence of portlandite was probably caused by the capillary action of the solution while the samples were kept in H₂SO₄. A direct contact of the cement matrix with the solution of sulfuric acid leads to a sulfate attack and the formation of gypsum. The non-aggressive solution penetrates to the higher parts of a sample, dissolves the surrounding Ca(OH)₂ and, during the drying of the sample, its crystallization occurs in the pores. For this reason, in the lowest parts of the samples, only gypsum as the primary product of the sulfate attack was identified. In addition to gypsum, the higher parts of the samples also contained ettringite and other by-products of the sulfate attack. In the case of the GBFS-concrete sample, crystals of portlandite were concentrated in the crevices around the partially reacted slag grains (**Figure 10**). Ettringite was identified on the surfaces of the pores. The FA-concrete sample contained a lot of damaged particles of fly ash and needle crystals of ettringite (**Figure 11**).

4 CONCLUSIONS

Microstructural changes in various types of fine-grained concrete after a six-month sulfate attack were investigated with mercury intrusion porosimetry and scanning electron microscopy. It was found that the total porosity of most samples was decreased after the sulfate attack, indicated by the products of the sulfate corrosion filling in the pores of the concrete. The most significant decrease was observed for the PC and FA concretes. The smallest changes in the microstructure occurred in the samples made from the sulfate-resisting cements. Thereby, the suitability of their use in the case of a sulfate attack was confirmed. The formation of the locations rich in sulfur, iron and aluminum during the sulfate attack on the concrete was determined by mapping the chemical-element distribution. Due to the presence of Al(OH)₃, which was identified in the aluminum-rich location, it can be concluded that, even during a six-month sulfate attack, ettringite is formed from C₄AF. The fate of the iron originating from C₄AF is still not clear.

Acknowledgement

This outcome was achieved with the financial support of the Czech Science Foundation (grant no. 13-22899P) and the European Union "Operational Programme Research and Development for Innovations", No. CZ.1.05/2.1.00/03.0097 (AdMaS).

5 REFERENCES

- ¹ A. Neville, *Cem. Concr. Res.*, 24 (2004), 1275–1296, doi:10.1016/j.cemconres.2004.04.004
- ² H. Yuan, P. Dangla, P. Chatellier, T. Chaussadent, *Cem. Concr. Res.*, 53 (2013), 267–277, doi:10.1016/j.cemconres.2013.08.002
- ³ D. Stein, *Instandhaltung von Kanalisationen*, 3rd ed., Ernst, Berlin 1999, 141
- ⁴ J. Skalný, J. Marchand, I. Odler, *Sulfate attack on concrete*, 1st ed., Spon Press, London 2002
- ⁵ H. F. W. Taylor, R. S. Gollop, *Mechanisms of chemical degradation of cement-based systems*, 1st ed., E & FN Spon, London 1997, 177–184
- ⁶ P. J. Monteiro, K. E. Kurtis, *Cem. Concr. Res.*, 33 (2003), 987–993, doi:10.1016/S0008-8846(02)01097-9
- ⁷ R. P. Khatari, V. Sirivivatnanon, *Cem. Concr. Com.*, 27 (1997), 1179–1189, doi:10.1016/S0008-8846(97)00119-1
- ⁸ H. F. W. Taylor, *Cement Chemistry*, 1st ed., Thomas Telford, London 1997, doi:10.1680/cc25929
- ⁹ B. Lothenbach, E. Wieland, *Waste Management*, 26 (2006), 706–719, doi:10.1016/j.wasman.2006.01.023
- ¹⁰ R. Gollop, H. F. W. Taylor, *Cem. Concr. Res.*, 26 (1996), 1013–1028, doi:10.1016/0008-8846(96)00089-0
- ¹¹ R. Gollop, H. F. W. Taylor, *Cem. Concr. Res.*, 22 (1992), 1027–1038, doi:10.1016/0008-8846(92)90033-R
- ¹² E. F. Irassar, V. L. Bonavetti, M. Gonzalez, *Cem. Concr. Res.*, 33 (2003), 31–41, doi:10.1016/S0008-8846(02)00914-6
- ¹³ J. Marchand, E. Samson, Y. Maltais, J. J. Beaudoin, *Cem. Concr. Com.*, 24 (2002), 317–329, doi:10.1016/S0958-9465(01)00083-X
- ¹⁴ M. Santhanam, M. D. Cohen, J. Olek, *Cem. Concr. Res.*, 31 (2001), 845–851, doi:10.1016/S0008-8846(01)00510-5
- ¹⁵ S. Diamond, *Cem. Concr. Com.*, 25 (2003), 1161–1164, doi:10.1016/S0958-9465(03)00138-0
- ¹⁶ M. Collepardi, *Cem. Concr. Com.*, 21 (1999), 147–154, doi:10.1016/S0958-9465(98)00044-4
- ¹⁷ D. Macphee, S. J. Barnett, *Cem. Concr. Res.*, 34 (2004), 1591–1598, doi:10.1016/j.cemconres.2004.02.022
- ¹⁸ N. J. Crammond, *Cem. Concr. Res.*, 15 (1985), 1039–1050, doi:10.1016/0008-8846(85)90095-X
- ¹⁹ G. R. Gouda, D. M. Roy, A. Sarkar, *Cem. Concr. Res.*, 5 (1975), 519–522, doi:10.1016/0008-8846(75)90026-5
- ²⁰ M. Romer, *Cem. Concr. Com.*, 25 (2003), 1173–1176, doi:10.1016/S0958-9465(03)00155-0
- ²¹ M. Romer, L. Holzer, M. Pfiffner, *Cem. Concr. Com.*, 25 (2003), 1111–1117, doi:10.1016/S0958-9465(03)00141-0
- ²² N. De Belie, J. Montanya, A. Beeldens, E. Vincke, D. Van Gemert, W. Verstraete, *Cem. Concr. Res.*, 34 (2004), 2223–2236, doi:10.1016/j.cemconres.2004.02.015

EFFECT OF THERMOMECHANICAL TREATMENT ON THE CORROSION BEHAVIOUR OF Si- AND Al-CONTAINING HIGH-Mn AUSTENITIC STEEL WITH Nb AND Ti MICRO-ADDITIONS

VPLIV TERMOMEHANSKE OBDELAVE NA KOROZIJSKO VEDENJE MANGANSKEGA AVSTENITNEGA JEKLA Z VSEBNOSTJO Si IN Al, MIKROLEGIRANEGA Z Nb IN Ti

Adam Grajcar, Aleksandra Plachcińska, Santina Topolska, Monika Kciuk

Silesian University of Technology, Institute of Engineering Materials and Biomaterials, Konarskiego Street 18a, 44-100 Gliwice, Poland
adam.grajcar@polsl.pl

Prejem rokopisa – received: 2014-07-31; sprejem za objavo – accepted for publication: 2014-12-19

doi:10.17222/mit.2014.148

The corrosion behavior of the 27Mn-4Si-2Al type austenitic steel micro-alloyed with Nb and Ti was evaluated in acidic 0.1 M H₂SO₄ and chloride 3.5 % NaCl environments using potentiodynamic polarization tests. The corrosion properties of solution-treated specimens were compared to thermomechanically processed specimens. In the acidic solution, the steel exhibited a lower corrosion resistance than in the chloride solution, independently of the heat treatment applied. SEM and light micrographs confirmed that the corrosion attack in the acidic solution was higher when compared to the chloride solution. The steel showed evidence of pitting and uniform corrosion in both the acidic and chloride solutions. The corrosion resistance of supersaturated specimens in both 0.1 M H₂SO₄ and 3.5 % NaCl media was lower when compared to the thermomechanically treated specimens. It was found that the corrosion behavior of the examined high-Mn steel depends on the passivation tendency of the alloying elements (Mn, Al) and the grain size.

Keywords: high-Mn steel, austenitic steel, corrosion resistance, passivity, thermomechanical treatment, potentiodynamic polarization test

Korozijsko vedenje avstenitnega jekla 27Mn-4Si-2Al, mikrolegiranega z Nb in Ti je bilo ocenjeno v kislem 0,1 M H₂SO₄ in v kloridnem okolju 3,5 % NaCl, s potenciodinamičnim polarizacijskim preizkusom. Korozijske lastnosti raztopno žarjenih vzorcev so bile primerjane s termomehansko izdelanimi vzorci. V kisli raztopini so bili vzorci manj korozijsko odporni kot v kloridni raztopini, neodvisno od uporabljene toplotne obdelave. SEM in svetlobni posnetki so potrdili, da je bil napad korozije v primerjavi s kloridno raztopino izrazitejši v kisli raztopini. Na jeklu so bili dokazi za jamičasto in splošno korozijo v obeh raztopinah, kisli in bazični. Korozijska odpornost prenasičenih vzorcev v 0,1 M H₂SO₄ in v 3,5 % NaCl je bila manjša v primerjavi s termomehansko obdelanimi vzorci. Ugotovljeno je, da je korozijsko vedenje preiskovanega visokomanganskega jekla odvisno od nagnjenosti k pasivaciji legirnih elementov (Mn, Al) in od velikosti zrn.

Ključne besede: visokomangansko jeklo, avstenitno jeklo, korozijska odpornost, pasivnost, termomehanska obdelava, preizkus potenciodinamične polarizacije

1 INTRODUCTION

High-manganese austenitic steels are being developed as advanced automotive structural materials due to their superior combination of strength, ductility, and crashworthiness. However, their application for automotive parts is limited because of their low corrosion resistance. The corrosion behavior of high-manganese austenitic steels depends on their chemical composition and the corrosion medium applied. It was found that additions of Al and Cr improve the corrosion resistance of high-Mn steels.¹⁻³ This is due to the passive-film-forming tendency of the steel surface. It is reported that a silicon addition to steel decreases its corrosion resistance.⁴ The tendency to create a passive protective layer on the steel surface depends on the type of corrosive environment. Kannan et al.¹ reported that 29Mn-3.1Al-1.4Si austenitic steel showed a lower corro-

sion resistance in an acidic solution than in a chloride solution.

The corrosion behavior of high-Mn austenitic steels also depends on the heat treatment applied and plastic deformation. Generally, cold working increases the corrosion rate because of the deformation twins, which represent the regions of different potentials from the matrix.^{5,6} The corrosion resistance of steel is also related to the dislocation density. In cold-rolled steels the dislocation amount is much higher when compared to hot-rolled steels because of the recrystallization effects reducing the dislocation density.⁷⁻⁹ The corrosion resistance of grain boundaries is poor because of a high dislocation density present at these regions. Di Schino et al.¹⁰ reported that the corrosion resistance of steel is also related to its grain size.

During the past decade, there were a number of reports on the corrosion properties of Fe-(high-Mn)-

Al-Si alloys. Most investigations focused on the effect of the alloying elements on the corrosion behaviour. There are few reports about the effects of heat treatment or plastic deformation on the corrosion resistance of high-Mn austenitic steels.^{5,11} Therefore, the corrosion properties of solution-treated and thermomechanically processed specimens were compared in this work.

2 EXPERIMENTAL PROCEDURE

The work addresses the corrosion behaviour of the vacuum-melted high-manganese steel containing 0.04 % C, 27.5 % Mn, 4.18 % Si, 1.96 % Al, 0.017 % S, 0.004 % P and 0.0028 % N. Carbon and manganese are the main austenite stabilizers. Silicon and aluminium should provide solid-solution strengthening. Additionally, micro-additions of Nb (0.033 %) and Ti (0.01 %) are added for precipitation strengthening and grain refinement. The ingots were hot forged and roughly rolled to a thickness of 4.5 mm. Two types of specimens were prepared using the thermomechanical rolling and the subsequent solution treatment. The thermomechanical processing consisted of hot rolling of flat samples in 3 passes to a final thickness of about 2 mm obtained at the finishing rolling temperature of 850 °C. Then, the samples were rapidly cooled in water to room temperature. The second group of samples was subsequently annealed at 900 °C for 20 min.

The corrosion properties of the 27Mn-4Si-2Al steel were evaluated using potentiodynamic polarization tests in two environments: acidic 0.1 M H₂SO₄ and 3.5 % NaCl solutions. The corrosion behavior of the solution-treated specimens was compared to the thermomechanically processed specimens. The corrosion tests were examined using the average of the measurement results for four supersaturated and two thermomechanically treated specimens. The exposed specimen surfaces (0.38 cm²) were ground with SiC paper of up to 800 grit. The samples were washed in distilled water and rinsed in acetone before the experiments. All the corrosion tests were conducted using freshly prepared electrolytes. Polarization studies were carried out using an Atlas 0531 electrochemical unit potentiostat/galvanostat driven by the AtlasCorr05 software and an electrochemical corrosion cell consisting of a specimen as the working electrode, stainless steel as the counter electrode and a silver/silver chloride (Ag/AgCl) reference electrode. A scan rate of 0.5 mV/s was employed during polarization. Potentiodynamic-scan data were collected to determine the electrochemical parameters – corrosion potential E_{corr} and corrosion current density i_{corr} – using Tafel slope extrapolation.

After the polarization tests, the samples were observed using a Zeiss SUPRA 25 scanning electron microscope (SEM) to assess the type of the corrosion attack. Subsequently, the depth of the corrosion pits on the cross-sectioned specimens using a Zeiss Axio Ob-

server Z1m light microscope was evaluated. For light microscopy, the samples were mechanically ground with SiC paper of up to 1500 grit, polished with Al₂O₃ with a granularity of 0.1 μm and then etched using 5 % nital to reveal the microstructure.

3 RESULTS AND DISCUSSION

A typical micrograph of a thermomechanically treated specimen is shown in **Figure 1a**. The light micrograph presents relatively coarse austenite grains elongated in the direction of hot rolling. The average grain size was estimated to be about 70 μm. Annealing twins and elongated sulfide inclusions were also observed. **Figure 1b** shows the light micrograph of a solution-treated specimen. The microstructure of the steel solution-treated from a temperature of 900 °C is characterized by a bimodal distribution of the grains. The average grain size was estimated to be about 40 μm. Relatively large elongated austenite grains and small recrystallized grains are apparent, indicating a strain accumulation that remains after the thermomechanical rolling. As a result, the driving force decreasing the accumulated energy leads to a partial recrystallization of

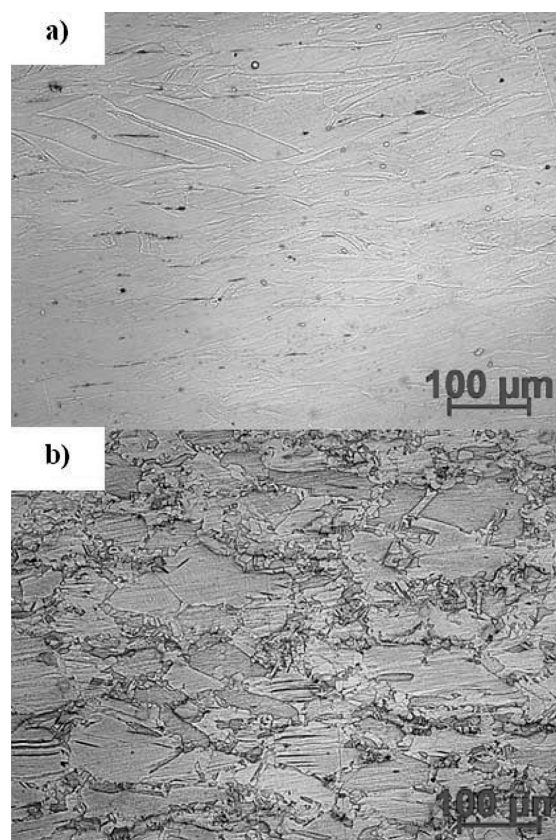


Figure 1: Austenitic microstructures of: a) thermomechanically treated and b) supersaturated steels

Slika 1: Avstenitna mikrostruktura: a) termomehansko obdelanega in b) prenasičenega jekla

the austenite grains during the subsequent annealing of the samples at 900 °C.

Based on the potentiodynamic curves (Figures 2 to 5), the corrosion potential E_{corr} and corrosion current density i_{corr} were determined. The average calculated values are shown in Table 1. The results of the corrosion tests are characterized by a small scatter. The lowest corrosion resistance was obtained in the acidic solution, independently of the heat-treatment type (thermomechanically treated or supersaturated specimens). The highest values of the corrosion current density were registered in the acidic solution. Kannan et al.¹ also reported that the 29Mn-3.1Al-1.4Si austenitic steel showed a lower corrosion resistance in an acidic medium than in a chloride solution.

Table 1: Electrochemical-polarization data of thermomechanically treated (t) and supersaturated (s) steels in two different environments

Tabela 1: Podatki o elektrokemijski polarizaciji termomehansko obdelanega (t) in prenasičenega (s) jekla v dveh različnih okoljih

	Type of heat treatment	3.5 % NaCl		0.1 M H ₂ SO ₄	
		$E_{corr}/$ mV	$i_{corr}/$ mA/cm ²	$E_{corr}/$ mV	$i_{corr}/$ mA/cm ²
average value	s	-774.4	0.30	-584.7	12.3
standard deviation		29.1	0.05	8.8	1.5
average value	t	-787.6	0.09	-583.9	1.4
standard deviation		6.5	0.007	6.2	0.2

The solution-treated specimens showed a higher corrosion-current-density values (12.29 mA/cm²) than the thermomechanically treated specimens (1.44 mA/cm²). In the chloride solution, the supersaturated specimens also showed a higher corrosion current density (0.24 mA/cm²) when compared to the thermomechanically treated specimens (0.09 mA/cm²). Generally, it is re-

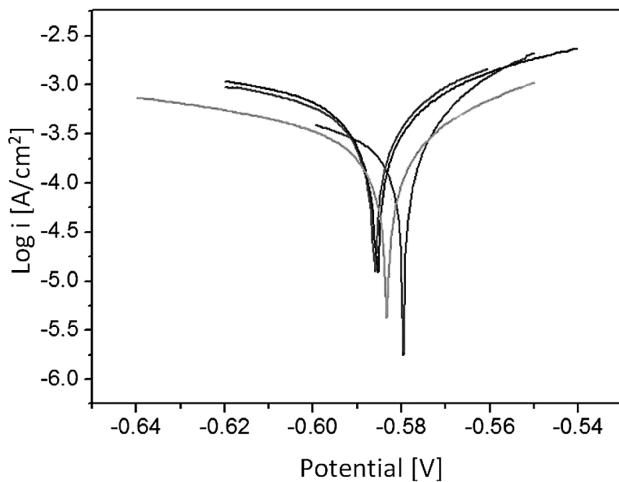


Figure 2: Potentiodynamic-polarization curves of the supersaturated steel obtained in 0.1 M H₂SO₄ solution (4 samples tested)

Slika 2: Potenciodinamične polarizacijske krivulje prenasičenega jekla, posnete v raztopini 0,1 M H₂SO₄ (preizkušeni so bili 4 vzorci)

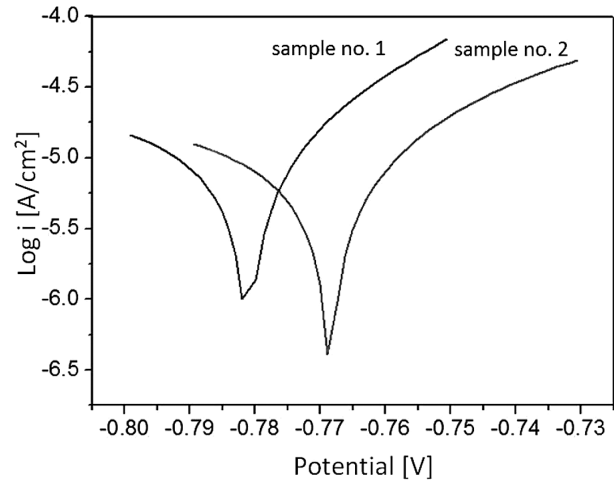


Figure 3: Potentiodynamic-polarization curves of the thermomechanically treated steel obtained in 3.5 % NaCl solution (2 samples tested)

Slika 3: Potenciodinamični polarizacijski krivulji termomehansko obdelanega jekla, posneti v raztopini 3,5 % NaCl (preizkušena sta bila 2 vzorca)

ported that cold working decreases the corrosion resistance of steel.^{5,6} Interestingly, the thermomechanically treated specimens showed a higher corrosion resistance than the supersaturated specimens independently of the corrosion medium. It should be noted that the examined steel was hot rolled. Hence, it has a much lower dislocation density than the cold-rolled specimens. Therefore, the higher corrosion resistance of the thermomechanically treated specimens is related to other factors.

The corrosion-potential values of the thermomechanically treated and supersaturated specimens are similar in both the acidic (Figure 2) and chloride solutions (Figure 3). The lowest corrosion-potential values were

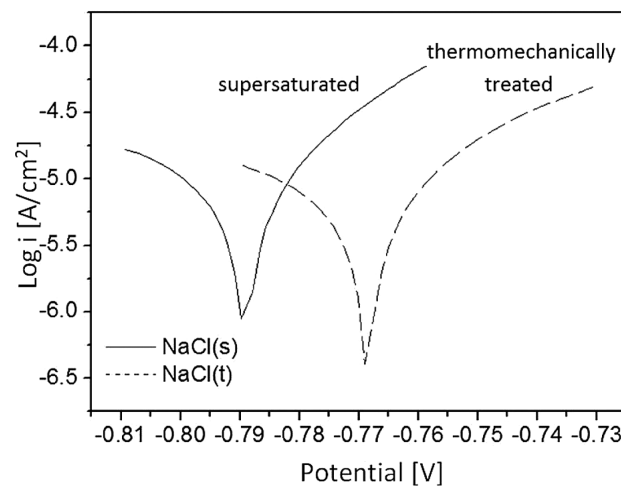


Figure 4: Potentiodynamic-polarization curves of the thermomechanically treated (t) and supersaturated (s) steels obtained in 3.5 % NaCl solution

Slika 4: Potenciodinamični polarizacijski krivulji termomehansko obdelanega (t) in prenasičenega (s) jekla, posneti v raztopini 3,5 % NaCl

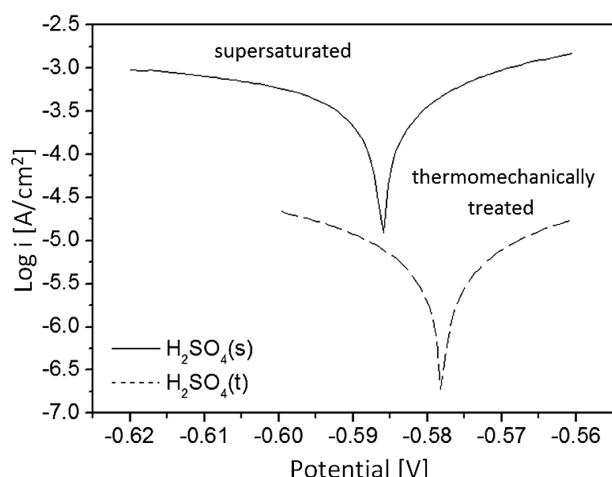


Figure 5: Potentiodynamic-polarization curves of the thermomechanically treated (t) and supersaturated (s) steels obtained in 0.1 M H₂SO₄ solution

Slika 5: Potenciodinamični polarizacijski krivulji termomehansko obdelanega (t) in prenasičenega (s) jekla, posneti v raztopini 0,1 M H₂SO₄

registered in the chloride solution (Figure 4). They are related to the earlier appearance of the corrosion pits in the chloride environment. In the 0.1 M H₂SO₄ medium,

higher (right-shifted) corrosion-potential values were registered (Figure 5). The lowest values of the corrosion potential in the chloride solution are also reported for the other high-Mn alloys.¹ However, it should be noted that the values of the corrosion current density were much higher in the acidic solution (Table 1). They are related to the stronger corrosion attack in this medium.

The SEM and light micrographs of the thermomechanically treated and supersaturated specimens after the polarization tests in two environments are shown in Figures 6 to 8. In the acidic solution, both steels showed extensive uniform corrosion. In addition to uniform corrosion, pitting corrosion can also be observed (Figure 6). In the thermomechanically treated specimens, after the corrosion tests in 0.1 M H₂SO₄ the maximum depth of corrosion pits was evaluated as 55 μm (Figure 6b). In the supersaturated specimens, the maximum depth of corrosion pits was slightly higher (Figure 7b). On both types of specimens, wide and shallow corrosion pits were observed. It was noted that corrosion pits were usually formed in the coarse-grained regions of the microstructure. Fine-grained regions were dominated by uniform corrosion and a smaller density of the corrosion pits. A similar relationship between the corrosion resis-

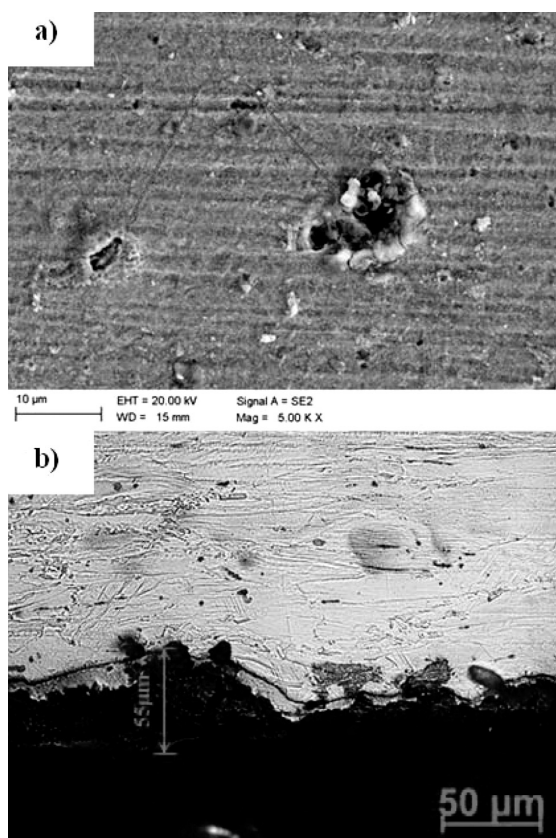


Figure 6: a) SEM micrograph of the surface and b) light micrograph of the cross-section of thermomechanically treated steel specimens, potentiodynamically polarized in acidic solution

Slika 6: a) SEM-posnetek površine in b) svetlobni posnetek prečnega prereza termomehansko obdelanega vzorca jekla, potenciodinamično polariziranega v kisli raztopini

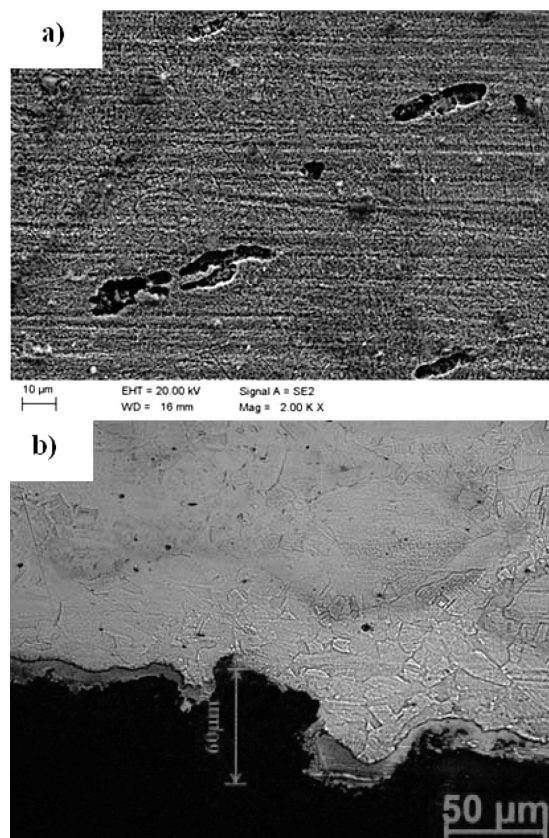


Figure 7: a) SEM micrograph of the surface and b) light micrograph of the cross-section of supersaturated steel specimens, potentiodynamically polarized in acidic solution

Slika 7: a) SEM-posnetek površine in b) svetlobni posnetek prečnega prereza prenasičenega vzorca jekla, potenciodinamično polariziranega v kisli raztopini

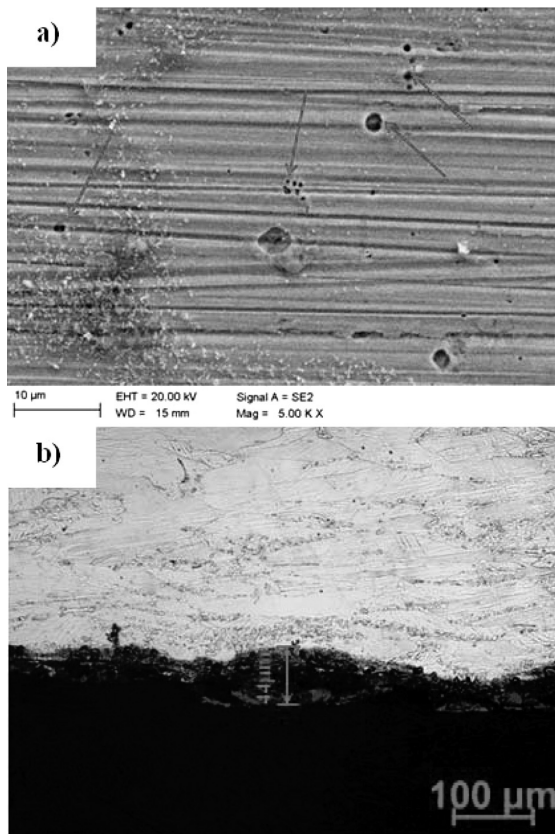


Figure 8: a) SEM micrograph of the surface and b) light micrograph of the cross-section of thermomechanically treated steel specimens, potentiodynamically polarized in chloride solution

Slika 8: a) SEM-posnetek površine in b) svetlobni posnetek prečnega prereza termomehansko obdelanega vzorca jekla, potenciodinamično polariziranega v raztopini klorida

tance and grain size was observed earlier by Di Schino et al.¹⁰ They observed that the pitting-corrosion rate decreased with the decreasing grain size, while the uniform-corrosion resistance was impaired by grain refining.

In the chloride solution, the thermomechanically treated specimens showed uniform corrosion. In addition to uniform corrosion, pitting-corrosion evidence was also observed (**Figure 8a**). Other authors^{1,12,13} also observed corrosion pits in different high-manganese steels after the polarization tests in a chloride solution. After the corrosion tests in 3.5 % NaCl, the maximum depth of the corrosion pits of the thermomechanically treated specimens was evaluated as 44 μm (**Figure 8b**). Similar corrosion pits can also be identified for the supersaturated specimens. Small pits are usually formed at non-metallic inclusions (**Figure 9**). The same nature of corrosion damages of high-Mn steels was also observed by Grajcar et al.⁶ on the samples subjected to immersion tests.

It was observed that pitting corrosion was usually initiated at sulfide inclusions. The negative impact of MnS inclusions on the corrosion resistance of austenitic steels was also observed by Donik et al.¹⁴ The density of

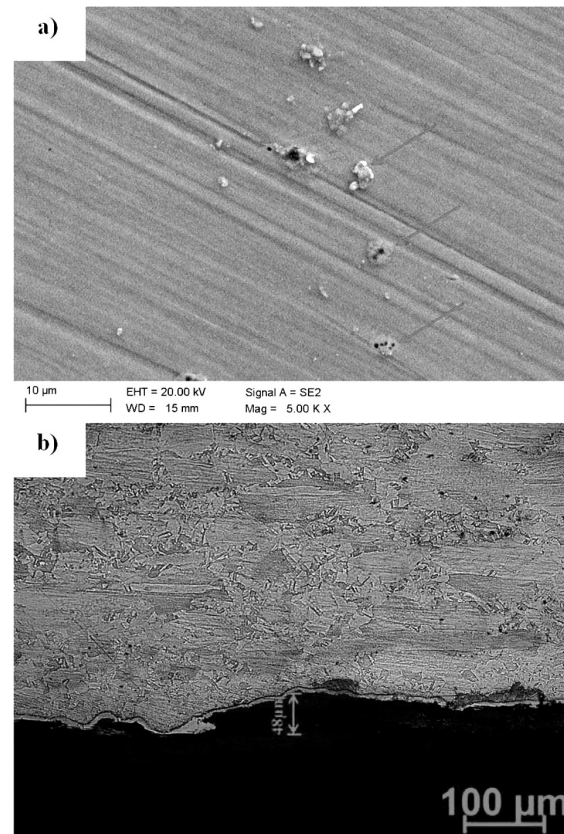


Figure 9: a) SEM micrograph of the surface and b) light micrograph of the cross-section of supersaturated steel specimens, potentiodynamically polarized in chloride solution

Slika 9: a) SEM-posnetek površine in b) svetlobni posnetek prečnega prereza prenasičenega vzorca jekla, potenciodinamično polariziranega v raztopini klorida

corrosion pits and corrosion products are greater in the acidic solution than in the chloride medium. Microscopic observations are confirmed by the potentiodynamic test results, which showed that the investigated steel has a better corrosion resistance in the chloride medium when compared to the acidic environment.

Corrosion resistance depends on the pH of corrosion solutions and the values of the corrosion potential (Pourbaix diagrams).¹⁵ In the 0.1 M H₂SO₄ (pH = 1) and 3.5 % NaCl solutions, manganese dissolves as Mn²⁺. It can be concluded that Mn showed a non-passivating tendency in these environments. In the acidic solution, aluminium dissolves as Al³⁺ ions, preventing the formation of the passive layer. In the 3.5 % NaCl solution, aluminium forms the oxide passive layer, slightly increasing the corrosion resistance of the investigated steel.

4 CONCLUSIONS

Potentiodynamic polarization tests showed that the 27Mn-4Si-2Al type austenitic steel is characterized by the lowest corrosion resistance in the 0.1 M H₂SO₄ solution, independently of the heat treatment applied (thermomechanically treated or solution-treated specimens).

Microscopic observations confirmed that corrosion damages are more numerous in the acidic solution. In both the acidic and chloride solutions wide and shallow corrosion pits of various depths were identified. In addition to pitting corrosion, extensive uniform corrosion was observed. The high density of the corrosion damages in the acidic solution is related to the non-passivating tendency of Mn and Al in this environment. Independently of the corrosion media, the thermomechanically treated specimens showed a better corrosion resistance than the supersaturated specimens. This means that the bimodal distribution of the grain size has a greater effect on decreasing the corrosion resistance of the investigated steel than the effect of hot working.

5 REFERENCES

- ¹ M. B. Kannan, R. K. S. Raman, S. Khoddam, *Corros. Sci.*, 50 (2008), 2879–2884, doi:10.1016/j.corsci.2008.07.024
- ² V. F. C. Lins, M. A. Freitas, E. M. P. Silva, *Appl. Surf. Sci.*, 250 (2005), 124–134, doi:10.1016/j.apsusc.2004.12.040
- ³ Y. S. Zhang, X. M. Zhu, S. H. Zhong, *Corros. Sci.*, 46 (2004), 853–876, doi:10.1016/j.corsci.2003.09.002
- ⁴ S. Suzuki, E. Matsubara, T. Komatsu, Y. Okamoto, K. Kanie, A. Muramatsu, H. Konishi, J. Mizuki, Y. Waseda, *Corros. Sci.*, 49 (2007), 1081–1096, doi:10.1016/j.corsci.2006.06.029
- ⁵ I. M. Ghayad, A. S. Hamada, N. N. Girgis, W. A. Ghanem, *Steel Grips*, 4 (2006) 4, 133–137
- ⁶ A. Grajcar, S. Kolodziej, W. Krukiewicz, *Arch. Mater. Sci. Eng.*, 41 (2010) 2, 77–84
- ⁷ A. Grajcar, M. Opiela, G. Fojt-Dymara, *Arch. Civ. Mech. Eng.*, 9 (2009) 3, 49–58, doi:10.1016/S1644-9665(12)60217-9
- ⁸ L. A. Dobrzański, A. Grajcar, W. Borek, *Mater. Sci. Forum*, 638–642 (2010), 3224–3229, doi:10.4028/MSF.638-642.3224
- ⁹ G. R. Razavi, M. S. Rizi, H. M. Zadeh, *Mater. Tehnol.*, 47 (2013) 5, 611–614
- ¹⁰ A. Di Schino, M. Barteri, J. M. Kenny, *J. Mater. Sci.*, 38 (2003) 15, 3257–3262, doi:10.1023/A:1025181820252
- ¹¹ S. Lasek, E. Mazancova, *Metalurgija*, 52 (2013), 441–444
- ¹² L. M. Roncercy, S. Weber, W. Theisen, *Metall. Mater. Trans. A*, 41 (2010), 2471–2478, doi:10.1007/s11661-010-0334-z
- ¹³ Y. S. Zhang, X. M. Zhu, *Corros. Sci.*, 41 (1999) 9, 1817–1833, doi:10.1016/S0010-938X(99)00017-7
- ¹⁴ C. Donik, I. Paulin, M. Jenko, *Mater. Tehnol.*, 44 (2010) 2, 67–72
- ¹⁵ N. Takeno, *Atlas of Eh-pH diagrams*, National Institute of Advanced Science and Technology, Tokyo 2005

SURFACE FREE ENERGY OF HYDROPHOBIC COATINGS OF HYBRID-FIBER-REINFORCED HIGH-PERFORMANCE CONCRETE

PROSTA ENERGIJA POVRŠINE HIDROFOBNIH PREMAZOV NA VISOKOZMOGLJIVEM BETONU, OJAČANEM S HIBRIDNIMI VLAKNI

Danuta Barnat-Hunek, Piotr Smarzewski

Lublin University of Technology, Faculty of Civil Engineering and Architecture, Nadbystrzycka Str. 40, 20-618 Lublin, Poland
d.barnat-hunek@pollub.pl

Prejem rokopisa – received: 2014-08-03; sprejem za objavo – accepted for publication: 2014-12-12

doi:10.17222/mit.2014.174

The aim of the research presented in the paper was to evaluate the feasibility of using hydrophobic preparations based on organosilicon compounds for the protection treatment of hybrid-fiber-reinforced high-performance concrete (FRHPC) surfaces. The wettability of concrete has a direct effect on the durability and corrosion resistance. The wetting properties of FRHPC were evaluated through the measurement of the contact angle between the surfaces of these materials with either water or glycerine used as probe liquids. On this basis, the surface free energy (SFE) was determined. The polar and disperse components of SFE were obtained by means of the Owens-Wendt method. Three different siloxane preparations were deposited onto seven types of concrete with the fiber content ranging from 0 % to 1 %. In order to investigate the effect on the strength, the granodiorite aggregate in concrete mixes 5, 6, 7 was replaced with granite. The basic characteristics of the concrete strength were examined: the tensile splitting strength, the compressive strength, the modulus of elasticity. A SEM examination of the coated concrete surfaces confirmed that preparations A–C can effectively cover the voids and pores present in the concrete surfaces. The presented results indicate that the surfaces of the concrete with a silane film had a wide range of SFE, depending on the kind of agent. SFE depended on the chemical reactivity of the silanes used, the type of solvent, the viscosity and surface tension of the solution. The evaluation of the contact angle and SFE helped to efficiently select the most appropriate preparation.

Keywords: surface free energy (SFE), contact angle, hydrophobization, high-performance concrete, hybrid fiber, Owens-Wendt method

Namen raziskave, predstavljene v članku, je bil oceniti izvedljivost uporabe hidrofobne obdelave na osnovi organosilikonskih spojin za zaščito površine zmogljivega betona (FRHPC), ojačanega s hibridnimi vlakni. Omočljivost betona ima neposreden vpliv na zdržljivost in odpornost proti koroziji. Omočljivost FRHPC je bila ocenjena z merjenjem stičnega kota med površino teh materialov pri uporabi vode in glicerina kot preizkusne tekočine. Na tej osnovi je bila določena prosta energija površine (SFE). Polarne in razpršilne komponente SFE so bile določene z Owen-Wendtovo metodo. Trije različni pripravki siloksana so bili naneseni na sedem vrst betona z vsebnostjo vlaken od 0 % do 1 %. Za preiskavo vpliva na trdnost je bil zrnati granodiorit nadomeščen v betonskih mešanica 5, 6 in 7 z granitom. Preiskovane so bile osnovne značilnosti trdnosti betona: natezna cepilna trdnost, tlačna trdnost in modul elastičnosti. SEM-preiskave pokrite površine betona so potrdile, da priprave A–C lahko učinkovito prekrivajo praznine in pore, ki so na površini betona. Prikazani rezultati kažejo, da ima površina betona s plastjo silanov velik razpon SFE, odvisno od vrste predstavnika. SFE je odvisna od kemijske reaktivnosti uporabljenega silana, vrste topila, viskoznosti in površinske napetosti raztopine. Ocena kota stika in SFE je pomagala pri izbiri najbolj primerne preparata.

Ključne besede: prosta energija površine (SFE), kot stika, hidrofobizacija, visokozmogljiv beton, hibridna vlakna, Owens-Wendt-ova metoda

1 INTRODUCTION

High-performance fiber-reinforced concrete is a cementitious material with a low water/cement ratio and a high cement content.^{1,2} Short, straight steel fibers are usually used to enhance the tensile strength and increase the ductility. As a result, the mechanical properties of hybrid-fiber-reinforced high-performance concrete are considerably enhanced compared to the normal concrete.^{2,3} High-performance concretes are often exposed to aggressive impacts of the environment and, therefore, they must have a high resistance to chemical corrosion, frost corrosion, weathering, impact of aggressive water and many other corrosive agents.

Moisture damage is a major factor in the deterioration of building materials. One of the methods used to protect the concrete surface is hydrophobization.^{4,5} It causes a decrease in the capillary water absorption, thus allowing free vapor permeability. Organosilicon compounds – siloxanes or methyl silicone resins^{6–8} – are mostly used as concrete hydrophobing agents. Research⁹ confirmed that a polyethylhydrosiloxane admixture has a beneficial effect on the durability of the concrete with large volumes of supplementary cementitious materials. Concrete is normally a hydrophilic material, which significantly reduces the durability of concrete structures. In the research to synthesize water-repellent concrete, the emulsion was enriched with the polymethyl-hydrogen

siloxane-oil hydrophobic agent.¹⁰ There are also tests aimed at increasing the strength and toughness using special techniques like polymer impregnation of the matrices of fibre-reinforced concretes.¹¹

Sustainability is the necessity for concrete and nanotechnology is the chance for the future of concrete-polymer composites.¹² In the case of impregnation, polymer-cement concrete (PCC) gained popularity. The most often used polymer-cement concretes are modified using styrene-butadiene co-polymer, acrylic polymers and epoxy resin.¹³

These coatings make the concrete surface non-wettable by water and corrosive compounds such as water-soluble salts. The fact that building materials can be wetted by liquids is of special importance, for example, during their hydrophobization, impregnation and in the production of anti-graffiti agents. The wettability of concrete by means of liquids which contain corrosive components is of great importance in practice; it may indicate adhesive properties of concrete as well as protective coatings applied to its surface. The wettability of concretes has a direct effect on the durability and corrosion resistance. In the research of concretes, their wettability and surface free energy (SFE) are considered to be important elements in assessing the adhesion properties. They are particularly useful in the analysis of the effects of modifying the surfaces of high-strength concretes by means of various protective coatings.

According to the literature data,¹⁴⁻¹⁶ the contact angle of the materials is an indicator of their wettability properties. High wettability – hydrophilicity – occurs at a low contact angle $< 90^\circ$, and insufficient wettability – hydrophobicity – occurs at a high contact angle $> 90^\circ$. The contact angle can be used to determine the surface tension¹² and define the surface free energy¹⁷⁻¹⁹ and adhesion operation.^{14,20,21}

The contact angle is influenced by many factors which include, but are not limited to, the following: surface physical and chemical homogeneity, surface roughness and impurities, type of the measured liquid, drop size of the measured liquid, humidity or ambient temperature.¹⁸⁻²¹ Among the most commonly used methods for determining the contact angle, one can mention the following: the air-bubble method, the geometric method, the liquid-capillary-rise methods tested on sample materials (among others, the Wilhelmy method) and the direct-measurement method.²²⁻²⁵ A very popular method to measure the contact angle is direct measurement using a contact-angle analyzer or a goniometer.^{26,27}

The surface free energy (the surface tension) is the key parameter while evaluating the physicochemical characteristics of solid surfaces. The surface may be of a dispersive nature (a dispersion component) or polar (a polar component). Knowing the properties of impregnating agents one can decrease or increase the SFE and, therefore, the surface tension of materials, causing their non-wettability, which is related, among others, to the

chemical corrosion and frost resistance. The highest decrease in SFE can be due to the coatings that hydrophobize a surface to the largest extent.²⁸

The surface free energy (SFE) is one of the thermodynamic quantities describing the state of equilibrium of the atoms in the surface layers of materials.^{14,29} SFE represents the state of imbalance of the intermolecular interactions present at the phase boundary of two different mediums. There are numerous methods for direct determination of the surface free energy of liquids. Owing to the fact that there are no direct methods for determining the SFE of solids, some indirect methods are used, which include, among others, the contact-angle measurement method, calculating the surface free energy on the basis thereon.^{21,22,30}

The main methods for determining SFE were formulated by Neumann, Wu, Owens and Wendt, Zisman and Fox, Fowkes, Van-Oss-Chaudhury-Good.²¹

The Owens-Wendt method is commonly used for determining the surface free energy of materials.¹⁹ This method consists of determining the dispersion and polar components of SFE. The polar component (γ_s^p), which is the measure of the surface polarity, is associated with, among others, the bond strength between the materials.

The analysis of the nature of a hydrophobized-concrete surface layer in terms of wettability presented in the article allowed us to assess, inter alia, the material behavior in the presence of water and corrosive compounds. In the cases where a significant resistance of a concrete surface layer to the impact of a corrosive environment is required, it is desirable to use preparations of the lowest SFE value.

2 MATERIALS AND METHODS

2.1 Concrete mixtures

In the laboratory, seven concrete mixtures were prepared using Portland cement 670.5 kg/m³ (CEM I 52.5 N-HSR/NA), aggregate 990 kg/m³, sand 500 kg/m³, water 178 L/m³, microsilica 74.5 kg/m³, superplasticizer 20 L/m³ and steel and polypropylene fibers in varied amounts.

Table 1: Fractions of fibers in various concretes

Tabela 1: Delež vlakna v različnih betonih

Concrete type	Fraction, %	
	Steel fibers	Polypropylene fibers
granodiorite aggregate		
HPC1	–	–
SFHPC	1 %	–
HFHPC1	0.75 %	0.25 %
granite aggregate		
HFHPC2	0.5 %	0.5 %
HFHPC3	0.25 %	0.75 %
PFHPC	–	1 %
HPC2	–	–

Table 2: Mechanical properties of concretes**Tabela 2:** Mehanske lastnosti betonov

	HPC1	SFHPC	HFHPC1	HFHPC2	HFHPC3	PFHPC	HPC2
Compressive strength (MPa)	151.0	154.9	144.7	133.9	122.3	94.6	129.5
Splitting tensile strength (MPa)	8.9	13.8	13.5	10.0	9.3	7.6	6.8
Modulus of elasticity (GPa)	38.37	39.74	34.27	32.45	29.60	29.42	32.55

Table 1 lists abbreviated names of the concretes and amounts of steel and polypropylene fibers for various batches. Granodiorite aggregate was used for the first three concretes and granite aggregate was used for the remaining four concretes.

The concrete samples were made on the basis of a recipe determined experimentally using the known mortar according to EN 206:2014-04. The mixing procedure was as follows: quartz sand and coarse aggregate were homogenized together and mixed with half quantity of water. Then, cement, silica fume and the remaining water were added and, finally, superplasticizer was added. After the components were thoroughly mixed, fibers were gradually added by hand to obtain homogeneous and workable mixtures. The fibers were dosed gradually so as not to be tried and not to sink to the bottom of the mixture. The samples were formed directly after the concrete compounds were mixed according to EN 12390-2:2011.

Molds coated with an anti-adhesive substance were filled with concrete batches and compacted on a vibrating table. All the samples were stored at a temperature of about 23 °C until removing them from the moulds after 24 h and they were then placed in a water tank for 7 d to cure. After 7 d the samples were removed from the tank to cure in laboratory conditions for up to 28 d.

2.2 Properties of the concrete

2.2.1 Compressive strength and splitting tensile strength

Cubic concrete samples with dimensions of 100 mm × 100 mm × 100 mm were applied. Research was conducted according to EN 12390-3:2002 regarding the compressive strength and EN 12390-6:2001 regarding the splitting tensile strength. The evaluation of the grades of the concretes was carried out using a Walter-Baj AG compression tester within 3 MN after 28 d of maturation, when the average compressive strength of the samples was obtained.

2.2.2 Modulus of elasticity

The determination of the modulus of elasticity was carried out on cylinders with a diameter of 150 mm and a height of 300 mm by measuring the deformation of the samples in a stress range from 0.5 MPa to 30 % of the concrete compressive strength. The examination was conducted by means of a Walter-Baj AG press and a modulus-measuring device with an extensometer.

The strength properties of the concretes adopted for the examination are shown in **Table 2**.

2.3 Hydrophobic materials used

Three hydrophobic preparations commonly used as construction chemicals were selected for the laboratory tests; they differed in the type of solvent, viscosity and concentration:

- A – the water-based solution of methylsilicone resin in the potassium hydroxide (1 : 6),
- B – the organic-solvent-based alkyl alkoxy silane oligomer,
- C – the organic-solvent-based methylsilicone resin.

Each preparation was applied with a brush in two layers. The first preparation was diluted in the proportion of 1 : 6 according to the manufacturer's requirements. The other hydrophobic preparations with organic solvents were not diluted. Thereafter, all the hydrophobized bricks were seasoned for a period of 7 d in the laboratory conditions to control the process of hydrolytic polycondensation of the hydrophobic coatings.

Producers do not provide full product characteristics of the examined hydrophobic preparations or how their solutions are applied in practice. For that purpose the following parameters were determined experimentally: the viscosity factor and the surface tension for all the examined preparations. The major characteristics of the applied preparations used in the research are listed in the **Table 3**. Viscosity factor η was determined by measuring the time of the solution flow in the Ostwald viscosimeter. The surface tension was measured by raising the fluid in the capillary. The research was executed at a room temperature of 22.5 °C.

Table 3: Basic characteristics of hydrophobic preparations**Tabela 3:** Osnovne značilnosti hidrofobnih preparatov

Type of formulation	Viscosity η / (Pa s × 10 ⁻³)	Density at 20 °C (g/cm ³)	Surface tension σ (N/ (m × 10 ⁻³))	Quotient of surface tension and viscosity σ/η
A	1.099	1.26	67.92	61.73
B	1.479	0.80	23.11	15.65
C	2.846	0.82	24.30	8.54

2.4 Determination of the contact angle and surface free energy

In order to calculate the surface free energy, the contact-angle measurements of the analyzed concretes were conducted. The method of directly measuring the angle formed by a drop of the measuring liquid with the surface measured was used, using a computer program for the image analysis. The measurement of the contact

angles of the measuring-liquid drops was carried out on a research stand consisting of a goniometer integrated with a camera for taking photos of the drops put onto the surfaces of the samples. The stand was described in³¹.

In order to examine the contact angle two measuring liquids were used – distilled water and glycerine required by the Owens-Wendt model used in the analyses. Measuring-liquid drops of 2 mm³ were deposited by means of a micropipette.^{14,32} Due to the heterogeneity of the material, six drops were put on each sample. The measurements were carried out twice: at the time of the application of the drops, i.e., at 0 min and at 40 min. Standard and hydrophobized surfaces HFRHPC1 during the examination of the contact angle of a glycerine drop are shown in **Figure 1**.

For the calculation of the wettability of the concrete surface, the SFE values of the measuring liquids (γ_L), and their dispersion (γ_L^d) and polar components (γ_L^p) were adopted as shown in **Table 4**.³³

Table 4: SFE values of measuring liquids, their dispersion and polar components³³

Tabela 4: SFE-vrednosti izmerjenih tekočin in njihovih disperzijskih in polarnih komponent³³

Measuring liquid	SFE and its components (mJ/m ²)		
	γ_L	γ_L^d	γ_L^p
Distilled water	72.8	21.8	51.0
Glycerine	62.7	21.2	41.5

In the Owens-Wendt model, the following equations were used – for the dispersion component:¹⁴

$$\gamma_s^d = \frac{\gamma_g (\cos \theta_g + 1) - \gamma_w (\cos \theta_w + 1) \sqrt{\gamma_g^p / \gamma_w^p}}{2(\sqrt{\gamma_g^d} - \sqrt{\gamma_g^p \gamma_w^d / \gamma_w^p})} \quad (1)$$

and for the polar component:

$$\sqrt{\gamma_s^p} = \frac{\gamma_w (\cos \theta_w + 1) - 2\sqrt{\gamma_s^d \gamma_w^d}}{2\sqrt{\gamma_w^p}} \quad (2)$$

where γ_w – the surface free energy of water, γ_w^d – the dispersion component of water SFE, γ_w^p – the polar component of water SFE, γ_g – the SFE of glycerine, γ_g^d – the dispersion component of glycerine SFE, γ_g^p – the polar component of glycerine SFE, γ_s^p – the polar component of SFE of the examined material, γ_s^d – the dispersion component of SFE of the examined material, θ_g – the contact angle of glycerine, θ_w – the contact angle of water.

The total value of SFE (γ_s) was determined as a sum of the polar and dispersion components:

$$\gamma_s = \gamma_s^p + \gamma_s^d \quad (3)$$

2.5 Scanning electron microscopy of the hydrophobized concrete

A qualitative analysis of the chemical compositions within the main mineral components of the standard and

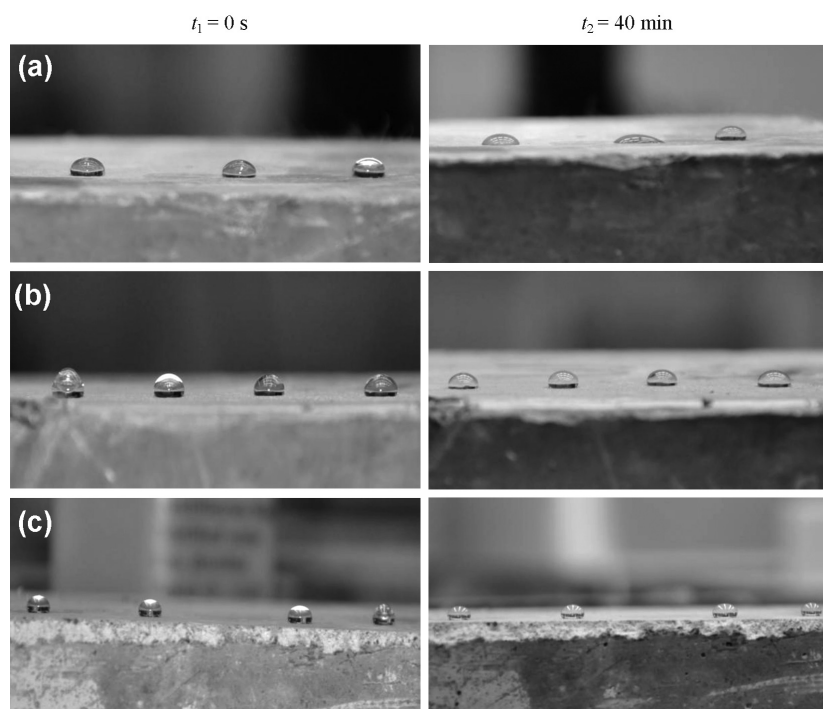


Figure 1: Standard and hydrophobized surfaces HFRHPC 1 during the examination of the contact angle of a glycerine drop: a) standard sample, b) water-soluble preparation – A, c) alkyl alkoxy silane oligomers – B

Slika 1: Navadna in hidrofobizirana površina HFRHPC 1 med preiskavo kontaktnega kota glicerinske kapljice: a) standardni vzorec, b) vodotopen preparat – A, c) alkil alkoxy silan oligomeri – B

hydrophobized concretes was carried out, and the morphology and microtopography were determined using a scanning electron microscope FEI Quanta 250 FEG equipped with a chemical-composition analysis system based on energy dispersion spectroscopy (EDS). The samples were prepared in the form of thin-layer plates, on which X-ray microanalyses were performed in the field mode and the compositions of the elements were determined for the seven batches of the concretes. The sample-preparation methodology excludes the formation of the microdefects associated with the cracking of the concrete surface and hydrophobic coatings. In order to avoid the formation of other surface defects, low vacuum and beam energy were used during the SEM analysis.

3 RESULTS AND ANALYSIS

3.1 Contact angle and surface free energy

The measured contact angles of water and glycerine and the calculated values of SFE and its components are included in **Tables 5** and **6**, respectively.

Graphic illustrations of the results obtained are shown in **Figures 2** to **4**.

Table 5: Concrete contact angles with water and glycerine

Tabela 5: Kontaktni koti vode in glicerina z betonom

Type of samples	Type of preparation	Contact angle			
		water $\theta_w/^\circ$		glycerine $\theta_g/^\circ$	
		$t_1 = 0$	$t_2 = 40$	$t_1 = 0$	$t_2 = 40$
HPC1	Standard	63.7	23.0	86.7	62.0
	A	83.5	74.1	86.6	77.3
	B	113.5	73.0	105.6	76.1
	C	122.7	98.3	127.3	102.1
SFHPC	Standard	67.8	32.4	86.2	66.7
	A	86.1	75.8	89.7	69.6
	B	107.5	103.3	108.7	106.7
	C	96.0	67.5	98.3	66.7
HFHPC1	Standard	39.4	20.1	67.0	43.5
	A	83.7	74.3	87.0	77.7
	B	109.3	104.0	109.7	105.7
	C	82.0	73.2	80.7	73.1
HFHPC2	Standard	42.3	12.6	71.0	45.4
	A	87.0	74.5	81.6	74.7
	B	103.4	111.6	106.3	104.1
	C	78.0	62.1	77.0	64.3
HFHPC3	Standard	55.5	26.0	73.4	47.8
	A	92.8	75.8	94.7	78.4
	B	113.4	103.3	106.8	103.6
	C	78.9	67.7	80.0	70.7
PFHPC	Standard	47.1	14.2	73.3	54.0
	A	100.7	78.3	103.3	82.1
	B	105.6	95.5	110.0	97.0
	C	101.8	83.7	94.5	85.7
HPC2	Standard	53.4	10.1	78.1	56.8
	A	102.5	83.4	100.4	79.3
	B	116.3	100.2	122.3	94.3
	C	116.1	100.5	119.8	105.6

Table 6: SFE and its components for hydrophobized and standard concretes

Tabela 6: SFE in njene komponente pri hidrofobiziranih in standardnih betonih

Type of sample	Type of preparation	SFE component				Total SFE $\gamma_s/(mJ/m^2)$	
		Dispersive $\gamma_s^d/(mJ/m^2)$		Polar $\gamma_s^p/(mJ/m^2)$		$t_1 = 0$	$t_2 = 40$
		$t_1 = 0$	$t_2 = 40$	$t_1 = 0$	$t_2 = 40$		
HPC1	Standard	1313.9	1873.8	266.9	342.5	1580.8	2216.3
	A	72.5	83.6	0.01	0.27	72.51	83.87
	B	65.5	82.0	4.95	0.45	70.45	82.45
	C	48.9	71.4	4.96	1.35	53.86	72.75
SFHPC	Standard	905.8	1833.5	160.04	345.60	1065.84	2179.1
	A	82.0	12.5	0.23	16.30	82.23	28.80
	B	17.9	56.1	0.63	0.94	18.53	57.04
	C	43.2	17.7	0.07	18.48	43.27	36.18
HFHPC1	Standard	1385.0	595.6	233.8	36.85	1618.8	632.45
	A	77.1	88.5	0.01	0.11	77.11	88.61
	B	9.4	26.6	2.00	0.24	11.40	26.86
	C	6.3	22.5	17.30	12.03	23.60	34.53
HFHPC2	Standard	1572.1	860.8	290.79	82.96	1862.89	943.79
	A	12.3	25.6	9.44	9.91	21.74	35.51
	B	46.4	57.0	0.29	2.95	46.69	59.95
	C	10.3	68.7	16.47	4.25	26.77	72.95
HFHPC3	Standard	803.5	641.1	111.2	47.24	914.70	688.34
	A	39.0	68.0	0.59	0.92	39.59	68.92
	B	40.4	11.0	1.17	3.08	41.57	14.08
	C	36.2	83.3	4.59	1.13	40.79	84.46
PFHPC	Standard	1426.9	1438.8	260.06	217.8	1686.96	1656.6
	A	43.9	95.4	0.03	0.07	43.93	95.47
	B	74.0	30.2	3.60	1.03	77.60	31.23
	C	49.8	48.6	0.31	1.20	50.11	49.80
HPC2	Standard	841.1	1798.1	127.99	309.91	1631.50	2108.0
	A	0.1	2.0	15.45	22.55	15.46	24.55
	B	88.3	25.4	10.92	0.81	99.22	26.21
	C	44.5	100.3	2.27	5.66	46.77	105.96

3.2 Scanning electron microscopy of the hydrophobized concrete

SEM microscopic analyses were performed to verify the distribution and effectiveness of hydrophobic coatings A, B, C in the pores of the concrete. For the analyses, the HFHPC1 concrete was adopted, for which

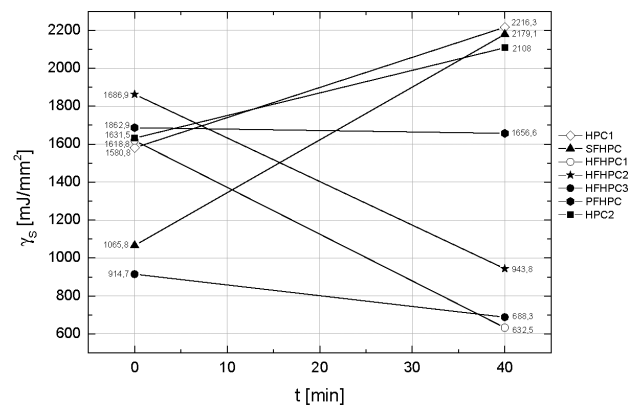


Figure 2: Total values of SFE of standard concretes at the beginning of the examination and after 40 min

Slika 2: Skupna vrednost SFE standardnih betonov na začetku preizkusa in po 40 min

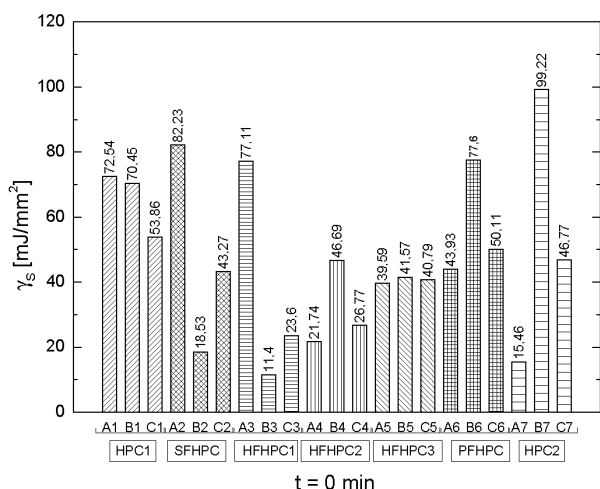


Figure 3: Total values of SFE of hydrophobized concretes at the beginning of the examination ($t = 0$)

Slika 3: Skupna vrednost SFE pri hidrofobiziranih betonih na začetku preizkusa ($t = 0$)

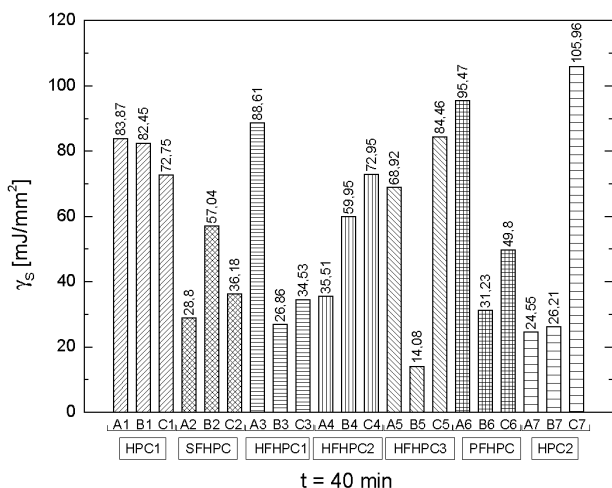


Figure 4: Total values of SFE of hydrophobized concretes after 40 min

Slika 4: Skupna vrednost SFE pri hidrofobiziranih betonih po 40 min the best hydrophobic properties of the coatings were obtained. Table 7 shows the analyses of the chemical

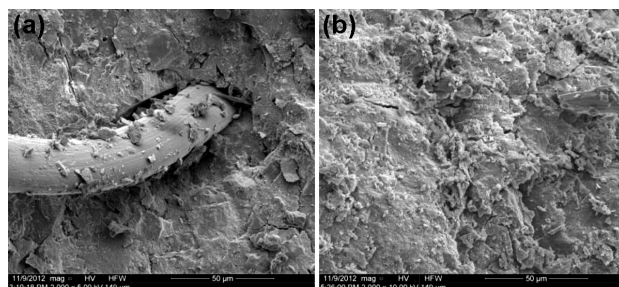


Figure 5: Microstructures of HFHPC1 and HPC2 concretes prior to hydrophobization, SEM

Slika 5: Mikrostruktura HFHPC1 in HPC2 betona pred hidrofobiziranjem, SEM

compositions in the field mode for standard HFHPC1 and hydrophobized concretes using preparations A, B and C, performed on the basis of energy dispersion spectroscopy (the results from the entire area of the study).

Table 7: Chemical compositions of standard and hydrophobized HFHPC1

Tabela 7: Kemijska sestava standardnih in hidrofobiziranih HFHPC1

HFHPC1	Component, w/%					
	Na ₂ O	MgO	Al ₂ O ₃	SiO ₂	K ₂ O	CaO
Standard	0.98	0.87	0.63	22.66	–	72.39
A	0.75	1.31	1.60	68.20	25.38	2.29
B	0.49	2.07	1.81	13.46	–	82.18
C	0.69	1.57	0.72	29.34	–	67.69

The microstructures of HFHPC1 and HPC2 are shown in Figure 5.

Distribution of polysiloxane gel in the structure of hydrophobized HFHPC1 is shown in Figure 6.

4 DISCUSSION

4.1 Contact angle and surface free energy

When analyzing the examination results presented in Tables 5 and 6, it can be noticed that the values of the contact angles and the surface free energy depend on the

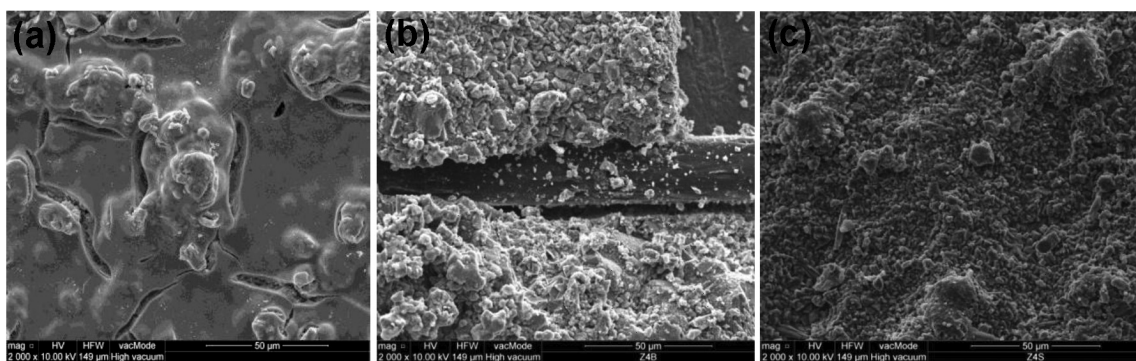


Figure 6: Organosilicon compounds in the microstructure of HFHPC1: a) water-soluble preparation – A, b) alkyl alkoxysilane oligomers – B, c) methylsilicone resin – C, SEM

Slika 6: Organosilikonske spojine v mikrostrukturi HFHPC1: a) vodotopen preparat – A, b) alkil alkilosilan oligomer – B, c) metilsilikonska smola – C, SEM

type of hydrophobic preparations and also on the type of concrete.

The results of the contact-angle measurements proved that in most cases the contact angle of glycerine (θ_g) is higher than the contact angle of water (θ_w), and it decreases in the course of time. The contact angles of water obtained for the standard samples at $t_1 = 0$ range from $\theta_w = 39.4^\circ$ for HFHPC1 to $\theta_w = 67.8^\circ$ for SFHPC; at $t_2 = 40$ min, they range from $\theta_w = 10.1^\circ$ for HPC2 to $\theta_w = 32.4^\circ$ for SFHPC. In the case of the standard samples, the contact angles of glycerine are higher than the contact angles of water (67.0 for HFHPC1 and 86.7 for HPC1 at $t_1 = 0$; 29.9 for HFHPC2 and 62.0 for HPC1 at $t_2 = 40$ min).

The highest contact angles of water, $\theta_w = 122.7^\circ$, and glycerine, $\theta_g = 127.3^\circ$, at $t_1 = 0$ were obtained for methylsilicone resin (C) used for HPC1. In all the other cases, the largest contact angle was obtained with alkyl alkoxysilane (B) and it ranged from 103.4° to 116.3° ($t_1 = 0$) and from 73.0° to 111.6° ($t_1 = 40$ min), which proved that a very good surface hydrophobicity was obtained with this preparation.

For the non-hydrophobized concretes, the value of the surface free energy is the highest and it amounts to $\gamma_s = 914.69$ mJ/m² for HFHPC3 and $\gamma_s = 1862.93$ mJ/m² for HFHPC2. With respect to the non-hydrophobized concretes, the SFE value is up to 142 times higher for the concrete with granite and up to 105 times higher for the concrete with granodiorite aggregate than in the case of the impregnated surfaces. The lowest value of SFE, $\gamma_s = 11.40$ mJ/m² (the weakest adhesion properties), was obtained for the HFHPC1 concrete hydrophobized with alkyl alkoxysilane in the organic solvent (B). In the cases of the PFHPC and HPC2 concretes with granite aggregate, preparation B showed much lower hydrophobic properties, since the value of SFE was higher by 27.55–83.77 mJ/m² than those of the other preparations. The concretes with granite aggregate obtained the highest hydrophobicity using the water-based solution of methylsilicone resin in potassium hydroxide ($\gamma_s = 15.46$ – 43.93 mJ/m²).

Furthermore, it can be noticed that in all the cases the SFE dispersive component (γ_s^d) constitutes a far larger share in the total SFE value (γ_s) than the polar component (γ_s^p).

Considering the variations in time it was observed that in the course of time (after 40 minutes) the total SFE value decreased in the case of the concretes containing steel and polypropylene fibers with both granodiorite and granite aggregates. In the other concretes without fibers, the SFE value decreased after 40 min, proving a decrease in the hydrophobicity.

4.2 Scanning electron microscopy of the hydrophobized concrete

A uniformly distributed silicon coating is formed in the microstructure of the concrete due to the water-

soluble preparation (A); however, it is too thick and shows numerous cracks. Analyzing the microstructure of the coating obtained from preparation A, it can be concluded that it creates the sealing for the fine subsurface pores of the concrete, resulting in a decrease in the water-vapor permeability of the concrete. The coating that is too thick does not provide an adequate adhesion to the concrete minerals, making the hydrophobization less effective. As a result of frost or chemical corrosion the coating will be damaged within a very short period of time.

The methylsilicone-resin coating (C) is of a homogeneous nature, as it is made from fine particles and does not create the sealing for the HFHPC1 structure. This ensures a good efficiency of the impregnation and does not disturb the diffusion of gases and vapors.

The alkyl-alkoxysilane-oligomer preparation (B), based on an organic solvent, is characterized by a fine-pore structure composed of even smaller particles than the macromolecular resin (C). Microscopic observations proved that the coating was uniformly distributed and it did not show any defects.

5 CONCLUSION

The measurement of the contact angle is one of the methods for monitoring the changes in the wettability of hydrophobized building materials.

The use of various preparations results in obtaining different wetting and adhesion properties of HFHPC, determined by the surface free energy. The SFE value decreases significantly on a hydrophobized surface, in particular when using a small molecule oligomer for the concretes with granodiorite aggregate or a water-based solution of methylsilicone resin in the potassium hydroxide for the concretes with granite aggregate. As proved, this may result from a more effective hydrophobization, due to macromolecular resins, of the materials characterized by the pores of bigger diameters like granite-aggregate-based concretes. Adding polypropylene and steel fibers contributes to an increased hydrophobicity in the course of time.

The application of organosilicon compounds in the near-concrete surface area results in a reduction in the SFE and surface tension of the concrete, depending on the chemical composition of the preparation. This causes a reduced penetration of the corrosive substances into the concrete structure, thus affecting its durability.

Evenly distributed silica gel is formed in the fine pores of the high-strength concrete by organic-solvent-based preparations B and C. This coating is characterized by a fine-pore microstructure; it shows an adequate adhesion to the concrete surface. Such properties of silicone resin ensure a good vapor permeability and effective hydrophobization.

6 REFERENCES

- ¹ P. Richard, M. Cheyrez, Composition of reactive powder concretes, *Cement Concrete Research*, 25 (1995) 7, 1501–1511, doi:10.1016/0008-8846(95)00144-2
- ² J. S. Barnett, J. Lataste, T. Parry, S. G. Millard, M. N. Soutsos, Assessment of fibre orientation in ultra-high performance fibre reinforced concrete and its effect on flexural strength, *Materials and Structures*, 43 (2010), 1009–1023, doi:10.1617/s11527-009-9562-3
- ³ A. M. Brandt, Fibre-reinforced cement-based (FRC) composites after over 40 years of development in building and civil engineering, *Composite Structures*, 86 (2008) 1–3, 3–9, doi:10.1016/j.compstruct.2008.03.006
- ⁴ Y. G. Zhu, S. C. Kou, C. S. Poon, J. G. Dai, Q. Y. Li, Influence of silane-based water repellent on the durability properties of recycled aggregate concrete, *Cement and Concrete Composites*, 35 (2013), 32–38, doi:10.1016/j.cemconcomp.2012.08.008
- ⁵ A. Johansson, M. Janz, J. Silfwerbrand, J. Trägårdh, Penetration depth for water repellent agents in concrete as a function of humidity, porosity and time, *International Journal Restoration of Buildings and Monuments*, 13 (2007), 3–16, doi:10.1515/rbm-2007-6102
- ⁶ F. Tittarelli, Oxygen diffusion through hydrophobic cement-based materials, *Cement and Concrete Research*, 39 (2009), 924–928, doi:10.1016/j.cemconres.2008.06.009
- ⁷ B. Felekoğlu, A method for improving the early strength of pumice concrete blocks by using alkyl alkoxy silane (AAS), *Construction and Building Materials*, 28 (2012), 305–310, doi:10.1016/j.conbuildmat.2011.07.026
- ⁸ R. Z. Homod, K. S. M. Sahari, Energy savings by smart utilization of mechanical and natural ventilation for hybrid residential building model in passive climate, *Energy and Buildings*, 60 (2013), 310–329, doi:10.1016/j.enbuild.2012.10.034
- ⁹ K. Sobolev, K. Batrakov, Effect of a Polyethylhydrosiloxane Admixture on the Durability of Concrete with Supplementary Cementitious Materials, *Journal of Materials in Civil Engineering*, 19 (2007) 10, 809–819, doi:10.1061/(ASCE)0899-1561(2007)19:10(809)
- ¹⁰ I. Flores-Vivian, V. Hejazi, M. I. Kozhukhova, M. Nosonovsky, K. Sobolev, Self-Assembling Particle-Siloxane Coatings for Superhydrophobic Concrete, *ACS Applied Materials & Interface*, 24 (2013) 5, 13284–13294, doi:10.1021/am404272v
- ¹¹ A. M. Brandt, Present trends in the mechanics of cement based fibre reinforced composites, *Construction and Building Materials*, 1 (1987) 1, 28–39, doi:10.1016/0950-0618(87)90057-2
- ¹² L. Czarnecki, Sustainable Concrete; Is Nanotechnology the Future of Concrete Polymer Composites?, *Advanced Materials Research*, 687 (2013), 3–11, doi:10.4028/www.scientific.net/AMR.687.3
- ¹³ L. Czarnecki, Polymer concretes, *Cement Lime Concrete*, 15 (2010) 2, 63–85 (in Polish)
- ¹⁴ A. Rudawska, Selected issues on establishing adhesion bonds – homogeneous and hybrid, *Monographs*, Lublin University of Technology, Lublin 2013
- ¹⁵ R. Sikora, Processing of macromolecular materials, *Wydawnictwo Edukacyjne*, Warsaw 1995
- ¹⁶ PN-EN 828:2000 Adhesives, Determining wettability by means of measuring the contact angle and critical surface tension of solid, 2000
- ¹⁷ E. Lugscheider, K. Bobin, The influence on surface free energy of PVD-coatings, *Surface Coatings Technology*, 142–144 (2001), 755–760, doi:10.1016/S0257-8972(01)01315-9
- ¹⁸ G. Cappelletti, S. Ardizzone, D. Meroni, G. Soliveri, M. Ceotto, C. Biaggi, M. Benaglia, L. Raimondi, Wettability of bare and fluorinated silanes: a combined approach based on surface free energy evaluations and dipole moment calculations, *Journal of Colloid and Interface Science*, 389 (2013), 284–291, doi:10.1016/j.jcis.2012.09.008
- ¹⁹ M. Żenkiewicz, Adhesion and modifying the surface layer of macromolecular materials, WNT, Warsaw 2000
- ²⁰ D. Sotiropoulou, S. Agathopoulos, P. Niklopoulos, Work of adhesion in ceramic oxide/liquid metal system, *Journal of Adhesion Science and Technology*, 10 (1996), 989–998, doi:10.1163/156856196X00058
- ²¹ A. Baldan, Adhesion phenomena in bonded joints, *International Journal of Adhesion and Adhesives*, 38 (2012), 95–116, doi:10.1016/j.ijadhadh.2012.04.007
- ²² E. Chibowski, F. Gonzalez-Caballero, Interpretation of contact angle hysteresis, *Journal of Adhesion Science and Technology*, 7 (1993), 1195–1209, doi:10.1163/156856193X00051
- ²³ C. W. Extrand, A thermodynamic model for contact angle hysteresis, *Journal of Colloid and Interface Science*, 27 (1998), 11–19, doi:10.1006/jcis.1998.5743
- ²⁴ S. Vedantam, M. V. Panchagnula, Constitutive modeling of contact angle hysteresis, *Journal of Colloid and Interface Science*, 321 (2008), 393–400, doi:10.1016/j.jcis.2008.01.056
- ²⁵ M. Zielecka, Methods of contact angle measurement as a tool for characterization of wettability of polymers, *Polymers*, 49 (2004), 327–332
- ²⁶ M. Żenkiewicz, P. Rytlewski, J. Czupryńska, J. Polański, T. Karasiewicz, W. Engelgard, Contact angle and surface free energy of electron-beam irradiated polymer composites, *Polymers*, 53 (2008), 446–451
- ²⁷ J. Shang, M. Flury, J. B. Harsh, R. L. Zollars, Comparison of different methods to measure contact angles of soil colloids, *Journal of Colloid and Interface Science*, 328 (2008), 299–307, doi:10.1016/j.jcis.2008.09.039
- ²⁸ U. Stachewicz, S. Li, E. Bilotti, A. H. Barber, Dependence of surface free energy on molecular orientation in polymer films, *Applied Physics Letters*, 100 (2012), 094104, doi:10.1063/1.3691186
- ²⁹ M. Żenkiewicz, Comparative study on the surface free energy of a solid calculated by different methods, *Polymer Testing*, 26 (2007) 1, 14–19, doi:10.1016/j.polymertesting.2006.08.005
- ³⁰ S. Ahadian, M. Mohseni, S. Morawian, Ranking proposed models for attaining surface free energy of powders using contact angle measurements, *International Journal of Adhesion and Adhesives*, 29 (2009), 458–469, doi:10.1016/j.ijadhadh.2008.09.004
- ³¹ A. Rudawska, J. Kuczmaszewski, Galvanized sheet bonding, *University Publishing*, Lublin University of Technology, Lublin 2005
- ³² A. Rudawska, E. Jacniacka, Analysis of Determining Surface Free Energy Uncertainty with the Owens-Wendt Method, *International Journal of Adhesion and Adhesives*, 29 (2009), 451–457, doi:10.1016/j.ijadhadh.2008.09.00
- ³³ D. Rossi, E. Mioni, M. Zancato, A. Bettero, S. Rossi, Development of a tensiometric model for surface energy characterization of raw coffee beans, *Journal of Food Engineering*, 112 (2012), 352–357, doi:10.1016/j.jfoodeng.2012.04.006

DEVELOPING CONTINUOUS-CASTING-PROCESS CONTROL BASED ON ADVANCED MATHEMATICAL MODELLING

UPORABA NAPREDNEGA MATEMATIČNEGA MODELIRANJA ZA RAZVOJ KONTROLE POSTOPKA KONTINUIRNEGA ULIVANJA

Jan Falkus, Katarzyna Miłkowska-Piszczek

Faculty of Metals Engineering and Industrial Computer Science, AGH University of Science and Technology, Al. Mickiewicza 30, 30-059
Kraków, Poland
jfalkus@agh.edu.pl

Prejem rokopisa – received: 2014-08-03; sprejem za objavo – accepted for publication: 2014-12-16

doi:10.17222/mit.2014.176

The method of continuous casting of steel – due to its ability to maximize the yield of liquid steel, along with substantially reducing the energy consumption of the production process – has become the fundamental method for obtaining steel semi-products. Nowadays, over 90 % of the global steel is cast with the continuous method. In recent years the ability to numerically model metallurgical processes – including the continuous process of steel casting – has been very important for creating new technologies, along with modifying those that already exist. The mathematical modelling of solidification processes with numerical methods allowed a full comprehensive reconstruction of the complex physical and chemical nature of the solidification processes. However, having to formulate a numerical model of the continuous-casting process is an extremely complex task because the requirements stipulate that a correct set of material parameters, along with the process data, have to be implemented. As regards the formulation of a mathematical model of the steel continuous-casting process, a comprehensive description of the heat transfer during the continuous casting is an important item. The complexity of this issue requires that conscious simplifications are made when formulating mathematical models for the calculation of the cast-strand solidification process. The number and type of the simplifications – which are necessary in this case – are the keys to the correctness of the results obtained, and they also influence the scope and accuracy when it comes to verifying the model. It is crucial to define the problem on the basis of the finite-element theory, and the elimination of numerical errors is obviously a necessary condition to ensure the correctness of the analysis performed. This paper contains a description of a number of solutions that are based on the finite-element method (FEM) for the models using the Euler, Lagrange and MiLE meshes. All the model concepts are illustrated with the examples of the calculations that were completed using the actual industrial data, along with the properties of the materials as determined by laboratory tests. The pivot of the considerations conducted is related to the verification of the correctness of the calculations, together with the sensitivity analysis of individual model types. The conclusions present an assessment of the progress of the current numerical models of the continuous-casting process, along with the directions for their further development.

Keywords: continuous casting, mathematical modelling, solidification, process control

Metoda kontinuirnega ulivanja jekla je postala osnovna metoda za pridobivanje jeklenih polproizvodov zaradi možnosti maksimalnega izkoristka staljenega jekla ter zmanjšanja porabe energije za proizvodni proces. Danes je okrog 90 % svetovne proizvodnje jekla ulitega z metodo kontinuirnega ulivanja. V preteklih letih je bila možnost modeliranja postopka ulivanja jekla zelo pomembna pri nastajanju novih tehnologij vključno z modificiranjem že obstoječih. Matematično modeliranje procesa strjevanja z numeričnimi metodami je omogočilo celovito rekonstrukcijo kompleksne fizikalne in kemijske narave procesa strjevanja. Vendar pa je postavitve numeričnega modela postopka kontinuirnega ulivanja zelo zahtevna naloga, ker zahteve določajo, da je treba uporabiti pravilne parametre materiala vključno s podatki procesa. Glede na postavitev matematičnega modela postopka kontinuirnega ulivanja je pomembna postavka celovit opis prenosa toplote med kontinuirnim ulivanjem. Kompleksnost tega vprašanja zahteva zavestne poenostavitve pri postavitvi matematičnih modelov za izračun procesa strjevanja žile. Število in vrsta poenostavitve, ki so v tem primeru nujne, sta ključ za pravilnost dobljenih rezultatov, vplivajo pa tudi na obseg in natančnost, ko pride do preverjanja modela. Ključnega pomena je definiranje problema, ki temelji na teoriji metode končnih elementov, odprava numeričnih napak pa je očitno potreben pogoj za zagotovitev pravilnosti izvršenih analiz. Članek vsebuje opis številnih rešitev, ki temeljijo na metodi končnih elementov (FEM), za modele, ki uporabljajo Euler-jevo, Lagrange-jevo in MiLE-mrežo. Prikazani so vsi koncepti modelov z izračuni, ki so bili dopolnjeni z uporabo pravih industrijskih podatkov, skupaj z lastnostmi materialov, kot je bilo določeno v laboratorijskih preizkusih. Težišče izvršenih obravnav je povezano s preverjanjem pravilnosti izračunov, skupaj z občutljivo analizo posameznih vrst modelov. V sklepih je predstavljena ocena glede napredovanja sedanjih numeričnih modelov postopka kontinuirnega ulivanja vključno z napotki za njihov nadaljnji razvoj.

Ključne besede: kontinuirno ulivanje, matematično modeliranje, strjevanje, kontrola procesa

1 INTRODUCTION

The history of the development of the steel continuous-casting process is an interesting example of the implementation of an idea that was well ahead of its time. After H. Bessemer had applied for the first patent in 1846, 34 years had to pass before the inventor made his first trials of steel casting at the semi-technical scale.¹

The reasons why the idea of the metal continuous-casting process was so inspiring for many metallurgical engineers are well known. The implementation of this process to steel casting significantly shortened the process line, definitely reducing both the process and the investment costs. The other indisputable reason for the advantage of steel continuous casting over ingot casting is the yield. Thanks to a yield increase of over 10 %, it

became possible to increase the steelworks output without increasing the steelmaking furnace capacity.

The reasons why the implementation of the steel continuous-casting process for the production took so long are as well understood as the reasons for its implementation. From the outset, the mechanical characteristics of a strand cast have been the main difficulty, as a strand is prone to cracking, especially at the initial formation stage; in an extreme case it may even break out. A small shell thickness of a strand leaving the mould is of key importance. This problem is exceptionally serious as regards steel and it arises from a relatively low value of the heat-conductivity coefficient of steel as compared to the other metals. For most non-ferrous metals, the liquid core of a strand cast continuously is much shorter and the solidification process ends right under the mould. For steel, the length of the liquid core most often ranges from a few metres to something between ten and twenty. This fact brings about the necessity of using advanced techniques of the process control and ensuring stable process conditions.

Note that despite the indisputable successes, the current development of the steel continuous-casting process cannot be considered finished. The problems related to the strand breakout or the occurrence of various defects of cast strands are still valid. The financial means earmarked for scientific research related to the continuous casting of steel indirectly prove that the problems still exist. An example of a research area that constitutes a huge challenge, both in theory and in practice, is the continuous casting of peritectic steels. Engineering new steel grades also involves the need for developing their casting process from scratch. Therefore, any projects related to the improvement of the mathematical description of the steel continuous-casting process are valuable for facilitating the process control problem.

2 STEEL CONTINUOUS-CASTING PROCESS AS AN OBJECT OF MODELLING

The effect of a continuous-casting-machine design on the method of mathematical modelling of the steel solidification process is significant. Without the knowledge of the machine technical documentation, it is difficult to make any attempt at modelling, aiming at obtaining the results intended for use for the process control.

Despite the existing differences in the design of individual machines, one should note that it is possible to generalise the problem and form the construction of a mathematical model assuming the occurrence of two cooling zones of the strand, i.e.:

- the primary cooling zone (including the mould)
- the secondary cooling zone (including the so-called cooling chamber and the division into the cooling zones independent of the cooling chamber).

Each of the two mentioned zones is characterised by two groups of parameters – the first one may be defined as a geometrical characteristic, and the other one as a set of parameters related to the heat transfer and the properties of the steel cast. The description of the heat-transfer model for the steel continuous-casting process is a complex task as all three heat-transfer mechanisms occur – conduction, radiation and convection^{2,4}. The following processes impact the heat transfer in the primary zone:

- conduction and convection in the liquid-steel area,
- conduction in the solidified shell,
- heat transfer between the outer layer of the solidified shell and the mould wall surface through an air gap forming in the mould,
- heat conduction in the mould,
- heat transfer in the mould between the channel walls and the cooling water.

The main processes in the secondary cooling zone are:

- heat transfer by convection,
- heat transfer by radiation,
- heat transfer by conduction between the solidifying strand and the rolls.

Additionally, thermal effects related to the phase transitions that accompany the solidification have a significant influence on the heat-transfer model.

The heat-transfer model was used for further considerations, wherein the temperature field could be determined by solving the Fourier Equation:

$$\frac{\partial(\rho c_p T)}{\partial t} = \frac{\partial}{\partial x} \left(\lambda \frac{\partial T}{\partial x} \right) + \frac{\partial}{\partial y} \left(\lambda \frac{\partial T}{\partial y} \right) + \frac{\partial}{\partial z} \left(\lambda \frac{\partial T}{\partial z} \right) + Q \quad (1)$$

where ρ is the density, kg m^{-3} ; c_p is the specific heat, $\text{kJ kg}^{-1} \text{K}^{-1}$; λ is the thermal conductivity, $\text{W m}^{-1} \text{K}^{-1}$; t is the time, s ; T is the temperature, K ; Q is the heat-source term, W m^{-3} ; x , y , z are 3D coordinate axes. The solution of the Fourier Equation should meet those boundary conditions declared on the strand surface. In the numerical model of the steel continuous-casting process discussed, these boundary conditions may be declared in three various ways. The Equation below describes the second and third types of boundary conditions:

$$Q = Flux + \alpha(T - T_a) + \sigma \varepsilon (T^4 - T_a^4) \quad (2)$$

where $Flux$ is the heat flux, W m^{-2} ; α is the heat-transfer coefficient, $\text{W m}^{-2} \text{K}^{-1}$; T_a is the ambient temperature, K ; σ is the Stefan-Boltzmann constant, $\text{W m}^{-2} \text{K}^{-4}$; ε is the emissivity. The heat flux in the model may be defined directly as the $Flux$ value (the Neumann condition), as well as with the convection (α – substitute heat-transfer coefficient) and with the radiation models (ε – emissivity).

It is a complicated task to formulate a model of the heat transfer in the mould. The main difficulty is the

effect of an air gap formed immediately after the steel has cooled to the solidus temperature, under the liquid-steel meniscus surface. The oscillatory movement of the mould and, in addition, the strand movement in the mould with a variable casting speed, strongly influence the actual dimensions of the gap. The presence of the mould powder and gases within the gap makes this description even more problematic. The physical properties and the chemical composition of the mould powders applied significantly influence the heat-resistance value. The development of the air gap causes a very high temperature gradient between the solidifying strand shell and the mould wall. Also, the change in the air-gap dimensions during the continuous-casting process may influence the stability of the process, having an impact on the thickness of the shell leaving the mould. The dimensions of the air gap increase with the distance from the liquid-steel meniscus, consequently causing an increase in the heat resistance (**Figure 1**).

The heat-transport mechanism between the solidifying strand shell and the mould wall may be divided into two components – conduction and radiation. The convection in this area may be neglected due to the small size of the air gap. The total air-transfer coefficient on the strand mould path may be presented with the following Equation:

$$q_{wk} = q_c + q_r \tag{3}$$

where:

q_{wk} – total heat-flux density,

q_c – conducted heat-flux density,

q_r – density of the heat flux transferred by radiation.

T_M – temperature of the mould, T_S – temperature of the strand surface, T_{SS} – temperature of the solid layer of the slag, T_{MS} – the melting point of the slag, T_{LS} – temperature of the liquid layer of the slag, T_{SO} – solidus temperature.⁵

Finally, the flux density of the heat flowing from the strand to the mould is calculated from the Newton law:

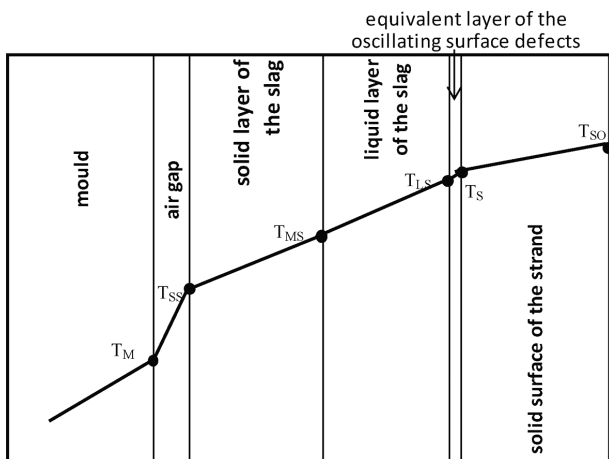


Figure 1: Structure of the layer between the mould and the shell
Slika 1: Zgradba područja med kokilo in strjeno skorjo

$$q_c = \frac{T_{wl} - T_{kr}}{r_{sz}} = \alpha_{sz} (T_{wl} - T_{kr}) \tag{4}$$

where:

α_{sz} – coefficient of the heat transfer through the air gap,

r_{sz} – air gap thermal resistance.

The outer side of the mould is intensely cooled with water, flowing through the channels. Here, the heat is transferred by forced convection. The calculation of the heat-transfer coefficient, with the water cooling in the mould channels, on the basis of the available formulas, is complex because of the method of heat transfer to the water flowing through the channel. Assuming the distribution of the channel density at the perimeter of the mould varies, it is possible to obtain a few cooling programs. To determine the average heat-transfer coefficient, the following formula may be applied to the outer surface of the mould:⁶

$$\alpha_w = \frac{Nu \lambda_w}{d_k} x_k \tag{5}$$

where:

x_k – water-cooled mould-surface share,

d_k – mould-channel diameter,

λ_w – heat-transfer coefficient for water,

Nu – Nusselt number.

For the forced convection (the water flowing in the mould channels) the Nusselt number is represented by the relationship between the Reynolds (Re) number and the Prandtl (Pr) number:

$$Nu = f(Re, Pr) \tag{6}$$

The Mikheyev formula may be selected to determine the Nusselt number:⁷

$$Nu = 0.021 Re^{0.8} Pr_w^{0.43} \left(\frac{Pr_w}{Pr_s} \right)^{0.25} \tag{7}$$

The Reynolds Re and Prandtl Pr numbers in Equation (7) are determined at the water properties for the mould-wall temperature (the s index) and the mean water temperature in the channel (the w index).

After leaving the mould, the slab surface is cooled with a water spray and in the air. The heat flux that is carried away from the surface of the solidifying strand is proportional to the temperature difference between the strand surface and the cooling medium temperature. In this zone it is recommended to maintain the cooling intensity which leads to gradual temperature changes. It ensures that the cracks generated by thermal stresses are avoided.⁸

In the secondary cooling zone, the heat exchange with the environment is accompanied by several mechanisms:

- direct impact of the water stream on the strand,
- cooling with the water flowing on the surface and with defected drops,

- cooling with the water lingering on the roll in the formed hollow,
- cooling the places located directly under the roll with the ambient air,
- cooling through the contact faces of the roll.

The heat transfer from the surface of the solidifying strand is a complex process due to the nature of the heat exchange accompanying the boiling effect. When the surface of the strand leaving the mould is cooled, film boiling prevails. At this stage, the main mechanism of the heat transfer is the conduction through the vapour film resulting from supplying water to the hot surface of the strand via the nozzles. The heat-transfer mechanism is also accompanied by radiation, therefore, the lower the strand surface temperature, the lower is the value of the heat-transfer coefficient.⁹ Drops of cooling water that fall onto the hot strand surface evaporate, forming a film that restricts water access at this spot. The water momentum is the highest in the centre of the cooling area, enabling the vapour film to be broken and allowing a direct contact between the water and the cooled strand surface. It intensifies the cooling process in this area, therefore, the amount of the heat received strongly depends on the liquid velocity.⁵

During further cooling, as the temperature falls below the Leidenfrost point, the transition-boiling effect occurs. In the vapour film, vapour bubbles form, consequently leading to a break and decay of the vapour film. It causes an increase in the heat-transfer coefficient.¹⁰ During further cooling we observe the effect of bubble boiling, along with a further decline in the heat-transfer coefficient. After the completion of the bubble-boiling stage and the cessation of the conditions for vapour forming, the strand surface is cooled by forced convection.¹¹ **Figure 2** presents the change in the heat-transfer coefficient for the water-boiling process.

A very important mechanism of the heat exchange in the secondary cooling zone is radiation due to the surface temperature of the strand that leaves the mould. To obtain a complete description of the effects, it is necessary to consider the heat-flux density resulting from the heat transfer by radiation. The radiation term may be expressed with the Stefan-Boltzman law:

$$q_{\text{rad}} = \varepsilon_{\text{wl}} \sigma (T_{\text{wl}}^4 - T_{\text{a}}^4) \quad (8)$$

where:

q_{rad} – heat-flux density lost by the strand surface to the environment,

σ – Stefan-Boltzman radiation constant,

ε_{wl} – total emissivity of the strand surface,

T_{a} – ambient temperature.

The strand emissivity-coefficient value may be adopted in the range of 0–1. Due to a simplification, the constant may be assumed to be 0.85.

The flux density of the heat transferred to the cooling water may be calculated from the following relationship:

$$q_{\text{spray}} = \alpha_{\text{spray}} (T_{\text{wl}} - T_{\text{spray}}) \quad (9)$$

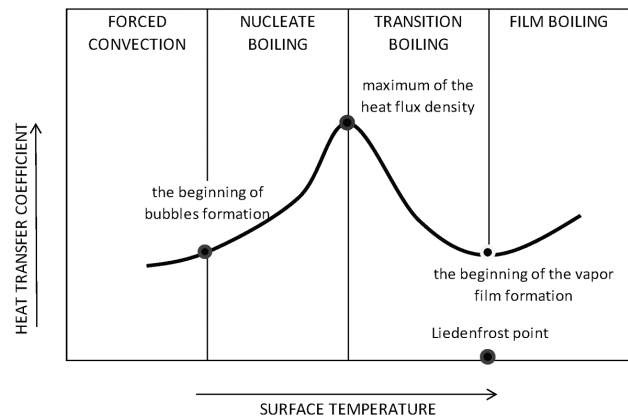


Figure 2: Flow diagram for the heat-transfer coefficient changing during the boiling process³

Slika 2: Potek spreminjanja koeficienta prenosa toplote med vrenjem³

where:

α_{spray} – coefficient of heat transfer by water,

T_{wl} – strand surface temperature,

T_{spray} – temperature of the water flowing through the nozzles.

In order to calculate the flux density of the heat transferred, it is necessary to know the heat-transfer coefficient α_{spray} . The relationship describing the heat-transfer coefficient of the heat transferred as a result of the water-spray impact may be expressed in a general form:⁴

$$\alpha_{\text{spray}} = A \dot{V}_{\text{spray}}^c (1 - bt_{\text{spray}}) \quad (10)$$

where:

α_{spray} – heat-transfer coefficient,

A, b, c – empirical constants,

\dot{V}_{spray}^c – cooling-water flux,

t_{spray} – temperature of the water flowing through the nozzles.

The heat-transfer coefficient depends on the conditions that occur during the contact of the water with the surface of the solidifying strand. The water-flux density, the velocity of the water flowing out of the spray nozzle,

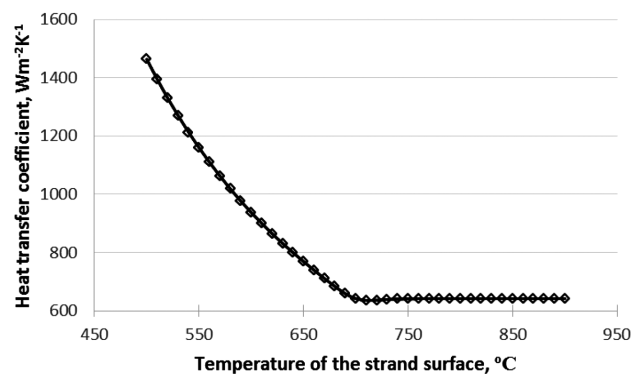


Figure 3: Heat-transfer coefficient during the cooling process with a water spray for $\dot{V}_{\text{spray}}^c = 3 \text{ dm}^3 \text{ m}^{-2} \text{ s}^{-1}$

Slika 3: Koeficient prenosa toplote med ohlajanjem z brizganjem vode pri $\dot{V}_{\text{spray}}^c = 3 \text{ dm}^3 \text{ m}^{-2} \text{ s}^{-1}$

the nozzle type and the water pressure all influence the value of the coefficient. A typical course of the changes in the heat-transfer coefficient as a function of the temperature is presented in **Figure 3**.

If the solidifying cast-strand surface temperature is not known, a simplified formula may be applied:¹

$$\alpha_{\text{spray}} = 10v + (107 + 0.688v)\dot{V}_{\text{spray}} \quad (11)$$

where: v – water-drop speed.

Equation (11) may be applied for water fluxes from $0.3 \text{ dm}^3 \text{ m}^{-2} \text{ s}^{-1}$ to $9.0 \text{ dm}^3 \text{ m}^{-2} \text{ s}^{-1}$ and speeds from 11 m s^{-1} to 32 m s^{-1} . The values obtained for a flux of $= 3 \text{ dm}^3 \text{ m}^{-2} \text{ s}^{-1}$ and the average water speeds are about $600 \text{ W m}^{-2} \text{ K}^{-1}$.

In the zone beyond the water sprays, in most of the continuous-casting machines, after a strand leaves the secondary-cooling chamber, a heat transfer occurs between the hot surface of the strand cooled and the ambient atmospheric air. Radiation is the prevailing mechanism of heat transfer; however, the heat is partly transported from the strand surface with free or forced convection.³

Even an abbreviated description of the heat-transfer mechanisms in the steel continuous-casting process indicates two basic difficulties accompanying the mathematical modelling of the process. First, it is impossible to identify every component of the model. If the description is very detailed, taking into account all the partial processes, then, at the verification stage, simplifications are usually made and substitute heat-transfer coefficients are determined. However, these simplifications do not cover all the problems that are encountered. The second stage of verification always requires us to find the relationship between the identified values of the heat-transfer coefficients and the intensity of the cooling-media supply. The fulfilment of this requirement is the key to the correctness of the forecast of each continuous-casting model and it is a problem most difficult to solve.

3 TYPES OF MATHEMATICAL MODELS

3.1 Lagrangian mesh model

The motion of a continuum may be described from two different standpoints – either with the Lagrangian or Eulerian method. The motion analysis, together with these methods, allows one to determine the position of any moving element of a body; in addition, these elements are treated as material points. The Lagrangian description is preferred in solid-body mechanics. In this model the "observer" follows the body's material points, observing their temperature and velocity being affected by specific boundary conditions. The initial positions of the material points influence the course of the process. As a result, the history of a numerically modelled process can be created on the basis of the temperature field and velocity (strain) field, allowing a calculation of the stress field in the body and the changes in the micro-structure and porosity. Another advantage of the Lagran-

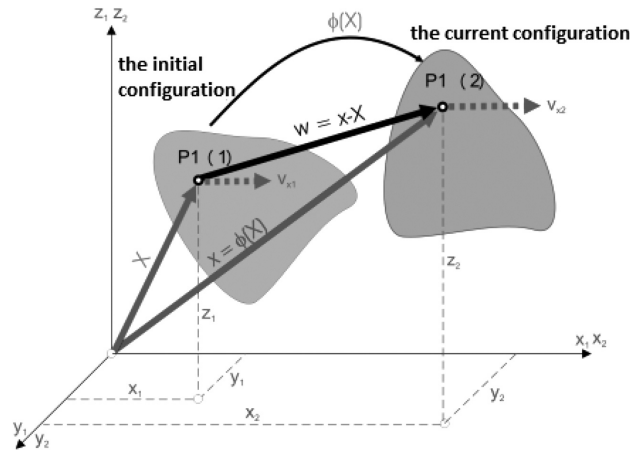


Figure 4: Lagrangian Method – description of the motion of the object⁵

Slika 4: Lagrange-jeva metoda – opis gibanja predmeta⁵

gian description is the fact that the mesh deforms together with the body, which is particularly relevant in the numerical modelling of body strains. In the Lagrangian method an object's motion (physical continuum) is described by the dependence of the coordinates of all the particles on the time and the initial position for $\tau = 0$ or the initial time τ_1 . A necessary condition is also the determination of all the properties of the object, taking into account the positions of its points at a specific time. By eliminating the time, we can obtain an equation of the trajectory of the object particles. In this method, the observer moving together with the object maintains contact with the same object particles at the set time.⁵ This is schematically presented in **Figure 4**.

3.2 Eulerian mesh model

The Eulerian method is usually used in fluid mechanics. Contrary to the Lagrangian description, the reference point is located outside the area, so the "observer" follows the behaviour of the area from the outside. In the Eulerian method, bodies move on the background of a mesh that represents a specific area. If, during the motion of the fluid in the system, the temperature, the velocity vector and the concentrations do not change with the time at the fixed points, the external "observer" interprets the system as a steady system. Only by analysing the

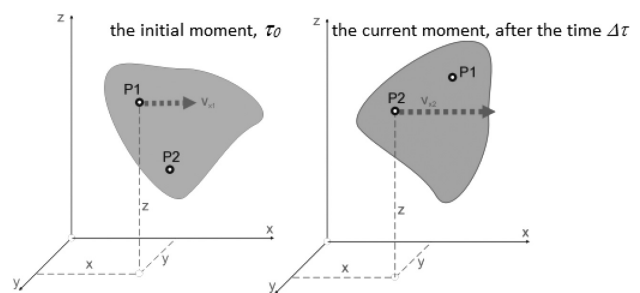


Figure 5: Euler Method – description of the motion of the object⁵

Slika 5: Euler-jeva metoda – opis gibanja predmeta⁵

data concerning the temperature field and the velocity, does it turn out that, in fact, the process of the system is transient.

The time and coordinates of the current configuration are independent variables. Such a description is called the Eulerian description or spatial description because the changes in the medium parameters at a specific place in the space are tracked. In **Figure 5** this place is determined by the coordinates x , y , z . At the initial moment, these coordinates describe the position of element $P1$ in the object, whereas after time $\Delta\tau$, at the moment of the current observation, they describe the position of a different element, $P2$. So, at various times various elements are located at the same place. This method of description is very favourable for the objects whose initial configuration has no influence, or their influence on the state of the configuration at a later time is of little significance. It is particularly significant for the description of the movement of fluids, i.e., liquids and gases.⁹

3.3 MiLE method

In the process of steel continuous casting, the solid and liquid phases occur simultaneously and, in the metallurgical part of the strand, these phases are adjacent. So, the problem of numerical modelling of this part of the process must be solved with both methods – the Lagrangian and Eulerian methods – or their combination. In the numerical model using the finite-element method, the Eulerian approximation is used to describe the temperature field and the liquid-metal flow. A fixed mesh with invariable geometry may be used here. The speed and temperature vectors are determined in fixed node points. To model the strain and stress of the solidified metal simultaneously, it is necessary to use the description with the Lagrangian coordinates.

At present, a new method combining the Lagrangian and Eulerian methods is used for a numerical simulation of the steel continuous-casting process – the MiLE (mixed Lagrangian-Eulerian method) method. In this method the continuous-casting-process area is divided into two parts. The upper, stationary, part is described by the Eulerian scheme. The lower part is described by the Lagrangian scheme as it moves at the casting speed. To maintain the strand integrity, at consecutive time steps,

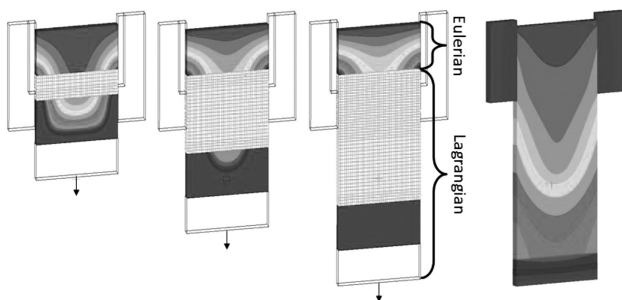


Figure 6: MiLE algorithm⁵
Slika 6: MiLE-algoritem⁵

layers are placed under the upper part; these layers bring, into the lower part, a mass of steel equivalent to the mass of the steel brought to the mould from the tundish.

The MiLE method allows linked modelling of the non-stationary temperature fields and of the liquid-steel flow in the process of steel continuous casting and modelling of the stresses caused by thermal effects.

The principle of the MiLE algorithm is presented in **Figure 6**. The first action is the division of the strand into two areas. After starting the casting process, the lower area moves downwards, whereas the upper area stays in its initial position. The calculations within this area are performed with the Eulerian model. To maintain the integrity between the areas, the mesh must be successively supplemented with additional layers of elements, forming a dynamic area. Therefore, a certain number of elements with the initial thickness of zero are stored within the area between the first two areas (the third area). In order to ensure the integrity of the temperature field and the velocity field between areas 1 and 3, in all the nodes of the “stored” (not yet used) layers, momentary boundary conditions are imposed. The same values of the temperature and velocity are assigned to the nodes with identical coordinates.^{5,12} In areas 2 and 3, the Lagrangian model is used for the calculations (**Figure 6**).

4 SENSITIVITY OF STEEL-CONTINUOUS-CASTING-PROCESS MODELS

4.1 Numerical parameters

The procedure of a mesh application arises from calculation tests and not from formal guidelines. For each new case, applying a FEM mesh is an individual issue for a specific model. For a new mesh (use of different elements or their sizes), a number of calculation tests should be performed in order to eliminate potential numerical errors. At the stage of the FEM mesh design, the places of the implementation of the boundary conditions should be taken into account due to the refinement of the mesh at those places, regardless of the applied mesh type. An observation of the obtained results, in particular the temperature distribution, allows an easy identification of the places where a numerical error related to the mesh-element size is generated. Usually a temperature-distribution asymmetry is noticeable. In addition, a high jump in the temperature values can be noticed. This is neither correlated with the boundary conditions nor justified by the change in the main process parameters in this area.

4.2 Material parameters

The thermophysical properties of steel – as determined by experimental research or calculated using thermodynamic databases – are the key input parameters for building a numerical model of the continuous-casting process. Based on the chemical composition of a steel

grade, and the algorithms implemented in the thermodynamic databases, a number of material properties, i.e., enthalpy, thermal conductivity, density, viscosity, solidus and liquidus temperatures, may be determined. The calculation of the material parameters of the steel grade tested based on its chemical composition is a common approach. However, it should be emphasised that the temperature distribution obtained with the numerical modelling is extremely sensitive to any changes in the basic thermophysical properties.

The starting point for the sensitivity analysis was the base variant, which took account of the specific heat values from the experimental tests, along with the latent heat value that was implemented in the numerical model as a numerical value. The calculations obtained for the base variant allowed the actual continuous-casting process for the S235 steel grade to be fully mapped for the declared strand casting speed of 1 m/min. The other variants were defined by the c_p declaration, as follows:

Variant 1, where the magnetic-transformation heat and the austenite-ferrite-transformation heat were considered. The heat of the fusion was declared as 113 kJ/kg.

Variant 2, where the magnetic-transformation heat, the austenite-ferrite-transformation heat and, additionally, the peritectic-transformation heat were considered. The heat of the fusion was declared as 113 kJ/kg.

Variant 3, where the magnetic-transformation heat, the austenite-ferrite-transformation heat, the peritectic-transformation heat and the heat of fusion were considered.

The obtained calculation results are presented in **Table 1**.

Table 1: Metallurgical length and shell thickness calculated for the selected variants

Tabela 1: Metalurška dolžina in debelina skorje, izračunana za izbrane variante

Specific heat, kJ/(kg K)	Metallurgical length, m	Thickness of the shell, cm
Basic	12.6	2.2
Variant 1	12.6	2.2
Variant 2	13.7	2.18
Variant 3	11.4	2.21

The method of determining the specific heat value, along with the solidifying heat, has a significant influence on the obtained results of the numerical model. By taking into account the values coming from the experimental research, the amount of the heat accompanying the individual phase transformations occurring during the solidification process may be accurately determined. In addition, the method determining the latent heat is very important. In extreme cases, an error in the enthalpy-value determination in relation to the verified specific-heat values may be as high as 178 °C.

4.3 Process parameters (boundary conditions)

The influence of the boundary conditions assumed for the calculations, apart from the thermophysical parameters, is the most important element of any mathematical model of the continuous-casting process. However, in professional references there is an extremely huge range of the values assumed. To illustrate the scale of the problem, the values of the heat-transfer coefficients (HTC) for 12 various models describing the heat transfer in a mould were collected in **Table 2**.^{3,13–25} Next, calculations with the specified HTC values were performed, maintaining the constant value of the other process parameters. The obtained calculation results are presented in **Table 3**.

Table 2: Heat-transfer coefficient in the primary cooling zone
Tabela 2: Koeficient prenosa toplote v primarni hladilni coni

No.	Average or maximum value	Reference
Group I – the average HTC value along the whole length of the mould		
1	$h = 1200 \text{ W}/(\text{m}^2 \text{ K})$	13,14
2	$h = 1300 \text{ W}/(\text{m}^2 \text{ K})$	15
3	$h = 1500 \text{ W}/(\text{m}^2 \text{ K})$	16,17
Group II – two values of heat-transfer coefficients		
4	$h_1 = 1163 \text{ W}/(\text{m}^2 \text{ K})$ for $z = 0.6 \text{ m}$ $h_2 = 1395.6 \text{ W}/(\text{m}^2 \text{ K})$ for $z > 0.6 \text{ m}$	18,19
Group III – linear variable		
5	$h = 2000\text{--}800 \text{ W}/(\text{m}^2 \text{ K})$	20
6	$h = 1500\text{--}600 \text{ W}/(\text{m}^2 \text{ K})$	20
Group IV – variable (various heat-transfer mechanisms)		
7	$h_{\text{max}} = 1300 \text{ W}/(\text{m}^2 \text{ K})$	21
8	$h_{\text{max}} = 2500 \text{ W}/(\text{m}^2 \text{ K})$	22
9	$h_{\text{max}} = 2000 \text{ W}/(\text{m}^2 \text{ K})$	23
10	$h_{\text{max}} = 1300 \text{ W}/(\text{m}^2 \text{ K})$	3
11	$h_{\text{max}} = 3097 \text{ W}/(\text{m}^2 \text{ K})$	24
12	$h_{\text{max}} = 1600 \text{ W}/(\text{m}^2 \text{ K})$	25

Table 3: Comparison of the shell thicknesses and temperatures for the selected models of the heat-transfer coefficient

Tabela 3: Primerjava debeline skorje in temperature pri izbranih modelih koeficienta prenosa toplote

Model	Thickness of the shell after leaving the mould, cm	Temperature, °C
1	2	836
2	2.3	812
3	2.75	772
4	2.27	833
5	2.38	900
6	1.94	956
7	1.98	976
8	1.92	1050
9	1.86	1090
10	1.82	1099
11	2.51	874
12	2.52	938

It should be stressed that model 12 is the author's own model, verified under industrial conditions. Its accuracy was checked with test-strand temperature measure-

ments. The results of this verification are presented in **Table 4**.

Table 4: Values of the strand surface temperature calculated and measured at the reference points

Tabela 4: Vrednosti izmerjene in izračunane temperature na površini žile v referenčnih točkah

	The average measured temperature, °C	The calculated temperature, °C
Measurement point I	855	861
Measurement point II	905	912

5 STRATEGY OF SELECTING THE STRAND COOLING PARAMETER

From the perspective of the applicable technology and the design of the slab-continuous-casting machine, it is essential to maintain the metallurgical length at a constant level. This is mostly related to the location of the soft reduction zone. The use of soft reduction of a strand allows an elimination of the axial porosity, consequently, improving the quality of the steel semi-products obtained. Maintaining a comparable metallurgical length for various strand casting speeds guarantees the safety during the continuous-casting process as the strand is fully solidified before shearing. For most of the continuous-casting machines, the best area where the total solidification of the strand should occur is the area before the exit from the secondary-cooling chamber. It is related to the location of the soft-reduction zone and the location of the last point of strand straightening.

The first step of the proposed method for determining the new cooling values is to calculate the influence of a change in the strand withdrawal speed on the metallurgical length, while verifying the shell thickness and the temperature at the reference points. An analysis of the sensitivity of the numerical model of the steel continuous-casting process to the casting speed allows a determination of the percentage impact of the change in the casting speed on the metallurgical length. Knowing this dependence allows us to calculate the influence of a change in the cooling parameters, which must always be correlated with the casting speed.

The simplest method of determining the new cooling values for the spray zones is using the percentage change in individual heat-transfer coefficients, taking into account the percentage change in the metallurgical length as a function of the casting speed. From the numerical perspective, the described method is an effective approach. However, determining the new sets of cooling values must be correlated with the existing technology and the relationships of the changes in the water-flow rates for individual spray zones. When the new values of heat-transfer coefficients were determined, minimum changes were applied to the heat-transfer coefficients within the first two cooling zones; more significant changes were introduced to the other spray zones, while

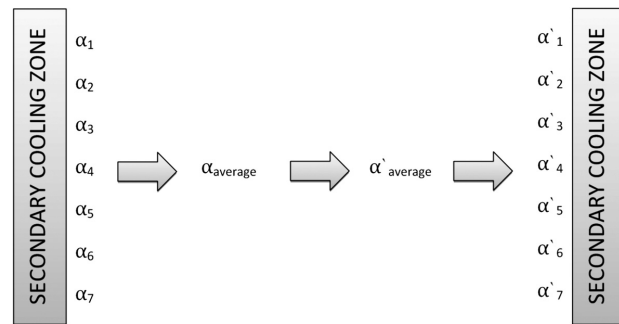


Figure 7: Diagram for a calculation of new heat-transfer coefficients²⁵
Slika 7: Prikaz izračuna novih koeficientov prenosa toplote²⁵

the temperature increase within the spray zones was controlled. Such an approach is extremely important for maintaining the safety of the steel continuous-casting process.

In the example discussed, for a speed of 1 m/min, the set of cooling factors remained unchanged, because the desired values of the metallurgical length, the temperature at the reference points and the shell thickness after leaving the mould were obtained. The simulation for the speed of 1 m/min was considered the reference for further considerations. **Figure 7** presents a diagram of the algorithm for determining the new values of heat-transfer coefficients.

The starting point of the algorithm includes the heat-transfer coefficients for seven spray zones; these were calculated on the basis of the actual flows of the water for the three speeds examined. Next, one heat-transfer coefficient for the whole secondary cooling zone $\alpha_{average}$ was calculated, using the proposed dependence presented with the formula below:

$$\alpha_{average} = \frac{\sum_1^n a_n s_n}{\sum_1^n s_n} \quad (12)$$

where:

α_n – heat-transfer coefficient for the selected spray zone,

s_n – surface area of the specific zone,

n – zone number.

The average heat-transfer coefficients for the secondary cooling zone were calculated from dependence 12. They were (305, 395 and 410) W m⁻² K⁻¹, for the speeds of (0.6, 0.8 and 1) m min⁻¹, respectively. Knowing the percentage impact of the casting speed on the metallurgical length, the new heat-transfer coefficients for the secondary cooling zone for the speeds of 0.6 m min⁻¹ and 0.8 m min⁻¹ were calculated; similar metallurgical lengths were obtained as for the speed of 1 m min⁻¹. The following dependence was used:

$$\alpha'_{average} = \frac{\alpha_{average}}{k} \quad (13)$$

where: k – coefficient based on the percentage relationship for the metallurgical length as a function of the casting speed.

The new heat-transfer coefficients for the secondary cooling zone were calculated from dependence 13. For the speed of 0.8 m min^{-1} the average heat-transfer coefficient was $315 \text{ W m}^{-1} \text{ K}^{-1}$ and for the speed of 0.6 m min^{-1} the average heat-transfer coefficient was about $205 \text{ W m}^{-2} \text{ K}^{-1}$. The numerical calculations conducted for the new average values of the heat-transfer coefficient for the secondary cooling zone α'_{average} confirmed the above method was correct. Similar metallurgical lengths of 15.7 m and 16.5 m were obtained for the speeds of 0.6 m min^{-1} and 0.8 m min^{-1} , respectively.

At the next stage, the heat-transfer coefficient was calculated using dependence 12 for each spray zone. The calculations resulted in a few sets of heat-transfer coefficients. The values of the heat-transfer coefficients that met the boundary conditions within the allowed percentage change in the heat-transfer coefficients for the individual spray zones were selected. The boundary conditions were determined on the basis of the actual change in the flows of the cooling water in the spray zones for a selected speed.

6 CONCLUSION

The development of a versatile method for the optimum determination of strand cooling parameters in the steel continuous-casting process is an extremely complex issue, requiring that many mutually contradictory criteria be met. The quality requirements related mainly to the structure of the solidified cast strand impose a clear restriction to increasing the casting speed. However, the continuous-casting-machine efficiency must be synchronised with the other nodes of the production line. The flexibility required in this case is related to the necessary response to unexpected events that may change the production rhythm of a steelmaking shop.

The cooling-program determination method in the steel continuous-casting process is based on the verification of the numerical models describing the strand solidification process. The determination of, possibly, all the properties of the cast steel as the function of the temperature is a very important step at the stage of determining the model parameters for the conditions defined as the standard. It mainly concerns the specific heat and the solidification heat, the dynamic viscosity, the density and the heat-transfer coefficient. Carrying out the measurements of the listed properties is, unfortunately, a very complex task, requiring the use of very specialised equipment.

For the mathematical description of the steel continuous-casting process at any particular level, we need to find the appropriate method of selecting the boundary conditions. The determination of the boundary conditions based on the process information is one of the fac-

tors that are crucial for the correctness of model calculations. Practically, this means that the amount of the used cooling water needs to be converted into the suitable heat-transfer coefficient.

The task of determining the cooling programme in the steel continuous-casting process is not a deterministic task. The selection of the variant for practical implementation depends largely on the experience of the user of the specific machine. However, the criteria that allow an assessment of the correctness of the assumed solution are strictly defined. The most important are:

- the shell thickness under the mould,
- the strand metallurgical length,
- the strand surface temperature at the selected measurement points,
- the critical stress at the temperature of the shell under the mould,
- the strand structure – in particular, the thickness of the chilled grain zone.

Acknowledgments

This research project was supported by the European Regional Development Fund – the Operational Programme "Innovative Economy", as a project New Concept for Selection of the Cooling Parameters in Continuous Casting of Steel, POIG.01.03.01-12-009/09.

7 REFERENCES

- ¹ H. F. Schrewe, *Continuous Casting of Steel*, Verlag Stahleisen, Dusseldorf 1989, p. 179
- ² T. Telejko, Z. Malinowski, M. Rywotycki, *Archives of Metallurgy and Materials*, 54 (2009) 3, 837–844
- ³ M. Rywotycki, K. Miłkowska-Piszczek, L. Trębacz, *Archives of Metallurgy and Materials*, 57 (2012) 1, 385–393, doi:10.2478/v10172-012-0038-z
- ⁴ Y. Meng, B. G. Thomas, *Metallurgical Transactions B*, 34B (2003) 3, 685–705, doi:10.1007/s11663-003-0040-y
- ⁵ J. Falkus, A. Buczek, A. Burbelko, P. Drożdż, M. Dziarmagowski, M. Karbowniczek, T. Kargul, K. Miłkowska-Piszczek, M. Rywotycki, K. Solek, W. Ślęzak, T. Telejko, L. Trębacz, E. Wielgosz, *Modelowanie procesu ciągłego odlewania stali*, Wydawnictwo Naukowe Instytutu Technologii Eksploatacji – Państwowy Instytut Badawczy, Radom 2012, p. 328
- ⁶ M. Rywotycki, Z. Malinowski, T. Telejko, *Hutnik Wiadomości Hutnicze*, 73 (2006) 4, 142–147
- ⁷ S. Wiśniewski, T. S. Wiśniewski, *Wymiana ciepła*, WNT, Warszawa 1997, p. 437
- ⁸ Z. Kudliński, *Technologie odlewania stali*, Wydawnictwo Politechniki Śląskiej, Gliwice 2006, p. 305
- ⁹ A. Buczek, *Metallurgy and Foundry Engineering*, 20 (1994) 3, 311–318
- ¹⁰ J. T. Cieśliński, *Modelowanie wrzenia pęcherzykowego*, Wydawnictwo Politechniki Gdańskiej, Gdańsk 2005, p. 148
- ¹¹ J. Sengupta, B. G. Thomas, M. A. Wells, *Metallurgical and Materials Transactions A*, 36 (2005) 1, 187–204, doi:10.1007/s11661-005-0151-y
- ¹² J. M. Drezet, M. Rappaz, *Metallurgical and Materials Transactions A*, 27A (1996) 10, 3214–3225, doi:10.1007/BF02663872

- ¹³ M. Biedrońska, R. Grzymkowski, *Krzepnięcie Metali i Stopów*, 19 (1994), 11–19
- ¹⁴ M. Biedrońska, R. Grzymkowski, *Krzepnięcie Metali i Stopów*, 18 (1993), 21–28
- ¹⁵ A. Kapusta, A. Wawrzynek, *Krzepnięcie Metali i Stopów*, 18 (1993), 87–94
- ¹⁶ A. Kapusta, A. Wawrzynek, *Krzepnięcie Metali i Stopów*, 16 (1987), 150–158
- ¹⁷ S. H. Seyedein, M. Hasan, *International Journal of Heat and Mass Transfer*, 40 (1997) 18, 4405–4423, doi:10.1016/S0017-9310(97)00064-1
- ¹⁸ X. K. Lan, J. M. Khodadadi, *International Journal of Heat and Mass Transfer*, 44 (2001) 5, 953–965, doi:10.1016/S0017-9310(00)00145-9
- ¹⁹ X. K. Lan, J. M. Khodadadi, *International Journal of Heat and Mass Transfer*, 44 (2001) 18, 3431–3442, doi:10.1016/S0017-9310(01)00005-9
- ²⁰ R. B. Mahaparta, J. K. Brimacombe, I. V. Samarasekera, *Metallurgical and Materials Transactions B*, 22B (1991) 6, 875–888, doi:10.1007/BF02651163
- ²¹ J. Falkus, K. Milkowska-Piszczek, M. Rywotycki, E. Wielgosz, *Journal of Achievements in Materials and Manufacturing Engineering*, 55 (2012) 2, 668–672
- ²² J. K. Park, B. G. Thomas, I. V. Samarasekera, *Ironmaking and Steelmaking*, 29 (2002) 5, 359–375, doi:10.1179/030192302225004601
- ²³ Z. Malinowski, T. Telejko, B. Hadala, *Archives of Metallurgy and Materials*, 57 (2012) 1, 325–331, doi:10.2478/v10172-012-0030-7
- ²⁴ J. S. Ha, J. R. Cho, B. Y. Lee, M. Y. Ha, *Journal of Materials Processing Technology*, 113 (2001) 1–3, 257–261, doi:10.1016/S0924-0136(01)00691-4
- ²⁵ K. Milkowska-Piszczek, J. Falkus, *Archives of Metallurgy and Materials*, 60 (2015) 1, 251–256, doi:10.1515/amm-2015-0040

ELASTIC BEHAVIOUR OF MAGNESIA-CHROME REFRACTORIES AT ELEVATED TEMPERATURES

ELASTIČNO VEDENJE OGNJEVZDRŽNIH GRADIV MAGNEZIJA-KROM PRI POVIŠANIH TEMPERATURAH

**Ilona Jastrzębska, Jacek Szczerba, Jakub Szlęzak, Edyta Śnieżek,
Zbigniew Pędzich**

AGH University of Science and Technology, al. A. Mickiewicza 30, 30-059 Kraków, Poland
ijastrz@agh.edu.pl

Prejem rokopisa – received: 2014-08-08; sprejem za objavo – accepted for publication: 2015-01-14

doi:10.17222/mit.2014.186

An investigation of the high-temperature elastic behaviour of four varieties of magnesia-chrome products was conducted in the present work. The starting materials were characterized with XRF, XRD and SEM/EDS analyses. The measurements of the dynamic Young's modulus were performed in a temperature range of 20–1300 °C, using the acoustic method. Moreover, the dynamic Young's moduli, shear moduli and Poisson's ratios were established at ambient temperature for the original and after-heating samples. The obtained results showed similar characteristics, but the elastic behaviours of all the refractory test materials were distinguishable. The curve of the Young's modulus changed as a function of temperature, exhibiting a close-to-hysteresis character, with a decreasing area between the lower and upper curve as the Cr₂O₃ content increased in the material. The Young's modulus and the shear modulus at ambient temperature were lower for the after-heating samples when compared to the original ones.

Keywords: Young's modulus, elastic properties, refractories, shear modulus, Poisson's ratio

V tem delu je opisana preiskava visokotemperaturnih elastičnih lastnosti magnezija-kromovih proizvodov. Začetni materiali so bili ocenjeni z analizo XRF, XRD in SEM/EDS. V območju temperatur 20–1300 °C so bile izvršene meritve dinamičnega Young-ovega modula z akustično metodo. Nadalje so bili določeni dinamični Young-ov modul, strižni modul in Poisson-ovo število pri sobni temperaturi originalnih in toplotno obdelanih vzorcih. Dobljeni rezultati so pokazali podoben karakter, vendar pa se je elastično vedenje vseh preizkušanih ognjevdržnih materialov razlikovalo. Krivulja Young-ovega modula se spreminja v odvisnosti od temperature, ima ozek histerezni karakter z zmanjšanjem področja med spodnjo in zgornjo krivuljo, ko vsebnost Cr₂O₃ v materialu narašča. Young-ov strižni modul je bil pri sobni temperaturi nižji pri žarjenih vzorcih v primerjavi z originalnimi.

Ključne besede: Young-ov modul, elastične lastnosti, ognjevdržna gradiva, strižni modul, Poisson-ovo število

1 INTRODUCTION

The rapidly growing interest in the high-temperature elastic properties arises from their great usefulness in the area of designing of refractory materials and predicting their lifetime. Notwithstanding, the literature about this issue is still scarce. The Young's modulus (E), as one of the most relevant elastic-material constants, is directly associated with the thermal-shock resistance, which is a very important property during the first heating stage of the refractory furnace lining, or when it is subjected to permanent thermal stresses as in steel ladles, tundishes or oxygen converters used for pig-iron production in the industrial metallurgy.

The commonly applied method for determining the Young's modulus includes the measurements of the speed of the ultrasonic-wave propagation in a material. This method allows us to measure the property at ambient temperatures only. However, in real working conditions the knowledge of the properties at elevated temperatures is more valuable.

The magnesia-chrome refractories (MgO-Cr₂O₃) are specific materials with multi-component complex micro-

structures composed of magnesia, introduced as a clinker, and a solid solution of spinels like chromite, magnesiochromite, magnesioferrite, a regular spinel or hercynite, introduced with a chromite-ore concentrate. Both components may also be introduced with a magnesia-chromite co-clinker, which is a burning product of these two components. This group of refractory materials is no longer developed to be used for rotary-kiln linings because of the toxicity of hexavalent chromium compounds, but it is still very important in the metallurgy of iron, lead or copper.^{1,2}

Therefore, the purpose of this work is to assess the elastic behaviour of a few magnesia-chrome refractory materials with slightly different chemical compositions, both at elevated and ambient temperatures.

2 EXPERIMENTAL WORK

The four varieties of magnesia-chrome (MCr) refractory products designated in order of increasing content of Cr₂O₃ as MCr1, MCr2, MCr3 and MCr4, industrially shaped and fired, were investigated. The test materials

were produced with the use of magnesia-chrome co-clinker, fused-magnesia clinker and a chrome-ore concentrate. As a result of different proportions between the used raw materials, the products contained slightly different amounts of Cr_2O_3 in the range of 18.0–21.8 % and MgO in the range of 61.3–68.4 %. The CaO/SiO_2 ratio for all of the materials was below 1.

Detailed chemical compositions determined with the XRF method, together with the basic properties of the examined products, are presented in **Table 1**. It can be observed from this table that the test samples exhibit slightly different open porosities which increase with the decreasing ferric-oxide content. The average thermal-shock resistance (*TSR*) of MCr1 is the same as for MCr4 (10 cycles) while for MCr2 it takes on the same value as for MCr3 (6 cycles).

Table 1: Basic properties of the examined materials
Tabela 1: Osnovne lastnosti preiskovanih materialov

Property	Material designation			
	MCr1	MCr2	MCr3	MCr4
Open porosity, %	14.0	13.8	12.1	15.6
Apparent density, g/cm^3	3.11	3.17	3.23	3.07
Compressive strength, MPa	62.2	94.8	100.7	48.3
Bending strength at 20 °C, MPa	6.8	9.7	8.6	7.2
Bending strength at 1450 °C, MPa	2.5	4.9	4.7	3.3
Average thermal-shock resistance (<i>TSR</i>), cycles at 950 °C, water	10	6	6	10
Oxide	Oxide content, w/%			
MgO	68.4	66.4	61.3	64.2
Cr_2O_3	18.0	18.45	19.9	21.8
Fe_2O_3	7.0	8.1	10.2	6.7
Al_2O_3	4.0	4.4	5.4	4.2
CaO	0.88	0.82	1.07	0.85
SiO_2	1.28	1.34	1.23	1.79

The XRD analysis of the investigated products was performed at room temperature, using a PANalytical X'Pert Pro MPD X-ray diffractometer with Bragg-Brentano geometry, and $\text{Cu-K}\alpha$ radiation ($\lambda = 0.154056 \text{ nm}$), in a range of $10^\circ \leq 2\theta < 90^\circ$. The obtained XRD patterns, illustrated in **Figure 1**, show two main compo-

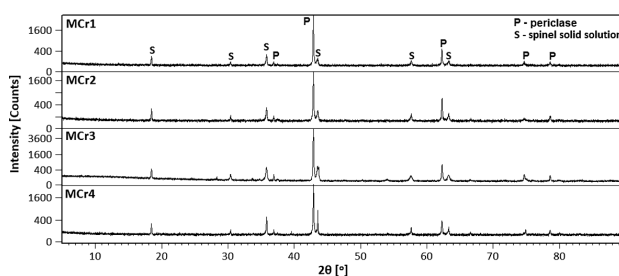


Figure 1: XRD patterns of test materials MCr1, MCr2, MCr3 and MCr4

Slika 1: XRD-posnetki preizkusnih materialov MCr1, MCr2, MCr3 in MCr4

nents which correspond to periclase (marked as P on the diffractogram) and a complex solid solution of spinels with an approximate chemical formula that can be expressed as $(\text{Mg, Fe})(\text{Cr, Al, Fe})_2\text{O}_4$ (marked as S on the diffractogram). The main difference between the registered patterns is associated with different intensities of the reflexes of the spinel solid solution, which generally increase with an increased content of Cr_2O_3 in the material.

The microstructures of the starting materials were observed under an ultra-high-definition scanning electron microscope, NovaNanosem200 equipped with an energy dispersive spectrometer, EDS. The samples for the BSE-SEM/EDS analysis were prepared as resin-embedded cross-sections using the traditional ceramographic method. The exemplary microstructures of the magnesia-chrome products are presented in **Figures 2 to 5**. As it can be observed from the figures, the test products do not differ significantly in their microstructures.

Periclase grains (visible in the SEM images as dark-grey areas) contain inclusions of the $(\text{Mg, Mn, Fe})(\text{Al, Cr, Fe})_2\text{O}_4$ solid solution (**Figures 2 and 3 – point 1, Figure 5 – point 4**). They represent magnesia co-clinker used as the raw material. Pure grains of magnesia clinker are also present in the material (**Figure 2 –**

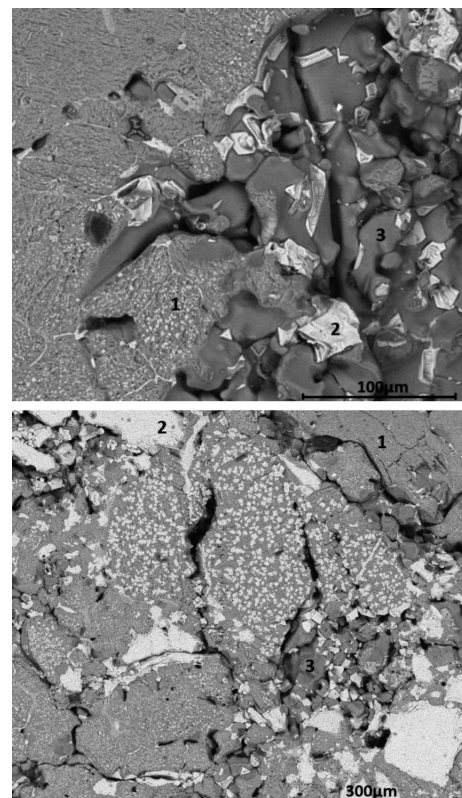


Figure 2: SEM images of MCr1 product: 1 – MgO with inclusions of solid solution $(\text{Mg, Fe})(\text{Al, Cr, Fe})_2\text{O}_4$, 2 – solid solution $(\text{Mg, Mn, Fe})(\text{Al, Cr, Fe})_2\text{O}_4$, 3 – MgO

Slika 2: SEM-posnetka proizvoda MCr1: 1 – MgO z vključki trdne raztopine $(\text{Mg, Fe})(\text{Al, Cr, Fe})_2\text{O}_4$, 2 – trdna raztopina $(\text{Mg, Mn, Fe})(\text{Al, Cr, Fe})_2\text{O}_4$, 3 – MgO

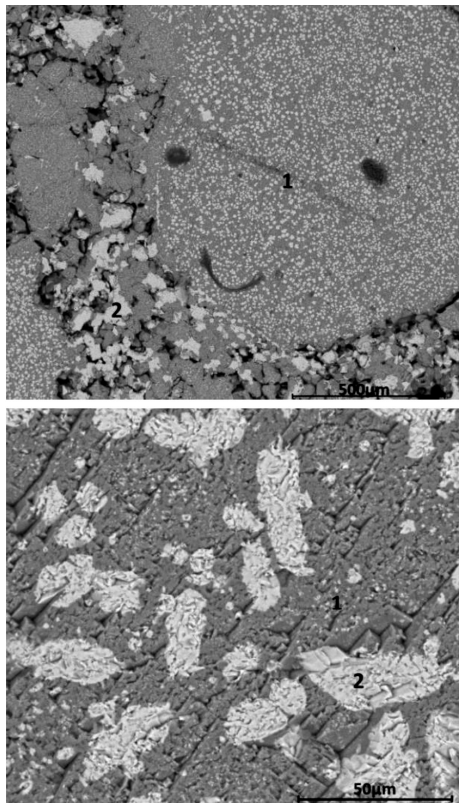


Figure 3: SEM images of MCr2 product: 1 – MgO with inclusions of solid solution (Mg, Fe)(Al, Cr, Fe)₂O₄, 2 – solid solution (Mg, Mn)(Al, Cr)₂O₄

Slika 3: SEM-posnetka produkta MCr2: 1 – MgO z vključki trdne raztopine (Mg, Fe)(Al, Cr, Fe)₂O₄, 2 – trdna raztopina (Mg, Mn)(Al, Cr)₂O₄

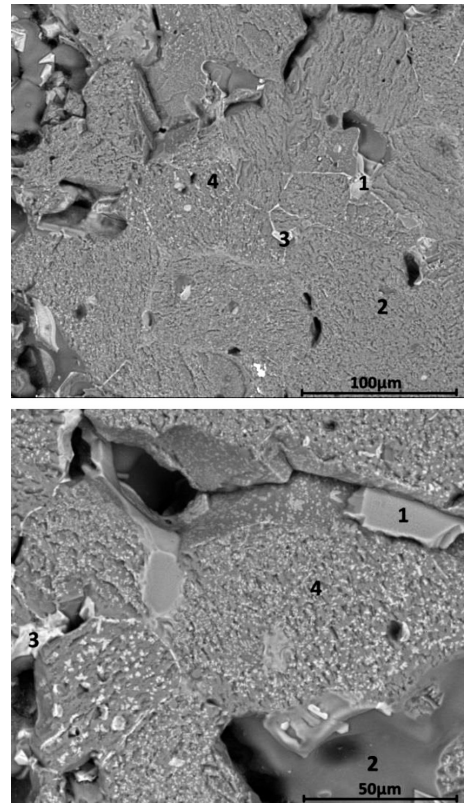


Figure 5: SEM images of MCr4 product: 1 – CaMgSiO₄, 2 – MgO, 3 – solid solution (Mg, Mn, Fe)(Al, Cr, Fe)₂O₄, 4 – MgO with large inclusions of solid solution (Mg, Mn, Fe)(Al, Cr, Fe)₂O₄

Slika 5: SEM-posnetka produkta MCr4: 1 – CaMgSiO₄, 2 – MgO, 3 – trdna raztopina (Mg, Mn, Fe)(Al, Cr, Fe)₂O₄, 4 – MgO z velikim vključkom trdne raztopine (Mg, Mn, Fe)(Al, Cr, Fe)₂O₄

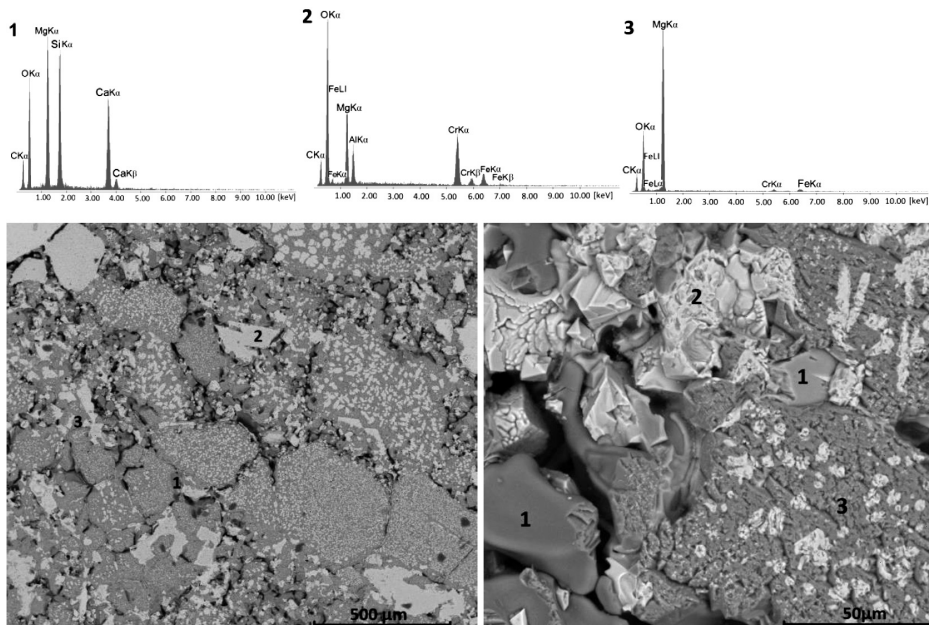


Figure 4: SEM images of the MCr3 product along with the EDS analysis for points 1, 2 and 3: 1 – CaMgSiO₄, 2 – (Mg, Fe)(Al, Cr, Fe)₂O₄, 3 – MgO enriched with iron and chromium

Slika 4: SEM-posnetka produkta MCr3 z EDS-analizo v točkah 1, 2 in 3: 1 – CaMgSiO₄, 2 – (Mg, Fe)(Al, Cr, Fe)₂O₄, 3 – MgO, obogaten z železom in kromom

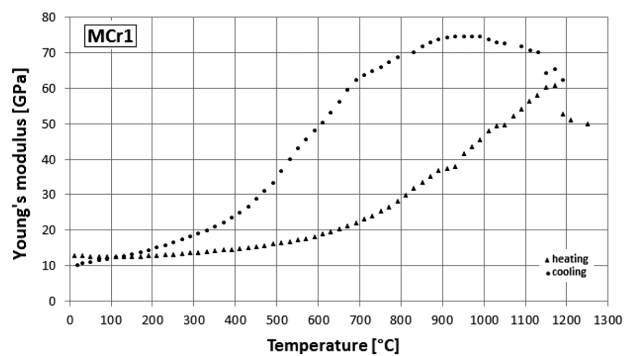


Figure 6: Young's modulus E versus the temperature during heating (triangles) and cooling (dots) for the material MCr1

Slika 6: Young-ov modul E v odvisnosti od temperature med ogrevanjem (trikotniki) in ohlajanjem (točke) za material MCr1

point 3, **Figure 5** – point 2). The lightest areas comprise a complex solid solution containing iron, (Mg, Mn, Fe^{2+})(Al, Cr, Fe^{3+}) $_2O_4$ (**Figures 2 and 4** – point 2, **Figure 5** – point 3), or without iron, (Mg, Mn) (Al, Cr) $_2O_4$ (**Figure 3** – point 2). Calcium magnesium silicate (monticellite) was also detected in the microstructures of the MCr3 and MCr4 products, visible as the light-grey areas located between the magnesia-chrome co-clinker grains (**Figures 4 and 5** – point 1).

The changes in the Young's modulus, depending on the temperature, were measured in the heating conditions at the maximum temperature of 1300 °C using a resonant-frequency and damping analyser RFDA HT-1600. The test samples, of rectangular cross-sections, had dimensions of 100 mm × 40 mm × 20 mm. The temperature increment during the heating was set to 2 °C/min while for the cooling it was 5 °C/min. The holding time at the maximum temperature was 20 min.

The ambient-temperature measurements of the dynamic Young's modulus, shear modulus (G) and Poisson's ratio (ν) were carried out on both the original samples and on the samples after the E -modulus measurements at elevated temperatures. Two samples, with rectangular cross-sections and the same dimensions, 100 mm × 40 mm × 20 mm, of each type of the material were sub-

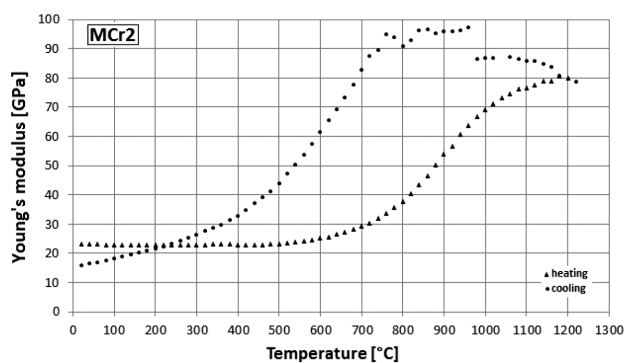


Figure 7: Young's modulus E versus the temperature during heating (triangles) and cooling (dots) for the material MCr2

Slika 7: Young-ov modul E v odvisnosti od temperature med ogrevanjem (trikotniki) in ohlajanjem (točke) za material MCr2

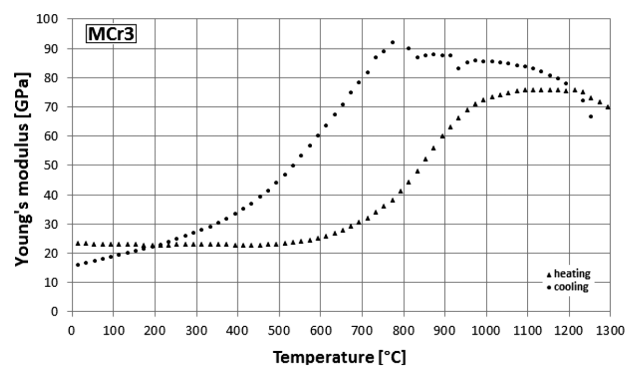


Figure 8: Young's modulus E versus the temperature during heating (triangles) and cooling (dots) for the material MCr3

Slika 8: Young-ov modul E v odvisnosti od temperature med ogrevanjem (trikotniki) in ohlajanjem (točke) za material MCr3

jected to an investigation. Therefore, the average modulus value for each sample was accounted for by the average value of the two measurements. The test was conducted with a RFTA Professional apparatus, in the flexural and torsion modes of vibrations, in accordance with the ASTM E 1876-09 standard.³

3 RESULTS

Figures 6 to 9 depict the dependence between the Young's modulus (E) and the temperature during the process of heating and cooling the samples. At the first sight, the sequences of the measured points for all of the examined materials look similar, exhibiting a "dolphin-like" shape. These measured-point sequences arrangement also resembles a hysteresis function, with a decreasing area between the lower and upper points as the Cr_2O_3 content increases in the material.

The common feature of all the investigated products is an evident increase of the heating slope which begins at about 600 °C. The MCr1 product, characterized by the lowest Cr_2O_3 content and a high open porosity, exhibited the widest hysteresis and the lowest value of the initial Young's modulus read off from the $E(T)$ dependence as 12.7 GPa (**Figure 6**). During the heating of this sample,

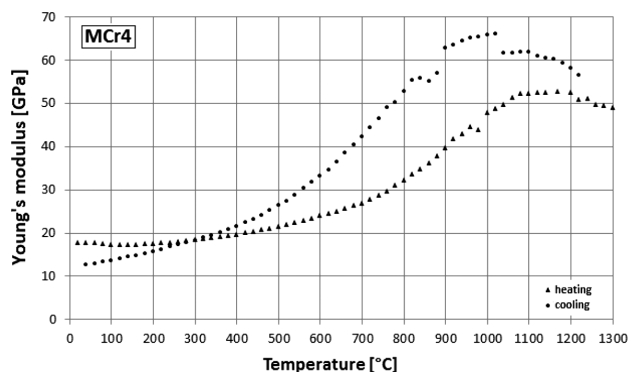


Figure 9: Young's modulus E versus the temperature during heating (triangles) and cooling (dots) for the material MCr4

Slika 9: Young-ov modul E v odvisnosti od temperature med ogrevanjem (trikotniki) in ohlajanjem (točke) za material MCr4

the maximum E value of 60.7 GPa was achieved at 1172 °C. Then, the elastic modulus decreased and reached the minimum value of 50 GPa at 1252 °C. Such an increase followed by a decrease in the Young's modulus during the heating cycles was observed for all the investigated samples. The maximum E value of 80.7 GPa, during the heating cycle, was registered for the MCr2 material at 1181 °C (Figure 7).

The cooling-cycle point sequence, for all the examined materials, showed an evident increase in the elastic modulus and a following gradual decrease, finally reaching an E value that was lower than the starting one, registered at the beginning of the test. In spite of the fact that the MCr1 and MCr4 products differ mostly in the area between the heating and cooling slopes, their values of the initial and final E moduli are the closest and so are their elastic moduli at the maximum temperature. On the other hand, the MCr2 and MCr3 materials, exhibiting similar sequences of the measured points and the areas between them, achieve similar E -modulus values both at the ambient and maximum temperatures of the test. It is worth to note that these two "pairs" of the materials exhibit the same thermal-shock resistance that can be observed from Table 1 (TSR : MCr2 = MCr3 = 6 and MCr1 = MCr4 = 10).

Table 2: Results of Young's modulus (E), shear modulus (G) and Poisson's (ν) ratio measured at ambient temperature

Tabela 2: Young-ov modul (E), strižni modul (G) in Poisson-ovo število (ν), izmerjeno pri sobni temperaturi

Sample designation	E /GPa	E decrease after heating, %	G /GPa	G decrease after heating, %	ν
MCr1 _o	13.80 ± 0.14	16.1	7.28 ± 0.07	17.4	-0.052
MCr1 _h	11.58 ± 0.12		6.01 ± 0.06		-0.038
MCr2 _o	21.51 ± 0.22	20.9	10.43 ± 0.10	18.5	0.031
MCr2 _h	17.02 ± 0.17		8.50 ± 0.09		0.001
MCr3 _o	24.41 ± 0.24	22.4	12.29 ± 0.12	22.8	-0.007
MCr3 _h	18.93 ± 0.19		9.49 ± 0.09		-0.003
MCr4 _o	17.62 ± 0.18	20.8	8.08 ± 0.08	20.4	0.091
MCr4 _h	13.96 ± 0.14		6.43 ± 0.06		0.086

Designation indexes: o – original sample, h – after-heating sample

Table 2 presents the results of the Young's moduli and shear moduli determined with the standard deviation as well as Poisson's ratios calculated with the equations given in ASTM E 1876-09 for the samples with a rectangular geometry. It can be observed that in each case the Young's and shear moduli of the after-heating samples are lower in comparison to the original ones. Here, the "pairs" of the test materials with similar E and G moduli can also be distinguished. The moduli for

MCr1 are the most similar to the ones for MCr4. A similar situation occurs when comparing the MCr2 and MCr3 materials.

It is worth emphasizing that the drops in the E values, for all the materials, entail a decrease in the shear moduli. The highest values of the E and G moduli for both the original and after-heating samples were obtained for the MCr3 sample, while the lowest values were registered for MCr1. The results obtained for Poisson's ratio ν showed that in each case its value was lower for the original sample when compared to the after-heating one. Moreover, for the MCr1 and MCr3 samples the ν ratios even reached negative values, whereas for the rest of the samples they were positive.

4 DISCUSSION

Firstly, it should be emphasized that magnesia-chrome materials are highly complex systems because they are composed of magnesia and a few spinel compounds that often form solid solutions with different proportions, making them even more complex. Among these spinels the following can be found: chromite $FeCr_2O_4$, magnesiochromite $MgCr_2O_4$, regular spinel $MgAl_2O_4$, magnesioferrite $MgFe_2O_4$, galaxite $MnAl_2O_4$ and hercynite $FeAl_2O_4$.

The present mixture of the mentioned spinels was found with the SEM observations and was also confirmed by the XRD analysis. It is worth noting that there is a good repeatability of the achieved results with regard to the curve shape created (Figures 6 to 9) by the obtained point sequences, despite the fact that these were industrial samples, in which an unavoidable spread of commercial properties may occur.

All the measured point sequences resemble a hysteresis function, which arises from the thermal history of a sample. The initial increasing character of an $E(T)$ curve is associated with a densification of the microstructure due to a partial oxidation of Fe^{2+} into Fe^{3+} , which starts above 300 °C,¹ leading to a modification of the existing spinel solid solution due to an incorporation of oxygen into the structure, or due to a grain reorganization as a result of the stress during the test and the increased temperature.

Above the temperature of 500 °C a more intense growth of the heating slope probably originates from an "order-disorder" phase transformation, occurring in the solid mixtures with a spinel structure. This phenomenon derives from the propensity of the ions to change their local positions in the structure. The ions in the 2+ oxidation states, which are regularly located in the tetrahedral (T) sites, pass to the octahedral (M) ones that are normally occupied by the 3+ ions, and vice versa.⁴ It is called a transition into an "inversion structure", which is followed by the changes in the structural-parameter values, like the oxygen parameter or the cation-anion distance in the T and M sites.

The literature quotes that cation disordering considerably affects the elasticity,⁵ the compressibility and the thermal-expansion coefficient.^{6–8} The beginning of an inversion transformation corresponds to different temperatures, depending on the type of spinel. After reaching the maximum value of the Young's modulus, the curve (the author has in mind a continuous sequence of measured points) starts to drop until reaching the maximum temperature of the test, which needs a further investigation. The cooling cycle after the maximum temperature starts with an increase in the E modulus reaching the maximum value for all the test materials. This behaviour exhibits the "strengthening" of the material in the average temperature range of 800–1000 °C, which may be the effect of the recrystallization process and filling the voids.

In the case of the MCr1 material the E -modulus change exhibits an almost continuous character during the cooling process, whereas in the cases of the other samples this dependence is discontinuous, requiring a further investigation. The following gradual drop in the $E(T)$ dependence is probably related with the stress relaxation due to a microcrack formation or, as previously reported by Podwórny et al.⁹, a channel-like pore formation, which triggers the loosening of the microstructure. Even though the test materials are not considerably different in their chemical and phase compositions, they exhibit distinguishable behaviours of the elastic-modulus change. Therefore, the $E(T)$ dependence may represent a "finger print" of the material. It proves that this method can be highly helpful for assessing the high-temperature behaviour of refractory materials.

The obtained lower values of the E moduli at ambient temperature for all the after-heating MCr samples (**Table 2**) are the results of microcracks or other defects formed during the heating of the materials. The decreased Young's moduli (E) are accompanied by simultaneous decreases in the shear moduli (G). These two moduli, together with Poisson's ratio (ν), are expressed with a well-known equation, $\nu = (E/2G) - 1$. It can be observed that the MCr1 and MCr3 products exhibit negative values of Poisson's ratio for both the original and after-heating samples. Such a behaviour of a material was also previously reported.^{9,10} The negative values of Poisson's ratio show that the material unfolds when it is subjected to stretching¹¹ and the negative ν obtained in this research can be ascribed to the rearrangement and rotation of the microstructural components such as large grains, used for the production of the material, or the pores that are always present in the microstructures of refractory materials.

Notwithstanding, it is difficult to relate these ratios with the elastic behaviour, chemical composition and type of the material investigated in this study. The calculated percentage changes in the E and G values after the heating (during the test at elevated temperatures) (**Table 2**) show that the tensile, compressive and shear stresses have almost equally destructive effects on materials MCr3 and MCr4. On the other hand, according

to the obtained results, the properties of the MCr1 material are more influenced by the shear stress, while for the MCr2 material the tensile and compressive stresses play prevailing roles.

5 CONCLUSIONS

1. The high-temperature investigation of the elastic properties of magnesia-chrome refractories showed hysteresis-like behaviours. The hysteresis range was the widest for the MCr1 product with the lowest amount of Cr_2O_3 and the narrowest for the MCr4 product with the largest amount of Cr_2O_3 .
2. Different E moduli obtained at elevated temperatures for the magnesia-chrome products prove that the used method may be helpful for predicting the high-temperature behaviour and lifetime of this kind of widely applied refractory materials.
3. The dynamic Young's moduli and shear moduli, measured at ambient temperature, were found to be lower for the after-heating samples when compared to the original ones, which was the result of the defects formed during the heating process.

Acknowledgements

This work was supported by grant no. UDA-POIG. 01.04.00-18-028/11-00.

6 REFERENCES

- 1 F. Nadachowski, Outline of refractory materials technology, Silesia Technical Publishing, Katowice 1995 (in Polish)
- 2 M. Szymaszek, J. Szczerba, W. Zelik, Directions in development of refractories for the cement and lime industry, *Ceramic Materials*, 63 (2011) 3, 608–613 (in Polish)
- 3 ASTM E 1876-09, 2009, doi:10.1520/E1876-09
- 4 K. E. Sickafus, J. M. Wills, N. W. Grimes, Spinel compounds: structure and property relations, *Journal of American Ceramic Society*, 82 (1999) 12, 3279–3292, doi:10.1111/j.1151-2916.1999.tb02241.x
- 5 R. C. Liebermann, I. Jackson, A. Ringwood, Elasticity and phase equilibria of spinel disproportionation reactions, *Geophys. J. Int.*, 50 (1977) 3, 553–586, doi:10.1111/j.1365-246X.1977.tb01335.x
- 6 R. M. Hazen, H. Yang, Effects of cation substitution and order-disorder on P-V-T equations of state of cubic spinels, *American Mineralogist*, 84 (1999), 1956–1960
- 7 J. Podwórny, Order-disorder phase transformation in 2:3 spinels, *Ceramika – Ceramics*, vol. 117, Polish Ceramic Society, Kraków 2014 (in Polish)
- 8 F. Martignago, A. Dal Negro, S. Carbonin, How Cr^{3+} and Fe^{3+} affect Mg-Al order-disorder transformations at high temperature in natural spinels, *Physics and Chemistry of Minerals*, 3 (2003), 401–408, doi:10.1007/s00269-003-0336-0
- 9 J. Podwórny, J. Wojsa, T. Wala, Variation of Poisson's ratio of refractory materials with thermal shocks, *Ceramics International*, 37 (2011), 2221–2227, doi:10.1016/j.ceramint.2011.03.070
- 10 R. Lakes, Deformation mechanism in negative Poisson's ratio materials: structural aspects, *Journal of Materials Science*, 26 (1991) 9, 2287–2292, doi:10.1007/BF01130170
- 11 R. Lakes, Foam structures with a negative Poisson's ratio, *Science*, 235 (1987) 4792, 1038–1040, doi:10.1126/science.235.4792.1038

STUDY ON THE MAGNETIZATION-REVERSAL BEHAVIOR OF ANNEALED Sm-Fe-Co-Si-Cu RIBBONS

ŠTUDIJ VEDENJA PRI OBRATU MAGNETIZACIJE ŽARJENIH TRAKOV Sm-Fe-Co-Si-Cu

Marcin Dośpiał, Sebastian Garus, Marcin Nabialek

Institute of Physics, Czestochowa University of Technology, Armii Krajowej Av. 19, 42-200 Czestochowa, Poland
mdospial@wp.pl

Prejem rokopisa – received: 2014-09-04; sprejem za objavo – accepted for publication: 2014-12-09

doi:10.17222/mit.2014.219

The paper presents the studies of Sm-Fe-Co-Si-Cu ribbons obtained with the melt-spinning technique, annealed at 1123 K for 3 h. The phase-composition studies were made using a D8 Advance Bruker X-ray diffractometer. It was found that the studied alloy has a multi-phase composition. These studies were of crucial importance in the interpretation of the magnetization reversal. Magnetic measurements, i.e., the major hysteresis loop and recoil curves were performed using a LakeShore vibrating-sample magnetometer with the maximum magnetic field of up to 2 T. On the basis of the recoil curves, the hysteresis loop was decomposed into the reversible and irreversible magnetization components. The decomposed curve was used to describe the processes that influence the reversal magnetization in the studied permanent magnets. Further, these components were used to model the recoil curves, using a modified hyperbolic $T(x)$ model based on the method described by Dośpiał. The modeled hysteresis loop and recoil curves revealed a high compliance with the experimental data, proving the validity of the assumptions made in the modeling procedure.

Keywords: permanent magnets, TbCu₇ structure, magnetization reversal, hysteresis model

Članek predstavlja študij trakov Sm-Fe-Co-Si-Cu, dobljenih s tehniko "melt-spinning", 3 h žarjenih pri 1123 K. Študij sestave faz je bil izvršen z rentgenskim difraktometrom D8 Advance Bruker. Ugotovljeno je bilo, da je preučevana zlitina sestavljena iz več faz. Te študije so bile ključnega pomena pri razlagi obrata magnetizacije. Magnetne meritve, to so glavna histerezna zanka in povratne krivulje, so bile izvršene z magnetometrom LakeShore z vibrirajočim vzorcem z uporabo največjih magnetnih polj do 2 T. Na podlagi povratnih krivulj je bila histerezna zanka razdeljena v komponente reverzibilne in ireverzibilne magnetizacije. Razstavljene krivulje so bile uporabljene za opis procesov, ki vplivajo na obrat magnetizacije pri preučevanih permanentnih magnetih. Nadalje so bile te komponente uporabljene za modeliranje povratnih krivulj z modificiranim hiperboličnim modelom $T(x)$ na podlagi metode, ki jo je opisal Dośpiał. Modelirane histerezne zanke in povratne krivulje so odkrile veliko ujemanje z eksperimentalnimi podatki, kar potrjuje veljavnost približkov, uporabljenih pri razvoju modela.

Ključne besede: permanentni magneti, strukture TbCu₇, obrat magnetizacije, histerezni model

1 INTRODUCTION

Alloys with the chemical composition close to SmCo_{7-8.5} are used for fabricating the materials with a TbCu₇ meta-stable structure that cannot exist steadily.¹⁻³ Doping elements, such as Si, Zr, Cu, etc., promote the crystallization of this type of disordered structure, whose main feature is a positive β intrinsic-coercivity temperature coefficient.^{4,5} The annealing process applied to these materials leads to the decomposition of the SmCo₇ phase into more stable structures, composed of the SmCo₅ and Sm₂Co₁₇ phases.⁶⁻⁸

One of the most popular methods for determining the reversal-magnetization process is an analysis of recoil loops. Reversal magnetization in multiphase, nanocomposite permanent magnets, such as annealed Sm_{12.5}Fe₈Co_{66.5}Si₂Cu₁₁ ribbons, is very complex and often described with more than one type of process.² On the basis of recoil curves, it is not only possible to determine the number of reversible and irreversible magnetization processes occurring in these materials, but also describing their parameters.⁶

Such information applied to hysteresis models can be used for simulating the major and minor hysteresis loops, the initial magnetization or recoil curves.

The aim of this paper is to present the theoretical description of the major hysteresis loop and recoil curves obtained using a hyperbolic $T(x)$ model modified by Dośpiał and its comparison with the experimental data.

2 MATERIALS AND EXPERIMENTAL PROCEDURE

Samples of the Sm_{12.5}Fe₈Co_{66.5}Si₂Cu₁₁ alloy were obtained from high-purity elements, by arc melting, in a protective argon atmosphere. The studied ribbons were prepared by rapidly quenching the liquid alloy on a rotating copper wheel with a high linear velocity of 20 m/s. Both ingots and the samples were prepared in a protective gas atmosphere under a pressure of 0.4×10^5 Pa. The obtained ribbons were encapsulated in the argon atmosphere, annealed at 1123 K for 3 h and slowly cooled to room temperature.

XRD patterns were measured using a Bruker X-ray diffractometer equipped with a Lynx Eye semiconductor counter. Diffraction patterns were made using a Cu- $K\alpha$ radiation source with a characteristic wave length of 0.1541 nm in the Bragg-Brentano geometry. The samples for the X-ray measurements were scanned in a 2θ range from 30° to 120° with an angle step of 0.02° and an exposition time of 3 s. A quantitative and qualitative analysis of the phase composition was carried out using the Bragg evaluation program applying the Rietveld profile-matching method.⁹

The major hysteresis loop and recoil curve were measured using a LakeShore VSM with the maximum external magnetic field of 2 T. The method of the recoil-curve decomposition into the constituent magnetization components was described elsewhere.^{10,11} The samples used for the magnetic measurements were in the form of ribbons of known dimensions. The demagnetization field resulting from their shape was taken into account and evaluated with the method described in¹².

2.1 Hysteresis model

In the original $T(x)$ model,^{13,14} the hysteresis loop can be described with the sum of sigmoid and linear functions. The sigmoid hysteretic function characterizes the irreversible magnetization changes. The linear one is used for describing the reversible magnetization changes. In this research the authors used the $T(x)$ model modified by Došpial,^{15,16} describing the reversible magnetization component with an anhysteretic sigmoid function. Based on this assumption, the whole reversal magnetization process was described with following Equations:

$$f_{r,+}^{\text{hys}} = \mu_0 M_R \sum_{i=1}^{n_{\text{irr}}} B_{0,i} (\tanh[C_{0,i}(x-a_{0,i})] + b_{+,i} - b_{1,i}) \quad (1a)$$

$$f_{r,+}^{\text{anhys}} = \mu_0 M_{\text{rev}}^{\text{max}} \cdot \left(\sum_{j=1}^{n_{\text{rev}}} B_{0,j} \frac{\tanh[C_{0,j}(x+a_{0,j})] + \tanh[C_{0,j}(x-a_{0,j})]}{2} \right) \quad (1b)$$

$$b_{+,i} = \tanh[C_{0,i}(x_k + a_{0,i})] - \tanh[C_{0,i}(x_k - a_{0,i})] \quad (1c)$$

$$f_{r,-}^{\text{hys}} = \mu_0 M_R \sum_{i=1}^{n_{\text{irr}}} B_{0,i} (\tanh[C_{0,i}(x+a_{0,i})] + b_{-,i} + b_{1,i}) \quad (2a)$$

$$f_{r,-}^{\text{anhys}} = \mu_0 M_{\text{rev}}^{\text{max}} \cdot \left(\sum_{j=1}^{n_{\text{rev}}} B_{0,j} \frac{\tanh[C_{0,j}(x+a_{0,j})] + \tanh[C_{0,j}(x-a_{0,j})]}{2} \right) \quad (2b)$$

$$b_{-,i} = \tanh[C_{0,i}(x_k - a_{0,i})] - \tanh[C_{0,i}(x_k + a_{0,i})] \quad (2c)$$

$$b_{1,i} = \frac{\tanh[C_{0,i}(x_m + a_{0,i})] - \tanh[C_{0,i}(x_m - a_{0,i})]}{2} \quad (3)$$

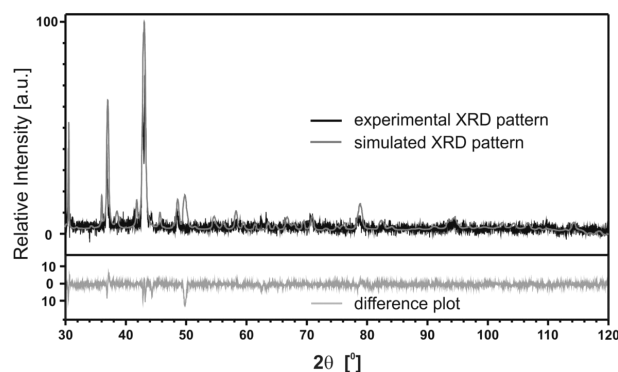


Figure 1: X-ray diffraction patterns: measured and calculated from the Rietveld refinement and the difference curve for a $\text{Sm}_{12.5}\text{Fe}_8\text{Co}_{66.5}\text{Si}_2\text{Cu}_{11}$ ribbon annealed at 850°C for 3 h

Slika 1: Rentgenogram, izmerjen in izračunan iz Rietveld-ovega približka, ter diferenčna krivulja za trak $\text{Sm}_{12.5}\text{Fe}_8\text{Co}_{66.5}\text{Si}_2\text{Cu}_{11}$, žarjen 3 h na 850°C

where (+) and (-) in the $f_{\pm}^{\text{hys,anhys}}$ functions represent the ascending and descending changes of the reversible (anhys) and irreversible (hys) components, respectively; x is the external-magnetic-field excitation, a_{0i} is the center of the i^{th} pinning/nucleation site, a_{0j} is the center of the j^{th} reversible process; $B_{0,i}$, $B_{0,j}$ are the amplitudes of the i^{th} and j^{th} magnetization components; $C_{0,i}$, $C_{0,j}$ are the sheering factors, while x_m represents the maximum-external-magnetic-field excitation. The i and j indexes refer to individual reversible and irreversible magnetization components, respectively, and $n_{\text{irr,rev}}$ is their total number.¹⁶

3 RESULTS AND DISCUSSION

Figure 1 presents the experimental X-ray diffraction pattern compared with the results of the Rietveld refinement simulation, obtained for the annealed $\text{Sm}_{12.5}\text{Fe}_8\text{Co}_{66.5}\text{Si}_2\text{Cu}_{11}$ thin ribbons.

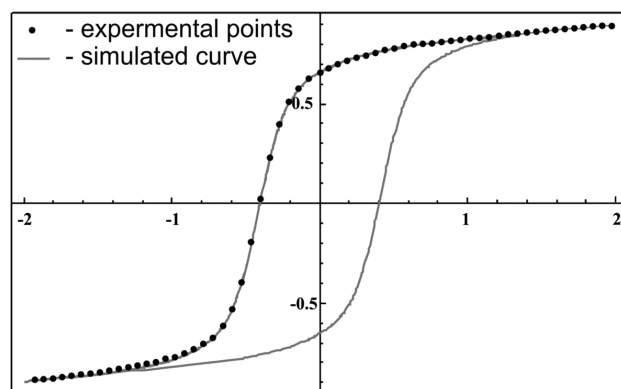


Figure 2: Measured demagnetization curve and the calculated hysteresis loop, obtained with the modified $T(x)$ model, for the $\text{Sm}_{12.5}\text{Fe}_8\text{Co}_{66.5}\text{Si}_2\text{Cu}_{11}$ ribbon annealed at 850°C for 3 h

Slika 2: Izmerjena krivulja razmagnetenja, izračunana z modificiranim modelom $T(x)$ histerezne zanke za trak $\text{Sm}_{12.5}\text{Fe}_8\text{Co}_{66.5}\text{Si}_2\text{Cu}_{11}$, žarjen 3 h na 850°C

According to the Rietveld refinement, it was found that the studied alloy was composed from $\text{Sm}_2\text{Co}_{17}$ (22.92 %), SmCo_7 (37.45 %) and SmCo_5 (39.63 %) phases. A lack of one of the less intense peaks on the experimental diffraction pattern, as compared with the simulation, can be associated with the preferred position, occupied by the Cu atoms in the TbCu_7 structure and the use of a copper X-ray source. Due to the overlapping peaks, originating from the presence of different crystalline phases, it was not possible to estimate the average grain size using the Bragg equation. However, it was possible to state that it was less than about 120 nm.

With the measured demagnetization curve and the simulated one, obtained with the modified hyperbolic $T(x)$ model, the major hysteresis loop is presented in **Figure 2**.

The experimentally determined hysteresis loop was used to estimate the basic magnetization parameters: saturation of the magnetization $\mu_0 M_S$ (0.90 T), remanence $\mu_0 M_R$ (0.70 T) and coercivity H_C (0.41 T).

The saturation of the magnetization and the remanence were also compared with those calculated from the initial magnetization curve and the irreversible magnetization dependence after the extrapolation to the infinite field, using the method described elsewhere.¹⁷ The calculated parameters were as follows: $\mu_0 M_S(\infty) = 0.91$ T and $\mu_0 M_R(\infty) = 0.70$ T; they were used to obtain the $M_r(\infty)/M_s(\infty)$ ratio which was 0.77.

On the basis of the $M_r(\infty)/M_s(\infty)$ ratio combined with the shape of the demagnetization curve and the estimated grain size, it was possible to conclude which type of interactions between the particles is dominant. According to the literature,^{18,19} a multiphase material with a smooth demagnetization curve (as observed on **Figure 2**) and the value of the M_R/M_S ratio higher than 0.5 is characteristic for exchange-coupled nanocomposites and/or anisotropic permanent magnets.

The measured demagnetization curve (the lower arm of the hysteresis is symmetric) was compared with the

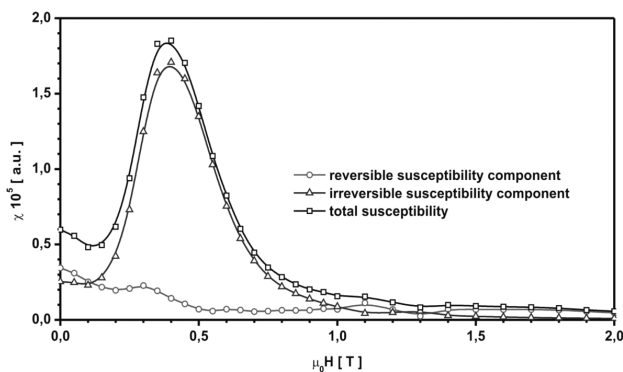


Figure 3: Reversible, irreversible and total susceptibilities determined from the magnetization components for a $\text{Sm}_{12.5}\text{Fe}_8\text{Co}_{66.5}\text{Si}_2\text{Cu}_{11}$ ribbon annealed at 850 °C for 3 h

Slika 3: Reverzibilna, ireverzibilna in skupna občutljivost, določena iz komponent magnetizacije za trak $\text{Sm}_{12.5}\text{Fe}_8\text{Co}_{66.5}\text{Si}_2\text{Cu}_{11}$, žarjen 3 h na 850 °C

theoretically simulated hysteresis loop (**Figure 2**). The simulation was done using the Mathematica software and Equations (1) to (3). The obtained results showed a high compliance with the experiment.

The startup data for simulating the major hysteresis loop and recoil curve was determined on the basis of the data obtained from the analysis of the reversible and irreversible magnetic susceptibilities (**Figure 3**).

As it can be seen on **Figure 3**, both reversible and irreversible susceptibilities are composed of at least three distribution sites. The fitting parameters determined from susceptibility curves are gathered in **Table 1**.

In order to simulate the irreversible magnetization changes, it was necessary to use a combination of three hysteretic functions, properly representing three pinning/nucleation sites. On the other hand, the reversible magnetization was represented by a combination of three anhysteretic functions, sourcing from the rotation of magnetization vectors, the free domain-wall movement of unpinned domain walls or the bowing of strongly pinned domain walls.

Table 1: Fitting parameters used in the simulation of the major hysteresis loop and recoil curve applying the modified $T(x)$ model, where: a_{0i} – the center of the i^{th} pinning/nucleation site (irreversible) or the peak resulting from the reversible process, B_{0i} – the amplitude of the i^{th} magnetization component, C_{0i} – the shearing factor of the i^{th} magnetization component

Tabela 1: Parametri ujemanja, uporabljeni pri simulaciji glavne histerezne zanke in povratne krivulje z uporabo modificiranega modela $T(x)$, kjer je: a_{0i} – sredina i^{th} nukleacije (ireverzibilno) ali vrh pri reverzibilnem procesu, B_{0i} – amplituda i^{th} magnetizacijske komponente, C_{0i} – strižni faktor i^{th} magnetizacijske komponente

Component		C_{0i}	a_{0i}	B_{0i}
rev	1	2.705	0.001	0.079
	2	0.107	0.320	0.354
	3	0.114	1.200	0.204
irr	1	0.039	0.022	0.355
	2	5.618	0.413	0.589
	3	2.672	0.749	0.081

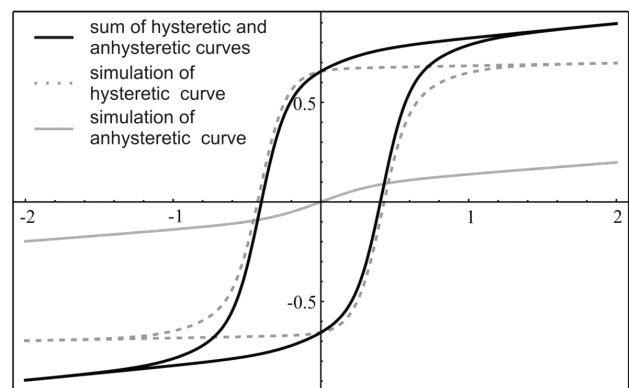


Figure 4: Decomposition of the hysteresis loop simulated with the modified $T(x)$ model into the hysteretic and anhysteretic functions

Slika 4: Razstavljanje z modificiranim modelom $T(x)$ simulirane histerezne zanke v histerezno in antihisterezno funkcijo

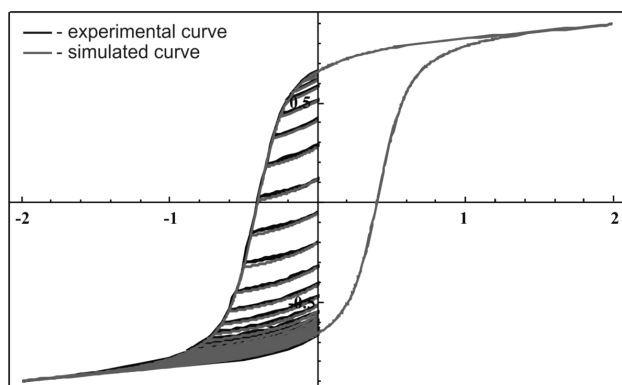


Figure 5: Comparison of the measured and simulated, with the modified $T(x)$ model, recoil loops for the $\text{Sm}_{12.5}\text{Fe}_8\text{Co}_{66.5}\text{Si}_2\text{Cu}_{11}$ ribbon annealed at $850\text{ }^\circ\text{C}$ for 3 h

Slika 5: Primerjava izmerjenih in z modificiranim modelom $T(x)$ simuliranih povratnih krivulj za trak $\text{Sm}_{12.5}\text{Fe}_8\text{Co}_{66.5}\text{Si}_2\text{Cu}_{11}$, žarjen 3 h na $850\text{ }^\circ\text{C}$

The decomposition of the hysteresis loop into the hysteretic and anhysteretic curves, representing irreversible and reversible magnetization processes, respectively, is presented in **Figure 4**.

The obtained results were also used for simulating the recoil curve in the demagnetization direction by applying Equations (1) to (3). The comparison of the simulated and measured recoil loops is presented in **Figure 5**.

As can be seen in **Figure 5**, the simulated and measured curves are similar. The observed small differences between the experiment and the simulation can be related to the recoil-loop openness effect that is, in turn, associated with the magnetic viscosity.

4 CONCLUSION

From the X-ray diffraction it was found that the studied sample was composed of three different phases, i.e., $\text{Sm}_2\text{Co}_{17}$ (22.92 %), SmCo_7 (37.45 %) and SmCo_5 .

The analysis of the parameters determined from the hysteresis loop and its shape revealed that the M_r/M_s ratio was higher than 0.5 (0.77). Such an increase in the value of the aforementioned ratio is typically met in the samples characterized by a high anisotropy²⁰ or strong exchange coupling between nanosized grains.^{18,19} The multiphase composition combined with a smooth, single-step demagnetization curve can be treated as a proof of strong exchange coupling between the grains of the constituent phases.²¹

The decomposition of the demagnetization curve into the reversible and irreversible magnetization components provided information on the quantity and type of the reversal-magnetization processes occurring in the studied material. Furthermore, using the obtained results and the $T(x)$ model modified by Dospial, it was possible to determine the anhysteretic and hysteretic curves forming the hysteresis. The same data was used to simulate the

recoil curve that showed a high compliance with the experimentally obtained one.

Acknowledgement

This work was supported by the Ministry of Science and Higher Education of Poland through Grant No. N N507 234940.

5 REFERENCES

- L. Peng, H. Zhang, J. Q. Xiao, Enhanced coercivity of melt-spun $\text{Sm}(\text{Co,Fe,Cu,Zr})_2$ ribbons annealed by improved process, *Journal of Magnetism and Magnetic Materials*, 320 (2008), 1377–1381, doi:10.1016/j.jmmm.2007.11.012
- M. Dospial, M. Nabialek, M. Szota, D. Plusa, The magnetization reversal processes of $\text{Sm}_2\text{Gd}_{10.5}\text{Fe}_8\text{Co}_{64}\text{Zr}_{2.5}\text{Cu}_{13}$ alloy in the as-quenched state, *Journal of Alloys and Compounds*, 509 (2011), S404–S407, doi:10.1016/j.jallcom.2010.12.043
- H. Tang, Y. Liu, D. J. Sellmyer, Nanocrystalline $\text{Sm}_{12.5}(\text{Co, Zr})_{87.5}$ magnets: synthesis and magnetic properties, *Journal of Magnetism and Magnetic Materials*, 241 (2002) 2–3, 345–356, doi:10.1016/S0304-8853(01)00978-7
- C. Jiang, M. Venkatesan, K. Gallagher, J. M. D. Cody, Magnetic and structural properties of $\text{SmCo}_{7-x}\text{Ti}_x$ magnets, *Journal of Magnetism and Magnetic Materials*, 236 (2001) 1, 49–55, doi:10.1016/S0304-8853(01)00451-6
- J. Zhou, I. A. Al-Omari, J. P. Liu, D. I. Sellmyer, Structure and magnetic properties of $\text{SmCo}_{7-x}\text{Ti}_x$ with TbCu_7 -type structure, *Journal of Applied Physics*, 87 (2000), 5299, doi:10.1063/1.373327
- M. J. Dospial, M. G. Nabialek, M. Szota, T. Mydlarz, K. Ozga, S. Lesz, Influence of heat treatment on structure and reversal magnetization processes of $\text{Sm}_{12.5}\text{Co}_{66.5}\text{Fe}_8\text{Cu}_{13}$ alloy, *Journal of Alloys and Compounds*, 536 (2012), S324–S328, doi:10.1016/j.jallcom.2011.11.096
- Y. Q. Guo, W. Li, J. Luo, W. C. Feng, J. K. Liang, Structure and magnetic characteristics of novel SmCo -based hard magnetic alloys, *Journal of Magnetism and Magnetic Materials*, 303 (2006), e367–e370, doi:10.1016/j.jmmm.2006.01.036
- Y. Guo, W. Li, W. Feng, J. Luo, J. Liang, Q. He, X. Yu, Structural stability and magnetic properties of $\text{SmCo}_{7-x}\text{Ga}_x$, *Applied Physics Letters*, 86 (2005), 192513, doi:10.1063/1.1926416
- Birkenstock, R. X. Fischer, T. Messner, BRASS 1.0 beta: The Bremen Rietveld Analysis and Structure Suite, *Zentrallabor für Kristallographie und Angewandte Materialwissenschaften, Fachbereich Geowissenschaften, University of Bremen*, 2003
- D. C. Crew, P. G. McCormick, R. Street, An investigation of reversible magnetization in NdFeB , *Journal of Applied Physics*, 86 (1999), 3278, doi:10.1063/1.371202
- M. Dospial, D. Plusa, Magnetization reversal processes in bonded magnets made from a mixture of $\text{Nd}(\text{Fe,Co})\text{-B}$ and strontium ferrite powder, *Journal of Magnetism and Magnetic Materials*, 330 (2013), 152–158, doi:10.1016/j.jmmm.2012.10.022
- A. K. Panda, S. Basu, A. Mitra, Demagnetization effect and its correction on the measurement of magnetic hysteresis loop of melt-spun ribbons, *Journal of Magnetism and Magnetic Materials*, 261 (2003), 190–195, doi:10.1016/S0304-8853(02)01472-5
- J. Takacs, *Mathematics of Hysteresis Phenomena*, Wiley-VCH Verlag, Weinheim 2003
- J. Takacs, I. Mészáros, Separation of magnetic phases in alloys, *Physica B*, 403 (2008), 3137–3140, doi:10.1016/j.physb.2008.03.023
- M. Dospial, M. Nabialek, M. Szota, P. Pietrusiewicz, K. Gruszka, K. Bloch, Modeling the hysteresis loop in hard magnetic materials using $T(x)$ model, *Acta Physica Polonica A*, 126 (2014), 170–171, doi:10.12693/APhysPolA.126.170

- ¹⁶ M. Dospial, Modeling the hysteresis loop of the nanocomposite material using modified hyperbolic T(x) model, *Acta Physica Polonica A*, 127 (2015), 415–417, doi:10.12693/APhysPolA.127.415
- ¹⁷ H. Zijlstra, *Experimental methods in magnetism*, Elsevier North-Holland, Amsterdam 1967
- ¹⁸ H. Kronmüller, D. Goll, Micromagnetic analysis of nucleation-hardened nanocrystalline PrFeB magnets, *Scripta Materialia*, 47 (2002) 8, 551–556, doi:10.1016/S1359-6462(02)00176-8
- ¹⁹ E. F. Kneller, R. Hawig, The exchange-spring magnet: a new material principle for permanent magnets, *Magnetics, IEEE Transactions*, 27 (1991) 4, 3588–3560, doi:10.1109/20.102931
- ²⁰ G. Ruwei, Z. Shouzheng, Z. Deheng et al., Coercivity and its dependence on the strength of alignment magnetic field in Nd-Fe-B sintered magnets, *Journal of Applied Physics*, 78 (1995) 2, 1156, doi:10.1063/1.360350
- ²¹ A. E. Ceglarek, D. Plusa, M. J. Dospial, M. G. Nabialek, P. Pietrusiewicz, Investigation of the Magnetization Reversal Process of High-Remanent Nd₁₀Fe₈₃Zr₁B₆ Alloy in the As-Cast State, *Acta Physica Polonica A*, 121 (2012) 5–6, 1279–1281

EVALUATION OF THE CHITOSAN-COATING EFFECTIVENESS ON A DENTAL TITANIUM ALLOY IN TERMS OF MICROBIAL AND FIBROBLASTIC ATTACHMENT AND THE EFFECT OF AGING

OCENA UČINKOVITOSTI NANOSA HITOZANA NA OPRIJEMANJE MIKROBOV IN FIBROBLASTOV NA DENTALNI TITANOVI ZLITINI TER NA POJAV STARANJA

Ulku Tugba Kalyoncuoglu¹, Bengi Yilmaz², Serap Gungor³, Zafer Evis⁴,
Pembegul Uyar^{5,6}, Gulcin Akca⁷, Gulay Kansu⁸

¹Balgat Oral and Dental Health Center, Baris Manco Street 22, 06520 Ankara, Turkey

²Middle East Technical University, Department of Biomedical Engineering, 06800 Ankara, Turkey

³Yuzuncu Yil University, Department of Mechanical Engineering, 65080 Van, Turkey

⁴Middle East Technical University, Department of Engineering Sciences, 06800 Ankara, Turkey

⁵Selcuk University, Department of Biology, 4207 Konya, Turkey

⁶Selcuk University, Advanced Technology Research and Application Center, 4207 Konya, Turkey

⁷Gazi University, Faculty of Dentistry, Department of Microbiology, 06500 Ankara, Turkey

⁸Ankara University, Faculty of Dentistry, Department of Prosthodontics, 06500 Ankara, Turkey
ulkutugbaterzi@gmail.com

Prejem rokopisa – received: 2014-09-23; sprejem za objavo – accepted for publication: 2015-01-08

doi:10.17222/mit.2014.239

The aim of this study was to obtain a biocompatible and antimicrobial implant surface by coating Ti6Al4V with chitosan which can be used to create a smooth transmucosal region for a faster and better wound healing and an increased bioactivity. Ti6Al4V plates were first abraded and ultrasonically cleaned and then coated with chitosan. In order to simulate the conditions of an oral environment, a group of coated plates were treated in a thermocycle apparatus. The coatings were evaluated with SEM, EDS, XRD and FTIR spectroscopy. The fibroblastic cell behavior was determined using HGF-1 cells. *P. gingivalis* was used to assess the effectiveness of chitosan as an antimicrobial coating.

It can be said that the Ti6Al4V plates were successfully coated with chitosan, indicated by the presence of the C, H and O elements in the EDS results. There were no significant differences between the XRD patterns of the coated and uncoated plates; however, the characteristic bands of chitosan were observed in the FTIR patterns of both the coated and aged samples. The fibroblast-cell attachment and proliferation were enhanced while the bacterial proliferation was inhibited by the chitosan coating. Chitosan was shown to be a biologically useful material that can be used as the coating material for transmucosal regions of dental implants.

Keywords: chitosan coating, dental implants, Ti6Al4V, HGF-1, *P. gingivalis*

Namen te študije je bil dobiti biokompatibilno in antimikrobno površino implantata z nanosom hitozana na Ti6Al4V, ki je primeren za gladko transmukozno področje, za hitrejše in boljše celjenje ran ter povečano bioaktivnost. Pri ploščah Ti6Al4V je bila najprej povečana hrupavost, nato so bile očiščene z ultrazvokom, potem pa je bil nanosen hitozan. Da bi simulirali razmere v ustih, je bila skupina plošč obdelana v napravi za termocikliranje. Nanosi so bili ocenjeni s SEM-, EDS-, XRD- in FTIR-spektroskopijo. Vedenje celic fibroblastov je bilo določeno z uporabo celic HGF-1. *P. gingivalis* je bil uporabljen za oceno učinkovitosti hitozana kot protimikrobnega nanosa.

Lahko trdimo, da so bile plošče Ti6Al4V uspešno prekrte s hitozanom, kar potrjuje prisotnost elementov C, H in O v EDS-rezultatih. Ni bilo opažene večje razlike pri rentgenski analizi vzorcev z nanosom in brez nanosa, vendar so bili opaženi karakteristični signali hitozana pri FTIR-analizi vzorcev tako pri vzorcih z nanosom kot tudi pri starih vzorcih. Oprijemanje in širjenje fibroblastičnih celic je bilo pospešeno, medtem ko je nanos hitozana zaviral širjenje bakterij. Pokazalo se je, da je hitozan biološko koristen material, ki ga je mogoče uporabiti za nanos na transmukozna področja dentalnih implantatov.

Ključne besede: nanos hitozana, dentalni implantati, Ti6Al4V, HGF-1, *P. gingivalis*

1 INTRODUCTION

Peri-implantitis, defined as an inflammatory reaction of the tissues surrounding a dental implant to a loss of the supporting bone,¹ is still the major challenge for the implant dentistry. It is known that the interface between an implant and the healthy soft tissue is similar to the one involving natural teeth.² A peri-implant soft-tissue cuff has to provide the same functions with the periodontal gingiva, such as inflammatory and immunological

defenses, growth factors and cytokine productions, filtering the seal around a tooth, an implant or prosthetic.³

Titanium (Ti), which is currently used for the production of dental implants, has remarkable properties, such as a good corrosion resistance, a very good biocompatibility and a high strength-to-weight ratio. A dioxide (or trioxide) layer that is a few nanometers thick (3–5 nm) spontaneously forms on the Ti surface. This is the layer that the biological fluids and tissues are in

contact with when Ti implants are inserted into the body.⁴ However, Ti is not able to function as an anti-microbial agent and, therefore, it cannot prevent the peri-implant infections.⁵

Surface modifications of implants with bioactive coatings stimulating the bone-cell attachment and growth is one way to increase the osseointegration and help stabilize the implant.⁶ Furthermore, in recent years, in order to decrease the bacterial activity around the Ti implants, studies focused on coating the transmucosal components with antimicrobial and biocompatible coating materials which are also efficient at wound healing and cellular attachment. On the other hand, the adhesion of gingival and epithelial cells is a desirable situation, providing a seal around the transmucosal component; however, a bacterial adhesion, which can provoke a breakdown of the attachment, is not wanted.⁴

For these kinds of applications, chitosan has many advantages, such as biocompatibility, antimicrobial efficiency and cheapness. It is a chitin-derived natural polymer produced by a deacetylation reaction. Chitin is mainly found in the exoskeleton of crustaceans and also in some fungi. Chitosan has been used in many biomedical applications including wound healing, skin grafting, homeostasis, hemodialysis, drug delivery, preventing dental plaque, calcium adsorption, etc.⁷

The objective of this study was to fabricate and characterize chitosan-coated Ti6Al4V plates. It is hypothesized that a chitosan coating would help with the human-gingival-fibroblast (HGF) attachment and antimicrobial effects. The influence of aging which simulates an oral environment was investigated *in vitro* as well.

2 MATERIALS AND METHODS

Titanium-alloy (Ti6Al4V) plates with dimensions of 20 mm × 20 mm × 2 mm were used in this study. The samples were divided into three groups: the control or un-treated Ti6Al4V ($n = 5$) (group 1), the chitosan-coated Ti6Al4V ($n = 5$) (group 2) and the chitosan-coated and aged Ti6Al4V ($n = 5$) (group 3). Before the coating process, the surfaces of the plates were air-borne-particle abraded with 50 μm aluminum-oxide particles for 10 s under 413.7 kPa (60 psi), with a distance from the tip of 0.5 mm, in a sandblaster (Heraeus Kulzer Combilabor, CL FSG 3, Germany). The aim of sandblasting was to increase the surface contact area and to obtain a higher surface roughness. All the samples were ultrasonically cleaned for 10 min in distilled water, 70 % ethanol, acetone, 70 % ethanol and distilled water sequence, respectively.

2.1 Chitosan coating

The coating procedure was performed as described by Yuan et al.⁸ Firstly, the plates were submerged in a volume fraction water : ethanol 5 % : 95 % solution. 3-iso-cyanatopropyltriethoxysilane was added at a con-

centration of $\varphi = 2$ % for 10 min at room temperature while maintaining the pH at 4.5–5.5 with NaOH or acetic acid. The samples were rinsed with ethanol and treated at 110 °C for 10 min in a vacuum oven (Nüve EV 018, Turkey). The samples were submerged into a volume fraction $\varphi = 2$ % glutaraldehyde solution at room temperature overnight and rinsed with distilled water. A mass fraction 1 % acetic-acid solution (aqueous) and 1 % chitosan (a medium molecular weight, Sigma Aldrich, Germany) in the acetic-acid solution were prepared. These solutions were mixed and stirred for 10 min and the resulting solution turned into a gel. The plates were submerged in this chitosan/acetic-acid solution at 4 °C overnight. The excess water was allowed to evaporate over 7 d (at ambient conditions).

The plates were briefly rinsed in 0.005 M NaOH followed by distilled water. After the coating process, a group of the coated plates (group 3) were treated with a thermocycle apparatus (Nüve, Turkey) to simulate a one-year oral environment. The aging process was performed for 1 week and the temperature of the water bath was alternated between 5–55 °C.⁹

The surface morphologies of the plates were observed using SEM (QUANTA 400F Field Emission SEM) at a voltage of 20 kV and the chemical composition was determined with EDS using a 30 keV ion beam. For the SEM observation the samples were coated with 5 μm AuPd. The XRD structural analysis was performed using an Ultima-IV X-ray diffractometer (Rigaku, Tokyo, Japan). The XRD was operated with a Cu- K_{α} radiation (40 kV/40 mA) and spectra were collected in the 2θ range of 10 ° to 80 ° with a scan speed of 2 ° min⁻¹. The surface functional groups of the coated samples were determined with a FTIR spectroscope (Bruker IFS 66/s, Bruker Optics, Germany) in wavenumber regions of 3800 cm⁻¹ to 300 cm⁻¹.

2.2 Cell culture and the MTT test

Before the biological experiments, for sterilization, the samples were washed in 95 % ethanol and placed under UV for 15 min, rinsed twice with sterile demineralized water and PBS. The HGF-1 cells (ATCC, CRL-2014) were donated by the Ankara University Faculty of Veterinary Medicine. The cells were cultured in Dulbecco's Modified Eagle Medium (DMEM) supplemented with 10 % of fetal-calf serum (FCS), 100 U/mL penicillin and 100 $\mu\text{g}/\text{mL}$ streptomycin in a $\varphi = 5$ % CO₂ incubator at 37 °C (all from Biochrom Ltd, Cambridge, UK). The proliferation of the cells was determined with a MTT (3-(4,5-dimethylthiazol-2-yl)-2,5-diphenyl-tetrazolium salt) test assay (Sigma, St Louis, MO, USA) and the morphology of the cells was examined with SEM.

HGF-1 cells were seeded on the Ti6Al4V plates, placed onto 6-well plates, at a density of cells 4 × 10⁵ mL⁻¹. The cells were incubated in 5 % CO₂ at 37 °C for 96 h. The Ti6Al4V plates were moved onto new 6-well plates after 96 h of incubation, and fresh media were

added. The media were then removed, a diluted MTT (5 mg/mL) solution was added into the wells and the incubation was continued in 5 % CO₂ at 37 °C for 4 h. After that, the incubation medium was removed and 400 µL of isopropanol with 0.04 N HCl was added to each well in order to dissolve the resulting formazan crystals. The absorbance of the formazan product at 570 nm and 690 nm was measured with a microplate reader (Biotek Epoch, Germany). The experiment was repeated independently in triplicate.

2.3 Cellular attachment and the morphology

The surfaces were analyzed using SEM in order to determine the cellular attachment and morphology of the cells. The HGF-1 cells cultured for 96 h on the Ti6Al4V plates were washed twice with a 0.1 M sodium-cacodylate buffer (pH 7.4), and the cells were fixed with 2.5 % glutaraldehyde prepared in 0.1 M sodium cacodylate for 1 h at room temperature. The excess glutaraldehyde solution was removed and the cells were rinsed twice in sterile distilled water and kept at -80 °C overnight before lyophilization. After the cells were dried to a critical point, the samples were coated with AuPd. The fixed cells on the discs were observed with SEM (Zeiss LS-10, Germany). The SEM images were recorded at 500-times and 5000-times magnifications.

2.4 Microbiological evaluation

The microbiological processes were done in the Medical Microbiology Laboratory at the Gazi University, the Faculty of Dentistry. In order to assess the microbial inhibition, *Porphyromonas gingivalis* (ATCC 33277) was used and cultured in Columbia Broth (Merck, Germany) supplemented with vitamin K (1 µg/mL), hemin (5 µg/mL) and 5 % sheep blood in an automated anaerobic chamber (Electrotek, United Kingdom) at 37 °C for 3–5 d with an atmosphere of 10 % H₂, 10 % CO₂ and 80 % N₂. The optical density of bacterial inoculum was adjusted to a 5 × 10⁸ colony-forming unit per mL (cfu/mL) using a spectrophotometer (BioTek ELx800, USA) according to the turbidity of the McFarland standard.

The same bacterial inoculum was spread onto a Schaedler agar media (Merck, Germany) supplemented with vitamin K (1 µg/mL), hemin (5 µg/mL) and 5 % sheep blood in the automated anaerobic chamber (Electrotek, UK) and the Ti6Al4V samples, coated with chitosan, were embedded into the infected agar plates with chitosan-coated faces. Then, the plates were incubated at 37 °C in an atmosphere of 10 % H₂, 10 % CO₂ and 80 % N₂ in the anaerobic chamber for 3–5 d. During the incubation period, the day after the incubation and every following day, a loopful of a sample was tested for the viability of the bacteria by culturing them on another Schaedler agar media, separately in the anaerobic chamber under the same conditions as mentioned before.

Then, the grown colonies of the bacteria were counted, calculated as cfu/mL and evaluated for the viability of the bacteria. All the samples were studied in triplicates in the experiment.

3 RESULTS

The SEM images of the uncoated, chitosan-coated and chitosan-coated and aged Ti6Al4V plates are given in **Figure 1**. As expected, the uncoated Ti6Al4V plate (**Figures 1a** and **1b**) was observed to have a rougher surface than the coated plates.

A chitosan aggregate was identified in the SEM micrographs of the chitosan-coated and aged plate. The chitosan was homogeneously distributed on the sand-blasted Ti6Al4V surface and conserved to a degree after the aging process. The chitosan aggregate can be seen more clearly at a high magnification even on the aged plate (**Figure 1f**). From **Figures 1c** and **1d**, it can be seen that the chitosan completely covered the Ti6Al4V substrate before the aging process was applied. The microcracks in the chitosan coating (**Figure 1c**) can be explained with the drying procedure in the ambient conditions. These cracks would have been prevented by freeze-drying the samples after the coating process. The coating was expected to be thicker than the chitosan phase on the aged plate due to the possible erosion

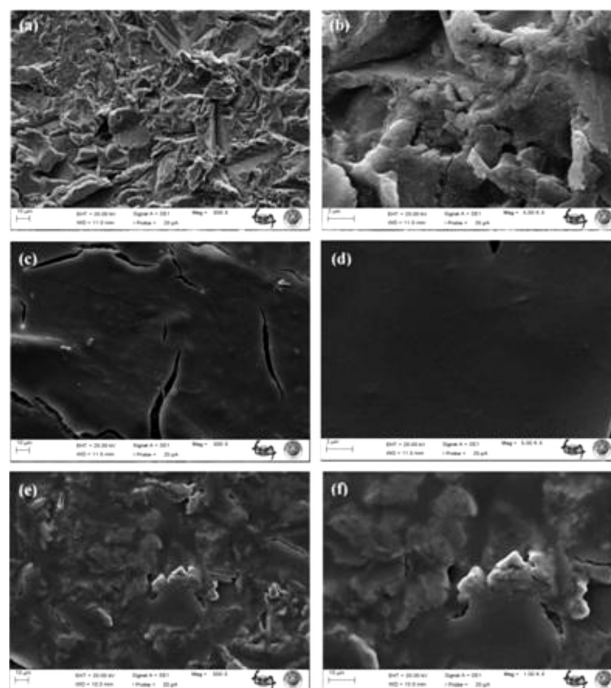


Figure 1: SEM images of Ti6Al4V plates: a) uncoated, 500-times, b) uncoated, 5000-times, c) chitosan-coated, 500-times, d) chitosan-coated, 5000-times, e) chitosan-coated and aged, 500-times, f) chitosan coated and aged, 5000-times

Slika 1: SEM-posnetki Ti6Al4V plošč: a) brez nanosa, povečava 500-kratna, b) brez nanosa, 5000-kratna, c) nanos hitozana, 500-kratna, d) nanos hitozana, 5000-kratna, e) nanos hitozana in starano, 500-kratna, f) nanos hitozana in starano, 5000-kratna

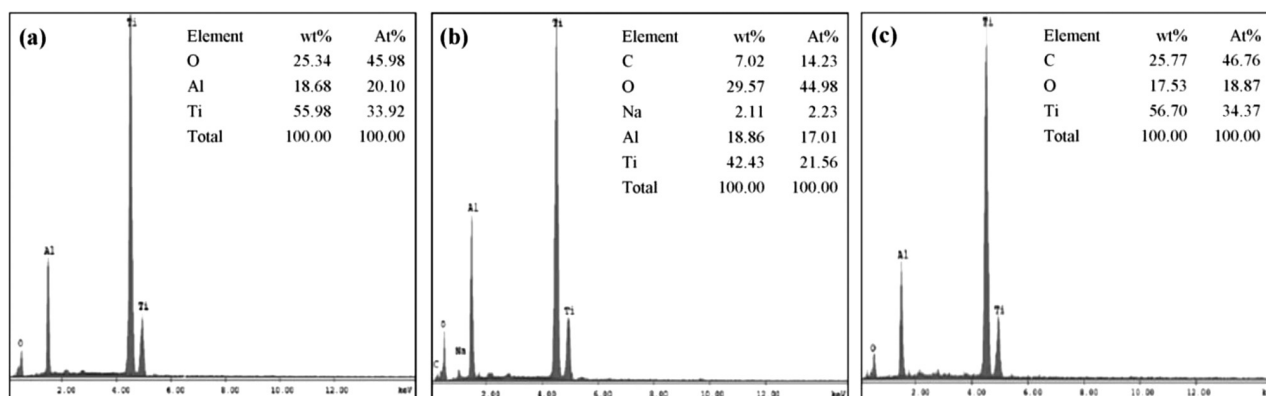


Figure 2: EDS spectra of Ti6Al4V plates: a) uncoated, b) chitosan-coated, c) chitosan-coated and aged
Slika 2: EDS-spektri Ti6Al4V plošč: a) brez nanosa, b) z nanosom hitozana, c) z nanosom hitozana in starano

caused by the aging process. When **Figures 1c to 1f** are compared, it can be seen that the rough-surface morphology, completely covered with the chitosan coating, reappears in the aged plates.

EDS was used to identify the elements and obtain semi-quantitative compositional information from the surfaces of the plates. The EDS results for the surfaces of the uncoated, chitosan-coated and chitosan-coated and aged Ti6Al4V plates are given in **Figure 2**.

The EDS analysis confirms the presence of the chitosan coating with the detected C and O elements on the Ti6Al4V plates even after the aging process. Without chitosan, due to the chemical content of the substrate material, the Ti and Al elements were detected together with the O element. The EDS spectrum of the chitosan-coated plate (**Figure 2b**) was observed to contain a low amount of the Na element.

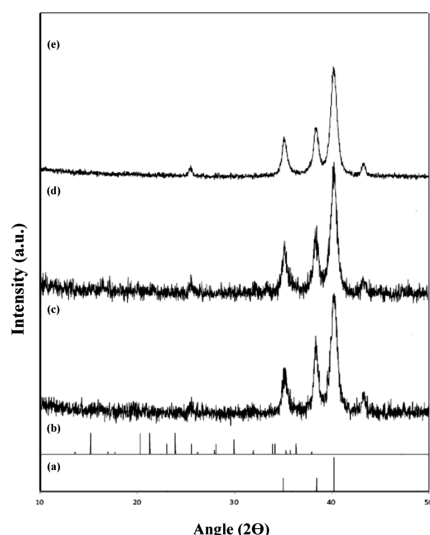


Figure 3: XRD patterns of: a) standard Ti (JCPDS # 01-1197), b) chitosan (JCPDS # 039-1894), c) uncoated Ti6Al4V plate, d) chitosan-coated Ti6Al4V plate, e) chitosan-coated and aged Ti6Al4V plate

Slika 3: Rentgenski posnetki vzorcev: a) Ti standard (JCPDS # 01-1197), b) hitozan (JCPDS # 039-1894), c) plošča Ti6Al4V brez nanosa, d) plošča Ti6Al4V z nanosom hitozana, e) plošča Ti6Al4V z nanosom hitozana in starana

The XRD patterns of the surfaces of the uncoated, chitosan-coated, chitosan-coated and aged Ti6Al4V plates are given, with the XRD peak positions of standard Ti and chitosan (**Figure 3**).

On **Figures 3a and 3c**, the substrate plates have the main standard Ti peaks at the 2θ values of 35.02° , 38.44° and 40.23° . The common XRD peaks at 25.42° and 42.22° were also attributed to the Ti6Al4V substrate. There were no distinct peaks of chitosan detected in the XRD patterns of both the coated or coated and aged plates.

The FTIR spectra of the surfaces of the chitosan-coated and chitosan-coated and aged Ti6Al4V plates are given in **Figure 4**. The FTIR spectra of the chitosan-coated Ti6Al4V plates show obvious differences after the aging process. If the FTIR spectrum of the coated and aged sample (**Figure 4b**) is compared with the one that was only coated, it can be seen that there are two additional bands at 2921 cm^{-1} and 2851 cm^{-1} which belong to the $-\text{CH}_2-$ and $-\text{CH}_3$ stretching vibrations, respectively.¹⁰ In addition, the intensities of the FTIR bands were decreased after the aging process. In the FTIR spectra of the chitosan-coated and aged sample, the band

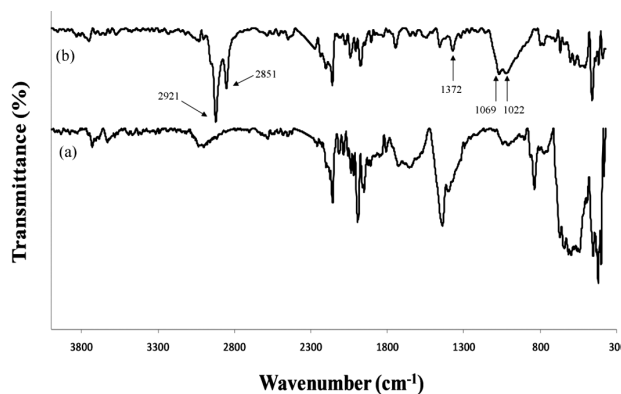


Figure 4: FTIR patterns of Ti6Al4V plates: a) chitosan-coated, b) chitosan-coated and aged

Slika 4: FTIR posnetka vzorcev Ti6Al4V-plošč: a) z nanosom hitozana, b) z nanosom hitozana in starano

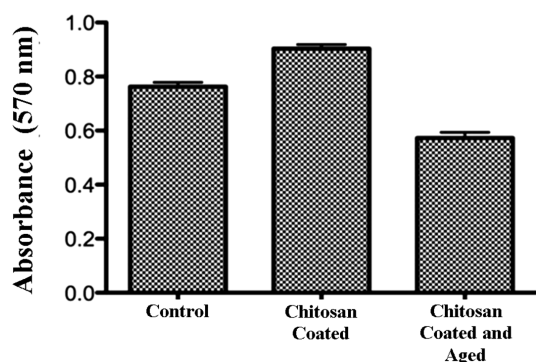


Figure 5: Survival/population of HGF-1 cells after 96 h of incubation on the control (untreated), chitosan-coated and chitosan-coated and aged Ti6Al4V plates. Data were expressed as the mean values (MV) of the \pm standard deviation (SD) of three independent experiments.

Slika 5: Preživela populacija celic HGF-1 po 96 h inkubacije na kontrolni plošči Ti6Al4V (brez nanosa), z nanosom hitozana in z nanosom hitozana ter staranju. Podatki za tri neodvisne preizkuse so prikazani kot srednja vrednost (MV) \pm standardna deviacija (SD).

at 1372 cm^{-1} was assigned to -NHCO of amide and the bands at 1069 cm^{-1} and 1022 cm^{-1} were ascribed to the saccharide structure.¹¹

The cellular viability of the HGF-1 cells of both the coated and coated and aged Ti6Al4V plates was evaluated using a MTT assay. The absorbances of the formazan produced by metabolically active HGF-1 cells on the experimental groups are given in **Figure 5**.

The cell morphology, cytoskeletal structure and adhesion behavior of the HGF-1 cells were observed

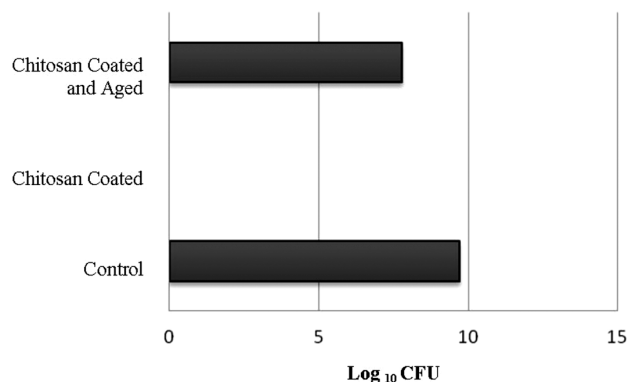


Figure 7: Number of viable *P. gingivalis* colonies (interpreted as \lg_{10})

Slika 7: Število živih kolonij *P. gingivalis* (prikazanih kot \lg_{10})

after 96 h of incubation on the control (untreated), chitosan-coated, and chitosan-coated and aged Ti6Al4V plates. The SEM micrographs, at two different magnifications, for each group are given in **Figure 6**.

In order to observe the inhibition effect of chitosan against the bacterial growth, the untreated Ti6Al4V plate (control), the chitosan-coated Ti6Al4V plate and the chitosan-coated Ti6Al4V plate after the ageing process were used as substrates. The numbers of viable *P. gingivalis* colonies proliferated on these substrates are given in **Figure 7**.

As can be seen from **Figure 7**, no *P. gingivalis* colonies were detected in the agar medium, on which the chitosan-coated samples were placed. On the other hand,

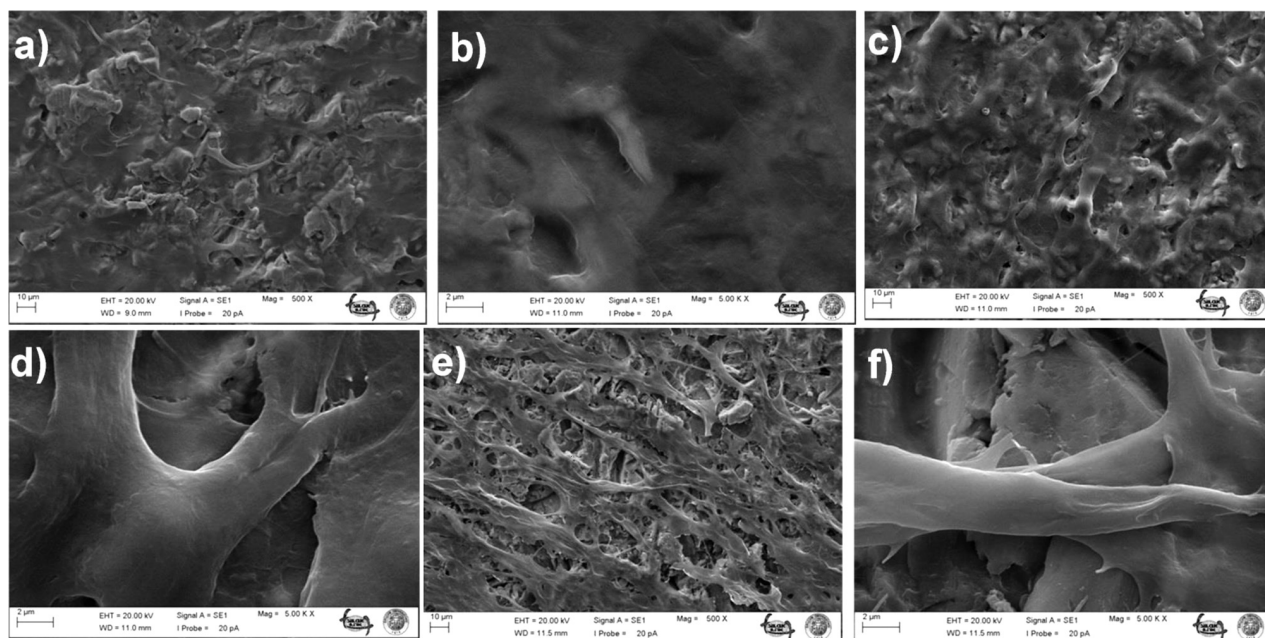


Figure 6: SEM micrographs of cultured human gingival fibroblast cells after 96 h of incubation on the Ti6Al4V plates: a), b) control (untreated), c), d) chitosan-coated, e), f) chitosan-coated and aged. Magnifications: 500-times (images on the left-hand side) and 5000-times (images on the right-hand side)

Slika 6: SEM-posnetki kultiviranih človeških gingivalnih fibroblastičnih celic po 96 h inkubacije na Ti6Al4V-ploščah: a), b) kontrolni (brez nanosa), c), d) z nanosom hitozana, e), f) z nanosom hitozana in starano. Povečave: 500-kratna (slike na levi strani) in 5000-kratna (slike na desni strani)

the bacterial growth was detected in the agar medium for the chitosan-coated and aged Ti6Al4V plates; however, the growth was much smaller than in the agar medium for the untreated Ti6Al4V plates.

4 DISCUSSION

Following the definition of osseointegration as a close contact between the bone and Ti and its alloys at the bone level,¹² the researchers focused on the surface-modification methods and implant-body design.

The major purposes for modifying dental implant surfaces are to positively modulate the host/implant tissue responses, prevent a microorganism attachment, a bone destruction, and also a failure of the implant, and decrease the healing period for osseointegration.¹² The aim of this study was to obtain an antibacterial coating for dental/craniofacial and orthopaedic implants and test the ability of the coating to promote the fibroblastic-cell growth before and after an aging process. For this purpose, chitosan, which is a biocompatible, biodegradable, antibacterial and inexpensive natural polymer with a good film-forming ability¹³, was applied on the Ti6Al4V substrate via silanization. The chitosan was successfully deposited on the plates, forming a uniform and yellowish transparent layer with some microcracks, possibly formed due to the ambient drying process.

The SEM micrographs revealed the existence of a chitosan layer on the plates even after the aging process. In addition, sandblasting increased the surface roughness and allowed a proper mechanical interlock with the coating. The elements belonging to the chitosan coating were detected with the EDS method on both the coated, and coated and aged plates. The presence of the oxygen (O) element in the EDS measurements of the Ti6Al4V plates (**Figure 2a**) can be attributed to the Al₂O₃ grains embedded in the surface during sandblasting¹⁴ or the oxide layer naturally forming on Ti and its alloys. The sodium (Na) element, which was detected in the EDS spectra of the chitosan-coated plate, was thought to originate from the NaOH solution that was used to remove the remaining acetic acid after the coating process.

The XRD pattern of the chitosan is characteristic of an amorphous polymer¹⁵ and yields broad peaks. Consequently, in the chitosan-coated plates there were no distinctive differences when compared to the substrate material. However, in the FTIR spectra of the chitosan-coated Ti6Al4V plates, characteristic bands of chitosan were observed and the aged sample showed obvious differences. The FTIR spectra showed molecular changes induced by the aging process. The main change observed was a decrease in the amide group 1372 cm⁻¹ and the formation of two -CH₂- and -CH₃ bands.

From the MTT absorbance values, it can be concluded that the degree of cell proliferation for the chitosan-coated Ti6Al4V group was higher than that of the control and chitosan-coated and aged groups after

96 h. Although the chitosan coating induced a proliferation of the HGF-1 cells, after the aging process their vitality decreased significantly. The general shape and growth pattern of the fibroblast cells can be seen directly from the SEM micrographs (**Figure 6**). After 96 h of culturing, the cells attached to all the different surfaces; the cells on the control samples were more flattened than on the other surfaces, with a broader contact area. In contrast, the cells on the chitosan-coated Ti6Al4V surface had a polygonal morphology with extensions in multiple directions.

In addition, the cells on the chitosan-coated and aged surface showed a spindle-like and elongated morphology, but they did not completely adhere to the surface. From the above we can conclude that the cells cultured on the chitosan coating showed higher initial-adhesion properties with an increased number of extremities of the cell bodies when compared to the control group. Since the thermal process applied during the aging induced chemical modifications in the structure of chitosan, the attachment and proliferation of the cells were then different. However, one week of aging, which was a simulation of one year of the oral environment, did not erode the coating much and the cellular response to this surface was not significantly affected.

In an in-vitro study, in which the initial attachment of oral bacteria on Ti surfaces was investigated¹⁶, it was shown that comparatively large amounts of *P. gingivalis* and *A. actinomycetemcomitans* adhered to a Ti surface even after polishing. These findings indicate that there is a considerable risk of adhesion of periodontopathic bacteria on Ti implants. The adhesion of bacteria is generally influenced by the physicochemical properties of the material surface, including the surface roughness, hydrophobicity (surface wettability) and electrical charge (zeta potential)¹⁷. Generally, rough surfaces allow a greater bacterial adhesion than smooth surfaces.

For the Ti6Al4V implant material, the electrical charge of the material's surface influences the adhesion capacity of bacteria. Bacteria are generally negatively charged, as are the Ti6Al4V surfaces. In this study, although having the same charge, the bacteria adhered to the untreated Ti6Al4V control samples. This proves that Ti and its alloys were unable to prevent a bacterial adhesion in long-term oral applications.

As chitosan was used for coating the Ti6Al4V material in this study, the electrically charged interaction between chitosan and the bacteria is also another important factor for assessing the bacterial adhesion. Nevertheless, positively charged chitosan can react easily with the negatively charged molecules and particles. Therefore, an electrical attraction can be expected between the positively charged chitosan-coated surface of the Ti6Al4V and negatively charged *P. gingivalis*. However, because of its different physicochemical properties, chitosan has an antibacterial effect instead of allowing a bacterial adhesion.

An ionic interaction between the cations due to the amino groups of chitosan and anionic parts of bacterial cell walls such as phospholipids and carboxylic acids was proposed as the mechanism for the antimicrobial activity of chitosan.¹⁸

It was reported that the antimicrobial effect between chitosan and bacteria was related to the following probable mechanisms: in the case of gram-positive bacteria, chitosan on the surfaces of cell walls forms a polymeric membrane which inhibits the food ingestion into the cells. Therefore, the cells cannot get food. In the case of gram-negative bacteria (such as *E. coli*), low-molecular-weight chitosan can pass into the cells easier; there it breaks the cell metabolism, forms flocculation and kills the bacteria by changing their physiological activities.¹⁹ In this study, the antibacterial effect of chitosan against *P. gingivalis* can be explained with the above mechanisms. On the other hand, bacterial inhibition was not provided on the samples that were exposed to the aging process, which can be explained with the chemical effects of the aging process.

In summary, chitosan was successfully applied to the Ti alloy and the aging process did not significantly erode the coating material. The chitosan coating allowed the adhesion and proliferation of human gingival fibroblast cells and it showed a high level of cytocompatibility while preventing the growth of the *P. gingivalis* bacteria. As determined with the FTIR studies, a one-week aging process, simulating a one-year oral environment, altered the chemical structure of the chitosan coating. The cell attachment decreased slightly; however, the coating was not able to perform its antibacterial activity after the aging process even though it was still better than the uncoated metal.

Acknowledgements

This research was supported by TUBITAK (the Scientific and Technological Research Council of Turkey) through project 111S515. The authors would also like to thank the Advanced Technology Research and Application Center at the Selcuk University for providing the resources (the cell culture and SEM facilities) necessary for the completion of this work.

5 REFERENCES

- ¹ F. Schwarz, M. Herten, M. Sager, K. Bieling, A. Sculean, J. Becker, *Clinical Oral Implants Research*, 18 (2007), 161–170, doi:10.1111/j.1600-0501.2007.01482.x
- ² H. L. Myshin, J. P. Wiens, *Journal of Prosthodontic Dentistry*, 94 (2005), 440–444, doi:10.1016/j.prosdent.2005.08.021
- ³ P. Schupbach, R. Glauser, *Journal of Prosthodontic Dentistry*, 97 (2007), 15–25, doi:10.1016/S0022-3913(07)60004-3
- ⁴ Y. A. D. Sitbon, *Epithelial cells attachment on five different dental implant abutment surface*, PhD Dissertation, University of Iowa, Iowa, USA, 2009
- ⁵ Å. Leonhardt, G. Dahlén, *European Journal of Oral Science*, 103 (1995) 6, 382–387, doi:10.1111/j.1600-0722.1995.tb01861.x
- ⁶ B. D. Ratner, A. S. Hoffman, F. J. Schoen, J. E. Lemons, *Biomaterials Science: an Introduction to Materials in Medicine*, Academic Press, San Diego, CA, USA 1996
- ⁷ F. Ezoddini-Ardakani, A. N. Azam, S. Yassaee, F. Fatehi, G. Rouhi, *Health*, 3 (2011), 200–205, doi:10.4236/health.2011.34036
- ⁸ Y. Yuan, B. M. Chesnutt, L. Wright, W. O. Haggard, J. D. Bumgardner, *Journal of Biomedical Materials Research, Part B*, 86B (2008), 245–252, doi:10.1002/jbm.b.31012
- ⁹ M. S. Gale, B. W. Darwell, *Journal of Dentistry*, 27 (1999) 2, 89–99, doi:10.1016/S0300-5712(98)00037-2
- ¹⁰ X. Wang, Y. Du, J. Yang, X. Wang, X. Shi, Y. Hu, *Polymer*, 47 (2006), 6738–6744, doi:10.1016/j.polymer.2006.07.026
- ¹¹ P. Renoud, B. Toury, S. Benayoun, G. Attik, B. Grosogoeat, *PLoS One*, e39367, 7 (2012), 1–10, doi:10.1371/journal.pone.0039367
- ¹² T. Albrektsson, A. Wennerberg, *International Journal of Prosthodontics*, 17 (2004) 5, 544–564
- ¹³ E. A. El-Hefian, M. M. Nasef, A. H. Yahaya, *E-Journal of Chemistry*, 9 (2012), 510–516, doi:10.1155/2012/285318
- ¹⁴ B. Burnat, M. Walkowiak-Przybyło, T. Błaszczak, L. Klimek, *Acta Bioengineering and Biomechanics*, 15 (2013), 87–95, doi:10.5277/abb130111
- ¹⁵ L. Qi, Z. Xu, X. Jiang, C. Hu, X. Zou, *Carbohydrate Research*, 339 (2004), 2693–2700, doi:10.1016/j.carres.2004.09.007
- ¹⁶ M. Yoshinari, Y. Oda, T. Kato, K. Okuda, A. Hirayama, *Journal of Biomedical Materials Research*, 52 (2000), 388–394, doi:10.1002/1097-4636(200011)52:2<388::AID-JBM20>3.0.CO;2-E
- ¹⁷ M. Egawa, T. Miura, T. Cato, A. Saito, M. Yoshinari, *Dental Materials Journal*, 32 (2013), 1001–106, doi:10.4012/djm.2012-156
- ¹⁸ G. İkinici, S. Şenel, H. Akıncıbay, S. Kaş, S. Erciş, C. G. Wilson, A. A. Hıncal, *International Journal of Pharmaceutics*, 235 (2002), 121–127, doi:10.1016/S0378-5173(01)00974-7
- ¹⁹ L. Y. Zheng, J. F. Zhu, *Carbohydrate Polymers*, 54 (2003), 527–530, doi:10.1016/j.carbpol.2003.07.009

STRUCTURE AND PROPERTIES OF THE CARBURISED SURFACE LAYER ON 35CrSiMn5-5-4 STEEL AFTER NANOSTRUCTURIZATION TREATMENT

STRUKTURA IN LASTNOSTI NAUGLIČENE POVRŠINE JEKLA 35CrSiMn5-5-4 PO NANOSTRUKTURNI OBDELAVI

Emilia Skolek, Krzysztof Wasiak, Wiesław A. Świątnicki

Warsaw University of Technology, Faculty of Materials Science and Engineering, Wołoska 141, 02-507 Warsaw, Poland
emilia.skolek@nanostal.eu

Prejem rokopisa – received: 2014-10-08; sprejem za objavo – accepted for publication: 2014-12-09

doi:10.17222/mit.2014.255

The aim of the paper was to investigate the structure and properties of the carburized surface layer of the 35CrSiMn5-5-4 steel after the nanostructuring with the austempering heat treatment. During vacuum carburizing the surface layer of the steel was enriched with carbon above $w = 0.6\%$. Steel samples were subsequently austenitized, quenched at two different temperatures, 260 °C and 320 °C, and annealed at these temperatures for the time necessary for the completion of the bainitic transformation. For comparison, one set of carbonized samples was subjected to the conventional heat treatment: martensitic quenching and low tempering. The microstructural characterisation of the steel after different heat treatments was performed using scanning (SEM) and transmission (TEM) electron microscopes. It was shown that both austempering treatments led to a carbide-free nano-bainitic structure composed of nanometric ferrite plates separated by thin layers of retained austenite. The microhardness and wear resistance of three kinds of steel samples were investigated: the two subjected to the austempering treatment at different temperatures and the one subjected to the conventional treatment. It was shown that the nano-bainitic structure containing an increased amount of retained austenite displays a higher wear resistance than the tempered martensite. The results confirm that austempering can be a competitive method of thermal treatment, in comparison to the conventional heat treatment, for the steels after the carburizing process.

Keywords: vacuum carburizing treatment, carburized surface layer, carbide-free bainite, austempering, wear resistance

Namen tega dela je preiskati strukturo in lastnosti naogljčene površine jekla 35CrSiMn5-5-4 po nanostrukturiranju s toplotno obdelavo austempranja. Med naogljčenjem v vakuumu se je površina jekla obogatila z ogljikom nad masnim deležem $w = 0,6\%$. Vzorci jekla so bili segreti v avstenitno področje, gašeni na dve različni temperaturi: 260 °C in 320 °C, in zadržani na teh temperaturah, potrebnih za popolno bainitno pretvorbo. Za primerjavo je bila serija naogljčenih vzorcev toplotno obdelana po navadni metodi: gašenje v martenzit in popuščano pri nizki temperaturi. Karakterizacija mikrostrukture jekla po različnih toplotnih obdelavah je bila izvršena z vrstičnim (SEM) in presevnim (TEM) elektronskim mikroskopom. Izkazalo se je, da obe toplotni obdelavi austempranja povzročita nastanek nanobainitne strukture brez karbidov in sestavljene iz nanometrskih feritnih ploščic, ločenih s tanko plastjo zaostalega avstenita. Pri treh različnih vzorcih je bila izmerjena mikrotrdota in odpornost proti obrabi; pri dveh z austempranjem pri različnih temperaturah in enem z navadno toplotno obdelavo. Izkazalo se je, da ima nanobainitna struktura s povečanim deležem zaostalega avstenita večjo odpornost proti obrabi kot pa popuščeni martenzit. Rezultati so potrdili, da je toplotna obdelava z austempranjem boljša metoda toplotne obdelave kot navadna toplotna obdelava za jekla po postopku naogljčenja.

Ključne besede: naogljčenje v vakuumu, naogljčena plast, bainit brez karbidov, austempranje, odpornost proti obrabi

1 INTRODUCTION

Carbide-free bainite obtained in the bottom range of bainitic transformation is characterised by exceptionally high mechanical properties such as hardness and tensile strength.¹⁻⁵ Moreover, its ductility is kept due to a high volume fraction of the retained austenite.⁵⁻⁷ Simultaneously, a lack of cementite precipitations as well as the presence of a great amount of the retained austenite in the form of thin layers placed between the bainitic plates, result in a high fracture toughness.^{8,9} The presence of the retained austenite may also increase the frictional wear resistance.^{10,11} It was postulated¹⁰⁻¹² that during the wear tests austenite may transform into the strain-induced martensite due to the stresses occurring during the friction. This would increase the hardness in the contact

zone as well as the frictional wear resistance in comparison to the samples containing tempered martensite after the conventional treatment.¹⁰⁻¹²

Initially, the carbide-free structure was produced in the types of steel with specifically designed chemical compositions. These contained the appropriate amounts of carbon, silicon and manganese.¹³ However, recently an attempt was made to obtain such a structure also in the commercial types of steel.^{5,14,15} The main objective of the present study was to produce a structure of carbide-free bainite in the surface layer of the 35CrSiMn5-5-4 steel after the carburising. The second objective was to determine the effect of the isothermal-quenching temperature on the structure and the surface properties of the examined material.

2 EXPERIMENTAL PROCEDURE

2.1 Vacuum carburizing

The carburizing process was carried out in a 15.0VPT-4022/24N vacuum furnace at the Seco/Warwick Company. The carburizing treatment was conducted with the FineCarb® technology in accordance with the patent.¹⁶ It was divided into ten subsequent processes of saturation and diffusion. The times of particular saturation and diffusion processes were selected in accordance with the simulations conducted with the SimVaC Plus® programme. The carburising atmosphere was a mixture of acetylene, ethylene and hydrogen. Due to the possibility of a significant growth of austenite grains, the pearlitisation process was carried out directly after the carburisation process. Afterwards, the furnace feed was heated up to 850 °C, held for 20 min and, finally, slowly cooled to the room temperature at the furnace-cooling rate.

2.2 Carbon-content measurements

The amount of carbon after the carburisation process was determined on the cross-section of the layer, using the Magellan Q8 Bruker optical emission spectrometer with spark excitation. The study was conducted from the front of the sample. 21 measurements were carried out at 0.1 mm – a surface layer of about 0.1 mm was removed after each measurement to obtain the cross-section of the carbon content. The measurements were performed in an accredited laboratory, in accordance with the 3/CHEM procedure, 3 ed., Sep 2010, with a precision of 0.02 % (0.001 % for sulphur and phosphorus).

2.3 Heat treatment

In order to form a nano-bainitic microstructure, the carburised samples of steel were austenitized for 30 min

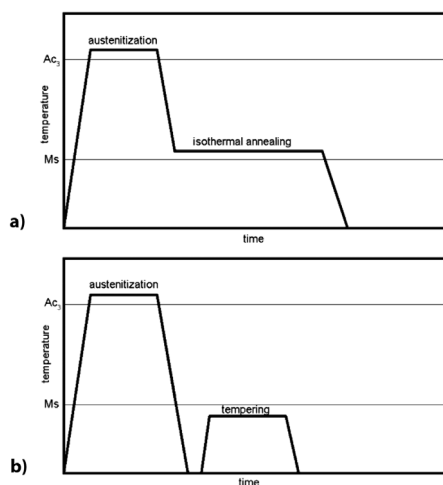


Figure 1: a) Scheme of the austempering and b) quenching and low-tempering treatment

Slika 1: Shematski prikaz toplotne obdelave: a) austempranje, b) gašenje in popuščanje pri nižji temperaturi

at a temperature of 900 °C, then cooled to the temperature range of the bainitic transformation and, finally, annealed at this temperature (**Figure 1**). The cooling medium used for isothermal quenching was composed of a liquid alloy of Sn-Ag heated up to the temperature of the isothermal step (260 °C and 320 °C). The time of isothermal quenching was selected in the way that ensured the end of the bainitic transformation at the temperature of isothermal annealing. The conventional heat treatment consisting of the martensitic quenching from the temperature of 900 °C and the subsequent tempering process at a temperature of 200 °C for 1h was performed in order to compare the properties of the layers obtained with two treatments. In this case, the oil quenching (WODOL) intended for structural steels was used as a cooling medium.

2.4 Microstructural observations

The microstructures of the austempered samples were examined with the use of light microscopy, SEM Hitachi S-3500N scanning electron microscopy and the TEM JEOL 1200 transmission electron microscope working at 120 kV. The LM and SEM observations were conducted just under the surface of the layer. At first, 50 µm of the examined material of the sample surface were grinded. Subsequently, the surfaces were etched with the Nital agent. The TEM observations were conducted at the surface zone of the layers at a depth of about 50–100 µm from the surface and in the core of the samples. Thin plates with a thickness of 200 µm were cut out of the samples, grinded to a thickness of 100 µm and, finally, electrolytically polished until perforation occurred. Phase constituents were identified according to the images of the electron diffraction analysis. The observations were carried out both in the bright field (BF) and in the dark field (DF), using the reflexions obtained from different phases.

The thickness of the ferrite plates and the austenite layers, observed on the TEM images, was determined in accordance with the following stereological Equation:¹⁷

$$d = \frac{2}{\pi} L \quad (1)$$

where d stands for the real size of the element of the microstructure (in the analysed case, the real thickness of a plate) and L means the size of the microstructure measured on the TEM image (in this case, the width measured on the image). The plate widths (L) were measured perpendicularly to the interphase boundaries.

The relative volume fraction of the phases was calculated on the assumption that the volume fraction of a given phase is equivalent to its area fraction observed on the image. Therefore, the n numbers of the secants of the l length were marked on the image of the microstructure. The volume fractions of phases V_V were calculated with the following formula:

Table 1: Chemical composition of the 35CrSiMn5-5-4 steel in mass fractions, w/%**Tabela 1:** Kemijska sestava jekla 35CrSiMn5-5-4 v masnih deležih, w/%

	C	Cr	Mn	Si	Ni	Cu	Al	Mo	W	Fe
w/%	0.35	1.31	0.95	1.3	0.14	0.15	0.04	0.018	<0.03	balance

$$V_v = \frac{\sum c_{ik}}{nl} \quad (2)$$

where $\sum c_{ik}$ is the sum of the widths of all the intersections of the secant line l with a given phase, l – the length of the secant line.

2.5 Microhardness measurements

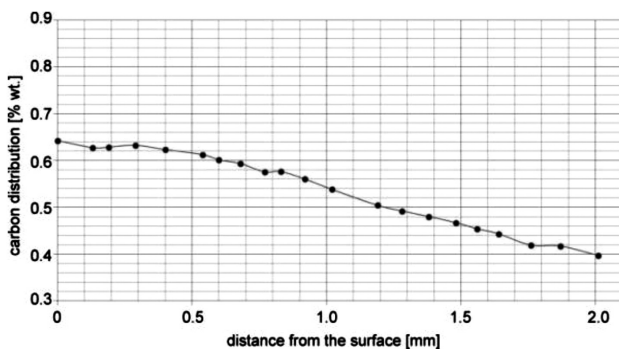
The measurements of the microhardness on the intersection of a layer were conducted with a LECO LM 248AT semi-automatic microhardness tester with the AMH43 v1.81 software in accordance with the PN-EN ISO 6507-1 norm.¹⁸ 1.96 N and 9.81 N loads, indenting the material for 10 s, were used in the investigation.

2.6 Wear-resistance measurements

The wear resistance measurements were carried out with the block-on-ring method using a T-05 tester, in conformity with the ASTM G77 norm.¹⁹ The examined sample was of a block shape and a width of 6.35 mm. The ring with an outer diameter of 34.99 mm was used as a counter specimen. The ring used in the research was made of the 100Cr6 bearing steel with a hardness of 62 HRC. The investigation lasted for 100 min and the applied unit load was 200 N mm⁻² and 400 N mm⁻². The rotation speed was 316 r/min (5.26 Hz) and the rubbing speed was 0.25 m/s. The track of the wear radius was 17.5 mm. Lux 10 oil was used as the grease.

3 RESULTS AND DISCUSSION

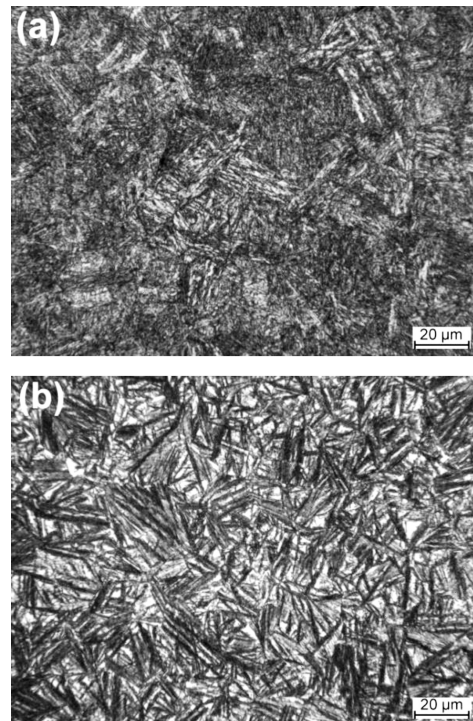
The previous research conducted on the 35CrSiMn5-5-4 steel indicated that the formation of carbide-free bainite structure with nanometric or submicron grain sizes can be achieved during isothermal quench-

**Figure 2:** Carbon-content profile for the carburized surface layer on 35CrSiMn5-5-4 steel**Slika 2:** Profil vsebnosti ogljika v naogljčeni plasti na jeklu 35CrSiMn5-5-4

ing.¹⁵ However, the amount of the retained austenite is relatively low due to a relatively low carbon content in this steel.¹⁵ In order to increase the carbon content in the surface layer, the 35CrSiMn5-5-4 steel with the chemical composition presented in **Table 1** was submitted to the vacuum carburizing treatment using the injection method. The increase in the carbon content facilitated the formation of a nano-bainitic structure in the steel.

The analysis of the chemical composition of the cross-section of the carburised layer of a steel sample indicated that the carbon content at the surface is $w = 0.64\%$. This value remains constant up to a depth of 0.5 mm from the surface. At a depth of 2 mm the carbon content is $w = 0.39\%$ (**Figure 2**).

A fine-grained acicular structure was formed during the isothermal quenching at the temperature of 260 °C, in the carburised layer of steel. The bainitic ferrite plates within this structure were either parallel to each other or arranged at different angles to each other. They formed groups or packages. An increase in the temperature of the treatment resulted in the microstructure in which small, unetched areas of the retained austenite occurred,

**Figure 3:** Microstructure of the carburized surface layer on 35CrSiMn5-5-4 steel after austempering at: a) 260 °C and b) 320 °C – LM images**Slika 3:** Mikrostruktura naogljčene površine jekla 35CrSiMn5-5-4 po austempranju na temperaturi: a) 260 °C in b) 320 °C (svetlobna mikroskopija)

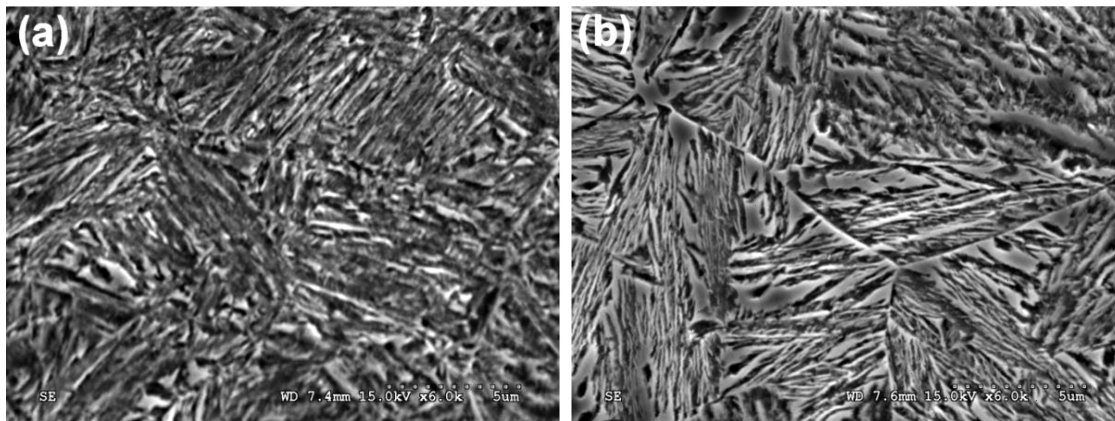


Figure 4: Microstructure of the carburized surface layer on 35CrSiMn5-5-4 steel after austempering at: a) 260 °C and b) 320 °C – SEM images
Slika 4: Mikrostruktura naogljicene plasti jekla 35CrSiMn5-5-4 po austempranju na temperaturi: a) 260 °C in b) 320 °C (SEM-posnetka)

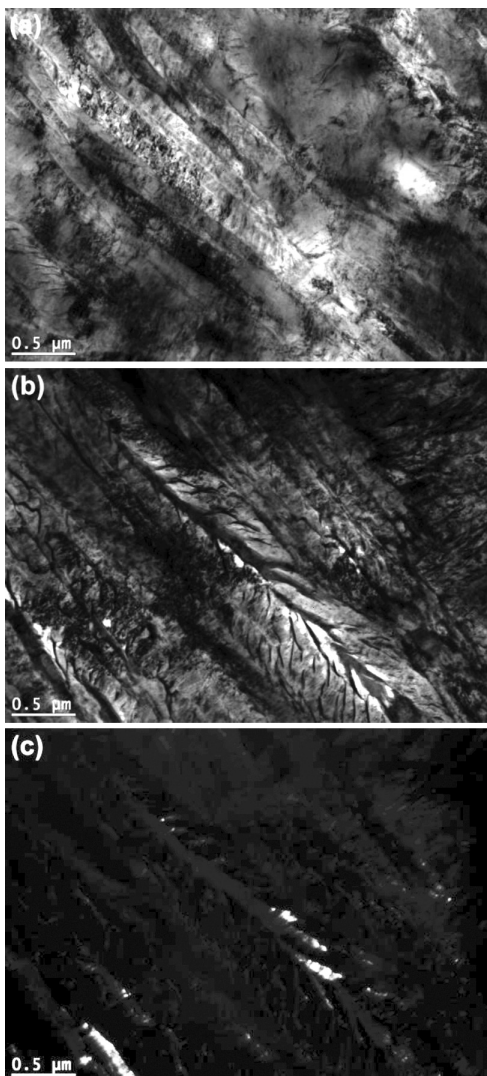


Figure 5: a) Microstructure of the carburized surface layer on 35CrSiMn5-5-4 steel after austempering at 260 °C, b) TEM BF image, c) TEM DF image of austenite reflection
Slika 5: a) Mikrostruktura naogljicene plasti na jeklu 35CrSiMn5-5-4 po austempranju na temperaturi 260 °C, b) TEM BF-posnetek, c) TEM DF-posnetek odboja avstenita

apart from the fine bainite plates arranged parallelly to each other (**Figures 3 and 4**).

A detailed investigation, conducted with TEM, of the microstructure of a steel sample treated at the temperature of 260 °C revealed the presence of martensite and carbide-free nano-bainite. The martensite and bainite were separated from each other with the layers of retained austenite (**Figure 5**). The average measured width of the ferritic and martensitic plates was (102 ± 7) nm, whereas the width of the layers of the retained austenite was (33 ± 3) nm. The increase in the temperature of the

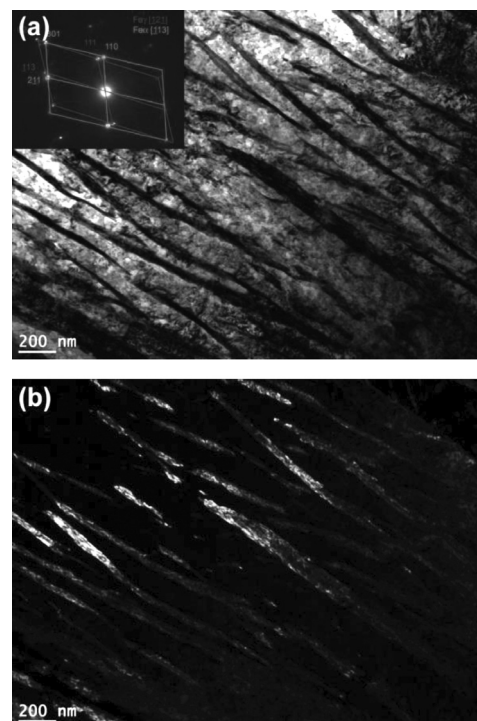


Figure 6: Microstructure of the carburized surface layer on 35CrSiMn5-5-4 steel after austempering at 320 °C: a) TEM BF image, b) TEM DF image of austenite reflection
Slika 6: Mikrostruktura naogljicene površine jekla 35CrSiMn5-5-4 po austempranju na 320 °C: a) TEM BF-posnetek, b) TEM DF-posnetek odboja avstenita



Figure 7: Block of retained austenite in the carburized surface layer on 35CrSiMn5-5-4 steel after austempering at 320 °C

Slika 7: Kos zaostalega avstenita v naogljiveni površini jekla 35CrSiMn5-5-4 po austempranju na 320 °C

treatment to 320 °C allowed the formation of a structure consisting of carbide-free bainite with the retained austenite. The bainitic plates have the average width of $65 \text{ nm} \pm 4 \text{ nm}$, whereas the layers of the retained austenite are $26 \text{ nm} \pm 2 \text{ nm}$ thick (**Figure 6**). Additionally, blocks of austenite with an area not exceeding $1 \text{ }\mu\text{m}^2$ were observed (**Figure 7**).

The relative volume fraction of the retained austenite in the surface layer, estimated on the basis of the TEM images was $(20.5 \pm 3.5) \%$ and $(20.2 \pm 3.5) \%$ for the samples isothermally quenched at 260 °C and 320 °C, respectively. The microstructure obtained through isothermal quenching at 320 °C was relatively homogenous

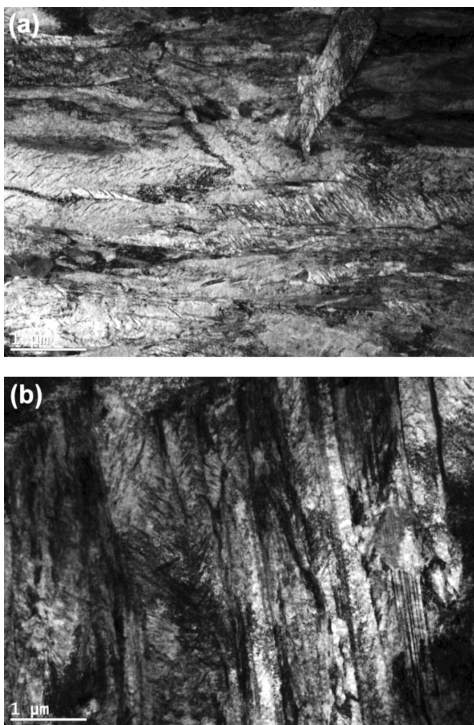


Figure 8: Microstructure of the core of the carburized steel after austempering at 260 °C

Slika 8: Mikrostruktura jedra pri naogljivenem jeklu po austempranju na 260 °C

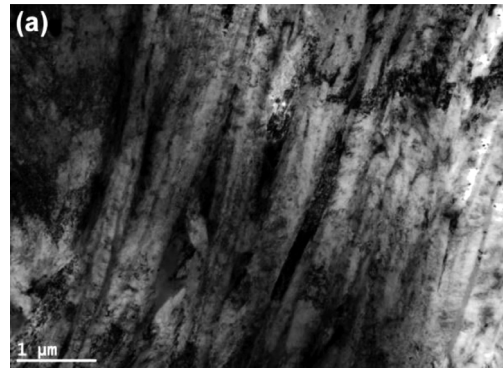


Figure 9: Microstructure of the core of the carburized steel after austempering at 320 °C

Slika 9: Mikrostruktura jedra pri naogljivenem jeklu po austempranju na 320 °C

in terms of the grain size. However, areas with different amounts of austenite were observed in the structure, as well as some individual secondary carbides that did not form clusters.

In the cores of the samples treated at 260 °C a martensitic-bainitic structure was formed. The presence of martensite resulted from the M_s temperature of 307 °C which is higher than the austempering temperature. The presence of highly dense carbides in martensite laths indicates that the tempering process occurred in the core of a sample during the austempering (**Figure 8**). The

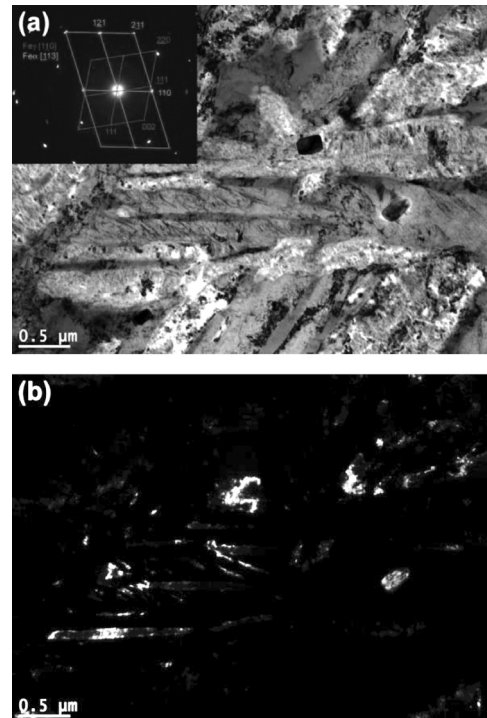


Figure 10: Austenite areas in the core of the carburized steel after austempering at 320 °C: a) TEM BF image, b) TEM DF image of austenite reflection

Slika 10: Avstenitna področja v jedru pri naogljivenem jeklu po austempranju na 320 °C: a) TEM BF-posnetek, b) TEM DF-posnetek odboja avstenita

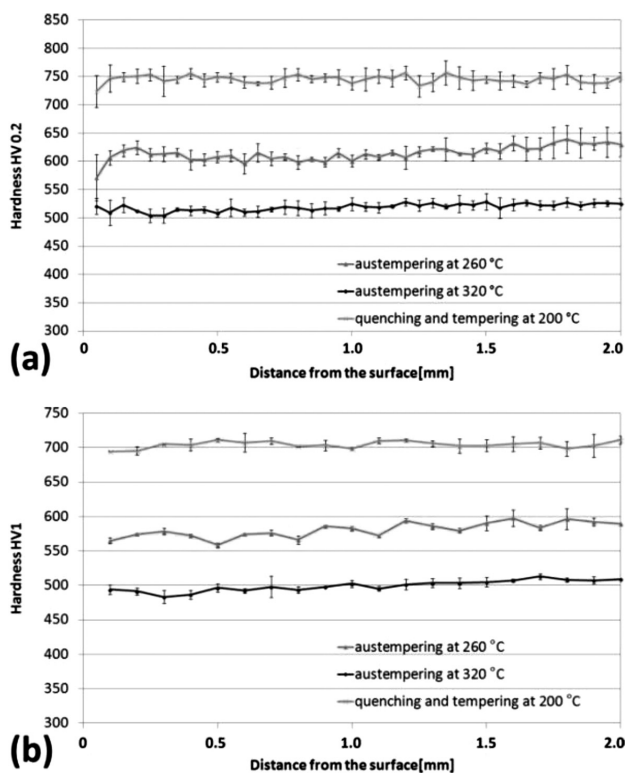


Figure 11: Hardness: a) HV_{0,2} and b) HV₁ profiles for the carburized surface layer on 35CrSiMn5-5-4 steel after various heat treatments
Slika 11: Profili trdote: a) HV_{0,2} in b) HV₁ v naogljivičeni plasti jekla 35CrSiMn5-5-4 po različnih toplotnih obdelavah

average grain size was (152 ± 23) nm. During the austempering at 320 °C carbide-free bainite of a submicron grain size $140 \text{ nm} \pm 10 \text{ nm}$ was formed in the core (**Figure 9**). However, a relatively large number of larger ferrite grains of about $0.5 \mu\text{m}$ were also observed (**Figure 10**). In both cases, the relative austenite volume fraction in the core, equal to $(13 \pm 3) \%$ and $(11.4 \pm 2.3) \%$ for the austempering at 260 °C and 320 °C, respectively, was significantly lower than in the carburised layer. Austenite mainly occurred in three different forms: as very thin layers (29 ± 4) nm in the case of the treatment carried out at 260 °C; as thicker layers (46 ± 6) nm; and small blocks $(0.086 \mu\text{m}^2\text{--}0.288 \mu\text{m}^2)$ in the case of the treatment conducted at 320 °C.

In the case of the austempering at 320 °C, which is higher than the M_s temperature, various factors may affect the structure of the core as well as the volume fractions of certain phases. The previous studies conducted on the 35CrSiMn5-5-4 steel revealed that the time necessary for completing the process of the bainitic transformation at 320 °C was slightly below 2 h.¹⁵ According to the literature,^{20,21} extending the time of isothermal treatment over the critical value results in a coalescence of ferritic grains and leads to the formation of austenite in the form of blocks. The increase in the grain sizes of particular phases may be also affected by the temperature of the treatment.²¹ Simultaneously, the

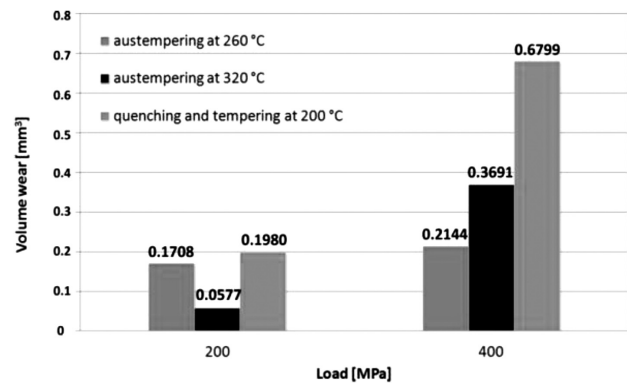


Figure 12: Volumetric wear of the carburized surface layer on 35CrSiMn5-5-4 steel after various heat treatments

Slika 12: Volumenska obraba naogljivičene plasti jekla 35CrSiMn5-5-4 po različnih toplotnih obdelavah

relative volume fraction of the retained austenite has a tendency to decrease with the increase in the time of the treatment.²⁰

The heat treatment described in the present study lasted for 24 h. Therefore, the grain sizes of ferrite and austenite in the core increased, whereas the relative austenite volume fraction decreased during the austempering in comparison with the previous treatment of this type of steel conducted for 2 h.¹⁵

The hardness of the layers was measured at different loads. In the case of a carburised, quenched and low-tempered layer, the hardness was higher than the hardness of the carburised steel submitted to isothermal quenching at 260 °C of approximately 130 HV_{0,2} and 125 HV₁ units. It was also higher than the hardness of the steel after the treatment at 320 °C of about 225 HV_{0,2} and 205 HV₁ units (**Figure 11**). This may be associated with a high amount of the relatively soft retained austenite in the nano-bainitic structure. The hardness does not change on the cross-section of a layer in the case of the steel subjected to the conventional treatment. After the nanostructuring process, the hardness of the steel slightly increased when the distance from the surface increased. With the increasing distance from the surface, the grain size also increases which should result in a decrease in the hardness. However, both the carbon content and the relative austenite volume fraction in the nano-bainitic structure decreased; therefore, the hardness in the core of the austempered samples is slightly higher.

The results of the investigations on the frictional wear resistance with the applied loads of 200 MPa and 400 MPa are presented in **Figure 12**. The level of the volume wear increases with an increase in the applied load. The wear tests indicate that the layer that was carburised and then austempered is characterised by a significantly higher frictional wear resistance in comparison to a much harder carburised layer, quenched and tempered in the conventional way. This difference is particularly pronounced in the case of the layer austempered at 260 °C. Most likely, this is associated with the amount of

the retained austenite in the layer with a nano-bainitic structure. Although the austenite is a relatively soft phase, it may transform into martensite under the stresses occurring during the friction due to the TRIP effect.⁹⁻¹² As a result of this effect, the hardness in the contact zone would increase significantly. This, in turn, may improve the frictional-wear resistance in comparison with the samples treated in the conventional way.¹⁰⁻¹² However, in order to prove this theory, a further study of the phase composition performed with XRD is required.

4 CONCLUSIONS

The austempering process conducted on the carburised 35CrSiMn5-5-4 steel allowed the formation of a nano-bainitic structure in the carburised layer as well as the formation of a martensite or carbide-free bainite structure with submicron grain sizes in the core of the examined material.

The increase in the carbon content in the layer during the carburizing favours the formation of the retained austenite, which may undergo a martensitic transformation due to the stresses during the wear test. The formed martensite may significantly increase the frictional-wear resistance of the examined steel.

Low-temperature isothermal quenching may be a new heat-treatment method applied on steel after carburisation. It is an alternative to the conventional treatment of quenching and low tempering. It seems beneficial in terms of the properties of a layer such as the increase in the frictional-wear resistance and lower quenching distortions.

Acknowledgements

The results presented in this paper were obtained within the project "Production of nanocrystalline steels using phase transformations" – NANOSTAL (contract no. POIG 01.01.02-14-100/09 made with the Polish Ministry of Science and Higher Education). The project is co-financed by the European Union from the European Regional Development Fund, within Operational Programme Innovative Economy 2007-2013.

5 REFERENCES

- ¹ C. Garcia-Mateo, F. G. Caballero, H. K. D. H. Bhadeshia, *ISIJ International*, 43 (2003) 11, 1821–1825, doi:10.2355/isijinternational.43.1821
- ² F. G. Caballero, H. K. D. H. Bhadeshia, K. J. A. Mawella, D. G. Jones, P. Brown, *Materials Science and Technology*, 18 (2002) 3, 279–284, doi:10.1179/026708301225000725
- ³ F. G. Caballero, H. K. D. H. Bhadeshia, *Current Opinion in Solid State and Materials Science*, 8 (2004) 3–4, 251–257, doi:10.1016/j.cossms.2004.09.005
- ⁴ C. Garcia-Mateo, F. G. Caballero, *ISIJ International*, 45 (2005) 11, 1736–1740, doi:10.2355/isijinternational.45.1736
- ⁵ W. A. Świątnicki, K. Pobiedzińska, E. Skołek, A. Gołaszewski, Sz. Marciniak, Ł. Nadolny, J. Szawłowski, *Materials Engineering (Inżynieria Materiałowa)*, 6 (2012), 524–529
- ⁶ H. K. D. H. Bhadeshia, *Proc. R. Soc. A*, 466 (2010) 2113, 3–18, doi:10.1098/rspa.2009.0407
- ⁷ H. K. D. H. Bhadeshia, *Mater. Sci. Eng. A*, 481–482 (2008), 36–39, doi:10.1016/j.msea.2006.11.181
- ⁸ C. Garcia-Mateo, F. G. Caballero, *Materials Transactions*, 46 (2005) 8, 1839–1846, doi:10.2320/matertrans.46.1839
- ⁹ B. Decooman, *Current Opinion in Solid State and Materials Science*, 8 (2004) 3–4, 285–303, doi:10.1016/j.cossms.2004.10.002
- ¹⁰ K. Wasiluk, E. Skołek, W. A. Świątnicki, *Materials Engineering (Inżynieria Materiałowa)*, 6 (2013), 911–915
- ¹¹ E. Skołek, K. Wasiak, J. Krasoń, W. A. Świątnicki, *Materials Engineering (Inżynieria Materiałowa)*, 6 (2013), 868–871
- ¹² P. Zhang, F. C. Zhang, Z. G. Yan, T. S. Wang, L. H. Qian, *Wear*, 271 (2011) 5–6, 697–704, doi:10.1016/j.wear.2010.12.025
- ¹³ H. K. D. H. Bhadeshia, C. Garcia-Mateo, P. Brown, *Bainite steel and methods of manufacture thereof*, Patent Application Publication, 2011, No US 2011/0126946 A1, available from World Wide Web: <https://www.google.com.ar/patents/US20110126946>
- ¹⁴ J. Dworecka, K. Pobiedzińska, E. Jezierska, K. Roźniatowski, W. Świątnicki, *Materials Engineering (Inżynieria Materiałowa)*, 2 (2014), 109–112
- ¹⁵ E. Skołek, Sz. Marciniak, W. Świątnicki, *Materials Engineering (Inżynieria Materiałowa)*, 2 (2014), 199–202
- ¹⁶ P. Kula, J. Olejnik, P. Heilman, *Hydrocarbon gas mixture for the under-pressure carburizing of steel*, European Patent No.: EP1558780, 2007, United States Patent No.: US 7513958, Available from World Wide Web <http://www.google.com/patents/EP1558780A1?cl=en>
- ¹⁷ L. C. Chang, H. K. D. H. Bhadeshia, *Materials Science and Technology*, 11 (1995) 9, 874–881
- ¹⁸ PN-EN ISO 6507-1:1999, *Metale – Pomiar twardości sposobem Vickersa - Metoda badań*, 1999
- ¹⁹ ASTM G77-93, *Standard Test Method for Ranking Resistance of Materials to Sliding Wear Using Block-on-Ring Wear Test*, 1993
- ²⁰ C. Liu, Z. Zhao, S. D. Bhole, *Materials Science and Engineering A*, 434 (2006) 1, 289–293, doi:10.1016/j.msea.2006.06.078
- ²¹ Y. K. Lee, H. C. Shin, Y. C. Jang, S. H. Kim, C. S. Choi, *Scripta Materialia*, 47 (2002) 12, 805–809, doi:10.1016/S1359-6462(02)00303-2

OPTIMIZATION OF THE SURFACE ROUGHNESS BY APPLYING THE TAGUCHI TECHNIQUE FOR THE TURNING OF STAINLESS STEEL UNDER COOLING CONDITIONS

UPORABA TAGUCHI-JEVE METODE ZA OPTIMIRANJE HRPAVOSTI POVRŠINE PRI STRUŽENJU NERJAVNEGA JEKLA Z OHLAJANJEM

Murat Sarıkaya

Department of Mechanical Engineering, Sinop University, 57030 Sinop, Turkey
msarikaya@sinop.edu.tr

Prejem rokopisa – received: 2014-11-14; sprejem za objavo – accepted for publication: 2015-01-16

doi:10.17222/mit.2014.282

This paper presents the optimization of the surface roughness using the Taguchi technique to assess the machinability of the AISI 316Ti steel with PVD coated carbide inserts under different cooling conditions such as dry, conventional (wet) and cryogenic cooling with liquid nitrogen (LN₂). Based on the Taguchi L₉ (3³) orthogonal-array design, the machinability tests were made utilizing a CNC lathe machine. Test parameters including the cutting speed, the cooling condition and the feed rate were taken and then the surface roughness (R_a) was measured to obtain the machinability indicator. An analysis of variance was performed to determine the importance of the input parameters for the surface roughness. The process parameters were optimized by taking the Taguchi technique into consideration. The Taguchi signal-to-noise ratio was employed with the smaller-the-better approach to obtain the best combination. On the basis of the first-order model, a mathematical model was created using the regression analysis to predict the R_a model. The results indicate that the feed rate is the parameter with the highest effect on the surface roughness and that the other parameters also have a statistical significance. In addition, cryogenic cooling is an alternative method for increasing the surface quality of machined parts.

Keywords: AISI 316Ti, cryogenic cooling, machinability, optimization, surface roughness, Taguchi method

Članek obravnava optimiranje hrapavosti površine z uporabo Taguchi-jeve metode za oceno obdelovalnosti jekla AISI 316Ti s karbidnimi vložki s PVD-nanosom v različnih razmerah ohlajanja, kot je suho, navadno (moko) in kriogensko hlajenje s tekočim dušikom (LN₂). Preizkusi obdelovalnosti so bili izvršeni s CNC-stružnico na osnovi Taguchi-jevega ortogonalnega niza L₉ (3³). Izbrani so bili parametri preizkusov, hitrost rezanja, razmere pri ohlajanju in hitrost podajanja, nato pa je bila izmerjena hrapavost površine (R_a) kot pokazatelj obdelovalnosti. Izvršene so bile analize variance, da bi ugotovili pomembnost vhodnih parametrov na hrapavost površine. Procesni parametri so bili optimirani z upoštevanjem Taguchi-jeve tehnike. Uporabljeno je bilo Taguchi-jevo razmerje signal – hrup s približkom čim manjše tem boljše za doseganje najboljše kombinacije. Na osnovi modela prvega reda je bil postavljen z uporabo regresijske analize matematični model za napovedovanje R_a. Rezultati kažejo, da je hitrost podajanja parameter z največjim učinkom na hrapavost površine, vsi drugi parametri imajo statistično značilnost. Dodatno je kriogensko ohlajanje alternativna metoda za povečanje kvalitete površine struženih delov.

Ključne besede: AISI 316Ti, kriogensko ohlajanje, obdelovalnost, optimizacija, hrapavost površine, Taguchi-jeva metoda

1 INTRODUCTION

Stainless steels were developed to obtain a better corrosion resistance compared to traditional carbon steels and they allow us to work at higher temperatures. There is a lot of stainless steel in the industry, but austenitic and ferritic stainless steels are commonly used in the manufacturing industry.¹ As a type of the AISI 316 steel, austenitic stainless steel AISI 316Ti contains low amounts of titanium (Ti), approximately 0.5 %. This steel type has the advantage of enduring higher temperatures for a longer time compared to the other stainless steels.² The physical and mechanical properties of the AISI 316Ti steel are similar to those of the other types of 316, but the corrosion resistance of 316Ti is better than those of the standard grades.² In recent years, due to its different properties, this steel has been extensively used for certain applications such as boat and ship parts,

medical and chemical handling equipment, heat exchangers, fastening tools, and in nuclear and construction industries where a low thermal conductivity, good heat resistance and corrosion resistance and a high strength are required in the high-temperature working conditions. However, the machining of this austenitic stainless steel is very difficult since it contains a high amount of strength-enhancing elements such as chromium, nickel and molybdenum.¹ One of the major problems is the heat generation at the cutting region during the machining of difficult-to-cut metals. The machining process requires more energy, so high temperatures occur throughout the deformation process and the friction at the tool-chip and tool-workpiece interfaces.³ Recently, the machining technology has been quickly improved to increase the processing productivity and machining performance in the cases of difficult-to-cut steels. An increase in the productivity can be achieved by decreasing the temperature

at the tool-chip and tool-workpiece interfaces thanks to the cooling/lubrication methods. As the cutting velocity and the feed rate increase during a machining process, due to an improvement in the coating technology, the cutting temperature increases as well. Thus, the use of cooling/lubrication is necessary during the metal-cutting operations. In recent years, certain cooling/lubrication methods such as cryogenic cooling, solid coolants/lubricants, wet cooling (traditional cooling), minimum-quantity lubrication, high-pressure coolants, compressed air/gases have been employed and these technologies have considerably increased the machining productivity.⁴ However, the use of mineral- or syntactic-based cutting fluids has led to certain problems like health risks and environmental pollution.^{5,6} In order to eliminate all the cutting fluids from the metal-cutting process, cryogenic cooling or high-pressure cooling with compressed air can be applied to protect the health and the environment.

Surface roughness is one of the most critical quality indicators of the machined surfaces of engineering materials used for important applications and the producers believe that it determines the degree of surface quality of the manufactured parts.⁶ A low surface roughness obtained from machining experiments contributes to some properties of workpiece including fatigue strength, corrosion and wear resistance, friction, etc.^{6,7} Surface roughness is affected by many parameters such as machined material, depth of cut, cutting-tool material, cutting speed, tool-nose radius, feed rate, coating type and cooling/lubrication conditions. Modern industry aims at producing high-quality parts, reducing the costs in a short time. To manufacture a product with a desired quality of the machining, the optimum process parameters should be chosen. Therefore, recently, certain statistical methods like the Taguchi technique, response-surface methodology (RSM), desirability function analysis, ANOVA and grey relational analysis (GRA) have been implemented to optimize and analyze process parameters.⁸⁻¹² In the engineering applications and academic studies of experimental design, the Taguchi method is very useful thanks to the orthogonal array that significantly reduces the number of the tests and, in addition, it attempts to eliminate the influence of uncontrollable factors on the test results. The main purpose of the Taguchi technique is to provide quality during the design stage. In this way, the cost and the test time decrease in a shorter period.^{12,13} Therefore, in this study, the Taguchi method with the L_9 orthogonal array was employed.

In some studies, the machinability of austenitic stainless steel was investigated by the researchers. For example, Kayir et al.¹ studied the effect of the tool geometry and the cutting parameters on the surface roughness in machining AISI 316Ti under dry cutting conditions. Their results demonstrated that the main parameters were the feed rate with a 73.97 % effect and the radius of the edge with a 13.26 % effect on the surface roughness. Xavier and Adithan¹⁴ explored the effects of cutting

fluids, cutting speed, depth of cut and feed rate on the tool wear and surface roughness in the turning of the AISI 304 austenitic stainless steel using a carbide tool. It was seen that the most important parameter was the feed rate having a 61.54 % effect on the surface roughness, while the cutting speed had a 46.49 % effect on the tool wear. Further, according to the ANOVA analysis, it was found that the cutting fluid had a considerable effect on both the surface roughness and the tool wear. Ciftci¹⁵ investigated the influence of the cutting speed and the tool coating on the surface roughness and the cutting force in the turning of the AISI 304 and AISI 316 austenitic stainless steels under dry cutting conditions. It was reported that the cutting speed considerably affected the surface roughness. Korkut et al.¹⁶ determined the best cutting parameters in the turning of the AISI 304 austenitic stainless steel with cemented carbide inserts. Their results showed that the surface roughness decreased with the increasing cutting speed. Tekiner and Yeşilyurt¹⁷ investigated the influences of the cutting parameters on the basis of the process noise in the turning of the AISI 304 austenitic stainless steel. It was found that the cutting speed of 165 m/min and the feed rate of 0.25 mm/r gave the best results.

The literature survey indicates that there are very few studies dealing with the turning of the AISI 316 stainless steel. When these studies are examined, it is seen that the surface roughness has not been evaluated with respect to different cutting conditions like dry, wet and cryogenic cooling procedures used during the turning of the AISI 316Ti stainless steel. In the light of the above information, this study can be summarized in three points: Firstly, the influences of the cutting parameters on the surface roughness in the turning of the AISI 316Ti stainless steel with a PVD coated carbide insert were investigated under dry, wet and cryogenic cooling conditions. Secondly, a mathematical model was formed to estimate the result of different levels of input parameters using a regression analysis. In the next process, an analysis of variance (ANOVA) was applied to determine the influences of the machining parameters. Lastly, the process parameters were optimized using the Taguchi technique. To achieve its goals, this paper employed a Taguchi L_9

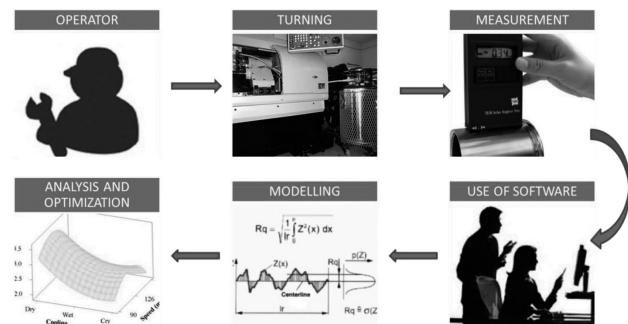


Figure 1: General flow diagram of the study

Slika 1: Prikaz poteka študije

(3³) orthogonal array for planning the experiments. An experimental design including three parameters (feed rate, cutting speed and cooling condition) with three levels was organized.

2 EXPERIMENTAL PROCEDURE

The workflow diagram of this study is illustrated in **Figure 1**. It shows the sequence of the performed study.

Table 1: Chemical composition of the material in mass fractions, w/%
Tabela 1: Kemijska sestava materiala v masnih deležih, w/%

C	Mn	Si	P	S	Cr	Ni	Mo	Cu	Ti
0.021	1.775	0.495	0.036	0.019	16.74	10.92	2.15	0.536	0.318

2.1 Material, machine tool, cutting tool and measurement

The AISI 316Ti workpiece material was used in the turning experiments and its chemical composition is given in **Table 1**. Recently, because of its unique properties including good heat resistance and corrosion resistance, a low thermal conductivity and a high strength at higher temperatures, this material has been used in many engineering operations involving boat and ship parts, medical and chemical handling equipment, heat exchangers, fastening tools, and in the nuclear and construction industry. The dimensions of the test material were \varnothing 60 mm \times 200 mm. All the turning tests were conducted using a Falco FI-8 model (Taiwan) CNC lathe machine with the maximum spindle speed of 4800 r/min and a 15 kW drive motor. An assembly produced by Sandvik including a PVD coated carbide insert of type SNMG 12 04 08-QM and a PSBNR 2020K-12 tool holder was utilized as the main tool arrangement with the following tool geometry: a rake angle of -6° , a clearance angle of 0° , the major cutting-edge angle of 75° , a cutting-edge inclination angle of -6° and a nose radius of 0.8 mm. The same type of cutting insert was employed for each test parameter. In engineering applications, surface quality is one of the most important quality indicators. For this reason, the average value of the surface roughness (R_a) was measured using a TIME TR 100 profilometer tester. Before the measurements of the surface roughness, the measuring device was calibrated with a special calibration. Each surface was machined by using a new cutting insert and after each test measurements were carried out on the workpiece.

2.2 Cutting conditions and design of the experiments

The cutting speed (V_c), the feed rate (f) and the cooling condition (C) were taken as the cutting parameters. The values of the cutting parameters were chosen from the plot experiments and the manufacturer’s handbook. During the machining tests, a constant depth of cut ($a_p = 1.6$ mm) was used; the other cutting parameters and their levels are given in **Table 2**. In this study, on the basis of

the control factors and their levels from **Table 2**, the Taguchi L₉ orthogonal array (OA) from the Minitab software was used, as shown in **Table 3** indicating the design of the experiments. It has nine rows and three columns. The rows correspond to the number of the tests; the columns correspond to the process parameters with three levels. In this array, the first, second and third columns represent the cutting speed, feed rate and cutting condition, respectively. The tests were conducted under different cutting conditions such as dry cutting, conventional wet cooling (flood coolant) and cryogenic cooling inside the tool with liquid nitrogen (LN₂). For wet cooling, a solution with boron oil and water (the ratio of boron oil/water = 1/20) was prepared.

Table 2: Process parameters and their levels

Tabela 2: Procesni parametri in njihovi nivoji

Code	Control parameter	Notation	Levels of factors		
			Level 1	Level 2	Level 3
A	Cooling condition	C	Dry	Wet	Cryogenic
B	Feed rate	$f/(mm/r)$	0.1	0.16	0.25
C	Cutting Speed	$V_c/(m/min)$	90	126	176

Table 3: Experimental design

Tabela 3: Načrt eksperimentov

Exp. no.	Coded values			Actual values		
	A	B	C	C	$f/(mm/r)$	$V_c/(m/min)$
1	1	1	1	Dry	0.1	90
2	1	2	2	Dry	0.16	126
3	1	3	3	Dry	0.25	176
4	2	1	2	Wet	0.1	126
5	2	2	3	Wet	0.16	176
6	2	3	1	Wet	0.25	90
7	3	1	3	Cryogenic	0.1	176
8	3	2	1	Cryogenic	0.16	90
9	3	3	2	Cryogenic	0.25	126

For the cryogenic cooling, liquid nitrogen was delivered directly from the liquid-nitrogen pressure tank to the tool holder at a pressure of 1.5 bar as shown in **Figure 2**. Three holes were drilled into the tool holder. The diameter of the first hole on the tool holder was 6 mm and it provided a connection between the tool holder

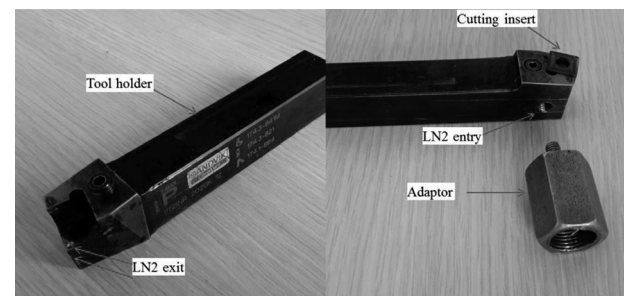


Figure 2: Modified tool holder and adaptor
Slika 2: Prirejen nosilec orodja in adapter

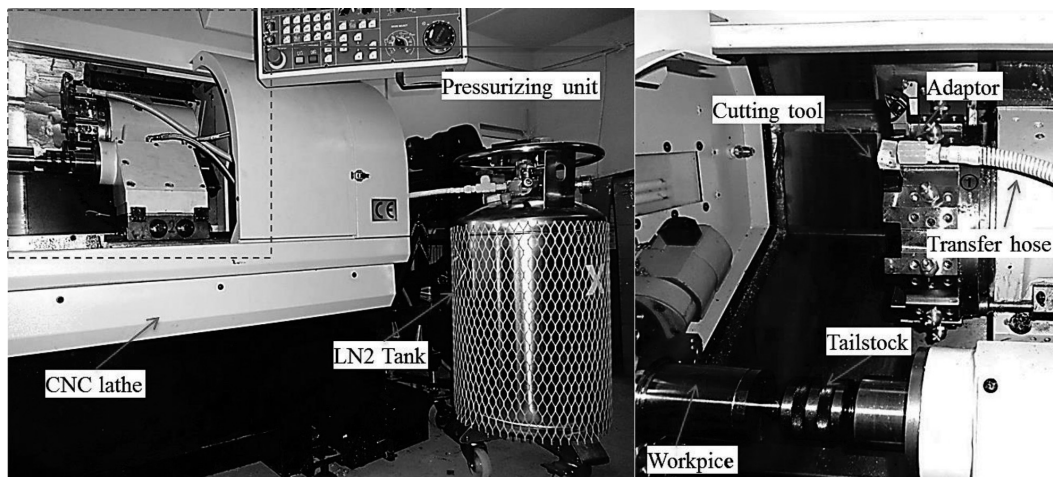


Figure 3: Experimental set-up
Slika 3: Eksperimentalni sestav

and the liquid-nitrogen container with the help of a hose and an adaptor. The liquid nitrogen accumulated inside the tool holder was released to the environment as a gas vapor with the help of the other two holes, taking the heat from the insert. The diameter of the gas exit holes was made to be 1.5 mm. The modified tool holder and the connection adaptor are seen in **Figure 2**, while **Figure 3** shows the experimental set-up for cryogenic cooling.

3 RESULTS AND DISCUSSION

3.1 Analysis of the experimental results

Surface roughness is one of the most important quality criteria for engineering materials. During the turning operations, the surface roughness can be controlled with the machining parameters. In this study, the surface roughness was evaluated using 3D surface plots in the graphs given in **Figure 4**. This figure shows that the surface roughness increased significantly with the increasing feed rate. The reason for this can be the fact that an

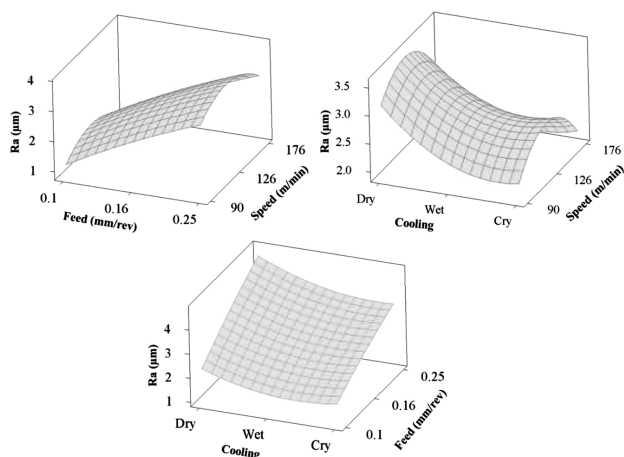


Figure 4: Effects of machining parameters on the surface roughness
Slika 4: Vpliv parametrov obdelave na hrapavost površine

increase in the feed rate leads to a vibration and increases the heat at the tool-chip interface; thereby a higher surface roughness occurs.¹⁸ To calculate the theoretical surface roughness, the abbreviated formula is expressed as follows:

$$R_a = \frac{f^2}{32 \cdot r} \quad (1)$$

According to Equation (1), in order to improve the surface quality, the feed rate can be decreased or, alternatively, the nose radius of the cutting insert can be increased since the surface roughness is a function both the nose radius and feed rate. The results obtained from the experiments are similar to this formula. In the literature, it is pointed out that surface roughness is affected negatively by an increase in feed rate and in order to obtain the better surface quality, the feed rate is reduced usually in machining processes.^{6,8,13} In present work, a similar result was detected when the surface roughness decreased with the increasing of feed rate.

According to **Figure 4**, the surface roughness showed a decreasing tendency with an increase in the cutting speed. An improvement in the surface quality was observed with the increasing cutting speed because the increasing temperature during the cutting process made the plastic deformation and the chip flow easier.^{6,18} Further, it is thought that because of a reduction in built-up edge (BUE) and built-up layer (BUL) formations, tool wear was affected positively, and so this situation gives rise to an improvement in the surface quality.⁶

During a manufacturing process, physical and chemical properties of the coolants allow a reduction in thermal/mechanical-based damages. When coolants are used efficiently, the dimensional accuracy and a better surface quality may occur; also, a longer life of the cutting tool may be obtained. **Figure 4** shows a significant change in the surface-roughness values, depending on the use of different roughness cooling methods. It can be seen that the surface roughness is minimum when using cryogenic

cooling. This may be due to a lower cutting temperature, a lower adhesion between the cutting insert and the machined-workpiece surface and a lower tool-wear rate compared to dry and wet cooling conditions.¹⁹ In addition, a reduction in the surface roughness due to wet cooling was determined in comparison with dry machining.

3.2 Signal-to-noise (S/N) analysis

The surface roughness (R_a) was evaluated with an orthogonal array for each combination of the test parameters using the Taguchi technique and an optimization of the process parameters was achieved with signal-to-noise (S/N) ratios. Here, the signal data includes the desired influence on the test results and the noise data includes the undesired influence on the test results. Therefore, the maximum S/N ratio provides the optimum results. There are three different ways of calculating the S/N ratios. These are the nominal-is-best, the smaller-the-better and the larger-the-better approaches. In the present study, the smaller-the-better option of the S/N quality characteristic was utilized to obtain the best combination for the surface roughness with respect to the desired low R_a . The smaller-the-better approach is expressed as follows:⁷

Smaller-the-better (minimize):

$$\frac{S}{N_{R_a}} = -10 \log \left[\frac{1}{n} \sum_{i=1}^n o_i^2 \right] \quad (2)$$

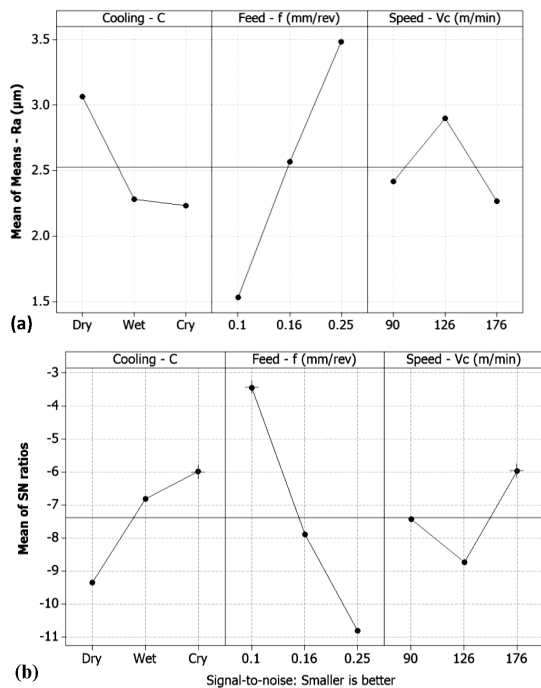


Figure 5: Main effect plots for: a) means and b) S/N ratios
Slika 5: Diagram učinka za: a) sredstva in b) razmerje S/N

In Equation (2), o_i is the response of the output characteristic for the i^{th} test and n is the number of the outputs of the test.

The experimental results and their S/N ratios were calculated using Equation (2) as given in Table 4. From this table, the mean surface roughness and the mean S/N ratio were calculated as $2.53 \mu\text{m}$ and -7.39 dB , respectively. The analysis of the process parameters like the cutting speed, feed rate and cooling condition was made using an S/N response table obtained with the Taguchi method as seen in Table 5. The S/N response table of the results gives the optimum points of the process parameters for the best surface roughness. Figure 5 was plotted to determine the optimum control factor of a machining parameter using the S/N response table. As seen in Figure 5, for the highest S/N ratio, the optimum parametric combination was found to be factor A (level 3, S/N = -5.985 dB , mean: $2.283 \mu\text{m}$), factor B (level 1, S/N = -3.450 dB , mean: $1.533 \mu\text{m}$) and factor C (level 3, S/N = -5.975 dB , mean: $2.267 \mu\text{m}$).

Under cryogenic cooling, the cutting speed was 176 m/min and the feed rate was 0.1 mm/r.

Table 4: Experimental results and their S/N values

Tabela 4: Rezultati eksperimentov in njihove S/N vrednosti

Test no.	Control parameters			Surface roughness $R_a/\mu\text{m}$	Signal to noise (S/N)/dB
	A Cooling condition	B Feed rate $f/(\text{mm/r})$	C Cutting speed $V_c/(\text{m/min})$		
1	Dry	0.1	90	1.90	-5.5751
2	Dry	0.16	126	3.55	-11.0046
3	Dry	0.25	176	3.75	-11.4806
4	Wet	0.1	126	1.65	-4.3497
5	Wet	0.16	176	2.00	-6.0206
6	Wet	0.25	90	3.20	-10.1030
7	Cryogenic	0.1	176	1.05	-0.4238
8	Cryogenic	0.16	90	2.15	-6.6488
9	Cryogenic	0.25	126	3.50	-10.8814

Table 5: Response table

Tabela 5: Tabela odgovorov

Levels	Control factors			Control factors		
	S/N ratios			Means		
	A	B	C	A	B	B
Level 1	-9.353	-3.450	-7.442	3.067	1.533	2.417
Level 2	-6.824	-7.891	-8.745	2.283	2.567	2.900
Level 3	-5.985	-10.822	-5.975	2.283	3.483	2.267
Delta	3.369	7.372	2.770	0.833	1.950	0.633
Rank	2	1	3	2	1	3

3.3 Analysis of variance

Analysis of variance (also known as ANOVA) is a statistical method and the significance of the machining parameters was identified with its help. The ANOVA analysis was performed with a 95 % confidence level and

5 % significance level. The *F* values of the control factors indicated the significance of the control factors determined with the ANOVA analysis. The percentage contribution of each parameter is shown in the last column of the ANOVA table. The column shows the effect rates of the input parameters on the outputs.⁶

In the present work, the ANOVA results are given in **Table 6** and, in addition, these results are graphically presented in **Figure 6**. The ANOVA results indicate that the cooling condition, the feed rate and the cutting speed influenced the surface roughness by 17 %, 74.1 % and 8.5 %, respectively. Therefore, the feed rate (factor *B*) is the most important factor affecting the surface roughness. According to **Table 6**, it can be said that the cooling condition, the feed rate and the cutting speed had a statistical and physical significance with regard to the surface roughness at the reliability level of 95 % because their *P* values are lower than 0.05.

Table 6: ANOVA analysis
Tabela 6: Analiza ANOVA

Factors	Degree of freedom	Sum of squares	Mean of squares	<i>F</i> ratio, $\alpha = 0.05$	<i>P</i>	Contribution (%)
Cooling method	2	1.3106	0.6553	48.14	0.020	17
Feed rate	2	5.7106	2.8553	209.78	0.005	74.1
Cutting speed	2	0.6572	0.3286	24.14	0.040	8.5
Error	2	0.0272	0.0136			0.35
Total	8	7.7056				100

3.4 Regression analysis

In many studies, a regression analysis was used to determine the relationship between the control factors and experimental results. In the present work, the control factors are the cutting speed (*V_c*), the feed rate (*f*) and the cooling condition (*C*) and the surface roughness (*R_a*) is the response. On the basis of the first-order model, a mathematical model was created using a regression analysis for predicting *R_a*. The first-order model can be expressed with Equation (3):

$$y = \beta_0 + \beta_1 \cdot v_1 + \beta_2 \cdot v_2 + \beta_3 \cdot v_3 \tag{3}$$

In this equation, *y* is the corresponding output, and *v₁*, *v₂*, and *v₃* are the values of the variable. The term β is the regression coefficient. The first-order model can be written as a function of the cooling condition (*C*), the feed rate (*f*) and the cutting speed (*V_c*). The relationship between the output and the turning parameters from Equation (3) was adapted as given in following Equation (4):

$$R_{a_{pre}} = \beta_0 + \beta_1 \cdot C + \beta_2 \cdot f + \beta_3 \cdot V_c \tag{4}$$

According to the above equations, a mathematical model for the surface roughness with coded values (**Table 3**) can be written in the following way:

$$R_{a_{pre}} = 1.56111 - 0.416667 \cdot C + 0.975 \cdot f - 0.075 \cdot V_c \tag{5}$$

$$R^2 = 87.98 \%$$

The determination coefficient, expressed as *R²*, shows the reliability of the predicted model. It was recommended that *R²* should be between 0.8 and 1.²⁰ In this study, the value of the determination coefficient is *R²* = 0.8798 and it is high enough, demonstrating a high significance of the predicted model. In order to evaluate the contents of the residual of the model, a graphical technique was employed. The sufficiency of the models was investigated by examining the residuals. The normal-probability plot of the residuals for the surface roughness is seen in **Figure 7**. It is seen that the residual rather appropriately tend towards a straight line, meaning that errors are normally delivered. This demonstrates that the predictive model is satisfactory.

3.5 Determining the optimum surface roughness

In the last phase of the Taguchi method, a verification experiment has to be made to check the reliability of the optimization.²¹ The verification experiment was conducted at the optimum levels of the variables determined as seen in **Figure 5**. *A₃-B₁-C₃* and their values from this figure were employed to calculate the estimated optimum surface roughness. The equation for estimating the optimum result (*R_{a_opt}*) was expressed as follows:

$$R_{a_{opt}} = (A_3 - T_{R_a}) + (B_1 - T_{R_a}) + (C_3 - T_{R_a}) + T_{R_a} \tag{6}$$

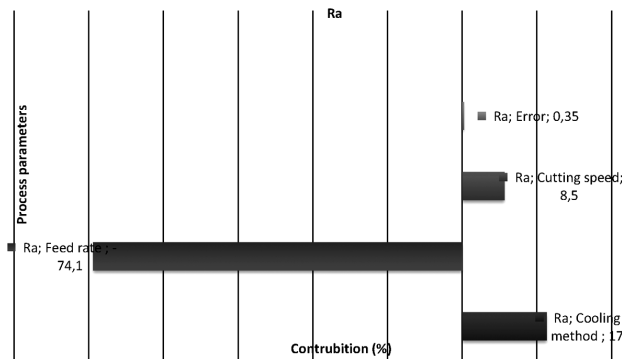


Figure 6: Graphical representation of the ANOVA results
Slika 6: Grafičen prikaz rezultatov ANOVA

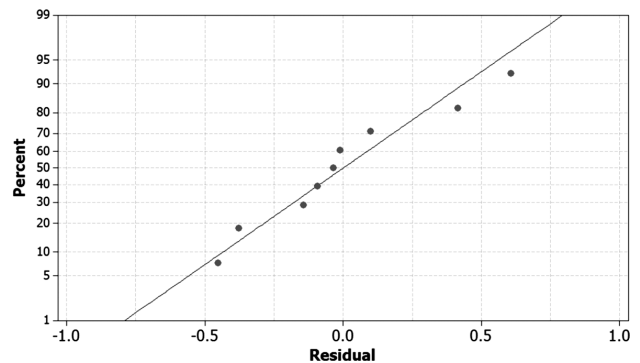


Figure 7: Normal-probability plot of the residuals
Slika 7: Diagram normalne verjetnosti preostankov

In Equation (6), A_3 , B_1 , and C_3 are the mean values of the surface roughness at the optimum level as seen in **Table 5**. T_{R_a} is the mean of all the R_a values obtained from the experimental results (**Table 4**). According to Equation (6), $R_{a,opt}$ is 1.023 μm .

In order to verify the result of the estimated surface roughness, the confidence interval (CI) was calculated using following equations:²²

$$CI = \sqrt{F_{\alpha,1,V_e} \cdot V_{ep} \cdot \left(\frac{1}{n_{eff}} + \frac{1}{R} \right)} \quad (7)$$

$$n_{eff} = \frac{N}{1 + T_{dof}} \quad (8)$$

In Equation (7), $F_{\alpha,1,V_e}$ is the F ratio at the 95 % confidence level, α is the significance level, V_e is the degree of freedom of the error, V_{ep} is the error variance, n_{eff} is the effective number of replications, R is the number of replications for the verification test. In Equation (8), N is the total number of tests and T_{dof} is the total main factor of the degree of freedom.

According to the F test table, $F_{\alpha,1,2}$ is 18.51. Further, $V_{ep} = 0.0136$, $R = 3$, $N = 9$, $T_{dof} = 6$ and, according to Equation (8), n_{eff} is 1.285. The confidence interval (CI) is found to be 0.528 using Equations (7) and (8). The predicted optimum surface roughness with the 95 % confidence interval is:

$$[R_{a,opt} - CI] < R_{a,exp} < [R_{a,opt} + CI], \text{ i.e., } [1.023 - 0.528] < 1.05 < [1.023 + 0.528] = 0.702 < 1.05 < 1.551.$$

The $R_{a,exp}$, which was found with the experiments, was within the confidence interval limit. Therefore, the system optimization was successfully achieved using the Taguchi method at a significance level of 0.05 in the turning of the AISI 316Ti stainless steel under different cutting conditions.

3.6 Experimental validation

Verification experiments of the process parameters were performed for the best result and the predictive model at the optimum and at random points. **Table 7** shows a comparison of the experimental results and the estimated results obtained with the Taguchi technique and mathematical model (Equation (5)). It was seen that the estimated results and the test results are quite close.

Table 7: Verification of the test results

Tabela 7: Preverjanje rezultatov preizkusov

Level	Taguchi technique			First-order model		
	Exp.	Pre-dicted	Error (%)	Exp.	Pre-dicted	Error (%)
$A_3B_1C_3$ (optimum)	1.05	1.023	1.8	1.05	1.06	0.9
$A_3B_2C_1$ (random)	2.15	2.19	1.82	2.15	2.16	0.4
$A_2B_1C_2$ (random)	1.65	1.55	6.06	1.65	1.66	0.6

The errors of the statistical analysis must be below 20 % for the reliability of the analysis.²⁰ Therefore, the results found in the verification experiment showed that the optimization was successful.

4 CONCLUSIONS

This study focused on the influences of the process parameters such as the cooling condition, the feed rate and the cutting speed on the surface roughness (R_a) in the turning of the AISI 316Ti stainless steel and an optimization was achieved on the basis of the Taguchi method. Cryogenic cooling using liquid nitrogen (LN_2) was applied from within a modified tool holder. The Taguchi S/N ratio was utilized with the smaller-the-better approach to obtain the optimum values. An analysis of variance was performed to define the importance of the process parameters for the outputs. Based on the first-order model, a mathematical model was created, namely $R_{a,pre}$, using the regression analysis. The results obtained from this study can be summarized as follows:

The best parameter levels were found to be $A_3-B_1-C_3$ (i.e., cutting condition = cryogenic cooling, feed rate = 0.1 mm/r and cutting speed = 176 m/min). Cryogenic cooling with LN_2 and a modified tool holder provided a better performance than dry and wet conventional cooling in terms of the surface roughness and may be recommended for use in the turning of the AISI 316Ti stainless steel.

Although the surface quality decreased with an increase in the feed rate, it showed an improvement tendency with an increase in the cutting speed and with the use of the cryogenic cooling and wet (traditional) cooling.

Using ANOVA, it was found that the feed rate is the dominant factor affecting the surface roughness, with a fraction of 74.1 %, followed by the cooling method and the cutting speed. Further, it was seen that the cooling condition, the feed rate and the cutting speed had statistical and physical significance for the surface roughness, with a reliability level of 95 %.

The regression model showed a high correlation between the experimental and predicted values. Further, the normal-probability plot of the residuals for the surface roughness showed that the residuals quite appropriately tended to a straight line, meaning that errors were normally delivered. This proved that $R_{a,pre}$ was satisfactory and quite reliable. In addition, the value of the determination coefficient was high enough.

In the verification experiment, the measured values were within the 95 % confidence interval (CI).

Future work may deal with analyzing the effects of some cooling/lubrication methods like the minimum-quantity lubrication (MQL), high-pressure cooling with a coolant, high-pressure cooling with compressed air, and external cryogenic cooling during the machining of the AISI 316Ti stainless steel. Further, other process para-

meters like the cutting-tool geometry, depth of cut, CVD coated inserts, uncoated carbide inserts, nose radius, and chip-breaker geometry may be considered by the researchers to define their influences on the tool life and surface quality in future academic studies.

5 REFERENCES

- ¹ Y. Kayır, S. Aslan, A. Aytürk, Analyzing the effects of cutting tools geometry on the turning of AISI 316Ti stainless steel with Taguchi method, *J. Fac. Eng. Arch. Gazi Univ.*, 28 (2013) 2, 363–372
- ² J. Brnic, G. Turkalj, M. Canadija, D. Lanc, AISI 316Ti (1.4571) steel – Mechanical, creep and fracture properties versus temperature, *Journal of Constructional Steel Research*, 67 (2011) 12, 1948–1952, doi:10.1016/j.jcsr.2011.06.011
- ³ E. O. Ezugwu, Improvements in the machining of aero-engine alloys using self-propelled rotary tooling technique, *Journal of Materials Processing Technology*, 185 (2007) 1, 60–71, doi:10.1016/j.jmatprotec.2006.03.112
- ⁴ V. S. Sharma, M. Dogra, N. M. Suri, Cooling techniques for improved productivity in turning, *Int. J. Mach. Tools Manufact.*, 49 (2009) 6, 435–453, doi:10.1016/j.ijmactools.2008.12.010
- ⁵ F. Pusavec, P. Krajnik, J. Kopac, Transition to sustainable production – Part I: application on machining technologies, *J. Clean. Prod.*, 18 (2010) 2, 174–184, doi:10.1016/j.jclepro.2009.08.010
- ⁶ M. Sarıkaya, A. Güllü, Multi-response optimization of MQL parameters using Taguchi-based GRA in turning of difficult-to-cut alloy Haynes 25, *J. Clean. Prod.*, 91 (2015), 347–357, doi:10.1016/j.jclepro.2014.12.020
- ⁷ T. Kivak, Optimization of surface roughness and flank wear using the Taguchi method in milling of Hadfield steel with PVD and CVD coated inserts, *Measurement*, 50 (2014), 19–28, doi:10.1016/j.measurement.2013.12.017
- ⁸ M. Sarıkaya, A. Gullu, Taguchi design and response surface methodology based analysis of machining parameters in CNC turning under MQL, *Journal of Cleaner Production*, 65 (2014), 604–616, doi:10.1016/j.jclepro.2013.08.040
- ⁹ A. Kadirvel, P. Hariharan, Optimization of the die-sinking micro-EDM process for multiple performance characteristics using the Taguchi-based grey relational analysis, *Mater. Tehnol.*, 48 (2014) 1, 27–32
- ¹⁰ E. Kabaklı, M. Bayramoğlu, N. Geren, Evaluation of the surface roughness and geometric accuracies in a drilling process using the Taguchi analysis, *Mater. Tehnol.*, 48 (2014) 1, 91–98
- ¹¹ T. Kivak, G. Samtaş, A. Çiçek, Taguchi method based optimisation of drilling parameters in drilling of AISI 316 steel with PVD monolayer and multilayer coated HSS drills, *Measurement*, 45 (2012) 6, 1547–1557, doi:10.1016/j.measurement.2012.02.022
- ¹² M. Sarıkaya, H. Dilipak, A. Gezgin, Optimization of the process parameters for surface roughness and tool life in face milling using the Taguchi analysis, *Mater. Tehnol.*, 49 (2015) 1, 139–147
- ¹³ İ. Asiltürk, H. Akkuş, Determining the effect of cutting parameters on surface roughness in hard turning using the Taguchi method, *Measurement*, 44 (2011) 9, 1697–1704, doi:10.1016/j.measurement.2011.07.003
- ¹⁴ M. A. Xavier, M. Adithan, Determining the influence of cutting fluids on tool wear and surface roughness during turning of AISI 304 austenitic stainless steel, *Journal of Materials Processing Technology*, 209 (2009) 2, 900–909, doi:10.1016/j.jmatprotec.2008.02.068
- ¹⁵ I. Ciftci, Machining of austenitic stainless steels using CVD multilayer coated cemented carbide tools, *Tribology International*, 39 (2006) 6, 565–569, doi:10.1016/j.triboint.2005.05.005
- ¹⁶ I. Korkut, M. Kasap, I. Ciftci, U. Seker, Determination of optimum cutting parameters during machining of AISI 304 austenitic stainless steel, *Materials & Design*, 25 (2004) 4, 303–305, doi:10.1016/j.matdes.2003.10.011
- ¹⁷ Z. Tekiner, S. Yeşilyurt, Investigation of the cutting parameters depending on process sound during turning of AISI 304 austenitic stainless steel, *Materials & Design*, 25 (2004) 6, 507–513, doi:10.1016/j.matdes.2003.12.011
- ¹⁸ R. Suresh, S. Basavarajappa, V. N. Gaitonde, G. L. Samuel, Machinability investigations on hardened AISI 4340 steel using coated carbide insert, *Int. J. Refract. Metals Hard Mat.*, 33 (2012), 75–86, doi:10.1016/j.ijrmhm.2012.02.019
- ¹⁹ M. Dhananchezian, M. P. Kumar, Cryogenic turning of the Ti–6Al–4V alloy with modified cutting tool inserts, *Cryogenics*, 51 (2011) 1, 34–40, doi:10.1016/j.cryogenics.2010.10.011
- ²⁰ M. H. Cetin, B. Ozcelik, E. Kuram, E. Demirbas, Evaluation of vegetable based cutting fluids with extreme pressure and cutting parameters in turning of AISI 304L by Taguchi method, *J. Clean. Prod.*, 19 (2011), 2049–2056, doi:10.1016/j.jclepro.2011.07.013
- ²¹ N. Mandal, B. Doloi, B. Mondal, R. Das, Optimization of flank wear using Zirconia Toughened Alumina (ZTA) cutting tool: Taguchi method and regression analysis, *Measurement*, 44 (2011), 2149–2155, doi:10.1016/j.measurement.2011.07.022
- ²² A. Divedi, P. Kumar, Surface quality evaluation in ultrasonic drilling through the Taguchi technique, *Int. J. Adv. Manuf. Technol.*, 34 (2007), 131–140, doi:10.1007/s00170-006-0586-3

EFFECT OF CRYOGENIC TREATMENT APPLIED TO M42 HSS DRILLS ON THE MACHINABILITY OF Ti-6Al-4V ALLOY

VPLIV PODHLAJEVANJA SVEDROV M42 HSS NA OBDELOVALNOST ZLITINE Ti-6Al-4V

Turgay Kivak¹, Ulvi Şeker²

¹Düzce University, Faculty of Technology, Department of Manufacturing Engineering, Düzce, Turkey

²Gazi University, Faculty of Technology, Department of Manufacturing Engineering, Ankara, Turkey
turgaykivak@duzce.edu.tr

Prejem rokopisa – received: 2014-11-16; sprejem za objavo – accepted for publication: 2014-12-16

doi:10.17222/mit.2014.283

This study investigated the effects of deep cryogenic treatment applied to M42 HSS drills on the tool wear, the tool life and the surface roughness during the drilling of a Ti-6Al-4V alloy under dry and wet cutting conditions. Drilling tests were carried out using untreated, cryogenically treated, cryogenically treated and tempered, and multi-layered TiAlN/TiN-coated HSS drills. Four different cutting speeds ((6, 8, 10, 12) m/min) and a constant feed rate of 0.06 mm/r were used as the cutting parameters and holes with a depth of 15 mm were drilled. At the end of the drilling tests, it was seen that the use of a coolant increased the tool life and decreased the surface roughness. Among the four tools, the best results in terms of the tool life and surface roughness were obtained with the multi-layered TiAlN/TiN-coated tool. The cryogenically treated and tempered drills exhibited an increase of 87 % in the tool life compared to the untreated drills. Scanning electron microscope (SEM) and X-ray diffraction (XRD) analyses showed that by reducing the size of the carbide particles in the microstructure, cryogenic treatment resulted in a more uniform carbide distribution and in the transformation of retained austenite to martensite. This played an important role in the increase in the hardness and wear resistance of the cutting tools.

Keywords: cryogenic treatment, microstructure, M42 HSS, drilling, tool life, surface roughness

V tej študiji je bil preiskovan vpliv globokega podhlajevanja svedrov M42 HSS na njihovo obrabo, zdržljivost in hrapavost površine med suhim in mokrim vrtnjem zlitine Ti-6Al-4V. Preizkusi vrtnja so bili izvršeni z uporabo HSS neobdelanih, podhlajenih, podhlajenih in popuščanih ter svedrov z večplastnim nanosom TiAlN/TiN. Uporabljene so bile štiri različne hitrosti rezanja ((6, 8, 10, 12) m/min) in konstantno podajanje 0,06 mm/r pri vrtnju 15 mm globokih izvrtin. Na koncu preizkusov vrtnja se je pokazalo, da uporaba hlajenja s tekočino poveča zdržljivost orodja in zmanjša hrapavost površine. Med štirimi orodji je bil glede na njihovo zdržljivost in hrapavost površine najboljši rezultat dosežen z orodji z večplastnim nanosom TiAlN/TiN. Podhlajeni in popuščani svedri so imeli povečano zdržljivost za 87 % v primerjavi z neobdelanimi svedri. Analize na vrstičnem elektronskem mikroskopu (SEM) in rentgenska difrakcija (XRD) sta pokazali, da z zmanjšanjem velikosti karbidnih zrn v mikrostrukturi pri podhlajevanju dobimo bolj enakomerno razporeditev karbidov, preostali avstenit pa se pretvori v martenzit. To ima pomembno vlogo pri povečanju trdote in odpornosti orodja za rezanje proti obrabi.

Ključne besede: obdelava s podhlajevanjem, mikrostruktura, M42 HSS, vrtnje, zdržljivost orodja, hrapavost površine

1 INTRODUCTION

With the rapid development of technology, the past few years have witnessed a rise in the expectations for the products made of resistant, lightweight materials and their production methods. In particular, the need for such materials in the electronics, computer, automotive and aerospace industries is increasing. Titanium and its alloys meet a great many of these expectations due to their low density, high resistance, and heat and corrosion resistance.¹⁻³ Among these alloys, all having different properties, Ti-6Al-4V is the most widely used and it is found in 60 % of industrial applications. This alloy has the properties of high resistance to fatigue and corrosion along with high strength and biocompatibility, and covers a wide application field, primarily in the aerospace industry.⁴ However, the Ti-6Al-4V alloy belongs to a group of materials which are difficult to machine because of their high chemical reactivity and high tendency to weld to the cutting tool,⁵ low heat conductivity, maintenance of strength at high temperatures and a low elasti-

city module. Furthermore, the production cost of these materials is high and errors during machining can cause serious increases in the cost of machining.⁶⁻¹⁰

The life of cutting tools plays a major role in increasing the productivity and, consequently, it is an important economic factor. In order to increase the life of cutting tools, a common approach in the past was to heat-treat the tool materials, thus providing a greater control over the range of the properties that a given tool material might have. In order to increase the life of cutting tools and improve their properties, the conventional heat treatment, applied especially to tool steel and high-speed steel (HSS), has been a widely used method for many years.¹¹ Cryogenic treatment is generally a complementary treatment to the heat treatment applied to increase the wear resistance of the materials exposed to high wear conditions. It is also known as the cold or subzero treatment.¹² It is cheap and permanent; it is done once and, unlike coatings, it affects the whole piece.¹³ Cryogenic treatment, depending on the temperatures

applied to the material, is classified as shallow cryogenic treatment (between $-50\text{ }^{\circ}\text{C}$ and $-100\text{ }^{\circ}\text{C}$) and deep cryogenic treatment (lower than $-125\text{ }^{\circ}\text{C}$).

After the conventional heat treatment, materials are first held at the temperatures of shallow or deep cryogenic treatment (generally for 24 h) and then brought gradually up to room temperature.¹⁴ In this way, the formation of fine carbide precipitates, a uniform carbide distribution and a conversion of the retained austenite to martensite are achieved. Thus, significant improvements are obtained in the mechanical properties of the materials such as the hardness and wear resistance.¹⁵⁻¹⁷ Cryogenic treatment, having been previously applied to tool/die steels, is now applied to the cutting tools in the machining and, as a result, important developments have been obtained in the tool wear, tool life and recovery of cutting conditions. Studies on cryogenically treated high-speed-steel tools show microstructural changes in the material that can considerably influence the tool life and productivity. In the literature, results showed tool-life improvements ranging from 92 % to 817 % for the cryogenically treated HSS tools in the industrial use.¹³

The influence of deep cryogenic treatment on the wear resistance and the tool life of M42 HSS drills with a high-speed dry-drilling configuration of carbon steels was studied and the experimental results indicated tool-life improvements of 77 % and 126 % for cryogenically treated and cryogenically treated + tempered drills, respectively.¹⁶ The improvement in the wear resistance and the significance of the treatment parameters for different materials were investigated in another study. It was found that cryogenic treatment provided an improvement in the tool life of nearly 110 %. The tool-life improvement was even higher with the use of TiN coatings.¹⁸

Compared to the other material-removal processes, the drilling process has quite a wide application field. Especially in the aerospace industry, drilling constitutes a large portion of the material-removal processes, up to 40–60 %.¹⁹ In the literature, studies investigating the machinability of titanium alloys are generally focused on turning and milling while those dealing with drilling are very limited.

In this study, cryogenic-treatment-induced changes in the microhardness and microstructure of M42 HSS tools and the effects of these changes on the tool wear, tool

life and surface roughness during the drilling of a Ti-6Al-4V alloy were investigated. Furthermore, the machining performance of cryogenically treated tools was examined in comparison with that of the untreated and multi-layered TiAlN/TiN-coated tools.

2 EXPERIMENTAL METHODS

2.1 Drilling experiments

Drilling tests were carried out using a JOHNFORD VMC 550-7.5 kW CNC vertical machining center under dry and wet cutting conditions. Four different cutting speeds (6, 8, 10 and 12) m/min were used for the experiments and the hole depth and feed rate were kept constant at 15 mm and 0.06 mm/r, respectively. The experimental set-up is shown in **Figure 1**. For the workpiece material, 100 mm \times 80 mm \times 15 mm blocks of the Ti-6Al-4V alloy were used. Before the experiments, the sample blocks were ground to eliminate the adverse effects of any surface defects. The chemical composition and mechanical properties of the workpiece material are shown in **Tables 1** and **2**, respectively.

Table 1: Chemical composition of Ti-6Al-4V alloy (w/%)

Tabela 1: Kemijska sestava zlitine Ti-6Al-4V (w/%)

Ti	Al	V	Fe	O	C	N	H
89.85	5.90	4.00	0.08	0.14	0.01	0.01	0.002

Table 2: Mechanical properties of Ti-6Al-4V

Tabela 2: Mehanske lastnosti zlitine Ti-6Al-4V

Tensile strength (MPa)	Yield strength (MPa)	Elongation 5D (%)	Hardness (R_c)
900-1100	830	10	36

In the wet cutting experiments, a 6 % concentration of a semi-synthetic emulsion was used as the coolant. For the elimination of the twisting effect, the distance from the tool holder to the drill tip was determined as 30 mm. This value was kept constant in all the experiments in order to validate the obtained values. Three holes were drilled under each machining condition for the comparison of the surface-roughness measurements. The average of each set of three measurements was used for the comparison. As the initial condition of each test, a new drill was used for each experiment. The surface roughness of the machined holes was measured using a Mohr Perthometer M1 portable surface-roughness tester for each machining condition and the average values of the surface roughness (R_a) were determined. In order to measure the surface roughness, the Ti-6Al-4V alloy blocks were sliced parallel to the hole axes and the measurements were taken at three different points. The average of these three measurements was used in the evaluations.

For the tool-wear experiments, as various wear mechanisms and types were formed on the drills and the

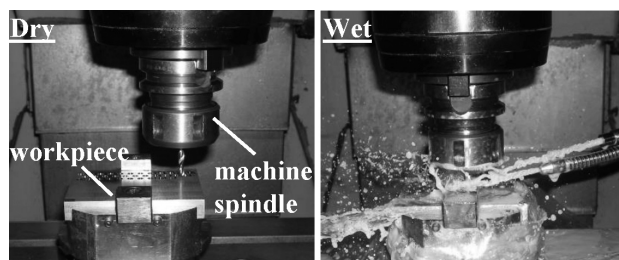


Figure 1: Details of the experimental set-up

Slika 1: Podrobnosti eksperimentalnega sestava

cost of the workpiece was high, the following were determined as the tool-life criteria:²⁰

- the average non-uniform flank wear $V_b = 0.15$ mm
- the maximum flank wear $V_{bmax} = 0.2$ mm
- the chipping = 0.2 mm
- the out-of-corner wear = 0.2 mm
- the fracture or catastrophic failure

As soon as one of the criteria mentioned above was realized, it was accepted that the tool was worn. A professional hand-held digital microscope (Dino-Lite, AM413ZT) and a JEOL JSM-6060 LV scanning electron microscope (SEM) were used to determine the wear mechanisms and types. Due to the limited amount and high cost of the workpiece material, the tool wear experiments were performed only at the cutting speed of 10 m/min. The tool life time was obtained by multiplying the total number of holes drilled by the drilling time at which the tool reached one of the wear criteria.

2.2 Cryogenic treatment and tempering

A number of uncoated and coated drills (Guhring) of a 5 mm diameter were cryogenically treated in order to observe the effect of cryogenic treatment on the drilling of the Ti-6Al-4V alloy with M42 HSS twist drills. Three types of uncoated drills were used: untreated drills (U), cryogenically treated drills (CT), and cryogenically treated and tempered (at 200 °C for 2 h) drills (CTT). Cryogenic treatment was not applied to the TiAlN/TiN-coated drills in order to compare the performance of the cryogenically treated material to that of the coated material. The chemical composition and properties of the M42 HSS twist drills used in the experiments are given in **Tables 3** and **4**, respectively.

Table 3: Chemical composition of M42 HSS drills (w/%)

Tabela 3: Kemijska sestava svedrov M42 HSS (w/%)

C	Cr	Co	Mo	W	V
1.1	4.2	8.0	10	1.8	1.2

Table 4: Properties of M42 HSS drills

Tabela 4: Lastnosti svedrov M42 HSS

	Uncoated HSS (U, CT, CTT)	Coated HSS (U)
Tool material	M42	M42
Tool reference	DIN 338	DIN 338
Point angle	135 °	135 °
Helix angle	35 °	35 °
Diameter	5 mm	5 mm
Coating	–	Multi-layer TiAlN/TiN
Coating thickness	–	4 µm
Hardness	–	3600 (HV _{0.05})

The cryogenic treatment of the M42 HSS drills was performed by gradually lowering the temperature from room temperature to –145 °C at the cooling rate of about 1–2 °C/min, holding the drills at this cryogenic temperature for 24 h, and then raising the temperature back to

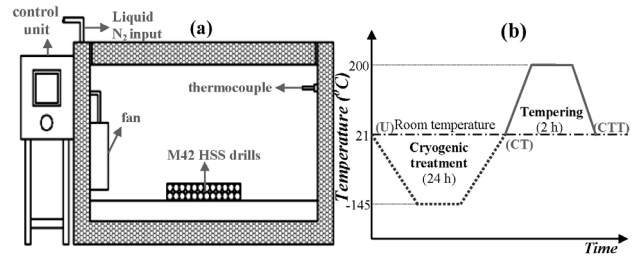


Figure 2: Details of the cryogenic-treatment process: a) schematic configuration of the cryogenic-treatment system, b) cryogenic treatment and tempering cycle used for M42 HSS drills

Slika 2: Podrobnosti postopka podhlajevanja: a) shematski prikaz sistema za podhlajevanje, b) cikel podhlajevanja in popuščanja, uporabljeneja pri svedrih M42 HSS

room temperature at the heating rate of 1–2 °C/min. **Figure 2** schematically illustrates the cryogenic treatment applied to the M42 HSS drills. To verify the formation of fine and homogeneous carbide particles and the transformation of the retained austenite to martensite, the microstructures of the untreated, cryogenically treated, and cryogenically treated and 2 h tempered drills were observed via SEM photographs and X-ray diffraction (XRD) profiles. The microstructure and phase distribution were characterized with SEM and the volume fraction of the retained austenite was determined using a GE-SEIFERT X-ray diffraction instrument with a Cr- $K\alpha_1$ X-ray source. From the X-ray diffractograms, the contents of the retained austenite and martensite in the alloy after different treatments were measured using the ASTM E975-84 standard.²¹

3 RESULTS AND DISCUSSION

3.1 Evaluation of cryogenic treatment of drills

In the HSS tools the main alloying elements which change the microstructure and the properties are C, Cr, Mo, V, W and Co. Except for Co, these elements precipitate in the microstructure and create carbides. Generally, seven groups of carbides precipitate in high-speed steels: (1) E carbide, $Fe_{2.4}C$ (hcp); (2) θ -carbide, M_3C (Fe_3C); (3) MC or M_4C_3 , (V_4C_3); (4) M_2C , (W_2C or Mo_2C); (5) λ -carbide, M_7C_3 (Cr_7C_3); (6) γ -carbide, $M_{23}C_6$ ($Cr_{23}C_6$); (7) η -carbide, M_6C (Fe_3W_3C or Fe_4W_2C), as expressed in²². The M_6C carbides were originally known as high-speed steels and they are similar to the complex surface-centered cubical carbides that are rich in tungsten and molybdenum and give red hardness to steel. The distribution of these carbide particles in the microstructure, their size, their amount and the distances between them affect the mechanical properties of the material.²³

In this study, profiles were obtained from the XRD analyses. These analyses were made to determine the differences in the amount of the carbide present in the cryo-treated (CT) and cryo-treated and tempered (CTT) drills compared to the untreated (U) tool (**Figure 3**). For the purpose of determining the residual-austenite vol-

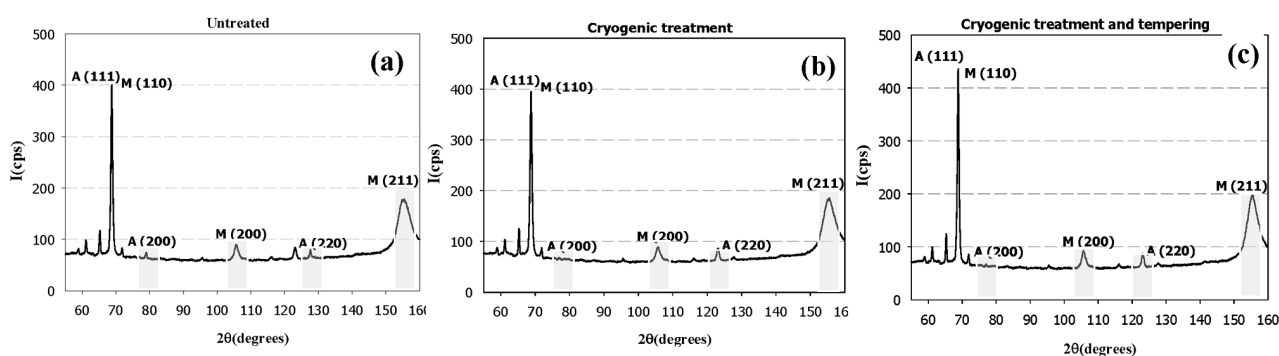


Figure 3: XRD profiles of HSS tools: a) untreated, b) cryo-treated, c) cryo-treated and tempered
Slika 3: Rentgenogram HSS-orođij: a) neobdelano, b) podhlajeno, c) podhlajeno in popuščano

ume, the peaks in the austenite (A200 and A220) and martensite (M200 and M211) planes were used. With the cryogenic treatment and cryogenic treatment + tempering, the austenite peaks in the A200 and A220 planes decreased, while the martensite peaks in the M200 and M211 planes increased. The volume proportion of the retained austenite in the untreated tool was measured as 6.5 % and in the cryo-treated and cryo-treated + tempered tools this proportion was 2.4 % and 1.8 %, respectively. Therefore, the cryogenic and tempering treatments played an important role in the transformation of the austenite (retained in the structure after the conventional heat treatment) into martensite. It is believed that the transformation of the retained austenite into martensite due to cryogenic treatment can provide significant improvements in the mechanical properties of cutting tools such as hardness. This was verified with the positive variations that occurred in the hardness and the microstructure.

After the cryogenic treatment, a Leica WMHT MOT microhardness tester was used to measure the Vickers HV microhardness on one cryogenically treated sample, one cryogenically treated and 2 h tempered sample and one untreated sample, with a minimum of eight indentations in each sample and the average used for the comparison. In **Table 5**, the differences in the microhardness values depending on the treatment applied to the M42 HSS tools are seen. On the untreated tool, the initial hardness was 703 HV and immediately after the cryo-

genic treatment it became 742 HV. After the cryogenic treatment, tempering was applied and the hardness was measured as 718 HV. With the cryogenic treatment and cryogenic treatment + tempering the percentages of the increase in the hardness were 5.5 and 2.1, respectively. It is thought that the increase in the hardness after the cryogenic treatment is the result of the transformation of the austenite retained after the conventional heat treatment to martensite.^{15,24} Moreover, the influence of cryogenic treatment on the increasing hardness can be found in the literature as well.^{13,25,26} Although hardness values differ depending on the material type and application method, increases in the hardness values of 1–3 HRC can be obtained with the cryogenic treatment.¹⁶ The tempering treatment caused some decrease in the hardness compared to the cryogenic treatment; however, it was observed that the hardness value was still higher than that of the untreated tool. It was assumed that this decrease in the hardness was the result of the dissociation

Table 5: Microhardness and retained-austenite volume after different treatment cycles

Tabela 5: Mikrotrdota in volumen zaostalega avstenita po različnih ciklih obdelave

Cutting tools	Retained austenite (p/%)	Microhardness (HV _{0.2})
Untreated	6.5	703
Cryo-treated	2.4	742
Cryo-treated and tempered	1.8	718

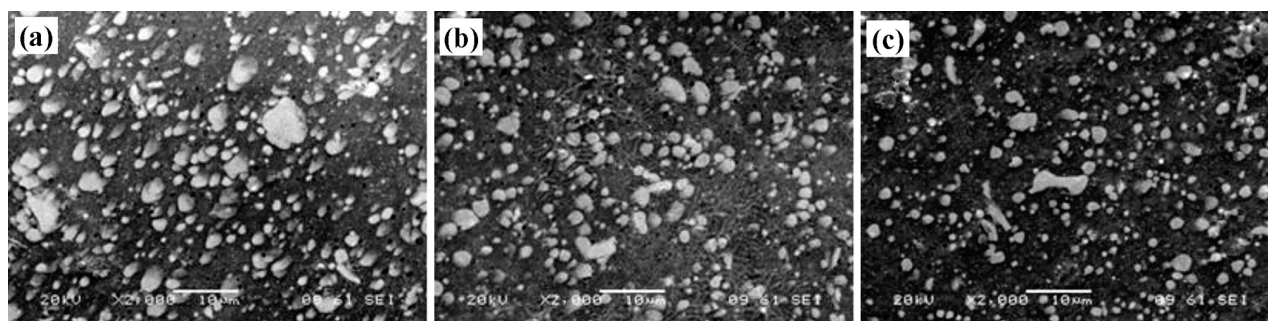


Figure 4: Microstructures of the drills: a) untreated, b) cryo-treated, c) cryo-treated and tempered
Slika 4: Mikrostruktura svedrov: a) neobdelano, b) podhlajeno, c) podhlajeno in popuščano

of some MC (Mo, V, W, Cr) carbides and precipitate phases.

In order to specify the changes in the microstructure caused by the cryogenic treatment and cryogenic treatment + tempering applied to the HSS tools compared to the untreated tools, SEM microstructure photographs were taken. The purpose of the microstructure examination was to explain the increasing hardness values and the improved tool life. The cutting-tool performance depends on the carbide properties in the microstructure. The microstructures of the U, CT and CTT HSS tools are shown in **Figure 4**. From the photograph of the untreated HSS-tool microstructure (**Figure 4a**), it is clear that the carbide particles in the matrix are large. As a result of the cryogenic treatment and cryogenic treatment and tempering, the carbide particles decreased in size and exhibited a much better distribution (**Figures 4b** and **4c**). Cryogenic treatment and tempering may cause a further increase in the particle volume fraction. Compared with **Figures 4a** and **4b**, in **Figure 4c**, it is possible to see a decrease in the size of the particles and a more uniform distribution of these particles due to the dissolution of the precipitates and the fracture of large particles.

With the decrease in the size of the carbide particles and their uniform distribution, the interior stresses in the martensite structure are relieved and the micro-cracking sensitivity is minimized, thus providing a significant improvement in the hardness and wear resistance. The precipitation of fine carbides as a result of cryogenic treatment is responsible for the improvement in the wear resistance.¹⁵ The increase in the microhardness as a result of cryogenic treatment seems to confirm this thesis. Uygur²⁷ showed that there was a strong relationship between the microstructure hardness and the wear properties of steel. Cryogenic treatment provides not only a carbide formation but also a uniform carbide distribution.^{15,16} The tempering after the cryogenic treatment provides the second carbide precipitation and plays an effective role in relieving interior stresses.¹⁶ Thus, in this study, it was thought that non-uniform

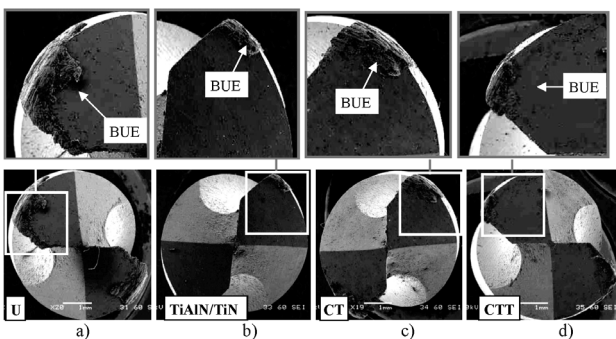


Figure 5: SEM images of drills tested under dry cutting conditions, at 10 m/min cutting speed and 0.06 mm/r feed rate: a) U, b) TiAlN/TiN, c) CT, d) CTT

Slika 5: SEM-posnetki svedrov, preizkušeni v suhih razmerah, hitrost rezanja 10 m/min in hitrost podajanja 0,06 mm/r: a) U, b) TiAlN/TiN, c) CT, d) CTT

carbides of different sizes were subjected to a size reduction by the cryogenic treatment, and then the tempering relieved the interior stresses.

3.2 Evaluation of the tool wear

A series of wear experiments was carried out in order to compare the performances of the U, TiAlN/TiN-coated, CT and CTT tools under dry and wet cutting conditions. In the wear experiments, holes with a depth of 15 mm were drilled at a cutting speed of 10 m/min and a feed rate of 0.06 mm/r. Under dry cutting conditions, the wear curve could not be obtained because the tool was subjected to a catastrophic failure due to an excessive adhesion without showing a regular wear tendency. **Figure 5** shows SEM images of the four different tools tested under dry cutting conditions. It was clearly observed that the high temperatures generated at the cutting area due to a lower coefficient of the heat conductivity of titanium in all of the drills caused a built-up edge (BUE).²⁸ Another BUE formation was observed at the outer corners, in particular where the cutting speed was at its maximum. This was because the outer-corner area was subjected to the extensive heat and chemical loads due to a greater heat generation. The adhesion tendency was higher with the untreated tool although fewer holes were drilled with it (**Figure 5a**). At the specified cutting parameters, the uncoated (U) tool completed its life after the drilling of four holes, the CT tool completed it after five holes, the CTT tool after six holes and the TiAlN/TiN-coated tool after seven holes. It was observed that the lower heat conductivity and friction coefficient of the coating reduced the friction at the tool-chip interface and decreased the BUE formation.

Under wet-cutting conditions, a more regular wear tendency was observed compared to dry cutting condi-

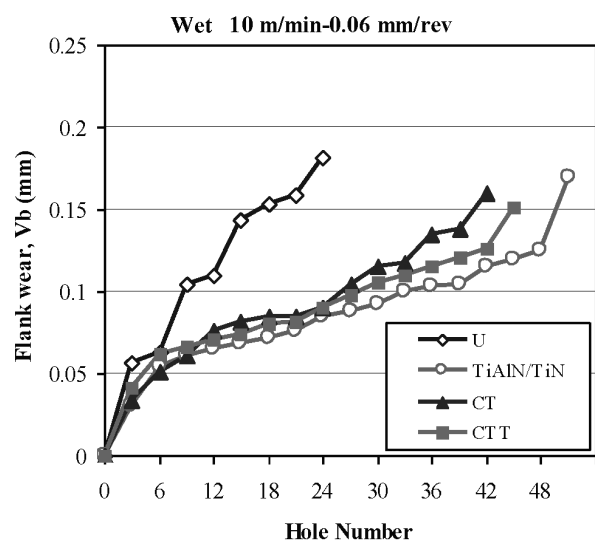


Figure 6: Number of holes and flank wear for drills under wet cutting conditions, at 10 m/min cutting speed and 0.06 mm/r feed rate

Slika 6: Število lukenj in obraba bokov pri svedrih v mokrih razmerah rezanja: hitrost rezanja 10 m/min, hitrost podajanja 0,06 mm/r

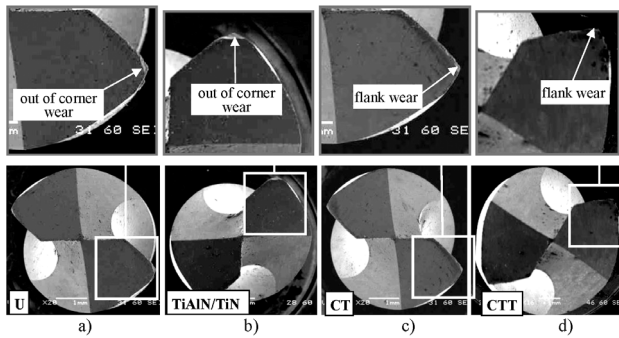


Figure 7: SEM images of drills tested under wet cutting conditions, at 10 m/min cutting speed and 0.06 mm/r feed rate: a) U, b) TiAlN/TiN, c) CT, d) CTT

Slika 7: SEM-posnetki svedrov, preizkušanih pri mokrem rezanju: hitrost rezanja 10 m/min in hitrosti podajanja 0,06 mm/r: a) U, b) TiAlN/TiN, c) CT, d) CTT

tions, and with the specified tool-wear criteria, the flank-wear curve was obtained, depending on the number of holes. In **Figure 6**, under wet cutting conditions, the differences in the number of holes and flank wear among the four different tools, at the cutting speed of 10 m/min and the feed rate of 0.06 mm/r, are given. The best performance in terms of the tool wear was obtained with the multi-layered TiAlN/TiN-coated tool, followed by the CTT, CT, and U tools, respectively. The U tool reached a flank wear value of 0.15 mm at the 24th hole, the CT tool at the 42nd hole, the CTT tool at the 44th hole, and the TiAlN/TiN-coated tool at the 51st hole. At this stage it is possible to state that cryogenic and tempering treatments created a change in the microstructure and provided an increase in the hardness, which had an important influence on the tool life. In general, while the TiAlN/TiN-coated, CT and CTT tools exhibited similar flank-wear values up to the 27th hole, after this hole, a wear difference began to be seen. In particular, the CT and CTT tools reached the tool wear criterion with a difference of a couple of holes.

In **Figure 7**, SEM images of the four different cutting tools tested under wet-cutting conditions are shown.

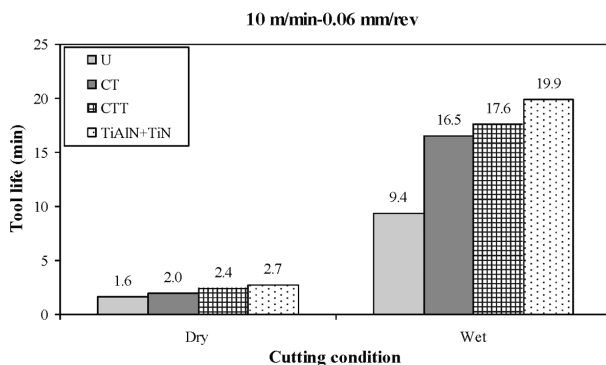


Figure 8: Tool-life differences depending on cutting conditions for the four tools at 10 m/min cutting speed and 0.06 mm/r feed rate

Slika 8: Razlike v zdržljivosti orodja v odvisnosti od razmer pri rezanju pri štirih orodjih pri hitrosti rezanja 10 m/min in hitrosti podajanja 0,06 mm/r

From these images it can be seen that here the tool wear is more regular in comparison with the dry cutting conditions. The tendency to form an excessive BUE formation that was observed with dry cutting conditions was minimized with the use of a coolant. It is known that during cutting operations, the coolant forms a thin film layer at the tool-chip interface and decreases the friction, at the same time making the chip removal easier and decreasing the temperatures at the cutting area,²⁹ thus delaying the wear of the cutting tool, compared to dry cutting. It was seen that the effective wear type of the U and TiAlN/TiN-coated tools was the outer-corner wear (**Figures 7a** and **7b**), while with the CT and CTT tools it was the flank wear (**Figures 7c** and **7d**). Furthermore, it was observed that with the CT and CTT tools, the wear at the outer corner did not form as rapidly as with the untreated tool, but instead it followed a more uniform feed along the cutting edges. This was thought to be the result of the improvement in the wear resistance of the cutting tool provided with the cryogenic treatment.

During the drilling of the Ti-6Al-4V alloy, a tool-life curve was prepared to determine the effects of dry and wet cutting conditions on the tool life (**Figure 8**). From the curve, it can be seen that wet cutting conditions provided a significant increase in the tool life in comparison with the dry cutting conditions. As the thermal properties of Ti-6Al-4V are poor, the use of cutting fluids (or coolants) is very important to improve the tool life³. The highest tool life obtained under dry cutting conditions was 2.7 min, while this value reached 19.9 min under wet cutting conditions. At this stage, the importance of using a coolant in the drilling of the Ti-6Al-4V alloy was once more confirmed. Under dry cutting conditions, the CT, CTT and TiAlN/TiN-coated tools exhibited life increases of (25, 50 and 68) % compared to the U tool. These values were (76, 87 and 112) % in the case of wet cutting conditions. It is believed that cryogenic treatment and cryogenic treatment + tempering have important roles in reducing the size of carbide particles, providing a uniform carbide distribution, transforming the retained austenite to martensite and increasing the hardness and wear resistance of cutting tools. The tool wear experiments confirmed this as well.

The CTT tools provided an increase in the tool life of 20 % under dry cutting conditions and 7 % under wet cutting conditions in comparison with the CT tools. The TiAlN/TiN-coated drills exhibited the best performance among the tested drills. It is thought that the TiAlN/TiN coating has a multi-layer structure and a lower friction coefficient and makes the chip flow more easily during the cutting; due to these properties it has an important influence on the increase in the tool life. Apart from that, its high hardness and lower friction coefficient, compared with the uncoated tool, affected the increase in the tool life. It is interesting to note that the TiAlN/TiN-coated tool had a longer tool life under wet cutting conditions. This was believed to be a result of the solid

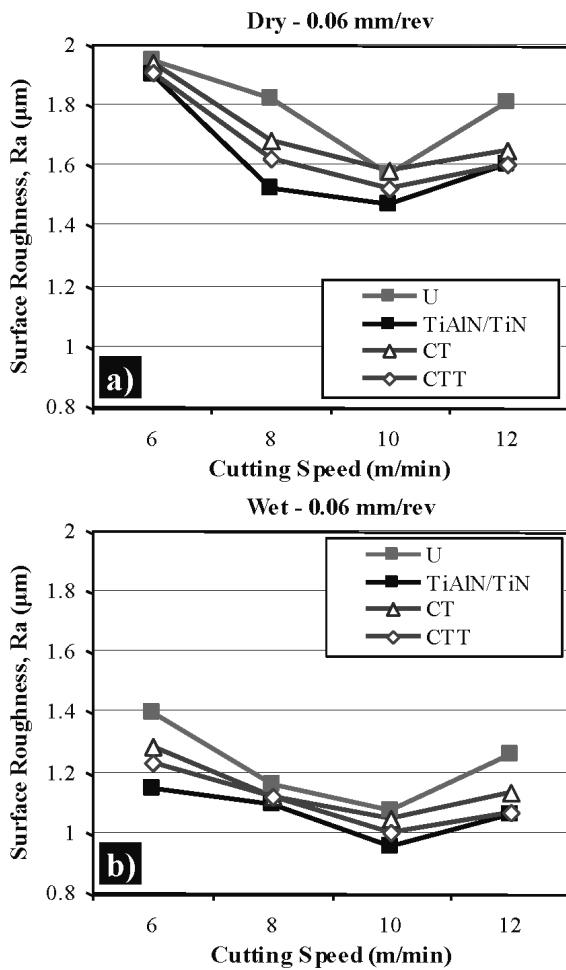


Figure 9: Different R_a values for the four tools, depending on cutting condition and cutting speed: a) dry, b) wet

Slika 9: Različne vrednosti R_a pri štirih orodjih v odvisnosti od razmer pri rezanju in hitrosti rezanja: a) suho, b) mokro

lubricating property of the coating acting together with the lubricating and cooling property of the coolant.

3.3 Evaluation of the surface roughness

Surface finish is also an important index of machinability or grindability because the performance and service life of the machined/ground components are often affected by their surface finish, the nature and extent of residual stresses and the presence of surface or subsurface microcracks, if any. This is particularly relevant when this component is to be used under dynamic loading or in conjugation with some other mating part(s).³⁰ Figure 9 shows the differences in the surface roughness (R_a) among the four different tools, depending on the cutting speed and cutting conditions. For all four tools, with the increase in the cutting speed, the R_a values decreased up to the cutting speed of 10 m/min, but with further increases in the cutting speed, some increase in R_a was observed. It is thought that the decrease in R_a values with the increase in the cutting speed was due to the reduction in the BUE size with the temperature inc-

rease at the tool-workpiece interface.³¹ Moreover, it is also believed that improved surface quality is influenced by the reduced friction resulting from the higher temperatures at the contact area at the tool-workpiece interface.³² The lowest R_a values among the four cutting tools were obtained for the holes drilled with the TiAlN/TiN-coated tools, followed by the CTT, CT and U tools, respectively. This sequence shows a parallelism with the one for the tool life. The average decreases in the R_a values of (6.5, 10.4 and 15) % were obtained with the CT, CTT and TiAlN/TiN-coated tools compared to the U tools. With the TiAlN/TiN-coated tool, compared to the other tools, less BUE formation and wear led to an improved surface quality (Figures 5 to 7). It was seen that the combination of the cryogenic and tempering treatments was the second most effective procedure with respect to improving the surface quality due to the positive microstructural changes and the increase in the hardness and wear resistance, surpassed only by the improvement achieved with the TiAlN/TiN coating. Wet cutting conditions provided important improvements for all four tools regarding the trend toward reduced R_a values. Under dry cutting conditions, the R_a values were between 1.4 µm and 1.94 µm whereas under wet cutting conditions, the values ranged from 0.95 µm to 1.4 µm. The main reasons for the difficult machinability of the Ti-6Al-4V alloy are its low heat-conductivity coefficient and high chemical reactivity. The use of a coolant makes the chip removal easier, inhibits the heat formation in the cutting area, and decreases the BUE formation to a large extent. Taken altogether, these factors increase the surface quality in parallel with the increase in the tool life.

4 CONCLUSIONS

From the observed performance of the U, CT, CTT and TiAlN/TiN-coated M42 HSS drills in the machining of Ti-6Al-4V, the following conclusions were drawn:

- Cryogenic treatment significantly improved the wear resistance and tool life of M42 HSS drills under dry and wet conditions in the drilling of the Ti-6Al-4V alloy. Cryogenic treatment and tempering increased the performance of the cutting tools.
- By reducing the size of the carbide particles, cryogenic and tempering treatment enabled their uniform distribution and increased the concentration as well. Furthermore, the treatment had an important influence on the transformation of the retained austenite to martensite, a process which contributes to the abrasive-wear resistance as a result of the increased hardness.
- The CT and CTT tools, unlike the U tools, exhibited a performance approaching that of the TiAlN/TiN-coated tools. It was seen that the use of a coolant also had a significant influence on the increase in the tool life and surface roughness. In dry cutting conditions,

the CT, CTT and TiAlN/TiN-coated tools exhibited an increase of (25, 50, and 68) % in the tool life, compared to the U tools. Under wet cutting conditions, these values were (76, 87 and 112) %. Under dry cutting conditions, the effective wear types were BUE and catastrophic failure, whereas under wet cutting conditions, flank wear and outer-corner wear were effective.

- The biggest advantage of cryogenic treatment compared to coatings is its cheapness and its influence on the whole piece of the material. In this study, the results that were obtained showed that cryogenic treatment, with some improvement, can serve as an alternative to coatings.

Acknowledgments

The authors wish to express their sincere thanks to the Gazi University Scientific Research Project Division for its financial support for Project No: 07/2010-38.

5 REFERENCES

- R. R. Boyer, An overview on the use of titanium in the aerospace industry, *Mater. Sci. Eng. A*, 213 (1996), 103–114, doi:10.1016/S0921-5093(96)10233-1
- F. Nabhani, Machining of Aerospace Titanium Alloys, *Robot. CIM-Int. Manuf.*, 17 (2001), 99–106, doi:10.1016/S0736-5845(00)00042-9
- E. O. Ezugwu, Z. M. Wang, Titanium Alloys and Their Machinability – a Review, *J. Mater. Process. Technol.*, 68 (1997), 262–274, doi:10.1016/S0924-0136(96)00030-1
- S. Sun, M. Brandt, M. S. Dargusch, Machining Ti–6Al–4V alloy with cryogenic compressed air cooling, *International Journal of Machine Tools & Manufacture*, 50 (2010), 933–942, doi:10.1016/j.ijmactools.2010.08.003
- J. L. Cantero, M. M. Tardío, J. A. Canteli, M. Marcos, M. H. Miguélez, Dry drilling of alloy Ti–6Al–4V, *Int. J. Mach. Tools Manuf.*, 45 (2005), 1246–1255, doi:10.1016/j.ijmactools.2005.01.010
- J. K. Schueller, J. Tlustý, S. Smith, E. Leigh, *Advanced Machining Techniques on Titanium Rotor Parts*, American Helicopter Society, 56th Annual Forum, Virginia Beach, VA, 2000
- L. Zeng, T. R. Bieler, Effects of Working, Heat Treatment, and Aging on Microstructural Evolution and Crystallographic Texture of α' , α'' , α'' and β Phases in Ti–6Al–4V Wire, *Mater. Sci. Eng. A*, 392 (2005), 403–414, doi:10.1016/j.msea.2004.09.072
- H. Fujii, Strengthening of $\alpha+\beta$ titanium alloys by thermomechanical processing, *Mater. Sci. Eng. A*, 243 (1998), 103–108, doi:10.1016/S0921-5093(97)00786-7
- S. Y. Hong, Y. Ding, Cooling approaches and cutting temperatures in cryogenic machining of Ti–6Al–4V, *Int. J. Mach. Tools Manuf.*, 41 (2001), 1417–1437, doi:10.1016/S0890-6955(01)00026-8
- A. K. Nady, M. C. Gowrishanka, S. Paul, Some studies on high-pressure cooling in turning of Ti–6Al–4V, *Int. J. Mach. Tools Manuf.*, 49 (2009), 182–198, doi:10.1016/j.ijmactools.2008.08.008
- S. S. Gill, R. Singh, H. Singh, J. Singh, Wear behaviour of cryogenically treated tungsten carbide inserts under dry and wet turning conditions, *Int. J. Mach. Tools Manuf.*, 49 (2009), 256–260, doi:10.1016/j.ijmactools.2008.11.001
- A. Bensely, A. Prabhakaran, D. Mohan Lal, G. Nagarajan, Enhancing the wear resistance of case carburized steel (En 353) by cryogenic treatment, *Cryogenics*, 45 (2006), 747–754, doi:10.1016/j.cryogenics.2005.10.004
- F. J. Da Silva, D. D. Franco, A. R. Machado, E. O. Ezugwu, A. M. Souza Jr, Performance of Cryogenically Treated HSS Tools, *Wear*, 261 (2006), 674–685, doi:10.1016/j.wear.2006.01.017
- A. Molinari, M. Pellizzari, S. Gialanella, G. Straffelini, K. H. Stiasny, Effect of Deep Cryogenic Treatment on the Mechanical Properties of Tool Steels, *J. Mater. Process. Tech.*, 118 (2001) 5, 350–355, doi:10.1016/S0924-0136(01)00973-6
- J. Y. Huang, Y. T. Zhu, X. Z. Liao, I. J. Beyerlein, M. A. Bourke, T. E. Mitchell, Microstructure of Cryogenic Treated M2 Tool Steel, *Mater. Sci. Eng. A*, 339 (2003), 241–244, doi:10.1016/S0921-5093(02)00165-X
- V. Firouzdar, E. Nejati, F. Khomamizadeh, Effect of deep cryogenic treatment on wear resistance and tool life of M2 HSS drill, *J. Mater. Process. Technol.*, 206 (2008), 467–472, doi:10.1016/j.jmatprotec.2007.12.072
- F. Cajner, V. Leskovšek, D. Landek, H. Cajner, Effect of Deep-Cryogenic Treatment on High Speed Steel Properties, *Mater. Manuf. Process.*, 24 (2009), 743–746, doi:10.1080/10426910902809743
- D. Mohan Lal, S. Renganarayanan, A. Kalanidhi, Cryogenic treatment to augment wear resistance of tool and die steels, *Cryogenics*, 41 (2001), 149–155, doi:10.1016/S0011-2275(01)00065-0
- P. T. Schroeder, Widening interest in twist drill, *Modern Mach. Shop*, 71 (1998) 4, 106–113
- S. Sharif, E. A. Rahim, Performance of coated- and uncoated-carbide tools when drilling titanium alloy-Ti–6Al4V, *Journal of Materials Processing Technology*, 185 (2007), 72–76, doi:10.1016/j.jmatprotec.2006.03.142
- ASTM E 975-84, Standard Practice for X-Ray Determination of Retained Austenite in Steel with Near Random Crystallographic Orientation, ASTM, 1989
- S. Gimenez, I. Iturriza, Microstructural characterisation of PM M35MHV as a function of the processing route, *Journal of Materials Processing Technology*, 143–144 (2003), 555–560, doi:10.1016/S0924-0136(03)00359-5
- J. Jeleńkowski, A. Ciski, T. Babul, Effect of deep cryogenic treatment on substructure of HS6-5-2 high speed steel, *Journal of Achievements in Materials and Manufacturing Engineering*, 43 (2010) 1, 80–87
- S. Zhirafar, A. Rezaeian, M. Pugh, Effect of cryogenic treatment on the mechanical properties of 4340 steel, *J. Mater. Process. Technol.*, 186 (2007), 298–303, doi:10.1016/j.jmatprotec.2006.12.046
- Y. Dong, X. Lin, H. Xiao, Deep cryogenic treatment of high-speed steel and its mechanism, *Heat Treatment of Metals*, 3 (1998), 55–59
- A. Çiçek, T. Kivak, İ. Uygur, E. Keci, Y. Turgut, Performance of cryogenically treated M35 HSS drills in drilling of austenitic stainless steels, *Journal of Advanced Manufacturing Technology*, 60 (2012) 1–4, 65–73, doi:10.1007/s00170-011-3616-8
- I. Uygur, Microstructure and wear properties of AISI 1038H steel weldments, *Lubr. Tribol. Ind.*, 58 (2006), 303–311, doi:10.1108/00368790610691383
- L. N. López de Lacalle, J. Pérez, J. I. Llorente, J. A. Sánchez, Advanced cutting conditions for the milling of aeronautical alloys, *Journal of Materials Processing Technology*, 100 (2000), 1–11, doi:10.1016/S0924-0136(99)00372-6
- S. Palanisamy, S. D. McDonald, M. S. Dargusch, Effects of coolant pressure on chip formation while turning Ti6Al4V alloy, *Int. J. Mach. Tools Manuf.*, 49 (2009), 739–743, doi:10.1016/j.ijmactools.2009.02.010
- N. R. Dhar, M. Kamruzzaman, M. Ahmed, Effect of minimum quantity lubrication (MQL) on tool wear and surface roughness in turning AISI-4340 steel, *J. Mater. Process. Technol.*, 172 (2006), 299–304, doi:10.1016/j.jmatprotec.2005.09.022
- C. Ibrahim, Machining of austenitic stainless steels using CVD multi-layer coated cemented carbide tools, *Tribol. Int.*, 39 (2006), 565–569, doi:10.1016/j.triboint.2005.05.005
- E. M. Trent, *Metal cutting*, Butterworths Press, London 1989, 1–171

LOAD-CAPACITY PREDICTION FOR THE CARBON- OR GLASS-FIBRE-REINFORCED PLASTIC PART OF A WRAPPED PIN JOINT

NAPOVED NOSILNOSTI PLASTIČNIH DELOV ZATIČNEGA SPOJA, OJAČANEGA Z OGLJIKOVIMI ALI STEKLASTIMI VLAKNI

Jan Krystek, Radek Kottner

University of West Bohemia in Pilsen, NTIS – New Technologies for the Information Society, Technická 8, 306 14 Plzeň, Czech Republic
krystek@kme.zcu.cz, kottner@kme.zcu.cz

Prejem rokopisa – received: 2014-11-28; sprejem za objavo – accepted for publication: 2015-01-09

doi:10.17222/mit.2014.289

A joint using a metal pin is one possibility of how to achieve a removable joint of composites. The load capacity of a wrapped pin joint depends on many parameters, especially on the types of fibres and resin, and geometric properties of the joint. The composite part of a wrapped pin joint is exposed to a combination of the tension in the longitudinal direction and local compression in the transverse direction. The values of the compressive stress in the transverse direction can exceed several times the uniaxial compressive strength. In this work, CFRP (carbon-fibre-reinforced plastic) and GFRP (glass-fibre-reinforced plastic) parts of wrapped pin joints were tested. Experimental specimens with different geometries were exposed to a quasi-static loading. A Zwick/Roell Z050 testing machine was used for the tensile tests. Moreover, the load capacities of the carbon or glass composite parts were determined using a finite-element analysis. A new measure based on the LaRC04 criterion was proposed for the prediction of the load capacity. The numerical and experimental results were compared.

Keywords: composite, finite-element method, load capacity, loop criterion, wrapped pin joint

Spoji z uporabo kovinskega zatiča so ena od možnosti, kako doseči odstranljivo kompozitno povezavo. Nosilnost zavite stične povezave je odvisna od mnogih parametrov, posebno od vrste vlaken in smole ter geometrijskih lastnosti povezave. Kompozitni del zavite zatične povezave je izpostavljen kombinaciji napetosti v vzdolžni smeri in lokalnim tlakom v prečni smeri. Vrednosti tlačnih napetosti v prečni smeri lahko večkrat presežejo enosno tlačno trdnost. V tem delu so bili preizkušeni zaviti zatični spoji z deli iz CFRP (plastika, ojačana z ogljikovimi vlakni) in GFRP (plastika, ojačana s steklenimi vlakni). Preizkusni vzorci z različno geometrijo so bili izpostavljeni kvazistatični obremenitvi. Za natezne preizkuse je bila uporabljena naprava Zwick/Roell Z050. Poleg tega je bila nosilnost kompozitnih delov z ogljikovimi ali steklastimi vlakni določena z uporabo analize končnih elementov. Novo merilo, ki temelji na merilu LaRC04, je bilo predlagano za napovedovanje nosilnosti. Primerjani so numerični in eksperimentalni rezultati.

Ključne besede: kompozit, metoda končnih elementov, nosilnost, merilo zanke, zaviti spoj s kovinskim zatičem

1 INTRODUCTION

Joints are often the critical parts of constructions. This work focuses on wrapped pin joints. The main principle of manufacturing the wrapped pin joints is to place the wrapping fibres of a composite directly around the metal pin, precisely following its shape. It allows creating a joint without any cutting fibres, which results in a high load capacity of the joint.¹

The curved composite part (loop – **Figure 1**) of a wrapped pin joint is exposed to a combination of the tension in the longitudinal direction (1 in **Figure 2**) and the compression in the transverse direction (3 in **Figure 2**) during a tensile loading of the joint. The tensile and compressive stresses in the loop reach significantly high values compared with the ultimate strengths in the principal material directions. No standard criterion for a correct failure prediction of the loop was found.^{1,2} Therefore, the LaRC04³ criterion was adjusted² so that the failure of the loop was also described. In the case of freely fastened (FF) loops, a matrix failure reduces the

loop's load capacity (if a matrix failure occurs). The matrix failure results in a separation of the wrapping's cross-section. In the case of tightly fastened (TF) loops, a matrix failure does not influence the loop's load capacity. The difference between the fastenings is explained in **Figure 3**.

However, the parameters of the adjusted LaRC04 criterion² depend on the types of the composite and fastening.⁴ Therefore, a new criterion was proposed in this work.

Experimental and numerical investigations of the loop's load capacity for a wrapped pin joint and a comparison of the experimental and numerical results were the aims of this work. Two types of composite fibres were used in these analyses.

2 EXPERIMENTS

Experimental specimens (unidirectional composite loops – **Figure 1**) were manufactured using the fila-

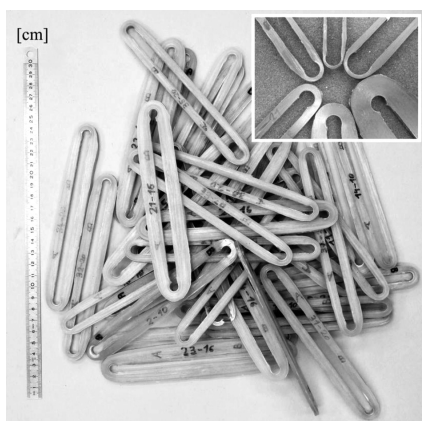


Figure 1: Loops with different geometries
Slika 1: Zanke z različno geometrijo

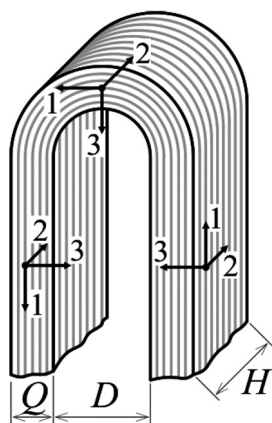


Figure 2: Geometric parameters of the loop and the principal material directions
Slika 2: Geometrijski parametri zanke in osnovne smeri materiala

ment-winding technology. Carbon or glass fibres and epoxy resin were used. Mechanical properties of the composites are presented in Table 1.

The joints were exposed to a tensile quasi-static loading (the loading speed was 0.5 mm/min) at a temperature of +22 °C. A Zwick/Roell Z050 testing machine was used. The description of geometric parameters is obvious from Figure 2: the diameter of pins (D) is 8 mm, the thickness of the loops (H) is 3 mm and the width (Q) is 1–9 mm. FF and TF loops were tested.

Table 1: Mechanical properties of the tested composites
Tabela 1: Mehanske lastnosti preizkušanih kompozitov

carbon fibres + epoxy (LG120 + EM100) ($V_f = 0.65$)						
E_1	E_2	G_{12}	ν_{12}	X^T	Y^C	S^L
(GPa)	(GPa)	(GPa)	–	(MPa)	(MPa)	(MPa)
118.9	4.7	2.0	0.35	3264	92	48
glass fibres + epoxy (LH298 + H512) ($V_f = 0.73$)						
E_1	E_2	G_{12}	ν_{12}	X^T	Y^C	S^L
(GPa)	(GPa)	(GPa)	–	(MPa)	(MPa)	(MPa)
52.6	8.6	4.7	0.30	2000	50	48

A comparison of force-displacement curves of the specimens with the same geometry ($Q = 5.5$ mm) and of

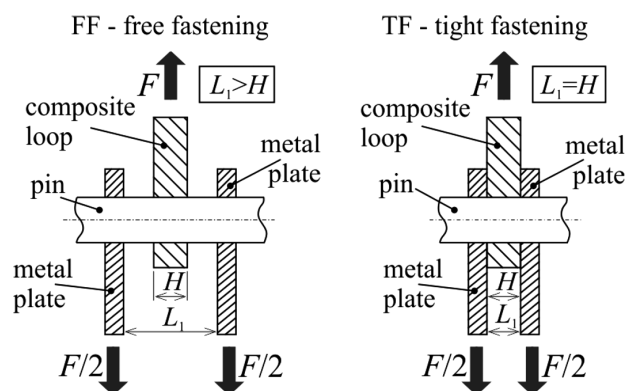


Figure 3: Types of loop fastening
Slika 3: Vrsta pritrditve zanke

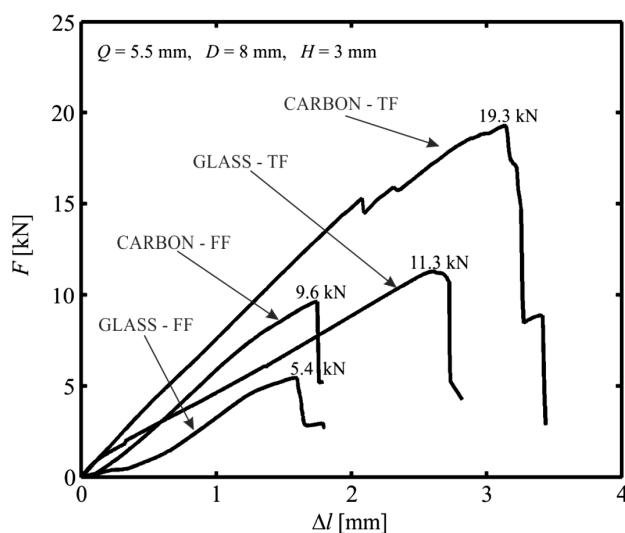


Figure 4: Comparison of force-displacement curves
Slika 4: Primerjava krivulj sila – raztezek

different materials and types of fastening is shown in Figure 4. Experimental dependencies of the load capacity F_{max} on the width Q are presented in Figure 5 (TF

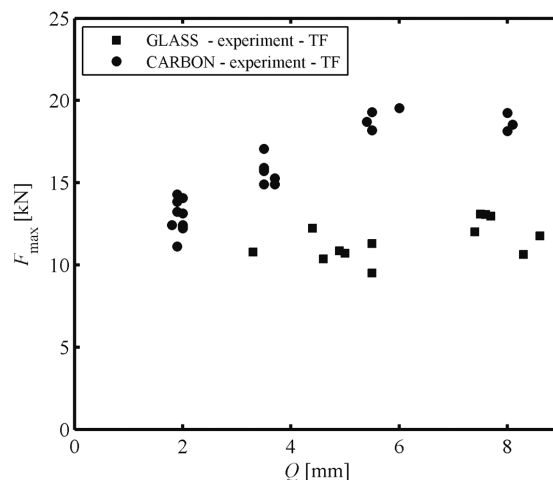


Figure 5: Load capacity of TF loops – experiment
Slika 5: Nosilnost TF-zank – preizkus

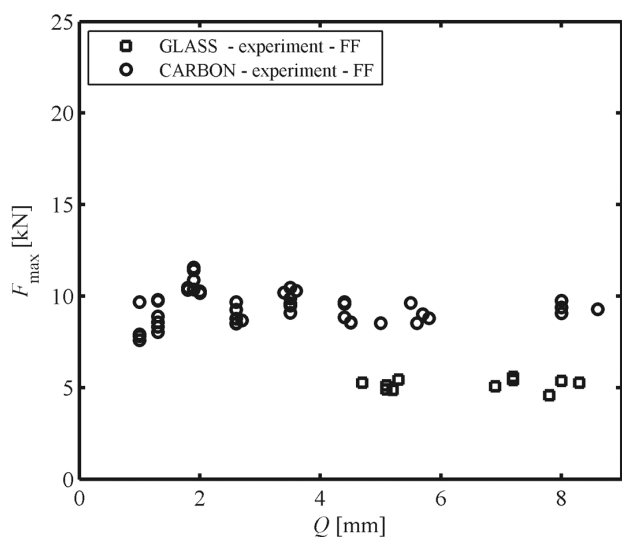


Figure 6: Load capacity of FF loops – experiment
Slika 6: Nosilnost FF-zanke – preizkus

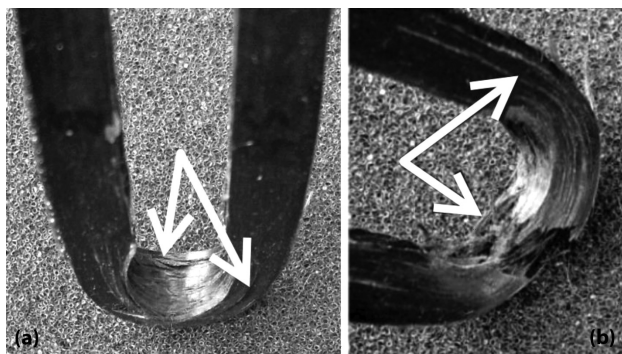


Figure 7: Failures of a) FF loop and b) TF loop
Slika 7: Porušitev: a) FF-zanke in b) TF-zanke

loops) and Figure 6 (FF loops). The diameter D was 8 mm and the thickness H was 3 mm. Typical failures of the FF and TF loops are presented in Figure 7.

2.1 Numerical simulations

The finite-element system MSC. Marc was used for the numerical simulation. Linear hexahedral elements with eight nodes (SOLID elements) were used in a parametrically created model. Due to the symmetry of the loop, only one eighth of the loop was modelled. The properties of transversely isotropic material were assigned to the elements considering the orientations of the fibres. The loading was controlled with a displacement of the rigid surface, which simulated the pin (Figure 8). The friction was neglected.

The loop criterion was proposed in this work. It is based on the LaRC04 criterion³ and respects the specific combination of the stresses in a loop.⁴ The failure index in the case of the fibre-failure mode ($\sigma_1 > 0$) of the loop criterion is:

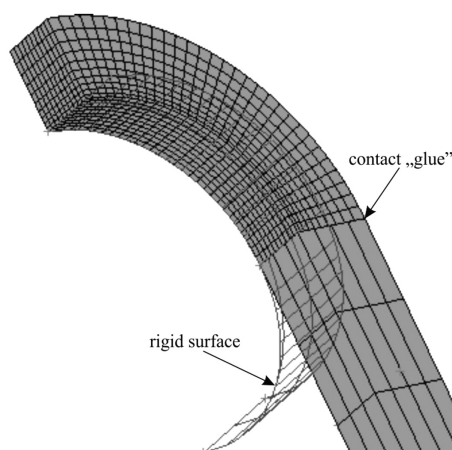


Figure 8: Mesh of the finite-element model
Slika 8: Mreža modela končnih elementov

$$FI_F = \frac{\sigma_1}{\frac{X^T - X^T \cdot P_f}{Y^C + X^T \cdot P_m} \cdot \sigma_3 \cdot P_f + X^T} \leq 1 \quad (1)$$

where P_f and P_m are the criterion parameters (the loop parameters), X^T is the tensile strength in the longitudinal direction and Y^C is the compressive strength in the transverse direction. The failure index in the case of the matrix-failure mode ($\sigma_3 < 0, \sigma_1 \geq 0$) of the loop criterion is:

$$FI_M = \left(\frac{\tau^T}{S^T - \eta^T \sigma_n + \sigma_1 P_m} \right)^2 + \left(\frac{\tau^L}{S^L - \eta^L \sigma_n + \sigma_1 P_m} \right)^2 \leq 1 \quad (2)$$

where τ^T and τ^L are the stresses in the plain of the failure (T – transverse direction, L – longitudinal direction), η^T and η^L are the coefficients of friction, S^T is the transverse shear strength and S^L is the longitudinal shear strength. The loop criterion was implemented into the finite-element system MSC. Marc.

3 RESULTS

The dependencies of the loop's load capacity F_{max} on the width Q , based on both the experimental and numerical results are presented in Figures 9 and 10. It is obvious that an increase in the width Q did not have a significant influence on the FF loop's load capacity. The load capacity of the TF loops increased with the width Q , but only up to the determinate width ($Q = 5$ mm).

The difference between the experimental and numerical results was minimized in the process of identifying the loop parameter P_f . The loop parameter $P_f = 0.87$ was identified for the carbon composite and it was $P_f = 0.65$ for the glass composite (the value of the loop parameter P_f does not depend on the fastening type). The influence of the loop parameter P_m on the load capacity was not investigated. P_m was assumed to be 0.05.²

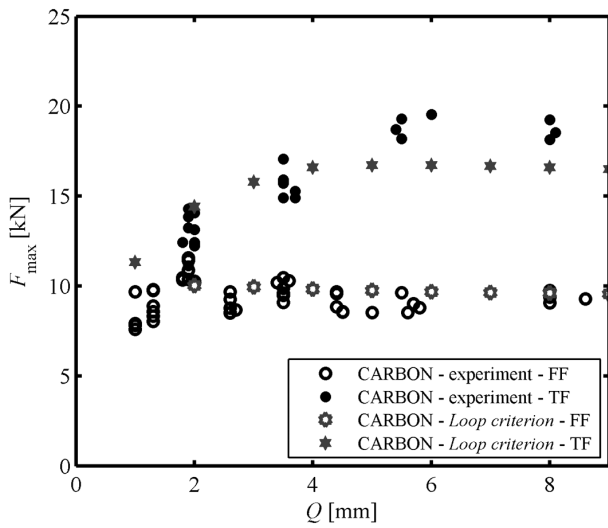


Figure 9: Load capacity of carbon loops
Slika 9: Nosilnost zank z ogljikovimi vlakni

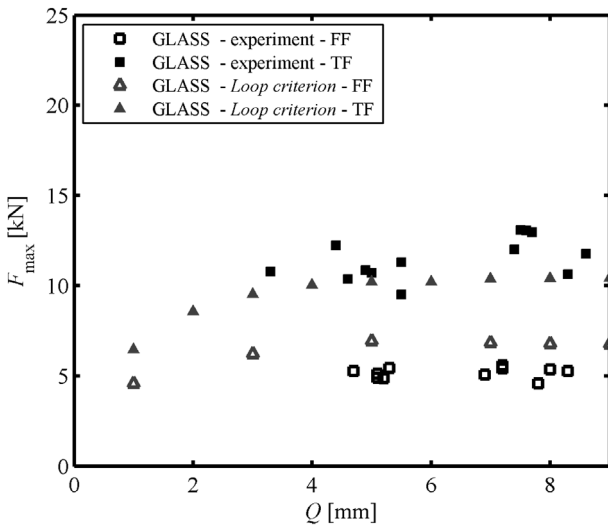


Figure 10: Load capacity of glass loops
Slika 10: Nosilnost zank s steklenimi vlakni

Very good agreement between the experimental and numerical results was achieved in the case of the FF carbon loops (**Figure 9**). In the case of the TF carbon loops, the difference between the experimental and numerical results was lower than 17 %. In the case of the glass composite, sufficient agreement between the experimental and numerical results was achieved for both types of

loop fastening (**Figure 10**). The difference between the experimental and numerical results was lower than 25 %.

4 CONCLUSION

Experimental dependency of a loop’s load capacity on the loop’s width was investigated. Carbon loops had a higher load capacity than glass loops. Irrespective of the type of fibres, the TF loops exhibited a higher load capacity than the FF loops. In the case of the FF loops, an increase in the width Q did not have a significant influence on the loop’s load capacity. In the case of the TF loops, the influence of the width Q was significant only up to its determinate value.

The loop criterion for determining the loop’s load capacity was proposed using the finite-element method. The values of the loop parameter P_f were identified for both analysed materials. With regard to the proposed loop criterion, this parameter does not depend on the type of the loop fastening. The maximum differences between the experimental and numerical results were 17 % for the carbon composite and 25 % for the glass composite.

Acknowledgement

This publication was supported by the project LO1506 of the Czech Ministry of Education, Youth and Sports.

5 REFERENCES

- ¹ T. Havar, E. Stuibler, Design and testing of advanced composite load introduction structure for aircraft high lift devices, ICAF 2009, Bridging the Gap between Theory and Operational Practice, Proceedings of the 25th Symposium of the International Committee on Aeronautical Fatigue, Rotterdam, 2009, 365–374, doi:10.1007/978-90-481-2746-7_21
- ² R. Kottner, J. Krýstek, R. Zemčik, J. Lomberský, R. Hynek, Strength analysis of carbon fiber-reinforced plastic coupling for tensile and compressive loading transmission, 52nd AIAA/ASME/ASCE/AHS/ASC Structures, Structural Dynamics and Materials, Denver, USA, 2011, doi:10.2514/6.2011-1982
- ³ S. T. Pinho, C. G. Dávila, P. P. Camanho, L. Iannucci, P. Robinson, Failure Models and Criteria for FRP under In-Plane or Three-Dimensional Stress States Including Shear Non-Linearity, Research report, NASA/TM-2005-213530, NASA Langley Research Center, 2005
- ⁴ J. Krýstek, Damage of composite components under various types of loading, Ph.D. thesis, University of West Bohemia, 2014 (in Czech)

A MESHLESS MODEL OF ELECTROMAGNETIC BRAKING FOR THE CONTINUOUS CASTING OF STEEL

BREZMREŽNI MODEL ELEKTROMAGNETNEGA ZAVIRANJA PRI KONTINUIRANEM ULIVANJU JEKLA

Katarina Mramor¹, Robert Vertnik², Božidar Šarler^{1,2}

¹University of Nova Gorica, Vipavska 13, 5000 Nova Gorica, Slovenia
²Institute of Metals and Technology, Lepi pot 11, 1000 Ljubljana, Slovenia
katarina.mramor@ung.si, bozidar.sarler@imt.si, robert.vertnik@imt.si

Prejem rokopisa – received: 2015-04-21; sprejem za objavo – accepted for publication: 2015-06-08

doi:10.17222/mit.2015.084

The application of magnetohydrodynamics in the continuous casting of steel enables improved control of the quality of the strand. The most common applications are electromagnetic braking (EMBR) and electromagnetic stirring (EMS). The former slows the flow by applying a static magnetic field and thus improves the steel flow pattern, reduces the velocity and the turbulence of the flow, increases the cleanliness of the material, improves the surface quality and reduces the number of inclusions, whereas the latter stirs the flow by applying an alternating magnetic field and thus improves the quality of the strand, reduces the surface and subsurface defects, enhances the solidification and reduces the number of breakouts.

In this contribution EMBR in a continuous-casting process is considered. The local radial basis function collocation method (LRBFCM) is used for the solution of coupled mass, energy, turbulent fluid flow, species and magnetic field equations. The explicit Euler time-stepping scheme and the collocation with multiquadrics radial basis functions on the five-noded overlapping influence domains are used to obtain the solution of the partial differential equations. The Abe-Kondoh-Nagano low Reynolds turbulence model is used to describe the turbulent fluid flow, whereas the fractional step method is used to solve the pressure-velocity coupling. The method has been thoroughly tested in several test cases. In the present article the influence of the application of electromagnetic braking on the macro-segregation in the continuous-casting process for carbon steel is presented.

Keywords: LRBFCM, continuous casting of steel, turbulent flow, magnetic field, macro-segregation

Uporaba magnetohidrodinamike pri kontinuiranem ulivanju jekla omogoča izboljšano kontrolo kakovosti žile. Najpogostejši aplikaciji sta elektromagnetno zaviranje (EMBR) in elektromagnetno mešanje (EMS). Prva zavira tok z uporabo statičnega magnetnega polja in tako izboljša tokovni vzorec jekla, zmanjša hitrost in turbulenco toka, poveča čistost materiala, izboljša kvaliteto površine in zmanjša število vključkov, medtem ko druga meša tok z uporabo izmeničnega magnetnega polja in tako izboljša kvaliteto žile, zmanjša nepravilnosti na površini in pod njo, pospeši strjevanje in zmanjša število prodorov.

V tem prispevku je obravnavano EMBR pri kontinuiranem ulivanju jekla. Lokalna kolokacijska metoda z radialnimi baznimi funkcijami (LRBFCM) je uporabljena za reševanje sklopljenih enačb za maso, energijo, turbulenten tok tekočine, koncentracijo sestavin in magnetno polje. Eksplisitna Euler-jeva časovna shema in kolokacija z multikvadrničnimi radialnimi baznimi funkcijami na pettočkovnih prekrivajočih se poddomenah sta uporabljena za rešitev parcialnih diferencialnih enačb. Abe-Kondoh-Naganov turbulentni model za nizka Reynolds-ova števila je uporabljen za opis turbulentnega toka, medtem ko je metoda delnih korakov uporabljena za rešitev tlačno-hitrostne sklopitve. Metoda je bila izdatno preizkušena na več preizkusnih primerih. V tem članku je predstavljen vpliv elektromagnetnega zaviranja na makroizcejanje pri kontinuiranem ulivanju ogljikovega jekla.

Ključne besede: LRBFCM, kontinuirano ulivanje jekla, turbulentni tok, magnetno polje, makroizcejanje

1 INTRODUCTION

In the manufacturing of steel,¹ which has in recent years greatly expanded, continuous casting is one of the most common processes in steel production.² The demand for cast steel of high quality fuels the need to further improve the casting process. One way to do that is to introduce either a static or an alternating electromagnetic (EM) field. In general, EM devices in the continuous casting of steel are divided into electromagnetic brakers (EMBR), which use a direct current to produce a static EM field, and into electromagnetic stirrers, which use an alternating current to produce an alternating magnetic field. The EM force, which is a result of the applied magnetic field in both cases, affects the velocity, temperature and concentration fields. By adjusting the magnetic field, the amount of defects, inclusions and air

bubbles in the material can be significantly reduced. In the present contribution, the application of an EMBR system and its effects on velocity, temperature and concentration fields are presented.

The quality of the final product depends on the magnitudes of velocity, temperature, concentration and magnetic fields. In the continuous-casting process the velocity, temperature, concentration and magnetic fields are difficult, if not impossible, to measure. The numerical models are therefore applied in order to help us better understand and further improve the process. The problem under consideration has already been considered with several different numerical models, among which are the Finite Volume Method (FVM),³⁻⁸ the Finite Element Method (FEM),⁹ and some more advanced meshless methods, like the Local Radial Basis Function

Collocation Method (LRBFCM),¹⁰ which is used in the present case as well. The purpose of this article is to present the results obtained for the application of EMBR in the CC process for carbon steel. The results are presented with and without magnetic field for the velocity, temperature and concentration fields.

2 GOVERNING EQUATIONS

The system of governing equations that describes the heat transfer, turbulent fluid flow, species concentration, and magnetic field in the continuous casting of steel, is based on the Reynolds time-averaging approach for modeling the turbulent flow¹¹ and mixture continuum formulation, first introduced by Bennon and Incropera.¹² Our model consists of six time-averaged equations:

$$\nabla \cdot \mathbf{v} = 0 \tag{1}$$

$$\frac{\partial(\rho \mathbf{v})}{\partial t} + \nabla \cdot (\rho \mathbf{v} \mathbf{v}) = -\nabla p + \nabla \cdot \left[\left(\mu_L + \mu_t \frac{\rho}{\rho_L} \right) (\nabla \mathbf{v} + (\nabla \mathbf{v})^T) \right] - \frac{2}{3} \nabla(\rho k) - \mu_L \frac{K_0(1-f_L)^2}{f_L^3} (\mathbf{v} - \mathbf{v}_s) + \rho \mathbf{g} (\beta_T(T - T_{ref}) + \beta_C(C - C_{ref})) + \mathbf{j} \times \mathbf{B} \tag{2}$$

$$\frac{\partial(\rho h)}{\partial t} + \nabla \cdot (\rho \mathbf{v} h) = \nabla \cdot (\lambda \nabla T) + \nabla \cdot (\rho f_s (h_L - h_s) (\mathbf{v} - \mathbf{v}_s)) + \nabla \cdot \left(f_L \frac{\rho_L v_t}{\sigma_t} \nabla h_L \right) + \frac{|\mathbf{j}|^2}{\sigma} \tag{3}$$

$$\frac{\partial(\rho C)}{\partial t} + \nabla \cdot (\rho C \mathbf{v}) = \nabla \cdot (\rho f_s D_s \nabla C_s + \rho f_L D_L \nabla C_L) + \nabla \cdot (\rho(C_L - C)(\mathbf{v} - \mathbf{v}_s)) + \nabla \cdot \left(\frac{f_L \mu_t}{\sigma_C} \nabla C_L \right) \tag{4}$$

$$\frac{\partial(\rho k)}{\partial t} + \nabla \cdot (\rho \mathbf{v} k) = \nabla \cdot \left[\left(\mu_L \frac{\rho}{\rho_L} + \frac{\mu_t}{\sigma_k} \right) \nabla k \right] + P_k + G_k - \rho \varepsilon - \rho D_{k-\varepsilon} + \mu_L \frac{K_0(1-f_L)^2}{f_L^3} \frac{\rho}{\rho_L} k \tag{5}$$

$$\frac{\partial(\rho \varepsilon)}{\partial t} + \nabla \cdot (\rho \mathbf{v} \varepsilon) = \nabla \cdot \left[\left(\mu_L \frac{\rho}{\rho_L} + \frac{\mu_t}{\sigma_\varepsilon} \right) \nabla \varepsilon \right] + \rho E_{k-\varepsilon} - \mu_L \frac{K_0(1-f_L)^2}{f_L^3} \varepsilon + [c_{1\varepsilon} f_1 (P_k + c_{3\varepsilon} G_k) - c_{2\varepsilon} f_2 \rho] \frac{\varepsilon}{k} \tag{6}$$

Where \mathbf{v} is the velocity of the mixture, $\rho = \rho_s = \rho_L$ is the density (assumed to be constant and equal in both phases). t stands for time and p for pressure. μ_t is the turbulent viscosity and μ_L is the dynamic viscosity, k represents the turbulent kinetic energy and K_0 is the permeability constant. \mathbf{v}_s , β_T , β_C , \mathbf{g} , T , T_{ref} , C , and C_{ref} represent the velocity of the solid phase, the thermal expansion coefficient, the solute expansion coefficient, the gravitational acceleration, the temperature, the refer-

ence temperature, the species concentration and the reference species concentration, respectively. $\mathbf{j} \times \mathbf{B}$ stands for the Lorentz force, h for the enthalpy, and λ for the thermal conductivity. f_s , f_L , h_s , and h_L represent the solid volume fraction, the liquid volume fraction, the enthalpy of the solid phase and the enthalpy of the liquid phase, ν_t is the turbulent kinematic viscosity and σ is the electrical conductivity. D_s , and D_L are diffusion coefficients for the solid and liquid phases, respectively. ε stands for the dissipation rate, σ_t , σ_C , σ_k , σ_ε , $c_{1\varepsilon}$, f_1 , $c_{2\varepsilon}$ and f_2 are closure coefficients. P_k , G_k , $D_{k-\varepsilon}$, and $E_{k-\varepsilon}$ are the shear production of turbulent kinetic energy, the generation of turbulence due to the buoyancy force, the source term in the k equation and the source term in the ε equation, respectively. In this contribution, only the porous zone is considered and is modelled using Darcy's law and the Kozeny-Carman relation. The closure relations, defined by Abe-Kondoh-Nagano,¹³ are used to set the turbulence closures. A detailed description of the closure coefficients, source terms and damping functions are given in the paper of Šarler et al.¹⁴ The Lorentz force is defined as:

$$\mathbf{F}_m = \mathbf{j} \times \mathbf{B} \tag{7}$$

where \mathbf{j} and \mathbf{B} are the current density and the magnetic flux density. The Maxwell's equations are used to calculate the current density:

$$\mathbf{j} = \sigma(-\nabla \phi + \mathbf{v} \times \mathbf{B}) \tag{8}$$

where ϕ is the fluid's electric potential. The assumption of a low magnetic Reynold's number ($Re_m \ll 1$) is made.

2.1 Boundary and initial conditions

The governing equations for velocity, species concentration and temperature in the continuous-casting process

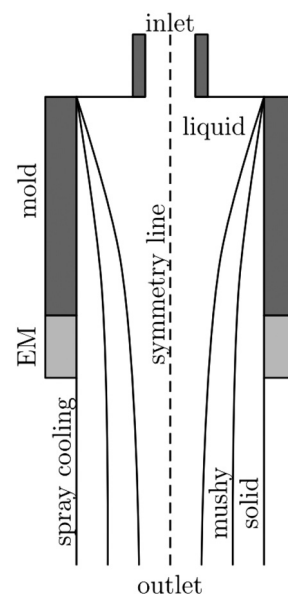


Figure 1: Simplified 2D model for continuous casting of steel
Slika 1: Poenostavljen 2D-model za kontinuirano ulivanje jekla

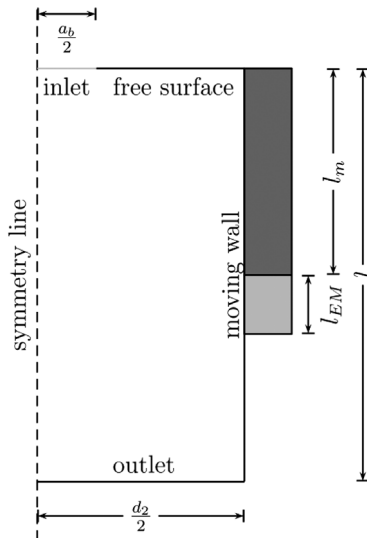


Figure 2: Computational domain scheme
Slika 2: Shema računске domene

are strongly coupled. Although the coupling between the magnetic field and the rest of the governing equations is weak, it is still very important for the solution to the problem of how the initial and boundary conditions are chosen. In present case, five different boundaries are chosen: inlet, free surface, wall, outlet and symmetry. The model of the domain is presented in **Figure 1**, the computational domain is depicted in **Figure 2**, and the initial and boundary conditions are given in **Figure 3**.

3 SOLUTION PROCEDURE

The explicit Euler time stepping and LRBFCM are used to solve the governing equations of the EMBR in the continuous-casting process. The pressure-velocity coupling is solved with the Fractional Step Method (FSM).¹⁵

The first step in the solution procedure is the calculation of the initial Lorentz force (Equation (7)). The procedure begins by solving the Poisson’s equation for electric potential:

$$\nabla^2\phi = \mathbf{v}\times\mathbf{B} \tag{9}$$

the solution of which is then inserted into Equation (7). The Lorentz force is inserted into the equation for the intermediate velocity \mathbf{v}^* , which is calculated from the momentum equation by omitting the pressure-gradient term. The pressure is then calculated from the Poisson’s equation by solving the pressure sparse matrix.¹⁴ The calculated pressure gradient is then used to correct the intermediate velocities of the final velocity field. After the solution of the velocity field, the equations for turbulent kinetic energy and dissipation rate are solved. This is followed by the solution of the enthalpy and species concentration equations. The enthalpy-temperature¹⁴ constitutive relation is used to calculate the temperature from the enthalpy. Finally, the turbulent

viscosity, velocity, temperature, species concentration, turbulent kinetic energy and dissipation rate are updated and the solution is ready for the next step.

The spatial discretization is solved using LRBFCM by constructing the approximation function θ , that is represented on each of the subdomains as a linear combination of the radial basis functions (RBFs) as:

$$\theta({}_l\mathbf{p}_n) = \sum_{i=1}^M {}_l\psi_i({}_l\mathbf{p}_n) {}_l\alpha_i \tag{10}$$

where M , ${}_l\alpha_i$, and ${}_l\psi_i$ represent a number of shape functions, an expansion coefficient, and RBF shape functions, centred at points ${}_l\mathbf{p}_n$, respectively. The most commonly used RBFs are Multiquadric RBF^{16,17}:

$${}_l\psi_i(\mathbf{p}) = \sqrt{{}_l r_i^2(\mathbf{p}) + c^2} \tag{11}$$

where c stands for a dimensionless shape parameter, which is in our case set to 32, and:

$${}_l r_i(\mathbf{p}) = \sqrt{\left(\frac{x-x_i}{{}_l x_{imax}}\right)^2 + \left(\frac{y-y_i}{{}_l y_{imax}}\right)^2} \tag{12}$$

is scaled by ${}_l x_{imax}$, and ${}_l y_{imax}$, the scaling parameters in the subdomains in the x and y directions, respectively (**Figure 3**).

A subdomain consists of the ${}_l M - 1$ nodes nearest to the node ${}_l\mathbf{p}_n$ and is formed around each of the calculation points. In this contribution, five-nodded overlapping subdomains are used. A linear system of equations is obtained by considering the collocation condition:

$$\theta({}_l\mathbf{p}_n) = \theta({}_l\mathbf{p}_n) \tag{13}$$

To construct the Partial Differential Equation (PDE) derivatives, originating from the governing equations, the first and the second derivatives of the function $\theta(\mathbf{p})$ have to be calculated:

$$\frac{\partial^j}{\partial \chi^j} \theta(\mathbf{p}) = \sum_{i=1}^M \frac{\partial^j}{\partial \chi^j} {}_l\psi_i(\mathbf{p}) {}_l\alpha_i \tag{14}$$

where the index j is used to denote the order of the derivative and $\chi = x, y$. A detailed explanation of the solution procedure is given in.^{18,19} The discretization scheme is shown in **Figure 3**.

4 RESULTS

The numerical procedure has so far been tested on the following benchmark test cases: lid driven cavity, natural convection in a cavity with a magnetic field, and a backward facing step with a transverse magnetic field and a test case for a simplified magnetic field in the continuous-casting process. As the results in all of the test cases are in good agreement with the reference results, both those calculated with the commercial code and those obtained from the literature, the method is now applied to the electromagnetic braking problem for the continuous casting of steel. The results of the EMBR

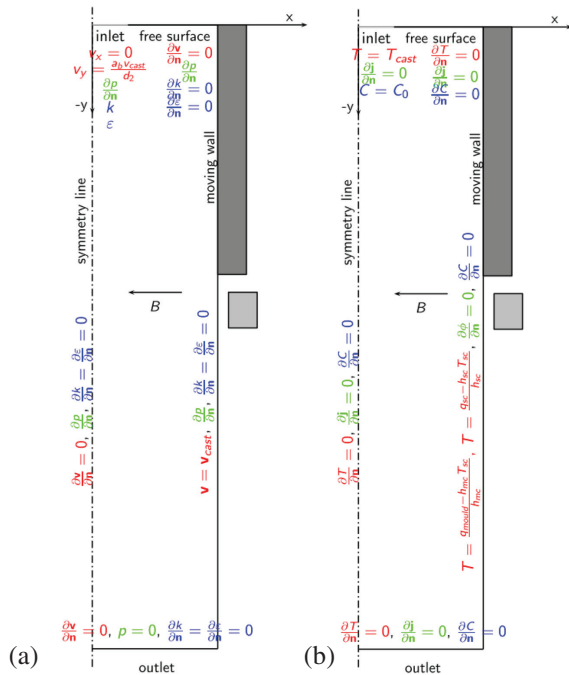


Figure 3: a) Boundary and initial conditions for velocity, pressure, turbulent kinetic energy and dissipation rate, b) boundary and initial conditions for temperature, magnetic field and species concentration
Slika 3: a) Robni in začetni pogoji za hitrost, tlak, turbulentno kinetično energijo in hitrost disipacije, b) robni in začetni pogoji za temperaturo, magnetno polje in koncentracijo

problem with continuous casting have been published in several articles.¹⁹⁻²¹

4.1 EM field calculations

The magnetic field for the EMBR is calculated analytically. The EMBR device consists of two coils, as shown in **Figure 4**. The magnetic fields in these coils can either face one another or point in a parallel direction, as shown in **Figures 5** and **6**. The magnetic field of both coil configurations is shown in **Figures 7** and **8**. The parallel coil configuration is chosen, as this is the default configuration for EMBR. As the coils in the EMBR device have iron cores, the magnetic field is

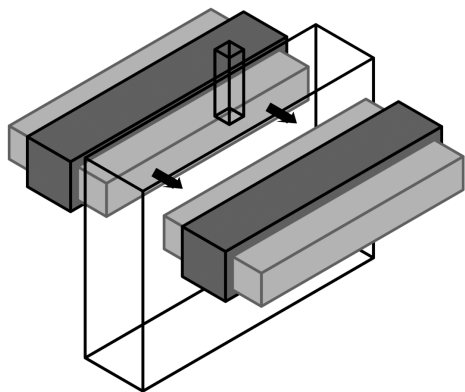


Figure 4: Scheme of EMBR
Slika 4: Shema EMBR

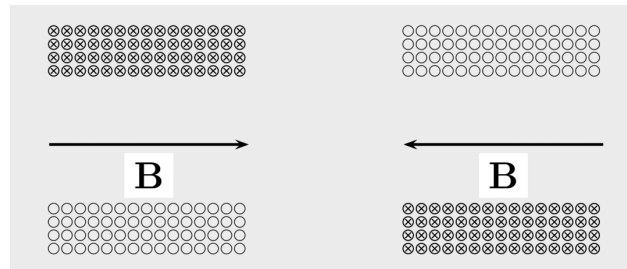


Figure 5: Scheme of the magnetic field for the coils facing each other
Slika 5: Shema magnetnega polja tuljav, obrnjenih druga proti drugi

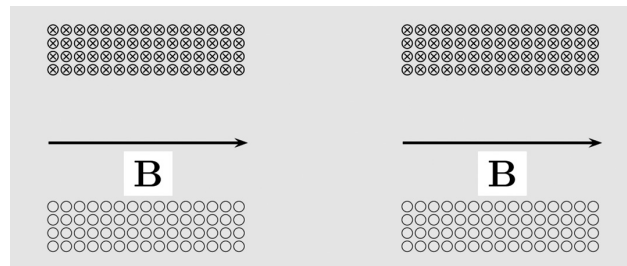


Figure 6: Scheme of the magnetic fields facing in the same direction
Slika 6: Shema magnetnega polja tuljav, obrnjenih v enako smer

enhanced due to the magnetization, as shown in **Figure 9**.

In general, steel is ferromagnetic, and thus the possibility of the influence of magnetization needs to be checked. The operating temperature in the strand is well above the Curie temperature, where steel is paramagnetic. The magnetic field in the molten steel in the strand is therefore not further influenced by the external magnetic field. The temperature dependence of the permeability of molten steel is shown in **Figure 10**.

The computational domain presents half of the longitudinal section of the billet, which is 1.8 m long and 14 cm wide. The SEN diameter is 3.5 cm, the mold

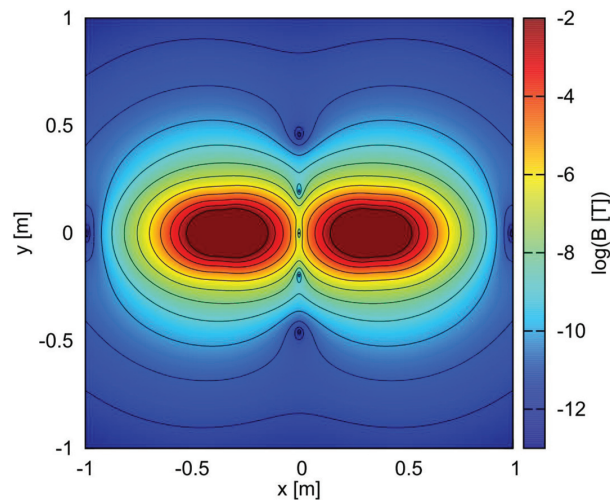


Figure 7: Magnetic field of coils facing each other
Slika 7: Magnetno polje tuljav, obrnjenih druga proti drugi

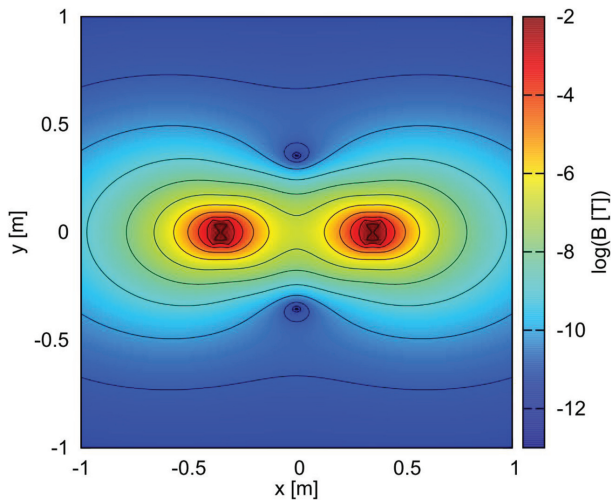


Figure 8: Magnetic field of coils facing in the same direction
Slika 8: Magnetno polje tuljav, obrnjenih v enako smer

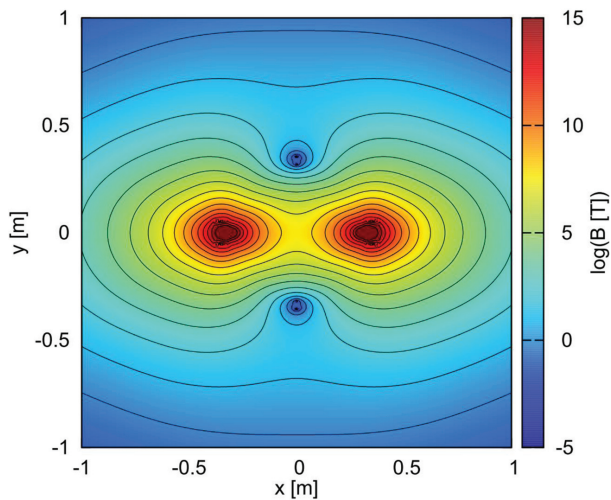


Figure 9: Magnetic field of parallel coils configuration (coils facing in the same direction) with an iron core
Slika 9: Magnetno polje paralelne postavitve tuljav (tuljave obrnjene v enako smer) z železnim jedrom

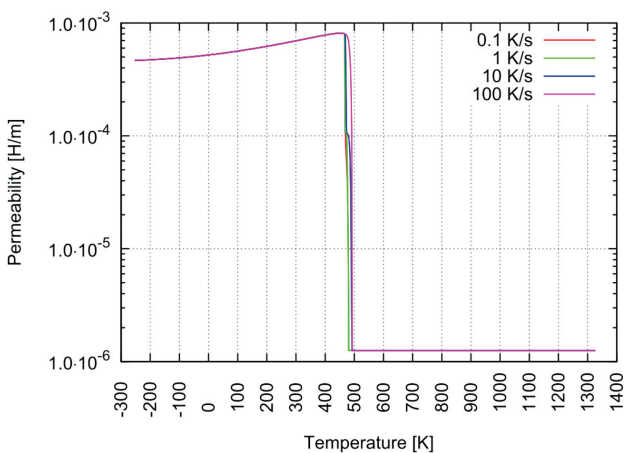


Figure 10: Temperature dependence of permeability for steel
Slika 10: Temperaturna odvisnost permeabilnosti jekla

height is 0.8 m and the coil height is 10 cm. The magnetic field is calculated for a coil configuration with 11 windings in the y direction and 25 windings in the x direction for coils placed 0.05 m away from the strand. The coils are placed just below the mold. A direct current with an amplitude of 50 A runs through the coils. Normally, the material properties of steel are temperature dependent. However, for the purpose of this simplified model, constant values are used for each of the phases. The values are given in **Table 1**.

Table 1: Material properties of steel

Tabela 1: Snovne lastnosti jekla

property	value
ρ	7200 kg/m ³
λ	30 W/(m K)
c_p	700 J/(kg K)
T_S	1680 K
T_L	1760 K
h_m	250000 J/kg
μ	0.006 Pa s
β_T	1·10 ⁻⁴ 1/K
β_C	4·10 ⁻³ 1/%
K_0	6.25·10 ⁹ m ⁻¹
C_{ref}	0.008
D_S	1.6·10 ⁻¹¹ m ² /s
D_L	1.0·10 ⁻⁸ m ² /s
σ	0.59·10 ⁶ /(Ω m)

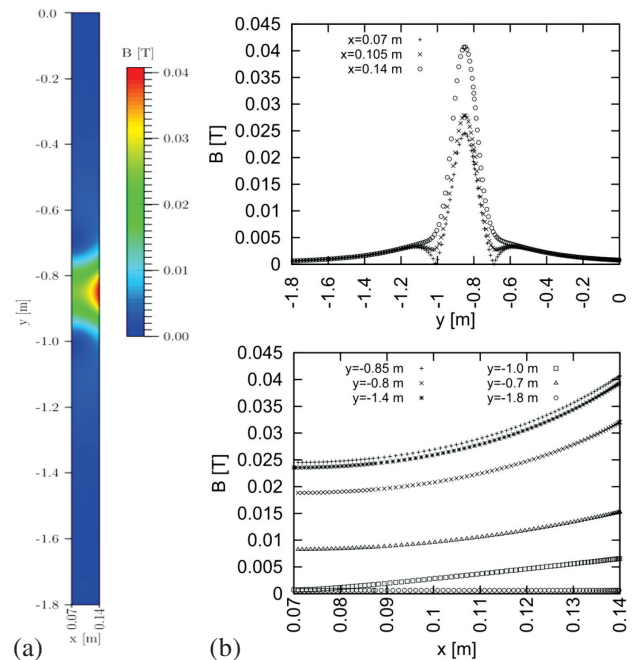


Figure 11: Magnetic field of parallel coils configuration with iron core: a) contour plot, b) top: vertical cross-section of the magnetic field at 0.07 m, 0.125 m and 0.14 m, b) bottom: horizontal cross-sections at -0.7 m, -0.8 m, -0.85 m, -1.0 m, -1.4 m and -1.8 m

Slika 11: Magnetno polje paralelne postavitve tuljav z železnim jedrom: a) konture magnetnega polja, b) zgoraj: navpični prerez magnetnega polja pri 0,07 m, 0,125 m in 0,14 m, b) spodaj: vodoravni prerez magnetnega polja pri -0,7 m, -0,8 m, -0,85 m, -1,0 m, -1,4 m in -1,8 m

4.2 EMBR for the continuous casting of steel

First the magnetic field in the strand for a default coil configuration with 25 windings in the x direction, 11 windings in the y direction, an electric current of 50 A, and a span distance of 0.05 m is calculated. The results are shown in **Figure 11**. The effect of this magnetic field is then investigated for the velocity, temperature and concentration fields. To better present the effect of the magnetic field the results are compared to the example without a magnetic field, as can be seen in **Figures 12 to 14**.

The effect of magnetic field on temperature is shown in **Figure 12**. The application of EMBR to the continuous casting of steels lowers the temperature throughout the mold. The lowering of the temperatures is the most apparent in the mold region.

In **Figure 13** a contour plot of the velocity field is shown together with several representative, both vertical and horizontal, cross-sections. The calculations confirm that the application of a magnetic field affects the velocity field. In the case of a parallel coil arrangement of the EMBR, the magnetic field slows down the velocity and diminishes the recirculation zones.

Finally, the effect of applying the EMBR to the continuous casting of steel is investigated for the concentration field. The results of the calculations are shown in **Figure 14**, from which it can be confirmed that the

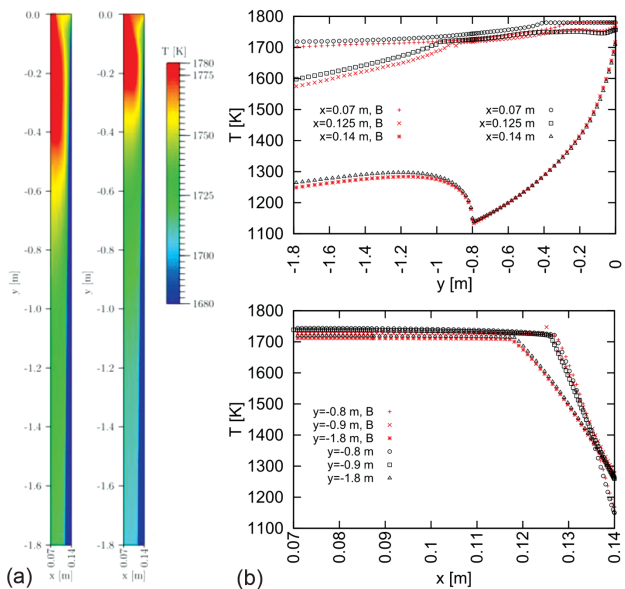


Figure 12: a) The velocity contour plots for configuration without (left) and with (right) a magnetic field, b) top: comparison of vertical cross-sections for velocities with and without magnetic field at 0.07 m, 0.125 m and 0.14 m, b) bottom: comparison of horizontal cross-sections for velocities with and without magnetic field at 0.8 m, 0.9 m and 1.8 m

Slika 12: a) Konture hitrostnega polja za konfiguracijo z magnetnim poljem (levo) in brez njega (desno), b) zgoraj: primerjava navpičnih prereзов hitrosti z magnetnim poljem in brez njega pri 0,07 m, 0,125 m in 0,14 m, b) spodaj: primerjava vodoravnih prereзов hitrosti z magnetnim poljem in brez njega pri 0,8 m, 0,9 m in 1,8 m

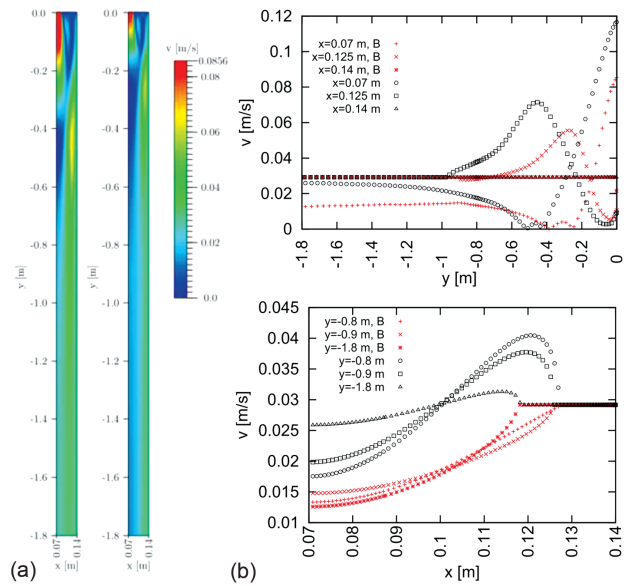


Figure 13: a) The temperature contour plots for configuration without (left) and with (right) magnetic field, b) top: comparison of vertical cross-sections for temperatures with and without magnetic field at 0.07 m, 0.125 m and 0.14 m, b) bottom: comparison of horizontal cross-sections for temperatures with and without magnetic field at 0.8 m, 0.9 m and 1.8 m

Slika 13: a) Konture temperaturnega polja za konfiguracijo z magnetnim poljem (levo) in brez njega (desno), b) zgoraj: primerjava navpičnih prereзов temperature z magnetnim poljem in brez njega pri 0,07 m, 0,125 m in 0,14 m, b) spodaj: primerjava vodoravnih prereзов temperature z magnetnim poljem in brez njega pri 0,8 m, 0,9 m in 1,8 m

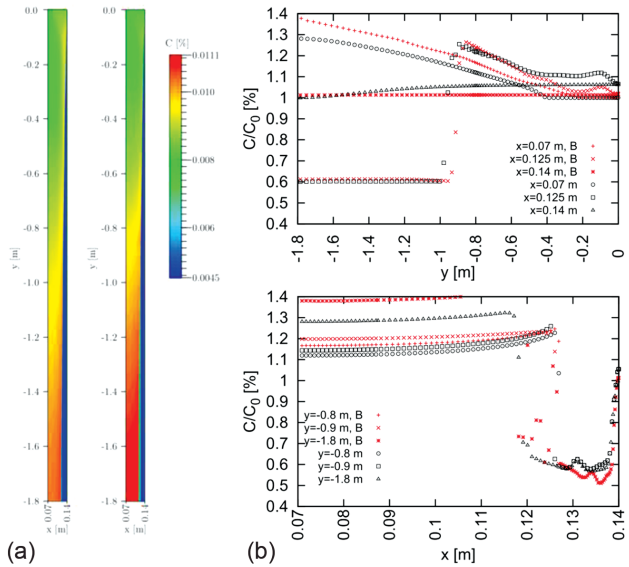


Figure 14: a) The concentration contour plots for configuration without (left) and with (right) magnetic field, b) top: comparison of vertical cross-sections for concentration with and without magnetic field at 0.07 m, 0.125 m and 0.14 m, b) bottom: comparison of horizontal cross-sections for concentration with and without magnetic field at 0.8 m, 0.9 m and 1.8 m

Slika 14: a) Konture koncentracijskega polja za konfiguracijo z magnetnim poljem (levo) in brez njega (desno), b) zgoraj: primerjava navpičnih prereзов koncentracije z magnetnim poljem in brez njega pri 0,07 m, 0,125 m in 0,14 m, b) spodaj: primerjava vodoravnih prereзов koncentracije z magnetnim poljem in brez njega pri 0,8 m, 0,9 m in 1,8 m

magnetic field affects the concentration. In present case, the binary mixture of carbon and iron is investigated for the mass fraction 0.08 % of carbon. It is shown that the magnetic field affects the pattern of the segregation in such a way that the levels of carbon are slightly decreased in the outer layers of the strand and increased in the middle of the strand.

5 CONCLUSIONS

In this paper, numerical calculations for electromagnetic braking in the continuous casting of steel are presented. The results, calculated with LRBFCM method, confirm that the application of a magnetic field affects the velocity of the fluid flow, as well as the temperature and species concentration. The present configuration of the coils produces a magnetic field that effectively slows down the velocity of the flow and decreases the temperature. It also affects the pattern of segregation in such a way that the concentration of carbon is decreased in the middle of the strand. In the future, an alternating magnetic field will be applied in order to calculate the electromagnetic stirring.

Acknowledgements

The research in this paper was sponsored by Centre of Excellence for Biosensors, Instrumentation and Process Control (COBIK) and Slovenian Grant Agency under Programme group P2-0357: Modelling and Simulation of Materials and Processes and applied project L2-6775 Modelling of Industrial Solidification Systems under Influence of Electromagnetic Field. This paper forms a part of the doctoral study of the first author that is partly co-financed by the European Union and by the European Social Fund respectively. The co-financing is carried out within the Human resources development operational programme for years 2007–2013, 1. Developmental priorities: Encouraging entrepreneurship and adaptation; Preferential directives 1.3: Scholarship schemes.

6 REFERENCES

- ¹ W. R. Irwing, *Continuous Casting of Steel*, The Institute of Materials, London 1993
- ² *Steel Statistical Yearbook 2013*, World Steel Association, Brussels 2013
- ³ H. K. Versteeg, *An Introduction to Computational Fluid Dynamics: the Finite Volume Method*, Pearson Education, India 1995
- ⁴ B. Zhao, B. G. Thomas, S. P. Vanka, R. J. O'Malley, *Metallurgical and Materials Transactions B*, 36 (2005) 6, 801–823, doi:10.1007/s11663-005-0083-3
- ⁵ M. R. Aboutalebi, M. Hasan, R. I. L. Guthrie, *Metallurgical and Materials Transactions B*, 26 (1995) 4, 731–744, doi:10.1007/bf02651719
- ⁶ D. S. Kim, W. S. Kim, K. H. Cho, *Iron and Steel Institute of Japan International*, 40 (2000) 7, 670–676, doi:10.2355/isijinternational.40.670
- ⁷ K. G. Kang, H. S. Ryou, N. K. Hur, *Numer. Heat Tr. A*, 48 (2005) 5, 461–481, doi:10.1080/10407780590911639
- ⁸ N. Kubo, T. Ishii, J. Kubota, T. Ikagawa, *Iron and Steel Institute of Japan International*, 44 (2004) 3, 556–564, doi:10.2355/isijinternational.44.556
- ⁹ C. H. Moon, S. M. Hwang, *International Journal for Numerical Methods In Engineering*, 57 (2003), 315–339, doi:10.1002/nme.679
- ¹⁰ B. Šarler, R. Vertnik, *Computers and Mathematics with Applications*, 51 (2006), 1269–1282, doi:10.1016/j.camwa.2006.04.013
- ¹¹ D. C. Wilcox, *Turbulence modeling for CFD*, DCW Industries, Inc., California 1993
- ¹² W. D. Bennon, F. P. Incropera, *Numerical Heat Transfer Part A-Applications*, 13 (1988) 3, 277–296, doi:10.1080/10407788808913614
- ¹³ K. Abe, T. Kondoh, Y. Nagano, *International Journal of Heat and Mass Transfer*, 37 (1994), 139–151, doi:10.1016/0017-9310(94)90168-6
- ¹⁴ B. Šarler, R. Vertnik, K. Mramor, *IOP Conference Series: Materials Science and Engineering*, 33 (2012), 12012–12021, doi:10.1088/1757-899x/33/1/012012
- ¹⁵ A. Chorin, *Mathematical Computation*, 22 (1968), 745–762
- ¹⁶ M. D. Buchmann, *Radial Basis Function: Theory and Implementations*, Cambridge University Press, Cambridge 2003, doi:10.1017/cbo9780511543241
- ¹⁷ R. Franke, *Mathematics of Computation*, 38 (1982), 181–200, doi:10.1090/s0025-5718-1982-0637296-4
- ¹⁸ K. Mramor, R. Vertnik, B. Šarler, *Computer Modeling in Engineering & Science*, 92 (2013) 4, 327–352, doi:10.3970/cmescs.2013.092.327
- ¹⁹ K. Mramor, *Modelling of Continuous Casting of Steel under the Influence of Electromagnetic Field with Meshless Method*, dissertation, UNG, Nova Gorica, 2014, p. 244
- ²⁰ K. Mramor, R. Vertnik, B. Šarler, *Engineering Analysis with Boundary Elements*, 49 (2014), 37–47, doi:10.1016/j.engabound.2014.04.013
- ²¹ K. Mramor, R. Vertnik, B. Šarler, *Mater. Tehnol.*, 48 (2014) 2, 281–288

NON-SINGULAR METHOD OF FUNDAMENTAL SOLUTIONS FOR THREE-DIMENSIONAL ISOTROPIC ELASTICITY PROBLEMS WITH DISPLACEMENT BOUNDARY CONDITIONS

NESINGULARNA METODA FUNDAMENTALNIH REŠITEV ZA DEFORMACIJO TRIDIMENZIJSKIH ELASTIČNIH PROBLEMOV Z DEFORMACIJSKIMI ROBNIMI POGOJI

Qingguo Liu¹, Božidar Šarler^{1,2}

¹University of Nova Gorica, Vipavska 13, 5000 Nova Gorica, Slovenia
²Institute of Metals and Technology, Lepi pot 11, 1000 Ljubljana, Slovenia
Qingguo.Liu@ung.si, bozidar.sarler@imt.si

Prejem rokopisa – received: 2015-04-23; sprejem za objavo – accepted for publication: 2015-10-09

doi:10.17222/mit.2015.086

The purpose of the present paper is to develop the Non-Singular Method of Fundamental Solutions (NMFS) based on the boundary-distributed source method for three-dimensional elasticity problems with displacement boundary conditions. In the NMFS, the source points and the collocation points coincide and both are positioned on the boundary of the problem domain. In this case, the fundamental solution is singular. In order to remove the singularities of the fundamental solution, the concentrated point sources are replaced by the distributed sources over the sphere around the singularity. The values of the distributed sources are calculated directly in the case of displacement boundary conditions for isotropic problems. The performance of the novel approach is shown on two three-dimensional elastic problems with displacement boundary conditions. The method requires the discretization of the boundary only and shows excellent accuracy. It represents an efficient alternative to the classic numerical methods. The developments lead to the possibility of modelling micromechanical problems without the discretization of the interior of each of the grains, like required in classic numerical methods.

Keywords: linear isotropic elasticity, non-singular method of fundamental solutions, boundary meshless method

Namen članka je razvoj nesingularne metode fundamentalnih rešitev (NMFS) na podlagi robno distribuirane metode izvirov za tridimenzijske probleme linearne elastičnosti z deformacijskimi robnimi pogoji. V NMFS se izvorne in kolokacijske točke skladajo in so pozicionirane na robu obravnavanega območja. V tem primeru je fundamentalna rešitev singularna. Za odstranitev singularnosti fundamentalne rešitve so koncentrirani izviri nadomeščeni s porazdeljenimi izviri po krogli okoli singularnosti. Vrednosti porazdeljenih izvirov so neposredno izračunane pri Dirichletovih robnih pogojih za izotropne probleme. Značilnosti novega načina so prikazane na dveh primerih tridimenzijskih problemov z deformacijskimi robnimi pogoji. Metoda zahteva zgolj diskretizacijo roba in prikazuje odlično natančnost. Pomeni tudi učinkovito alternativo klasičnim numeričnim metodam. Opisani razvoj vodi do možnosti simulacije mikromehanskih problemov brez diskretizacije notranjosti zrn, kot je to potrebno pri klasičnih numeričnih metodah.

Ključne besede: linerna izotropna elastičnost, nesingularna metoda fundamentalnih rešitev, robna brez mrežna metoda

1 INTRODUCTION

The main idea of MFS¹ consists of approximating the solution of the partial differential equation by a linear combination of fundamental solutions, defined in source points. The expansion coefficients are calculated by collocation or a least-squares fit of the boundary conditions. The fundamental solution is usually singular in the source points and this is the reason why the source points are located outside the domain in the MFS. In this case, the original problem is reduced to determining the unknown coefficients of the fundamental solutions and the coordinates of the source points by requiring the approximation to satisfy the boundary conditions and hence solving a non-linear problem. If the source points are a priori fixed, then the coefficients of the MFS approximation are determined by solving a linear problem. The MFS has become very popular in recent years because of its simplicity²⁻⁵ and for 3D problems.^{6,7}

In the traditional MFS, a fictitious boundary, positioned outside the problem domain, is required to place the source points. This is very impractical or even impossible, particularly when solving multi-body problems. In recent years, various efforts have been made, with the aim being to remove this barrier in the MFS, so that the source points can be placed on the real boundary directly⁸⁻¹². In the present paper, we use a Non-Singular MFS based on⁸ to deal with the three-dimensional isotropic elasticity problems with displacement boundary condition. The application of a non-singular method of fundamental solutions (NMFS) in two-dimensional isotropic and anisotropic linear elasticity has been originally developed.¹³⁻¹⁵ We respectively used area-distributed sources covering the source points to replace the concentrated point sources. This NMFS approach also does not require any information about the neighboring points for each source point, thus it is a truly a meshfree

boundary method. The present developments are dedicated to enabling NMFS for solving three-dimensional micromechanical elasticity problems. This is of utmost importance in the simulation of an effective Young's modulus and Poisson's ratio for multigrain systems that appear in many engineering systems.

The rest of the paper is structured as follows. The governing equations are shown in matrix form. The solution procedure is given for MFS and NMFS. A three-dimensional example in two cases, translation and deformation, is given, followed by the conclusions and future research.

2 GOVERNING EQUATIONS

Consider a 3D domain Ω with the boundary Γ filled with isotropic elasticity materials. Let us introduce a 3D Cartesian coordinate system with the orthonormal base vectors $\mathbf{i}_x, \mathbf{i}_y$ and \mathbf{i}_z and the coordinates p_x, p_y and p_z of the position vector \mathbf{p} , i.e., $\mathbf{p} = p_x \mathbf{i}_x + p_y \mathbf{i}_y + p_z \mathbf{i}_z$. To simplify the calculations we shall assume that (i) the solid is free of body forces and (ii) the thermal strains can be neglected. Under these conditions the general equation of elasticity¹⁶ is:

$$C_{\zeta\xi v\tau} \frac{\partial^2 u_v(\mathbf{p})}{\partial p_\zeta \partial p_\tau} = 0, \quad \zeta, \xi, v, \tau = x, y, z \quad (1)$$

where u_v are the displacements, $C_{\zeta\xi v\tau}$ are the elastic stiffnesses and the components of a fourth rank stiffness tensor:¹⁷

$$\mathbf{C} = C_{\zeta\xi v\tau} \begin{bmatrix} C_{xxxx} & C_{xxyy} & C_{xxzz} & C_{xxyz} & C_{xxxz} & C_{xxxxy} \\ C_{xxyy} & C_{yyyy} & C_{yyzz} & C_{yyyz} & C_{xyzy} & C_{xyyy} \\ C_{xxzz} & C_{yyzz} & C_{zzzz} & C_{yzzz} & C_{xzzz} & C_{xyzz} \\ C_{xxyz} & C_{yyyz} & C_{yzzz} & C_{yzyz} & C_{xzyz} & C_{xyyz} \\ C_{xxxz} & C_{xzyy} & C_{xzzz} & C_{xzyz} & C_{xzxz} & C_{xyxz} \\ C_{xxxxy} & C_{xyyy} & C_{xyzz} & C_{xyyz} & C_{xyxz} & C_{xyxy} \end{bmatrix} = \begin{bmatrix} c_{11} & c_{12} & c_{13} & c_{14} & c_{15} & c_{16} \\ c_{12} & c_{22} & c_{23} & c_{24} & c_{25} & c_{26} \\ c_{13} & c_{23} & c_{33} & c_{34} & c_{35} & c_{36} \\ c_{14} & c_{24} & c_{34} & c_{44} & c_{45} & c_{46} \\ c_{15} & c_{25} & c_{35} & c_{45} & c_{55} & c_{56} \\ c_{16} & c_{26} & c_{36} & c_{46} & c_{56} & c_{66} \end{bmatrix} \quad (2)$$

In subsequent discussions, it will be convenient to write the equilibrium Equation (1) in matrix form as:

$$\begin{bmatrix} \frac{\partial}{\partial p_x} & 0 & 0 & \frac{\partial}{\partial p_y} & \frac{\partial}{\partial p_z} & 0 \\ 0 & \frac{\partial}{\partial p_y} & 0 & \frac{\partial}{\partial p_x} & 0 & \frac{\partial}{\partial p_z} \\ 0 & 0 & \frac{\partial}{\partial p_z} & 0 & \frac{\partial}{\partial p_x} & \frac{\partial}{\partial p_y} \end{bmatrix} \begin{bmatrix} \frac{\partial u_x}{\partial p_x} \\ \frac{\partial u_y}{\partial p_y} \\ \frac{\partial u_z}{\partial p_z} \\ \frac{\partial u_y}{\partial p_z} + \frac{\partial u_z}{\partial p_y} \\ \frac{\partial u_x}{\partial p_z} + \frac{\partial u_z}{\partial p_x} \\ \frac{\partial u_x}{\partial p_y} + \frac{\partial u_y}{\partial p_x} \end{bmatrix} = 0 \quad (3)$$

The stresses $\sigma_{\zeta\xi}$ are related to the strains through the generalized Hooke's law:

$$\boldsymbol{\sigma} = \mathbf{C}\boldsymbol{\varepsilon} \quad (4)$$

where $C_{\zeta\xi v\tau}$ satisfy the fully symmetrical conditions:

$$C_{\zeta\xi v\tau} = C_{\xi\zeta v\tau}, C_{\zeta\xi v\tau} = C_{\zeta\xi tv}, C_{\zeta\xi v\tau} = C_{v\tau\xi\xi} \quad (5)$$

$\boldsymbol{\varepsilon}$ is the strains vector:

$$\boldsymbol{\varepsilon} \equiv \begin{bmatrix} \varepsilon_{xx} \\ \varepsilon_{yy} \\ \varepsilon_{zz} \\ 2\varepsilon_{yz} \\ 2\varepsilon_{xz} \\ 2\varepsilon_{xy} \end{bmatrix} = \begin{bmatrix} \frac{\partial u_x}{\partial p_x} \\ \frac{\partial u_y}{\partial p_y} \\ \frac{\partial u_z}{\partial p_z} \\ \frac{\partial u_y}{\partial p_z} + \frac{\partial u_z}{\partial p_y} \\ \frac{\partial u_x}{\partial p_z} + \frac{\partial u_z}{\partial p_x} \\ \frac{\partial u_x}{\partial p_y} + \frac{\partial u_y}{\partial p_x} \end{bmatrix} \quad (6)$$

3 SOLUTION PROCEDURE

The fundamental solution for the isotropic elasticity is given¹⁸ in three dimensions (3D) by:

$$U_{\zeta\xi}(\mathbf{p}, \mathbf{s}) = \frac{1}{16\pi\mu(1-\nu)r} \left\{ (3-4\nu)\delta_{\zeta\xi} + \frac{(p_\zeta - s_\zeta)(p_\xi - s_\xi)}{r^2} \right\}, \quad \zeta, \xi = x, y, z \quad (7)$$

where $U_{\zeta\xi}(\mathbf{p}, \mathbf{s})$ represents the displacement in the direction ζ at point \mathbf{p} due to a unit point force acting in the direction ξ at point \mathbf{s} . $r = [(p_x - s_x)^2 + (p_y - s_y)^2 + (p_z - s_z)^2]^{1/2}$ is the distance between the point \mathbf{p} and the source point \mathbf{s} . Equation (7) is expanded as follows:

$$\begin{aligned}
 U_{xx} &= \frac{1}{16\pi\mu(1-\nu)r} \left[(3-4\nu) + \frac{(p_x - s_x)^2}{r^2} \right] \\
 U_{yy} &= \frac{1}{16\pi\mu(1-\nu)r} \left[(3-4\nu) + \frac{(p_y - s_y)^2}{r^2} \right] \\
 U_{zz} &= \frac{1}{16\pi\mu(1-\nu)r} \left[(3-4\nu) + \frac{(p_z - s_z)^2}{r^2} \right] \\
 U_{xy} = U_{yx} &= \frac{1}{16\pi\mu(1-\nu)r} \frac{(p_x - s_x)(p_y - s_y)}{r^2} \\
 U_{xz} = U_{zx} &= \frac{1}{16\pi\mu(1-\nu)r} \frac{(p_x - s_x)(p_z - s_z)}{r^2} \\
 U_{yz} = U_{zy} &= \frac{1}{16\pi\mu(1-\nu)r} \frac{(p_y - s_y)(p_z - s_z)}{r^2}
 \end{aligned} \tag{8}$$

It can be shown that the following u_x , u_y and u_z satisfy the governing Equations (3):

$$u_x(\mathbf{p}) = U_{xx}(\mathbf{p}, \mathbf{s})\alpha + U_{xy}(\mathbf{p}, \mathbf{s})\beta + U_{xz}(\mathbf{p}, \mathbf{s})\gamma \tag{9}$$

$$u_y(\mathbf{p}) = U_{yx}(\mathbf{p}, \mathbf{s})\alpha + U_{yy}(\mathbf{p}, \mathbf{s})\beta + U_{yz}(\mathbf{p}, \mathbf{s})\gamma \tag{10}$$

$$u_z(\mathbf{p}) = U_{zx}(\mathbf{p}, \mathbf{s})\alpha + U_{zy}(\mathbf{p}, \mathbf{s})\beta + U_{zz}(\mathbf{p}, \mathbf{s})\gamma \tag{11}$$

where α , β and γ represent arbitrary constants. The fundamental solution $U_{\zeta\xi}(\mathbf{p}, \mathbf{s})$ is singular when $\mathbf{p} = \mathbf{s}$. We use the desingularization technique, proposed by Liu⁸ for evaluating the singular values. We modify his approach in a sense of preserving the original fundamental solution at all the points except the singularity, and by scaling the singularity with the area of the sphere over which the desingularization integration is performed. This allows us to treat the MFS and the NMFS in formally the same way. The desingularization (transformation of $U_{\zeta\xi}(\mathbf{p}, \mathbf{s})$ into $\tilde{U}_{\zeta\xi}(\mathbf{p}, \mathbf{s})$) is thus performed in the following way:

$$\tilde{U}_{\zeta\xi}(\mathbf{p}, \mathbf{s}) = \begin{cases} U_{\zeta\xi}(\mathbf{p}, \mathbf{s}) & r > R \\ \frac{1}{\pi R^2} \int_{A(\mathbf{s}, R)} U_{\zeta\xi}(\mathbf{p}, \mathbf{s}) dA & r \leq R \end{cases} \tag{12}$$

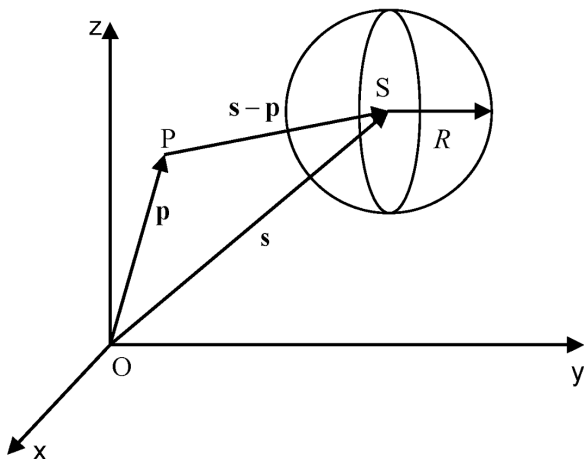


Figure 1: Distributed source on a sphere $A(\mathbf{s}, R)$ with radius R
 Slika 1: Porazdeljeni izviri na krogli $A(\mathbf{s}, R)$ z radijem R

where $A(\mathbf{s}, R)$ represents a sphere with radius R , centered around \mathbf{s} . The involved integrals can be calculated as follows (by using the integration in polar coordinates $p_x - s_x = r \sin\varphi \cos\theta$, $p_y - s_y = r \sin\varphi \sin\theta$ and $p_z - s_z = r \cos\varphi$, **Figure 1**):

$$\begin{aligned}
 \tilde{U}_{xx}(\mathbf{p}, \mathbf{p}) = \tilde{U}_{yy}(\mathbf{p}, \mathbf{p}) = \tilde{U}_{zz}(\mathbf{p}, \mathbf{p}) &= \frac{5-6\nu}{16\pi\mu(1-\nu)R} \\
 \tilde{U}_{xy}(\mathbf{p}, \mathbf{p}) = \tilde{U}_{yx}(\mathbf{p}, \mathbf{p}) &= 0 \\
 \tilde{U}_{xz}(\mathbf{p}, \mathbf{p}) = \tilde{U}_{zx}(\mathbf{p}, \mathbf{p}) &= 0 \\
 \tilde{U}_{yz}(\mathbf{p}, \mathbf{p}) = \tilde{U}_{zy}(\mathbf{p}, \mathbf{p}) &= 0
 \end{aligned} \tag{13}$$

It can also be shown that the following u_x , u_y and u_z satisfy the governing Equations (3):

$$u_x(\mathbf{p}) = \tilde{U}_{xx}(\mathbf{p}, \mathbf{s})\alpha + \tilde{U}_{xy}(\mathbf{p}, \mathbf{s})\beta + \tilde{U}_{xz}(\mathbf{p}, \mathbf{s})\gamma \tag{14}$$

$$u_y(\mathbf{p}) = \tilde{U}_{yx}(\mathbf{p}, \mathbf{s})\alpha + \tilde{U}_{yy}(\mathbf{p}, \mathbf{s})\beta + \tilde{U}_{yz}(\mathbf{p}, \mathbf{s})\gamma \tag{15}$$

$$u_z(\mathbf{p}) = \tilde{U}_{zx}(\mathbf{p}, \mathbf{s})\alpha + \tilde{U}_{zy}(\mathbf{p}, \mathbf{s})\beta + \tilde{U}_{zz}(\mathbf{p}, \mathbf{s})\gamma \tag{16}$$

The solution of the problem is sought in the form:

$$\begin{aligned}
 u_x(\mathbf{p}) &= \sum_{n=1}^N \tilde{U}_{xx}(\mathbf{p}, \mathbf{p}_n) \alpha_n + \sum_{n=1}^N \tilde{U}_{xy}(\mathbf{p}, \mathbf{p}_n) \beta_n + \\
 &+ \sum_{n=1}^N \tilde{U}_{xz}(\mathbf{p}, \mathbf{p}_n) \gamma_n
 \end{aligned} \tag{17}$$

$$\begin{aligned}
 u_y(\mathbf{p}) &= \sum_{n=1}^N \tilde{U}_{yx}(\mathbf{p}, \mathbf{p}_n) \alpha_n + \sum_{n=1}^N \tilde{U}_{yy}(\mathbf{p}, \mathbf{p}_n) \beta_n + \\
 &+ \sum_{n=1}^N \tilde{U}_{yz}(\mathbf{p}, \mathbf{p}_n) \gamma_n
 \end{aligned} \tag{18}$$

$$\begin{aligned}
 u_z(\mathbf{p}) &= \sum_{n=1}^N \tilde{U}_{zx}(\mathbf{p}, \mathbf{p}_n) \alpha_n + \sum_{n=1}^N \tilde{U}_{zy}(\mathbf{p}, \mathbf{p}_n) \beta_n + \\
 &+ \sum_{n=1}^N \tilde{U}_{zz}(\mathbf{p}, \mathbf{p}_n) \gamma_n
 \end{aligned} \tag{19}$$

The coefficients α_n , β_n and γ_n are calculated from a system of $3N$ algebraic equations:

$$\mathbf{Ax} = \mathbf{b} \tag{20}$$

where \mathbf{A} stands for a $3N \times 3N$ matrix with the entries A_{ij} , \mathbf{x} is a $3N \times 1$ vector with the entries x_i , and \mathbf{b} is a $3N \times 1$ vector with entries b_i :

$$\begin{aligned}
 A_{ij} &= \tilde{U}_{xx}(\mathbf{p}_i, \mathbf{p}_j), \quad A_{i(N+j)} = \tilde{U}_{xy}(\mathbf{p}_i, \mathbf{p}_j) \\
 A_{i(2N+j)} &= \tilde{U}_{xz}(\mathbf{p}_i, \mathbf{p}_j), \quad A_{(N+i)j} = \tilde{U}_{yx}(\mathbf{p}_i, \mathbf{p}_j) \\
 A_{(N+i)(N+j)} &= \tilde{U}_{yy}(\mathbf{p}_i, \mathbf{p}_j), \quad A_{(N+i)(2N+j)} = \tilde{U}_{yz}(\mathbf{p}_i, \mathbf{p}_j) \\
 A_{(2N+i)j} &= \tilde{U}_{zx}(\mathbf{p}_i, \mathbf{p}_j), \quad A_{(2N+i)(N+j)} = \tilde{U}_{zy}(\mathbf{p}_i, \mathbf{p}_j) \\
 A_{(2N+i)(2N+j)} &= \tilde{U}_{zz}(\mathbf{p}_i, \mathbf{p}_j), \quad i, j = 1, 2, \dots, N
 \end{aligned} \tag{21}$$

$$x_i = \alpha_i, \quad x_{(N+i)} = \beta_i, \quad x_{(2N+i)} = \gamma_i, \quad i = 1, 2, \dots, N \tag{22}$$

$$b_i = u_x(\mathbf{p}_i), \quad b_{(N+i)} = u_y(\mathbf{p}_i), \quad b_{(2N+i)} = u_z(\mathbf{p}_i), \quad i = 1, 2, \dots, N \tag{23}$$

By knowing all the elements A_{ij} and b_i of the system (20), we can determine the values of x_i (i.e., α_n, β_n and γ_n). Afterwards, we can calculate the solution of the governing equation from:

$$u_\zeta(\mathbf{p}) = \sum_{n=1}^N \tilde{U}_{\zeta x}(\mathbf{p}, \mathbf{p}_n) \alpha_n + \sum_{n=1}^N \tilde{U}_{\zeta y}(\mathbf{p}, \mathbf{p}_n) \beta_n + \sum_{n=1}^N \tilde{U}_{\zeta z}(\mathbf{p}, \mathbf{p}_n) \gamma_n, \quad \zeta = x, y, z \tag{24}$$

where \mathbf{p} is any point inside the domain or on the boundary.

4 NUMERICAL EXAMPLES

We consider a cube with the side length $a = 2$ m centered around $p_x = 0$ m, $p_y = 0$ m, $p_z = 0$ m. The elastic media is defined by $E = 1$ N/m², $\nu = 0.3$.

4.1 Translation

We consider a solution of the governing equations in this cube subject to the boundary conditions $\bar{u}_x = 2$ m, $\bar{u}_y = 2$ m, $\bar{u}_z = 2$ m. The analytical solution is:

$$u_x = 2 \text{ m}, \quad u_y = 2 \text{ m}, \quad u_z = 2 \text{ m}, \tag{25}$$

A plot of the translation, obtained with the analytical solution and the numerical solutions with MFS and NMFS, is shown in **Figure 2** for the case with 150 nodes (25 nodes on each side of the cube). The distance of the fictitious boundary from the true boundary for the MFS is set $R_M = 5d$, where d is the smallest distance between two nodes on the boundary. The radius of the sphere for the distributed area source covering each node is set to $R = d/3$.

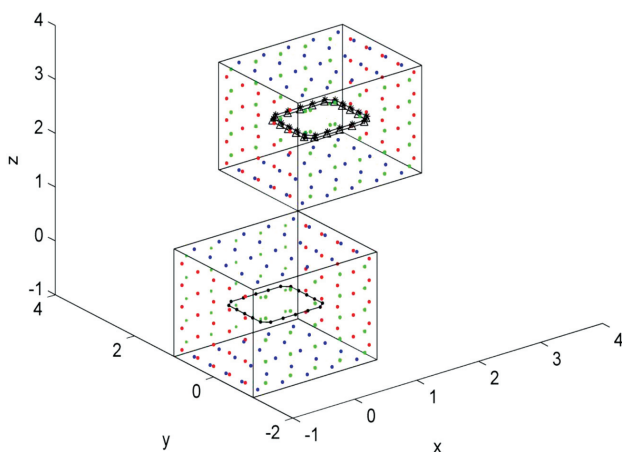


Figure 2: The analytical solution and the numerical solution of MFS and NMFS for the translation case with $N = 150$, $R = d/3$, $R_M = 5d$ (•: collocation points, +: analytical solution, x: MFS solution, Δ: NMFS solution)

Slika 2: Analitična in numerična rešitev z MFS in NMFS za translacijski primer z $N = 150$, $R = d/3$, $R_M = 5d$ (•: kolokacijske točke, +: analitična rešitev, x: MFS rešitev, Δ: NMFS rešitev)

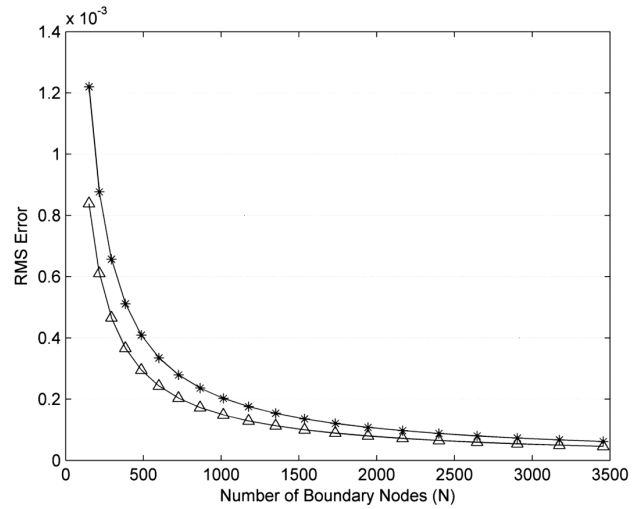


Figure 3: The relationship between the RMS errors and the number of boundary nodes for translation case, calculated by NMFS. $R = d/3$ (+: e_x , x: e_y , Δ: e_z).

Slika 3: Odvisnost med RMS-napakami in številom robnih točk za translacijski primer, izračunan z NMFS. $R = d/3$ (+: e_x , x: e_y , Δ: e_z).

The solution of the points on a square with the side length $a = 1$ m centered around $p_x = 0$ m, $p_y = 0$ m, $p_z = 0$ m on the plane $p_z = 0$ are computed and compared with the analytical solutions. The root-mean-square (RMS) errors of the numerical solution are defined as:

$$e_\zeta = \sqrt{\frac{1}{N} \sum_{n=1}^N (u_{\zeta n} - u_{\zeta n}^a)^2}, \quad \zeta = x, y \tag{26}$$

Table 1: RMS errors of NMFS solutions for the translation case with $R = d/3$

Tabela 1: RMS-napake NMFS-rešitev za translacijski primer z $R = d/3$

Num. of boundary nodes (N)	$e_x(\times 10^{-3})$	$e_y(\times 10^{-3})$	$e_z(\times 10^{-3})$
150	1.2200	1.2200	0.8390
216	0.8769	0.8769	0.6109
294	0.6570	0.6570	0.4658
384	0.5112	0.5112	0.365
486	0.4091	0.4091	0.2950
600	0.3348	0.3348	0.2428
726	0.2791	0.2791	0.2033
864	0.2363	0.2363	0.1727
1014	0.2026	0.2026	0.1485
1176	0.1757	0.1757	0.1291
1350	0.1538	0.1538	0.1132
1536	0.1357	0.1357	0.1001
1734	0.1207	0.1207	0.0891
1944	0.1080	0.1080	0.0799
2166	0.0973	0.0973	0.0720
2400	0.0880	0.0880	0.0652
2646	0.0800	0.0800	0.0594
2904	0.0731	0.0731	0.0543
3174	0.0670	0.0670	0.0498
3456	0.0617	0.0617	0.0459

where u_{zk} and $u_{zk}(\zeta = x, y)$ are the analytical and the numerical solutions, respectively. The number of boundary nodes used is from 150 to 3 456.

Figure 3 shows the RMS errors of the results obtained using the NMFS. The errors are already less than 10^{-3} with $N = 216$ and the solution converges to the analytical solution with an increasing number of nodes (Table 1). The MFS result is shown in Table 2 for $R_M = 5d$. Here it should be noted that the MFS solution error is relatively small; however, the convergence is not uniform. This fact is due to the choice of the artificial boundary position, which was for all node arrangements $R_M = 5d$ and thus most probably not optimally varying.

Table 2: RMS errors of MFS solutions for the translation case with $R_M = 5d$

Tabela 2: RMS- napake MFS-rešitev za translacijski primer z $R_M = 5d$

Num. of boundary nodes (N)	$e_x(\times 10^{-14})$	$e_y(\times 10^{-14})$	$e_z(\times 10^{-14})$
150	0.2204	0.2204	0.5548
216	1.7907	1.7907	4.8854
294	0.0364	0.0364	0.0794
384	0.1590	0.1590	0.1617
486	0.0348	0.0348	0.0017
600	0.0058	0.0058	0.0015
726	0.1103	0.1102	0.1631
864	0.0004	0.0004	0.0001
1014	0.0475	0.0445	0.0478
1176	0.0033	0.0050	0.0025
1350	0.0005	0.0003	0.0010
1536	0.0038	0.0295	0.0238
1734	0.0000	0.0000	0.0000
1944	0.0000	0.0000	0.0000
2166	0.0004	0.0004	0.0006
2400	0.0000	0.0000	0.0000
2646	0.0000	0.0000	0.0000
2904	0.0000	0.0000	0.0000
3174	0.0000	0.0001	0.0000
3456	0.0000	0.0000	0.0000

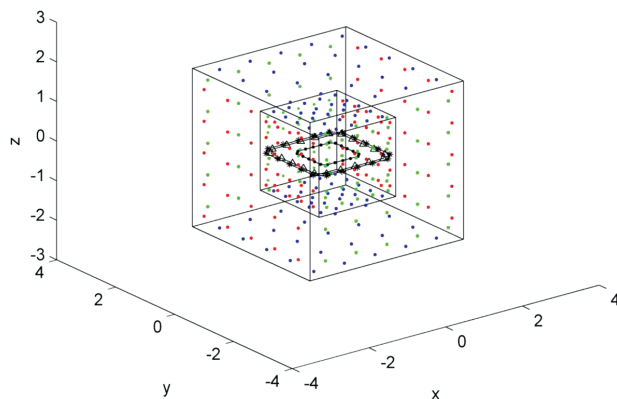


Figure 4: The analytical solution and the numerical solution of MFS and NMFS for the deformation case with $N = 150, R = d/3, R_M = 5d$ (*: collocation points, +: analytical solution, x: MFS solution, Δ: NMFS solution)

Slika 4: Analitična in numerična rešitev z MFS in NMFS za deformacijski primer z $N = 150, R = d/3, R_M = 5d$ (*: kolokacijske točke, +: analitična rešitev, x: MFS rešitev, Δ: NMFS rešitev)

4.2 Deformation

We consider a solution of the governing equations in this cube subject to the boundary conditions $\bar{u}_x = p_x, \bar{u}_y = p_y, \bar{u}_z = p_z$. The analytical solution is:

$$u_x = p_x, u_y = p_y, u_z = p_z \tag{27}$$

A plot of the deformation, obtained with the analytical solution and the numerical solutions with MFS and NMFS, is shown in Figure 4 for the case with 150 nodes

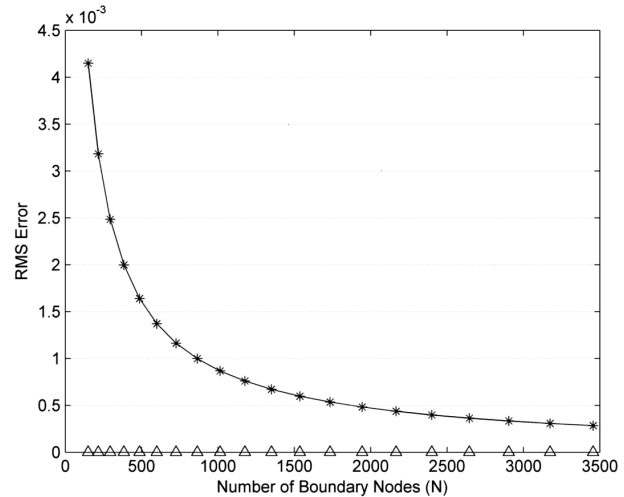


Figure 5: The relationship between the RMS errors and the number of boundary nodes for the deformation case, calculated by NMFS. $R=d/3$ (+: e_x , x: e_y , Δ: e_z).

Slika 5: Odvisnost med RMS- napakami in številom robnih točk za deformacijski primer, izračunan z NMFS. $R = d/3$ (+: e_x , x: e_y , Δ: e_z).

Table 3: RMS errors of the NMFS solutions for the deformation case with $R=d/3$

Tabela 3: Odvisnost med RMS- napakami in številom robnih točk za deformacijski primer, izračunan z NMFS, $R = d/3$

Num. of boundary nodes (N)	$e_x(\times 10^{-3})$	$e_y(\times 10^{-3})$	$e_z(\times 10^{-3})$
150	4.1487	4.1487	0.0000
216	3.1826	3.1826	0.0000
294	2.4837	2.4837	0.0000
384	1.9972	1.9972	0.0000
486	1.6395	1.6395	0.0000
600	1.3703	1.3703	0.0000
726	1.1623	1.1623	0.0000
864	0.9983	0.9983	0.0000
1014	0.8667	0.8667	0.0000
1176	0.7596	0.7596	0.0000
1350	0.6711	0.6711	0.0000
1536	0.5973	0.5973	0.0000
1734	0.5350	0.5350	0.0000
1944	0.4820	0.4820	0.0000
2166	0.4365	0.4365	0.0000
2400	0.3971	0.3971	0.0000
2646	0.3629	0.3629	0.0000
2904	0.3329	0.3329	0.0000
3174	0.3064	0.3064	0.0000
3456	0.2830	0.2830	0.0000

(25 nodes on each side of the cube). The same R and R_M as with example 4.1 are used.

Figure 5 shows the RMS errors of the results obtained using the NMFS and the solution converges to the analytical solution with an increasing number of nodes (**Table 3**). The MFS results are shown in **Table 4** for $R_M = 5d$.

Table 4: RMS errors of the MFS solutions for the deformation case with $R_M = 5d$

Tabela 4: RMS-napake MFS-rešitev za deformacijski primer $R_M = 5d$

Num. of boundary nodes (N)	$e_x(\times 10^{-11})$	$e_y(\times 10^{-11})$	$e_z(\times 10^{-11})$
150	0.1410	0.1410	0.0000
216	0.0256	0.0256	0.0000
294	0.0018	0.0018	0.0000
384	0.0012	0.0012	0.0000
486	0.0014	0.0014	0.0000
600	2.1088	2.1088	0.0000
726	0.0010	0.0010	0.0000
864	0.0001	0.0001	0.0000
1014	0.0000	0.0000	0.0000
1176	0.0000	0.0000	0.0000
1350	0.0010	0.0008	0.0019
1536	0.0000	0.0002	0.0001
1734	0.0000	0.0000	0.0000
1944	0.0002	0.0001	0.0001
2166	0.0005	0.0005	0.0008
2400	0.0000	0.0000	0.0000
2646	0.0000	0.0000	0.0000
2904	0.0000	0.0000	0.0000
3174	0.0000	0.0000	0.0000
3456	0.0000	0.0000	0.0000

5 CONCLUSION

A new, non-singular method of fundamental solutions¹³ is extended in the present paper to solve 3D linear elasticity problems. In this approach, the singular values of the fundamental solution are integrated over a small sphere, so that the coefficients in the system of equations can be evaluated analytically and consistently, leading to an extremely simple computer implementation of this method. The method essentially gives similar results as the classic MFS. It has the advantage that the artificial boundary is not present; however, the problems with the traction boundary condition have not yet been solved. The main advantage of the method is that the discretisation is performed only on the boundary of the domain and no polygonisation is needed, like in the finite-element method. The NMFS, presented in this paper, can be adapted or extended to handle many related problems, such as anisotropic elasticity, and multi-body problems, which all represent directions for our further investigations. The advantage of not having to generate the

artificial boundary is particularly welcome in these types of problems. The method will be used in the future for the calculation of 3D engineering deformation problems in steel and aluminium alloys, with realistic grain shapes, obtained from microscope images. The developed method is believed to represent the simplest state-of-the-art way to numerically cope with these types of problems.

Acknowledgement

This paper forms a part of the project L2-6775 Simulation of industrial solidification processes under influence of electromagnetic fields. This work was partially performed within the Creative Core program (AHA-MOMENT) contract no. 3330-13-500031, co-supported by RSMIZS and European Regional Development Fund Research.

6 REFERENCES

- C. S. Chen, A. Karageorghis, Y. S. Smyrlis, *The Method of Fundamental Solutions - A Meshless Method*, Dynamic Publishers, Atlanta 2008
- V. D. Kupradze, *Ž. Vyčisl. Mat. i Mat. Fiz.*, 4 (1964), 1118–1121
- V. D. Kupradze, M. A. Aleksidze, *Methods Math. Phys.*, 4 (1964), 82–126, doi:10.1016/0041-5553(64)90006-0
- A. Poullikkas, A. Karageorghis, G. Georgiou, *Computers & Structures*, 80 (2002), 365–370, doi:10.1016/S0045-7949(01)00174-2
- Y. S. Smyrlis, *Mathematics of Computation*, 78 (2009), 1399–1434, doi:10.1090/S0025-5718-09-02191-7
- D. Redekop, R. S. W. Cheung, *Comput Struct*, 26 (1987), 703–707, doi:10.1016/0045-7949(87)90017-4
- G. S. A. Fam, Y. F. Rashed, *Engineering Analysis with Boundary Elements*, 33 (2009), 330–341, doi:10.1016/j.enganabound.2008.07.002
- Y. J. Liu, *Engineering Analysis with Boundary Elements*, 34 (2010), 914–919, doi:10.1016/j.enganabound.2010.04.008
- B. Šarler, *Engineering Analysis with Boundary Elements*, 33 (2009), 1374–1382, doi:10.1016/j.enganabound.2009.06.008
- D. L. Young, K. H. Chen, J. T. Chen, J. H. Kao, *CMES: Computer Modeling in Engineering & Sciences*, 19 (2007), 197–222, doi:10.3970/cmcs.2007.019.197
- D. L. Young, K. H. Chen, C. W. Lee, *Journal of Computational Physics*, 209 (2005), 290–321, doi:10.1016/j.jcp.2005.03.007
- W. Chen, F. Z. Wang, *Engineering Analysis with Boundary Elements*, 34 (2010), 530–532, doi:10.1016/j.enganabound.2009.12.002
- Q. G. Liu, B. Šarler, *CMES: Computer Modeling in Engineering and Sciences*, 91 (2013), 235–266, doi:10.3970/cmcs.2013.091.235
- Q. G. Liu, B. Šarler, *Mater. Tehnol.*, 47 (2013) 6, 789–793
- Q. G. Liu, B. Šarler, *Engineering Analysis with Boundary Elements*, 45 (2014), 68–78, doi:10.1016/j.enganabound.2014.01.020
- A. F. Bower, *Applied Mechanics of Solids*, CRC Press, USA Florida 2009
- T. C. T. Ting, *Anisotropic Elasticity*, Oxford Science Publications, Oxford 1996
- M. H. Aliabadi, *The Boundary Element, Applications in Solids and Structures*, 2ed, John Wiley & Sons, Chichester 2006

SOLID-STATE SINTERING OF $(K_{0.5}Na_{0.5})NbO_3$ SYNTHESIZED FROM AN ALKALI-CARBONATE-BASED LOW-TEMPERATURE CALCINED POWDER

SINTRANJE V TRDNEM KERAMIKE $(K_{0.5}Na_{0.5})NbO_3$, SINTETIZIRANE IZ NIZKOTEMPERATURNO KALCINIRANEGA PRAHU, PRIPRAVLJENEGA NA OSNOVI ALKALIJSKIH KARBONATOV

Mahdi Feizpour¹, Touradj Ebadzadeh¹, Darja Jenko²

¹Department of Ceramic Engineering, Materials and Energy Research Center, P.O. Box 31787-316, Karaj, Alborz, Iran

²Institute of Metals and Technology, Lepi pot 11, 1000 Ljubljana, Slovenia
m-feizpour@merc.ac.ir, iusteng@gmail.com

Prejem rokopisa – received: 2015-10-10; sprejem za objavo – accepted for publication: 2015-10-19

doi:10.17222/mit.2015.315

Potassium sodium niobate $K_{0.5}Na_{0.5}NbO_3$ (KNN) was synthesized by the double calcination of a homogenized mixture of potassium and sodium carbonates and niobium pentoxide for 4 h at 625 °C. The calcination temperature was chosen on the basis of the thermal analyses of the mixture of precursors, where the weight loss being the function of the temperature reaches the plateau. The calcined powder was investigated by X-ray Diffraction (XRD) and Transmission Electron Microscopy (TEM) and was found to be without unreacted materials or secondary phases. Before sintering, the powder compacts were annealed for 4 h at 450 °C, while the sintering was carried out for 2 h at 1115 °C using two different configurations: 1) in a closed crucible where the KNN pellets were in close physical proximity to, but not in direct contact with, the KNN packing powder, and 2) in a completely open crucible without any packing powder. The Archimedes' density of the sintered samples was 91.5 % of theoretical density for the first configuration, while it was 93.4 % for the second configuration. The Field-Emission Scanning Electron Microscopy (FE-SEM) and XRD analyses of the sintered ceramics showed that by using a calcination temperature as low as 625 °C a typical sintered microstructure of KNN could be achieved with both sintering configurations.

Keywords: potassium sodium niobate, low-temperature calcination, solid-state synthesis, sintering, microstructure

Keramiko kalij-natrijevega niobata $K_{0.5}Na_{0.5}NbO_3$ (KNN) smo sintetizirali z dvojno kalcinacijo homogenizirane zmesi kalijevega in natrijevega karbonata ter niobijevega oksida 4 h pri temperaturi 625 °C. Temperaturo kalcinacije smo izbrali glede na termično analizo mešanice prekurzorjev, kjer se izguba mase v odvisnosti od temperature ni več spreminjala in je dosegla plato. Kalciniran prah smo preiskovali z rentgensko fazno analizo (XRD) in presevno elektronsko mikroskopijo (TEM), ki sta pokazali, da prah ne vsebuje nezreagiranih materialov ali sekundarnih faz. Stisnjene tablete kaciniranega prahu so bile pred sintranjem segrevane 4 h pri 450 °C, samo sintranje pa je potekalo 2 h pri 1115 °C z uporabo dveh različnih konfiguracij: 1) v zaprtem lončku, kjer so bile tablete KNN v neposredni fizični bližini, a ne v neposrednem stiku z zasipom KNN in 2) v popolnoma odprtem lončku brez zasipa. Povprečna Arhimedova gostota sintranih vzorcev je bila za prvo konfiguracijo 91,5 % teoretične gostote, medtem ko je bila za drugo konfiguracijo 93,4 %. Vrstična elektronska mikroskopija z emisijo polja (FE-SEM) in analiza XRD sintrane keramike sta pokazali, da lahko že pri nižji temperaturi kalciniranja 625 °C dosežemo tipično sintrano mikrostrukturo KNN za obe konfiguraciji sintranja.

Ključne besede: kalij-natrijev niobat, nizkotemperaturna kalcinacija, sinteza v trdnem stanju, sintranje, mikrostruktura

1 INTRODUCTION

Pb-based piezoceramics are the main group of piezoelectric materials with high electromechanical properties.¹ However, with the beginning of the 21st Century, some legislation was imposed to limit the fabrication and usage of substances that contain lead, due to its toxicity, and to develop environmentally friendlier replaceable materials.² During the past 15 years, different families of known lead-free piezoelectrics were restudied and several attempts were focused on obtaining functional properties close to those of the lead-based piezoelectrics.³⁻⁵

Among the different groups of lead-free piezoelectric ceramics, the potassium sodium niobate $K_{0.5}Na_{0.5}NbO_3$ [KNN] family is a widely investigated candidate for the replacement of $Pb(Zr,Ti)O_3$ and the other lead-based

piezoelectric ceramics, mainly due to its fair electromechanical properties, high Curie point and its compatibility with base-metal electrodes like Ni.⁶⁻¹⁴ Dealing with KNN-based materials involves some difficulties, mainly concerning the preservation of the stoichiometry during the powder synthesis and the sintering of the powder compact, because of the high potential of the alkali elements for evaporation, especially at elevated temperatures.^{15,16}

Up to now, numerous studies have been conducted on maximizing the piezoelectric response of pure and/or doped KNN-based lead-free piezoelectric ceramics. However, since the major and cheapest source for providing alkali elements for the synthesis of KNN is alkali carbonates of Na_2CO_3 and K_2CO_3 , the calcination of the homogenized KNN precursors is an important step

in the solid-state synthesis of KNN. The most widely used temperatures for the calcination of KNN from the alkali carbonates are in the range between 750 °C and 950 °C.⁹ But as Popovic et al.¹⁶ have thermodynamically shown, the vapor pressure of alkali elements over the respective niobates increases by 4 to 5 orders of magnitudes when increasing the temperature from 627 °C to 927 °C. This makes the low-temperature calcination process an easy solution to overcome the off-stoichiometry problem for the synthesized KNN powder due to the evaporation of the alkali elements at elevated temperatures. On the other hand, using lower calcination temperatures may lead to powders with a lower crystallinity and still-unreacted precursors. Based on the literature and the best of our knowledge, up to now, the lowest temperature of synthesis for KNN powder from a Na_2CO_3 , K_2CO_3 and Nb_2O_5 mixture was 700 °C.¹⁷ The aim of this study is to explore whether this temperature can be even more reduced and the sintered properties of samples still remain good enough or not.

2 MATERIALS AND METHODS

Na_2CO_3 (99.95–100.05 % purity), K_2CO_3 (99+ % purity) and Nb_2O_5 (99.9 % purity), all from Sigma-Aldrich, Germany, were dried overnight at 200 °C and weighed according to the $K_{0.5}Na_{0.5}NbO_3$ stoichiometry in a dry-box and homogenized in a PM-400 Retsch planetary mill for 4 h at 175 r/min using 125 mL grinding zirconia jar and zirconia balls (3 mm in diameter) and 99.8 % purity acetone as the medium. The homogenized mixture of KNN precursors (hereafter, HOM powder) was dried for 1 h at 90 °C and at least 2 h at 200 °C and stored in a desiccator.

Differential Thermal Analysis (DTA) and Thermo-Gravimetry (TG) of the HOM powder were recorded from 200 °C to 750 °C with a heating rate of 10 °C/min by means of a Netzsch STA 409 C/CD under a constant flow rate of 100 cm³/min of dried synthetic air. Prior to the measurement, the sample was isothermally held for 3 h at 200 °C. In addition, the dimensional changes vs. the temperature of the HOM and calcined powder compact (100 MPa, uniaxial press) were recorded from 200 °C to 1200 °C with a heating rate of 5 °C/min under synthetic air using a Leitz optical dilatometry. The X-ray Diffraction (XRD) patterns of the calcined powders and the crushed sintered pellets were recorded at room temperature using a PANalytical X'Pert PRO MPD diffractometer with $Cu-K\alpha_1$ radiation of 0.15406 nm in the 2θ range 10–90 ° with a step of 0.017 ° and an integration time of 200 s.

The particle size distribution of the calcined powder was analyzed with a Microtrac S3500 static light-scattering particle size analyzer. The specific surface area of the calcined powder was analyzed by nitrogen adsorption/desorption at –196 °C (BET method, Belsorp-mini II) using an automated gas-adsorption analyzer. Prior to the measurement, the powders were degassed under vacuum for 2 h at 250 °C. The morphology, crystal structure and

elemental composition of the calcined powder were observed and analyzed with a High-Resolution Transmission Electron Microscope (HR-TEM – JEOL JEM-2100) using an accelerating voltage 200 kV with an attached Energy-Dispersive X-ray Spectrometer EDS (JEOL JED-2300 Series) and a Scanning Transmission Electron Microscope (STEM) unit with a Bright-Field (BF) detector (EM-24511SIOD, JEOL).

After the calcination process, the powders were compacted at 200 MPa using a cold isostatic press. Before sintering, the powder compacts were annealed for 4 h at 450 °C in order to remove the adsorbed moisture and CO_2 from the powder before the sintering process started. The sintering was carried out for 2 h at 1115 °C using two different configurations: 1) in a closed, double-crucible (high-purity alumina, total volume: \approx 16 cm³) where the KNN pellets were put in a small Pt crucible (volume: \approx 2 cm³), which was surrounded by KNN packing powder (2.5 g, after the first calcination at 800 °C), hereafter the CC/wPP configuration, and 2) in a completely open crucible where the KNN pellets were put in a small Pt crucible without using any packing powder, hereafter the OC/woPP configuration. The density of the sintered ceramics was measured based on Archimedes' principle using the ASTM C373 standard and reported as an average value of three measurements. The sintered pellets were cut, mounted, and polished using standard ceramography techniques and finished with 3 μ m and 1/4 μ m diamond-paste polishes. The microstructure of the sintered ceramics was characterized using a Field-Emission Scanning Electron Microscope (FE-SEM – JEOL JSM-7600F). Prior to the analysis, the samples were coated with a thin layer of carbon.

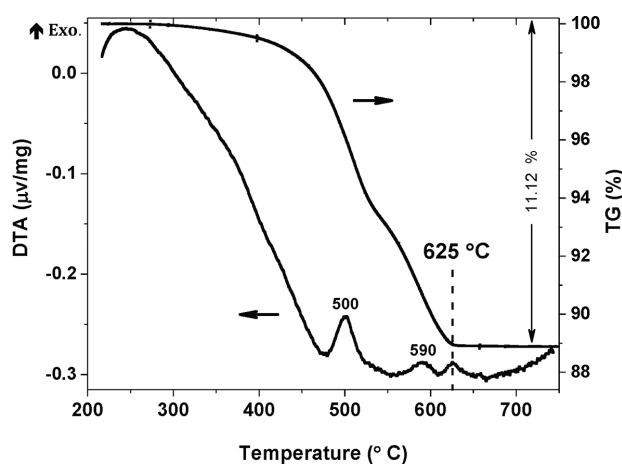


Figure 1: DTA/TG thermal analyses curves of the homogenized mixture of KNN precursors (the HOM powder)

Slika 1: Krivulji termične analize DTA/TG homogenizirane zmesi prekurzorjev KNN (prah HOM)

3 RESULTS AND DISCUSSION

3.1 Synthesis of the KNN powder at a low calcination temperature

The DTA/TG thermal analyses of the HOM powder are shown in **Figure 1**. There is a pronounced exothermic peak around 500 °C, which is accompanied by a sharp weight loss in this temperature region, which is related to the decomposition of the alkali carbonates and also to the formation of the $(K,Na)_2Nb_4O_{11}$ intermediate phase and the KNN perovskite phase from the precursors. However, there are still two minor exothermic peaks at 590 °C and 625 °C, which can be attributed to the completion of the synthesis and the final formation of KNN.^{18,19} According to the TG curve, the amount of weight loss is almost zero above 625 °C. In addition, this temperature coincides with the last exothermic DTA peak.

To further explore the possible low calcination temperature, optical dilatometry of the HOM powder was performed, which is shown in **Figure 2**. The expansion started from 390 °C and it underwent a large expansion of $\approx 26\%$ by heating the powder compact further from 495 °C to 625 °C. Again, the temperature of 625 °C became an important temperature since the dimensional change of the sample reached a plateau at 625 °C. The dimension of the powder compact stayed constant up to 910 °C and underwent a shrinkage of $\approx 3\%$ during heating to 940 °C.

According to the thermal analyses of the HOM powder and the dimensional changes of the HOM powder compact, 625 °C was chosen as a possible temperature for the calcination of the KNN precursors at low temperature. The HOM powder was calcined two times for 4 h with a heating rate of 5 °C/min at 625 °C with an intermediate and final milling step similar to the homogenization process.

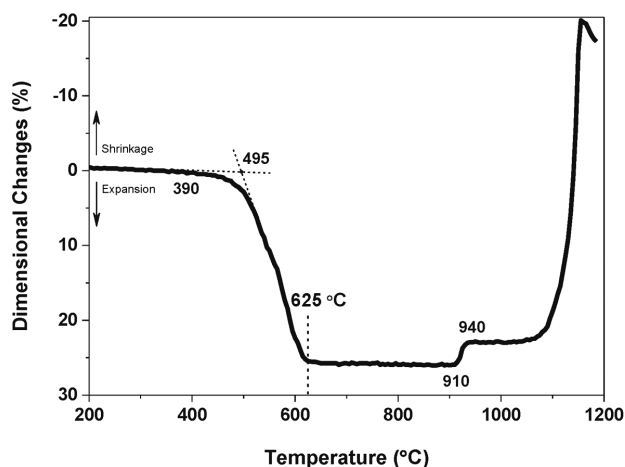


Figure 2: Dimensional changes of the powder compact of the homogenized mixture of the KNN precursors (the HOM powder)

Slika 2: Spremembe dimenzij stisnjene tabletko iz homogenizirane zmesi prekurzorjev KNN (prah HOM)

XRD patterns of the KNN calcined powders after the first and second calcinations at 625 °C are shown in **Figure 3**. For comparison, the patterns of the HOM powder that was calcined for 4 h at 800 °C and the HOM powder that was held for only 30 min at the sintering temperature of KNN, i.e., 1115 °C, are also shown in **Figure 3**. It is clear that all the peaks in these patterns can be indexed as the KNN perovskite phase and, based on the detection limit of the XRD technique, there is no trace of secondary phases or unreacted precursors in the patterns of the first and second calcined KNN powders at 625 °C. By increasing the calcination temperatures, the peaks sharpened and split, which are indications of the more homogenous structures and the growth of the crystallites.

The densification behavior of the double-calcined KNN powder at 625 °C and subsequently milled is shown in **Figure 4**. There is no change in the dimensions of the powder compact until 895 °C, but similar to the HOM powder, it again underwent a small shrinkage of $\approx 2\%$ during heating from 895 °C to 925 °C. We tried to decode the reason for such behavior at this temperature region and it is also a topic of another of our papers that will be published soon. However, the powder compact underwent a large shrinkage due to the sintering process, which started from ≈ 1090 °C and finally, it melted at 1150 °C. This narrow sintering window is typical for KNN-based ceramics and it is not related to the calcination temperature of the KNN.^{20,21} In the inset of **Figure 4**, the particle size distribution of the double-calcined KNN powder at 625 °C and subsequently milled is shown. The d_{10} , d_{50} and d_{90} of this powder are 0.19 μm , 0.41 μm and 0.82 μm , respectively, and the powder has a unimodal distribution. The specific surface area of this powder was 18.0 m^2/g .

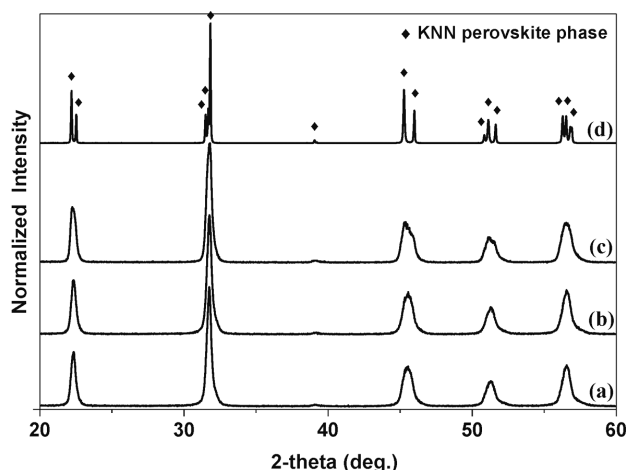


Figure 3: XRD patterns of KNN powder after: a) first calcination for 4 h at 625 °C, b) double calcination for 4 h at 625 °C, c) first calcination for 4 h at 800 °C, d) holding for 30 min at the sintering temperature of KNN (1115 °C)

Slika 3: Rentgenogram prahov KNN po: a) prvi kalcinaciji 4 h pri 625 °C, b) dvakratni kalcinaciji 4 h pri 625 °C, c) prvi kalcinaciji 4 h pri 800 °C in d) segrevanju 30 min pri temperaturi sintranja KNN (1115 °C)

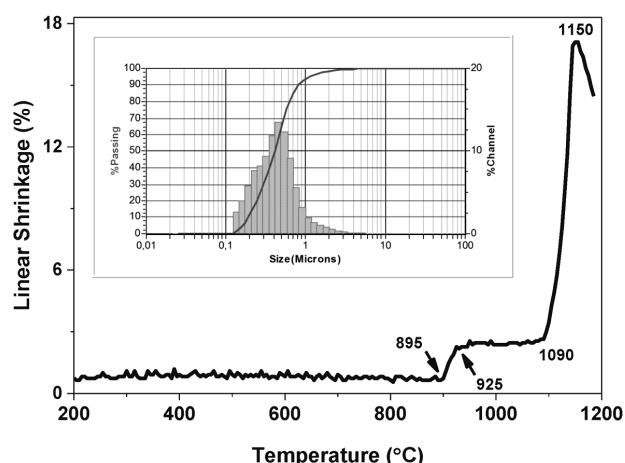


Figure 4: Densification behavior of double-calcined KNN powder for 4 h at 625 °C and subsequently milled recorded by optical dilatometry. Inset shows the particle size distribution of this powder.

Slika 4: Potek zgoščevanja dvakrat kalciniranega in mletega prahu KNN 4 h pri 625 °C, dobljen z uporabo optične dilatometrije. Vstavljena slika prikazuje porazdelitev velikosti delcev tega prahu.

The morphology, crystallite size, crystal structure and elemental composition of the double calcined KNN powder at 625 °C and subsequently milled is shown in **Figure 5**. The lower-magnification TEM BF image revealed that the calcined powder was agglomerated (**Figure 5a**). The powder was composed of agglomerates of around 500–700 nm or smaller, and of individual particles as small as 20 nm or larger (**Figure 5c**). A Selected-Area Electron Diffraction (SAED) pattern, taken from the dashed-line circled area and included as the inset in **Figure 5a**, shows a characteristic diffraction of a ring pattern with relatively continuous rings, which means the crystallites are small, in the nm range, and in a random orientation. The SAED pattern contains some brighter and more distinct spots in the rings, which indicates the presence of some larger crystallites. The electron-diffraction spots can be described by a perovskite phase with indices as shown in the inset image of **Figure 5a**.

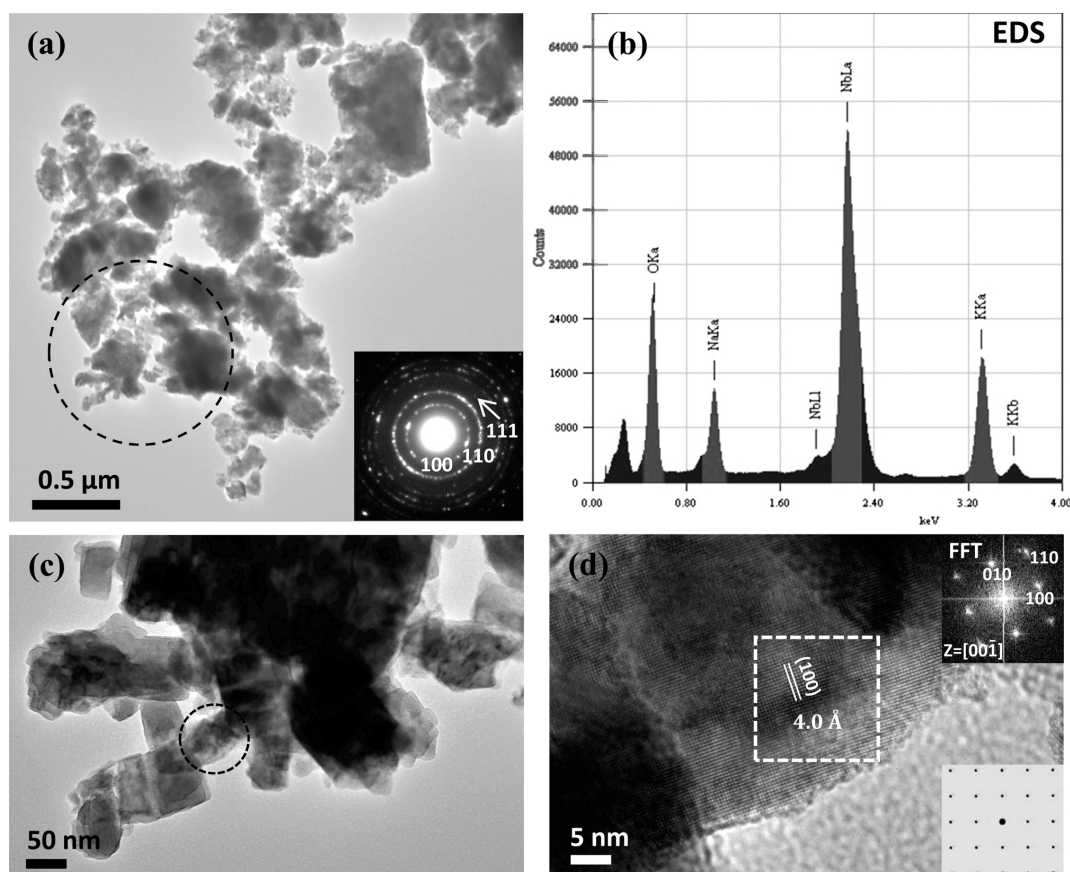


Figure 5: a) Lower magnification TEM BF image of the morphology and crystallite size of the double-calcined KNN powder at 625 °C and subsequently milled with the SAED pattern of the selected dashed-line circled area included as the inset, and b) typical EDS spectrum from the same selected dashed-line circled area in **Figure a**. c) Higher magnification TEM BF and d) HR-TEM images of this powder. From the selected dashed-line circled area of the TEM BF image, the HR-TEM image was taken. From the dashed-line circled area in the HR-TEM image, the 2D FFT and simulation image were calculated and included as the insets.

Slika 5: a) Posnetek TEM v svetlem polju (BF) pri nizki povečavi prikazuje morfologijo in velikost kristalinitov dvakrat kalciniranega in mletega prahu KNN pri 625 °C z vključeno sliko uklonskega posnetka (SAED) iz izbranega obkroženega področja in b) značilno kemijsko analizo z rentgensko spektroskopijo (EDS) iz istega izbranega obkroženega področja na **sliki a**; c) posnetek TEM BF in d) visokoločljivostna slika (HR-TEM) pri višji povečavi istega prahu. Iz označenega črtkano krožnega mesta na sliki TEM BF je bil narejen posnetek HR-TEM. Iz izbranega črtkano kvadratnega področja na sliki HR-TEM sta bili izračunani vstavljene sliki 2D hitre Fourierjeve transformacije (FFT) in simulacija.

The elemental composition was determined with EDS. A typical EDS spectrum of a selected analysis of KNN powder from the dashed-line circled area in **Figure 5a** is shown in **Figure 5b**. The analyses confirmed the presence of Nb, Na, K and O in ratios close to the KNN stoichiometry. An observation at higher magnification

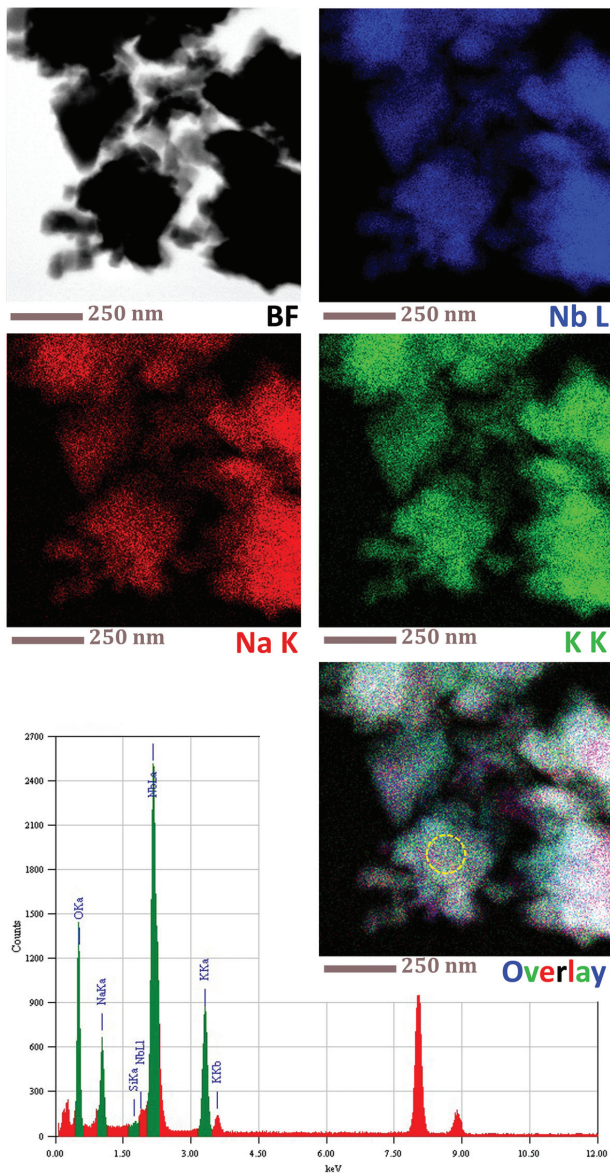


Figure 6: STEM/EDS elemental mapping of the double-calcined KNN powder at 625 °C and subsequently milled with EDS spectrum of the selected dashed-line circled area shown in the overly STEM image. Unmarked peaks at 8.04 keV and 8.90 keV belong to the $Cu-K\alpha_1$ and $K\beta_1$ characteristic X-rays, respectively, which came from the Cu TEM grid that was used as a sample holder.

Slika 6: Površinska kemijska analiza z rentgensko spektroskopijo (STEM/EDS) dvakrat kalciniranega in mletega prahu KNN pri 625 °C s spektrom EDS iz izbranega obkroženega področja, prikazanega na prekrivni sliki STEM. Neoznačeni vrhovi pri 8,04 keV in 8,90 keV pripadajo $Cu-K\alpha_1$ in $K\beta_1$ karakterističnim rentgenskim žarkom, ki izvirajo iz Cu-mrežice TEM, in ki je bila uporabljena kot nosilec vzorca.

(**Figure 5c**) revealed particles with cuboidal shapes, which is typical for KNN powders.

The HR-TEM image with a 2D Fast Fourier Transform (FFT) inset (**Figure 5d**) shows a small KNN particle at an atomic resolution in the $[00-1]$ zone axis. The simulated image in the inset of **Figure 5d** shows the position of the atoms in the $[00-1]$ zone axis and corresponds to the FFT image calculated from the experimental HR-TEM image. The measured distance between the atoms from the HR-TEM image in the (100) direction is 0.40 nm, which is in very good agreement with the cell parameters of the KNN.²²

STEM/EDS elemental mapping of the double-calcined KNN powder at 625 °C and subsequently milled is shown in **Figure 6**, with a distribution of the important comparable elements of Nb, Na and K and their overlay. The analysis nicely showed a homogeneous distribution of all three elements in the range of the detection limit of the EDS. As shown in the EDS spectrum, in some areas a small amount of Si was also detected. However, this

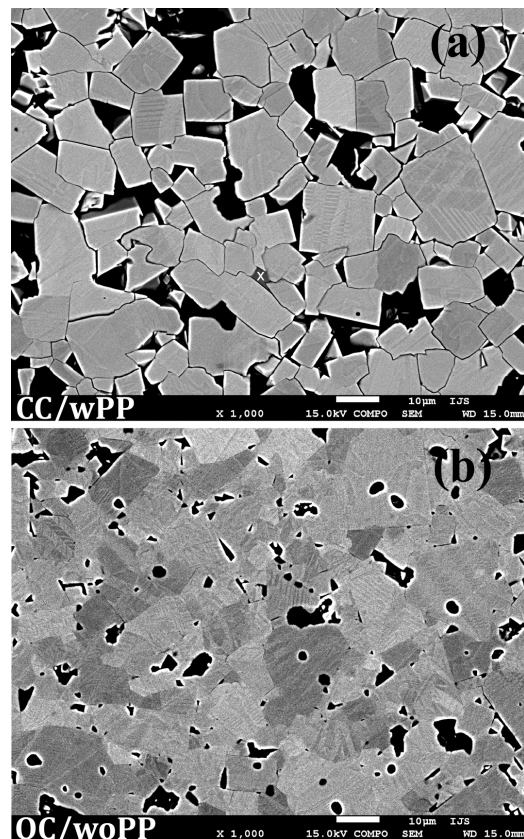


Figure 7: Orientation-contrast SEM images of a polished surface of KNN ceramics sintered under two different configurations: a) closed crucible with KNN packing powder – CC/wPP and b) open crucible without KNN packing powder – OC/wOPP. The × sign in **Figure a** marks a Si-containing grain with a stoichiometry close to $K_6Nb_6Si_4O_{26}$.

Slika 7: Posnetki SEM v načinu orientacijskega kontrasta poliranih površin keramike KNN, sintrane pri dveh različnih konfiguracijah: a) zaprt lonček z zasipom KNN – CC/wPP in b) odprt lonček brez zasipa KNN – OC/wOPP. Znak × na **sliki a** označuje zrno, ki vsebuje Si, katerega sestava je blizu $K_6Nb_6Si_4O_{26}$.

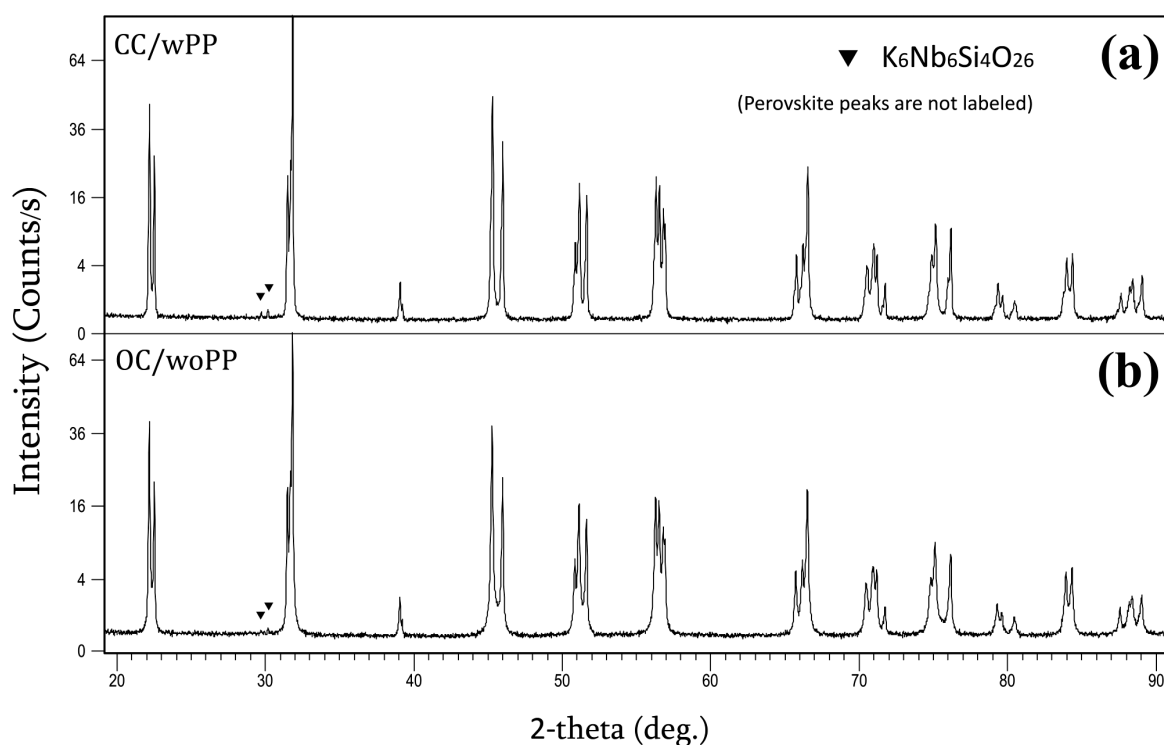


Figure 8: XRD patterns of ceramics sintered under two different configurations: a) closed crucible with KNN packing powder – CC/wPP and b) open crucible without KNN packing powder – OC/woPP

Slika 8: Rentgenogram keramike KNN, sintrane pri dveh različnih konfiguracijah: a) zaprt lonček z zasipom KNN – CC/wPP in b) odprt lonček brez zasipa KNN – OC/woPP

amount is very low for the exact characterization and its determination.

3.2 Sintering of the 625 °C-calcined KNN powder

The relative density of the ceramics sintered under the CC/wPP and OC/woPP configurations were 91.5 % and 93.4 %, respectively. **Figure 7** shows the orientation-contrast SEM images of the polished surface of the KNN ceramics sintered under the two different configurations mentioned above. The percentages of porosity, which are visible as black areas in the images, were evaluated using ImageTool version 3.00 software and measured approximately as 17.5 % and 6.5 % for the samples sintered under CC/wPP and OC/woPP configurations, respectively. Some grains may have been pulled out, which typically happens during the grinding and polishing of KNN-based ceramics. Therefore, these values are not necessarily representative of the amount of porosity in the bulk ceramics. Apart from the percentages of the porosity, the shapes of the grains are also different in these two microstructures. The CC/wPP configuration mainly resulted in cuboidal grains with plane grain boundaries, whereas the OC/woPP configuration led to almost non-polyhedral grain shapes with intragranular porosities. According to Acker et al.²³ more faceted grains can be achieved for the KNN with the amount fraction 2 % excess on the A-site. Later on, they explained that for stoichiometric KNN the excess alkali

elements from the packing powder atmosphere drives the ceramic composition towards the A-site excess regime and consequently away from the ideal stoichiometric conditions for sintering dense materials.²⁴ This may explain why using packing powder for the suppression of the evaporation of alkali elements during sintering may cause the density of the ceramic to be even lower than the density of the unprotected sample.²⁵ This contradicts the popular belief about the sintering of KNN-based ceramics and raises an interesting question on the use of KNN packing powder, to what extent the addition of an alkali-rich atmosphere during sintering is beneficial for the properties of KNN-based ceramics? In addition, based on our observations, the weight losses of samples during the sintering process were significantly similar for both sintering configurations.

Figure 8 shows the XRD patterns of ceramics sintered under different sintering configurations of CC/wPP and OC/woPP. Though the KNN powder was calcined only at 625 °C and, thus, has a lower crystallinity and homogeneity compared to the usual higher-calcination-temperature powders, both sintered ceramics have highly crystalline and homogenous structures. All the main peaks can be indexed as the KNN perovskite phase with a monoclinic structure.²² However, in both patterns, a trace of a secondary phase was found at around $2\theta \approx 30^\circ$. These two extra visible peaks, which are not related to the KNN perovskite phase, are in a very good accordance with the main peaks of $K_6Nb_6Si_4O_{26}$ with JCPDS

card number 01-072-0558. The existence of a Si-containing phase was also proved in the compositional analyses of the sintered samples from both sintering configurations. For example, the grain which is marked with × in **Figure 7a** represents a phase with the following atomic stoichiometry for Na : K : Nb : Si : O as (0.47 : 13.34 : 15.09 : 9.11 : 62.00) %, which matches very well with the nominal atomic stoichiometry of K₆Nb₆Si₄O₂₆, i.e., (14.29 : 14.29 : 9.52 : 61.90) %.

4 CONCLUSIONS

For the first time, 625 °C is suggested as the possible low-calcination temperature for the solid-state synthesis of K_{0.5}Na_{0.5}NbO₃ from an alkali-carbonates source. A microstructural analysis of the KNN sample processed from double-calcined KNN powder at 625 °C shows that a typical microstructure of KNN, otherwise processed with higher calcination temperatures (≈ 800 °C), can be achieved. The sintering of KNN in an open-crucible setup without using packing powder contributed to a higher density. A trace of K₆Nb₆Si₄O₂₆ secondary phase was found in the SEM and XRD of sintered samples, but its origin requires further investigation.

Acknowledgement

The authors would like to dedicate this paper to the memory of the late Professor Marija Kosec on the third anniversary of her death, 23rd Dec.

This work was financially supported by Ministry of Science, Research and Technology of Iran with the grant No. 38-1392-063 from Materials and Energy Research Center. In addition, the support of Jožef Stefan Institute – Electronic Ceramics Department (K5) and Institute of Metals and Technology (IMT), both from Ljubljana, Slovenia, is greatly appreciated. The contributions of Mohammad Ali Bahrevar, Alireza Aghaei, Andreja Benčan Golob, Tadej Rojac, Goran Dražić, Jurij Koruza, Katarina Vojisavljević, Julian Walker, Jernej Pavlič, Jitka Hreščak, Tina Bakarič, Marko Vrabelj, Andraž Bradeško, Maja Makarovič, Jerca Praprotnik, Tina Rucigaj, Jena Cilenšek, Silvo Drnovšek, Edi Kranjc and Maja Koblar are much appreciated. Special thanks from Mahdi go to Prof. Barbara Malič, the head of K5, for her kind and generous hosting at K5 during the visiting research period of 2014, and to Assist. Prof. Matjaž Godec, the director of IMT, for his special attention to the TEM investigations and our mutual cooperation.

5 REFERENCES

- B. Jaffe, W. R. Cook, H. Jaffe, *Piezoelectric Ceramics*, Academic Press, New York 1971
- European Parliament, Directive 2002/95/EU of the European Parliament and of the Council of 27 January 2003 on the restriction of the use of certain hazardous substances in electrical and electronic equipment, *Official Journal of the European Union*, L37 (2003), 19–23
- T. Shrout, S. Zhang, Lead-free piezoelectric ceramics: Alternatives for PZT?, *Journal of Electroceramics*, 19 (2007) 1, 111–124, doi:10.1007/s10832-007-9095-5
- J. Rödel, W. Jo, K. T. P. Seifert, E. M. Anton, T. Granzow, D. Damjanovic, Perspective on the development of lead-free piezoceramics, *Journal of the American Ceramic Society*, 92 (2009) 6, 1153–1177, doi:10.1111/j.1551-2916.2009.03061.x
- D. Damjanovic, N. Klein, J. Li, V. Porokhonsky, What can be expected from lead-free piezoelectric materials?, *Functional Materials Letters*, 3 (2010) 1, 5–13, doi:10.1142/S1793604710000919
- Y. Saito, H. Takao, T. Tani, T. Nonoyama, K. Takatori, T. Homma, T. Nagaya, M. Nakamura, Lead-free piezoceramics, *Nature*, 432 (2004) 7013, 84–87, doi:10.1038/nature03028
- D. Jenko, A. Benčan, B. Malič, J. Holc, M. Kosec, Electron microscopy studies of potassium sodium niobate ceramics, *Microscopy and Microanalysis*, 11 (2005) 6, 572–580, doi:10.1017/S1431927605050683
- R. Zuo, J. Rödel, R. Chen, L. Li, Sintering and electrical properties of lead-free Na_{0.5}K_{0.5}NbO₃ piezoelectric ceramics, *Journal of the American Ceramic Society*, 89 (2006) 6, 2010–2015, doi:10.1111/j.1551-2916.2006.00991.x
- B. Malič, A. Benčan, T. Rojac, M. Kosec, Lead-free piezoelectrics based on alkaline niobates: Synthesis, sintering and microstructure, *Acta Chimica Slovenica*, 55 (2008) 4, 719–726
- K. Shinichiro, K. Masahiko, H. Yukio, T. Hiroshi, (K,Na)NbO₃-based multilayer piezoelectric ceramics with nickel inner electrodes, *Applied Physics Express*, 2 (2009) 11, 111401, doi:10.1143/APEX.2.111401
- M. Kosec, B. Malič, A. Benčan, T. Rojac, J. Tellier, Alkaline niobate-based piezoceramics: Crystal structure, synthesis, sintering and microstructure, *Functional Materials Letters*, 3 (2010) 1, 15–18, doi:10.1142/S1793604710000865
- J. F. Li, K. Wang, F. Y. Zhu, L. Q. Cheng, F. Z. Yao, (K, Na)NbO₃-based lead-free piezoceramics: Fundamental aspects, processing technologies, and remaining challenges, *Journal of the American Ceramic Society*, 96 (2013) 12, 3677–3696, doi:10.1111/jace.12715
- J. Rödel, K. G. Webber, R. Dittmer, W. Jo, M. Kimura, D. Damjanovic, Transferring lead-free piezoelectric ceramics into application, *Journal of the European Ceramic Society*, 35 (2015) 6, 1659–1681, doi:10.1016/j.jeurceramsoc.2014.12.013
- J. Wu, D. Xiao, J. Zhu, Potassium–sodium niobate lead-free piezoelectric materials: Past, present, and future of phase boundaries, *Chemical Reviews*, 115 (2015) 7, 2559–2595, doi:10.1021/cr5006809
- A. B. Haugen, F. Madaro, L. P. Bjørkeng, T. Grande, M. A. Einarsrud, Sintering of sub-micron K_{0.5}Na_{0.5}NbO₃ powders fabricated by spray pyrolysis, *Journal of the European Ceramic Society*, 35 (2015) 5, 1449–1457, doi:10.1016/j.jeurceramsoc.2014.11.011
- A. Popovic, L. Bencze, J. Koruza, B. Malič, Vapour pressure and mixing thermodynamic properties of the KNbO₃-NaNbO₃ system, *RSC Advances*, 5 (2015) 93, 76249–76256, doi:10.1039/C5RA11874C
- X. Vendrell, J. E. García, X. Bril, D. A. Ochoa, L. Mestres, G. Dezanneau, Improving the functional properties of (K_{0.5}Na_{0.5})NbO₃ piezoceramics by acceptor doping, *Journal of the European Ceramic Society*, 35 (2015) 1, 125–130, doi:10.1016/j.jeurceramsoc.2014.08.033
- B. Malič, A. Kupec, M. Kosec, Thermal Analysis, In: T. Schneller, R. Waser, M. Kosec, D. Payne (Eds.), *Chemical Solution Deposition of Functional Oxide Thin Films*, Springer, Vienna 2013, 163–179, doi:10.1007/978-3-211-99311-8_7
- B. Malič, D. Jenko, J. Holc, M. Hrovat, M. Kosec, Synthesis of sodium potassium niobate: A diffusion couples study, *Journal of the American Ceramic Society*, 91 (2008) 6, 1916–1922, doi:10.1111/j.1551-2916.2008.02376.x
- M. Kosec, D. Kolar, On activated sintering and electrical properties of NaNbO₃, *Materials Research Bulletin*, 10 (1975) 5, 335–339, doi:10.1016/0025-5408(75)90002-1

- ²¹ J. Hreščak, A. Benčan, T. Rojac, B. Malič, The influence of different niobium pentoxide precursors on the solid-state synthesis of potassium sodium niobate, *Journal of the European Ceramic Society*, 33 (2013) 15–16, 3065–3075, doi:10.1016/j.jeurceramsoc.2013.07.006
- ²² J. Tellier, B. Malič, B. Dkhil, D. Jenko, J. Cilenšek, M. Kosec, Crystal structure and phase transitions of sodium potassium niobate perovskites, *Solid State Sciences*, 11 (2009) 2, 320–324, doi:10.1016/j.solidstatesciences.2008.07.011
- ²³ J. Acker, H. Kungl, M. J. Hoffmann, Influence of alkaline and niobium excess on sintering and microstructure of sodium-potassium niobate $(K_{0.5}Na_{0.5})NbO_3$, *Journal of the American Ceramic Society*, 93 (2010) 5, 1270–1281, doi:10.1111/j.1551-2916.2010.03578.x
- ²⁴ J. Acker, H. Kungl, R. Schierholz, S. Wagner, R. A. Eichel, M. J. Hoffmann, Microstructure of sodium-potassium niobate ceramics sintered under high alkaline vapor pressure atmosphere, *Journal of the European Ceramic Society*, 34 (2014) 16, 4213–4221, doi:10.1016/j.jeurceramsoc.2014.06.021
- ²⁵ P. Bomlai, P. Wichianrat, S. Muensit, S. J. Milne, Effect of calcination conditions and excess alkali carbonate on the phase formation and particle morphology of $Na_{0.5}K_{0.5}NbO_3$ powders, *Journal of the American Ceramic Society*, 90 (2007) 5, 1650–1655, doi:10.1111/j.1551-2916.2007.01629.x

STABILITY OF CLOSE-CELL Al FOAMS DEPENDING ON THE USAGE OF DIFFERENT FOAMING AGENTS

STABILNOST ALUMINIJEVIH PEN Z ZAPRTO POROZNOSTJO GLEDE NA UPORABO RAZLIČNIH PENILNIH SREDSTEV

Irena Paulin

Institute of Metals and Technology, Lepi pot 11, 1000 Ljubljana, Slovenia
irena.paulin@imt.si

Prejem rokopisa – received: 2015-10-21; sprejem za objavo – accepted for publication: 2015-10-28

doi:10.17222/mit.2015.322

Close-cell Al foams produced by the powder-metallurgy (PM) route can be made with different foaming agents, regarding the type of liberated gas. Most commonly, H₂ gas is used as the liberation agent, but there is a huge improvement made with CO₂ gas liberating agents, such as calcite and dolomite. In order to determine the benefits and/or disadvantages of foaming agents, studies of the foam pores' stability, depending on the type of liberated gas, were performed.

The stability of Al foams was studied by different analytical techniques, i.e., AES, expandometer, heating microscopy and SEM/EDS. AlSi12 aluminium powder as the matrix material and TiH₂ and CaCO₃ as the foaming agents liberating different gases – one based on H₂ and another on CO₂ – were used. Based on the obtained results, the mechanism of foam stability was studied and a comparison of the two foaming agents was made and evaluated.

Keywords: Al foams, CaCO₃, TiH₂, stability of pores, oxide layers

Aluminijeve pene z zaprto poroznostjo, narejene po postopku metalurgije prahov, se lahko pripravi z različnimi penilnimi sredstvi glede na plin, ki se pri penjenju sprošča. Najbolj pogosto je uporabljeno penilno sredstvo na osnovi H₂ plina, vendar se v zadnjem času veliko uporabljajo tudi penila na osnovi CO₂, kot sta kalcit in dolomit. Da bi ugotovili prednosti in slabosti različnih penilnih sredstev, so bile narejene študije stabilnosti por glede na tip izhajajočega plina.

Stabilnost aluminijevih pen je bila raziskovana z različnimi analitskimi tehnikami – z AES, ekspanzometrom, segrevalnim mikroskopom in SEM/EDS analizo. Za raziskavo smo uporabili aluminijev prah AlSi12 in TiH₂ ter CaCO₃ kot penilni sredstvi z različnimi tipoma sproščenega plina – en na osnovi H₂ in drugi na osnovi CO₂. Glede na rezultate raziskave smo opisali mehanizem za stabilizacijo aluminijevih pen in primerjali ter ocenili obe penilni sredstvi.

Ključne besede: Al pene, CaCO₃, TiH₂, stabilnost por, oksidne plasti

1 INTRODUCTION

Al foams as a promising class of materials with great chances for applicative use¹⁻³ due to their mechanical, chemical and physical properties were analyzed from different viewpoints. Most studies were performed on the synthesis, characterization and mechanical testing of foams, but few investigated the stability of foams by adding ceramic particles into the matrix and no analysis was made to explain the stability of the interior of the pores and the properties of the material depending on this stability.

The PM production process starts with mixing metal powders – elementary-metal powders, or alloyed powders or metal powder blends – and a foaming agent, after which the mixture is compacted to yield a dense, semi-finished product.^{4,5} The method depends on the preparation of the precursors⁶, which in principle can be made by any technique that ensures the embedding of the foaming agent into the metal matrix without any observable residual open porosity. In general, precursors consist of a compacted metallic powder and a foaming agent that are sintered at a pre-determined temperature. Due to the high temperature of the thermal treatment, the

foaming agent decomposes into a solid component that is incorporated into the matrix material, and a gas component that causes foaming of the matrix material.⁷

The metal matrix is a semi-solid, thus the gas liberated from the agent is forming pores that give a specific shape and mechanical properties to the foams. The obtained foam must be rapidly and properly cooled down to retain the bloated structure. Pore formation depends on the amount and the type of the liberated gas, the time and temperature of the thermal treatment and the cooling process. All those parameters influence the stability of the pores and thus the stability of the material properties. The quantitative expansion and collapsing behaviors of the samples were characterized with a mechanical expandometer and heating microscopy.

This investigation is focused on the closed-cell Al foam produced by the powder metallurgy (PM) process using different gas-liberating foaming agents, such as TiH₂ and CaCO₃. The aim of the study was to investigate the mechanism of the stability of the Al foams to understand the process of pore formation, the possibility of predicting the foam properties and for the optimal selection of the foaming agent, depending on the expected properties.

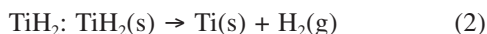
2 EXPERIMENTAL PROCEDURES

In the present study of Al-foam stability, the interior surfaces of the pores were carefully studied. AlSi12 aluminium powder, TiH₂ and CaCO₃ as the foaming agents liberating different gases – one based on H₂ and the other on CO₂ – were used. The decomposition of both foaming agents could be described by the two chemical reactions given below, and the volume of liberated gas was calculated from the ideal gas law:

$$pV = nRT \quad (1)$$

where p is the pressure, V is the volume of gas, n is the amount of substance ($n = m/M$, where m is the mass and M is the molar mass), R is the gas constant and T is the temperature.

The decomposition of:



1 g of TiH₂ liberates at $T = 923 \text{ K}$ (650 °C) a gas volume of $V = 1.51 \text{ L}$



1 g of CaCO₃ liberates at $T = 923 \text{ K}$ (650 °C) a gas volume of $V = 0.76 \text{ L}$

The calculation of the gas liberation at standard temperature and pressure shows that the volume of liberated gas is relatively high, but in the real foaming process, where the pressure of gas in the material is higher, the volume of gas is smaller. On the other hand, some of the liberated gas escapes out of the material when the pressure in the formed bubbles is too high.^{8,9} The process of pore formation can be explained by the theory of soap bubbles.

A calculation of the amount of liberated gas shows that the largest amount of gas liberated under the same conditions is obtained with the TiH₂ decomposition, while the amount of liberated gas with the decomposition of CaCO₃ is just a half of that. A calculation of the volumes of liberated gas gives how much foaming agent is needed for similar results of foaming.

All the samples were prepared by the same procedure, i.e., mixing the AlSi12 powder with mass fractions 1 % TiH₂ and 3 % CaCO₃, respectively, cold compaction at 1200 MPa⁶ into semi-products, called precursors, and foaming at a temperature that is specific for each foaming agent.¹⁰ After preparing the foams, some in a lab furnace and some in the expandometer, specimens were analyzed with different techniques: SEM/EDS (SEM JEOL 6500F with Oxford INCA EDX analyzer) was used for micro-chemical analyses of the inclusions in the foam thin walls, while the surface of the interior of the pores and the exterior of the foams were investigated by AES (Microlab 310 F VG–Scientific). AES depth profiles were performed by ion etching with a velocity of 0.125 nm/min. The AES surface analyses were also performed for the initial powder particles to confirm the presence of an oxide layer on the surface.

The mechanism of foam stability was explained by the investigation with heating microscopy and the expandometer. Both methods were used to determine the time and the temperature of foaming the material. In heating microscopy, small samples of precursor material with different foaming agents were put into the furnace within the microscope and heated up to 800 °C with a heating rate of 7 °C/min. Precursors were inserted at room temperature into the microscope and heated up until the foaming process did not stop and foams started to collapse. During the heating, changes to the shape and the size of the investigated material were observed. This method enabled us to determine the temperature of the foaming process start and the temperature of the foam collapse.

The mechanical expandometer was used to measure the expansion of the foamable precursors inside a cylindrical mould as a function of time and temperature.¹¹ The temperature of the expandometer furnace was held constant at 750 °C for the TiH₂ foaming agent and at 800 °C for the CaCO₃ foaming agent.

3 RESULTS AND DISCUSSION

The foaming process was studied by observing precursors in the heating microscope during heating. Samples began to change their shape and volume at a certain temperature, depending on the type of foaming agent. The results obtained with the heating microscope enabled us to determine the approximate time and temperature of the beginning of the process. Changes of the foam expansion (precursor was made with AlSi12 + TiH₂) are represented in **Figure 1**.

The heating microscope also enabled us to observe the collapsing of the foams after extended foaming times at individual temperatures. This resulted in gas escaping from the bubbles that were formed inside the matrix material. At a certain temperature, the matrix material became viscous, which prevented the escape of gas from the material. Higher temperatures caused a drop in the material viscosity, and due to pressure in the gas bubbles the gas escaped and the foam collapsed. That was the reason that the foams had to be cooled down fast after the desired expansion of material was achieved. Cooling could be achieved either by immersing the foamed product into water or with cold compressed air. In our case cooling in water was applied.

Foams prepared with different foaming agents were cut into smaller pieces and samples for the investigation with SEM/EDS were prepared, using a standard metallographic procedure with grinding and polishing. **Figures 2 and 3** show SE (secondary electron) and BE (back-scattered) images of the polished foamed material, where residuals of solid particles of foaming agents captured in the walls of the foams after the gas liberation are visible.

In^{12,13} the authors confirmed that those ceramic particles helped to stabilize the Al foams. In analyses of

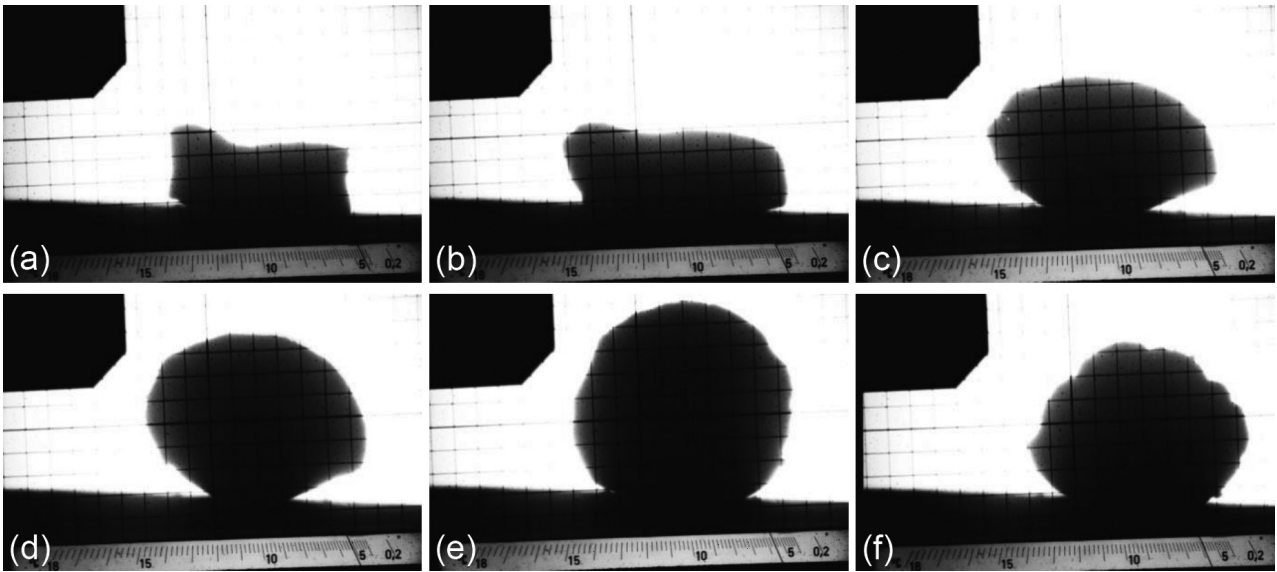


Figure 1: Heating microscope – change of precursor AlSi12 + TiH₂ size: a) 420 °C, no changes, b) 500 °C, first noticed change, c) 520 °C, precursor starts rapidly to bloat, d) 525 °C, still rapidly bloating, e) 580 °C, maximum expansion, f) 600 °C, collapse of sample, keeping the shape of a loaf

Slika 1: Segrevalna mikroskopija – sprememba velikosti prekurzorja iz AlSi12 + TiH₂: a) 420 °C, še nobenih sprememb velikosti, b) 500 °C, prve spremembe, c) 520 °C, vzorec začne hitro naraščati, d) 525 °C, vzorec zelo hitro narašča, e) 580 °C, vzorec doseže največjo velikost, f) 600 °C, vzorec se sesede, vendar obdrži obliko hlebčka

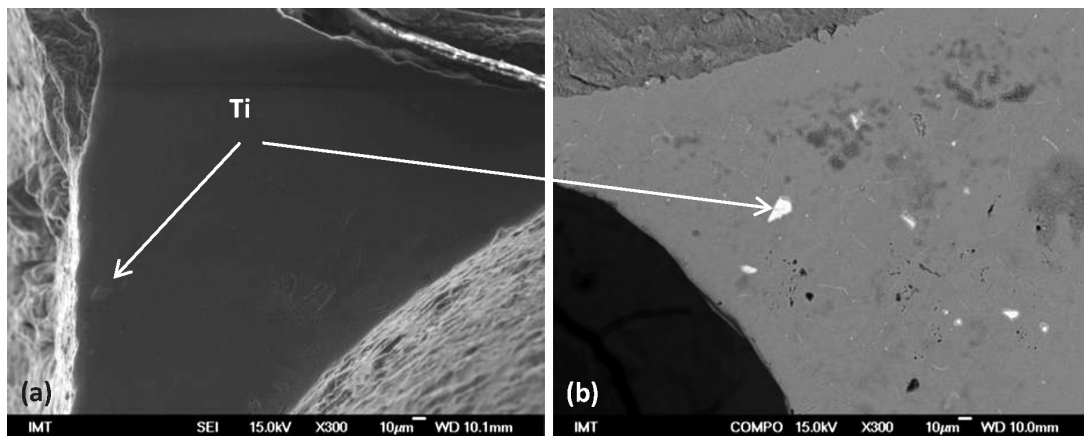


Figure 2: SEM images of thin foam-cell wall with Ti residuals of TiH₂ foaming agent: a) SE image and b) BE image

Slika 2: SEM posnetka tanke celične stene aluminijeve pene z ostanki Ti iz penilnega sredstva TiH₂: a) SE posnetek in b) BE posnetek

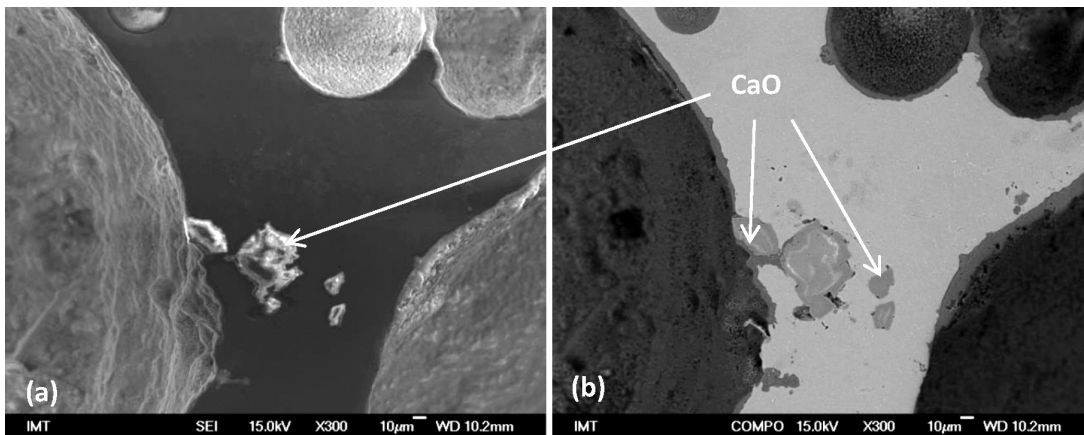


Figure 3: SEM images of thin foam-cell wall with residuals of CaCO₃ foaming agent: a) SE image and b) BE image; the same spot

Slika 3: SEM posnetka tanke celične stene z ostanki penila CaCO₃: a) SE posnetek in b) BE posnetek; isto mesto

ceramic additions to Al foams during preparation, a special emphasis was given to the positive effects of CaO particles.

One of the important properties of aluminium foams is also their stability during the foaming process. The quantitative expansion and collapse behavior of the samples were characterized with the mechanical expandometer, in which the precursor was exposed to a constant temperature of 750 °C for AlSi12 + TiH₂ and 800 °C for AlSi12 + CaCO₃. The expansion was measured with seven samples prepared using TiH₂ and CaCO₃ agents, respectively, and it was approximately 245 % with the CaCO₃ and up to 285 % with the TiH₂ precursors. Nevertheless, the TiH₂ precursors appeared to collapse faster than the CaCO₃ precursors.

Observations in the mechanical expandometer and in the heating microscope revealed that the foams prepared with a foaming agent based on the liberation of CO₂ gas were more stable than those that were prepared with the liberation of H₂. The obtained results were confirmed by the AES analysis of the interior surfaces of the pores where the oxide layers were analyzed and thus the stability can be explained.^{6,14,15} Two interior pore surfaces, obtained by foaming AlSi12 + TiH₂ and AlSi12 + CaCO₃ mixtures, were analyzed, and the results were compared (Figures 4 and 5). Also, the external surface of the foam was analyzed to see the difference in the interior and exterior surfaces of the foam (Figure 6).

The results showed differences in the thicknesses of the oxide layers on the surface of the pore interior depending on the applied foaming agent and on the surface of the foam exterior. The thickness of the oxide layer on the interior pore surface obtained by foaming with TiH₂ was 10–15 nm, while the thickness of the oxide layer on the external surface of the foam was 35–40 nm. On the other hand, the thickness of the oxide layer on the interior pore surface obtained by foaming with CaCO₃ was 90–125 nm, while the oxide layer on the external surface of the foam was about 45–60 nm thick. The difference in

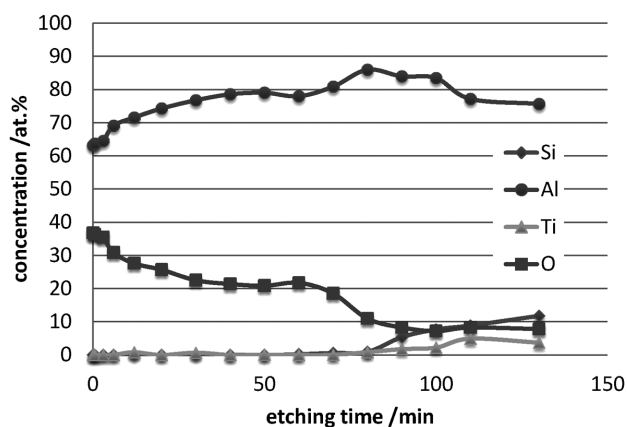


Figure 4: AES depth profiles of the interior surface of the AlSi12 + TiH₂ foam pores

Slika 4: Globinski profili AES notranje površine v pori pene AlSi12 + TiH₂

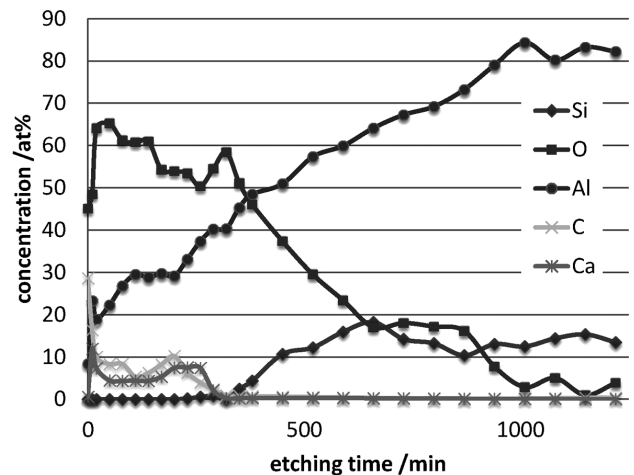


Figure 5: AES depth profiles of the interior surface of the AlSi12 + CaCO₃ foam pores

Slika 5: Globinski profili AES notranje površine v pori pene AlSi12 + CaCO₃

the oxide layer thicknesses was explained by the fact that H₂ represented a reduction atmosphere in the material, and oxygen formed on the surface of the matrix material only a thin oxide layer. Oxide was present in the material as a thin oxide layer on the surface of the powder particles. On the other hand, the CaCO₃ powder created a CO₂ atmosphere during the foaming process, so that the oxide layer on the pore surface was easily formed. Thick oxide layers enabled better stability of the foams produced by foaming agents based on CO₂. However, in both cases there was no great difference in the thicknesses of the oxide layers on the external surface.

The question appears, why CO₂-based foaming agents are not yet more widely used? And the answer is that agents releasing CO₂ need higher temperatures for the liberation of the gas and the needed temperature is approximately 100 °C above the melting point of pure aluminium¹⁰. In such a case, the matrix material is already molten and the viscosity of such material is not high enough to prevent gas escaping out of the material.

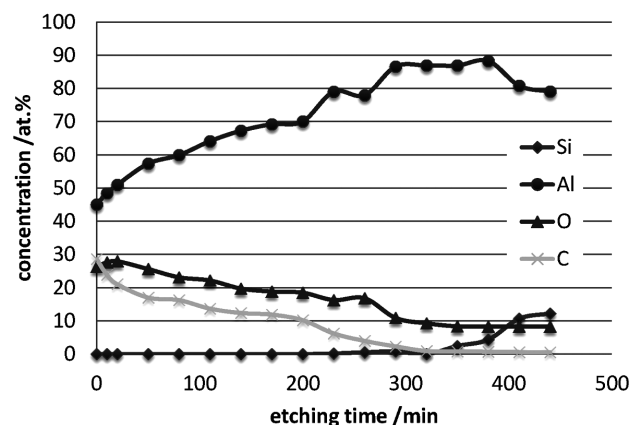


Figure 6: AES depth profiles of the exterior AlSi12 + TiH₂ foam surface

Slika 6: Globinski profili AES zunanje površine pene AlSi12 + TiH₂

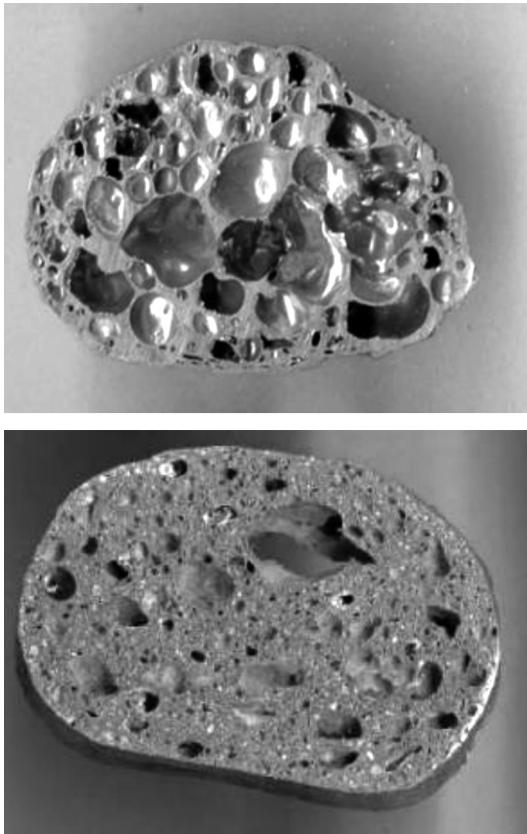


Figure 7: Images of Al foam, cut from loaf: a) AlSi12 + TiH₂ and b) AlSi12 + CaCO₃

Slika 7: Posnetka Al pene, odrezan Al hlebček: a) AlSi12 + TiH₂ in b) AlSi12 + CaCO₃

The solution is to pre-heat the precursors for some time before the foaming process begins. When foaming agents in those precursors are then exposed to an elevated temperature, decomposition has already started and the agent did not need such a long time to decompose completely, while the matrix aluminium has insufficient time to melt completely.

The sizes and shapes of the pores in the foams prepared by exposure to H₂ or CO₂ gas are different. H₂ gas forms spherical pores, while CO₂ forms smaller pores of not completely spherical shape; they are slightly elongated in the horizontal direction (**Figure 7**). However, the stability of foams is better when a CO₂-based foaming agent is used, but the pore shapes and consequently the mechanical properties in the vertical direction are better when using H₂-based foaming agents. The final application of the foamed material determines the selection of the foaming agent as well as the selection of the matrix material. On the other hand, the use of a combination of both foaming agents in a well-defined proportion can be an alternative.

4 CONCLUSIONS

CaCO₃ is a good substitute for the expensive and more widely used TiH₂ foaming agent, though some properties of foams, like the stabilization of pores, are in this case even better. Natural oxidation of the pore surfaces inside the material, as well as the oxidation of external surfaces, helps to stabilize foams so that they do not collapse after the completed foaming.

The oxide layers detected by the AES analysis on the surface of aluminium powders helped to prevent premature melting of the matrix material and enabled foaming agents to decompose before the matrix material melted and lost sufficient viscosity. Similar case is observed when using TiH₂ foaming agent that decomposes at a relatively low temperature, but the additional oxide layer on the surface of the powder delays the beginning of the decomposition as it was pre-studied and confirmed in the literature.

According to^{12,13} and from our research the conclusion can be made that a thicker oxide layer and the residuals of the ceramic solid particles from the CaCO₃ foaming agent give an opportunity to foaming agents based on CO₂ to be used more often in the production of aluminium foams.

Nevertheless, the stability of the foams is better when a CO₂-based foaming agent is used, but the pore shapes are more spherical and consequently the mechanical properties, as known from the literature, are higher when H₂-based foaming agents are used, so the use of a combination of both foaming agents in a well-defined proportion can be an alternative.

Acknowledgements

This work was supported by the “Physics and chemistry of porous aluminium for Al panels capable of highly efficiently energy absorption” project L2-2410 (D), funded by the Slovenian Research Agency.

5 REFERENCES

- ¹ A. H. Benouali, L. Froyen, J. F. Delerue, M. Wevers, Mechanical analysis and microstructural characterisation of metal foams, *Materials Science and Technology*, 18 (2002) 5, 489–494, doi:10.1179/026708302225002056
- ² M. Nosko, F. Simancik, R. Florek, Reproducibility of aluminum foam properties: Effect of precursor distribution on the structural anisotropy and the collapse stress and its dispersion, *Materials Science and Engineering A*, 527 (2010) 21–22, 5900–5908, doi:10.1016/j.msea.2010.05.073
- ³ M. Haesche, J. Weise, F. Garcia-Moreno, J. Banhart, Influence of particle additions on the foaming behaviour of AlSi11/TiH₂ composites made by semi-solid processing, *Materials Science and Engineering A*, 480 (2008) 1–2, 283–288, doi:10.1016/j.msea.2007.07.040
- ⁴ J. Banhart, Manufacture, characterisation and application of cellular metals and metal foams, *Progress in Materials Science*, 46 (2001) 6, 559–632, doi:10.1016/S0079-6425(00)00002-5

I. PAULIN: STABILITY OF CLOSE-CELL Al FOAMS DEPENDING ON THE USAGE OF DIFFERENT FOAMING AGENTS

- ⁵ I. Duarte, J. Banhart, A study of aluminium foam formation – Kinetics and microstructure, *Acta Materialia*, 48 (2000) 9, 2349–2362, doi:10.1016/S1359-6454(00)00020-3
- ⁶ I. Paulin, B. Šuštaršič, V. Kevorkijan, S. Škapin, M. Jenko, Synthesis of aluminium foams by powder-metallurgy process: compacting of precursors, *Mater. Tehnol.*, 45 (2011) 1, 13–19
- ⁷ I. Duarte, P. Weigand, J. Banhart, Foaming kinetics of aluminium alloys, In: J. Banhart, N. A. Ashby, N. A. Fleck (Eds.), *Metal Foams and Porous Metal Structures*, MIT Verlag, Bremen, Germany 1999, 97-104
- ⁸ I. Jeon, T. Asahina, K. J. Kang, S. Im, T. J. Lu, Finite element simulation of the plastic collapse of closed-cell aluminum foams with X-ray computed tomography, *Mechanics of Materials*, 42 (2010) 3, 227–236, doi:10.1016/j.mechmat.2010.01.003
- ⁹ A. E. Markaki, T. W. Clyne, The effect of cell wall microstructure on the deformation and fracture of aluminium-based foams, *Acta Materialia*, 49 (2001) 9, 1677–1686
- ¹⁰ I. Paulin, Synthesis and characterization of Al foams produced by powder metallurgy route using dolomite and titanium hydride as a foaming agents, *Mater. Tehnol.*, 48 (2014) 6, 943–947
- ¹¹ P. Weigand, *Untersuchung der Einflussfaktoren auf die pulvermetallurgische Herstellung von Aluminiumschäumen*, Dissertation, RWTH Aachen University, Aachen 1999
- ¹² J. Baumeister, J. Weise, A. Jeswein, M. Busse, M. Haesche, *Metallic foam production from AlMg4.5Mn recycling machining chips by means of thixocasting and the effects of different additions for stabilization*, MetFoam 2007, Montreal, Canada 2007
- ¹³ A. R. Kennedy, S. Asavavisitchai, Effect of ceramic particle additions on foam expansion and stability in compacted Al-TiH₂ powder precursors, *Adv. Eng. Mater.*, 6 (2004) 6, 400–402, doi:10.1002/adem.200405145
- ¹⁴ J. Banhart, *Metal foams: Production and stability*, *Adv. Eng. Mater.*, 9 (2006) 8, 781–794, doi:10.1002/adem.200600071
- ¹⁵ A. Haibel, A. Rack, J. Banhart, Why are metal foams stable?, *Applied Physics Letters*, 89 (2006), 154102, doi:10.1063/1.2357931

EVOLUTION OF THE MICROSTRUCTURE AND MAGNETIC PROPERTIES OF A COBALT-SILICON-BASED ALLOY IN THE EARLY STAGES OF MECHANICAL MILLING

RAZVOJ MIKROSTRUKTURE IN MAGNETNIH LASTNOSTI ZLITINE Co-Si V ZAČETNEM STADIJU MEHANSKEGA LEGIRANJA

Watcharee Rattanasakulthong¹, Chitnarong Sirisathitkul², Peter Franz Rogl³

¹Department of Physics, Faculty of Science, Kasetsart University, Bangkok, Thailand
²Magnet Laboratory, Molecular Technology Research Unit, School of Science, Walailak University, Nakhon Si Thammarat, Thailand
³Institute of Materials Chemistry and Research, University of Vienna, Vienna, Austria
chitnarong.siri@gmail.com

Prejem rokopisa – received: 2014-12-11; sprejem za objavo – accepted for publication: 2014-12-22

doi:10.17222/mit.2014.300

The early stages in the mechanical alloying of amount fractions $x = 40$ % cobalt (Co) and $x = 60$ % silicon (Si) powders were investigated using X-ray diffractometry (XRD), scanning electron microscopy (SEM), differential thermal analysis (DTA) and vibrating-sample magnetometry (VSM). After 2–8 h of ball-milling, the characteristic XRD peaks of the face-centered-cubic (fcc) Si and hexagonal close-packed (hcp) Co phases remained sharp without a cobalt-silicide phase. As the milling progressed, the particle size observed by SEM tended to reduce, being accompanied by smoother edges and a narrow size distribution. On the DTA curves, between 200 °C and 1200 °C, exothermic peaks indicated a ferromagnetic-to-paramagnetic transition, whereas endothermic peaks corresponded to the lattice recovery, the transition from a hcp to a fcc Co and melting. The longest milling of up to 8 h significantly increased the magnetic squareness and the coercive field.

Keywords: Co-Si alloys, ball milling, XRD, VSM, DTA

Preiskovan je bil začetni stadij mehanskega legiranja zlitine, sestavljene iz prahov z množinskim delom $x = 40$ % kobalta (Co) in $x = 60$ % silicija (Si). Uporabljena je bila rentgenska difraktometrija (XRD), vrstična elektronska mikroskopija (SEM), diferencialna termična analiza (DTA) in vibracijska magnetometrija vzorcev (VSM). Po mletju od 2 h do 8 h v krogljčnem mlinu so še ostali ostri značilni XRD-vrhovi faz fcc Si in hcp Co brez Co-silicidne faze. S podaljševanjem časa mletja se s SEM opazi zmanjšanje velikosti delcev prahov, zožanje njihove velikostne porazdelitve in povečanje zaobljenja robov delcev. Na DTA-krivuljah se je med 200 °C in 1200 °C pojavil eksotermni vrh, ki je posledica prehoda iz feromagnetne v paramagnetno fazo, endotermni vrh pa je posledica poprave rešetke zaradi prehoda iz hcp v fcc Co in nato taljenja. Najdaljši časi mletja (do 8 h) pomembno vplivajo na magnetno koercitivnost in povečanje kvadratičnosti histerezne zanke.

Ključne besede: zlitina na osnovi Co-Si, krogljčno mletje, XRD, VSM, DTA

1 INTRODUCTION

Mechanical milling has been successfully used in producing a variety of magnetic amorphous alloys, intermetallic compounds, nanocomposites and nanocrystalline powders.^{1,2} Milling ferromagnetic powders (i.e., Co, Fe, Ni) with non-magnetic metals (e.g., Au, Cu, Ag) gives rise to mechanical alloys with a giant magnetoresistance (GMR) effect.³ Since an addition of Si reduces the magnetic anisotropy and the eddy-current loss in commercial steels, Fe–Si mechanical alloys also received much interest.^{4–7} By contrast, Co–Si alloys only gained attention in the last decade after being recognized as hydrogen-storage materials for nickel-metal hydride batteries. The discharge capacity and cycling ability of negative electrodes are reportedly improved when using 1 : 1 or 2 : 1 Co–Si milled for 10–80 h.^{8–10} In addition to homogenizing their sizes and shapes, the ball milling leads to several compounds as shown by the Co–Si phase diagram.¹¹ The Co₂Si, CoSi and CoSi₂ phases affect the

magnetic and hydrogen-storage properties of the alloys.^{10–14}

In this work, the evolution of the phases during the initial period of the milling of Co with $x = 60$ % Si is examined. The thermal and magnetic properties of these Co–Si powders from the early stage of the ball-milling for up to 8 h are also reported.

2 EXPERIMENTAL WORK

Elemental crystalline cobalt powder (a 99.8 % purity with the average particle size of less than 2 μm) and silicon powder (a 99 % purity with the average particle size of less than 44 μm) were mixed in an atomic ratio of 40 : 60 in a steel vial loaded with steel balls of 3 mm in diameter. The ball-to-powder mass ratio was around 15 : 1. The vial was spun at 595 r/min on a vario-planetary mill (Fritsch) for (2, 4, 6 and 8) h in a dry condition under air. The structural and magnetic properties of the milled powders were characterized with X-ray diffrac-

tion (XRD) using Cu- $K\alpha$ radiation and vibrating sample magnetometry (VSM), respectively. The coercive field was determined from the x-intercept of the hysteresis loop obtained with VSM, whereas the y-intercept corresponded to the remanent magnetization. A ratio of the remanent magnetization to the saturation magnetization is referred to as the magnetic squareness in **Table 1**. The thermal properties were studied using a differential thermal analysis (DTA) with a heating rate of $5\text{ }^\circ\text{C min}^{-1}$.

Table 1: Magnetic squareness and coercive field of Co - x(Si) = 60 % powders

Tabela 1: Magnetna kvadratnost in koercitivno polje prahov iz Co - x(Si) = 60 %

Milling time (h)	Magnetic squareness	Coercive field (kA m^{-1})
2	0.28	15.15
4	0.29	15.32
6	0.28	15.48
8	0.37	19.41

3 RESULTS AND DISCUSSION

The XRD patterns of the Co-Si powders after the milling shown in **Figure 1** have characteristic peaks of the fcc Si phase ($2\theta = 28.440^\circ$, 47.300° and 56.120°) and the hcp Co phase ($2\theta = 47.220^\circ$, 44.080° and 41.440°). According to the literature¹⁵, allotropic Co undergoes a transition from the hcp to the fcc structure at a temperature around $450\text{ }^\circ\text{C}$. Previous works suggested that the ball milling can also induce such an allotropic transformation by virtue of a defect accumulation.¹⁶⁻¹⁹ The mixed phase may be converted into a highly distorted hcp structure in the early stage of milling but further milling leads to a fcc structure as a result of the stacking faults from the plastic deformation.¹⁷ The CoSi and CoSi₂ phases are not clearly detected. The formation of silicide compounds generally requires prolonged milling and, as demonstrated with Pd-Si¹, it is dependent

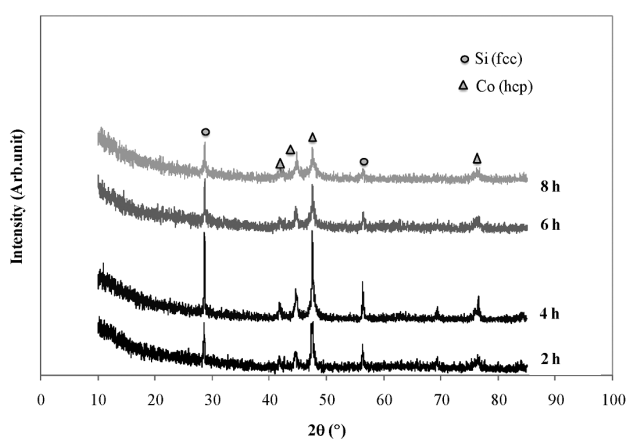


Figure 1: XRD patterns of Co - x(Si) = 60 % powders after milling for 2–8 h

Slika 1: XRD-posnetki prahov Co - x(Si) = 60 % po mletju od 2 h do 8 h

on the volume fractions of the two elemental powders. In some cases, the milling is carried out at a high temperature to stimulate the formation of compounds.¹ In our case, all Co and Si peaks are rather sharp indicating a high degree of crystallinity. However, the peaks clearly broaden and their intensities are decreased after the milling for 8 h. The small peaks of Si slightly below 70° in the case of milling for 2 h and 4 h disappear after the longer milling.

The morphologies of the Co-Si powders at various milling times obtained with SEM are shown in **Figure 2**. After the milling for 2 h, several particles are still bulky, with straight and sharp edges. The edges are gradually broken or rubbed off and the particles become smoother as the milling progresses. Furthermore, the particle size is clearly reduced after the longest milling time of 8 h. It was also reported that a decrease in the particle size of Fe-Si powders began to be noticeable only after 5 h of ball milling.⁷ It is known that milling modifies the size of ball-milled powders by virtue of fracturing and cold welding. Each process dominates in a different stage of milling and the welding of particles is dominant in the initial milling time of up to 3 h.^{5,6} The narrower size distribution seen in the case of 8 h milling is a result of simultaneous fracturing of larger particles and cold welding of smaller particles. The powder from the early stage of milling can be modeled as brittle Si embedded in more ductile Co particles.

It is seen from the DTA curves in **Figure 3** that after 2 h to 8 h of milling, the samples exhibit a broad exothermic peak centered around $600\text{ }^\circ\text{C}$. The area is increased with the milling time because more energy is released in the case of prolonged milling. Another exothermic peak is observed that was shifted from above to

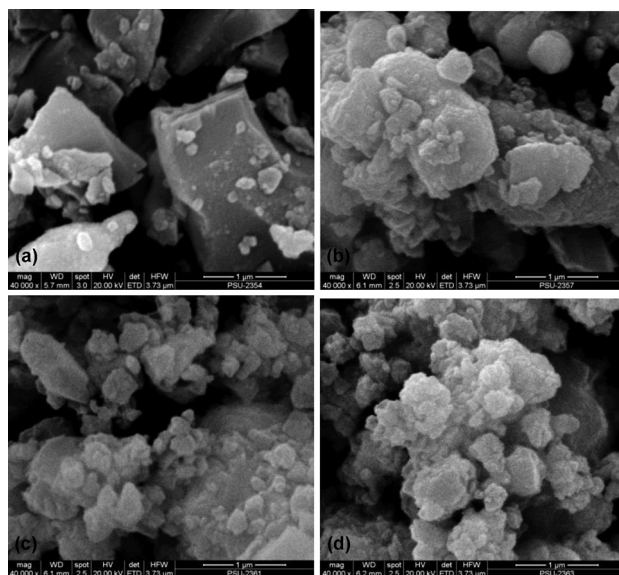


Figure 2: SEM micrographs of Co - x(Si) = 60 % powders after milling for: a) 2h, b) 4h, c) 6h and d) 8 h

Slika 2: SEM-posnetki prahov Co - x(Si) = 60 % po mletju: a) 2 h, b) 4 h, c) 6 h in d) 8 h

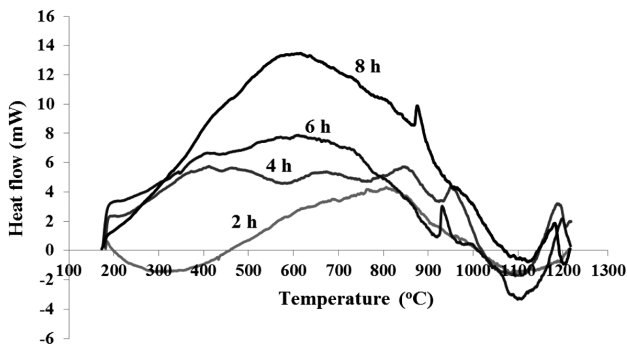


Figure 3: DTA curves of Co – x(Si) = 60 % powders after milling for 2–8 h

Slika 3: DTA-krivulje prahov Co – x(Si) = 60 % po mletju od 2 h do 8 h

below 900 °C due to the increase in the milling time. This small exothermic peak may correspond to the ferromagnetic-to-paramagnetic transition. In addition to both exothermic peaks, there are endothermic peaks at around 1100 °C corresponding to the melt appearing in the system and at around 450 °C resembling the transition from hcp to fcc in bulk Co.¹⁵ The latter is less notable in the case of a longer milling time because the defect accumulation due to milling already facilitates the transformation to the fcc phase. The heat absorption also reduces the defect and dislocation density in the lattice-recovery process at around 200–300 °C which is clearly detected only in the case of 2 h milling.

The hysteresis loops of the milled Co–Si powders are shown in **Figure 4** and their magnetic parameters are summarized in **Table 1**. Like the other granular Co alloys³, the magnetization is not saturated under the magnetic field of about 200 kA m⁻¹. Both the coercive field and squareness (approximated from the ratio of the remanence to the maximum magnetization in 200 kA m⁻¹) remain rather constant in the case of 2–6 h milling but increase significantly after the milling for 8 h. Interestingly, the size of Co particles is slightly modified during the 2–6 h milling. This can then be related to the dependence of the magnetic properties on the particle size of magnetic mechanical alloys. The coercive field is also related to the lattice imperfections as the milling is progressed because they impede the domain-wall movement.^{4,5} Although Co has a strong crystalline anisotropy²⁰, it is noted that these coercive-field values are comparable to those of the Fe alloys with a high fraction of Si, which could be further reduced with heat treatments.^{5,7}

4 CONCLUSION

The ball-milling of Co – 60 % Si for up to 8 h does not significantly induce silicide and amorphous phases. However, there are some modifications in the morphology and particle size during this early stage of milling. As a result, the thermal and magnetic properties of

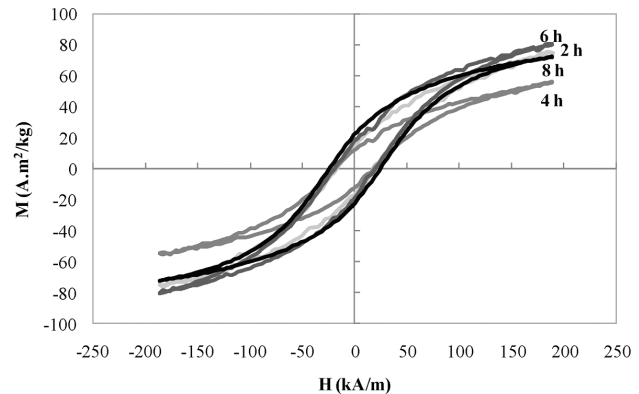


Figure 4: Hysteresis loops of Co – x(Si) = 60 % powders after milling for 2–8 h

Slika 4: Histerezne zanke prahov Co – x(Si) = 60 % po mletju od 2 h do 8 h

Co–Si powders are considerably influenced by the milling time. In addition to the endothermic DTA peaks corresponding to the lattice recovery, the allotropic Co transition, the melting and the ferromagnetic-to-paramagnetic transition give rise to an exothermic peak, which shifts to a lower temperature as the milling progresses. The considerable reduction in the particle size after the milling for 8 h results in an enhanced coercive field and magnetic squareness.

Acknowledgements

This work was funded by Faculty of Science, Kasetsart University (ScRF-E5-2553). The authors would like to thank Scientific Equipments Center, Prince of Songkla University for the characterization facilities and Jureeporn Noodam for her assistance in the characterizations.

5 REFERENCES

- D. L. Zhang, Processing of advanced materials using high-energy mechanical milling, *Progress in Materials Science*, 49 (2004), 537–560, doi:10.1016/S0079-6425(03)00034-3
- K. Ociepka, A. Bajorek, A. Chrobak, G. Chelkowska, K. Prusik, Magnetic properties of Tb(Ni_{1-x}Fe_x)₃ (x = 0.2, 0.6) crystalline compounds and powders, *Acta Physica Polonica A*, 126 (2014) 1, 180–181, doi:10.12693/APhysPolA.126.180
- W. Rattanasakulthong, C. Sirisathitkul, Effects of oxidation and cluster distribution on thermal and magnetotransport properties of mechanically alloyed Co–Cu powders, *Applied Physics A*, 83 (2006) 1, 77–81, doi:10.1007/s00339-005-3455-2
- T. J. Zhou, Z. Yu, Y. W. Du, The effective magnetic anisotropy in nanocrystalline Fe_{100-x}Si_x alloys, *Journal of Magnetism and Magnetic Materials*, 202 (1999) 2–3, 354–358, doi:10.1016/S0304-8853(99)00384-4
- J. Ding, Y. Lee, L. F. Chen, C. R. Deng, Y. Shi, Y. S. Chow, T. B. Gang, Microstructure and soft magnetic properties of nanocrystalline Fe–Si, *Journal of Alloys and Compounds*, 314 (2001) 1–2, 262–267, doi:10.1016/S0925-8388(00)01234-2
- B. Zuo, N. Saraswati, T. Sritharan, H. H. Hng, Production and annealing of nanocrystalline Fe–Si and Fe–Si–Al alloy powders, *Materials Science and Engineering A*, 371 (2004) 1–2, 210–216, doi:10.1016/j.msea.2003.11.046

- ⁷ S. H. Kim, Y. J. Lee, B. H. Lee, K. H. Lee, K. Narasimhan, Y. D. Kim, Characteristics of nanostructured Fe-33 at.%Si alloy powders produced by high-energy ball milling, *Journal of Alloys and Compounds*, 424 (2006) 1–2, 204–208, doi:10.1016/j.jallcom.2005.10.085
- ⁸ G. He, L. F. Jiao, H. T. Yuan, Y. Y. Zhang, Y. J. Wang, Preparation and electrochemical hydrogen storage property of alloy CoSi, *Electrochemistry Communications*, 8 (2006) 10, 1633–1638, doi:10.1016/j.elecom.2006.07.023
- ⁹ Y. Zhang, L. Jiao, Y. Wang, Q. Wang, Y. Zhang, L. Liu, H. Yuan, Influence of CoSi on the electrochemical hydrogen storage properties of MgNi alloy, *International Journal of Hydrogen Energy*, 33 (2008) 18, 4819–4823, doi:10.1016/j.ijhydene.2008.05.098
- ¹⁰ Y. Wang, J. M. Lee, X. Wang, An investigation of the origin of the electrochemical hydrogen storage capacities of the ball-milled Co-Si composites, *International Journal of Hydrogen Energy*, 35 (2010) 4, 1669–1673, doi:10.1016/j.ijhydene.2009.12.026
- ¹¹ H. Okamoto, Co-Si (Cobalt-Silicon), *Journal of Phase Equilibria and Diffusion*, 29 (2008) 3, 295, doi:10.1007/s11669-008-9311-2
- ¹² J. S. Tsay, Y. D. Yao, Y. Liou, Magnetic phase diagram study of ultrathin Co/Si(111) films, *Surface Science*, 454-456 (2000) 1–2, 856–859, doi:10.1016/S0039-6028(00)00158-8
- ¹³ S. W. Kim, Y. Mishima, D. C. Choi, Effect of process conditions on the thermoelectric properties of CoSi, *Intermetallics*, 10 (2002) 2, 177–184, doi:10.1016/S0966-9795(01)00122-4
- ¹⁴ S. Abhaya, G. V. Rao, S. Kalavathi, V. S. Sastry, G. Amarendra, Silicide formation in Co/Si system investigated by depth-resolved positron annihilation and X-ray diffraction, *Surface Science*, 600 (2006) 13, 2762–2765, doi:10.1016/j.susc.2006.04.043
- ¹⁵ C. Xie, J. Hu, R. Wu, H. Xia, Structure transition comparison between the amorphous nanosize particles and coarse-grained polycrystalline of cobalt, *Nanostructured Materials*, 11 (1999) 8, 1061–1066, doi:10.1016/S0965-9773(99)00394-3
- ¹⁶ J. Y. Huang, Y. K. Wu, H. Q. Ye, K. Lu, Allotropic transformation of cobalt induced by ball milling, *Nanostructured Materials*, 6 (1995) 5–8, 723–726, doi:10.1016/0965-9773(95)00160-3
- ¹⁷ J. Sort, J. Nogués, S. Suriñach, M. D. Baró, Microstructural aspects of the hcp-fcc allotropic phase transformation induced in cobalt by ball milling, *Philosophical Magazine*, 83 (2003) 4, 439–455, doi:10.1080/0141861021000047159
- ¹⁸ M. Baricco, N. Cowlam, L. Schiffrini, P. P. Macrí, R. Frattini, S. Enzo, Copper-cobalt f.c.c. metastable phase prepared by mechanical alloying, *Philosophical Magazine B*, 68 (1993) 6, 957–966, doi:10.1080/13642819308217953
- ¹⁹ F. Cardellini, G. Mazzone, Thermal and structural study of the h.c.p.-to-f.c.c. transformation in cobalt, *Philosophical Magazine A*, 67 (1993) 6, 1289–1300, doi:10.1080/01418619308225355
- ²⁰ T. H. Lee, H. C. Koo, H. Kim, S. H. Han, S. H. Lim, Crystalline anisotropy effect on magnetic properties and its competition with shape anisotropy, *Metals and Materials International*, 17 (2011) 3, 509–513, doi:10.1007/s12540-011-0632-z

IN MEMORIAM

prof. dr. Milanu Trbižanu, zaslužnemu profesorju Univerze v Ljubljani



Poslovil se je dr. Milan Trbižan, zaslužni profesor Univerze v Ljubljani. Bil je eden tistih, ki so v zadnjih desetletjih bistveno prispevali k uspešnemu razvoju livarstva v Sloveniji na več področjih.

S prvo generacijo kamniških maturantov je leta 1953 končal gimnazijo in se vpisal na študij metalurgije na takratni Fakulteti za rudarstvo, metalurgijo in kemijsko tehnologijo, kjer je diplomiral leta 1960. Praktične izkušnje si je kot mlad inženir pridobival v livarni Titan, leta 1964 pa je bil izvoljen za asistenta na Katedri za železarstvo.

Njegovo raziskovalno delo so bile preiskave litih kovinskih materialov, predvsem vpliv termošoka na toplotno utrujenost litega železa. Iz te tematike je leta 1973 tudi doktoriral na Montanistični univerzi v Leobnu. Razvil je lastno preiskovalno napravo za ponavljajoče se obremenitve s termošokom. Leta 1976 je bil izvoljen za docenta, leta 1986 za izrednega ter leta 1992 za rednega profesorja in predstojnika Katedre za livarstvo; naziv zaslužnega profesorja mu je bil podeljen leta 2011.

Njegova raziskovalna dejavnost je bila usmerjena v probleme v livarstvu. Že pri diplomski je preiskoval materiale za izdelavo livarskih form in jeder.

Takoj po zaposlitvi na Univerzi je začel sodelovati s podjetjem Termit Moravče pri razvoju oplaščenih peskov za postopek izdelave ulitkov Croning.

Poleg rednega dela je pomembno oblikoval Društvo livarjev Slovenije. Leta 1965 je bil izvoljen za tajnika Društva livarjev in opravljal to delo vse do leta 1992, ko je postal predsednik društva. V tej vlogi je ostal do leta 2005.

S predavanji je sodeloval na mnogih nacionalnih, mednarodnih in svetovnih kongresih livarjev. Bil je tudi pobudnik letnega posvetovanja livarjev v Portorožu, ki vsako leto privabi več kot 250 udeležencev iz številnih držav.

Prof. Trbižan je s svojim pedagoško-vzgojnim, raziskovalnim, inovativnim in društvenim delovanjem prispeval tudi k uspehu naših livarn, ki z visokotehnološkimi ulitki uspešno konkurirajo na mednarodnem trgu in zagotavljajo lepo število delovnih mest.

S svojim značilnim temperamentom je odkrival nova obzorja in nas razveseljeval v človeškem in strokovnem smislu. Profesor Trbižan je bil še poln načrtov, organiziral je že srečanje ob svoji 80-letnici, a nepričakovana smrt mu je preprečila vse nadaljnje načrte.

Zaslužnega profesorja dr. Milana Trbižana bomo ohranili v najboljši luči v svojih spominih.

Prof. dr. Primož Mrvar
Predstojnik Oddelka za materiale
in metalurgijo NTF UL

MATERIALI IN TEHNOLOGIJE

MATERIALS AND TECHNOLOGY

Letnik / Volume 49 2015

ISSN 1580-2949

© Materiali in tehnologije
IMT Ljubljana, Lepi pot 11, 1000 Ljubljana, Slovenija

MATERIALI IN TEHNOLOGIJE / MATERIALS AND TECHNOLOGY

VSEBINA / CONTENTS
LETNIK / VOLUME 49, 2015/1, 2, 3, 4, 5, 6

2015/1

Boron-doped hydrogenated amorphous semiconductor MEMS

Z borom dopirani hidrogenirani amorfni polprevodnik MEMS

M. Galindo, C. Zúñiga, R. Palomino-Merino, F. López, W. Calleja, J. de la Hidalga, V. M. Castaño 3

Wear behaviour of B₄C reinforced hybrid aluminum-matrix compositesVedenje hibridnega kompozita na osnovi aluminija, ojačanega z B₄C, pri obrabi

T. Thiagarajan, R. Subramanian, S. Dharmalingam, N. Radika, A. Gowrisankar 9

Influence of the HIP process on the properties of as-cast Ni-based alloys

Vpliv vročega izostatskega stiskanja na lastnosti Ni-zlitin z lito strukturo

J. Malcharecziková, M. Pohludka, V. Michenka, T. Čegan, J. Juřica, M. Kursá 15

Corrosion of CrN-coated stainless steel in a NaCl solution (w = 3 %)

Korozija nerjavnega jekla s CrN-prevleko v raztopini NaCl (w = 3 %)

I. Kucuk, C. Sarioglu 19

Preparation and properties of master alloys Nb-Al and Ta-Al for melting and casting of γ -TiAl intermetallicsPriprava in lastnosti predzlitin Nb-Al in Ta-Al za taljenje in ulivanje intermetalnih zlitin γ -TiAl

J. Juřica, T. Čegan, K. Skotnicová, D. Petlák, B. Smetana, V. Matějka 27

Decreasing the carbonitride size and amount in austenitic steel with heat treatment and thermomechanical processing

Zmanjšanje velikosti karbonitridov v avstenitem jeklu s toplotno obdelavo in termomehansko predelavo

P. Martínek, P. Podaný, J. Nacházek 31

Deep cryogenic treatment of H11 hot-working tool steel

Globoka kriogenska obdelava orodnega jekla H11 za delo v vročem

P. Suchmann, D. Jandova, J. Niznanska 37

Numerical prediction of the compound layer growth during the gas nitriding of Fe-M binary alloys

Numerično napovedovanje rasti spojinske plasti med plinskim nitriranjem binarnih zlitin Fe-M

R. Kouba, M. Keddám 43

Antibacterial composite based on nanostructured ZnO mesoscale particles and a poly(vinyl chloride) matrix

Protibakterijski kompozit na osnovi nanostrukturnih delcev ZnO in osnove iz polivinil klorida

J. Sedlák, P. Bažant, J. Klofáč, M. Pastorek, I. Kuřitka 55

Water-soluble cores – verifying development trends

Jedra, topna v vodi – preverjanje smeri razvoja

E. Adámková, P. Jelínek, J. Beňo, F. Mikšovský 61

Mathematical modelling and physical simulation of the hot plastic deformation and recrystallization of steel with micro-additives

Matematično modeliranje in fizikalna simulacija vroče plastične predelave in rekristalizacije jekla z mikrododatki

E. Kalinowska-Ozgowicz, W. Wajda, W. Ozgowicz 69

Synthesis of NiTi/Ni-TiO₂ composite nanoparticles via ultrasonic spray pyrolysisSinteza kompozitnih nanodelcev NiTi/Ni-TiO₂ z ultrazvočno razpršilno pirolizo

P. Majerič, R. Rudolf, I. Anžel, J. Bogović, S. Stopić, B. Friedrich 75

Hydroxyapatite coatings on Cp-Titanium Grade-2 surfaces prepared with plasma spraying

Nanos hidroksiapatita na površino Cp-Titana Grade-2 z nabrizgavanjem s plazmo

R. Rudolf, D. Stamenković, Z. Aleksić, M. Jenko, I. Đorđević, A. Todorović, V. Jokanović, K. T. Raić 81

Heat-transfer characteristics of a non-Newtonian Au nanofluid in a cubical enclosure with differentially heated side walls

Značilnosti prenosa toplote newtonske Au nanotekočine v kockastem ohišju z različno gretima stranskima stenama

P. Ternik, R. Rudolf, Ž. Žunič 87

Amplitude–frequency response of an aluminium cantilever beam determined with piezoelectric transducers

Amplitudno-frekvenčni odziv konzolnega nosilca iz aluminija, ugotovljen s piezoelektričnimi pretvorniki

Z. Lašová, R. Zemčík 95

Micromechanical model of the constituents of a unidirectional fiber-reinforced composite and its response to the tensile cyclic loading

Mikromehanski model nadomestkov kompozitov, ojačanih z enosmernimi vlakni, in njihov odgovor na ciklično natezno obremenjevanje

T. Kroupa, H. Srbová, R. Zemčík 99

Dry-cutting options with a chainsaw at the Hotavlje I natural-stone quarry Možnosti suhega rezanja z verižno žago v kamnolomu naravnega kamna Hotavlje I. J. Kortnik, B. Markoli	103
Effect of sliding speed on the frictional behavior and wear performance of borided and plasma-nitrided W9Mo3Cr4V high-speed steel Vpliv hitrosti drsenja na vedenje in obrabo boriranega in v plazmi nitriranega hitroreznega jekla W9Mo3Cr4V I. Gunes	111
Tribological behaviour of A356/10SiC/3Gr hybrid composite in dry-sliding conditions Tribološko vedenje hibridnega kompozita A356/10SiC/3Gr pri suhem drsenju B. Stojanović, M. Babić, N. Miloradović, S. Mitrović	117
New solid-polymer-electrolyte material for dye-sensitized solar cells Novi elektrolitni material na osnovi trdnega polimera za sončne celice, občutljive za svetlobo V. K. Singh, B. Bhattacharya, S. Shukla, P. K. Singh	123
Compacting the powder of Al-Cr-Mn alloy with SPS Kompaktiranje prahu zlitine Al-Cr-Mn s SPS T. F. Kubatík, Z. Pala, P. Novák	129
Effect of tempering on the microstructure and mechanical properties of resistance-spot-welded DP980 dual-phase steel Vpliv popuščanja na mikrostrukturo in mehanske lastnosti točkasto varjenega dvofaznega jekla DP980 F. Nikoosohbat, S. Kheirandish, M. Goodarzi, M. Pouranvari	133
Optimization of the process parameters for surface roughness and tool life in face milling using the Taguchi analysis Optimizacija procesnih parametrov glede na hrupavost površine in trajnostno dobo orodja pri čelnem rezkanju z uporabo Taguchijeve analize M. Sarikaya, H. Dilipak, A. Gezgin	139
Thin tin monosulfide films deposited with the HVE method for photovoltaic applications Tanka plast HVE kositrovega monosulfida za uporabo v fotovoltaiki N. Revathi, S. Bereznev, J. Lehner, R. Traksmaa, M. Safonova, E. Mellikov, O. Volobujeva	149
Mechanical properties of the austenitic stainless steel X15CrNiSi20-12 after recycling Mehanske lastnosti avstenitnega nerjavnega jekla X15CrNiSi20-12 po recikliranju A. Delić, O. Kablar, A. Zulić, D. Kovačević, N. Hodžić, E. Barčić	153
Comparison of refractory coatings based on talc, cordierite, zircon and mullite fillers for lost-foam casting Primerjava ognjevdržnih premazov na osnovi smucka, kordierita, cirkona in mulitnih polnil za ulivanje v forme z izparljivim modelom Z. Aćimović-Pavlović, A. Terzić, Lj. Andrić, M. Pavlović	157
Selection of the most appropriate welding technology for hardfacing of bucket teeth Izbira najbolj primerne tehnologije trdega navarjanja zoba zajemalke V. Lazić, A. Sedmak, R. R. Nikolić, M. Mutavdžić, S. Aleksandrović, B. Krstić, D. Milosavljević	165
Characterization of TiO₂ nanoparticles with high-resolution FEG scanning electron microscopy Karakterizacija nanodelcev TiO ₂ z visokoločljivostno FEG vrstično elektronsko mikroskopijo Z. Samardžija, D. Lapornik, K. Gradišek, D. Verhovšek, M. Čeh	173
2015/2	
Editor's Preface / Predgovor urednika M. Torkar	181
Pitting corrosion of TiN-coated stainless steel in 3 % NaCl solution Jamičasta korozija nerjavnega jekla s prevleko TiN v 3-odstotni raztopini NaCl I. Kucuk, C. Sarioglu	183
Design of a wideband planar antenna on an epoxy-resin-reinforced woven-glass material Širokopasovna ploskovna antena na epoksi smoli, ojačani s steklenimi vlakni R. Azim, M. T. Islam	193
Influence of the strain rate on the PLC effect and acoustic emission in single crystals of the CuZn30 alloy compressed at an elevated temperature Vpliv hitrosti deformacije na pojav PLC in akustično emisijo monokristalov zlitine CuZn30, stiskane pri povišani temperaturi W. Osgowicz, B. Grzegorzcyk, A. Pawelek, A. Piątkowski, Z. Ranachowski	197
Determination of elastic-plastic properties of Alporas foam at the cell-wall level using microscale-cantilever bending tests Določanje elastičnih in plastičnih lastnosti pene Alporas na ravni celične stene z upogibnimi preizkusi z mikroskopsko iglo T. Doktor, D. Kytýř, P. Koudelka, P. Zlámal, T. Fíla, O. Jiroušek	203
Electrochemical behavior of biocompatible alloys Elektrokemijsko vedenje biokompatibilnih zlitin I. Petrášová, M. Losertová	207
Materiali in tehnologije / Materials and technology 49 (2015) 6, 995–1018	997

Preparation and thermal stability of ultra-fine and nano-grained commercially pure titanium wires using CONFORM equipment	
Priprava komercialne ultradrobne in nanozrnate Ti-žice z opremo CONFORM in njena termična stabilnost T. Kubina, J. Dlouhý, M. Köver, M. Dománková, J. Hodek	213
Estimation of the thermal contact conductance from unsteady temperature measurements	
Določanje kontaktne toplotne prevodnosti iz neravnotežnega merjenja temperature J. Kvapil, M. Pohanka, J. Horský	219
Potentiodynamic and XPS studies of X10CrNi18-8 steel after ethylene oxide sterilization	
Potenciodinamične in XPS analize jekla X10CrNi18-8 po sterilizaciji z etilen oksidom W. Walke, J. Przondziona	223
TEM replica of a fluoride-miserite glass-ceramic glaze microstructure	
TEM-replike mikrostrukture steklokeramične fluor-mizeritne glazure J. Ma. Rincón, R. Casasola	229
Experimental analysis and modeling of the buckling of a loaded honeycomb sandwich composite	
Eksperimentalna analiza in modeliranje upogibanja obremenjenega satatega sendvičnega kompozita A. Bentouhami, B. Keskes	235
Fatigue behaviour of X70 steel in crude oil	
Vedenje jekla X70 pri utrujanju v surovi nafti E. Gajdoš, M. Šperl, J. Bystrianský	243
Use of Larson-Miller parameter for modeling the progress of isothermal solidification during transient-liquid-phase bonding of IN718 superalloy	
Uporaba Larson-Millerjevega parametra za modeliranje izotermnega strjevanja pri spajanju z vmesno tekočo fazo superzlitine IN718 M. Pouranvari, S. M. Mousavizadeh	247
Effect of severe air-blast shot peening on the wear characteristics of CP titanium	
Vpliv intenzivnega površinskega kovanja s peskanjem z zrakom na obrabne lastnosti CP-titana A. C. Karaoglanli	253
Finite-element minimization of the welding distortion of dissimilar joints of carbon steel and stainless steel	
Uporaba končnih elementov za zmanjšanje popačenja oblike pri varjenju ogljikovega in nerjavnega jekla E. Ranjbarnodeh, M. Pouranvari, M. Farajpour	259
Magnesium-alloy die forgings for automotive applications	
Izkovki iz magnezijevih zlitin za avtomobilsko industrijo M. Madaj, M. Greger, V. Karas	267
Resistance to electrochemical corrosion of the extruded magnesium alloy AZ80 in NaCl solutions	
Odpornost ekstrudirane magnezijeve zlitine AZ80 proti elektrokemijski koroziji v raztopini NaCl J. Przondziona, E. Hadasik, W. Walke, J. Szala, J. Michalska, J. Wiczorek	275
Microwave-assisted hydrothermal synthesis of Ag/ZnO sub-microparticles	
Hidrotermična sinteza podmikrometrskih delcev Ag/ZnO z mikrovalovi L. Münster, P. Bažant, M. Machovský, I. Kuřitka	281
Determination of the cause of the formation of transverse internal cracks on a continuously cast slab	
Ugotavljanje vzrokov za nastanek notranjih prečnih razpok v kontinuirno ulitem slabu Z. Franěk, M. Masarik, J. Šmíd	285
Effective preparation of non-linear material models using a programmed optimization script for a numerical simulation of sheet-metal processing	
Učinkovita priprava nelinearnih modelov materiala s programiranim optimizacijskim zapisom za numerično simulacijo obdelave pločevine M. Urbánek, F. Tikal	291
Neutralization of waste filter dust with CO₂	
Nevtralizacija odpadnega filterskega prahu s CO ₂ A. Kračun, I. Anžel, L. Fras Zemljič, A. Stergaršek	297
The influence of the morphology of iron powder particles on their compaction in an automatic die	
Vpliv morfologije delcev železovega prahu na njegovo sposobnost za avtomatsko enosno stiskanje B. Šuštaršič, M. Godec, Č. Donik, I. Paulin, S. Glodež, M. Šori, M. Ratej, N. Javornik	303
2015/3	
Wear mechanisms and surface engineering of forming tools	
Obrabni mehanizmi in inženiring površine preoblikovalnih orodij B. Podgornik, V. Leskovšek	313
Predicting the physical properties of drawn Nylon-6 fibers using an artificial-neural-network model	
Napovedovanje fizikalnih lastnosti vlečenih vlaken iz najlona 6 z uporabo modela umetne nevronske mreže R. Semnani Rahbar, M. Vadood	325

Influence of the impact angle and pressure on the spray cooling of vertically moving hot steel surfaces Vpliv vpadnega kota in tlaka na ohlajanje z brizganjem na vertikalno premikajoče se vroče površine jekla M. Hnízdil, M. Chabičovský, M. Raudenský	333
Techniques of measuring spray-cooling homogeneity Tehnike merjenja homogenosti hlajenja z brizganjem M. Chabičovský, M. Raudenský	337
Mineralogical and geochemical characterization of roman slag from the archaeological site near Mošnje (Slovenia) Mineraloška in geokemična karakterizacija rimske žindre z arheološkega najdišča pri Mošnjah (Slovenija) S. Kramar, J. Lux, H. Pristacz, B. Mirtič, N. Rogan - Šmuc	343
Reynolds differential equation singularity using processes of small straining with lubrication Reynoldsova diferencialna enačba pri procesih majhne deformacije z mazanjem D. Čurčija, F. Vodopivec, I. Mamuzić	349
Prediction of the catastrophic tool failure in hard turning through acoustic emission Napovedovanje katastrofične poškodbe keramičnih vložkov pri struženju z akustično emisijo M. Čilliková, B. Mičieta, M. Neslušan, R. Čep, I. Mrkvica, J. Petrů, T. Zlámal	355
Erosive wear resistance of silicon carbide-cordierite ceramics: influence of the cordierite content Odpornost keramike silicijev karbid-kordierit proti obrabi pri eroziji: vpliv vsebnosti kordierita M. Pošarac-Marković, Dj. Veljović, A. Devečerski, B. Matović, T. Volkov-Husović	365
Influence of the substrate temperature on the structural, optical and thermoelectric properties of sprayed V₂O₅ thin films Vpliv temperature podlage na strukturne, optične in termoelektrične lastnosti napršene tanke plasti V ₂ O ₅ Y. Vijayakumar, K. N. Reddy, A. V. Moholkar, M. V. R. Reddy	371
Deep micro-hole drilling for hadfield steel by electro-discharge machining (EDM) Vrtanje globokih mikrolukenj v jekla hadfield z metodo elektrorazreza (EDM) V. Yilmaz, M. Sarıkaya, H. Dilipak	377
Surface analysis of electrochromic Cu_xO films in their colored and bleached states Površinska analiza elektrokromiznih plasti Cu _x O v njihovih obarvanih in obeljenih stanjih M. M. Ristova, M. Milun, B. Pejova	387
Thermodynamic analysis of the precipitation of carbonitrides in microalloyed steels Termodinamska analiza izločanja karbonitridov v mikrolegiranih jeklih M. Opiela	395
Experimental investigation of the crack-initiation moment of Charpy specimens under impact loading Eksperimentalna preiskava trenutka iniciacije razpoke pri udarni obremenitvi Charpyjevih vzorcev V. Kharchenko, E. Kondryakov, A. Panasenko	403
Structural, thermal and magnetic properties of Fe-Co-Ni-B-Si-Nb bulk amorphous alloy Strukturne, termične in magnetne lastnosti masivne amorfne zlitine Fe-Co-Ni-B-Si-Nb S. Lesz, M. Nabiałek, R. Nowosielski	409
The nano-wetting aspect at the liquid-metal/SiC interface Vidik nanoomakanja na stiku staljena kovina-SiC M. Mihailović, K. Raić, A. Patarić, T. Volkov - Husović	413
The effect of a superplasticizer admixture on the mechanical fracture parameters of concrete Vpliv dodatka superplastifikatorja na parametre mehanskega zloma betona H. Šimonová, I. Havlíková, P. Daněk, Z. Keršner, T. Vymazal	417
Properties and structure of Cu-Ti-Zr-Ni amorphous powders prepared by mechanical alloying Lastnosti in struktura amorfni praškov Cu-Ti-Zr-Ni, pripravljenih z mehanskim legiranjem A. Guwer, R. Nowosielski, A. Lebeda	423
Interaction of Cr₂N and Cr₂N/Ag thin films with CuZn-brass counterpart during ball-on-disc testing Interakcija Cr ₂ N in Cr ₂ N/Ag tankih plasti v paru s CuZn-medenino med preizkusom krogla na disk P. Bílek, P. Jurči, P. Dulová, M. Hudáková, J. Ptačinová, M. Pašák	429
Using simulated spectra to test the efficiency of spectral processing software in reducing the noise in Auger electron spectra Uporaba simuliranega spektra za preizkus učinkovitosti programske opreme predelave spektra pri zmanjšanju šuma spektra Augerjevih elektronov B. Poniku, I. Belič, M. Jenko	435
Surface behavior of AISI 4140 modified with the pulsed-plasma technique Lastnosti površine AISI 4140, spremenjene s tehniko pulzirajoče plazme Y. Y. Özbek, M. Durman	441
Preparation and dielectric properties of thermo-vaporous BaTiO₃ ceramics Priprava in dielektrične lastnosti termo-parno porozne keramike BaTiO ₃ A. Kholodkova, M. Danchevskaya, N. Popova, L. Pavlyukova, A. Fionov	447
Materiali in tehnologije / Materials and technology 49 (2015) 6, 995–1018	999

Hybrid sol-gel coatings doped with cerium to protect magnesium alloys from corrosion Hibridni sol-gel-nanosi, dopirani s cerijem, za korozijsko zaščito magnezijevih zlitin N. V. Murillo-Gutiérrez, F. Ansart, J.-P. Bonino, M.-J. Menu, M. Gressier	453
Influence of the tool geometry and process parameters on the static strength and hardness of friction-stir spot-welded aluminium-alloy sheets Vpliv geometrije orodja in parametrov procesa na statično trdnost in trdoto pri vrtilno-tornem točkastem varjenju pločevin iz Al-zlitine H. Güler	457
The stabilization of nano silver on polyester filament for a machine-made carpet Stabilizacija nanodelcev srebra na poliestrskem vlaknu za strojno izdelavo preprog K. M. Shojaei, A. Farrahi, H. Farrahi, A. Farrahi	461
Evaluation of the thermal resistance of selected bentonite binders Ocena toplotne upornosti izbranih bentonitnih veziv J. Beňo, J. Vontorová, V. Matějka, K. Gál	465
Development of numerical models for the heat-treatment-process optimisation in a closed-die forging production Razvoj numeričnih modelov za optimizacijo postopka toplotne obdelave pri proizvodnji odkovkov v zaprtih utopnih orodjih L. Maleček, M. Fedorko, F. Vančura, H. Jirková, B. Mašek	471
Alojz Prešern, dipl. inž. metalurgije (1920–2015)	477
2015/4	
Impact-toughness investigations of duplex stainless steels Preiskave udarne žilavosti dupleksnega nerjavnega jekla S. Topolska, J. Łabanowski	481
Effects of the artificial-aging temperature and time on the mechanical properties and springback behavior of AA6061 Vpliv temperature in časa umetnega staranja na mehanske lastnosti in vzmetnost AA6061 A. Polat, M. Avsar, F. Ozturk	487
Monitoring of polyurethane dispersions after the synthesis Spremljanje poliuretanskih disperzij po sintezi M. Ocepek, J. Zabret, J. Kecej, P. Venturini, J. Golob	495
Spectroscopic and porosimetric analyses of Roman pottery from an archaeological site near Mošnje, Slovenia Spektroskopske in porozimetrične preiskave rimske lončenine z arheološkega najdišča pri Mošnjah, Slovenija S. Kramar, J. Lux	503
Non-linear finite-element simulations of the tensile tests of textile composites Nelinearna simulacija nateznih preizkusov tekstilnih kompozitov s končnimi elementi T. Kroupa, K. Kunc, R. Zemčík, T. Mandys	509
Influence of the type and number of prepreg layers on the flexural strength and fatigue life of honeycomb sandwich structures Vpliv vrste in števila plasti na utrditev upogibne trdnosti in zdržljivosti pri utrujanju satastih sendvičnih konstrukcij L. Fojtl, S. Rusnakova, M. Zaludek, V. Rusnák	515
Potential for obtaining an ultrafine microstructure of low-carbon steel using accumulative roll bonding Možnosti doseganja ultradrobnozrnate mikrostrukture pri spajanju maloogljičnega jekla z akumulativnim valjanjem T. Kubina, J. Gubiš	521
Optimization of the annealing of plaster moulds for the manufacture of metallic foams with an irregular cell structure Optimiranje postopka žarjenja mavčnih form za izdelavo kovinskih pen z nepravilno strukturo celic I. Kroupová, P. Lichý, F. Radkovský, J. Beňo, V. Bednářová, I. Lána	527
The kinetics of small-impurity grain-boundary-segregation formation in cold-rolled deep-drawing 08C-Al and IF steels during post-deformation annealing Kinetika nastanka segregacije nečistoč po mejah zrn med žarjenjem po hladnem valjanju jekel 08C-Al in IF za globoki vlek A. Rashkovskiy, A. Kovalev, D. Wainstein, I. Rodionova, Y. Bykova, D. Zakharova	531
Application of a control-measuring apparatus and peltier modules in the bulk-metallic-glass production using the pressure-casting method Uporaba kontrolno-merilne naprave in peltierjevih modulov pri izdelavi masivnih kovinskih stekel po postopku tlačnega litja W. Pilarczyk, A. Pilarczyk	537
Evaluation of the structural changes in 9 % Cr creep-resistant steel using an electrochemical technique Ocena sprememb strukture v jeklu z 9 % Cr, odpornem proti lezenju, z uporabo elektrokemijske tehnike J. Rapouch, J. Bystriansky, V. Seřl, M. Svobodova	543
Effect of the by-pass cement-kiln dust and fluidized-bed-combustion fly ash on the properties of fine-grained alkali-activated slag-based composites Vpliv prahu iz peči za cement in letečega pepela iz vrtnčaste plasti na lastnosti drobnozrnatega, z alkalijami aktiviranega kompozita na osnovi žlindre V. Břlek Jr., L. Pařízek, L. Kalina	549

Microstructure, magnetic and mechanical properties of the bulk amorphous alloy Fe₆₁Co₁₀Ti₄Y₅B₂₀ Mikrostruktura, magnetne in mehanske lastnosti masivne amorfne zlitine Fe ₆₁ Co ₁₀ Ti ₄ Y ₅ B ₂₀ K. Bloch, M. Nabialek, J. Gondro	553
Modified cement-based mortars: crack initiation and volume changes Modificirane malte na osnovi cementa: iniciacija razpok in volumenske spremembe I. Havlikova, V. Bilek Jr., L. Topolar, H. Simonova, P. Schmid, Z. Kersner	557
Fracture properties of plain and steel-polypropylene-fiber-reinforced high-performance concrete Lastnosti loma navadnega in visokozmogljivega betona, ojačanega s polipropilenskimi vlakni P. Smarzewski, D. Barnat-Hunek	563
Preparation of porous ceramic materials based on CaZrO₃ Priprava porozne keramike na osnovi CaZrO ₃ E. Śnieżek, J. Szczerba, I. Jastrzębska, E. Kleczyk, Z. Pędzich	573
DP780 dual-phase-steel spot welds: critical fusion-zone size ensuring the pull-out failure mode Točkasti zvari jekla DP780 z dvofazno strukturo: kritična velikost staljene cone, ki zagotavlja porušenje z izpuljenjem M. Pouranvari, S. P. H. Marashi, H. L. Jaber	579
Application of computed tomography in comparison with the standardized methods for determining the permeability of cement-composite structures Uporaba računalniške tomografije v primerjavi s standardiziranimi metodami določanja prepustnosti cementnih kompozitnih struktur T. Komárková, M. Králíková, P. Kovács, D. Kocáb, T. Stavař	587
Properties of polymer-filled aluminium foams under moderate strain-rate loading conditions Lastnosti aluminijevih pen, napoljenih s polimernimi materiali, pri zmernih obremenitvah T. Doktor, P. Zlámal, T. Fíla, P. Koudelka, D. Kytýř, O. Jiroušek	597
Quality of the structure of ash bodies based on different types of ash Kvaliteta strukture telesa iz pepela na osnovi različnih vrst pepela V. Cerny	601
Sintered board materials based on recycled glass Sintrani ploščati materiali na osnovi recikliranega stekla T. Melichar, J. Bydžovský	607
Mechanical and wetting properties of nanosilica/epoxy-coated stainless steel Mehanske in površinske lastnosti premaza iz silicijevih nanodelcev in epoksidne smole na nerjavnem jeklu M. Conradi, G. Intihar, M. Zorko	613
Development of composite salt cores for foundry applications Razvoj kompozitnih slanih jeder za uporabo v livarstvu J. Beňo, E. Adámková, F. Mikšovský, P. Jelínek	619
Carbide morphology and ferrite grain size after accelerated carbide spheroidisation and refinement (ASR) of C45 steel Morfologija karbidov in velikost feritnih zrn po pospešeni sferoidizaciji in rafinaciji (ASR) jekla C45 J. Dlouhy, D. Hauserova, Z. Novy	625
Use of micromachining to shape the structure and electrical properties of the front electrode of a silicon solar cell Uporaba mikroobdelovanja za oblikovanje strukture in električnih lastnosti prednje elektrode silicijeve sončne celice M. Muszyfaga-Staszuk	629
Fabrication of TiO₂ nanotubes for bioapplications Izdelava TiO ₂ -nanocevk za biomedicinsko uporabo M. Kulkarni, K. Mrak-Poljšak, A. Flašker, A. Mazare, P. Schmuki, A. Kos, S. Čučnik, S. Sodin-Šemrl, A. Iglič	635
Assessment of the impact-echo method for monitoring the long-standing frost resistance of ceramic tiles Ocena metode impact-echo za kontrolo dolgotrajne odpornosti keramičnih ploščic proti zmrzali M. Matysik, I. Plskova, Z. Chobola	639
Investigation on new creep- and oxidation-resistant materials Preiskava novega materiala, odpornega proti lezenju in oksidaciji O. Khalaj, B. Masek, H. Jirkova, A. Ronsova, J. Svoboda	645
Effect of preheating on mechanical properties in induction sintering of metal-powder material Fe and w(Cu) = 3 % Vpliv predgrevanja na mehanske lastnosti indukcijsko sintranega materiala, izdelanega iz kovinskega prahu Fe in w(Cu) = 3 % G. Akpınar, E. Atik	653
2015/5	
Kinetic study and characterization of borided AISI 4140 steel Študij kinetike in karakterizacija boriranega jekla AISI 4140 M. Keddad, M. Ortiz-Domínguez, O. A. Gómez-Vargas, A. Arenas-Flores, M. Á. Flores-Rentería, M. Elias-Espinosa, A. García-Barrientos	665
Materiali in tehnologije / Materials and technology 49 (2015) 6, 995–1018	1001

Kinetics of the precipitation in austenite HSLA steels

Kinetika izločanja v avstenitnih HSLA-jeklih

E. Kalinowska-Ozgowicz, R. Kuziak, W. Ozgowicz, K. Lenik 673

Combined influence of V and Cr on the AISi10MgMn alloy with a high Fe level

Vzajemni vpliv V in Cr na zlitino AISi10MgMn z visoko vsebnostjo Fe

D. Bolibruchová, M. Žihalová 681

A reliable approach to a rapid calculation of the grain size of polycrystalline thin films after excimer laser crystallization

Zanesljiv način hitrega izračuna velikosti zrn v polikristalni tanki plasti po UV-laserski kristalizaciji

C. C. Kuo 687

Effects of different stirrer-pin forms on the joining quality obtained with friction-stir welding

Vpliv različnih oblik vrtilnih konic na kvaliteto spoja pri tornem vrtilnem varjenju

H. Basak, K. Kaptan 693

Monitoring early-age concrete with the acoustic-emission method and determining the change in the electrical properties

Pregled svežega betona z metodo akustične emisije in določanjem sprememb električnih lastnosti

L. Pazdera, L. Topolar, M. Korenska, T. Vymazal, J. Smutny, V. Bilek 703

Effect of the aggregate type on the properties of alkali-activated slag subjected to high temperatures

Vpliv vrste agregata na lastnosti z alkalijo aktivirane žindre, izpostavljene visokim temperaturam

P. Rovnaník, Á. Dufka 709

Microstructure evolution of advanced high-strength TRIP-aided bainitic steel

Razvoj mikrostrukture naprednega visokotrdnostnega bainitnega jekla z uporabo TRIP

A. Grajcar 715

Effect of electric current on the production of NiTi intermetallics via electric-current-activated sintering

Vpliv električnega toka pri izdelavi intermetalne zlitine NiTi s sintranjem, aktiviranim z električnim tokom

T. Yener, S. Siddique, F. Walther, S. Zeytin 721

Control of soft reduction of continuous slab casting with a thermal model

Kontrola mehke redukcije pri kontinuirnem litju slabov s termičnim modelom

J. Stetina, P. Ramik, J. Katolicky 725

Optimization of operating conditions in a laboratory SOFC testing device

Optimizacija obratovalnih razmer laboratorijske gorivne celice SOFC

T. Skalar, M. Lubej, M. Marinšek 731

Production of shaped semi-products from AHS steels by internal pressure

Izdelava polproizvodov iz AHS-jekel, oblikovanih z notranjim tlakom

I. Vorel, H. Jirková, B. Mašek, P. Kurka 739

Composite-material printed antenna for a multi-standard wireless application

Tiskana antena iz kompozitnega materiala za večstandardno brezžično uporabo

T. Alam, M. R. I. Faruque, M. T. Islam, N. Misran 745

Friction and wear behaviour of ulexite and cashew in automotive brake pads

Odpornost proti trenju in obrabi avtomobilskih zavornih oblog z uleksitom in prahom iz indijskega oreha

İ. Sugözü, İ. Mutlu, A. Keskin 751

Diffusion kinetics and characterization of borided AISI H10 steel

Kinetika difuzije in karakterizacija boriranega jekla AISI H10

I. Gunes, M. Ozcatal 759

Application of the Taguchi method to optimize the cutting conditions in hard turning of a ring bore

Uporaba Taguchi-jeve metode za optimizacijo trdega struženja roba izvrtine

M. Boy, I. Ciftci, M. Gunay, F. Ozhan 765

Thermal fatigue of single-crystal superalloys: experiments, crack-initiation and crack-propagation criteria

Toplotno utrujanje monokristalnih superzlitin: preizkusi, merila za nastanek in napredovanje razpoke

L. Getsov, A. Semenov, S. Semenov, A. Rybnikov, E. Tikhomirova 773

Investigating the effects of cutting parameters on the built-up-layer and built-up-edge formation during the machining of AISI 310 austenitic stainless steels

Preiskava vplivov parametrov rezanja na nastanek nakopičene plasti in nakopičenega roba med struženjem avstenitnega nerjavnega jekla AISI 310

M. B. Bilgin 779

Mortar-type identification for the purpose of reconstructing fragmented Roman wall paintings (Celje, Slovenia)

Analiza ometov za rekonstrukcijo fragmentov rimskih stenskih poslikav (Celje, Slovenija)

M. Gutman, M. Lesar Kikelj, J. Kuret, S. Kramar 785

Au-nanoparticle synthesis via ultrasonic spray pyrolysis with a separate evaporation zone Sinteza nanodelcev zlata z ultrazvočno razpršilno pirolizo z ločeno cono izhlapevanja P. Majerič, B. Friedrich, R. Rudolf	791
Determination of the critical fraction of solid during the solidification of a PM-cast aluminium alloy Določanje kritičnega deleža strjene faze med strjevanjem v PM ulite aluminijeve zlitine R. Kayıkcı, M. Colak, S. Sirin, E. Kocaman, N. Akar	797
Microstructural evolution of Inconel 625 during hot rolling Mikrostrukturni razvoj Inconela 625 med vročim valjanjem F. Tehovnik, J. Burja, B. Podgornik, M. Godec, F. Vode	801
Thermophysical properties and microstructure of magnesium alloys of the Mg-Al type Termofizikalne lastnosti in mikrostruktura magnezijevih zlitin tipa Mg-Al P. Lichý, J. Beňo, I. Kroupová, I. Vasková	807
Micro-encapsulated phase-change materials for latent-heat storage: thermal characteristics Mikroenkapsulirani materiali s fazno premeno za shranjevanje latentne toplote: toplotne značilnosti M. Ostrý, D. Dostálová, T. Klubal, R. Příkryl, P. Charvát	813
Ceramic masonry units intended for the masonry resistant to high humidity Keramični gradbeni elementi, namenjeni za zgradbe, odporne proti visoki vlagi J. Zach, V. Novák, J. Hroudová, M. Sedlmajer	817
Flame resistance and mechanical properties of composites based on new advanced resin system FR4/12 Negorljivost in mehanske lastnosti kompozitov na osnovi novih naprednih sistemov smol FR4/12 V. Rusnák, S. Rusnáková, L. Fojtl, M. Žaludek, A. Čapka	821
Effect of process parameters on the microstructure and mechanical properties of friction-welded joints of AISI 1040/AISI 304L steels Vpliv procesnih parametrov na mikrostrukturo in mehanske lastnosti tornjo varjenih spojev jekel AISI 1040/AISI 304L İ. Kirik, N. Özdemir	825
Influence of inoculation methods and the amount of an added inoculant on the mechanical properties of ductile iron Vpliv metod modifikacije in količine dodanega modifikatorja na mehanske lastnosti duktilnega železa H. Avdušinić, A. Gigović-Gekić, D. Čubela, R. Sunulahpašić, N. Mujezinović	833
One-step green synthesis of graphene/ZnO nanocomposites for non-enzymatic hydrogen peroxide sensing Enostopenjska zelena sinteza nanokompozita grafen-ZnO za neencimatsko detekcijo vodikovega peroksida S. S. Low, M. T. T. Tan, P. S. Khiew, H. S. Loh, W. S. Chiu	837
Material parameters for a numerical simulation of a compaction process for sintered double-height gears Materialni parametri za numerično simulacijo postopka stiskanja sintranih dvovišinskih zobnikov T. Verlak, M. Šori, S. Glodež	841
2015/6	
Problems and normative evaluation of bond-strength tests for coated reinforcement and concrete Problemi in normativna ocena preizkusov trdnosti vezi med armaturo s prekritjem in betonom P. Pokorný, M. Kouřil, J. Stouřil, P. Bouřka, P. Simon, P. Juránek	847
Modeling of occurrence of surface defects of C45 steel with genetic programming Modeliranje pojava površinskih napak pri jeklu C45 z genetskim programiranjem M. Kovačič, R. Jager	857
Effects of various helically angled grinding wheels on the surface roughness and roundness in grinding cylindrical surfaces Vpliv različnih kotov vijačnice pri brusilnih kolutih na hrapavost površine in okroglost pri brušenju valjastih površin M. Gavas, M. Kina, U. Köklü	865
Characterization of cast-iron gradient castings Karakterizacija litoželeznega gradientnega ulitka D. Mitrović, P. Mrvar, M. Petrič	871
Comparative mechanical and corrosion studies on magnesium, zinc and iron alloys as biodegradable metals Primerjalna študija mehanskih in korozijskih lastnosti biorazgradljivih zlitin magnezija, cinka in železa D. Vojtěch, J. Kubásek, J. Čapek, I. Pospíšilová	877
Microstructural changes of fine-grained concrete exposed to a sulfate attack Mikrostrukturne spremembe drobnozrnatega betona, izpostavljenega sulfatu M. Vyšvařil, P. Bayer, M. Rovnaníková	883
Effect of thermomechanical treatment on the corrosion behaviour of Si- and Al-containing high-Mn austenitic steel with Nb and Ti micro-additions Vpliv termomehanske obdelave na korozijsko vedenje manganskega avstenitnega jekla z vsebnostjo Si in Al, mikrolegiranega z Nb in Ti A. Grajcar, A. Plachcińska, S. Topolska, M. Kciuk	889
Materiali in tehnologije / Materials and technology 49 (2015) 6, 995–1018	1003

Surface free energy of hydrophobic coatings of hybrid-fiber-reinforced high-performance concrete Prosta energija površine hidrofobnih premazov na visokozmogljivem betonu, ojačanem s hibridnimi vlakni D. Barnat-Hunek, P. Smarzewski	895
Developing continuous-casting-process control based on advanced mathematical modelling Uporaba naprednega matematičnega modeliranja za razvoj kontrole postopka kontinuirnega ulivanja J. Falkus, K. Miłkowska-Piszczek	903
Elastic behaviour of magnesia-chrome refractories at elevated temperatures Elastično vedenje ognjevdržnih gradiv magnezija-krom pri povišanih temperaturah I. Jastrzębska, J. Szczerba, J. Szlęzak, E. Śniezek, Z. Pędzich	913
Study on the magnetization-reversal behavior of annealed Sm-Fe-Co-Si-Cu ribbons Študij vedenja pri obratu magnetizacije žarjenih trakov Sm-Fe-Co-Si-Cu M. Dośpiał, S. Garus, M. Nabialek	919
Evaluation of the chitosan-coating effectiveness on a dental titanium alloy in terms of microbial and fibroblastic attachment and the effect of aging Ocena učinkovitosti nanosa hitozana na oprijemanje mikrobov in fibroblastov na dentalni titanovi zlitini ter na pojav staranja U. T. Kalyoncuoglu, B. Yilmaz, S. Gungor, Z. Evis, P. Uyar, G. Akca, G. Kansu	925
Structure and properties of the carburised surface layer on 35CrSiMn5-5-4 steel after nanostructurization treatment Struktura in lastnosti naogljjičene površine jekla 35CrSiMn5-5-4 po nanostrukturni obdelavi E. Skoček, K. Wasiak, W. A. Świątnicki	933
Optimization of the surface roughness by applying the Taguchi technique for the turning of stainless steel under cooling conditions Uporaba Taguchi-jeve metode za optimiranje hrapavosti površine pri struženju nerjavnega jekla z ohlajanjem M. Sarıkaya	941
Effect of cryogenic treatment applied to M42 HSS drills on the machinability of Ti-6Al-4V alloy Vpliv podhlajevanja svedrov M42 HSS na obdelovalnost zlitine Ti-6Al-4V T. Kivak, U. Şeker	949
Load-capacity prediction for the carbon- or glass-fibre-reinforced plastic part of a wrapped pin joint Napoved nosilnosti plastičnih delov zatičnega spoja, ojačanega z ogljikovimi ali steklastimi vlakni J. Krystek, R. Kottner	957
A meshless model of electromagnetic braking for the continuous casting of steel Brezmrežni model elektromagnetnega zaviranja pri kontinuirnem ulivanju jekla K. Mramor, R. Vertnik, B. Šarler	961
Non-singular method of fundamental solutions for three-dimensional isotropic elasticity problems with displacement boundary conditions Nesingularna metoda fundamentalnih rešitev za deformacijo tridimenzijskih elastičnih problemov z deformacijskimi robnimi pogoji Q. Liu, B. Šarler	969
Solid-state sintering of (K_{0,5}Na_{0,5})NbO₃ synthesized from an alkali-carbonate-based low-temperature calcined powder Sintranje v trdnem keramike (K _{0,5} Na _{0,5})NbO ₃ , sintetizirane iz nizkotemperaturno kalciniranega prahu, pripravljenega na osnovi alkalijskih karbonatov M. Feizpour, T. Ebadzadeh, D. Jenko	975
Stability of close-cell Al foams depending on the usage of different foaming agents Stabilnost aluminijevih pen z zaprti poroznostjo glede na uporabo različnih penilnih sredstev I. Paulin	983
Evolution of the microstructure and magnetic properties of a cobalt-silicon-based alloy in the early stages of mechanical milling Razvoj mikrostrukture in magnetnih lastnosti zlitine Co-Si v začetnem stadiju mehanskega legiranja W. Rattanasakulthong, C. Sirisathitkul, P. F. Rogl	989
In memoriam prof. dr. Milan Trbižan	993
Letnik 49 (2015), 1–6 – Volume 49 (2015), 1–6	995

MATERIALI IN TEHNOLOGIJE / MATERIALS AND TECHNOLOGY

AVTORSKO KAZALO / AUTHOR INDEX

LETNIK / VOLUME 49, 2015, 1–6, A–Ž

A

Aćimović-Pavlović Z. 157
 Adámková E. 61, 619
 Akar N. 797
 Akca G. 925
 Akpınar G. 653
 Alam T. 745
 Aleksandrović S. 165
 Aleksić Z. 81
 Andrić Lj. 157
 Ansart F. 453
 Anžel I. 75, 297
 Arenas-Flores A. 665
 Atik E. 653
 Avdušinović H. 833
 Avsar M. 487
 Azim R. 193

B

Babić M. 117
 Barčić E. 153
 Barnat-Hunek D. 563, 895
 Basak H. 693
 Bayer P. 883
 Bažant P. 55, 281
 Bednářová V. 527
 Belič I. 435
 Beňo J. 61, 465, 527, 619, 807
 Bentouhami A. 235
 Bereznev S. 149
 Bhattacharya B. 123
 Bílek Jr. V. 549, 557
 Bílek P. 429
 Bilek V. 703
 Bilgin M. B. 779
 Bloch K. 553
 Bogović J. 75
 Bolibruchová D. 681
 Bonino J.-P. 453
 Bouška P. 847
 Boy M. 765
 Burja J. 801
 Bydžovský J. 607
 Bykova Y. 531
 Bystrianský J. 243, 543

C

Calleja W. 3
 Casasola R. 229
 Castaño V. M. 3
 Cerny V. 601
 Chabičovský M. 333, 337
 Charvát P. 813
 Chiu W. S. 837
 Chobola Z. 639
 Ciftci I. 765
 Colak M. 797
 Conradi M. 613

Č

Čubela D. 833
 Čurčija D. 349

Č

Čapek J. 877
 Čapka A. 821
 Čegan T. 15, 27
 Čeh M. 173
 Čep R. 355
 Čilliková M. 355
 Čučnik S. 635

D

Danchevskaya M. 447
 Daněk P. 417
 Delić A. 153
 Devečerski A. 365
 Dharmalingam S. 9
 Dilipak H. 139, 377
 Dlouhý J. 213, 625
 Doktor T. 203, 597
 Dománková M. 213
 Donik Č. 303
 Došpial M. 919
 Dostálová D. 813
 Dufka Á. 709
 Dulová P. 429
 Durman M. 441

Đ

Đordević I. 81

E

Ebadzadeh T. 975

Elias-Espinosa M. 665
 Evis Z. 925

F

Falkus J. 903
 Farajpour M. 259
 Farrahi A. 461
 Farrahi H. 461
 Faruque M. R. I. 745
 Fedorko M. 471
 Feizpour M. 975
 Fíla T. 203, 597
 Fionov A. 447
 Flašker A. 635
 Flores-Rentería M. Á. 665
 Fojtl L. 515, 821
 Franěk Z. 285
 Fras Zemljič L. 297
 Friedrich B. 75, 791

G

Gajdoš E. 243
 Gál K. 465
 Galindo M. 3
 García-Barrientos A. 665
 Garus S. 919
 Gavas M. 865
 Getsov L. 773
 Gezgin A. 139
 Gigović-Gekić A. 833
 Glodež S. 303, 841
 Godec M. 303, 801
 Golob J. 495
 Gómez-Vargas O. A. 665
 Gondro J. 553
 Goodarzi M. 133
 Gowrisankar A. 9
 Gradišek K. 173
 Grajcar A. 715, 889
 Greger M. 267
 Gressier M. 453
 Grzegorzczak B. 197
 Gubiš J. 521
 Gunay M. 765
 Gunes I. 111, 759
 Gungor S. 925
 Gutman M. 785

Guwer A. 423
Güler H. 457

H

Hadasik E. 275
Hauserova D. 625
Havlíková I. 417, 557
Hidalga de la J. 3
Hnízdil M. 333
Hodek J. 213
Hodžic N. 153
Horský J. 219
Hroudová J. 817
Hudáková M. 429

I

Iglič A. 635
Intihar G. 613
Islam M. T. 193, 745

J

Jaber H. L. 579
Jager R. 857
Jandova D. 37
Jastrzębska I. 573, 913
Javornik N. 303
Jelínek P. 61, 619
Jenko D. 975
Jenko M. 81, 435
Jirková H. 471, 645, 739
Jiroušek O. 203, 597
Jokanović V. 81
Jurči P. 429
Juránek P. 847
Juřica J. 15, 27

K

Kablar O. 153
Kalina L. 549
Kalinowska-Ozgowicz E. 69, 673
Kalyoncuoglu U. T. 925
Kansu G. 925
Kaptan K. 693
Karaoglanli A. C. 253
Karas V. 267
Katolický J. 725
Kayikci R. 797
Kciuk M. 889
Kecelj J. 495
Keddám M. 43, 665
Keršner Z. 417, 557
Keskes B. 235
Keskin A. 751
Khalaj O. 645
Kharchenko V. 403

Kheirandish S. 133
Khiew P. S. 837
Kholodkova A. 447
Kina M. 865
Kirik I. 825
Kivak T. 949
Kleczyk E. 573
Klofáč J. 55
Klupal T. 813
Kocáb D. 587
Kocaman E. 797
Komárková T. 587
Kondryakov E. 403
Korenska M. 703
Kortnik J. 103
Kos A. 635
Kottner R. 957
Kouba R. 43
Koudelka P. 203, 597
Kouřil M. 847
Kovačević D. 153
Kovačič M. 857
Kovács P. 587
Kovalev A. 531
Kračun A. 297
Králíková M. 587
Kramar S. 343, 503, 785
Kroupa T. 509
Kroupa T. 99
Kroupová I. 527, 807
Krstić B. 165
Krystek J. 957
Kubásek J. 877
Kubatík T. F. 129
Kubina T. 213, 521
Kucuk I. 19, 183
Kulkarni M. 635
Kunc K. 509
Kuo C. C. 687
Kuret J. 785
Kuřitka I. 55, 281
Kurka P. 739
Kursa M. 15
Kuziak R. 673
Kvapil J. 219
Kytýř D. 203, 597
Köklü U. 865
Köver M. 213

L

Łabanowski J. 481
Lána I. 527
Lapornik D. 173

Lašová Z. 95
Lazić V. 165
Lebuda A. 423
Lehner J. 149
Lenik K. 673
Lesar Kikelj M. 785
Leskovšek V. 313
Lesz S. 409
Lichý P. 527, 807
Liu Q. 969
Loh H. S. 837
López F. 3
Losertová M. 207
Low S. S. 837
Lubej M. 731
Lux J. 343, 503

M

Machovský M. 281
Madaj M. 267
Majerič P. 75, 791
Malcharcziková J. 15
Maleček L. 471
Mamuzić I. 349
Mandys T. 509
Marashi S. P. H. 579
Marinšek M. 731
Markoli B. 103
Martínek P. 31
Masarik M. 285
Mašek B. 471, 645, 739
Matějka V. 27, 465
Matović B. 365
Matysik M. 639
Mazare A. 635
Melichar T. 607
Mellikov E. 149
Menu M.-J. 453
Mičieta B. 355
Michalska J. 275
Michenka V. 15
Mihailović M. 413
Mikšovský F. 61, 619
Miłkowska-Piszczek K. 903
Miloradović N. 117
Milosavljević D. 165
Milun M. 387
Mirtič B. 343
Misran N. 745
Mitrović D. 871
Mitrović S. 117
Moholkar A. V. 371
Mousavizadeh S. M. 247

- Mrak-Poljšak K. 635
 Mramor K. 961
 Mrkvica I. 355
 Mrvar P. 871
 Mujezinović N. 833
 Murillo-Gutiérrez N. V. 453
 Musztyfaga-Staszuk M. 629
 Mutavdžić M. 165
 Mutlu İ. 751
 Münster L. 281
- N**
 Nabiałek M. 409, 553, 919
 Nacházel J. 31
 Neslušán M. 355
 Nikolić R. R. 165
 Nikoosohbat F. 133
 Niznanska J. 37
 Novák P. 129
 Novák V. 817
 Nowosielski R. 409, 423
 Novy Z. 625
- O**
 Ocepek M. 495
 Opiela M. 395
 Ortiz-Domínguez M. 665
 Ostrý M. 813
 Ozcatal M. 759
 Ozgowicz W. 69, 197, 673
 Ozhan F. 765
 Ozturk F. 487
 Özbek Y. Y. 441
 Özdemir N. 825
- P**
 Pala Z. 129
 Palomino-Merino R. 3
 Panasenko A. 403
 Pařízek L. 549
 Pastorek M. 55
 Pašák M. 429
 Patarić A. 413
 Paulin I. 303, 983
 Pawełek A. 197
 Pavlović M. 157
 Pavlyukova L. 447
 Pazdera L. 703
 Pędzich Z. 573, 913
 Pejova B. 387
 Petlák D. 27
 Petrášová I. 207
 Petrič M. 871
 Petrů J. 355
- Piątkowski A. 197
 Pilarczyk A. 537
 Pilarczyk W. 537
 Plachcińska A. 889
 Plskova I. 639
 Pošarac-Marković M. 365
 Podaný P. 31
 Podgornik B. 313, 801
 Pohanka M. 219
 Pohludka M. 15
 Pokorný P. 847
 Polat A. 487
 Poniku B. 435
 Popova N. 447
 Pospíšilová I. 877
 Pouranvari M. 133, 247, 259, 579
 Pristacz H. 343
 Přikryl R. 813
 Przondziono J. 223, 275
 Ptačinová J. 429
- R**
 Radika N. 9
 Radkovský F. 527
 Raić K. T. 81, 413
 Ramik P. 725
 Ranachowski Z. 197
 Ranjbarnodeh E. 259
 Rapouch J. 543
 Rashkovskiy A. 531
 Ratej M. 303
 Rattanasakulthong W. 989
 Raudenský M. 333
 Raudenský M. 337
 Reddy K. N. 371
 Reddy M. V. R. 371
 Revathi N. 149
 Rincón J. Ma. 229
 Ristova M. M. 387
 Rodionova I. 531
 Rogan - Šmuc N. 343
 Rogl P. F. 989
 Ronsova A. 645
 Rovnaník P. 709
 Rovnaníková M. 883
 Rudolf R. 75, 81, 87, 791
 Rusnák V. 515, 821
 Rusnáková S. 515, 821
 Rybnikov A. 773
- S**
 Safonova M. 149
 Samardžija Z. 173
 Sarikaya M. 139, 377, 941
- Sarioglu C. 19, 183
 Schmid P. 557
 Schmuki P. 635
 Sedlák J. 55
 Sedlmajer M. 817
 Sedmak A. 165
 Sefl V. 543
 Şeker U. 949
 Semenov A. 773
 Semenov S. 773
 Semnani Rahbar R. 325
 Shojaei K. M. 461
 Shukla S. 123
 Siddique S. 721
 Simon P. 847
 Simonova H. 557
 Singh P. K. 123
 Singh V. K. 123
 Sirin S. 797
 Sirisathitkul C. 989
 Skalar T. 731
 Skołek E. 933
 Skotnicová K. 27
 Smarzewski P. 563, 895
 Smetana B. 27
 Smutny J. 703
 Śnieżek E. 573, 913
 Sodin-Šemrl S. 635
 Srbová H. 99
 Stamenković D. 81
 Stavař T. 587
 Stergaršek A. 297
 Stetina J. 725
 Stojanović B. 117
 Stopić S. 75
 Stoulil J. 847
 Subramanian R. 9
 Suchmann P. 37
 Sugözü İ. 751
 Sunulahpašić R. 833
 Świątnicki W. A. 933
 Svoboda J. 645
 Svobodova M. 543
 Szala J. 275
 Szczerba J. 573, 913
 Szlęzak J. 913
- Š**
 Šarler B. 961, 969
 Šimonová H. 417
 Šmíd J. 285
 Šori M. 303, 841
 Šperl M. 243

Šuštaršič B. 303

T

Tan M. T. T. 837
 Tehovnik F. 801
 Ternik P. 87
 Terzić A. 157
 Thiyagarajan T. 9
 Tikal F. 291
 Tikhomirova E. 773
 Todorović A. 81
 Topolar L. 557, 703
 Topolska S. 481, 889
 Torkar M. 181
 Traksmaa R. 149

U

Urbánek M. 291
 Uyar P. 925

V

Vadood M. 325
 Vančura F. 471
 Vasková I. 807

Veljović Dj. 365
 Venturini P. 495
 Verhovšek D. 173
 Verlak T. 841
 Vertnik R. 961
 Vijayakumar Y. 371
 Vode F. 801
 Vodopivec F. 349
 Vojtěch D. 877
 Volkov - Husović T. 365, 413
 Volobujeva O. 149
 Vontorová J. 465
 Vorel I. 739
 Vyšvařil M. 883
 Vymazal T. 417, 703

W

Wainstein D. 531
 Wajda W. 69
 Walke W. 223, 275
 Walther F. 721
 Wasiak K. 933
 Wieczorek J. 275

Y

Yener T. 721
 Yilmaz B. 925
 Yilmaz V. 377

Z

Zabret J. 495
 Zach J. 817
 Zakharova D. 531
 Zaludek M. 515
 Zemčík R. 95, 99, 509
 Zeytin S. 721
 Zlámal P. 203, 597
 Zlámal T. 355
 Zorko M. 613
 Zulić A. 153
 Zúñiga C. 3

Ž

Žaludek M. 821
 Žihalová M. 681
 Žunič Z. 87

MATERIALI IN TEHNOLOGIJE / MATERIALS AND TECHNOLOGY

VSEBINSKO KAZALO / SUBJECT INDEX

LETNIK / VOLUME 49, 2015, 1–6

Kovinski materiali – Metallic materials

Boron-doped hydrogenated amorphous semiconductor MEMS

Z borom dopirani hydrogenirani amorfni polprevodnik MEMS

M. Galindo, C. Zúñiga, R. Palomino-Merino, F. López, W. Calleja, J. de la Hidalga, V. M. Castaño 3

Wear behaviour of B₄C reinforced hybrid aluminum-matrix composites

Vedenje hibridnega kompozita na osnovi aluminija, ojačanega z B₄C, pri obrabi

T. Thiyagarajan, R. Subramanian, S. Dharmalingam, N. Radika, A. Gowrisankar 9

Influence of the HIP process on the properties of as-cast Ni-based alloys

Vpliv vročega izostatskega stiskanja na lastnosti Ni-zlitin z lito strukturo

J. Malcharcziková, M. Pohludka, V. Michenka, T. Čegan, J. Juřica, M. Kurska 15

Corrosion of CrN-coated stainless steel in a NaCl solution (w = 3 %)

Korozijska nerjavnega jekla s CrN-prevleko v raztopini NaCl (w = 3 %)

I. Kucuk, C. Sarioglu 19

Preparation and properties of master alloys Nb-Al and Ta-Al for melting and casting of γ -TiAl intermetallics

Priprava in lastnosti predzlitin Nb-Al in Ta-Al za taljenje in ulivanje intermetalnih zlitin γ -TiAl

J. Juřica, T. Čegan, K. Skotnicová, D. Petlák, B. Smetana, V. Matějka 27

Decreasing the carbonitride size and amount in austenitic steel with heat treatment and thermomechanical processing

Zmanjšanje velikosti karbonitridov v avstenitem jeklu s toplotno obdelavo in termomehansko predelavo

P. Martínek, P. Podaný, J. Nacházek 31

Deep cryogenic treatment of H11 hot-working tool steel

Globoka kriogenska obdelava orodnega jekla H11 za delo v vročem

P. Suchmann, D. Jandova, J. Niznanska 37

Numerical prediction of the compound layer growth during the gas nitriding of Fe-M binary alloys

Numerično napovedovanje rasti spojinske plasti med plinskim nitriranjem binarnih zlitin Fe-M

R. Kouba, M. Keddou 43

Amplitude–frequency response of an aluminium cantilever beam determined with piezoelectric transducers

Amplitudno-frekvenčni odziv konzolnega nosilca iz aluminija, ugotovljen s piezoelektričnimi pretvorniki

Z. Lašová, R. Zemčík 95

Effect of sliding speed on the frictional behavior and wear performance of borided and plasma-nitrided W9Mo3Cr4V high-speed steel

Vpliv hitrosti drsenja na vedenje in obrabo boriranega in v plazmi nitriranega hitroreznega jekla W9Mo3Cr4V

I. Gunes 111

Tribological behaviour of A356/10SiC/3Gr hybrid composite in dry-sliding conditions

Tribološko vedenje hibridnega kompozita A356/10SiC/3Gr pri suhem drsenju

B. Stojanović, M. Babić, N. Miloradović, S. Mitrović 117

Compacting the powder of Al-Cr-Mn alloy with SPS

Kompaktiranje prahu zlitine Al-Cr-Mn s SPS

T. F. Kubatík, Z. Pala, P. Novák 129

Effect of tempering on the microstructure and mechanical properties of resistance-spot-welded DP980 dual-phase steel

Vpliv popuščanja na mikrostrukturo in mehanske lastnosti točkasto varjenega dvofaznega jekla DP980

F. Nikoosohbat, S. Kheirandish, M. Goodarzi, M. Pouranvari 133

Optimization of the process parameters for surface roughness and tool life in face milling using the Taguchi analysis

Optimizacija procesnih parametrov glede na hrupavost površine in trajnostno dobo orodja pri čelnem rezkanju z uporabo Taguchijeve analize

M. Sarıkaya, H. Dilipak, A. Gezgin 139

Mechanical properties of the austenitic stainless steel X15CrNiSi20-12 after recycling

Mehanske lastnosti avstenitnega nerjavnega jekla X15CrNiSi20-12 po recikliranju

A. Delić, O. Kablar, A. Zulić, D. Kovačević, N. Hodžić, E. Barčić 153

Selection of the most appropriate welding technology for hardfacing of bucket teeth Izbira najbolj primerne tehnologije trdega navarjanja zoba zajemalke V. Lazić, A. Sedmak, R. R. Nikolić, M. Mutavdžić, S. Aleksandrović, B. Krstić, D. Milosavljević	165
Pitting corrosion of TiN-coated stainless steel in 3 % NaCl solution Jamičasta korozija nerjavnega jekla s prevleko TiN v 3-odstotni raztopini NaCl I. Kucuk, C. Sarioglu	183
Influence of the strain rate on the PLC effect and acoustic emission in single crystals of the CuZn30 alloy compressed at an elevated temperature Vpliv hitrosti deformacije na pojav PLC in akustično emisijo monokristalov zlitine CuZn30, stiskane pri povišani temperaturi W. Ozgowicz, B. Grzegorzcyk, A. Pawelek, A. Piątkowski, Z. Ranachowski	197
Determination of elastic-plastic properties of Alporas foam at the cell-wall level using microscale-cantilever bending tests Določanje elastičnih in plastičnih lastnosti pene Alporas na ravni celične stene z upogibnimi preizkusi z mikroskopsko iglo T. Doktor, D. Kytýř, P. Koudelka, P. Zlámal, T. Fíla, O. Jiroušek	203
Electrochemical behavior of biocompatible alloys Elektrokemijsko vedenje biokompatibilnih zlitin I. Petrášová, M. Losertová	207
Preparation and thermal stability of ultra-fine and nano-grained commercially pure titanium wires using CONFORM equipment Priprava komercialne ultradrobne in nanozrnate Ti-žice z opremo CONFORM in njena termična stabilnost T. Kubina, J. Dlouhý, M. Köver, M. Dománková, J. Hodek	213
Estimation of the thermal contact conductance from unsteady temperature measurements Določanje kontaktne toplotne prevodnosti iz neravnotežnega merjenja temperature J. Kvapil, M. Pohanka, J. Horský	219
Potentiodynamic and XPS studies of X10CrNi18-8 steel after ethylene oxide sterilization Potenciodinamične in XPS analize jekla X10CrNi18-8 po sterilizaciji z etilen oksidom W. Walke, J. Przdonziono	223
Experimental analysis and modeling of the buckling of a loaded honeycomb sandwich composite Eksperimentalna analiza in modeliranje upogibanja obremenjenega satastega sendvičnega kompozita A. Bentouhami, B. Keskes	235
Fatigue behaviour of X70 steel in crude oil Vedenje jekla X70 pri utrujanju v surovi nafti L. Gajdoš, M. Šperl, J. Bystrianský	243
Use of Larson-Miller parameter for modeling the progress of isothermal solidification during transient-liquid-phase bonding of IN718 superalloy Uporaba Larson-Millerjevega parametra za modeliranje izotermnega strjevanja pri spajanju z vmesno tekočo fazo superzlitine IN718 M. Pouranvari, S. M. Mousavizadeh	247
Effect of severe air-blast shot peening on the wear characteristics of CP titanium Vpliv intenzivnega površinskega kovanja s peskanjem z zrakom na obrabne lastnosti CP-titana A. C. Karaoglanli	253
Finite-element minimization of the welding distortion of dissimilar joints of carbon steel and stainless steel Uporaba končnih elementov za zmanjšanje popačenja oblike pri varjenju ogljikovega in nerjavnega jekla E. Ranjbarnodeh, M. Pouranvari, M. Farajpour	259
Magnesium-alloy die forgings for automotive applications Izkovki iz magnezijevih zlitin za avtomobilsko industrijo M. Madaj, M. Greger, V. Karas	267
Resistance to electrochemical corrosion of the extruded magnesium alloy AZ80 in NaCl solutions Odpornost ekstrudirane magnezijeve zlitine AZ80 proti elektrokemijski koroziji v raztopini NaCl J. Przdonziono, E. Hadasik, W. Walke, J. Szala, J. Michalska, J. Wiczorek	275
Determination of the cause of the formation of transverse internal cracks on a continuously cast slab Ugotavljanje vzrokov za nastanek notranjih prečnih razpok v kontinuirno ulitem slabu Z. Franěk, M. Masarik, J. Šmíd	285
Neutralization of waste filter dust with CO₂ Nevtralizacija odpadnega filtrskega prahu s CO ₂ A. Kračun, I. Anžel, L. Fras Zemljič, A. Stergaršek	297
The influence of the morphology of iron powder particles on their compaction in an automatic die Vpliv morfologije delcev železovega prahu na njegovo sposobnost za avtomatsko enosno stiskanje B. Šuštaršič, M. Godec, Č. Donik, I. Paulin, S. Glodež, M. Šori, M. Ratej, N. Javornik	303

Wear mechanisms and surface engineering of forming tools Obrabni mehanizmi in inženiring površine preoblikovalnih orodij B. Podgornik, V. Leskovšek	313
Influence of the impact angle and pressure on the spray cooling of vertically moving hot steel surfaces Vpliv vpadnega kota in tlaka na ohlajanje z brizganjem na vertikalno premikajoče se vroče površine jekla M. Hnízdil, M. Chabičovský, M. Raudenský	333
Techniques of measuring spray-cooling homogeneity Tehnike merjenja homogenosti hlajenja z brizganjem M. Chabičovský, M. Raudenský	337
Reynolds differential equation singularity using processes of small straining with lubrication Reynoldsova diferencialna enačba pri procesih majhne deformacije z mazanjem D. Čurčija, F. Vodopivec, I. Mamuzić	349
Prediction of the catastrophic tool failure in hard turning through acoustic emission Napovedovanje katastrofične poškodbe keramičnih vložkov pri struženju z akustično emisijo M. Čilliková, B. Mičieta, M. Neslušan, R. Čep, I. Mrkvica, J. Petrů, T. Zlámal	355
Deep micro-hole drilling for hadfield steel by electro-discharge machining (EDM) Vrtanje globokih mikrolukenj v jekla hadfield z metodo elektrorazreza (EDM) V. Yilmaz, M. Sarıkaya, H. Dilipak	377
Surface analysis of electrochromic Cu₂O films in their colored and bleached states Površinska analiza elektrokromiznih plasti Cu ₂ O v njihovih obarvanih in obeljenih stanjih M. M. Ristova, M. Milun, B. Pejova	387
Thermodynamic analysis of the precipitation of carbonitrides in microalloyed steels Termodinamska analiza izločanja karbonitridov v mikrolegiranih jeklih M. Opiela	395
Experimental investigation of the crack-initiation moment of Charpy specimens under impact loading Eksperimentalna preiskava trenutka iniciacije razpoke pri udarni obremenitvi Charpyjevih vzorcev V. Kharchenko, E. Kondryakov, A. Panasenko	403
Structural, thermal and magnetic properties of Fe-Co-Ni-B-Si-Nb bulk amorphous alloy Strukturne, termične in magnetne lastnosti masivne amorfne zlitine Fe-Co-Ni-B-Si-Nb S. Lesz, M. Nabiałek, R. Nowosielski	409
The nano-wetting aspect at the liquid-metal/SiC interface Vidik nanoomakanja na stiku staljena kovina-SiC M. Mihailović, K. Raić, A. Patarić, T. Volkov - Husović	413
Properties and structure of Cu-Ti-Zr-Ni amorphous powders prepared by mechanical alloying Lastnosti in struktura amorfnihih prahov Cu-Ti-Zr-Ni, pripravljenih z mehanskim legiranjem A. Guwer, R. Nowosielski, A. Lebuda	423
Interaction of Cr₂N and Cr₂N/Ag thin films with CuZn-brass counterpart during ball-on-disc testing Interakcija Cr ₂ N in Cr ₂ N/Ag tankih plasti v paru s CuZn-medenino med preizkusom krogla na disk P. Břílek, P. Jurči, P. Dulová, M. Hudáková, J. Ptačinová, M. Pašák	429
Surface behavior of AISI 4140 modified with the pulsed-plasma technique Lastnosti površine AISI 4140, spremenjene s tehniko pulzirajoče plazme Y. Y. Özbek, M. Durman	441
Hybrid sol-gel coatings doped with cerium to protect magnesium alloys from corrosion Hibridni sol-gel-nanosi, dopirani s cerijem, za korozijsko zaščito magnezijevih zlitin N. V. Murillo-Gutiérrez, F. Ansart, J.-P. Bonino, M.-J. Menu, M. Gressier	453
Influence of the tool geometry and process parameters on the static strength and hardness of friction-stir spot-welded aluminium-alloy sheets Vpliv geometrije orodja in parametrov procesa na statično trdnost in trdoto pri vrtilno-tornem točkastem varjenju pločevin iz Al-zlitine H. Güler	457
Impact-toughness investigations of duplex stainless steels Preiskave udarne žilavosti dupleksnega nerjavnega jekla S. Topolska, J. Łabanowski	481
Effects of the artificial-aging temperature and time on the mechanical properties and springback behavior of AA6061 Vpliv temperature in časa umetnega staranja na mehanske lastnosti in vzmetnost AA6061 A. Polat, M. Avsar, F. Ozturk	487
Influence of the type and number of prepreg layers on the flexural strength and fatigue life of honeycomb sandwich structures Vpliv vrste in števila plasti na utrditev upogibne trdnosti in zdržljivosti pri utrujanju satastih sendvičnih konstrukcij L. Fojtl, S. Rusnakova, M. Zaludek, V. Rusnák	515

Potential for obtaining an ultrafine microstructure of low-carbon steel using accumulative roll bonding Možnosti doseganja ultradrobnozrnatne mikrostrukture pri spajanju maloogljivega jekla z akumulativnim valjanjem T. Kubina, J. Gubiš	521
Optimization of the annealing of plaster moulds for the manufacture of metallic foams with an irregular cell structure Optimiranje postopka žarjenja mavčnih form za izdelavo kovinskih pen z nepravilno strukturo celic I. Kroupová, P. Lichý, F. Radkovský, J. Beňo, V. Bednářová, I. Lána	527
The kinetics of small-impurity grain-boundary-segregation formation in cold-rolled deep-drawing 08C-Al and IF steels during post-deformation annealing Kinetika nastanka segregacije nečistoč po mejah zrn med žarjenjem po hladnem valjanju jekel 08C-Al in IF za globoki vlek A. Rashkovskiy, A. Kovalev, D. Wainstein, I. Rodionova, Y. Bykova, D. Zakharova	531
Application of a control-measuring apparatus and peltier modules in the bulk-metallic-glass production using the pressure-casting method Uporaba kontrolno-merilne naprave in peltierjevih modulov pri izdelavi masivnih kovinskih stekel po postopku tlačnega litja W. Pilarczyk, A. Pilarczyk	537
Evaluation of the structural changes in 9 % Cr creep-resistant steel using an electrochemical technique Ocena sprememb strukture v jeklu z 9 % Cr, odpornem proti lezenju, z uporabo elektrokemijske tehnike J. Rapouch, J. Bystriansky, V. Seřl, M. Svobodova	543
Microstructure, magnetic and mechanical properties of the bulk amorphous alloy Fe₆₁Co₁₀Ti₄Y₅B₂₀ Mikrostruktura, magnetne in mehanske lastnosti masivne amorfnе zlitine Fe ₆₁ Co ₁₀ Ti ₄ Y ₅ B ₂₀ K. Bloch, M. Nabiałek, J. Gondro	553
DP780 dual-phase-steel spot welds: critical fusion-zone size ensuring the pull-out failure mode Točkasti zvari jekla DP780 z dvofazno strukturo: kritična velikost staljene cone, ki zagotavlja porušenje z izpuljenjem M. Pouranvari, S. P. H. Marashi, H. L. Jaber	579
Properties of polymer-filled aluminium foams under moderate strain-rate loading conditions Lastnosti aluminijevih pen, napoljenih s polimernimi materiali, pri zmernih obremenitvah T. Doktor, P. Zlámal, T. Fíla, P. Koudelka, D. Kytýř, O. Jiroušek	597
Carbide morphology and ferrite grain size after accelerated carbide spheroidisation and refinement (ASR) of C45 steel Morfoloģija karbidov in velikost feritnih zrn po pospešeni sferoidizaciji in rafinaciji (ASR) jekla C45 J. Dlouhy, D. Hauserova, Z. Novy	625
Investigation on new creep- and oxidation-resistant materials Preiskava novega materiala, odpornega proti lezenju in oksidaciji O. Khalaj, B. Masek, H. Jirkova, A. Ronesova, J. Svoboda	645
Effect of preheating on mechanical properties in induction sintering of metal-powder material Fe and w(Cu) = 3 % Vpliv predgrevanja na mehanske lastnosti indukcijsko sintranega materiala, izdelanega iz kovinskega prahu Fe in w(Cu) = 3 % G. Akpınar, E. Atik	653
Kinetic study and characterization of borided AISI 4140 steel Študij kinetike in karakterizacija boriranega jekla AISI 4140 M. Keddām, M. Ortiz-Domínguez, O. A. Gómez-Vargas, A. Arenas-Flores, M. Á. Flores-Rentería, M. Elias-Espinosa, A. García-Barrientos	665
Kinetics of the precipitation in austenite HSLA steels Kinetika izločanja v avstenitnih HSLA-jeklih E. Kalinowska-Ozgowicz, R. Kuziak, W. Ozgowicz, K. Lenik	673
Combined influence of V and Cr on the AISi10MgMn alloy with a high Fe level Vzajemni vpliv V in Cr na zlitino AISi10MgMn z visoko vsebnostjo Fe D. Bolibruchová, M. Žihalová	681
Effects of different stirrer-pin forms on the joining quality obtained with friction-stir welding Vpliv različnih oblik vrtilnih konic na kvaliteto spoja pri tornem vrtilnem varjenju H. Basak, K. Kaptan	693
Microstructure evolution of advanced high-strength TRIP-aided bainitic steel Razvoj mikrostrukture naprednega visokotrdnostnega bainitnega jekla z uporabo TRIP A. Grajcar	715
Effect of electric current on the production of NiTi intermetallics via electric-current-activated sintering Vpliv električnega toka pri izdelavi intermetalne zlitine NiTi s sintranjem, aktiviranim z električnim tokom T. Yener, S. Siddique, F. Walther, S. Zeytin	721
Control of soft reduction of continuous slab casting with a thermal model Kontrola mehke redukcije pri kontinuirnem litju slabov s termičnim modelom J. Stetina, P. Ramik, J. Katolicky	725

Production of shaped semi-products from AHS steels by internal pressure Izdelava polproizvodov iz AHS-jekel, oblikovanih z notranjim tlakom I. Vorel, H. Jirková, B. Mašek, P. Kurka	739
Diffusion kinetics and characterization of borided AISI H10 steel Kinetika difuzije in karakterizacija boriranega jekla AISI H10 I. Gunes, M. Ozcatal	759
Application of the Taguchi method to optimize the cutting conditions in hard turning of a ring bore Uporaba Taguchi-jeve metode za optimizacijo trdega struženja roba izvrtine M. Boy, I. Ciftci, M. Gunay, F. Ozhan	765
Thermal fatigue of single-crystal superalloys: experiments, crack-initiation and crack-propagation criteria Toplotno utrujanje monokristalnih superzlitin: preizkusi, merila za nastanek in napredovanje razpoke L. Getsov, A. Semenov, S. Semenov, A. Rybnikov, E. Tikhomirova	773
Investigating the effects of cutting parameters on the built-up-layer and built-up-edge formation during the machining of AISI 310 austenitic stainless steels Preiskava vplivov parametrov rezanja na nastanek nakopičene plasti in nakopičenega roba med struženjem avstenitnega nerjavnega jekla AISI 310 M. B. Bilgin	779
Determination of the critical fraction of solid during the solidification of a PM-cast aluminium alloy Določanje kritičnega deleža strjene faze med strjevanjem v PM ulite aluminijeve zlitine R. Kayikci, M. Colak, S. Sirin, E. Kocaman, N. Akar	797
Microstructural evolution of Inconel 625 during hot rolling Mikrostrukturni razvoj Inconela 625 med vročim valjanjem F. Tehovnik, J. Burja, B. Podgornik, M. Godec, F. Vode	801
Thermophysical properties and microstructure of magnesium alloys of the Mg-Al type Termofizikalne lastnosti in mikrostruktura magnezijevih zlitin tipa Mg-Al P. Lichý, J. Beňo, I. Kroupová, I. Vasková	807
Effect of process parameters on the microstructure and mechanical properties of friction-welded joints of AISI 1040/AISI 304L steels Vpliv procesnih parametrov na mikrostrukturo in mehanske lastnosti torno varjenih spojev jekel AISI 1040/AISI 304L İ. Kirik, N. Özdemir	825
Influence of inoculation methods and the amount of an added inoculant on the mechanical properties of ductile iron Vpliv metod modifikacije in količine dodanega modifikatorja na mehanske lastnosti duktilnega železa H. Avdušinović, A. Gigović-Gekić, D. Čubela, R. Sunulahpašić, N. Mujezinović	833
Modeling of occurrence of surface defects of C45 steel with genetic programming Modeliranje pojava površinskih napak pri jeklu C45 z genetskim programiranjem M. Kovačič, R. Jager	857
Effects of various helically angled grinding wheels on the surface roughness and roundness in grinding cylindrical surfaces Vpliv različnih kotov vijačnice pri brusilnih kolutih na hrapavost površine in okroglost pri brušenju valjastih površin M. Gavas, M. Kına, U. Köklü	865
Characterization of cast-iron gradient castings Karakterizacija litoželeznega gradientnega ulitka D. Mitrović, P. Mrvar, M. Petrič	871
Comparative mechanical and corrosion studies on magnesium, zinc and iron alloys as biodegradable metals Primerjalna študija mehanskih in korozijskih lastnosti biorazgradljivih zlitin magnezija, cinka in železa D. Vojtěch, J. Kubásek, J. Čapek, I. Pospíšilová	877
Effect of thermomechanical treatment on the corrosion behaviour of Si- and Al-containing high-Mn austenitic steel with Nb and Ti micro-additions Vpliv termomehanske obdelave na korozijsko vedenje manganskega avstenitnega jekla z vsebnostjo Si in Al, mikrolegiranega z Nb in Ti A. Grajcar, A. Plachcińska, S. Topolska, M. Kciuk	889
Study on the magnetization-reversal behavior of annealed Sm-Fe-Co-Si-Cu ribbons Študij vedenja pri obratu magnetizacije žarjenih trakov Sm-Fe-Co-Si-Cu M. Došpial, S. Garus, M. Nabialek	919
Evaluation of the chitosan-coating effectiveness on a dental titanium alloy in terms of microbial and fibroblastic attachment and the effect of aging Ocena učinkovitosti nanosa hitozana na oprijemanje mikrobov in fibroblastov na dentalni titanovi zlitini ter na pojav staranja U. T. Kalyoncuoglu, B. Yilmaz, S. Gungor, Z. Evis, P. Uyar, G. Akca, G. Kansu	925
Structure and properties of the carburised surface layer on 35CrSiMn5-5-4 steel after nanostructurization treatment Struktura in lastnosti naogljíčene površine jekla 35CrSiMn5-5-4 po nanostrukturni obdelavi E. Skolek, K. Wasiak, W. A. Świątnicki	933
Materiali in tehnologije / Materials and technology 49 (2015) 6, 995–1018	1013

Optimization of the surface roughness by applying the Taguchi technique for the turning of stainless steel under cooling conditions	
Uporaba Taguchi-jeve metode za optimiranje hrapavosti površine pri struženju nerjavnega jekla z ohlajanjem	
M. Sarıkaya	941
Effect of cryogenic treatment applied to M42 HSS drills on the machinability of Ti-6Al-4V alloy	
Vpliv podhlajevanja svedrov M42 HSS na obdelovalnost zlitine Ti-6Al-4V	
T. Kırık, U. Şeker	949
Stability of close-cell Al foams depending on the usage of different foaming agents	
Stabilnost aluminijevih pen z zaprtjo poroznostjo glede na uporabo različnih penilnih sredstev	
I. Paulin	983
Evolution of the microstructure and magnetic properties of a cobalt-silicon-based alloy in the early stages of mechanical milling	
Razvoj mikrostrukture in magnetnih lastnosti zlitine Co-Si v začetnem stadiju mehanskega legiranja	
W. Rattanasakulthong, C. Sirisathitkul, P. F. Rogl	989
Anorganski materiali – Inorganic materials	
Water-soluble cores – verifying development trends	
Jedra, topna v vodi – preverjanje smeri razvoja	
E. Adámková, P. Jelínek, J. Beňo, F. Mikšovský	61
Hydroxyapatite coatings on Cp-Titanium Grade-2 surfaces prepared with plasma spraying	
Nanos hidroksiapatita na površino Cp-Titana Grade-2 z nabrizgavanjem s plazmo	
R. Rudolf, D. Stamenković, Z. Aleksić, M. Jenko, I. Đorđević, A. Todorović, V. Jokanović, K. T. Raić	81
Dry-cutting options with a chainsaw at the Hotavlje I natural-stone quarry	
Možnosti suhega rezanja z verižno žago v kamnolomu naravnega kamna Hotavlje I.	
J. Kortnik, B. Markoli	103
Thin tin monosulfide films deposited with the HVE method for photovoltaic applications	
Tanka plast HVE kositrovega monosulfida za uporabo v fotovoltaiki	
N. Revathi, S. Bereznev, J. Lehner, R. Traksmaa, M. Safonova, E. Mellikov, O. Volobujeva	149
Comparison of refractory coatings based on talc, cordierite, zircon and mullite fillers for lost-foam casting	
Primerjava ognjevdzdržnih premazov na osnovi smucka, kordierita, cirkona in mulitnih polnil za ulivanje v forme z izparljivim modelom	
Z. Aćimović-Pavlović, A. Terzić, Lj. Andrić, M. Pavlović	157
TEM replica of a fluoride-miserite glass-ceramic glaze microstructure	
TEM-replike mikrostrukture steklokeramične fluor-mizeritne glazure	
J. Ma. Rincón, R. Casasola	229
Microwave-assisted hydrothermal synthesis of Ag/ZnO sub-microparticles	
Hidrotermična sinteza podmikrometrskih delcev Ag/ZnO z mikrovalovi	
L. Münster, P. Bažant, M. Machovský, I. Kuřitka	281
Mineralogical and geochemical characterization of roman slag from the archaeological site near Mošnje (Slovenia)	
Mineraloška in geokemična karakterizacija rimske žlindre z arheološkega najdišča pri Mošnjah (Slovenija)	
S. Kramar, J. Lux, H. Pristacz, B. Mirtič, N. Rogan - Šmuc	343
Erosive wear resistance of silicon carbide-cordierite ceramics: influence of the cordierite content	
Odpornost keramike silicijev karbid-kordierit proti obrabi pri eroziji: vpliv vsebnosti kordierita	
M. Pošarac-Marković, Dj. Veljović, A. Devečerski, B. Matović, T. Volkov-Husović	365
Influence of the substrate temperature on the structural, optical and thermoelectric properties of sprayed V₂O₅ thin films	
Vpliv temperature podlage na strukturne, optične in termoelektrične lastnosti napršene tanke plasti V ₂ O ₅	
Y. Vijayakumar, K. N. Reddy, A. V. Moholkar, M. V. R. Reddy	371
Preparation and dielectric properties of thermo-vaporous BaTiO₃ ceramics	
Priprava in dielektrične lastnosti termo-parno porozne keramike BaTiO ₃	
A. Kholodkova, M. Danchevskaya, N. Popova, L. Pavlyukova, A. Fionov	447
Spectroscopic and porosimetric analyses of Roman pottery from an archaeological site near Mošnje, Slovenia	
Spektroskopske in porozimetrične preiskave rimske lončenine z arheološkega najdišča pri Mošnjah, Slovenija	
S. Kramar, J. Lux	503
Effect of the by-pass cement-kiln dust and fluidized-bed-combustion fly ash on the properties of fine-grained alkali-activated slag-based composites	
Vpliv prahu iz peči za cement in letečega pepela iz vrtinčaste plasti na lastnosti drobnozrnatega, z alkalijami aktiviranega kompozita na osnovi žlindre	
V. Břílek Jr., L. Pařízek, L. Kalina	549

Preparation of porous ceramic materials based on CaZrO₃ Priprava porozne keramike na osnovi CaZrO ₃ E. Śnieżek, J. Szczerba, I. Jastrzębska, E. Kleczyk, Z. Pędzich	573
Quality of the structure of ash bodies based on different types of ash Kvaliteta strukture telesa iz pepela na osnovi različnih vrst pepela V. Cerny	601
Sintered board materials based on recycled glass Sintrani ploščati materiali na osnovi recikliranega stekla T. Melichar, J. Bydžovský	607
Development of composite salt cores for foundry applications Razvoj kompozitnih slanih jeder za uporabo v livarstvu J. Beňo, E. Adámková, F. Mikšovský, P. Jelínek	619
Use of micromachining to shape the structure and electrical properties of the front electrode of a silicon solar cell Uporaba mikroobdelovanja za oblikovanje strukture in električnih lastnosti prednje elektrode silicijeve sončne celice M. Muszyfaga-Staszuk	629
Assessment of the impact-echo method for monitoring the long-standing frost resistance of ceramic tiles Ocena metode impact-echo za kontrolo dolgotrajne odpornosti keramičnih ploščic proti zmrzali M. Matysik, I. Plskova, Z. Chobola	639
A reliable approach to a rapid calculation of the grain size of polycrystalline thin films after excimer laser crystallization Zanesljiv način hitrega izračuna velikosti zrn v polikristalni tanki plasti po UV-laserski kristalizaciji C. C. Kuo	687
Effect of the aggregate type on the properties of alkali-activated slag subjected to high temperatures Vpliv vrste agregata na lastnosti z alkalijo aktivirane žlindre, izpostavljene visokim temperaturam P. Rovnaník, Á. Dufka	709
Optimization of operating conditions in a laboratory SOFC testing device Optimizacija obratovalnih razmer laboratorijske gorivne celice SOFC T. Skalar, M. Lubej, M. Marinšek	731
Friction and wear behaviour of ulexite and cashew in automotive brake pads Odpornost proti trenju in obrabi avtomobilskih zavornih oblog z uleksitom in prahom iz indijskega oreha İ. Sugözü, İ. Mutlu, A. Keskin	751
Elastic behaviour of magnesia-chrome refractories at elevated temperatures Elastično vedenje ognjevdružnih gradiv magnezija-krom pri povišanih temperaturah I. Jastrzębska, J. Szczerba, J. Szlęzak, E. Śnieżek, Z. Pędzich	913
Solid-state sintering of (K_{0,5}Na_{0,5})NbO₃ synthesized from an alkali-carbonate-based low-temperature calcined powder Sintranje v trdnem keramike (K _{0,5} Na _{0,5})NbO ₃ , sintetizirane iz nizkotemperaturno kalciniranega prahu, pripravljenega na osnovi alkalijskih karbonatov M. Feizpour, T. Ebadzadeh, D. Jenko	975
Polimeri – Polymers	
Antibacterial composite based on nanostructured ZnO mesoscale particles and a poly(vinyl chloride) matrix Protibakterijski kompozit na osnovi nanostrukturiranih delcev ZnO in osnove iz polivinil klorida J. Sedlák, P. Bažant, J. Klofáč, M. Pastorek, I. Kuřitka	55
Micromechanical model of the constituents of a unidirectional fiber-reinforced composite and its response to the tensile cyclic loading Mikromehanski model nadomestkov kompozitov, ojačanih z enosmernimi vlakni, in njihov odgovor na ciklično natezno obremenjevanje T. Kroupa, H. Srbová, R. Zemčík	99
New solid-polymer-electrolyte material for dye-sensitized solar cells Novi elektrolitni material na osnovi trdnega polimera za sončne celice, občutljive za svetlobo V. K. Singh, B. Bhattacharya, S. Shukla, P. K. Singh	123
Design of a wideband planar antenna on an epoxy-resin-reinforced woven-glass material Širokopasovna ploskovna antena na epoksi smoli, ojačani s steklenimi vlakni R. Azim, M. T. Islam	193
Predicting the physical properties of drawn Nylon-6 fibers using an artificial-neural-network model Napovedovanje fizikalnih lastnosti vlečenih vlaken iz najlona 6 z uporabo modela umetne nevronske mreže R. Semnani Rahbar, M. Vadood	325
Monitoring of polyurethane dispersions after the synthesis Spremljanje poliuretanskih disperzij po sintezi M. Oceppek, J. Zabret, J. Kecelj, P. Venturini, J. Golob	495
Materiali in tehnologije / Materials and technology 49 (2015) 6, 995–1018	1015

Composite-material printed antenna for a multi-standard wireless application

Tiskana antena iz kompozitnega materiala za večstandardno brezžično uporabo
T. Alam, M. R. I. Faruque, M. T. Islam, N. Misran 745

Flame resistance and mechanical properties of composites based on new advanced resin system FR4/12

Negorljivost in mehanske lastnosti kompozitov na osnovi novih naprednih sistemov smol FR4/12
V. Rusnák, S. Rusnáková, L. Fojtl, M. Žaludek, A. Čapka 821

Load-capacity prediction for the carbon- or glass-fibre-reinforced plastic part of a wrapped pin joint

Napoved nosilnosti plastičnih delov zatičnega spoja, ojačanega z ogljikovimi ali steklastimi vlakni
J. Krystek, R. Kottner 957

Nanomateriali in nanotehnologije – Nanomaterials and nanotechnology**Synthesis of NiTi/Ni-TiO₂ composite nanoparticles via ultrasonic spray pyrolysis**

Sinteza kompozitnih nanodelcev NiTi/Ni-TiO₂ z ultrazvočno razpršilno pirolizo
P. Majerič, R. Rudolf, I. Anžel, J. Bogović, S. Stopić, B. Friedrich 75

Heat-transfer characteristics of a non-Newtonian Au nanofluid in a cubical enclosure with differentially heated side walls

Značilnosti prenosa toplote nenewtonske Au nanotekočine v kockastem ohišju z različno gretima stranskima stenama
P. Ternik, R. Rudolf, Z. Žunič 87

Characterization of TiO₂ nanoparticles with high-resolution FEG scanning electron microscopy

Karakterizacija nanodelcev TiO₂ z visokoločljivostno FEG vrstično elektronsko mikroskopijo
Z. Samardžija, D. Lapornik, K. Gradišek, D. Verhovšek, M. Čeh 173

The stabilization of nano silver on polyester filament for a machine-made carpet

Stabilizacija nanodelcev srebra na poliestrskem vlaknu za strojno izdelavo preprog
K. M. Shojaei, A. Farrahi, H. Farrahi, A. Farrahi 461

Mechanical and wetting properties of nanosilica/epoxy-coated stainless steel

Mehanske in površinske lastnosti premaza iz silicijevih nanodelcev in epoksidne smole na nerjavnem jeklu
M. Conradi, G. Intihar, M. Zorko 613

Fabrication of TiO₂ nanotubes for bioapplications

Izdelava TiO₂-nanocevk za biomedicinsko uporabo
M. Kulkarni, K. Mrak-Poljšak, A. Flašker, A. Mazare, P. Schmuki, A. Kos, S. Čučnik, S. Sodin-Šemrl, A. Igljič 635

Au-nanoparticle synthesis via ultrasonic spray pyrolysis with a separate evaporation zone

Sinteza nanodelcev zlata z ultrazvočno razpršilno pirolizo z ločeno cono izhlapevanja
P. Majerič, B. Friedrich, R. Rudolf 791

One-step green synthesis of graphene/ZnO nanocomposites for non-enzymatic hydrogen peroxide sensing

Enostopenjska zelena sinteza nanokompozita grafen-ZnO za neencimatsko detekcijo vodikovega peroksida
S. S. Low, M. T. T. Tan, P. S. Khiew, H. S. Loh, W. S. Chiu 837

Gradbeni materiali – Materials in civil engineering**The effect of a superplasticizer admixture on the mechanical fracture parameters of concrete**

Vpliv dodatka superplastifikatorja na parametre mehanskega zloma betona
H. Šimonová, I. Havlíková, P. Daněk, Z. Keršner, T. Vymazal 417

Evaluation of the thermal resistance of selected bentonite binders

Ocena toplotne upornosti izbranih bentonitnih veziv
J. Beňo, J. Vontorová, V. Matějka, K. Gál 465

Modified cement-based mortars: crack initiation and volume changes

Modificirane malte na osnovi cementa: iniciacija razpok in volumenske spremembe
I. Havlíková, V. Bilek Jr., L. Topolar, H. Simonova, P. Schmid, Z. Kersner 557

Fracture properties of plain and steel-polypropylene-fiber-reinforced high-performance concrete

Lastnosti loma navadnega in visokozmogljivega betona, ojačanega s polipropilenskimi vlakni
P. Smarzewski, D. Barnat-Hunek 563

Application of computed tomography in comparison with the standardized methods for determining the permeability of cement-composite structures

Uporaba računalniške tomografije v primerjavi s standardiziranimi metodami določanja prepustnosti cementnih kompozitnih struktur
T. Komárková, M. Králíková, P. Kovács, D. Kocáb, T. Stavař 587

Monitoring early-age concrete with the acoustic-emission method and determining the change in the electrical properties

Pregled svežega betona z metodo akustične emisije in določanjem sprememb električnih lastnosti
L. Pazdera, L. Topolar, M. Korenska, T. Vymazal, J. Smutny, V. Bilek 703

Mortar-type identification for the purpose of reconstructing fragmented Roman wall paintings (Celje, Slovenia) Analiza ometov za rekonstrukcijo fragmentov rimskih stenskih poslikav (Celje, Slovenija) M. Gutman, M. Lesar Kikelj, J. Kuret, S. Kramar	785
Micro-encapsulated phase-change materials for latent-heat storage: thermal characteristics Mikroenkapsulirani materiali s fazno premeno za shranjevanje latentne toplote: toplotne značilnosti M. Ostrý, D. Dostálová, T. Klubal, R. Příkryl, P. Charvát.	813
Ceramic masonry units intended for the masonry resistant to high humidity Keramični gradbeni elementi, namenjeni za zgradbe, odporne proti visoki vlagi J. Zach, V. Novák, J. Hroudová, M. Sedlmajer	817
Problems and normative evaluation of bond-strength tests for coated reinforcement and concrete Problemi in normativna ocena preizkusov trdnosti vezi med armaturo s prekritjem in betonom P. Pokorný, M. Kouřil, J. Stoužil, P. Bouška, P. Simon, P. Juránek	847
Microstructural changes of fine-grained concrete exposed to a sulfate attack Mikrostrukturne spremembe drobnozrnatega betona, izpostavljenega sulfatu M. Vyšvařil, P. Bayer, M. Rovnaníková.	883
Surface free energy of hydrophobic coatings of hybrid-fiber-reinforced high-performance concrete Prosta energija površine hidrofobnih premazov na visokozmogljivem betonu, ojačanem s hibridnimi vlakni D. Barnat-Hunek, P. Smarzewski	895
Numerične metode – Numerical methods	
Mathematical modelling and physical simulation of the hot plastic deformation and recrystallization of steel with micro-additives Matematično modeliranje in fizikalna simulacija vroče plastične predelave in rekristalizacije jekla z mikrododatki E. Kalinowska-Ozgowicz, W. Wajda, W. Ozgowicz	69
Effective preparation of non-linear material models using a programmed optimization script for a numerical simulation of sheet-metal processing Učinkovita priprava nelinearnih modelov materiala s programiranim optimizacijskim zapisom za numerično simulacijo obdelave pločevine M. Urbánek, F. Tikal	291
Using simulated spectra to test the efficiency of spectral processing software in reducing the noise in Auger electron spectra Uporaba simuliranega spektra za preizkus učinkovitosti programske opreme predelave spektra pri zmanjšanju šuma spektra Augerjevih elektronov B. Poniku, I. Belič, M. Jenko	435
Development of numerical models for the heat-treatment-process optimisation in a closed-die forging production Razvoj numeričnih modelov za optimizacijo postopka toplotne obdelave pri proizvodnji odkovkov v zaprtih utopnih orodjih L. Maleček, M. Fedorko, F. Vančura, H. Jirková, B. Mašek	471
Non-linear finite-element simulations of the tensile tests of textile composites Nelinearna simulacija nateznih preizkusov tekstilnih kompozitov s končnimi elementi T. Kroupa, K. Kunc, R. Zemčík, T. Mandys	509
Material parameters for a numerical simulation of a compaction process for sintered double-height gears Materialni parametri za numerično simulacijo postopka stiskanja sintranih dvovišinskih zobnikov T. Verlak, M. Šori, S. Glodež	841
Developing continuous-casting-process control based on advanced mathematical modelling Uporaba naprednega matematičnega modeliranja za razvoj kontrole postopka kontinuirnega ulivanja J. Falkus, K. Miłkowska-Piszczek	903
A meshless model of electromagnetic braking for the continuous casting of steel Brezmrežni model elektromagnetnega zaviranja pri kontinuirnem ulivanju jekla K. Mramor, R. Vertnik, B. Šarler	961
Non-singular method of fundamental solutions for three-dimensional isotropic elasticity problems with displacement boundary conditions Nesingularna metoda fundamentalnih rešitev za deformacijo tridimenzijskih elastičnih problemov z deformacijskimi robnimi pogoji Q. Liu, B. Šarler	969
Editor's Preface – Predgovor urednika	
Editor's Preface / Predgovor urednika M. Torkar	181
In Memoriam	
Alojz Prešern, dipl. inž. metalurgije (1920–2015)	477
Prof. dr. Milan Trbižan	993
Materiali in tehnologije / Materials and technology 49 (2015) 6, 995–1018	1017

Letno kazalo – Index	
Letnik 49 (2015), 1–6 – Volume 49 (2015), 1–6	995